

Advances of Smoothed Particle Hydrodynamics: the Proceedings of the 2017 SPHERIC Beijing International Workshop

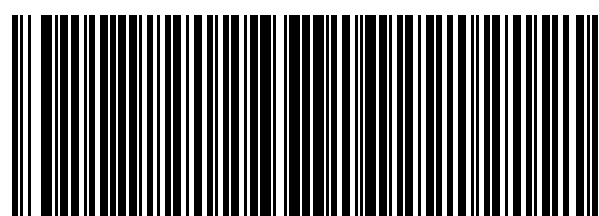
Introduction:

Smoothed particle hydrodynamics (SPH) is a most popular mesh-free particle method in the broad area of computational engineering sciences. The SPHERIC workshops are the only worldwide events which exclusively focus on the SPH methodology and related simulation approaches. **The 2017 SPHERIC Beijing International Workshop** (or SPHERIC Beijing 2017) is the first time that the SPHERIC Workshop is held in Asia.

This proceedings contains 43 papers presented at the SPHERIC Beijing 2017, and shows the latest development of SPH, ranging from computational modelling using SPH, theoretical and numerical aspects of SPH, numerics, alternative formulation and particle-based simulation techniques, and diversified applications.

Sponsor organizations:

- National Natural Science Foundation of China (NSFC)
- Chinese Society of Theoretical and Applied Mechanics (CSTAM)
- College of Engineering, Peking University
- Institute of Ocean Research, Peking University
- BIC-ESAT, Peking University
- State Key Laboratory of Turbulence and Complex System, PKU



978-1-946018-02-1



Advances of Smoothed Particle Hydrodynamics: the Proceedings of the 2017 SPHERIC Beijing International Workshop

Peking University, Beijing, China, 2017

中国
北京



Advances of

Smoothed Particle Hydrodynamics:

the Proceedings of the 2017 SPHERIC Beijing International Workshop

Editors

- Moubin Liu**
- Can Huang**



ScienTech Publisher



Advances of Smoothed Particle Hydrodynamics:

the Proceedings of the 2017 SPHERIC Beijing International Workshop

Editors

Moubin Liu
Peking University

Can Huang
Zhejiang University

ScienTech Publisher

**Advances of Smoothed Particle Hydrodynamics: the Proceedings of the 2017
SPHERIC Beijing International Workshop**

Edited by M. B. Liu, C. Huang

Published by ScienTech Publisher, USA, 2017

PO Box 891, Mason, OH 45040, USA

Website at <http://www.sci-en-tech.com/>

International Standard Book Number:

ISBN-13: 978-1-946018-02-1 (online)

ISBN-10: 1-946018-02-3 (online)

No claim to original U.S. Government works



This book contains information obtained from authentic and highly regarded sources. The editors and publishers cannot assume responsibility for the validity of all materials or the consequences of their usage.

No part of this book may be copied, reprinted, reproduced, transmitted, or shared utilization in any form by any electronic, photocopying, mechanical, microfilming, recording or other means, or in any information storage or retrieval system, without written permission from the publishers or from the corresponding authors. For permission to use material electronically or other means from this work, please contact the publisher or the corresponding authors.

Acknowledgement

SPHERIC Beijing 2017 has been supported by

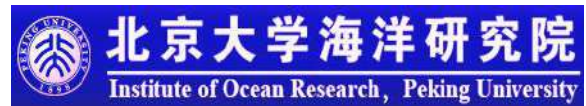
National Natural Science Foundation of China
(NSFC)



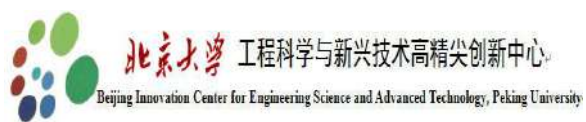
Chinese Society of Theoretical and Applied Mechanics (CSTAM)



Institute of Ocean Research, Peking University



Beijing Innovation Centre for Engineering Science and Advanced Technology (BIC-ESAT), Peking University



State Key Laboratory for Turbulence and Complex Systems, Peking University



SPHERIC Workshops

Smoothed Particle Hydrodynamics (SPH) is a Lagrangian, meshfree and particle method. It has recently gained enhanced attention in the area of scientific computing. Exemplary applications refer to the development of galaxies in astrophysics, environmental engineering, applied solid mechanics, marine and coastal engineering, nuclear power engineering, and medical engineering or geotechnical problems.

The **SPH European Research Interest Community** (SPHERIC) was founded in 2005 as a Special Interest Group of the ERCOFTAC community and aims at encouraging and facilitating the spread of the SPH method throughout Europe and the wider international community. Since that time, the SPHERIC community continues both to grow and to play an important role in helping the development of SPH for academia, industry and government organizations. The successful concept of SPHERIC is due to a methodological focus in an interdisciplinary application environment, integrating the know-how of physicists, mathematicians, IT experts and engineers from academia and industry.

Scientific Committee

- Prof. David Le Touz é(Ecole Centrale de Nantes, France)
- Dr. Damien Violeau (Electricité de France, France)
- Dr. Nathan Quinlan (National Univ. of Ireland, Ireland)
- Dr. Ben Rogers (University of Manchester, UK)
- Prof. Stefano Sibilla (University of Pavia, Italy)
- Dr. Jean-Christophe Marongiu (ANDRITZ Hydro, France)
- Dr. Alex Crespo (Universidade de Vigo, Spain)
- Dr. Andrea Colagrossi (INSEAN, Italy)
- Dr. Xiangyu Hu (Technical University of Munich, Germany)
- Prof. Rade Vignjevic (Brunel University of London, UK)
- Prof. Thomas Rung (Technical University of Hamburg-Harburg, Germany)
- Dr. Antonio Souto-Iglesias (Technical University of Madrid, Spain)
- Dr. Renato Vacondio (University of Parma, Italy)
- Dr. Matthieu De Leffe (Nextflow Software, France)
- Prof. Moncho Gómez-Gesteira (Universidade de Vigo, Spain)
- Dr. Abbas Khayyer (University of Kyoto, Japan)
- Prof. Walter Dehnen (University of Leicester, UK)
- Dr. Raj Das (University of Auckland, New Zealand)
- Prof. Robert A. Dalrymple (Johns Hopkins University , USA)
- Prof. Alexis Hérault (Conservatoire National des Arts et Métiers, France)
- Prof. Joe Monaghan (Monash University, Australia)
- Prof. Peter Eberhard (University of Stuttgart, Germany)
- Prof. Moubin Liu (Peking University, China)
- Dr Mehmet Yildiz (Sabanci University, Turkey)

Organizing Committee

Chair

- Prof. M. B. Liu, Peking University

Co-Chairs

- Prof. H. F. Qiang, Xi'an Hi-Tech Institute, China
- Prof. A. M. Zhang, Harbin Engineering University, China
- Prof. L. Zou, Dalian University of Technology, China
- Prof. D. A. Hu, Hunan University, China
- Prof. F. Xu, Northwestern Polytechnical University, China
- Prof. Z. R. Li, Wenzhou University, China

Preface

SPH is a most popular mesh-free particle method in the broad area of computational engineering sciences and it is opening up the possibility of research into fields that have been beyond conventional modelling capabilities. The SPHERIC workshops are the only worldwide events which exclusively focus on the SPH methodology and related simulation approaches. **The 2017 SPHERIC Beijing International Workshop** (or SPHERIC Beijing 2017) is held at Peking University, a top university in China, during October 17-20, 2017. This is the first time that the SPHERIC Workshop is held in Asia.

The SPHERIC Beijing 2017 organization committee received abstracts from China, France, Germany, UK, Italy, Spain, Switzerland, Ireland, USA, Japan and Australia. After peer-review, 56 abstracts were selected to present in the SPHERIC Beijing 2017, while 43 of them were included in the present proceedings. The works in the proceedings range from computational modelling using SPH, theoretical and numerical aspects of SPH, numerics, alternative formulation and particle-based simulation techniques, and diversified applications. The proceedings is therefore organized into five sections.

Section I presents different computational modeling techniques using SPH. Diversified numerical models, including standard SPH, Riemann-ALE SPH, δ ALE-SPH and SPH models with turbulence, are used to compute free surface and moving boundary flows. Fluid and structure interactions are simulated by standard SPH method, ISPH-SPH coupled method and MPS-FEM coupled method. SPH or relevant particle models are also used to simulate and investigate multiple continua and multi-phase flows.

Section II contains works related to theoretical and numerical aspects of SPH. Some benchmark problems are simulated to test numerical convergence and stability of SPH or modified approaches. Several adaptive (variable resolution) technologies are investigated to reduce the computational cost while ensuring computational accuracy.

Section III introduces numerics including high-performance computing and visualization techniques with SPH. Based on CPU or GPU parallel techniques, it is feasible to resolve challenges arising from solving large-scale, highly complex, nonlinear and distorted flow applications. SPH and its improved versions are used to deal with digital image processing including scaling, rotating and repairing.

Section IV introduces alternative formulations and particle-based simulation techniques. Alternative approaches, such as Material Point Method (MPM), Finite Volume Particle Method (FVPM), Reproducing Kernel Particle Method (RKPM), Physics Evoked Cloud Method (PECM), possess

many similarities, enrich big family of meshfree, particle methods and are therefore helpful for the development of SPH.

Section V introduces diversified SPH applications in hydraulic engineering, ocean engineering, impact engineering, environmental engineering and even applications in melting process of quartz glass and root growth. These demonstrate the powerful capabilities of the SPH method, offer ample opportunities to further improvements, and extend the SPH method for more complex and practical applications in engineering and sciences.

Finally, we would like to express our gratitude to all authors and referees for their critical contributions and valuable assistance. Supports from the National Natural Science Foundation of China (NSFC), the Chinese Society of Theoretical and Applied Mechanics (CSTAM), Beijing Innovation Centre for Engineering Science and Advanced Technology (BIC-ESAT), Institute of Ocean Research and State Key Laboratory for Turbulence and Complex Systems of Peking University are highly appreciated. Special thanks are given to Miss Jing Xu for her efforts in artwork design. We also wish to thank the ScienTech Publisher, for providing us this opportunity to publish this book.

Editors

Moubin Liu
Peking University

Can Huang
Zhejiang University

Table of Contents

SECTION I – COMPUTATIONAL MODELLING USING SPH

1.1	“High speed water impacts of flat plates in different ditching configurations through a Riemann-ALE SPH model”	1
	<i>S. Marrone, A. Colagrossi, L. Chiron, M. De Leffe, D. Le Touze</i>	
1.2	“SPH numerical investigation of oscillating characteristics of hydraulic jumps at an abrupt drop”	9
	<i>D. De Padova, M. Mossa, S. Sibilla</i>	
1.3	“The δALE-SPH model: an improved δ-SPH scheme containing particle shifting and ALE formulation”	15
	<i>P. N. Sun, A. M. Zhang, A. Colagrossi, S. Marrone, M. Antuono</i>	
1.4	“An enhanced ISPH-SPH coupled method for incompressible fluid-elastic structure interactions”	23
	<i>A. Khayyer, H. Gotoh, Y. Shimizu, H. Falahaty</i>	
1.5	“SPH modeling of fluid-structure interaction”	30
	<i>L. H. Han, X. Y. Hu</i>	
1.6	“Investigation of interaction between solitary wave and horizontal plate based on MPS-FEM coupled method”	37
	<i>C. P. Rao, D. C. Wan</i>	
1.7	“Implement of the MPS-FEM coupled method for the FSI simulation of the 3-D dam-break problem”	43
	<i>Y. L. Zhang, D. C. Wan</i>	
1.8	“A new numerical method for SPH fluid-solid coupling simulation and its preliminary verification”	50
	<i>X. J. Ma, G. Maitminin, A. F. Jin</i>	
1.9	“Numerical simulation of Rayleigh-Taylor instability by multiphase MPS method”	57
	<i>X. Wen, D. C. Wan</i>	
1.10	“Modeling of single film bubble and numerical study of the Plateau structure in foam system”	63
	<i>Z. G. Sun, N. Ni, Y. J. Sun, G. Xi</i>	
1.11	“A two-phase SPH model for sediment transport in free surface flows”	71
	<i>H. B. Shi, X. P. Yu</i>	
1.12	“Numerical simulation of water-entry problems using an improved multiphase SPH method”	78
	<i>H. Cheng, F. R. Ming, A. M. Zhang</i>	
1.13	“SPH numerical simulation of lift-off by impact of sand particles on flat sand bed”	86
	<i>J. Zhao, A. F. Jin, G. Maitminin, X. J. Ma</i>	

SECTION II – THEORETICAL AND NUMERICAL ASPECTS OF SPH

2.1 “Multiphase Godunov-typed smoothed particle hydrodynamics method with approximate Riemann solvers”	92
Z. W. Cai, Z. Zong, L. Zhou, Z. Chen, C. Tiao	
2.2 “SPH energy balance during the generation and propagation of gravity waves”	100
D. D. Meringolo, Y. Liu, A. Colagrossi	
2.3 “Particle trajectory calculation in SPH”	108
J. Y. Shen, W. H. Lu, Y. X. Xing, Darcy Q. Hou, Arris S. Tijsseling	
2.4 “Adaptive particle splitting in the Finite Volume Particle Method”	115
Nathan J. Quinlan	
2.5 “The study on SPH method with space variable smoothing length and its applications to multi-phase flow”	121
W. K. Shi, Y. M. Shen , J. Q. Chen	
2.6 “A dynamic refinement strategy in SPH for simulating the water entry of an elastomer”	129
L. Wang, F. Xu, Y. Yang	
2.7 “Simulating shock waves with corrective smoothed particle method (CSPM)”	136
C. Y. Huang, J. Deng, Y. X. Xing, Darcy Q. Hou, Arris S. Tijsseling	

SECTION III – NUMERICS

3.1 “Developing an extensible, portable, scalable toolkit for massively parallel incompressible smoothed particle hydrodynamics (ISPH)”	142
X. H. Guo, Benedict D. Rogers, Steven Lind, Rebecca Fair, Peter K. Stansby	
3.2 “The simulation of three-dimensional flow by using GPU-based MPS method”	149
X. Chen, D. C. Wan	
3.3 “GPU-based SPH modeling of flood with floating bodies in urban underground spaces”	157
J. S. Wu, N. Li, W. Y. Liu, H. Zhang	
3.4 “Image processing with the SPH method”	163
C. Y. Huang, W. H. Lu, Y. X. Xing, Darcy Q. Hou, X. Cheng	

SECTION IV – ALTERNATIVE FORMULATIONS AND PARTICAL-BASED SIMULATION TECHNIQUE

4.1 “On the efficacy of augmenting SPH simulations of mixed-mode failure with the Material Point Method” .	169
Sam Raymond, Bruce Jones, R. Pramanik, Kai Pan, T. Douillet-Grellier, John Williams	
4.2 “Suppression of non-physical voids in the finite volume particle method”	177
Mohsen H. Moghimi, Nathan J. Quinlan	
4.3 “The Hermit-type reproducing kernel particle method for piezoelectric materials”	184
J. C. Ma, G. F. Wei	
4.4 “A Physics Evoked Meshfree Method”	192

Z. B. Ma, Y. Z. Zhao 1

SECTION V – SPH APPLICATIONS

5.1 “Analysis of the hydrological safety of dams using numerical tools: Iber and DualSPHysics”	199
<i>J. González-Cao, O. García-Feal, A. J. C. Crespo, J. M. Domínguez, M. Gómez-Gesteira</i>	
5.2 “Numerical simulation of water entry with improved SPH method”	206
<i>J. R. Shao, M. B. Liu</i>	
5.3 “Construction of two-dimensional SPH numerical wave tank”.....	213
<i>J. Y. Wang, F. Xu, Y. Yang</i>	
5.4 “SPH for the interaction between tsunami wave and upright cylindrical groups”	217
<i>J. J. Li, L. Tian, Y. S. Yang, L. C. Qiu, Y. Han</i>	
5.5 “Numerical and experimental investigation of two porous wave - breaking structures”.....	224
<i>W. Q. Hu, Q. Fan, J. M. Zhan, W. H. Cai</i>	
5.6 “DualSPHysics: a numerical tool to simulate real breakwaters”	228
<i>F. Zhang, S. P. Shang, Alejandro Crespo, José Domínguez, Moncho Gómez-Gesteira, Corrado Altomare, Andrea Marzocca</i>	
5.7 “Numerical simulation of green water using SPH method”	236
<i>L. J. Wen, Q. D. Feng</i>	
5.8 “Application of improved SPH solid-wall boundary model in missile water exiting”	242
<i>H. L. Zheng, H. F. Qiang, F. Z. Chen, X. Y. Sun</i>	
5.9 “Aircraft tire water spray simulation using SPH”.....	247
<i>Y. K. Hu, Y. F. Rong, D. X. Leng, F. Xu, X. Y. Gao, R. G. Cao, W. Ding, J. Lv</i>	
5.10 “Numerical simulation research on multi-floor building breaking by conical projectile with SPH methods”	251
<i>H. F. Qiang, X. Y. Sun, F. Z. Chen, H. L. Zheng, C. Shi, G. X. Zhang</i>	
5.11 “Numerical study of the mechanism of explosive/impact welding using an improved SPH method”	257
<i>Z. L. Zhang, M. B. Liu</i>	
5.12 “A SPH model of root growth”	267
<i>Matthias Mimault, Mariya Ptashnyk, Lionel X. Dupuy</i>	
5.13 “Modeling the melting process of quartz glass using SPH method”	274
<i>Z. Y. Liu, Q. L. Ma, H. S. Fang</i>	
5.14 “An elasto-plastic- μ (I) SPH model for landslide induced debris flow”	281
<i>W. T. Zhang, Y. An, Q. Q. Liu</i>	
5.15 “Overview of SPH- ALE applications for hydraulic turbines in ANDRITZ Hydro”	285
<i>M. Rentschler, J.C. Marongiu, M. Neuhäuser, E. Parkinson</i>	
Author Index.....	293

High-speed water impacts of flat plates in different ditching configurations through a Riemann-ALE SPH model

S. Marrone, A. Colagrossi
CNR-INSEAN
Marine Technology Research Institute
Rome, Italy
salvatore.marrone@cnr.it

L. Chiron, M. De Leffe
NEXTFLOW Software,
Nantes, France

D. Le Touzé
LHEEA Lab. (UMR CNRS)
École Centrale de Nantes
Nantes, France

Abstract—The violent water entry of flat plates is investigated through a Riemann-ALE SPH model. The test conditions are of interest for problems related to aircraft and helicopter emergency landing in water. Three main parameters are considered: the horizontal velocity, the approach angle (i.e. vertical to horizontal velocity ratio) and the pitch angle, α . Regarding the latter, small angles are considered in this study. As described in the theoretical work by Zhao and Faltinsen (1993), for small α a very thin, high-speed jet of water is formed, and the time-spatial gradients of the pressure field are extremely high. Further, air-entrainment can take place making even more complex the loading process of the plate. These test conditions are very challenging for numerical solvers. In the present study an enhanced SPH model is firstly tested on a purely vertical impact with deadrise angle $\alpha = 4^\circ$. An in-depth validation against analytical solutions and experimental results is carried out, highlighting the several critical aspects of the numerical modelling of this kind of flow, especially when pressure peaks are to be captured. A discussion on the main difficulties when comparing to model scale experiments is also provided. Then, the more realistic case of a plate with both horizontal and vertical velocity components is discussed and compared to ditching experiments recently carried out at CNR-INSEAN. In the latter case both single and two-phase models are considered to take into account possible air-cushion effects.

I. INTRODUCTION

The problem of the high-speed water entry is classically of interest in the naval field as far as slamming loads on ships are concerned. In this context several theoretical solution have been derived for simplified conditions and a large literature of experimental data is available. Water-entry problems are also very important in the aircraft ditching, that is, the emergency landing on water. The response of the vehicle to this kind of water impact is critical in terms of safety of the passengers and certifications issued by airworthiness authorities includes the success of the airframe in ditching tests. In this context few high-fidelity numerical methods have been developed so far (examples can be found in [1], [2]).

The SPH method has already shown promising results for the simulation of violent water impacts thanks to its accuracy and easiness in following the free-surface deformations (see e.g. [3]–[5]). In the present work an in-depth study and validation of the SPH model is provided for 2D water

entries of flat panels with small deadrise angle. Both purely vertical and oblique impact velocity with high horizontal velocity component are studied (sections III and IV). These conditions are of interest for, respectively, helicopter and airplane ditching situations. To this aim the numerical outcome will be compared to experimental measurements and analytical solutions when available. The influence of the air phase is also addressed for the oblique water entry through a multiphase SPH model. In order to accurately resolve the high and localized pressure peaks developed at the impact a Riemann-based SPH solver is used within an Arbitrary Eulerian-Lagrangian (ALE) framework. The choice of the numerical parameters to be adopted, as e.g. the liquid compressibility, is critically and extensively discussed on the base of physical considerations peculiar of water-impact flows.

II. ADOPTED SPH SCHEME

In the present work Euler equations for compressible fluids are solved. Indeed, since the Reynolds number of the flow is quite high and only the impact stage is simulated (short time-range regime) viscous effects can be considered negligible. The weakly-compressible model is adopted; the fluid is, therefore, assumed to be barotropic and a classical stiffened state equation is used:

$$p(\rho) = \frac{c_0^2 \rho_0}{\gamma} \left[\left(\frac{\rho}{\rho_0} \right)^\gamma - 1 \right] + p_0, \quad (1)$$

where ρ_0 and p_0 are constant, c_0 is the speed of sound, and γ is a dimensionless parameter greater than 1 (in all of the following examples $\gamma = 7$ is used).

When considering violent free-surface flows, the proper identification of the reference velocity U_{ref} is crucial, as is discussed in the following sections. Considering the Mach number $Ma = U_{ref}/c_0$, the constraint $Ma < 0.1$ is enforced to make compressibility effects negligible. Additionally, during violent impact events (i.e., flat impacts) the acoustic pressure $p = \rho u c_0$ can be reached, and in this case the pressure peak intensity becomes proportional to $1/Ma$. On the other hand, in such a condition an incompressible constraint can induce

singularities on the pressure field (see [6] for a discussion on the difference between these two models in impact situations). This is linked to the fact that for this kind of impacts the presence of the air phase is generally crucial and the single-phase approach can lead to incorrect pressure evaluations under the incompressible/weakly-compressible hypothesis (for a deeper discussion see also [4]). Being aware of these limits of the single-phase model, the results obtained in this paper have been produced considering a possible Mach dependency.

In the present work the Riemann-based solver described in [7] is adopted. In that work the ALE formalism is used allowing for maintaining a regular particle spatial distribution and smooth pressure fields while preserving the whole scheme conservation and consistency of the classical SPH scheme. The introduction of the Riemann-based solver in the SPH scheme leads to an increased stability and robustness of the scheme with respect to the standard SPH formulation. The formalism proposed by [8], Thanks to the introduction of Riemann-solvers the fluxes between particles are upwind oriented and the resulting scheme is characterized by good stability properties. The discrete Euler equations are written as follows:

$$\left\{ \begin{array}{l} \frac{D\mathbf{r}_i}{Dt} = \mathbf{v}_{0i}, \\ \frac{D\mathbf{V}_i}{Dt} = \mathbf{V}_i \sum_j (\mathbf{v}_{0j} - \mathbf{v}_{0i}) \nabla W_{ij} \mathbf{V}_j \\ \frac{D(V_i \rho_i)}{Dt} = -V_i \sum_j 2\rho_E (\mathbf{v}_E - \mathbf{v}_0(\mathbf{r}_{ij})) \nabla W_{ij} \mathbf{V}_j \\ \frac{D(V_i \rho_i \mathbf{v}_i)}{Dt} = -V_i \sum_j 2[\rho_E \mathbf{v}_E \otimes (\mathbf{v}_E - \mathbf{v}_0(\mathbf{r}_{ij}))] \nabla W_{ij} \mathbf{V}_j \\ \quad - V_i \sum_j 2P_E \mathbf{I} \nabla W_{ij} \mathbf{V}_j + \omega_i \rho_i \mathbf{g} \end{array} \right. \quad (2)$$

where ρ_E , P_E and \mathbf{v}_E are the solutions of the Riemann problem at the interface $\mathbf{r}_{ij} = (\mathbf{r}_i + \mathbf{r}_j)/2$, between particles i and j . The particle transport velocity v_0 is obtained as the summation of the particle velocity plus a small perturbation which helps preserving a regular particle distribution (details about the adopted model can be found in [7]).

III. VERTICAL WATER ENTRY OF A FLAT PANEL

In this first section the vertical impact of a flat plate is numerically investigated and validated. Specifically, results of the 2D single-phase simulations are described and compared to the experimental data from a wet drop test performed in [9]. In that work a flat panel (panel length L equal to 64 cm) impacting with a deadrise angle of 4° and a vertical impact velocity U of 6.0 m/s is studied. Measures of pressures at several positions along the plate are taken, allowing for a detailed control of the pressure peak repeatability and for possible 3D effects.

As described in the theoretical work by [10], for these small deadrise angles a very thin, high-speed jet of water is

formed, and the time-spatial gradients of the pressure field are extremely high. This makes the test conditions very demanding for numerical solvers. From the potential flow theory by [10], the jet thickness at model scale is about 0.1 mm. It is worth noting that the theory in [10] is formulated for symmetric wedge impacts whereas in the present case the impact of a inclined single plate is considered. More details about the reference solution to be adopted are given in section III-B.

On the base of this theoretical data, the 2D simulation has been conducted using a very high spatial resolution, corresponding to a particle size $\Delta x = 15.6 \mu\text{m}$; by referring the latter to the panel length L , the ratio $L/\Delta x$ is equal to 41,000. The whole tank depth and width are, respectively, 3 m and 6 m. In order to manage such a small particle size a variable-h technique has been used. Specifically, the particle size gradually changes with a maximum magnification factor of 3,200 between the most refined region and the lowest resolution one (see figure 1). The total number of particles is about 3 million.

For small dead-rise angles water compressibility cannot be neglected when calculating the speed of the water jet U_{jet} (see e.g. [11]–[13]). In the experimental conditions the speed of sound in water is $c_0^* = 1481 \text{ m/s} \approx 247 U$, therefore the Mach number $\text{Ma} = U/c_0^*$ is about 4×10^{-3} . Under such a condition an estimate of the jet speed is $U_{jet} \sim 42U \sim 250 \text{ m/s}$. As noted in [11], this very thin, high-speed jet disintegrates at some distance from the root due to interaction with both the surrounding air and the surface of the body. In this case surface tension plays an important role on the jet evolution. This local and complex physics is not taken into account in the present numerical method but it is not supposed to play a relevant role on the pressure distribution.

A. Selection of the speed of sound for the SPH model

Before starting the SPH simulations the speed of sound needs to be specified. As mentioned in section II, the numerical Mach number usually adopted within the SPH simulations is $\text{Ma} = U/c_0 = 0.1$, which guarantees the weakly-compressible regime (i.e., compressibility plays a negligible role). Nonetheless, for this kind of impact the reference speed for the Mach

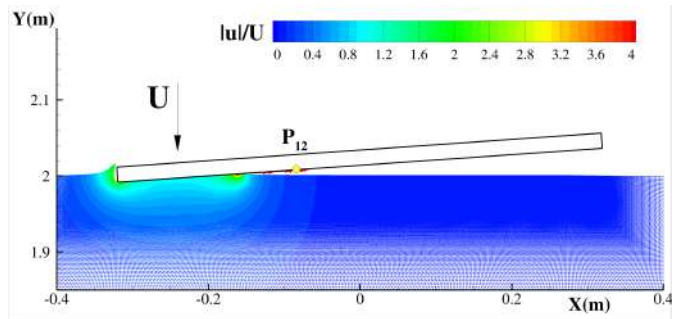


Fig. 1. Vertical impact of a flat panel. Colors are representative of the SPH velocity intensity. Pressure probe number 12, which is the gauge used for the comparison with the experimental data, is also depicted.

number can not be the impact velocity U . Indeed, considering that the intersection point between the horizontal undisturbed free-surface and the wedge surface has a speed equal to $U_{inters} = U/\sin(\alpha) \approx 14U$. According to Wagner theory the water jet formed during the impact has a speed higher than U_{inters} . Therefore, if one chooses the speed of sound using the wedge speed U , i.e., $c_0 = 10U$, the jet would not form at all, its speed being in the supersonic regime. This is a clear example where the weakly-compressible rule $\text{Ma} \leq 0.1$ needs to be enforced in a proper way, considering the specific problem at hand.

In the present case the reference speed should be the water jet speed U_{jet} which, however, is an unknown of the problem. Using the theory in [11], the estimate $U_{jet} = 40U$ can be used. Note that, using the latter constraint, the speed of sound in water would result even higher than the real one, $c_0 = 400U$ versus $c_0^* = 247U$. This means that for the adopted model scale water compressibility effects are not negligible, at least inside the jet region. However, considering that in the jet zone the pressure is close to the ambient pressure, water compressibility effects should not play a relevant role on the local impact loads.

In order to satisfy the weakly-compressible assumption, at least in the impact region, the reference velocity used is $U_{ref} = \sqrt{P_{max}/\rho}$, where P_{max} is an unknown of the problem and needs to be estimated. Then, an ex-post facto verification of the SPH simulations is required. Using the Wagner theory (which is valid for small deadrise angles as far as the air presence is negligible) the maximum pressure predicted is:

$$P_{max} = \frac{1}{2} \rho U^2 \frac{\pi^2/4}{[\tan(\alpha)]^2} \stackrel{\alpha=4^\circ}{\simeq} 252 \rho U^2 \quad (3)$$

corresponding to about 91 bar in our experiment.

The water-hammer pressure for this impact is $\rho c_0^* U = 88$ bar which is the maximum pressure level that can be physically reached in the experiments. The P_{max} predicted by potential flow theory is higher than the acoustic pressure, and this is a further indication that water compressibility cannot be neglected for this problem. Thus, considering $P_{max} \sim 80$ bar, the reference velocity is $U_{ref} = \sqrt{P_{max}/\rho} \sim 15U$ which is smaller than $U_{jet} = 40U$.

Taking this into account, a good compromise for the SPH speed of sound can be obtained by adopting a reference velocity $U_{ref} = 10U$ which implies a speed of sound $c_0 = 100U$ (i.e., Mach number $\text{Ma} = U/c_0 = 0.01$). The resulting time step is equal to $\Delta t = 1.5 \Delta x/c_0 \approx 0.04 \mu\text{s}$ which is 250 times smaller than the sampling rate of the pressure probes used in the experiments (i.e., the SPH sample frequency is 25 MHz versus the 100 kHz of the experimental pressure probes). This aspect is expected to influence the observed pressure peak which, for the considered configuration, needs a high time/space resolution to be captured. Further, in order to verify the appropriateness of such a choice, also a simulation using $c_0^* = 247U$ has been run, the results will be shown at the end of section III-B.

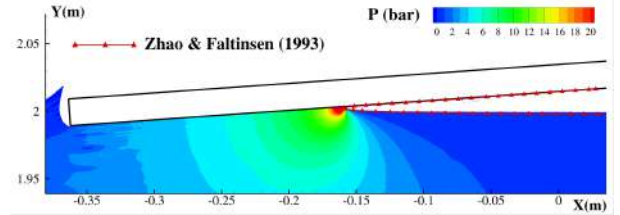


Fig. 2. Vertical impact of a flat panel: colors are representative of the SPH pressure field. Red solid line is the free surface extracted from [10].

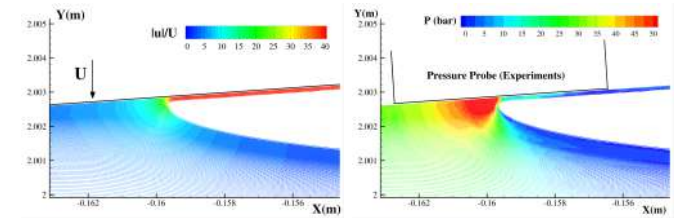


Fig. 3. Vertical impact of a flat panel: enlarged view of the impact zone. Left: contours of the velocity module. Right: contours of the SPH pressure field. The size of the pressure gauges used in the experiments is also depicted.

B. Comparison between SPH results, analytical solution and experimental data

Figure 2 shows the pressure field predicted by the SPH for the flat panel impact. In the same plot the free surface deformation evaluated by the potential flow theory by [10] is reported. Left plot of figure 3 shows an enlarged view of the flow velocity predicted by the SPH in the area of the highest pressure levels. A thin water jet is formed with a thickness of about 0.1 mm corresponding to about ten particles, thus justifying the high $L/\Delta x$ ratio needed to properly solve such a flow.

In the right plot of the same figure an enlarged view of the pressure field is shown (in this case the displayed pressure range is enlarged too). From this plot it is seen that the high-pressure region is limited to an area of 1 mm² with a pressure peak of about 60 bar. In the same figure the size of the probe used in the experiments is depicted. Clearly, the pressure sensor has a size much larger than the pressure bulb formed below the water-jet root. This aspect will be discussed in the following section.

In figure 4 the time histories of the pressure measured at probe P_{12} are shown. This probe is positioned 23.6 cm from the left-hand edge of the panel (see figure 1). The SPH solution is compared with the experiments and with the pressure peak predicted by Wagner theory. The SPH prediction is between the two reference data sets, and is characterized by high-frequency components due to the fragmented jet of water that pass over the numerical pressure probe. The latter has a dimension of 0.125 mm (which is the size of the SPH kernel support) and the SPH sampling rate is 25 MHz. Both the SPH and the analytical predictions overestimate the experimental data for which the maximum pressure recorded is 34 bar (in the SPH solution the pressure peak reaches 70 bar whereas

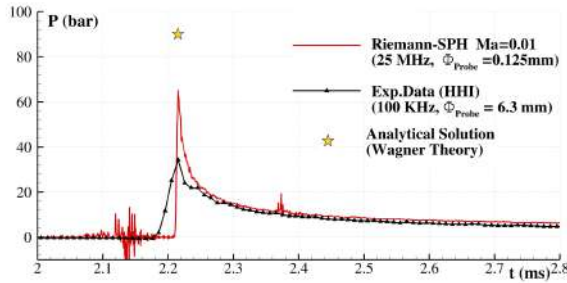


Fig. 4. Vertical impact of a flat panel: SPH pressure time histories at probe P_{12} compared with experimental data and with analytical solution Wagner theory.

the analytical prediction is 91 bar). It has to be noted that, even though the Wagner theory is referred to the case of a symmetric wedge entry, according to [14] and [15] the value of the pressure peak should be substantially the same of the case of an oblique flat panel impact (it will be shown in section III-C that this approximation can be quite rough for the present case). Conversely, regarding the entire pressure signal, it is not possible to compare to classical analytical solutions, such as in [10], since they are all formulated for the symmetric wedge entry case.

As mentioned above, air entrainment is expected to play a minor role for deadrise angles greater than 3° [10], [15]. Notwithstanding that, most of the experimental measurements available in the literature for angles close to 4° exhibit pressure peaks much smaller than the one predicted by potential theory (cf., [15]–[18]) and the values measured in the present study are in fair agreement with previous experiments by [15], [16]. As for possible 3D effects, these have been checked by comparing the pressure values on gauges aligned at the same distance from the piercing edge. For the probes positioned in the most central region no relevant differences have been observed. However, the maximum pressure impact measured in the experiment for small dead-rise angles can be also affected by:

- 1) Changes of the body velocity during the impact stage
- 2) Rotations of the body during the impact stage
- 3) Deformations of the wedge surface
- 4) Sampling rate of the pressure signals
- 5) Size of the pressure gauge

Thanks to the experimental setup adopted the first three points can be neglected, while the last two can play an important role. In order to take into account the experimental sampling rate, the SPH signal has first been filtered using a moving average filter (MAF) reducing the numerical sampling rate from 25 MHz to 100 kHz. The result is illustrated in figure 5. The reduction of the SPH peak due to this filtering procedure is not enough to get a good agreement with the experimental data.

As a further step the SPH pressure has been measured integrating on a circular area equal to the size of the experimental pressure probes and then filtered at 100 kHz.

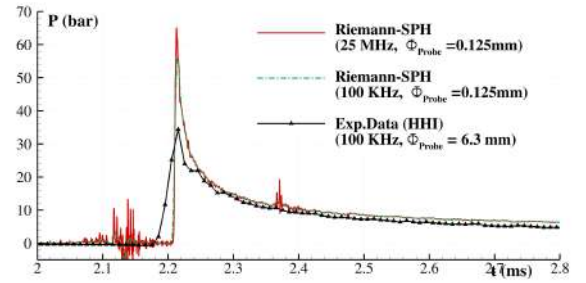


Fig. 5. Vertical impact of a flat panel: SPH pressure time histories versus experimental data. The SPH signal is filtered with a running average filters (MAF) at 100 kHz (dashed-dotted line).

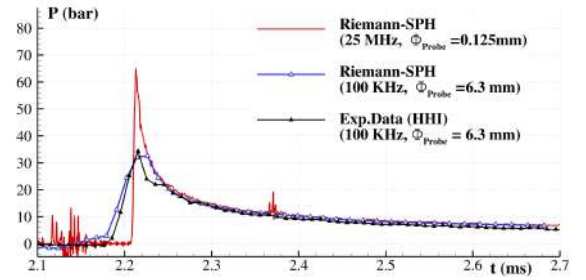


Fig. 6. Vertical impact of a flat panel: SPH pressure time histories versus experimental data. The SPH signal recorded using the size of the experimental pressure gauges and filtered at 100 kHz is also shown.

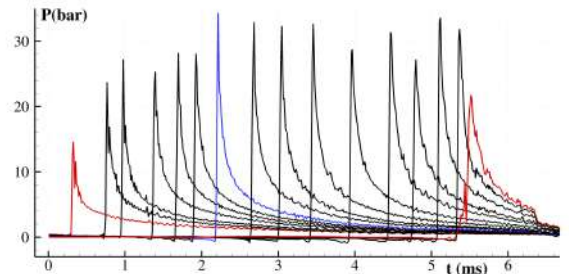


Fig. 7. Vertical impact of a flat panel: experimental data for the pressure time histories on a row of probes (not equispaced). The time history from the first and last probes on the panel impacting the water are colored in red. The time history in blue is from probe P_{12} , used in the previous figures for comparison with the SPH solution.

This result is shown in figure 6. In this case the SPH output is much closer to the pressure recorded in the experiment.

Summarizing, according to the analytical solution very narrow pressure peaks are expected for this kind of impact. Using pressure gauges with a size of few millimeters and a sampling rate of 100 kHz it is not possible to record such a localized event. Having in mind such limits, through SPH it is possible to get predictions close to the experimental data if the pressures are integrated over the experimental gauge area, even when using a speed of sound c_0 smaller than the real one c_0^* .

In figure 7 the experimental pressure time histories recorded

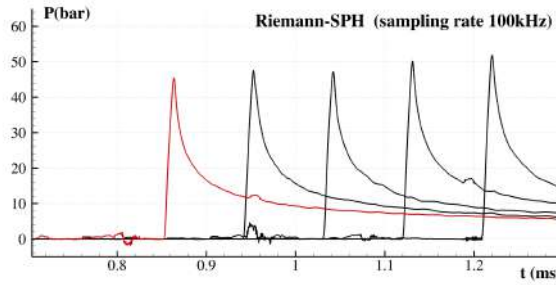


Fig. 8. Vertical impact of a flat panel: SPH pressure time histories on a row of probes. The original SPH signals have been filtered with a MAF at 100 kHz as in the experimental signals. The time history from the first probe on the panel impacting the water is colored in red.

	U_P (m/s)	$1/2\rho U_P^2$ (bar)	P_{max} (bar)	C_P
Exp.	104	54	30	0.56
SPH Ma=0.01	117	68	70	1.03
SPH Ma=0.004	119	71	75	1.06

TABLE I

AVERAGE OF THE PEAK PROPAGATION VELOCITY U_P PLOTTED IN FIG. 9. THE CORRESPONDING PRESSURE PEAK $1/2\rho U_P^2$, THE ACTUAL AVERAGE PRESSURE PEAK MEASURED AT THE PROBES P_{max} AND THE RELATED PRESSURE COEFFICIENT C_P (4) ARE ALSO REPORTED.

on a sequence of pressure probes is reported. Even if the experimental pressure peaks present some fluctuations, very similar pressure evolutions are recorded with an almost constant time shift at each probe. The SPH results show quite good repeatability of the pressure peaks along the wedge surface as well (see figure 8). In this regard, it is worth comparing the propagation velocity of the pressure peak along the plate, U_P . Indeed, in water entry flows the value of the pressure peak should correlate to U_P^2 (see e.g. [19], [20]) as:

$$C_P = \frac{P_{max}}{1/2\rho U_P^2} = 1. \quad (4)$$

In figure 9 the calculated values of U_P for both SPH and experimental results are reported for several probes. Only the probes far from the panel edges have been considered to avoid influences of either the initial impact stage or the final stage, for which the flow self-similarity is not applicable. In the same figure the values of U_P obtained from a simulation adopting the real speed of sound $c_0^* = 247U$ (Ma=0.004) are also reported. The difference between the simulation with Ma=0.01 and Ma=0.004 is very small (about 2% of the average value), confirming that within the weakly-compressible regime the Mach number effect is limited. For the sake of completeness in the same plot also the analytical value of U_P (valid for a wedge entry problem) is reported, i.e.:

$$U_P = \frac{\pi}{2} U \cot(\alpha). \quad (5)$$

In Table I The average values of U_P are reported. For the simulation at Ma=0.01 the average value of U_P is about 117 m/s corresponding to a pressure coefficient $C_P = 1.03$ which

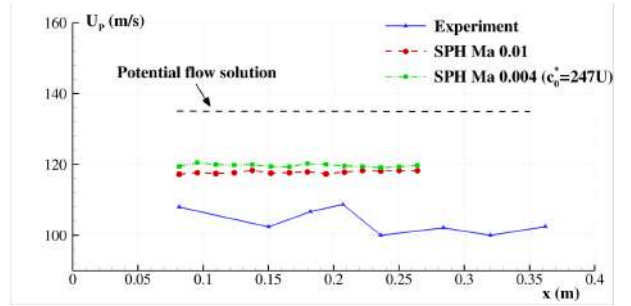


Fig. 9. Vertical impact of a flat panel: Peak propagation velocity U_P calculated on several positions along the panel for the experiment (triangles), SPH simulation at Ma=0.01 (circles) and Ma=0.004 (squares), and analytical value from potential flow theory (dashed line). The origin of the x-axis is set at the left-hand edge of the panel.

is close to the expected value (eq. 4). On the other hand, since the value of U_P predicted by the SPH is smaller than the analytical one, maximum pressure of the SPH cannot be equal to the one predicted by the Wagner theory as shown above. This difference is essentially due to the fact that Wagner theory is referred to a symmetric wedge entry, while the present case is asymmetric (see section III-C).

When considering the experimental pressure probes an average value of U_P equal to 104 m/s is obtained (with a standard deviation $\sigma = 3.1$). This propagation velocity of the pressure peak corresponds to a pressure coefficient C_P equal to 0.56. This confirms that the measurement system adopted is not able to record the real pressure peaks which are therefore underestimated as shown in this section.

C. Comparison between symmetric and asymmetric water entry

In the last subsection it has been shown that the pressure peak predicted by SPH is consistent with the water impact theory. Indeed, the calculated peak propagation velocity U_P and the pressure peak P_{max} give a pressure coefficient C_P close to unity (see eq. 4). Nonetheless, it still remains a significant discrepancy between SPH results and the analytical solution for this impact angle. In order to investigate the source of this incongruity a further simulation has been performed.

The symmetric problem has been set by retaining the initial particle configuration of the asymmetric case and closing the fluid domain at the left edge of the panel with a vertical wall

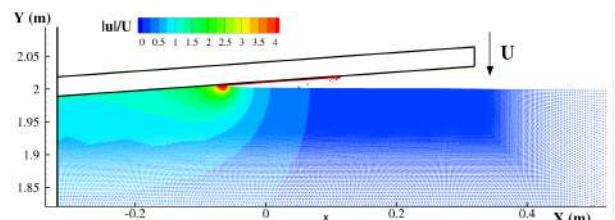


Fig. 10. Vertical impact of a flat panel: fluid domain adopted in the symmetric problem configuration. Colors refer to the module of the velocity field.

(see figure 10). The simulation has been run with $Ma=0.01$.

In figure 11 the peak propagation velocity for both symmetric and asymmetric problems are shown. It is clear that in the symmetric configuration the SPH solution is now much closer to the potential flow prediction and, because of this increase in the value of U_p , a larger pressure peak is expected on the panel surface. The recorded pressure at 0.16 m from the left-hand edge of the panel is shown in figure 12 for both symmetric and asymmetric SPH solutions.

Consistently with the observed value of U_p , the pressure peak of the symmetric solution is about 88 bar. In the same figures the analytical solutions from [21] and [10] are also reported. Evidently, the symmetric SPH solution is now much closer to the analytical prediction and the remaining difference can be mainly attributed to fluid compressibility. This is in agreement with the analytical work in [22]. In that work it is shown that, generally, asymmetric impacts induce smaller pressure peaks with respect to the symmetric case. This effect is emphasized when the deadrise angle is smaller (in [22] the smallest angle considered is 10°).

IV. WATER ENTRY WITH HIGH HORIZONTAL SPEED AT 4° PITCH ANGLE

In this section the ditching problem including a large horizontal velocity component is studied, comparing the SPH outcome to model test experiments. Given the higher complexity of the problem, in this section also possible influences of the air phase are investigated, since its role can not be a priori neglected.

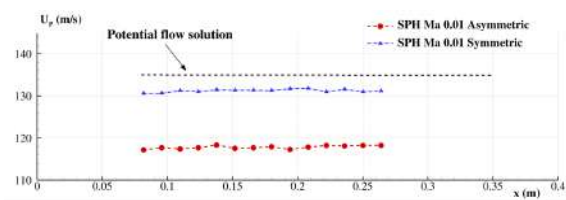


Fig. 11. Vertical impact of a flat panel: Peak propagation velocity U_p calculated on several positions along the panel for the asymmetric (circles) and symmetric (triangles) SPH simulations, and analytical value from potential flow theory (dashed line). The origin of the x-axis is set at the left-hand edge of the panel.

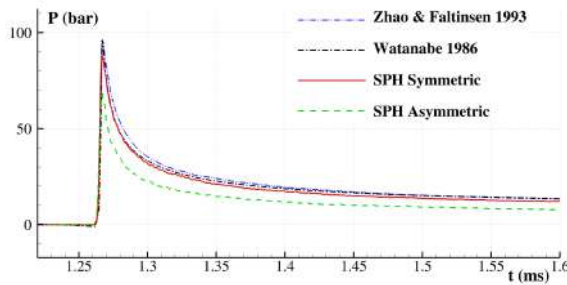


Fig. 12. Vertical impact of a flat panel: pressure time histories of symmetric (solid line) and asymmetric (dashed) solutions measured at 0.16 m from the left-hand edge of the panel. Analytical solutions by [21] (dash-dot line) and by [10] (dash-dot-dot line) are also reported.

A. Description of the experimental data

Guided ditching impact experiments [19], [23] were performed in the CNR-INSEAN towing tank, which is 470 m long, 13.5 m wide and 6.5 m deep. The dimension of the flat plate were 500 mm by 1000 mm (Fig. 13). Pressures at 18 points are measured through Kulite XTL123B pressure transducers. The sampling rate of the latter is 200 kS.s^{-1} while their dimension is 3.8 mm. The horizontal and vertical velocities at the impact are respectively 40 m.s^{-1} and -1.5 m.s^{-1} . In the experiments, these velocities are assumed to remain constant during the whole ditching impact.

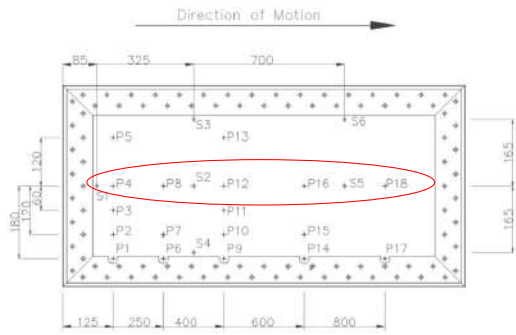


Fig. 13. Top view of the plate. Red ellipse shows pressure probes considered for 2D SPH simulations (measures are in mm).

B. Numerical methodology

In this second test case series, simulations have been conducted using Adaptive Particle Refinement (APR) technique [24]. This technique allows keeping a high spatial resolution around the flat plate during the simulation as the refinement areas move at the same speed of the plate. In order to avoid the pressure filtering described in section III, the numerical adopted pressure sensor size is the same as in the experiments (*i.e.* 3.8 mm).

For both single-phase and two-phases models, simulations were performed with a nominal sound speed $c_0^{\text{water}} = 1480 \text{ m/s}$ and a nominal density $\rho_0^{\text{water}} = 1000 \text{ kg/m}^3$ for water. For the two-phases approach, the nominal sound speed of air was $c_0^{\text{air}} = 343 \text{ m/s}$ and the nominal density was $\rho_0^{\text{air}} = 1 \text{ kg/m}^3$. More details about the two-phases model adopted can be found in [25], [26]. Comparisons with experiments are established in terms of pressure coefficient, which is defined as :

$$C_p = \frac{P}{0.5\rho_0^{\text{water}} U^2 \left[1 + \left(\frac{V}{U} \right)^2 \right]} \quad (6)$$

where U and V refer respectively to the horizontal and vertical velocities.

C. Flat panel impact : single-phase approach

The numerical tank is 20 m long and 6 m deep. Simulations involving 6 refinement levels ($\Delta x_{\min} = 1.5625 \text{ mm}$) and 8 refinement levels ($\Delta x_{\min} = 0.390625 \text{ mm}$) were performed

(Fig. 14). At initialization, the total number of particles for simulation involving 6 and 8 refinement levels are respectively about 67,000 and 110,000. Figure 15 shows the pressure coefficient field predicted by the single-phase SPH simulation in the area of the highest pressure levels. It is worth nothing that the field appears very regular despite the contour lines cross several refinement interfaces. In Figure 16, SPH pressure time histories for two different probes are compared with the experimental data from [19], [23]. The origin of the time axis is based on P4 pressure peak. A good agreement between the finest SPH solution and the experimental data is observed in terms of loading process and peak maxima. The phase shift in the pressure peak is due to the different peak propagation velocity which can be attributed in this case to 3D effects.

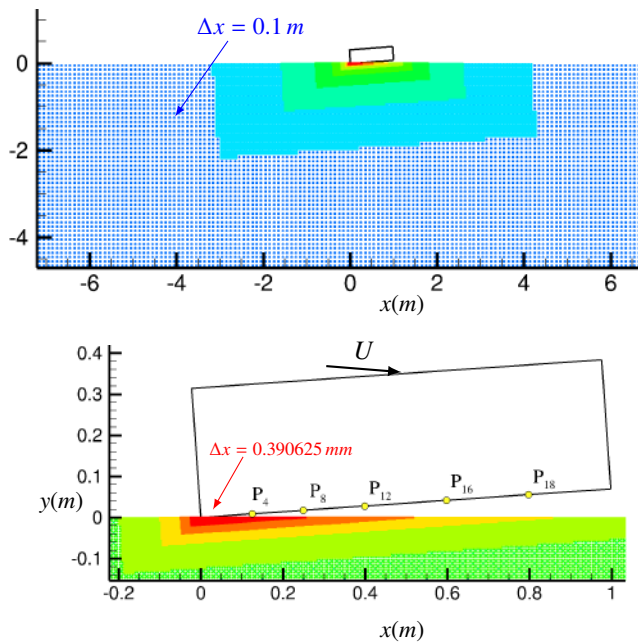


Fig. 14. Sketch of the single-phase simulation involving 8 refinement levels (top: global view, bottom: zoomed view). Colors refer to refinement depth.

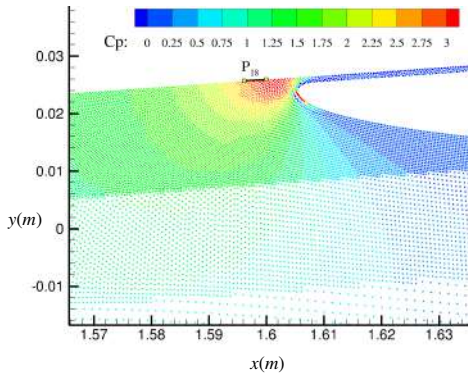


Fig. 15. Pressure coefficient field of the single-phase APR simulation involving 8 refinement levels at time $t = 0.02$ s. The size of the pressure gauge P_{18} is depicted.

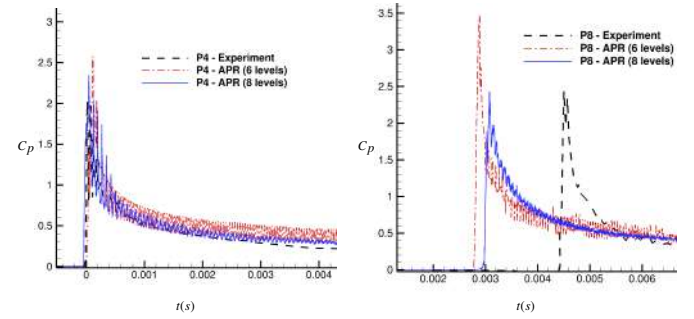


Fig. 16. Comparison between experimental data and SPH APR simulations (single-phase model): pressure time histories for probes P4 and P8.

D. Flat panel impact : two-phases approach

Simulations involving 6 refinement levels ($\Delta x_{min} = 1.5625$ mm) and 8 refinement levels ($\Delta x_{min} = 0.390625$ mm) were performed also for the two-phase simulations (Fig. 17). At initialization, the total number of particles are about 125,000 and 300,000 for the simulations involving, respectively, 6 and 8 refinement levels. In order to take into account air-cushion effects, the bottom left corner of the flat plate is located 3 mm above the interface at initial time. In Figure 19, SPH pressure time histories for two different probes are compared with the experimental data in [19], [23]. The origin of the time axis is based on the pressure peak registered at P4. Since differences between single-phase and two-phases approaches are small, one can conclude that the influence of air is negligible for this deadrise angle.

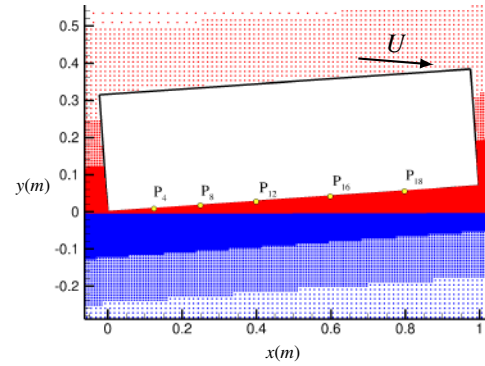


Fig. 17. Sketch of the two-phases simulation involving 8 refinement levels (top: refinement levels, bottom: phase configuration)

ACKNOWLEDGEMENTS

The research leading to these results has partially received funding from the European Union's Horizon 2020 research and innovation programme under grant agreement No 724139. The SPH simulations performed under the present research have been obtained using the SPH-Flow solver, software developed within a collaborative consortium composed of Ecole Centrale de Nantes, NextFlow Software company and CNR-INSEAN.

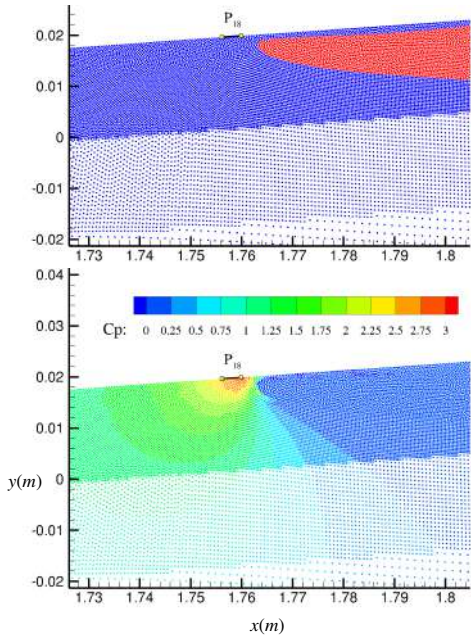


Fig. 18. Phase configuration (top) and pressure coefficient field (bottom) of the two-phases APR simulation involving 8 refinement levels at time $t = 0.024$ s. The size of the pressure gauge P_{18} is depicted.

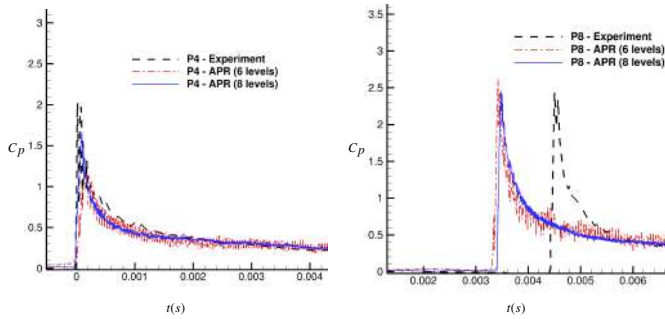


Fig. 19. Comparison between experimental data and SPH APR simulations (two-phases model): pressure time histories for 4 different probes

REFERENCES

- [1] H. Streckwall, O. Lindenau, and L. Bensch, “Aircraft ditching: a free surface/free motion problem,” *Archives of Civil and Mechanical Engineering*, vol. 7, no. 3, pp. 177–190, 2007.
- [2] B. Guo, P. Liu, Q. Qu, and J. Wang, “Effect of pitch angle on initial stage of a transport airplane ditching,” *Chinese Journal of Aeronautics*, vol. 26, no. 1, pp. 17–26, 2013.
- [3] G. Oger, M. Doring, B. Alessandrini, and P. Ferrant, “Two-dimensional SPH simulations of wedge water entries,” *J. Comp. Phys.*, vol. 213 (2), pp. 803–822, 2006.
- [4] D. Meringolo, A. Colagrossi, S. Marrone, and F. Aristodem, “On the filtering of acoustic components in weakly-compressible SPH simulations,” *Journal of Fluids and Structures*, vol. to appear, 2017.
- [5] S. Lind, P. Stansby, and B. D. Rogers, “Incompressible-compressible flows with a transient discontinuous interface using smoothed particle hydrodynamics (SPH),” *Journal of Computational Physics*, vol. 309, pp. 129–147, 2016.
- [6] S. Marrone, A. Colagrossi, A. Di Mascio, and D. Le Touzé, “Prediction of energy losses in water impacts using incompressible and weakly compressible models,” *Journal of Fluids and Structures*, vol. 54, pp. 802–822, 2015.
- [7] G. Oger, S. Marrone, D. Le Touzé, and M. De Leffe, “SPH accuracy improvement through the combination of a quasi-Lagrangian shifting transport velocity and consistent ALE formalisms,” *Journal of Computational Physics*, vol. 313, pp. 76–98, 2016.
- [8] J. Vila, “On particle weighted methods and Smooth Particle Hydrodynamics,” *Mathematical Models & Methods in Applied Sciences*, vol. 9, no. 2, pp. 161–209, 1999.
- [9] S. Marrone, A. Colagrossi, J. Park, and E. Campana, “Challenges on the numerical prediction of slamming loads on LNG tank insulation panels,” *Ocean Engineering*, vol. 141, pp. 512–530, 2017.
- [10] R. Zhao and O. M. Faltinsen, “Water entry of two-dimensional bodies,” *Journal of Fluid Mechanics*, vol. 246, pp. 593–612, 1993.
- [11] A. A. Korobkin and A. Iafrati, “Numerical study of jet flow generated by impact on weakly compressible liquid,” *Physics of Fluids*, vol. 18, no. 3, p. 032108, 2006.
- [12] E. Campana, A. Carcaterra, E. Ciappi, and A. Iafrati, “Some insights into slamming forces: compressible and incompressible phases,” *Proceedings of the Institution of Mechanical Engineers, Part C: Journal of Mechanical Engineering Science*, vol. 214, no. 6, pp. 881–888, 2000.
- [13] A. Carcaterra and E. Ciappi, “Prediction of the compressible stage slamming force on rigid and elastic systems impacting on the water surface,” *Nonlinear Dynamics*, vol. 21, no. 2, pp. 193–220, 2000.
- [14] O. M. Faltinsen and Y. A. Semenov, “Nonlinear problem of flat-plate entry into an incompressible liquid,” *Journal of fluid mechanics*, vol. 611, p. 151, 2008.
- [15] S. Okada and Y. Sumi, “On the water impact and elastic response of a flat plate at small impact angles,” *Journal of marine science and technology*, vol. 5, no. 1, pp. 31–39, 2000.
- [16] S.-L. Chuang, “Experiments on slamming of wedge-shaped bodies,” *Journal of Ship Research*, vol. 11, no. 3, pp. 190–198, 1967.
- [17] S. Mizoguchi and K. Tanizawa, “Impact wave loads due to slamming—a review,” *Ship Technology Research*, vol. 43, no. 4, pp. 139–154, 1996.
- [18] M. Tenzer, O. e. Moctar, and T. E. Schellin, “Experimental investigation of impact loads during water entry,” *Ship Technology Research*, vol. 62, no. 1, pp. 47–59, 2015.
- [19] A. Iafrati, “Experimental investigation of the water entry of a rectangular plate at high horizontal velocity,” *Journal of Fluid Mechanics*, vol. 799, pp. 637–672, 2016.
- [20] J. Armand and R. Cointe, “Hydrodynamic impact analysis of a cylinder,” *Journal of offshore mechanics and Arctic engineering*, vol. 109, no. 3, pp. 237–243, 1987.
- [21] T. Watanabe, “Analytical expression of hydrodynamic impact pressure by matched asymptotic expansion technique,” *Trans. West-Japan Soc. Naval Arch.*, no. 71, pp. 77–85, 1986.
- [22] Y. A. Semenov and A. Iafrati, “On the nonlinear water entry problem of asymmetric wedges,” *Journal of Fluid Mechanics*, vol. 547, pp. 231–256, 2006.
- [23] A. Iafrati, S. Grizzi, M. Siemann, and L. B. Montañés, “High-speed ditching of a flat plate: Experimental data and uncertainty assessment,” *Journal of Fluids and Structures*, vol. 55, pp. 501–525, 2015.
- [24] L. Chiron, G. Oger, M. D. Leffe, and D. L. Touzé, “Improvements on Particle Refinement method with SPH,” *Proceedings of the 11th International SPHERIC workshop*, 2016.
- [25] J. Leduc, J. Marongiu, F. Leboeuf, M. Lance, and E. Parkinson, “Multiphase SPH: a new model based on acoustic Riemann solver,” in *Proc of 4th Int SPHERIC Workshop*, May 2009, pp. 8–13.
- [26] J. Leduc, F. Leboeuf, and M. Lance, “Improvement of multiphase model using preconditioned Riemann solvers,” *5th international SPHERIC workshop, Manchester*, 2010.

SPH numerical investigation of oscillating characteristics of hydraulic jumps at an abrupt drop

Diana De Padova, Michele Mossa

Department of Civil, Environmental, Building Engineering
and Chemistry
Polytechnic University of Bari
Bari, Italy
diana.depadova@poliba.it
michele.mossa@poliba.it

Stefano Sibilla

Department of Civil Engineering and Architecture
University of Pavia
Pavia, Italy
stefano.sibilla@unipv.it

Abstract—This paper shows the results of the SPH modelling of the transition from supercritical to subcritical flow at an abrupt drop based on the laboratory experiments by Mossa et al. (2003). At an abrupt drop the transition from supercritical to subcritical flow is characterised by several flow patterns depending upon the inflow and tailwater flow conditions. SPH simulations are obtained by a pseudo-compressible XSPH scheme with pressure smoothing; turbulent stresses are represented either by an algebraic mixing-length model, or by a two-equation $k-\varepsilon$ model. The numerical model is applied to analyse the occurrence of oscillatory flow conditions between two different jump types characterised by quasi-periodic oscillation, and the results are compared with experiments performed at the hydraulics laboratory of Bari Technical University. The purpose of this paper is to obtain a deeper understanding of the physical features of a flow which is in general difficult to be reproduced numerically, owing to its unstable character. In particular, relying on previous SPH analyses of vorticity-dominated flows (De Padova et al. 2016), vorticity fields, velocity, water depth and pressure spectra downstream of the jump, and velocity and pressure cross-correlations can be computed and analysed.

I. INTRODUCTION

At an abrupt drop the transition from supercritical to subcritical flow is characterised by several flow patterns depending upon the inflow and tailwater flow conditions. Figure 1 summarises well acknowledged flow patterns: (a) the A-jump, (b) the wave jump or W-jump, (c) the wave train, (d) the B-jump (or maximum plunging condition) characterised by a plunging jet mechanisms and (e) the minimum B-jump (or limited jump) with a limited hydraulic jump [1]. Some researchers pointed out the existence of oscillating phenomena [2-5]. These oscillating characteristics can be: (i) change from one type of hydraulic jump to another; (ii) horizontal

movement of the jump toe; (iii) cyclic variation of velocity components and pressure in the region close to the jump roller; (iv) formation, development and coalescence of the large-scale flow structures.

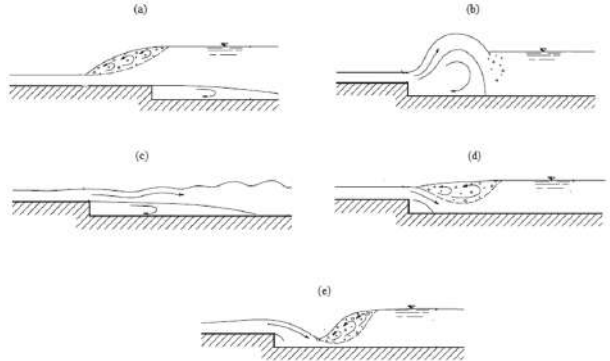


Figure 1. Flow conditions (from Ohtsu and Yasuda, 1991). From the top: (a) A-jump; (b) wave jump; (c) wave train; (d) B-jump (maximum plunging condition); (e) minimum B-jump (limited jump).

As shown by [6], specific flow conditions can lead to cyclic oscillations between jump types, resulting in the cyclic formation and evolution of jump vortices.

Meshless Lagrangian techniques appear to be particularly suitable to represent the complex and highly-unsteady free-surface patterns which characterize a hydraulic jump: a number of realizations obtained with Smoothed Particle Hydrodynamics (SPH) have shown that this method can be successfully applied to the simulation of standing waves [7-9], of hydraulic jumps [10-11] and of spilling breakers [12], being able to reproduce, both qualitatively and quantitatively, their average and time-dependent features.

The purpose of this paper is therefore to use a Weakly-Compressible SPH (WCSPH) scheme, together with a suitable turbulence model, to study the oscillating characteristics and cyclic mechanisms which can occur in a hydraulic jump at an abrupt drop in certain conditions, leading to an alternate shift of the flow pattern between the B-jump and the wave jump. The numerical results are eventually compared to the laboratory experiments by Mossa et al. [6], in order to obtain a deeper understanding of the physical features of this particular kind of unsteady flow.

II. EXPERIMENTAL SET UP

Experimental investigations were carried out in the laboratory of the Civil and Environmental Engineering Department – Water Engineering Division (hereafter referred to as SIA) of Bari Polytechnic University in a 0.40 m wide, 24.4 m long channel (with sidewalls 0.5 m height). The walls and bottoms of both channels were made of Plexiglas (Fig. 2). In the SIA channel, the abrupt drop was made of Plexiglas and located 0.8m downstream of the gate. The tested elevation drops s were equal to 3.20 or 6.52 cm. Discharges were measured by a triangular sharp-crested weir. Measurements of upstream and downstream water depths were carried out with electric hydrometers type point gauges supplied with electronic integrators, which yielded directly the estimate of the time-averaged flow depth. The hydrometers, supplied with verniers, had a measurement accuracy of ± 0.1 mm. Water discharge and tailwater depth were regulated by two gates placed, respectively, at the upstream and downstream ends of the channel. For some runs, pressure measurements under the jumps were obtained using a pressure transducer type 4310 of Society TransInstruments with a relative pressure difference range equal to 0–7500 Pa. The pressure tap was connected to the transducer using a rigid tube with 2mm diameter and 0.4m of length. An amplifier and a conditioner were used to adjust the signal output of the transducer for resolution and acceptable range of the A/D board. In addition, a videocamera was used to film the jump for some runs.

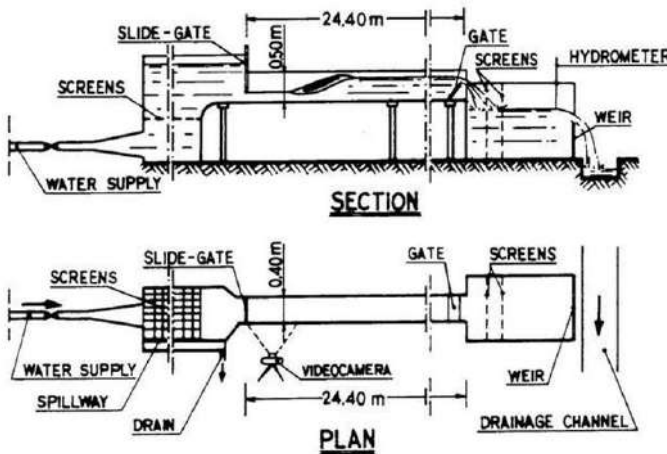


Figure 2. Sketch of the channel at the hydraulic laboratory of the laboratory of the Civil and Environmental Engineering Department – Water Engineering Division (hereafter referred to as SIA) of Bari Polytechnic University.

TABLE I. PARAMETERS OF THE ANALYSED UNDULAR HYDRAULIC JUMP

Run no. Mossa et al. (2003) [6]	y_I [cm]	y_t [cm]	V_I [m/s]	V_t [m/s]	F_I [cm]	y_I/y_t	s	Jump type
B32	3.5	16.63	1.93	0.4	3.3	4.75	3.2	B - wave

Table 1 lists the main experimental parameters of the investigated hydraulic jump: y_I is the inflow water depth; y_t is the water depth downstream of the jump; $F_I = V_I/(gy_I)^{0.5}$ is the inflow Froude number and Re is the Reynolds number defined as $Re=V_Iy_I/v=V_Iy_t/v$ where V_I and V_t are the flow velocities at water depths y_I and y_t , respectively, and v the kinematic water viscosity at the run temperature.

III. SPH NUMERICAL METHOD

The SPH code was developed at the Fluid Mechanics Laboratory of the Department of Civil Engineering and Architecture of the University of Pavia.

SPH simulations were obtained by a standard weakly compressible SPH (WCSPH) scheme [13-14], where a reduced compressibility modulus of 10^6 Pa is assumed for water and a pressure smoothing procedure is applied at every time step to the difference between local and hydrostatic pressure in order to reduce the numerical noise in pressure evaluation [10].

An algebraic mixing-length model and a two-equation model were tested to represent turbulent stresses.

The mixing-length model is based on the introduction of a mixing-length $l_m = f_i \min(\kappa z, l_{max})$, where $\kappa = 0.41$ is the Von Kármán constant, z is the distance from the wall, l_{max} is a cutoff maximum value and

$$f_i = \min \left[1, \left| \sum_j \frac{m_j}{\rho_j} \nabla W_{ij} \right|^3 \right] \quad (1)$$

is a damping function which is less than unity only near the free surface. The effect of f_i is to bound l_m near the free surface, where a non-physical growth of the eddy viscosity may lead to numerical instabilities [15-16].

The two-equation model is a SPH version of the Standard $k-\varepsilon$ turbulence model [17]:

$$\begin{aligned} \frac{Dk_i}{Dt} &= P_{k_i} + \frac{1}{\sigma_k} \sum_j m_j \frac{\nu_{T_i} + \nu_{T_j}}{\rho_i + \rho_j} \frac{k_i - k_j}{r_{ij}^2 + 0.01h^2} \vec{r}_{ij} \cdot \vec{\nabla} W_{ij} - \varepsilon_i \\ \frac{D\varepsilon_i}{Dt} &= \frac{1}{\sigma_\varepsilon} \sum_j m_j \frac{\nu_{T_i} + \nu_{T_j}}{\rho_i + \rho_j} \frac{\varepsilon_i - \varepsilon_j}{r_{ij}^2 + 0.01h^2} \vec{r}_{ij} \cdot \vec{\nabla} W_{ij} + \\ &+ C_{\varepsilon_1} \frac{\varepsilon_i}{k_i} P_{k_i} + C_{\varepsilon_2} \frac{\varepsilon_i}{k_i} \sum_j \frac{m_j}{\rho_j} \varepsilon_j W_{ij} \end{aligned} \quad (2)$$

where P_k is the production of turbulent kinetic energy depending on the local rate of deformation, ν_T is the eddy viscosity and $\sigma_k = 1$, $\sigma_\varepsilon = 1.3$, $C_{\varepsilon 1} = 1.44$ and $C_{\varepsilon 2} = 1.92$ are model constants whose values are those proposed for the standard $k-\varepsilon$ formulation.

According to the standard XSPH approach, at each time step a new particle velocity \vec{v}^T is obtained by explicit integration of the momentum equation (2) while a smoothed value of velocity \vec{v}^S is obtained by:

$$\vec{v}^S(\vec{x}_i) = (1-\varphi)\vec{v}^T(\vec{x}_i) + \varphi \frac{\sum_j \frac{m_j}{\rho_j} \vec{v}^T(\vec{x}_j) W_{ij}}{\sum_j \frac{m_j}{\rho_j} W_{ij}} \quad (3)$$

and used for particle movement. The smoothing parameter φ controls the intensity of velocity filtering. According a sensitivity analysis the SPH simulation of the experimental test on hydraulic jump was performed by adopting a velocity smoothing coefficient in the XSPH scheme $\varphi = 0.01$.

IV. NUMERICAL TEST AND RESULTS

The SPH 2D simulation of the hydraulic jump reported in table 1, were performed in a physical domain consisting in a rectangle 2 m long and 0.4 m high, shorter than the real channel in the test facility. The shorter domain was chosen in order to reduce the computational cost without influencing the quality of the numerical solution. A schematic figure of the problem setup can be seen in Figure 3.



Figure 3. Schematic figure of the geometrical setup. Solid black lines indicates solid walls, dashed blue lines the initial free surface and dashed red lines show the position of the periodic open boundaries.

The ratio of the smoothing length to the initial particle spacing Σ , which influences the efficiency of the SPH kernel function [18], was maintained to a constant value of $\eta/\Sigma = 1.5$ [19]. According to a sensitivity analysis, the SPH simulation of the case here studied was performed by adopting an initial particle spacing $\Sigma = 0.001$ m.

According to the sensitivity analysis shown by [9] the test T1a was performed by adopting a mixing length turbulence model with $l_{max} = 0.5 h_2$. It was chosen to adopt two-equation model (2) for test T1b. Some of the results are here summarized. Table 2 lists the principal characteristics of SPH simulations.

TABLE II. NUMERICAL PARAMETERS OF THE SPH SIMULATIONS IN THE SENSITIVITY ANALYSIS.

Test	Turbulence model	η/Σ	N_p
T1a	Mixing – length model	1.5	3000
T1b	k- ϵ turbulence model	1.5	3000

The results of the SPH simulations were carried out to analyze oscillations of different jump types. Their analysis was useful for the study of the phenomena, which appeared cyclic as well, of the formation, evolution of the jump vortices. Both the mixing length model and the $k-\epsilon$ model yield similar results and are able to predict the oscillating characteristics and cyclic mechanisms in hydraulic jumps.

The instantaneous vorticity fields (Figs. 4a ÷ 5d) of the configuration with oscillations between the B and wave jump clearly indicate that the transition phase between the two jump types is well reproduced by both turbulence models (T1a and T1b). Vortices are characterized by a clockwise or anti-clockwise rotation, depending on which type of jump is present. In particular, vortices are characterized by a clockwise rotation when the wave jump occurs (Figs. 4b ÷ 4d and Figs. 5b ÷ 5d) and by an anti-clockwise one for the B jump (Figs. 4a ÷ 4c and Figs. 5a ÷ 5c), respectively.

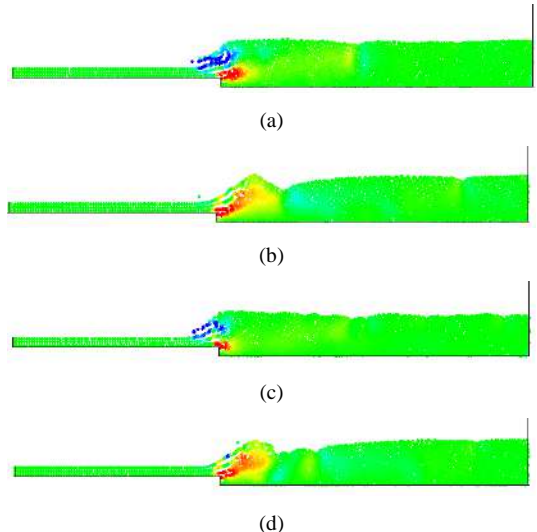


Figure 4. Instantaneous SPH vorticity field in the SPH simulation of Test T1a: (a) $t = 8$ s; (b) $t = 17$ s; (c) $t = 22$ s; (d) $t = 27$ s.

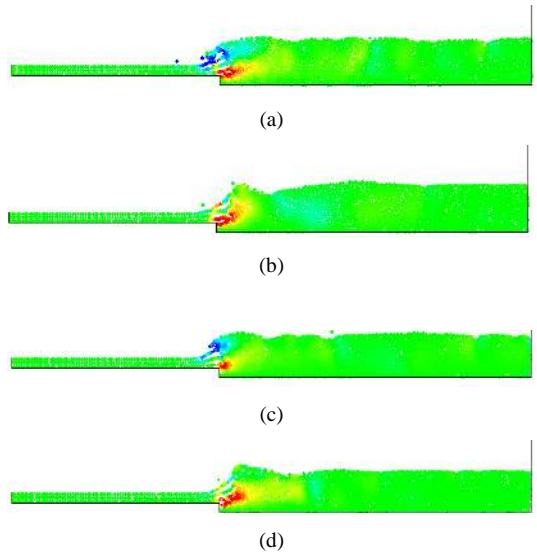


Figure 5. Instantaneous SPH vorticity field in the SPH simulation of Test T1b: (a) $t = 15$ s; (b) $t = 21$ s; (c) $t = 26$ s; (d) $t = 30$ s.

Figure 6 show the amplitude spectrum of the pressure fluctuations computed in tests T1a and T1b, compared with the measurements under the hydraulic jump B32 of Table 1, where the pressure tap was located at a distance of 26 cm from the time-averaged position of the jump toe.

From the analysis of the spectrum it is clear that even the pressure fluctuations are quasi-periodic and strongly influenced by the oscillations between the B and wave jump types; furthermore, it is possible to observe the existence of a peak in each spectrum, as it was shown in the experiments by [6].

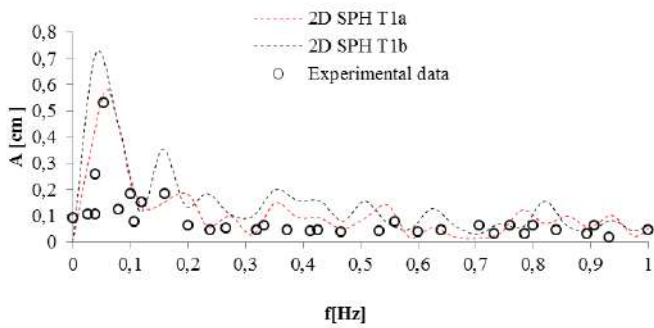


Figure 6. Amplitude spectrum of pressure fluctuations under hydraulic jump (configuration B32 of Table 1) for the SPH simulations of test T1 and two different turbulence models: mixing-length (T1a) and $k-\varepsilon$ (T1b).

Although both turbulence models yield similar results, the detailed comparison of the computed amplitude spectra with the measured ones shows that the results obtained with the mixing-length model are closer to the experimental data than the $k-\varepsilon$ ones (Fig. 6). The peak frequency is slightly higher than 0.1 Hz for test T1a, as shown by [6], while it is lower than 0.1 Hz for test T1b.

Figures 7a÷7c show a part of the time series of the pressure, the horizontal (u) and vertical (v) velocity components measured at the bottom under the hydraulic jump T1a of Table 2, near the time-averaged position of the hydraulic jump toe.

From the analysis of the figures 7a÷7c , it is clear that velocity components and pressure fluctuations, are strongly influenced by the oscillations between the B and wave jump types. The time histories (Fig. 7a) show that low pressures (low water depths) can be correlated with the horizontal flow upstream of the wave-jump, while higher pressures (and depths) can be correlated with the upward flow caused by the roller in the B-jump phase. Therefore, the analysis of the oscillating phenomena indicates a correlation among the velocity components and pressure fluctuations.

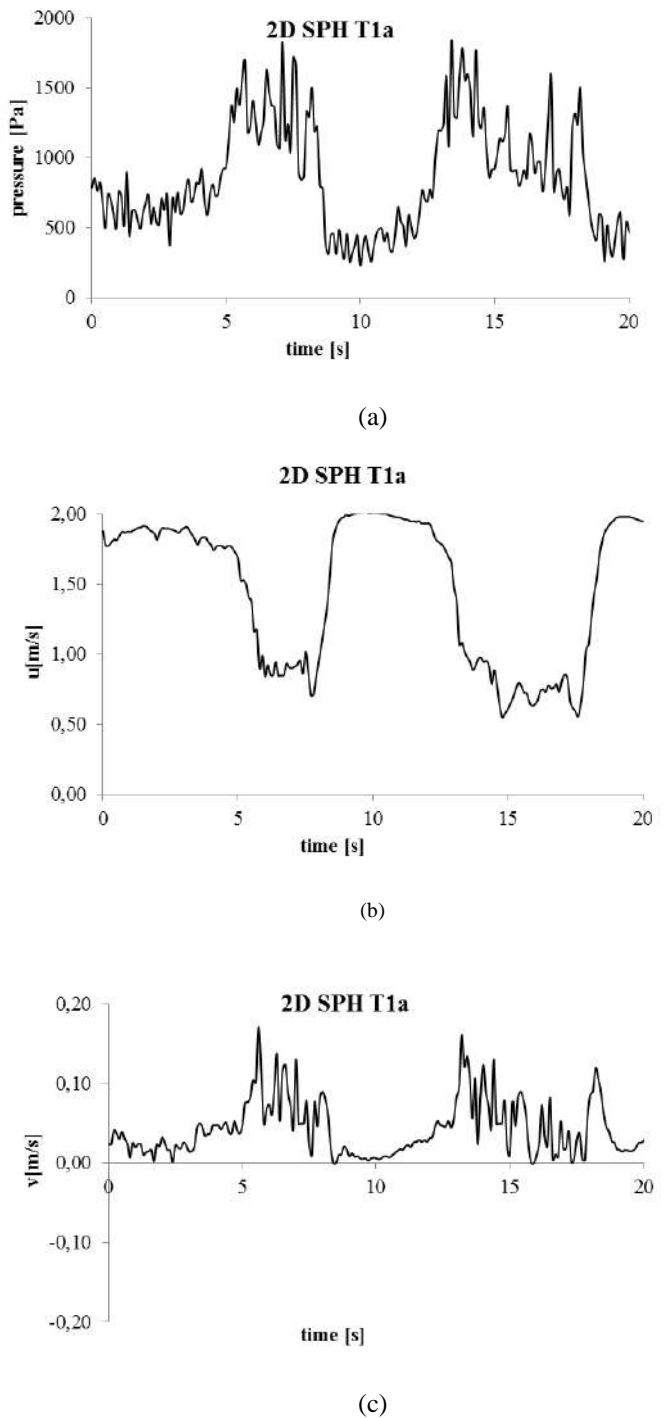


Figure 7. Time series of (a) the pressure; (b) the horizontal (u) velocity component and (c) the vertical (v) velocity component measured at the bottom under the hydraulic jump

Correlation coefficients can also be easily computed from SPH results. The correlation coefficient r is defined as:

$$r = \frac{\sum_{i=1}^n (x_{1i} - \bar{x}_1)(x_{2i} - \bar{x}_2)}{\sqrt{\sum_{i=1}^n (x_{1i} - \bar{x}_1)^2 \sum_{i=1}^n (x_{2i} - \bar{x}_2)^2}} \quad (4)$$

where x_1 and x_2 are two variables, respectively, while the bar denotes a time average. Figure 8 shows the correlation coefficient $r(p,u)$ at different locations downstream of the average position of the jump toe. It can be seen that pressures and streamwise velocities are strongly anti-correlated near the jump (i.e. lower pressures, and levels, occur when the streamwise velocity is higher, and viceversa), while they show a positive correlation downstream. The correlations coefficient $r(u,v)$ between the velocity components exhibits a similar behaviour.

This result is consistent with the oscillation between the B-jump (Fig. 5a and 5c) and the wave-jump (Fig. 5b and 5d) patterns.

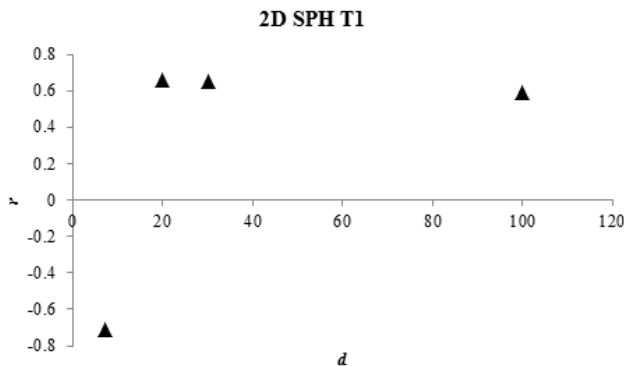


Figure 8. Correlation coefficient between pressure and streamwise velocity component as a function of the distance d from the average toe position.

V. CONCLUSIONS

The 2D SPH model was applied to the modelling of the transition from supercritical to subcritical flow at an abrupt drop based on the laboratory experiments by [6]. Oscillating characteristics in the hydraulic jump are investigated and reproduced using a weakly-compressible XSPH scheme, together with either an algebraic mixing-length or a two-equation turbulence model to represent turbulent stresses: a sensitivity analysis was therefore performed on the influence of different turbulence model.

Although both turbulence models yield similar results, the detailed comparison of the computed amplitude spectra with the measured ones shows that the results obtained with the

mixing-length model are closer to the experimental data than the $k-\varepsilon$ ones.

As observed experimentally by [6], these numerical results show the existence of a peak at a similar frequency in the amplitude spectra of the time series of the surface elevations upstream and downstream of the jump, in the amplitude spectra of the pressure and in the amplitude spectra of the velocity components fluctuations measured under the hydraulic jump.

It is possible to conclude that the SPH numerical simulations yield results which are in qualitative and quantitative agreement with the experiments: hence SPH can be used as a reliable “numerical experiment” which allows one to get a better insight in the unsteady flow phenomenon, performing detailed evaluations which can be complicated to be obtained during laboratory experiments.

For instance, the analysis of amplitude spectra, of the vorticity fields and of the correlation coefficients indicates that velocity components and pressure fluctuations, are strongly influenced by the oscillations between the B and wave jump types, and that a strong correlation exists among the velocity and vorticity fields and the pressure fluctuations even far downstream of the jump position.

REFERENCES

- [1] I. Ohtsu, and, Y. Yasuda. ‘Transition from supercritical to subcritical flow at an abrupt drop’, Journal of Hydraulic Research, IAHR, vol. 29, no. 3, pp. 309-328, 1991.
- [2] G. Nebbia. “Su taluni fenomeni alternativi in correnti libere”, L’Energia Elettrica, fasc. I – vol. XIX, pp. 1-10, 1942.
- [3] A. Abdel Ghafar, M. Mossa, and A. Petrillo. ‘Scour from flowdownstream of a sluice gate after a horizontal apron’, Sixth International Symposium on River Sedimentation - Management of Sediment - Philosophy, Aims, and Techniques, New Delhi, Editors C.V.J. Varma and A.R.G. Rao, Oxford & IBH Publishing Co. Pvt. Ltd., pp. 1069-1088, 1995.
- [4] M. Mossa. On the oscillating characteristics of hydraulic jumps, Journal of Hydraulic Research. Taylor & Francis 37 (4), 541e558, 1999.
- [5] H. Wang, H. Chanson. “Experimental study of turbulent fluctuations in hydraulic jumps”. J. Hydraul. Eng. 141 (7) [http://dx.doi.org/10.1061/\(ASCE\) HY.1943-7900.0001010](http://dx.doi.org/10.1061/(ASCE) HY.1943-7900.0001010), 2015.
- [6] M. Mossa, A. Petrillo, and H. Chanson. “Tailwater Level Effects on Flow Conditions at an Abrupt Drop”. Journal of Hydraulic Research, 41, 39-51,2003.
- [7] Dalrymple, R.A., Rogers, B.D. (2006). Numerical modelling of waves with the SPH method. Coastal Eng. 53, 131–147
- [8] T. Capone, A. Panizzo, JJ. Monaghan. “SPH modelling of water waves generated by submarine landslides”. Journal of Hydraulic Research, 48, 80–84, 2010.
- [9] D. De Padova, R.A. Dalrymple, M. Mossa. “Analysis of the artificial viscosity in the smoothed particle hydrodynamics modelling of regular waves”. J Hydraulic Res 52, 836-848, 2014.
- [10] D De Padova, M Mossa , S. Sibilla, E. Torti “3D SPH modelling of hydraulic jump in a very large channel”. J Hydraulic Res 51, 158-173, 2013.
- [11] P. Jonsson, P. Andreasson, J. Gunnar, I. Hellströma, Pär Jonsén and T. Staffan Lundströma. “Smoothed Particle Hydrodynamic simulation of hydraulic jump using periodic open boundaries” Applied Mathematical Modelling, 40 (19–20), 8391–8405, 2016.

- [12] D. De Padova, M. Mossa, S. Sibilla. "SPH numerical investigation of the velocity field and vorticity generation within a hydrofoil-induced spilling breaker". *Environmental Fluid Mechanics* 16 (1), 267-287, 2016.
- [13] GR Liu, MB Liu. "Smoothed particle hydrodynamics—a meshfree particle methods". World Scientific Publishing, Singapore, 2005.
- [14] JJ. Monaghan. "Simulating free surface flows with SPH". *J Comp Phys* 110 (2): 399–406, 1992.
- [15] D. De Padova, M. Mossa, and S. Sibilla."Laboratory experiments and SPH modelling of hydraulic jumps". *Proc. Int. Conf. 4th Spheric Workshop*, Nantes, 255–257, 2009.
- [16] D. De Padova, M. Mossa, S. Sibilla, and E. Torti "Hydraulic jump simulation by SPH". *Proc. Int. Conf. 5th Spheric Workshop*, Manchester, 50–55, 2010
- [17] B.E. Launder, D.B. Spalding "The numerical computation of turbulent flows". *Comp Meth Appl Mech Eng* 3:269–289, 1974.
- [18] W. Dehnen, H. Aly. " Improving convergence in smoothed particle hydrodynamics simulations without pairing instability". *Monthly Not. Royal Astr. Soc.* 425: 1068-1082, 2012.
- [19] D. De Padova, R.A. Dalrymple, M. Mossa, A.F.Petrillo. "An analysis of SPH smoothing function modelling a regular breaking wave". *Proc. Nat. Conf. XXXI Convegno Nazionale di Idraulica e Costruzioni Idrauliche*, Perugia, Italy, pp 182-182, 2008.

The δ ALE-SPH model: an improved δ -SPH scheme containing particle shifting and ALE formulation

P.N. Sun, A.M. Zhang

College of Shipbuilding Engineering,
Harbin Engineering University,
Harbin, China

sunpengnan@hrbeu.edu.cn; zhangaman@hrbeu.edu.cn

A. Colagrossi, S. Marrone & M. Antuono

Marine Technology Research Institute,
CNR-INSEAN,
Rome, Italy

andrea.colagrossi@cnr.it; salvatore.marrone@cnr.it;
matteo.antuono@cnr.it

Abstract—In the present work we derive a novel model, named δ ALE-SPH scheme, by merging the δ^+ SPH scheme and the Arbitrary Lagrangian Eulerian (ALE) formulation. Differently from the δ^+ SPH scheme, the use of the ALE framework allows for an inclusion of the Particle Shifting Technique (PST) for recovering the consistency of particles' masses, volumes and positions. In the proposed scheme, a diffusive term is included in the density equation to ensure a regular pressure field. Furthermore, different constraints on the mass flux equation are investigated. Indeed we discovered that the accuracy of the solution as well as the properties of the scheme strongly depend on how this equation is numerically handled. Suitable algorithms for the numerical treatment near the free surface and on the solid wall boundary are implemented. These treatments improve the particle distribution and the pressure evaluation close to the fluid boundary. Finally, the δ ALE-SPH scheme is tested against several challenging benchmark test cases, proving to be more robust and accurate than the other SPH schemes.

I. INTRODUCTION

δ -SPH is a popular SPH variant and has been shown to be robust in solving violent fluid-structure interactions [1-3]. Nevertheless, there are still some drawbacks that limit the application of this model, and more in general of the SPH itself, in some areas where traditional CFD methods perform very well, such as the flows past bodies at high Reynolds numbers, flow evolutions with negative pressures which excite tensile instability, etc. In Sun et al. [4], a Particle Shifting Technique (PST) was first combined with the δ -SPH scheme, which was called δ^+ SPH scheme, to tackle these challenging problems. A shifting formula under weakly-compressible hypothesis was proposed in that work. It was shown that PST allows for a uniform particle configuration through small continuous resettlements. Indeed, to achieve a convergence rate larger than 1, a uniform particle distribution should be guaranteed, see [5]. δ^+ SPH has shown remarkable improvements in solving some challenging benchmark test cases characterized by negative pressures [6]. However, the particle repositioning by PST leads to consistency issues due to violation of the link between particle mass, volume and position which, in turn, can induce conservation problems.

The present work is dedicated to further extend the δ^+ SPH scheme combining with an Arbitrary Lagrangian Eulerian (ALE) formulation as recently proposed in Oger et al. [7]. A new scheme based on the δ -SPH model is developed, namely

δ ALE-SPH, aiming to improve the consistency and conservation of the δ^+ -SPH model.

In the literature, when a particle shifting is imposed, the generic variables of the particle is recalculated by the Taylor Series with its gradient evaluated on the particle location [8]. Another solution is to maintain these variables unchanged [4] if the resettlement is small enough. In the present δ ALE-SPH scheme, the variables are updated based on the ALE formulation. The use of the ALE framework allows for the inclusion of the Particle Shifting Technique (PST) in order to recover the consistency of particle masses, volumes and positions.

In the proposed scheme, the diffusive term of the δ -SPH is added in the continuity equation of the ALE scheme to ensure a regular pressure field. However, a straightforward application of the ALE scheme in [7] does not provide satisfying results. In particular, three different constraints on the mass flux equation are investigated in this work. In addition to that, suitable algorithms for the numerical treatment near the free surface and on the solid wall boundary are implemented. These treatments improve the particle distribution and the pressure evaluation close to the boundaries.

The present paper is arranged as follows. In the second section, the δ ALE-SPH scheme is introduced with different numerical treatments for the mass flux equation. In the third section, benchmarks are employed to test the proposed numerical scheme. The improvements in the numerical accuracy of δ ALE-SPH scheme with respect to the other SPH schemes are shown on the selected benchmarks. The different treatments for the mass flux equation are compared and discussed. Conclusion and future works are presented in the last section.

II. THE δ ALE-SPH SCHEME

A. Governing equations

In the SPH framework, the fluid domain is discretized into uniformly distributed particles which transport the main physical quantities (namely, density, volume, pressure, velocity etc.). We consider here Navier-Stokes equations for compressible fluids. In this framework, the discrete ALE-SPH scheme reads:

$$\begin{cases} \frac{d\mathbf{r}_i}{dt} = \mathbf{v}_i + \delta\mathbf{v}_i, \\ \frac{dV_i}{dt} = V_i \sum_j V_j (\mathbf{v}_j - \mathbf{v}_i) \cdot \nabla_i W_{ij} + V_i \sum_j V_j (\delta\mathbf{v}_j - \delta\mathbf{v}_i) \cdot \nabla_i W_{ij}, \\ \frac{dm_i}{dt} = V_i \sum_j^* V_j (\rho_i \delta\mathbf{v}_i + \rho_j \delta\mathbf{v}_j) \cdot \nabla_i W_{ij}, \\ \frac{d(m_i \mathbf{v}_i)}{dt} = V_i \sum_j (\rho_i \mathbf{v}_i \otimes \delta\mathbf{v}_i + \rho_j \mathbf{v}_j \otimes \delta\mathbf{v}_j) \cdot \nabla_i W_{ij} + \rho_i V_i \mathbf{f}_i - V_i \sum_j V_j (p_i + p_j) \nabla_i W_{ij} + \mu V_i \sum_j V_j \pi_{ij} \nabla_i W_{ij}, \end{cases} \quad (1)$$

where \mathbf{r}_i indicates the i -th particle position and the symbol d/dt denotes the Lagrangian derivative. m_i is the particle mass which is equal to the product between density and volume, i.e. $m_i = \rho_i V_i$. The kernel function $W_{ij} = W(\|\mathbf{r}_i - \mathbf{r}_j\|)$ is assumed to be a positive radial function with a compact support characterized by a reference length h (hereinafter called smoothing length). Here, a C2-Wendland kernel is used and about 50 neighbour particles (in a 2D framework) are considered in the kernel support, which corresponds to $h = 2\Delta x$ where Δx indicates the initial particle distance. The starred summation in the mass flux equation in (1) indicates that the sum is restricted to fluid particles only and this ensures the mass conservation. As usual, symbols \mathbf{v}_i and p_i indicate the velocity and pressure of the i -th particle while $\delta\mathbf{v}_i$ represents an arbitrary velocity change (more details in the following). In particular, the fluid is assumed to be weakly-compressible and barotropic and the following linear state equation is adopted:

$$p_i = c_0^2 (\rho_i - \rho_0), \quad (2)$$

where ρ_0 is the reference density (for example, the density along the free surface) and c_0 is the reference speed of sound. Within a weakly-compressibility assumption, c_0 has to satisfy the following constraint (see[4]):

$$c_0 \geq 10 \max\left(U_{\max}, \sqrt{\frac{p_{\max}}{\rho_0}}\right), \quad (3)$$

where U_{\max} and p_{\max} denote the maximum expected velocity and pressure. Finally, \mathbf{f}_i represents a generic volume force acting on the i -th particle.

The viscous term is represented through the formula in [4]. Here, μ denotes the dynamic viscosity while π_{ji} is given below:

$$\pi_{ji} = K \frac{(\mathbf{v}_j - \mathbf{v}_i) \cdot (\mathbf{r}_j - \mathbf{r}_i)}{\|\mathbf{r}_j - \mathbf{r}_i\|^2}, \quad (4)$$

where $K = 2(n+2)$ and n is the number of spatial dimensions. For the inviscid cases in the third section, μ is replaced by $\alpha c_0 h \rho_0 / K$ and $\alpha = 0.01$ is used in this work.

With the following relation:

$$\frac{d(\rho_i V_i)}{dt} = \frac{d(\rho_i)}{dt} V_i + \frac{d(V_i)}{dt} \rho_i, \quad (5)$$

we replace the volume equation with a density equation in the standard ALE scheme (1). In addition, a density diffusive term D_i is added in the density equation to prevent high frequency pressure oscillations (as in the normal δ -SPH scheme).

In the standard ALE scheme, a mass flux between the particles is introduced consequently to the position arbitrary shifting. However, from the numerical point of view, the mass flux equation in system (1) leads to error cumulation in long-time simulations, particularly in the problems with considerable free surface deformations. Therefore, a numerical correction in the mass flux equation is also added. Finally, the system (1) becomes:

$$\begin{cases} \frac{d\mathbf{r}_i}{dt} = \mathbf{v}_i + \delta\mathbf{v}_i, \\ \frac{d\rho_i}{dt} = -\rho_i \sum_j V_j (\mathbf{v}_j - \mathbf{v}_i) \cdot \nabla_i W_{ij} - \rho_i \sum_j V_j (\delta\mathbf{v}_j - \delta\mathbf{v}_i) \cdot \nabla_i W_{ij} + \delta h c_0 D_i^\rho, \\ \frac{dm_i}{dt} = V_i \sum_j^* V_j (\rho_i \delta\mathbf{v}_i + \rho_j \delta\mathbf{v}_j) \cdot \nabla_i W_{ij} + \Theta_m, \\ \frac{d(m_i \mathbf{v}_i)}{dt} = V_i \sum_j (\rho_i \mathbf{v}_i \otimes \delta\mathbf{v}_i + \rho_j \mathbf{v}_j \otimes \delta\mathbf{v}_j) \cdot \nabla_i W_{ij} + \rho_i V_i \mathbf{f}_i - V_i \sum_j V_j (p_i + p_j) \nabla_i W_{ij} + \mu V_i \sum_j V_j \pi_{ij} \nabla_i W_{ij}, \end{cases} \quad (6)$$

where D_i^ρ is the density diffusive term as adopted in the δ -SPH [9], namely:

$$D_i^\rho = 2 \sum_j \psi_{ji} \frac{\mathbf{r}_{ji} \cdot \nabla_i W_{ij}}{\|\mathbf{r}_{ji}\|^2} V_j, \quad (7)$$

with

$$\psi_{ij} = (\rho_j - \rho_i) - 0.5 [\langle \nabla \rho \rangle_i^L + \langle \nabla \rho \rangle_j^L] \cdot \mathbf{r}_{ji}, \quad (8)$$

where $\mathbf{r}_{ji} = \mathbf{r}_j - \mathbf{r}_i$ and the superscript ‘L’ indicates that the gradient is evaluated using the renormalized gradient equation [9].

The velocity deviation $\delta\mathbf{v}_i$ is computed by using a formula similar to the Particle Shifting Technique (PST), that is:

$$\delta\mathbf{v}_i = \sum_j -Ma \cdot (2h) \cdot c_0 \cdot \left[1 + R \left(\frac{W_{ij}}{W(\Delta x)} \right)^n \right] \nabla_i W_{ij} V_j. \quad (9)$$

where $Ma = U_{\max} / c_0$ and Δx is the mean particle distance and the constants R and n are set equal to 0.2 and 4 respectively. If one sets the shifting velocity equal to $\delta\mathbf{v} = -\mathbf{v}$, the particle displacement becomes zero which means the governing equations are solved in the Eulerian framework.

In order to limit the action of the shifting term to ensure the particles are transported in a nearly Lagrangian way, the following modified velocity deviation $\delta\mathbf{v}^*$ is considered:

$$\delta\mathbf{v}_i^* = \min \left(\|\delta\mathbf{v}_i\|, \frac{U_{\max}}{2} \right) \frac{\delta\mathbf{v}_i}{\|\delta\mathbf{v}_i\|} \quad (10)$$

The system (6) is integrated in time by using a fourth-order Runge-Kutta scheme for the cases in this paper.

B. Particles' masses treatments

The term Θ_m for the mass flux equation plays an important role. Here three different alternatives are proposed.

In the **mass treatment 1**, a correction term Θ_m that forces $dm_i/dt = 0$ is added in the mass flux equation. Θ_m can be written as

$$\Theta_m = -V_i \sum_j^* V_j (\rho_i \delta v_i + \rho_j \delta v_j) \cdot \nabla_i W_{ij} . \quad (11)$$

This treatment is similar to the one used in the transport-velocity formulation [10]. In that work, a constant mass is assigned to the particle which is transported by a modified velocity modified with respect to the physical velocity of the particle. Only a momentum flux is allowed between the particles while mass flux is prevented.

In the **mass treatment 2**, a mass diffusive term similar to the density diffusion as used in the δ -SPH scheme is proposed. Θ_m can be written as

$$\Theta_m = \delta h c_0 D_i^m \quad (12)$$

where D_i^m is given below

$$D_i^m = 2 \sum_j (m_j - m_i) \frac{(\mathbf{r}_j - \mathbf{r}_i) \cdot \nabla_i W_{ij}}{\|\mathbf{r}_j - \mathbf{r}_i\|^2} \sqrt{V_i V_j}, \quad (13)$$

In the **mass treatment 3**, $\Theta_m = 0$ is adopted, which recovers the same mass flux equation as in the standard ALE-SPH scheme [7]. In the third section of the present paper, the three forms of Θ_m will be numerically studied for different benchmark test cases.

C. The numerical treatment for the shifting velocity close to the free surface

As discussed in Sun et al. [4], in order to not violate the kinematic boundary condition on the free surface, the shifting velocity for the particles close to it has to be modified by nullifying the normal component of δv_i to the free surface and maintaining its tangential component. Recently, a similar approach has been also proposed by Khayyer et al. [11] in the MPS context. For the ease of the reader, we first recall some results from the work of Marrone et al. [12] to detect the free surface particles. We indicate by λ_i the minimum eigenvalue of the renormalized matrix \mathbf{L}_i defined by:

$$\mathbf{L}(\mathbf{r}_i) = \left[\sum_j \nabla_i W_{ij} \otimes (\mathbf{r}_j - \mathbf{r}_i) V_j \right]^{-1} \quad (14)$$

The value of λ_i allows for the identification of a region in the particle domain that is close to the free surface. Hereinafter, we denote by \mathcal{T} such a region, see more in Marrone et al. [12] and Sun et al. [4].

The normal to the free surface in such a region is defined through the following formula:

$$\hat{\mathbf{n}}_i = \frac{\langle \nabla \lambda \rangle_i}{|\langle \nabla \lambda \rangle_i|} \text{ with } \langle \nabla \lambda \rangle_i = - \sum_j (\lambda_j - \lambda_i) \mathbf{L}_i \nabla_i W_{ij} V_j \quad (15)$$

However, as pointed out in [4], when considering violent flows the free surface can be characterized by the formation of thin jets, the normal evaluated form Eq. (15) can be less accurate due to the small number of neighbouring particles.

Since λ_i is a good measure of the number of the neighbouring particles, it has been further adopted to correct the shifting velocities. Finally, the shifting velocity is corrected as $\delta \hat{v}_i$ in the following formula:

$$\delta \hat{v}_i = \begin{cases} 0 & \text{if } \lambda_i < 0.55 \text{ and } i \in \mathcal{T} \\ \kappa_i (\mathbb{I} - \mathbf{n}_i \otimes \mathbf{n}_i) \delta v_i^* & \text{if } \lambda_i \geq 0.55, \mathbf{n}_i \cdot \delta v_i^* \geq 0 \text{ and } i \in \mathcal{T} \\ \delta v_i^* & \text{if } \lambda_i \geq 0.55, \mathbf{n}_i \cdot \delta v_i^* \leq 0 \text{ and } i \in \mathcal{T} \\ \delta v_i^* & \text{if } i \notin \mathcal{T} \end{cases} \quad (16)$$

where \mathbb{I} is the identity tensor and

$$\kappa_i = \begin{cases} 0 & \text{if } \min_j (\mathbf{n}_i \cdot \mathbf{n}_j) \leq 0.966 \\ 1 & \text{otherwise} \end{cases} \quad (17)$$

In Eq. (17), index j refers to the neighbour particles of i . Eq. (17) is used to remove the shifting velocity in the corner of the flow region. Since \mathbf{n}_i and \mathbf{n}_j are both unit vectors, $\mathbf{n}_i \cdot \mathbf{n}_j \rightarrow 1$ when they are pointing in the same direction while $\mathbf{n}_i \cdot \mathbf{n}_j \rightarrow 0$ when they are perpendicular to each other. $\mathbf{n}_i \cdot \mathbf{n}_j = 0.966$ occurs when the \mathbf{n}_i and \mathbf{n}_j have the included angle as about 15° , and when this angle is larger, their shifting velocities are blocked to zero. This treatment is important to ensure the numerical stability in the flow regions with high curvature like thin jets.

D. The numerical treatment for the shifting velocity close to a solid wall boundary

A careful treatment for the shifting velocity should also be conducted on the particles close to a solid wall boundary, particularly for those in the vicinity of both a solid wall and free surface. In the present work, the technique of “fixed ghost particle” boundary [1] is applied to model all the solid walls, the shifting velocity of all the ghost particles are all set to be zero. The following algorithm is mainly introduced for the modification of the shifting velocity of the fluid particles.

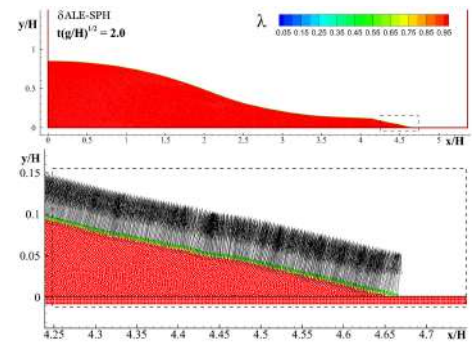


Figure 1. The distribution of λ used for the evaluation of free surface normal. (top) an overall distribution of λ ; (bottom) zoom view of the dashed rectangular box of the top figure and the free surface normal.

A dam-break flow is taken as an example, (see Figure 1). In this case, before the liquid tongue hits the vertical solid wall, a very thin flow tip is formed and it freely slips on the flat bottom. In order to ensure a stable evolution of the thin tip, careful treatments should be imposed for the shifting velocity of the particles presenting in this flow region. Firstly, a correct

and accurate evaluation of the normal for the free surface particles (including the particles on the flow tip) should be evaluated. Eq. (15) can be employed for this aim. However, it depends on a reasonable evaluation of λ by using Eq.(14). Firstly, we note that, for the ghost particles, we assign λ of the ghost particle to be 1. Then Eq. (14) is employed to evaluate the λ for the fluid particles, taking into account the existing of ghost particles with their 2D volumes as $(\Delta x)^2$ being Δx the particle size. On the top of Figure 1, the distribution of λ at $t(g/H)^{1/2} = 2$ is depicted for a dam-break case. As can be seen, on the ghost particles, λ are all set to be 1, which helps to ensure the normal for the particles in the free surface region to be corrected, even for the particle on the flow tip, see the bottom plot of Figure 1.

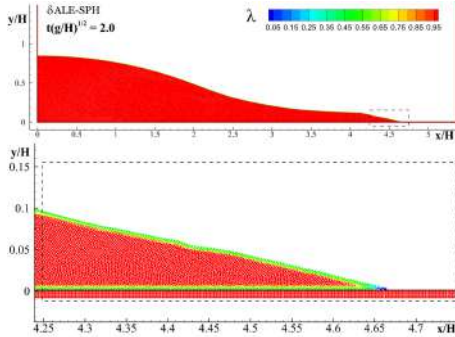


Figure 2. The distribution of λ used as a threshold for the blocking of the shifting velocity for the particles in the flow tips or splashing droplet. (top) The overall distribution; (bottom) zoom view in the dashed rectangular box of the top figure.

Since in Eq.(16), λ is employed again to block the shifting velocity for the particles with few neighbours. Here we note that the ghost particles need to be not taken into account when using Eq.(14) to evaluate the λ as a threshold in Eq.(16), see the corresponding distribution of λ in Figure 2. That means the flows tip which is slipping attached on a solid wall is treated as a splashing jet. This numerical treatment is crucial in maintaining the simulation stable in some violent interactions between the fluid and solid wall, e.g. dam-breaking and sloshing.

III. NUMERICAL RESULTS

A. Benchmark test No. 1: Taylor Green flow

One of the most used benchmark test in the SPH literature is the periodic Taylor-Green flow problem. This case is particularly challenging for SPH and the absence of solid or free boundaries make this problem suitable for the validation of the consistency and accuracy of novel numerical schemes. In the literature, more attention has been paid to the formation and breaking of filament structure at the initial stage, see e.g. [7]. The filament structure is due to the inherent Lagrangian characteristic of SPH method and it can be removed by using Particle Shifting Technique (PST). However, in weakly compressible SPH models, PST has to be implemented carefully; otherwise the inconsistency due to particle repositioning may lead to a completely wrong evolution. In this section the adopted benchmark tests have two main aims:

(1) Simple implementation of PST in a weakly compressible SPH model (δ -SPH model) may lead to a non-

physical evolution of pressure for the flow in a closed flow region. Conversely, the proposed δ ALE-SPH model is able to give a correct pressure evolution.

(2) The numerical treatment proposed for the mass flux equation in δ ALE-SPH will be shown to be necessary, especially in viscous flows with higher Reynolds numbers.

In the Taylor Green flow, four vortices with anti-rotational directions are placed in a squared fluid domain with the size of $[0, L] \times [0, L]$, closed by periodical boundaries. The initial velocity and pressure distribution for this problem can be referred to [7]. According to the analytic solution of this problem under an incompressible hypothesis, the time evolution of the total energy in the flow and the pressure on a fixed spatial position can be written in the formulation as

$$f(t) = f(t_0) e^{(-16\pi^2/Re)tU/L} \quad (18)$$

where $f(t)$ denotes the total kinetic energy or pressure in the time domain and t_0 indicates the initial time.

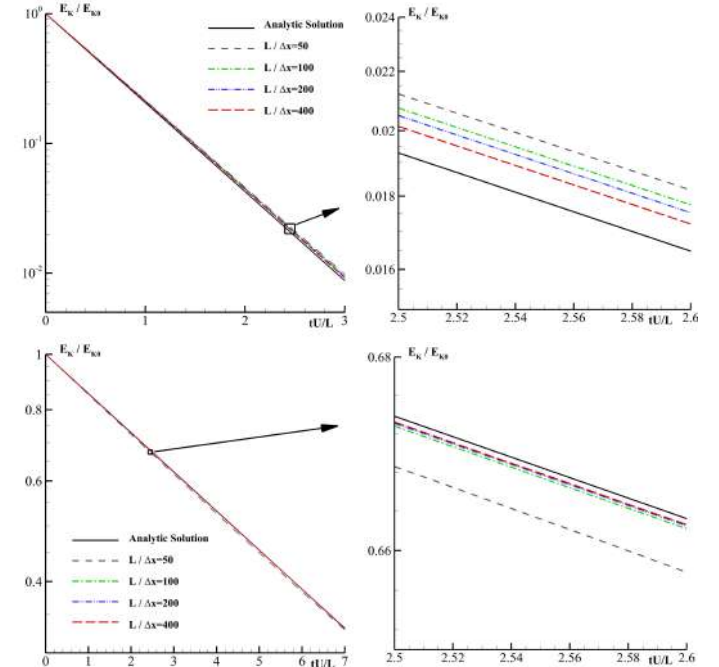


Figure 3. Time evolutions of the overall kinetic energy for the flow Taylor Green vortices at two Reynolds numbers: $Re = 100$ (up) and $Re = 1000$ (bottom). On the right hand-side shows the enlarged views for the square regions on the left-hand side.

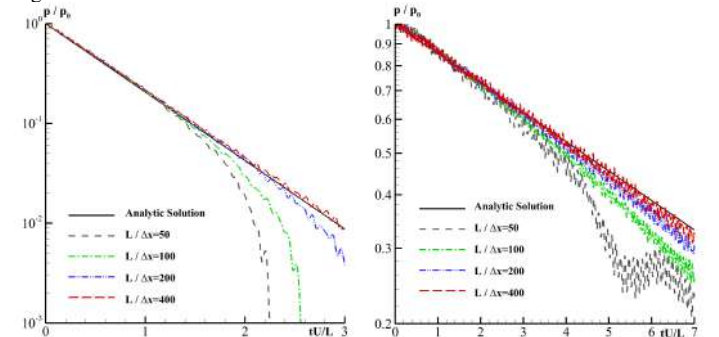


Figure 4. Time evolutions of the pressure measured on the centre of the flow regions at two Reynolds numbers: $Re = 100$ (left) and $Re = 1000$ (right). The results of the δ ALE-SPH in different particle resolutions are compared with the analytic solutions.

Two Reynolds numbers, $Re = \rho UL/\mu$ where U is the reference velocity [7], have been tested for this case, respectively $Re=100$ and $Re=1000$. Firstly, the δ ALE-SPH model with a constant mass constrain (i.e. **the mass treatment 1** for the mass flux equation, see Eq. (11)) is tested with four different particle resolutions.

The time evolutions of the decays of the overall kinetic energy and the pressure measured on the centre of the domain are plotted in Figure 3 and Figure 4 respectively. From these two groups of plots, it is found that as the particle resolution is refined, the SPH results converge to the analytic solutions. It is worth noting that, to the authors' knowledge, this is the first time that the pressure evolution in the Taylor Green flow is compared with an analytic solution. Thanks to the novel proposed density equation with a density diffusion involved, the pressure evolution is stable and agrees fairly well with the analytic solution when the particle resolution is fine enough.

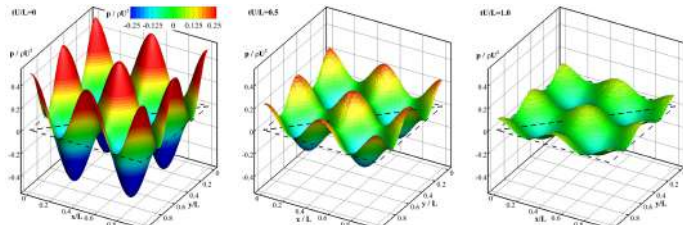


Figure 5. Pressure distribution on the fluid domain occupied by the Taylor Green vortices at 3 time instants when $Re=100$: the vertical axis shows the pressure amplitude and the two horizontal axes show the positions.

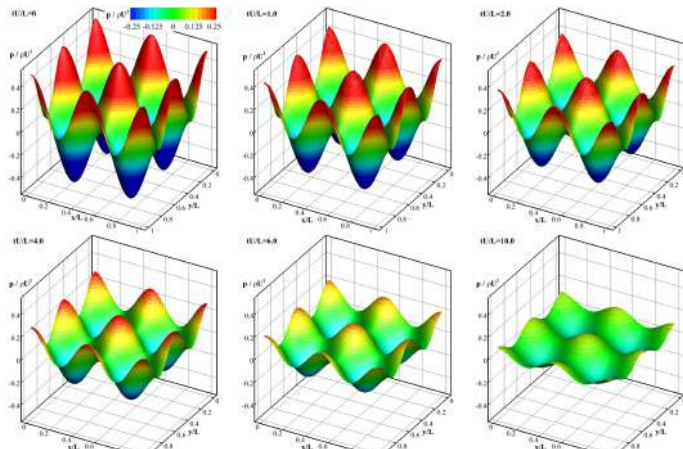


Figure 6. Pressure distribution on the fluid domain occupied by the Taylor Green vortices at 6 time instants when $Re=1000$: the vertical axis shows the pressure amplitude and the two horizontal axes show the positions.

The pressure distribution on the whole fluid region is plotted in 3D views in Figure 5 and Figure 6 in order to better show the pressure distributions at different time instants. In both the two Reynolds numbers ($Re=100$ and $Re=1000$), the pressure distribution is smooth thanks to the density diffusive term in the density equation. As expected, in case of the larger Reynolds number, the pressure decay is slower with respect to the one of the smaller Reynolds number.

Three other schemes are also tested in this benchmark. They are respectively the δ^+ SPH model (simply implementing the PST into the δ -SPH model) and the δ ALE-SPH but with the mass treatment 2 and 3. The particle resolution $L/\Delta x = 200$ is adopted for these cases.

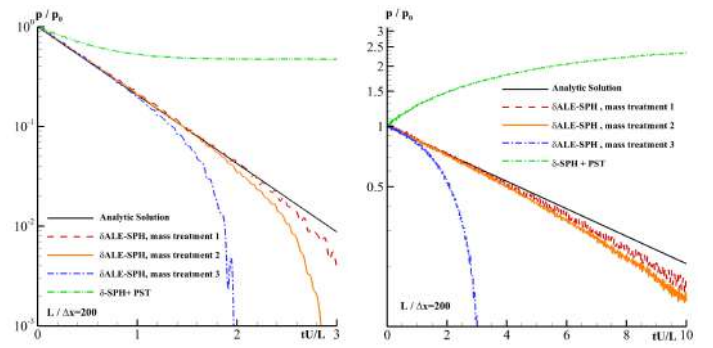


Figure 7. Time evolutions of the pressure measured on the centre of the flow at two Reynolds numbers: $Re = 100$ (left) and $Re = 1000$ (right). Comparisons are made between different schemes, respectively δ ALE-SPH with different mass treatments in Section II. B and δ -SPH with PST implemented.

The pressure evolutions on the centre of the fluid region are plotted in Figure 7 for the two Reynolds numbers. The results of the mass treatment 1 and mass treatment 2 are similar but faster pressure decay is observed in the latter case. When using the mass treatment 3 in δ ALE-SPH, the pressure decays correctly at the initial stage, but after that, the pressure evolution deviates from the reference solution quickly due to the error cumulation for the particle mass. When the Reynolds number is enlarged, this pressure error occurs earlier. In the results of the δ^+ SPH, we find that simply implementing a particle shifting to the particle position leads the pressure to evolve in a completely wrong direction.

B. Benchmark test No. 2: Flow past an inclined elliptical cylinder at $Re=500$

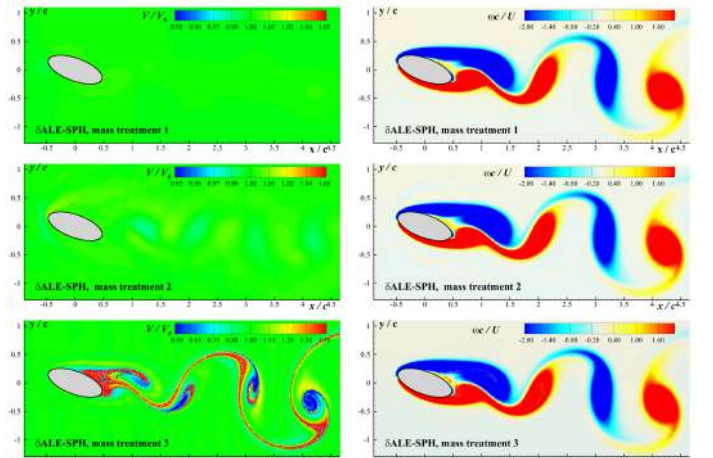


Figure 8. Flow past an inclined elliptical cylinder at $Re = 500$ at $tU/t = 11.4$. From the top to bottom shows the volume distributions (left) and vorticity distributions (right) by the δ ALE-SPH model using mass treatment from 1 to 3 presented in Section II. B.

In this part, a benchmark test case involving the flow past an inclined elliptical cylinder with the angle of attack of 20° and axis ratio of 0.4 at $Re = Uc/v = 500$ (c is the length of the major axis of the ellipse and U is the velocity of the free stream) is simulated. In the numerical set up, the centre of the ellipse is placed at the origin of the frame of reference. The inflow boundary is placed $x = -5c$ and outflow at $x = 10c$. The lateral boundaries are placed at $y = \pm 5c$ in order to avoid the blockage effect.

Firstly, simulations with the particle resolution $c/\Delta x = 100$ are run to make a comparative study between the

different mass treatments in the mass flux equation. The volume and vorticity distributions at $tU/c = 11.4$ for the three different schemes are shown in Figure 8. In the mass treatment 3, due to the lack of a correction term in the mass flux equation, at $tU/c = 11.4$, the particle volume has been distributed in a large range. It is observed that inside the vortex cores, the particles volumes are dramatically reduced while on the vortex boundary, the volumes are increased. In the results of mass treatment 1 and 2, the volume variations are both within 1%, which is within the limitation of the weakly compressible hypothesis. Regarding the vorticity distributions, all the three schemes present smooth vorticity fields; only in the results of mass treatment 3, the wide variation of particle volumes introduces some perturbations of vorticity close to the elliptical cylinder.

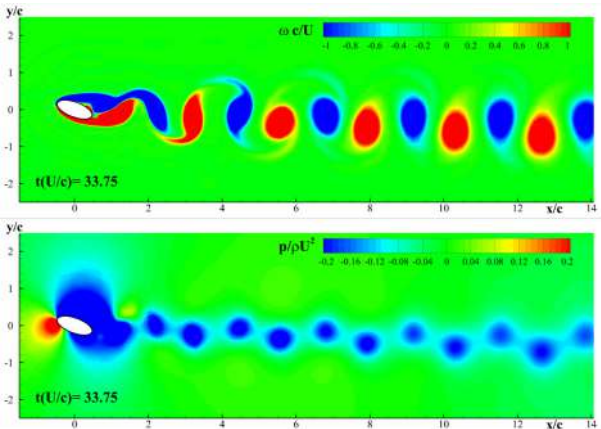


Figure 9. The flow past an inclined elliptical cylinder with an angle of attack of 20° at $Re=500$, solved by δ ALE-SPH with the mass treatment 1. (Top) vorticity field; (Bottom) pressure field.

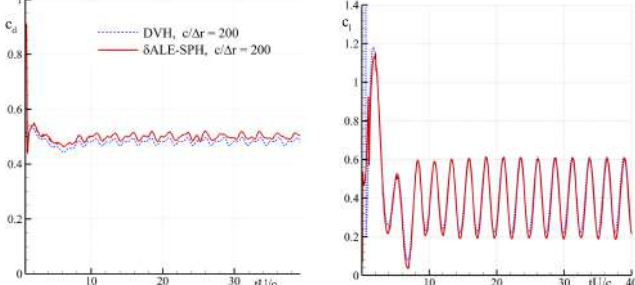


Figure 10. Time evolutions of the drag and lift force coefficients in the flow past the elliptical cylinder at $Re=500$, solved by δ ALE-SPH with the mass treatment 1. SPH results are compared with the DVH [13] solutions.

In the following part, the **mass treatment 1** is adopted in δ ALE-SPH to rerun this case with a finer particle resolution $c/\Delta x = 200$. The vorticity and pressure distributions at $tU/c = 33.75$, when a steady vortex shedding stage is reached, are depicted in Figure 9. Thanks to the shifting of the particle positions, very smooth vorticity and pressure distributions are obtained. No tensile instability is observed in the region characterized by negative pressure. Figure 10 shows the time evolutions of the drag and lift force coefficients measured on the ellipse. The reference solution is calculated by the recently developed Vortex Particle Method called Diffused Particle Hydrodynamics (DVH), see [13]. A fairly good agreement is achieved between the results of δ ALE-SPH and DVH.

C. Benchmark test No. 3: Rotation of a free-surface square fluid patch

Rotation of a free-surface square fluid patch has become a basic but challenging benchmark test for testing the mesh free numerical models, see [4, 11, 14]. The challenging aspect of this test is the strong negative pressure inside the fluid and the four elongated thin fluid arms. The former may excite the tensile instability while the latter is accompanied with the sharp free surface shape. Initially, the square fluid patch with the boundary length of L is subjected to a rotating velocity field defined as:

$$\mathbf{u}(x, y, t = 0) = (\omega y; -\omega x) \quad (19)$$

With the assumption of the fluid to be incompressible, the initial pressure field can be obtained by solving the Poisson equation, see more in [14].

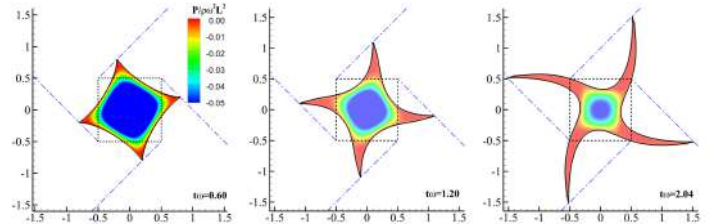


Figure 11. The deformations of the rotational fluid patch and the pressure distributions at three time instants. The fluid surfaces obtained by δ ALE-SPH with mass treatment 1 are compared against the results of LFDM [14].

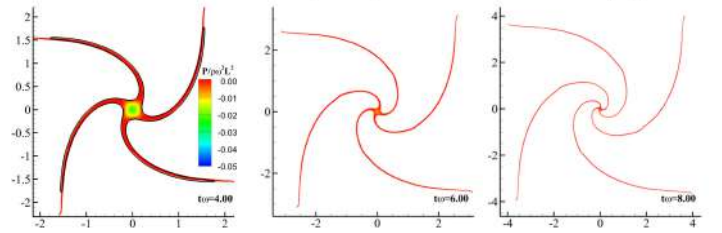


Figure 12. Rotation of the fluid patch at different time instants. (left) $t\omega = 4.0$; (middle) $t\omega = 6.0$; (right) $t\omega = 8.0$. The black-dashed line at $t\omega = 4.0$ indicates the BEM result [14].

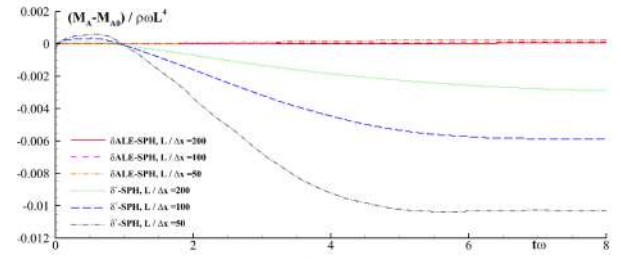


Figure 13. Time evolutions of the variation of angular momentum.

It has been demonstrated in [4] that δ -SPH failed to simulate this case due to the tensile instability and δ^+ -SPH model is able to solve this problem, but the error in the angular-momentum conservation is considerable. In this part, δ ALE-SPH with **mass treatment 1** is employed to model this case. The fluid shapes along with the pressure distributions at different time instants are compared with the free surface obtained with a Lagrangian Finite Difference Method (LFDM) in [14]. Fairly good agreements between the surface shapes are achieved. In addition, pressure field of δ ALE-SPH are free of noise thanks to the density diffusive term added in the density equation. Due to the distortion of the mesh in the

LFDM solver, the simulation terminates at $t\omega = 2.04$. Therefore, a solver based on a boundary element method (BEM) is employed to further predict the free surface shape after $t\omega = 2.04$. In the first subplot of Figure 12, the free surface shape at $t\omega = 4.00$ is compared against the result of a Boundary Element Method (BEM) solver. Again a good agreement is obtained. After that, since the four fluid arms have been extremely thin and it is impossible for the BEM solver to continue predicting this problem. But the fluid shapes at $t\omega = 6.00$ and $t\omega = 8.00$ can still be predicted by δALE-SPH, as shown in Figure 12.

Regarding the conservation of momentum in the SPH results, it is found that the error of the linear momentum is again negligible ($\sim 10^{-8} \rho UL^2$) and, therefore, they are not shown here. Figure 13 plots the time history of the errors of angular momentum in δ^+ -SPH and δALE-SPH results with three different particle resolutions. The performance of δALE-SPH in conserving the angular momentum is shown to be superior than δ^+ -SPH.

D. Benchmark test No. 4: Shallow water sloshing

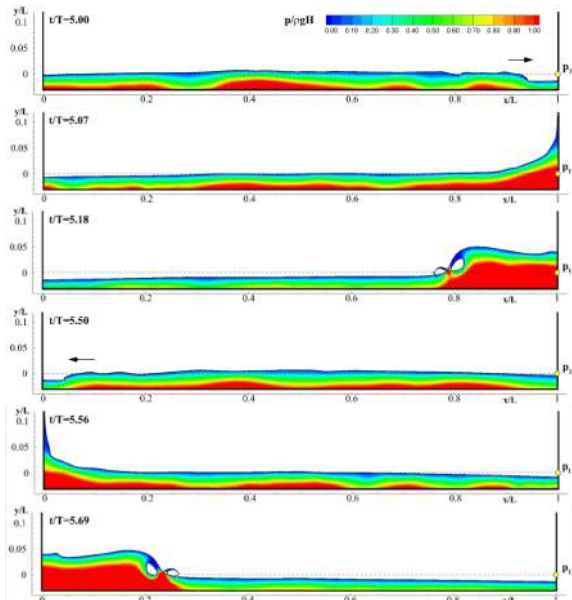


Figure 14. The fluid patterns and pressure distributions at some characteristic time instants after 5 sloshing periods when the flow reaches a steady stage.

In the simulation of free surface flows within a body force field, as described in [4], the shifting of the particle positions alters the potential energy of particles and therefore the conservation property of SPH is destroyed. Even in [4], an equation of symmetric particle shifting is proposed but the error on free surface boundary may still induce error cumulation on energy conservation in long duration simulations.

In this part, simulations of a shallow water sloshing with a violent free surface deformation are tested for the proposed δALE-SPH scheme. The experimental case named as Series 5 in [2] is adopted here as a benchmark. In this case, the water tank has a length of $L = 1\text{m}$, width of $W = 0.1\text{m}$ and filled with the water depth denoted by H . The shallow water inside a rectangular water tank is excited by a periodic swaying

motion which can be expressed as $x = A\cos(\omega t) - A$ where ω is the exciting frequency. The natural frequency of the sloshing phenomenon can be obtained by a first-order approximated as $\omega_r^{(n)} = \sqrt{gnk \tan(kH)}$ where n is the order of the natural frequency. In the Series 5 case in [2], the parameters $A/H = 2.333$ and $H/L = 0.03$ are adopted. The exciting frequency ω is set as $1.231\omega_r^{(1)}$. In all the SPH simulations, The fluid domain is discretized with the particle resolution as $H/\Delta x = 24$ and we set the fluid viscosity considering both the dissipation in the fluid bulk and the dissipation due to the boundary layer, see more in [2].

Firstly the new proposed δALE-SPH with the **mass treatment 1** is adopted to simulate this problem. The fluid patterns and pressure distributions at some characteristic time instants after 5 sloshing periods are shown in Figure 14. Under the swaying excitation, the water waves are generated inside the tank and hits the side walls. Water climbing on the wall induces a pressure impulse and the fluid rolling down generates a breaking wave. Such a periodic violent fluid-structure interacting case demands rigorous mass and momentum conservations and numerical stability of the numerical scheme. Particularly when a particle shifting is involved, it is hard to maintain these conservations and stability on the fluid surface. A stable free surface configuration and smooth pressure distribution are obtained as primarily shown in Figure 14. An experimental result for the fluid surface evolution at $x/L = 0.05$ is available thanks to the experimental campaign conducted in Bouscasse et al.[2]. As plotted in Figure 15, a good agreement is obtained between the experimental data and the result of δALE-SPH.

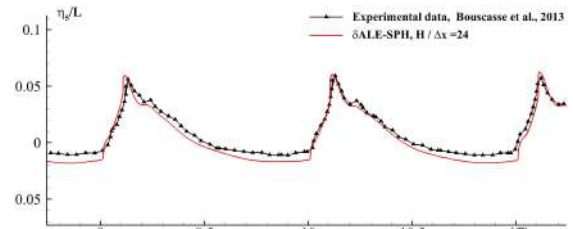


Figure 15. Time evolutions of the fluid surface elevation measured at $x/L = 0.05$. The results of δALE-SPH is compared against the experimental data [2].

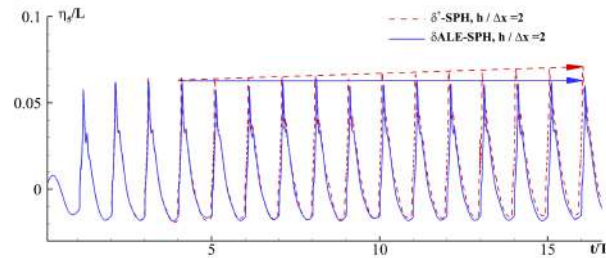


Figure 16. Time evolutions of the fluid surface elevation measured at $x/L = 0.05$. The results of δ^+ -SPH and δALE-SPH are compared.

In order to demonstrate the effect of the ALE formulation when the PST is implemented in a violent free surface flow, in the second simulation, δ^+ -SPH is simply applied for the same sloshing problem to show its difference with respect to δALE-SPH. As stated in [4], in the δ^+ -SPH model, due to the shifting

of the particle position close to the free surface and the solid wall, the momentum conservations cannot be strictly maintained. Therefore inconsistency gradually develops in a long duration simulation. This inconsistency can be demonstrated from the time evolution of the free surface elevation at $x/L = 0.05$. In Figure 16, time evolutions of the surface elevation of both the δ^+ -SPH and δ ALE-SPH are compared in long time duration. When $t/T \leq 5$, the results of the two solvers almost coincide. However, due to the cumulation of the errors in δ^+ -SPH, during $t/T > 5$, the surface is gradually raised up due to the over gaining of the potential energy after using PST.

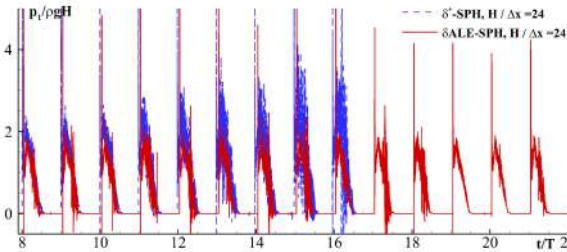


Figure 17. Time evolutions of the pressure measured on the side wall with a height equal to the still water depth. The results of δ^+ -SPH and δ ALE-SPH with mass treatment 1 are compared.

A further comparison is made in Figure 17 for the pressure evolutions measured on the side wall with a height equal to the still water depth $H = 0.03m$, see the pressure probe p_1 in Figure 14. It is shown that δ ALE-SPH model always gives the impact pressure with similar peak pressure in each period. This behaviour agrees well with the one predicted by the δ -SPH model which has shown its superiority in solving sloshing problems [2]. However, when $t/T > 8$, δ^+ -SPH failed in correctly predicting the impact pressure due to inconsistency introduced by PST. In conclusion, the present comparison clearly shows the effect of the ALE formulation in maintaining the conservation and consistency properties when a particle shifting is imposed.

IV. CONCLUSIONS

In the present work, PST and ALE formulations are combined in the framework of δ -SPH scheme. Differently to the simple application of PST into δ -SPH (δ^+ -SPH scheme), when the ALE formulation is considered, mass and momentum flux between the particle pairs makes the scheme more sensitive to stability problems. Therefore, special attention has been paid to the treatment on the free surface and solid wall, and the consideration of the mass corrections in the mass flux equation. Benchmark cases are employed to show the improvements of δ ALE-SPH with respect to δ^+ -SPH.

The δ ALE-SPH scheme further improves the consistency and momentum conservation when PST is adopted to regularize the particle positions. Through the test of the Taylor-Green flow, δ ALE-SPH scheme is shown to be able to correctly predict the pressure decay on the center of the fluid. From the test of rotating square fluid patch, it is shown that the conservation of angular momentum is significantly improved than in the results of δ^+ -SPH. In the shallow water sloshing test, for a long term simulation, the δ ALE-SPH scheme avoids the non-physical free surface rising up and gives a correct prediction of the impact pressure.

The δ ALE-SPH scheme with mass treatment 1 or 2 supplies a nearly homogeneous volume or mass distribution. Through the test of flow past an inclined elliptical cylinder, it is shown that due to the strong vortex motion in the long duration simulation, the mass or volume distribution can be quite disordered if no numerical term is adopted in the mass flux equation. The mass diffusion (the mass treatment 2) is similar to the density diffusion adopted in the δ -SPH scheme, and the former has been shown to effectively regularize the mass distributions. In the mass treatment 1, the mass flux is blocked to be zero (a constant mass constrain), but it gives the most satisfactory numerical results. The mechanism behind this behavior is still an ongoing research and will be discussed in detail in the future articles.

ACKNOWLEDGEMENT

This work has been funded by: the National Natural Science Foundation of China (Grant No. U1430236) and the PhD Student Research and Innovation Fund of the Fundamental Research Funds for the Central Universities (Grant No. HEUGIP201701), to which the authors are most grateful.

REFERENCES

- [1] Marrone, S., Antuono, M., Colagrossi, A., Colicchio, G., Le Touzé, D., Graziani, G. δ -SPH model for simulating violent impact flows. Computer Methods in Applied Mechanics and Engineering. 2011, 200, 1526-42.
- [2] Bouscasse, B., Antuono, M., Colagrossi, A., Lugni, C. Numerical and Experimental Investigation of Nonlinear Shallow Water Sloshing. International Journal of Nonlinear Sciences & Numerical Simulation. 2013, 14, 313-71.
- [3] Zhang, A.-m., Sun, P.-n., Ming, F.-r., Colagrossi, A. Smoothed particle hydrodynamics and its applications in fluid-structure interactions. Journal of Hydrodynamics, Ser. B. 2017, 29, 187-216.
- [4] Sun, P., Colagrossi, A., Marrone, S., Zhang, A. The δ plus-SPH model: simple procedures for a further improvement of the SPH scheme. Computer Methods in Applied Mechanics and Engineering. 2017, 315, 25-49.
- [5] Antuono, M., Bouscasse, B., Colagrossi, A., Marrone, S. A measure of spatial disorder in particle methods. Computer Physics Communications. 2014, 185, 2609-21.
- [6] Sun, P., Colagrossi, A., Marrone, S., Zhang, A. Detection of Lagrangian Coherent Structures in the SPH framework. Computer Methods in Applied Mechanics and Engineering. 2016, 305, 849-68.
- [7] Oger, G., Marrone, S., Le Touzé, D., De Leffe, M. SPH accuracy improvement through the combination of a quasi-Lagrangian shifting transport velocity and consistent ALE formalisms. Journal of Computational Physics. 2016, 313, 76-98.
- [8] Lind, S., Xu, R., Stansby, P., Rogers, B.D. Incompressible smoothed particle hydrodynamics for free-surface flows: A generalised diffusion-based algorithm for stability and validations for impulsive flows and propagating waves. Journal of Computational Physics. 2012, 231, 1499-523.
- [9] Antuono, M., Colagrossi, A., Marrone, S., Molteni, D. Free-surface flows solved by means of SPH schemes with numerical diffusive terms. Computer Physics Communications. 2010, 181, 532-49.
- [10] Adami, S., Hu, X., Adams, N.A. A transport-velocity formulation for smoothed particle hydrodynamics. Journal of Computational Physics. 2013, 241, 292-307.
- [11] Khayyer, A., Gotoh, H., Shimizu, Y. Comparative study on accuracy and conservation properties of two particle regularization schemes and proposal of an optimized particle shifting scheme in ISPH context. Journal of Computational Physics. 2017, 332, 236-56.
- [12] Marrone, S., Colagrossi, A., Le Touzé, D., Graziani, G. Fast free-surface detection and level-set function definition in SPH solvers. Journal of Computational Physics. 2010, 229, 3652-63.
- [13] Rossi, E., Colagrossi, A., Bouscasse, B., Graziani, G. The Diffused Vortex Hydrodynamics Method. Communications in Computational Physics. 2015, 18, 351-79.
- [14] Le Touzé, D., Colagrossi, A., Colicchio, G., Greco, M. A critical investigation of smoothed particle hydrodynamics applied to problems with free - surfaces. International Journal for Numerical Methods in Fluids. 2013, 73, 660-91.

An Enhanced ISPH-SPH Coupled Method for Incompressible Fluid-Elastic Structure Interactions

Abbas Khayyer, Hitoshi Gotoh

Department of Civil and Earth Resources Engineering
Kyoto University
Kyoto, Japan
khayyer@particle.kuciv.kyoto-u.ac.jp

Yuma Shimizu, Hosein Falahaty

Department of Civil and Earth Resources Engineering
Kyoto University
Kyoto, Japan

Abstract—An enhanced fully Lagrangian computational method is developed for simulation of interactions in between incompressible fluid flows and deformable elastic structures. The developed computational method corresponds to a novel coupled solver based on Smoothed Particle Hydrodynamics (SPH). A projection-based Incompressible SPH (ISPH) fluid model is coupled with a SPH-based structure model in a mathematically-physically consistent manner via a careful attention to the mathematical concept of projection-based particle methods, i.e. Helmholtz-Leray decomposition. The fluid model is founded on the solution of Navier-Stokes and continuity equations, while the structure model is based on conservation laws for linear and angular momenta corresponding to an isotropic elastic solid. A set of previously developed enhanced schemes are incorporated for the ISPH fluid model. Hence, the developed coupled method is referred to as enhanced ISPH-SPH. Performance of the structure model is first verified in reproduction of the dynamic response of a cantilever elastic plate and then the enhanced ISPH-SPH is validated through simulation of Fluid-Structure Interaction (FSI) problems including dam break with elastic gate, high speed impact of an elastic aluminum wedge on undisturbed water free surface and hydroelastic slamming of marine panel. To the best of our knowledge, the paper presents the first semi-implicit/explicit ISPH-SPH coupled method for FSI related to deformable elastic structures.

I. INTRODUCTION

The dynamics of complex systems dominated by violent Fluid-Structure Interactions (FSI) have been always of great interest in a variety of fields of engineering (e.g. hydrodynamic slamming on marine vessels, tsunami/storm surge impact on onshore structures, sloshing in liquid containers, etc.). Indeed, advancement of techniques for scrupulous, comprehensive and (mathematically-physically) consistent modeling of FSI problems can present magnificent contributions to various industrial subjects.

In the view of intrinsic difficulties usually encountered in numerical modeling of the most challenging FSI problems (e.g. existence of violent free-surface flows as well as presence of large/abrupt hydrodynamics loads and consequently large structural deformations), Lagrangian meshfree methods (e.g. Smoothed Particle Hydrodynamics

[1, 2] or Moving Particle Semi-implicit [3]) appear to be appropriate candidates for computational modeling of such important phenomena. Consequently, in several studies, simulations of FSI problems were targeted using meshfree methods [4-9]. In particular, a number of fully Lagrangian SPH-based coupled FSI solvers have been developed during the last decade [4-6]. However, to the best knowledge of authors, most of the coupled SPH-based FSI solvers have been founded on fully explicit computations in which the stability of calculations is guaranteed through incorporation of numerical stabilizers that often require tuning and usually result in an unphysical gap in between fluid and structure.

In this study, a projection-based particle method, namely Incompressible SPH (ISPH) [10], is coupled with a newly developed SPH-based structure model in a mathematically-physically consistent manner via a careful attention to the mathematical concept of Helmholtz-Leray decomposition [11]. The ISPH-based fluid model is founded on the solution of Navier-Stokes and continuity equations, while the SPH-based structure model is based on conservation laws for linear and angular momenta corresponding to an isotropic elastic solid. A set of previously developed enhanced schemes are incorporated in the ISPH fluid model. Hence, hereafter the developed coupled method is referred to as Enhanced ISPH-SPH.

At first, the performance of the SPH-based structure model is validated through calculation of the dynamic response of a free oscillating cantilever plate [12]. Then the SPH-based structure model is coupled with enhanced ISPH fluid model in reproduction of a number of violent benchmark test cases including dam break with elastic gate [4] high speed impact of an elastic beam on undisturbed water free surface [6, 13] and hydroelastic slamming of a marine panel corresponding to the experiments [14,15,16].

II. NUMERICAL METHOD

A. Fluid Model

Fluid model is founded on the solution of Navier-Stokes and continuity equations (Eqs. 1 and 2) in the framework of projection-based ISPH method. The Navier-Stokes equation is expressed as:

$$\left(\frac{D\mathbf{u}}{Dt} \right)_F = - \left(\frac{\nabla p}{\rho} \right)_F + v_F \nabla^2 \mathbf{u}_F + \mathbf{g} + \mathbf{F}_{S \text{ to } F} \quad (1)$$

where D/Dt stands for Lagrangian time derivative, ρ_F represents fluid density, t stands for time, \mathbf{u} denotes particle velocity vector, p symbolizes particle's pressure, \mathbf{g} signifies gravitational acceleration and v_F represents laminar kinematic viscosity; $\mathbf{F}_{S \text{ to } F}$ corresponds to the interaction force imposed by the neighbouring structure particles (S) to fluid target particle (F).

The continuity is imposed by projecting the intermediate velocity field into velocity divergence free condition (Eq. 2) via Poisson Pressure Equation.

$$\nabla \cdot \mathbf{u}_F = 0 \quad (2)$$

The fluid model benefits from a set of enhanced schemes, i.e. Corrected Incompressible SPH (CISPH); Higher-order Source term of PPE (HS); Higher-order Laplacian model (HL); Error Compensating Source term of PPE (ECS); Gradient Correction (GC); and Dynamic Stabilization (DS). Also, a 5th order Wendland kernel [17] is utilized. A comprehensive description is presented for the aforementioned schemes in [18] and [19].

B. Structure Model

The structure model is configured according to SPH-based discretization of equations of conservation of linear and angular momenta in Lagrangian form (Eqs. 3 and 10). The equation for conservation of linear momentum is described as (according to Hooke's law):

$$\left(\frac{D\mathbf{u}}{Dt} \right)_S = - \frac{1}{\rho_S} \nabla \cdot \boldsymbol{\sigma}_S + \mathbf{F}_{F \text{ to } S} + \mathbf{g} \quad (3)$$

$$\boldsymbol{\sigma}_S = \lambda_S \text{tr}(\boldsymbol{\varepsilon}_S) \mathbf{I} + 2\mu_S \boldsymbol{\varepsilon}_S \quad (4)$$

where ρ_S stands for density of structure particle, $\boldsymbol{\sigma}_S$ represents the stress tensor of structure particle, $\boldsymbol{\varepsilon}$ is strain tensor, $\mathbf{F}_{F \text{ to } S}$ corresponds to the interaction force acting on interface from fluid (F) to structure (S) particles and \mathbf{I} is the unit tensor. In Eq. (4), λ_S and μ_S are Lame's constants, i.e. mechanical properties of the material calculated from Young's modulus E_S and the Poisson's ratio ν_S .

The SPH-based discretization of the divergence of stress is carried out as follows:

$$\begin{aligned} \frac{1}{\rho_i} \langle \nabla \cdot (\lambda_S \text{tr}(\boldsymbol{\varepsilon}) \mathbf{I}) \rangle_i \\ = \lambda_S \sum_j \frac{m_j}{\rho_i \rho_j} (\text{tr}(\boldsymbol{\varepsilon}_i) \mathbf{I} + \text{tr}(\boldsymbol{\varepsilon}_j) \mathbf{I}) \cdot \nabla_i w_{ij}^0 \end{aligned} \quad (5)$$

$$\frac{1}{\rho_i} \langle \nabla \cdot (2\mu_S \boldsymbol{\varepsilon}) \rangle_i = 2\mu_S \sum_j \frac{8m_j}{(\rho_i + \rho_j)^2} \mathbf{s}_{ij} \frac{\mathbf{r}_{ij} \cdot \nabla_i w_{ij}^0}{|\mathbf{r}_{ij}| |\mathbf{r}_{ij}^0|} \quad (6)$$

where components of strain tensor $\boldsymbol{\varepsilon}$ are defined as:

$$\boldsymbol{\varepsilon}_{\eta\zeta} = -\frac{1}{2} \left(\frac{\partial s_\eta}{\partial r_\zeta} + \frac{\partial s_\zeta}{\partial r_\eta} \right) \quad (7)$$

and subscripts i and j represent target particle and its neighbouring (structure) particles, respectively. Superscript "0" denotes the values evaluated with respect to reference configuration, m represents the mass of particle and η and ζ correspond to spatial coordinates; \mathbf{s}_{ij} stands for pure elastic deformation (with exclusion of rigid body rotation) of position vector \mathbf{r}_{ij} , which is described as follows:

$$\mathbf{s}_{ij} = \mathbf{r}_{ij} - 0.5 (\mathbf{R}_j \mathbf{r}_{ij}^0 + \mathbf{R}_i \mathbf{r}_{ij}^0) \quad (8)$$

$$\mathbf{R}_i = \begin{bmatrix} \cos \theta_i & -\sin \theta_i \\ \sin \theta_i & \cos \theta_i \end{bmatrix} \quad (9)$$

where \mathbf{R} is the rigid body rotation tensor while θ is updated at each time step from the solution of the following equation of conservation of angular momentum:

$$I_i \frac{\partial \boldsymbol{\omega}_i}{\partial t} = 2\mu_S \frac{m_i}{\rho_i} \sum_j \frac{1}{2} \mathbf{R}_i \mathbf{r}_{ij}^0 \times \mathbf{s}_{ij} \frac{\mathbf{r}_{ij} \cdot \nabla_i w_{ij}^0}{|\mathbf{r}_{ij}| |\mathbf{r}_{ij}^0|} \quad (10)$$

In the above equation I , $\boldsymbol{\omega}$ represent moment of inertia and angular velocity vector, respectively.

C. Fluid-Structure Coupling Scheme

Fluid-structure coupling is set in a mathematically-physically consistent manner by considering the prediction-correction feature of projection-based particle methods, via extension of the linear momentum equation (Eq. 1) all over the surrounding particles of the interface. In other words, structure particles are considered as a moving boundary for the fluid. After the computation of fluid's pressure field, the interaction term $\mathbf{F}_{F \text{ to } S}$ is imposed to the structure particles based on the pressure gradient at the fluid-structure interface (Fig. 1). Therefore, the interface boundary conditions in between fluid and structure ([4] and [20]), i.e.

$$\begin{aligned} \mathbf{u}_S &= \mathbf{u}_F \\ \boldsymbol{\sigma}_S \mathbf{n}_S &= -\boldsymbol{\sigma}_F \mathbf{n}_F \end{aligned} \quad (11)$$

are satisfied automatically, where, \mathbf{n}_S and \mathbf{n}_F are normal vectors to structure and fluid interface particles, respectively.

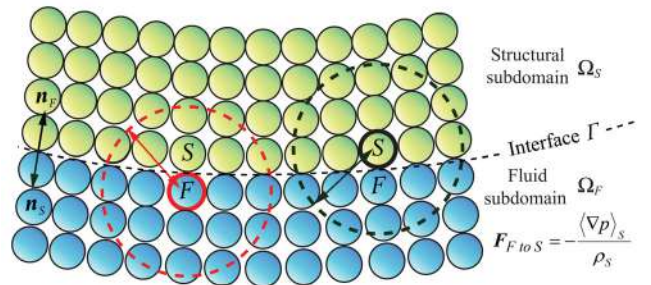


Figure 1 Schematic sketch of fluid-structure coupling scheme [4, 20]

III. VERIFICATION

A. Free Oscillations of Cantilever Elastic Plate

The performance of SPH-based structure model is firstly verified in reproduction of the dynamic response of a free oscillating cantilever rubber plate subjected to an initial velocity distribution of $v(x)$ as for principal mode of vibration [12], (**Fig. 2a**). In Fig. 2(a), parameter c stands for sound speed; k is the wave number while for principal mode of vibration, $kl = 1.875$.

Fig. 2(b) demonstrates a snapshot corresponding to stress field simulated by the SPH-based structure model. From Fig. 2(b), the stress field reproduced by the structure model appears to be smooth and qualitatively consistent. From **Fig. 2(c)**, the simulated time history of deflection of the plate's free end is shown to be in a good agreement with the analytical solution.

B. Dam Break with Elastic gate

The proposed Enhanced ISPH-SPH FSI solver is implemented into simulation of dam break impacting elastic gate [4].

The initial setup of the dam break benchmark test consist of a water column of 0.14 m height isolated by a vertical gate. The gate is composed of two part; rigid upper part and lower elastic part with the length of 0.079 m. The elastic gate is of 0.005 m thickness with the Young's modulus and Poisson's ratio of 12 MPa and 0.4, respectively. The water has a density ρ_F and kinematic viscosity ν_F of 1000 kg/m³ and 1.0×10^{-6} m²/s, respectively. The initial particle spacing was set as $d_0 = 0.001$ m.

Fig. 3 indicates the snapshots corresponding to the simulation of dam break with elastic gate using Enhanced ISPH-SPH FSI solver. According to **Fig. 3**, the Enhanced ISPH-SPH solver has performed well in reproducing the stress/pressure fields. As can be seen, the Enhanced ISPH-SPH has produced smooth and stable fields of stress in the structure and pressure in the fluid. Also, the deformation of the elastic structure is well consistent with fluid flow, preventing formation of unphysical gap in between two continuums.

Fig. 4 shows the time histories of the displacement of the free end of elastic gate reproduced by Enhanced ISPH-SPH FSI solver. From **Fig. 4**, it can be seen that ISPH-SPH has provided sufficient level of accuracy in terms of both horizontal and vertical displacements of the free end of elastic gate and the simulated displacements are well consistent with those of experiment.

C. High Speed Impact of Elastic Wedge on Still Water Free Surface

The Enhanced ISPH-SPH FSI solver is employed in the simulation of high speed impact of an elastic aluminum beam wedge with still water surface, for which semi-analytical solutions exist [13].

In the mentioned test case, the deformable beam wedge of the length of $l = 0.6$ m and thickness of $h_e = 0.04$ m directs downward and eventually impacts the free surface with a dead-rise angle of $\theta = 10^\circ$ and a constant velocity of $v = 30$ m/s (v is in vertical direction). According to the theory [13], all the degrees of freedom are restrained at the centre of the wedge as well as the extremities. The Young's modulus and Poisson's ratio of aluminum wedge are set as $E_s = 67.5$ GPa and $\nu_s = 0.34$, respectively.

Figs. 5(a-c) present a set of snapshots of particle distributions together with pressure and stress fields corresponding to simulation of the impact of elastic beam wedge on still water free surface by using Enhanced ISPH-SPH solver. From Figs. 5(a-c), the developed FSI solver has performed well in production of smooth pressure and stress

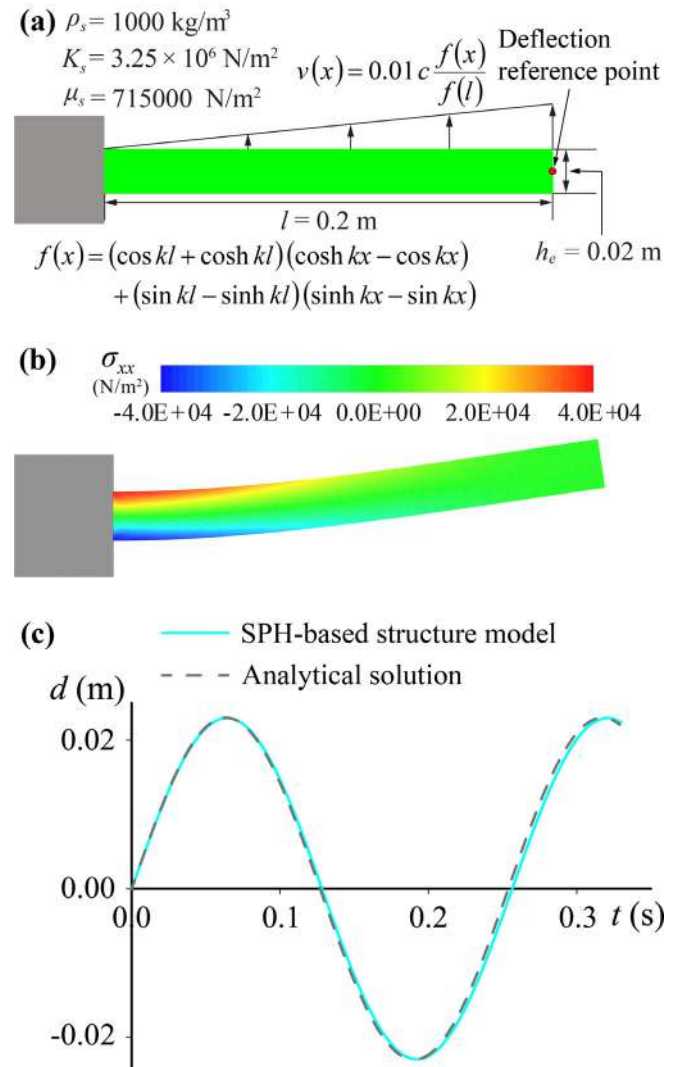


Figure 2 Verification of SPH-based structure model **(a)** set up of the benchmark test [12], **(b)** normal stress σ_{xx} at $t = 0.05$ s **(c)** time history of deflection (d) of plate's free end

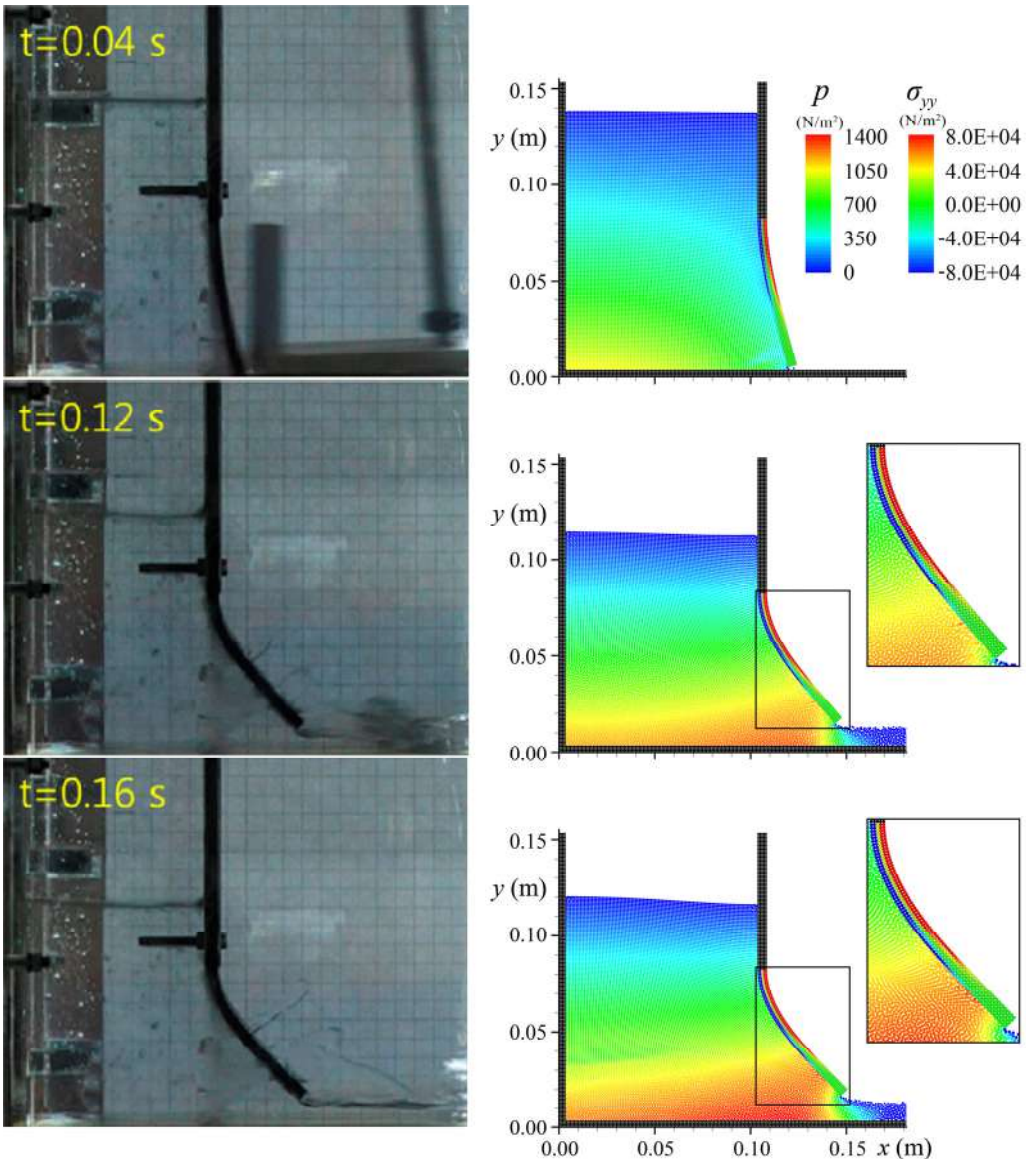


Figure 3 Snapshots corresponding to the stress/pressure fields reproduced by ISPH-SPH FSI solver in simulation of dam break with elastic gate [4]

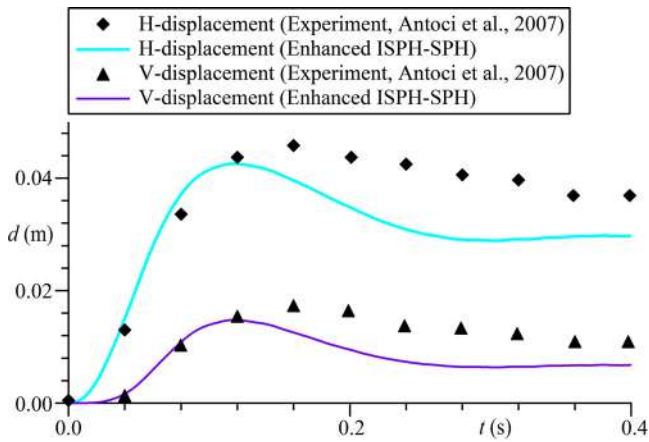


Figure 4 Time histories of horizontal and vertical displacements of the free end of elastic gate [4]

fields without driving unphysical gap in between fluid and structure. **Figs. 5(d-f)** demonstrate the pressure/deflection time histories reproduced by the developed Enhanced ISPH-SPH method in comparison with the semi-analytical solution at several reference points. As it can be seen from Figs. 5(d-f), the reproduced time histories of deflection and pressure are in good agreement with semi-analytical solution.

D. Hydroelastic Slamming of Marine Panels

For further validation of the developed FSI solver, hydroelastic slamming of a marine panel, corresponding to the experiments by Allen [14] and Stenius et al. [15], are considered. These tests were conducted using a Servo-hydraulic Slam Testing System (SSTS) with sets of different panels. In the present study, the hydroelastic slamming

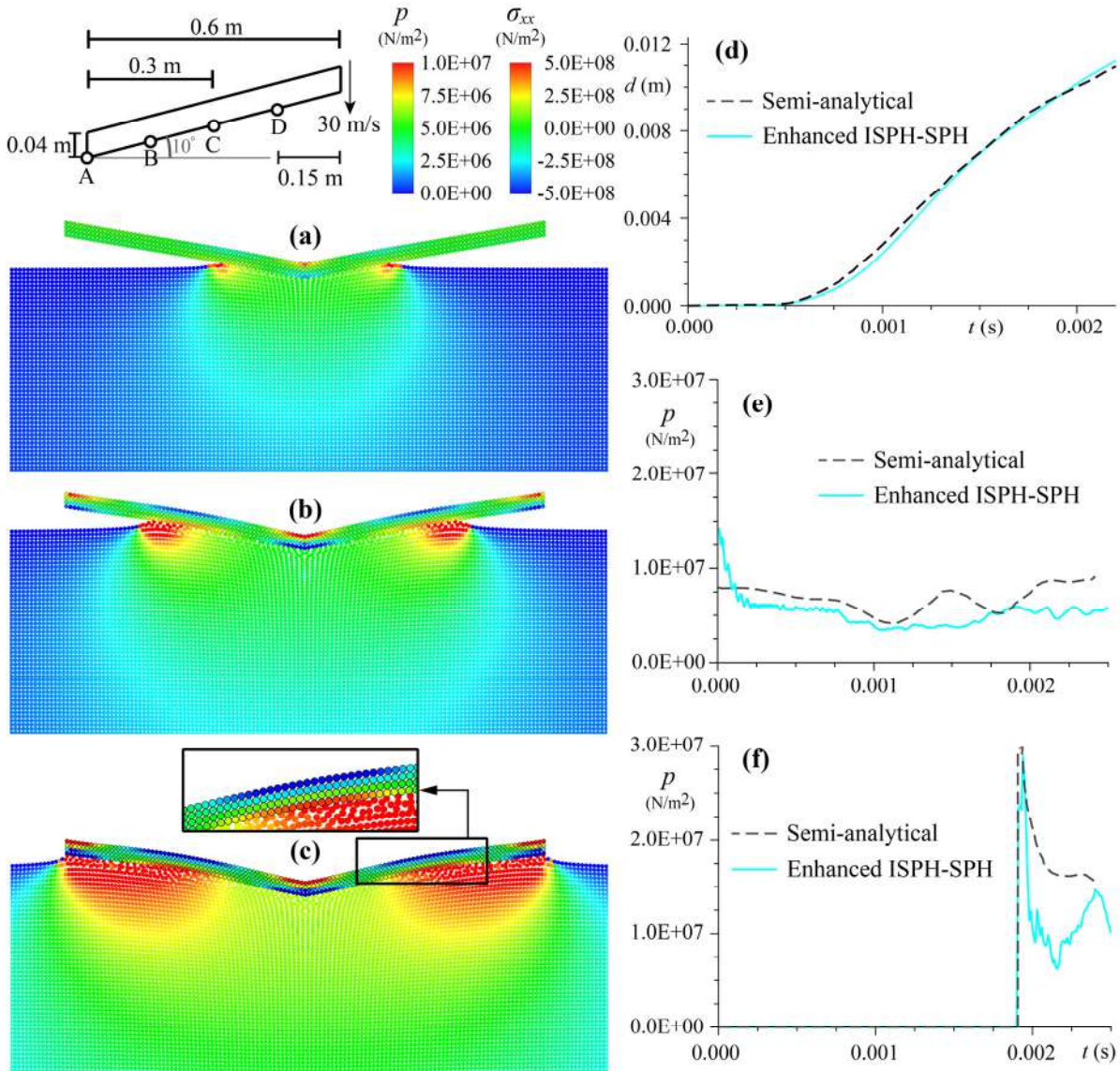


Figure 5 Simulation results by enhanced ISPH-SPH FSI solver corresponding to high speed ($v = 30 \text{ m/s}$) impact of an elastic aluminium beam [6, 13] (a-c) snapshots of particles together with pressure/stress fields at $t = 0.0009 \text{ s}$, $t = 0.0017 \text{ s}$ and $t = 0.0025 \text{ s}$, respectively, and time histories of (d) deflection at reference point C, (e) pressure at reference point A, and (f) pressure at reference point D

corresponding to a Solid Glass-fibre single skin panel [14, 15] are reproduced. The panel is of 1.03 m length, 0.6 m width and 0.0095 m thickness. The bending and shear stiffness are set as 1.52 kNm and $44.0\text{E}+03 \text{ kN/m}$, respectively. The details of the experimental and numerical setup are shown in **Fig. 6**. The hydrodynamic pressure and panel deflections are measured at reference points P3 and D3, respectively.

Figs. 6(a-d) portray typical snapshots corresponding to the SG (Solid Glass-fiber) panel that slams the water surface with a velocity of $v = 4 \text{ m/s}$. From these figures, the Enhanced ISPH-SPH has provided stable pressure/stress fields all through the instants of slamming simulation. The deformation of elastic panel is well consistent with variation

of the free surface configuration at all the instants shown in Figs. 6(a-d). Also, **Figs. 7(a) and (b)** illustrate a quantitative validation by considering time histories of deflection and pressure at reference points D3 and P3. From Fig. 7, the Enhanced ISPH-SPH FSI solver has provided an appropriate level accuracy in reproduction of the results corresponding to a hydroelastic slamming phenomenon [14].

The time history of deflection of elastic panel at reference point D3, for $v = 4 \text{ m/s}$, is well matched with that of experiment. In terms of time history of variations of reproduced pressure field at P3 for the case of $v = 3 \text{ m/s}$, there is an absolute agreement both in terms of magnitude and instant of occurrence for the peak pressure in between

the results by ISPH-SPH FSI solver and experiment. Also, the trend of variation of simulated pressure field at P3 is generally consistent with that of experiment, all through the time history of pressure variation.

IV. CONCLUDING REMARKS

An enhanced fully Lagrangian meshfree computational method is developed for simulation of incompressible fluids interacting with deformable elastic structures. The

developed computational method corresponds to a novel (Smoothed Particle Hydrodynamics)-based Fluid-Structure Interaction (FSI) solver. The developed method comprises of a projection-based semi-implicit Incompressible SPH (ISPH) as the fluid model which is coupled with a SPH-based structure model. The coupling is performed in a mathematically-physically consistent manner via a careful attention to the mathematical concept of Helmholtz-Leray decomposition. In the mentioned coupling procedure, structure particles are considered as a moving

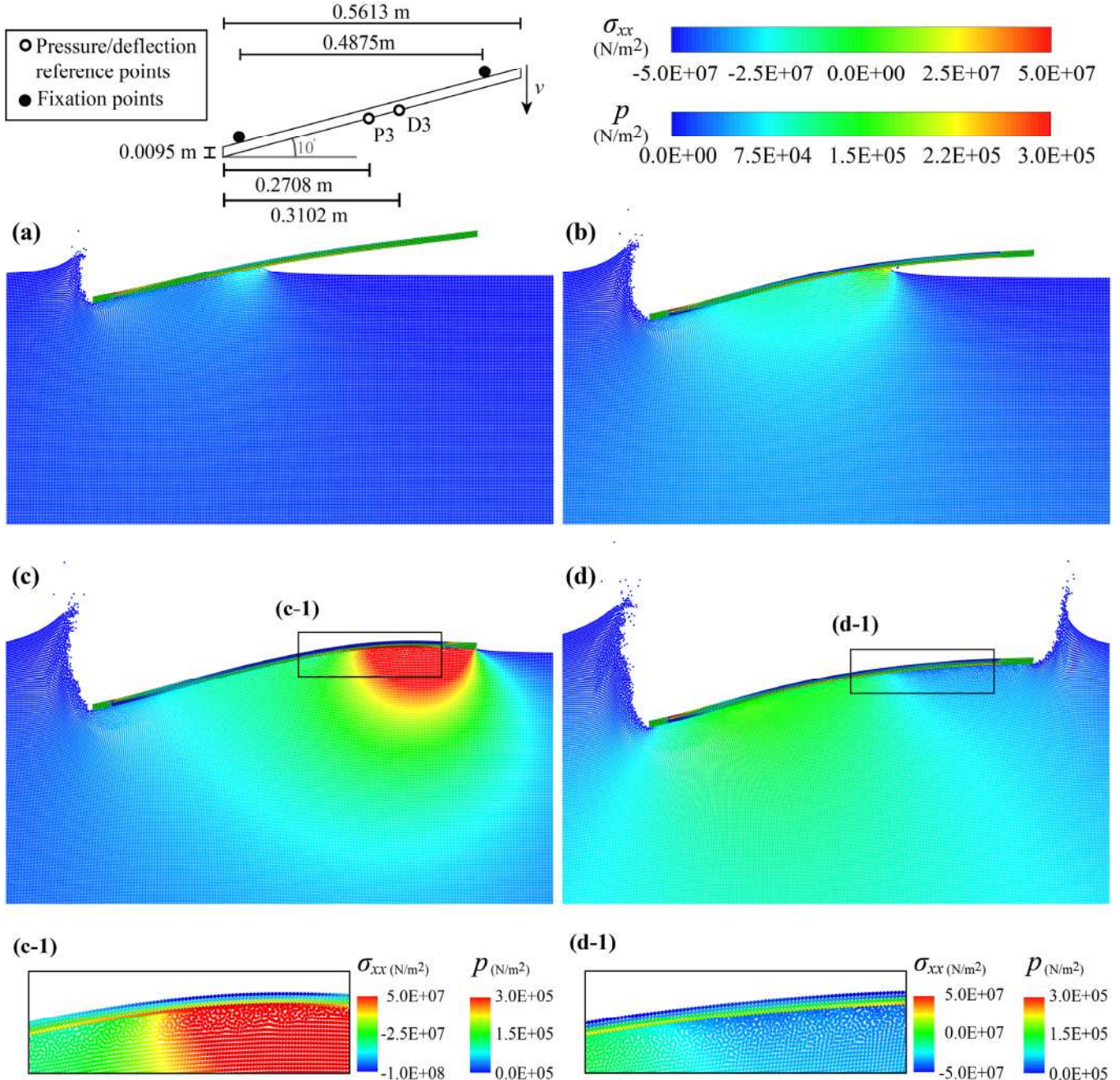


Figure 6 Simulation results by the developed enhanced ISPH-SPH FSI solver corresponding to hydroelastic slamming of a SG panel [14, 15] (a-d) snapshots of particles together with pressure/stress fields for the case of impact velocity $v = 4$ m/s at $t = 0.01$ s, $t = 0.015$ s, $t = 0.020$ s and $t = 0.025$ s, respectively

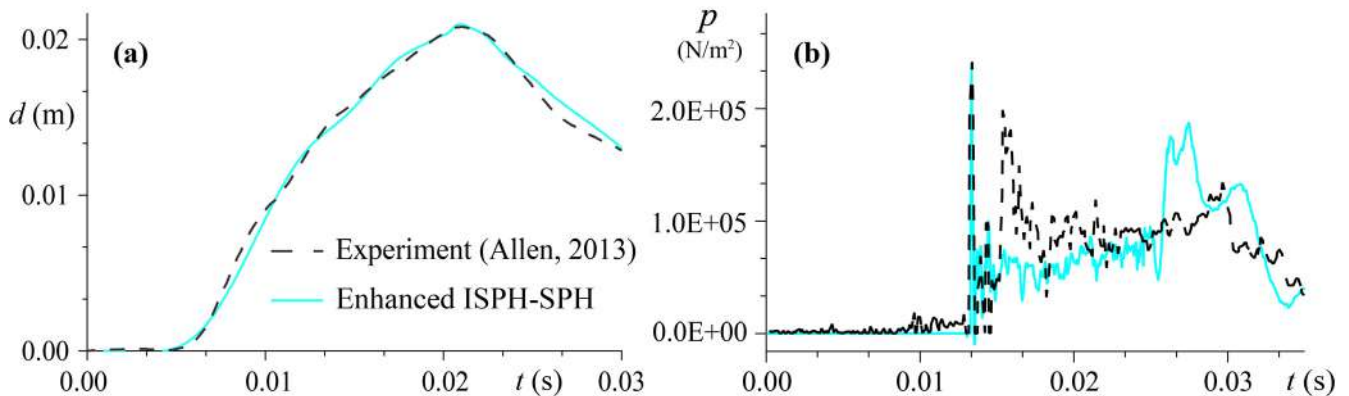


Figure 7 Time histories of (a) deflection (d) at reference point D3 for the case of $v = 4$ m/s (b) pressure (p) at reference point P3 for the case of $v = 3$ m/s, reproduced by enhanced ISPH-SPH FSI solver for slamming of SG panel [14, 15, 16]

boundary for the fluid particles, providing proper velocity/position boundary conditions in calculation of fluid's pressure. In addition, a set of previously developed enhanced schemes are incorporated to improve the accuracy of ISPH fluid model. Thus, the coupled ISPH-SPH FSI solver is referred to as enhanced ISPH-SPH. Unlike most previous studies, the developed FSI solver is free of artificial stress/force for stabilization and stability is guaranteed through the applied coupling scheme as well as fluid's error minimizing schemes that are founded on clear physical/mathematical concepts.

The SPH-based structure model is first validated in simulation of dynamic response of a free oscillating cantilever plate [12]. Then, the enhanced ISPH-SPH FSI solver is applied into simulation of dam break with elastic gate [4], high speed impact of an elastic aluminium beam [13] and hydroelastic slamming of a marine panel [14]. The results of the simulations are evaluated in terms of stability and accuracy. From the presented snapshots, the Enhanced ISPH-SPH has provided acceptable level of stability in reproduction of pressure and stress fields. The accuracy of the proposed method is validated in terms of reproduced pressure and deflection time histories.

Future works comprise of further validations, extension of FSI simulations into multi-phase flows and development of reliable schemes for multi-physics and multi-scale simulations.

REFERENCES

- [1] T. L. B Lucy, "A numerical approach to the testing of fission hypothesis," *Astronom. J.*, vol. 82, pp. 1013-1024, 1977.
- [2] R. A. Gingold, and J. J. Monaghan, "Smoothed particle hydrodynamics: theory and application to non-spherical stars," *Mon. Not. R. Astron. Soc.*, vol. 181, pp. 375-389, 1977.
- [3] S. Koshizuka, and Y. Oka, "Moving-particle semi-implicit method for fragmentation of incompressible fluid," *Nucl. Sci. Eng.*, vol. 123, pp. 421-434, 1996.
- [4] C. Antoci, M. Gallati and S. Sibilla, "Numerical simulation of fluid-structure interaction by SPH," *Comput. Struct.*, vol. 85, pp. 879-890, 2007.
- [5] A. Rafiee and K. P. Thiagarajan, "An SPH projection method for simulating fluid-hydroelastic structure interaction," *Comput. Methods Appl. Mech. Eng.*, vol. 198, pp. 2785-2795, 2009.
- [6] G. Oger, L. Brosset, P. M. Guilcher, E. Jacquin, J. B. Deuff and D. Le Touzé, "Simulations of hydro-elastic impacts using a parallel SPH model," *International Journal of Offshore and Polar Engineering*, vol. 20(3), pp. 181-189, 2010.
- [7] S. C. Hwang, A. Khayyer, H. Gotoh, and J. C. Park, "Development of a fully Lagrangian MPS-based coupled method for simulation of fluid-structure interaction problems," *J. Fluids Struct.*, vol. 50, pp. 497-511, 2014.
- [8] S. C. Hwang, J. C. Park, H. Gotoh, A. Khayyer and K. J. Kang, "Numerical simulations of sloshing flows with elastic baffles by using a particle-based fluid-structure interaction analysis method," *Ocean Eng.*, vol. 118, pp. 227-241, 2016.
- [9] A. Khayyer, H. Falahaty, H. Gotoh and T. Koga, "An Enhanced coupled Lagrangian solver for incompressible fluid and non-linear elastic structure interactions," *Journal of JSCE (Coastal Eng.)*, vol. 72(2), pp. 1117-1122, 2016.
- [10] S. Shao and E. Y.M. Lo, "Incompressible SPH method for simulation of Newtonian and non-Newtonian flows with a free surface," *Adv. Water Resour.*, vol. 26, pp. 787-800, 2003.
- [11] C. Foias, O. Manley, R. Rosa and R. Temam, *Navier-Stokes Equations and Turbulence*, Cambridge University Press, ISBN: 978-0511546754, 2001, 364 pp.
- [12] J. P. Gray, J. J. Monaghan and R. P. Swift, "SPH elastic dynamics," *Comput. Meth. Appl. Mech. Engrg.*, vol. 190, pp. 6641-6662, 2001.
- [13] Y. M. Scolan, "Hydro-elastic behavior of a conical shell impacting on a quiescent-free surface of an incompressible liquid," *Journal of Sound and Vibration*, vol. 277, pp 163-203, 2004.
- [14] T. Allen, "Mechanics of flexible composite hull panels subjected to water impacts," a dissertation for Doctoral of Philosophy in Mechanical Engineering, University of Auckland, 2013.
- [15] I. Stenius, A. Rosén, M. Battley and T. Allen, "Experimental hydroelastic characterization of slamming loaded marine panels," *Ocean Eng.*, vol. 74, pp. 1-15, 2013.
- [16] M. Battley, T. Allen, P. Pehrson, I. Stenius and A. Rosen, "Effects of panel stiffness on slamming responses of composite hull panels," In: 17th International Conference on Composite Materials, Edinburgh International Convention Centre (EICC), Edinburgh, UK, 2009.
- [17] H. Wendland, "Piecewise polynomial, positive definite and compactly supported radial functions of minimal degree," *Adv. Comput. Math.*, vol. 4, pp. 389-396, 1995.
- [18] H. Gotoh and A. Khayyer, "Current achievements and future perspectives for projection-based particle methods with applications in ocean engineering," *J. Ocean Eng. Mar. Energy*, vol. 2(3), pp. 251-278, 2016.
- [19] A. Khayyer, H. Gotoh, Y. Shimizu and K. Gotoh, "On enhancement of energy conservation properties of projection-based particle methods," *European Journal of Mechanics B/Fluids*, vol. 66, pp. 20-37, 2017.
- [20] S. Koshizuka, Ryushiho (Particle Method), Maruzen, (in Japanese), 2005, 144 pp.

SPH modeling of fluid-structure interaction

Luhui Han and Xiangyu Hu

Department of Mechanical Engineering
Technical University of Munich

85747 Garching, Germany

Luhui.han@tum.de, Xiangyu.hu@tum.de

Abstract—This work concerns numerical modeling of FSI (fluid-structure interaction) problems in a uniform SPH (smoothed particle hydrodynamics) framework. It combines a transport-velocity SPH scheme advancing fluid motions with a total Lagrangian SPH formulation dealing with the structure deformations. Since both fluid and solid governing equations are solved in SPH framework, coupling becomes straightforward and meanwhile the momentum of the FSI system is strictly conservative. A well-known FSI benchmark test case has been performed to validate the modeling and demonstrate its potential.

I. INTRODUCTION

Fluid-structure interaction (FSI) can be found in many natural phenomena, such as birds flying and fish swimming. Meanwhile, it also plays a very important role in the design of many engineering systems, e.g. aircraft, engines and bridges. Although their mechanical behaviors are quite different, essentials of them are interactions of some movable or deformable structures with internal or surrounding fluid flows [1].

Since FSI problems usually involve flow nonlinearity and multi-physics, which are too complex to solve analytically, they have to be analyzed by means of experiments or numerical simulations, and the maturity of computational fluid dynamics (CFD) and computational solid dynamics (CSD) in past decades enables it [2]. Accordingly, a small number of numerical approaches have already been developed, such as the space-time finite-element method (FEM) [3] and arbitrary Lagrangian Eulerian formulation (ALE) [4]. Because all of these mesh-based methods discretize the domain into individual meshes, they have to take significant efforts on mesh generation to prevent the occurrence of severe mesh distortion [5]. In comparison to conventional mesh-based methods, particle-based meshless methods are intended to approximate mathematic equations in the domain only by nodes (particles) without being connected by meshes [6]. Typical meshless methods, which have already been used successfully in solving FSI, are coupled models like SPH-DEM (Smoothed particle hydrodynamics and Discrete Element Method) [6] and LBM-DEM (Lattice Boltzmann Method) [7]. A common advantage of all these meshless methods is that the identification of moving interfaces and deformable boundaries can be handled straightforwardly [8],

nevertheless these coupled methods for FSI are still limited for more general applications. They both chose partitioned solution in the form of “CFD-CSD” by using different discretization schemes to simulate the separate behaviors of fluid and structure, and usually require elaborate consideration for the momentum conservation at fluid-structure interfaces.

SPH technique was first developed in astrophysics by Lucy [9] and by Gingold and Monaghan [10], and has recently been adapted to many relevant engineering problems, including heat and mass transfer, molecular dynamics, fluid and solid mechanics. Owing to both its significant advantages of handling large deformations in a purely Lagrangian frame in simulation of solid dynamics and its great convenience of capturing breaking, merging, and splashing features in free surface flows, Antoci et al. [11] successfully performed an FSI study in a uniform SPH framework. Since the same discretization method allowed for a common description of both the fluid and the solid dynamics in terms of pressure and velocity, both the kinematic and dynamic interface conditions at fluid and solid interfaces became straightforward and easy to implement conservatively. Like in Gray et al.’s work [12], starting from continuum mechanics, the linear elastic relation between stress and deformation tensors was derived from the incremental formulation of Hooke’s law corrected by the Jaumann rate therein. As pointed out in Ref. [11], this relation is rate-independent, incrementally linear and reversible. If it is integrated in time with a conveniently small time step, it can be adopted as a constitutive model when small finite deformations are considered. Other applications by using the same constitutive equation in solving solid dynamics problems can be found in [13, 14]. However, observing their simulation results in [11, 14], one can clearly see that the particle distributions had some sort of shift after a period of simulation. The initial uniformly distributed particles finally formed into another pattern even in areas without stresses. That is because the conventional SPH method has a shortcoming of inconsistency and the fore-mentioned incremental constitutive model is just an approximation of Hooke’s law. To overcome this limit, Vignjevic et al. [15] proposed a total Lagrangian framework for simulating solid dynamics, where Lagrangian kernels were employed directly to solve momentum equation with respect to the reference configuration. Besides, this total Lagrangian formalism takes another advantage of not suffering from tensile instability problems [16].

Inherited from Antoci et al.'s work [11], we proposed a new numerical modeling for FSI problems in this work, where fluid governing equations are discretized with conventional Eulerian kernels in current configuration while solid governing equations are solved with Lagrangian kernels in the reference configuration. Finally, several FSI benchmark test cases have been performed to validate the current uniform SPH modelling and demonstrate its potential.

II. GOVERNING EQUATIONS

A. Fluid equations

The governing equations for the motion of an isothermal, Newtonian fluid in a Lagrangian frame of reference are the continuity equation

$$\frac{d\rho}{dt} = -\rho \nabla \cdot \mathbf{v} \quad (1)$$

and the momentum-conservation equation

$$\rho \frac{d\mathbf{v}}{dt} = -\nabla p + \mathbf{F}^{(v)} + \rho \mathbf{g} \quad (2)$$

with ρ , \mathbf{v} , t , p , $\mathbf{F}^{(v)}$ and \mathbf{g} denoting the density of the fluid, the velocity, the time, the pressure, the viscous force and a body-force, respectively.

Based on the weakly compressible SPH approach [11, 17], which is often used to simulate incompressible flows, a linearized equation of state is introduced to estimate the pressure from the density field via

$$p = c_0^2(\rho - \rho_0), \quad (3)$$

where artificial sound speed $c_0 = \sqrt{\frac{\varepsilon}{\rho_0}}$ with ε denoting the

compressibility of the fluid. In particular, Monaghan [18] suggests that, in order to limit the admissible density variation to 1%, the maximal Mach number, i.e. the ratio between the maximal flow velocity and c_0 , must be lower than 0.1.

Assuming incompressibility of the fluid, the viscous force $\mathbf{F}^{(v)}$ simplifies to

$$\mathbf{F}^{(v)} = \eta \nabla^2 \mathbf{v} \quad (4)$$

with the dynamic viscosity η .

B. Structural equations

In this work, the structure is considered to be elastic and compressible. The governing equations for the motion of a structure derive from the balance laws including balance of mass and momentum.

Following the convention in continuum mechanics, the vector \mathbf{X} is used to define the undeformed reference configuration, and vector \mathbf{x} defines the deformed current

configuration. Assuming the initial state corresponds to the undeformed reference state, the displacement \mathbf{u} of a material point, given by the difference between its current position and its original position, can be defined as

$$\mathbf{u} = \mathbf{x} - \mathbf{X}. \quad (5)$$

Thus, the deformation gradient \mathbf{F} , an important variable in the description of body kinematics, can be given by

$$\mathbf{F} = \frac{\partial \mathbf{x}}{\partial \mathbf{X}} = \frac{\partial(\mathbf{X} + \mathbf{u})}{\partial \mathbf{X}} = \mathbf{I} + \frac{\partial \mathbf{u}}{\partial \mathbf{X}} \quad (6)$$

where \mathbf{I} is a 2nd rank identity matrix.

From a total Lagrangian point of view, the balance of mass adopts the algebraic form given by

$$\rho J - \rho^0 = 0 \quad (7)$$

where the Jacobian J is the determinant of \mathbf{F} . Meanwhile, the momentum balance equation is reformed to

$$\rho^0 \frac{d^2 \mathbf{x}}{dt^2} = \nabla^0 \cdot \mathbf{P} + \rho^0 \mathbf{g}. \quad (8)$$

In the above, ρ^0 is the mass density in the reference configuration, and \mathbf{P} is the 1st Piola-Kirchhoff stress tensor. In contrast to the Cauchy stress tensor σ which expresses the stress relative to the current configuration, the 1st Piola-Kirchhoff stress tensor \mathbf{P} relates forces in the current configuration with areas in the reference configuration. Similarly, there is another important stress tensor \mathbf{S} , named by the 2nd Piola-Kirchhoff stress tensor, which relates forces in the reference configuration to areas also in the reference configuration. The relationship among them can be formalized as

$$\mathbf{P} = J \sigma \cdot \mathbf{F}^{-T}, \quad (9)$$

and

$$\mathbf{S} = J \mathbf{F}^{-1} \cdot \sigma \cdot \mathbf{F}^{-T}. \quad (10)$$

According to the knowledge in continuum mechanics, the 2nd Piola-Kirchhoff stress tensor \mathbf{S} is energy conjugate to the Green-Lagrange strain tensor \mathbf{E} and can be obtained by

$$\mathbf{S} = \mathbf{C} : \mathbf{E} \quad (11)$$

where the stiffness tensor, \mathbf{C} , is a 4th rank quantity and can represent any material behavior, isotropic or orthotropic, as long as it is linear, and \mathbf{E} can be evaluated in terms of \mathbf{F} by

$$\mathbf{E} = \frac{1}{2} (\mathbf{F}^T \cdot \mathbf{F} - \mathbf{I}). \quad (12)$$

In particular, for isotropic materials under Hooke's law, (11) simplifies to

$$\mathbf{S} = \lambda \operatorname{tr}(\mathbf{E}) \mathbf{I} + 2\mu \mathbf{E} \quad (13)$$

with Lame coefficients λ and μ . Given a kind of material characterized by the Poisson ratio ν^s ($\nu^s < 0.5$ for a compressible structure) and by the Young modulus E^s , bulk modulus K^s , shear modulus G^s and fore-mentioned Lame coefficients λ and μ can be expressed as

$$K^s = \frac{E^s}{3(1-2\nu^s)}, \quad (14)$$

$$\mu = G^s = \frac{E^s}{2(1+\nu^s)}, \quad (15)$$

$$\lambda = \frac{E^s \nu^s}{(1+\nu^s)(1-2\nu^s)}. \quad (16)$$

Substituting (10), (13) into (9), we finally calculate the 1st Piola-Kirchhoff stress tensor \mathbf{P} in (8) with

$$\mathbf{P} = \mathbf{F}(\lambda \operatorname{tr}(\mathbf{E}) \mathbf{I} + 2\mu\mathbf{E}). \quad (17)$$

III. NUMERICAL MODELLING

In this section, we present our modelling in details. We initialize all our simulations with Cartesian particles using a constant particle spacing Δx . Each particle is assigned a constant mass, which might be different between fluid and structure according to their individual densities. For convenience of explanation, we make some remarks in advance. In the following SPH equations, the labels a and b are used to denote fluid particles while labels i and j indicating structure particles. An identical kernel function is employed for formulating both fluid and structure equations. Smoothing length h is constant in the entire computational domain.

A. SPH discretization for fluid equations

Density evolution equation: The density of a fluid particle a is calculated from a summation over all its neighboring particles by

$$\rho_a = m_a \sum_b W_{ab} + m_a \sum_j W_{aj} \quad (18)$$

where ρ_a and m_a denote the density and mass of particle a , W_{ab} is short for kernel function $W(|\mathbf{r}_{ab}|, h)$ with $\mathbf{r}_{ab} = \mathbf{r}_a - \mathbf{r}_b$. Note that equation (18) allows for density discontinuities across fluid-structure interfaces, and the two terms on the right hand side represent the density contribution from neighbouring fluid and structure particles, respectively.

1) Momentum equation: Considering FSI effects, the momentum-conservation equation (2) for fluid particle a can be reformed to

$$\frac{d\mathbf{v}_a}{dt} = \mathbb{F}_a^{f:p} + \mathbb{F}_a^{f:v} + \mathbb{F}_a^{s:p} + \mathbb{F}_a^{s:v} + \mathbf{g}. \quad (19)$$

Here \mathbb{F}_a^f denotes force per unit mass due to the other fluid particles while \mathbb{F}_a^s due to structure particles. Both of them consist of two parts, resulting from pressure and viscous force respectively, denoted by $\mathbb{F}_a^{f:p}$, $\mathbb{F}_a^{f:v}$, $\mathbb{F}_a^{s:p}$ and $\mathbb{F}_a^{s:v}$.

According to Hu and Adams' work [19], $\mathbb{F}_a^{f:p}$ can be approximated by

$$\mathbb{F}_a^{f:p} = -\frac{1}{m_a} \sum_b (V_a^2 + V_b^2) p_{ab} \nabla_a W_{ab} \quad (20)$$

where the density-weighted inter-particle averaged pressure p_{ab} is formulated by

$$p_{ab} = \frac{\rho_a p_b + \rho_b p_a}{\rho_a + \rho_b}, \quad (21)$$

$\nabla_a W_{ab} = \nabla_a W(\mathbf{r}_{ab}, h)$ is the gradient of the kernel function, V_a and V_b denote the two interacting particle volumes.

Using the inter-particle-averaged shear viscosity

$$\eta_{ab} = \frac{2\eta_a \eta_b}{\eta_a + \eta_b}, \quad (22)$$

the viscous force $\mathbb{F}_a^{f:v}$ can be obtained through

$$\mathbb{F}_a^{f:v} = \frac{1}{m_a} \sum_b \eta_{ab} (V_a^2 + V_b^2) \frac{\mathbf{v}_{ab}}{r_{ab}} \frac{\partial W_{ab}}{\partial r_{ab}}. \quad (23)$$

with $\mathbf{v}_{ab} = \mathbf{v}_a - \mathbf{v}_b$ and $r_{ab} = |\mathbf{r}_{ab}|$ representing the relative velocity and distance between two interacting particles.

Based on the analysis of Turek et al. [20], the boundary condition on the fluid-structure interface can be achieved by exerting a no-slip condition for the flow with moving boundaries. Following the implementation of Adami et al.'s wall boundary condition [21] and assuming the dummy particles in structure region used to mimic the interaction on the fluid-structure interface just coincide with the real structure particles, for each interacting particle pair (a, i) , we can simply approximate the imaging pressure p_i^d and velocity \mathbf{v}_i^d on dummy particle i with

$$p_i^d = p_a, \quad (24)$$

and

$$\mathbf{v}_i^d = 2\mathbf{v}_i - \mathbf{v}_a. \quad (25)$$

Alternatively, one can also choose the same extrapolation scheme proposed in [21] to evaluate them.

Consequently, the forces per unit mass due to structure particles $\mathbb{F}_a^{s:p}$ and $\mathbb{F}_a^{s:v}$ can be given by

$$\mathbb{F}_a^{s:p} = -\frac{1}{m_a} \sum_j (V_a^2 + V_j^2) p_a \nabla_a W_{aj} \quad (26)$$

and

$$\begin{aligned}\mathbb{F}_a^{s,v} &= \frac{1}{m_a} \sum_j \eta_a (V_a^2 + V_j^2) \frac{\mathbf{v}_a - \mathbf{v}_j^d}{r_{aj}} \frac{\partial W_{aj}}{\partial r_{aj}} \\ &= \frac{2}{m_a} \sum_j \eta_a (V_a^2 + V_j^2) \frac{\mathbf{v}_a - \mathbf{v}_j}{r_{aj}} \frac{\partial W_{aj}}{\partial r_{aj}}\end{aligned}\quad (27)$$

Since the negative pressure occurs in the wake in the FSI benchmark cases, which usually leads to particle clumping and void regions during the simulation, one also needs a remedy to solve this tensile instability problem in fluid regions. A number of solutions have already been proposed and validated, such as in Refs. [16, 17]. In this work, we choose transport-velocity scheme exactly the same as that in Ref. [17] (see details therein).

B. SPH discretization for structure equations

Before formulizing the momentum balance equation (8) for structure with SPH approximation, we must make some preparations first. It is well known that the conventional SPH method has a shortcoming of inconsistency, not even zero order consistency [22]. It may not be that important in fluid dynamics, however, it leads to artificial strain and stress in solid dynamics, especially when a rigid coordinate transformation occurs on a structure, where no actual strain and stress should be yielded. To remedy this defect, a correction matrix \mathbf{B}^0 is introduced by

$$\mathbf{B}_i^0 = \left(\sum_j V_j^0 (\mathbf{X}_j - \mathbf{X}_i) \otimes \nabla_i^0 W_{ij} \right)^{-1} \quad (28)$$

where

$$\nabla_i^0 W_{ij} = \frac{\partial W(|\mathbf{r}_{ij}^0|, h)}{\partial r_{ij}^0} \mathbf{e}_{ij}^0 \quad (29)$$

is the gradient of a Lagrangian kernel function. Here we make an important remark that all variables and operators with superscript 0 relate to the reference configuration, i.e. the initial state. Consequently, equations (28) and (29) are only calculated once at the beginning.

Multiplying by the same matrix \mathbf{B}^0 , the deformation gradient \mathbf{F} can be computed with SPH approximation by

$$\mathbf{F}_i = \left(\sum_j V_j^0 (\mathbf{u}_j - \mathbf{u}_i) \otimes \nabla_i^0 W_{ij} \right) \mathbf{B}_i^0 + \mathbf{I}. \quad (30)$$

1) *Density evolution equation:* According to Eq. (7), the density of each structure particle i can be obtained algebraically by

$$\rho_i = \frac{1}{J_i} \rho_i^0 \quad (31)$$

with $J_i = \det(\mathbf{F}_i)$.

2) *Momentum balance equation:* Similar as that in fluids, when considering FSI effects, the momentum balance equation (8) for structure particle i should be reformed with additional terms to

$$\frac{d^2 \mathbf{x}_i}{dt^2} = \mathbb{F}_i^{s:\mathbf{P}} + \mathbb{F}_i^{f:p} + \mathbb{F}_i^{f:v} + \mathbf{g} \quad (32)$$

where $\mathbb{F}_i^{s:\mathbf{P}}$ denotes the acceleration caused by inner stress of a structure. It can be represented by

$$\mathbb{F}_i^{s:\mathbf{P}} = \frac{1}{m_i} \sum_j \left((V_i^0)^2 + (V_j^0)^2 \right) \frac{\mathbf{P}_i \mathbf{B}_i^0 + \mathbf{P}_j \mathbf{B}_j^0}{2} \cdot \nabla_i^0 W_{ij} \quad (33)$$

with the 1st Piola-Kirchhoff stress tensor on particle i being

$$\mathbf{P}_i = \mathbf{F}_i (\lambda \operatorname{tr}(\mathbf{E}_i) \mathbf{I} + 2\mu \mathbf{E}_i). \quad (34)$$

and Green-Lagrange strain tensor

$$\mathbf{E}_i = \frac{1}{2} (\mathbf{F}_i^T \cdot \mathbf{F}_i - \mathbf{I}). \quad (35)$$

Finally, according to the Newton's third law of motion, each structure particle involved in (26) and (27) takes an equal and opposite reaction from the interacting fluid particle, therefore, the forces per unit mass owing to fluid-structure interactions can be given easily by

$$\mathbb{F}_i^{f:p} = -\frac{1}{m_i} \sum_b (V_i^2 + V_b^2) p_b \nabla_i W_{ib}, \quad (36)$$

and

$$\mathbb{F}_i^{f:v} = \frac{2}{m_i} \sum_b \eta_b (V_i^2 + V_b^2) \frac{\mathbf{v}_i - \mathbf{v}_b}{r_{ib}} \frac{\partial W_{ib}}{\partial r_{ib}}. \quad (37)$$

Notice that, the gradient of elastic stress in structures is calculated in the reference configuration within the total Lagrangian formulation, however, the fluid-structure interaction forces must be obtained in the current configuration.

IV. NUMERICAL TEST

In this section, we present the validation results for the well-known 2D benchmark FSI problem, defined by Turek and Hron [20], as shown in the Fig. 1, where the flow passes a fixed circular cylinder with a flexible beam attached to its downstream side. This test model has been frequently used as a large-displacement benchmark validation case for 2D FSI solvers [5, 23].

In Fig. 1, the computational domain is sketched out along with all its geometric parameters. By choosing the cylinder diameter $D = 0.1\text{m}$ as the characteristic length, all other special measurements can be represented by D , such as the domain length $L = 11D$, the domain height $H = 4.1D$, and the length and height of the flexible beam being $l = 3.5D$ and $h = 0.2D$, respectively. Note that, the cylinder centre is located at $C = (0.2D, 0.2D)$ (measured from the

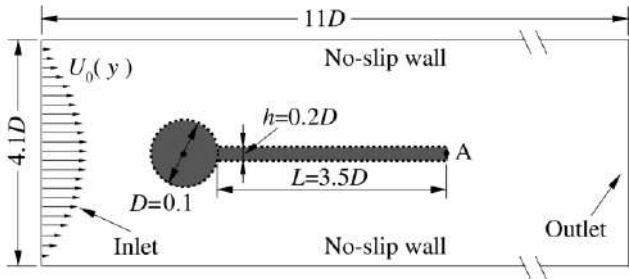


Figure 1. Model setup for flow-induced vibration of a flexible beam attached to a rigid cylinder [5].

left bottom corner of the domain), which is intentionally non-symmetric to prevent the dependence of the onset of any possible oscillation on the precision of the computation [20].

Concerning boundary conditions, no-slip walls are exerted on the top and bottom sides of the domain while outflow condition on the right side. Fluid flows into the domain from the left side with a parabolic velocity profile

$$U_0(y) = 1.5\bar{U} \frac{y(H-y)}{(H/2)^2}, \quad (38)$$

where \$\bar{U}\$ is the mean inflow velocity with the value of 1m/s in this paper. As suggested by Turek and Hron [20], for this kind of non-steady test case, a starting procedure is usually applied by employing a smooth increase of the velocity profile in time as

$$U(t, y) = \begin{cases} \frac{1 - \cos(\pi t / 2)}{2} U_0(y) & \text{if } t < T_s, \\ U_0(y) & \text{otherwise.} \end{cases} \quad (39)$$

where \$T_s\$ denotes the end time of the starting procedure.

With the same configuration shown above, Turek and Hron [20] defined three different test cases FSI1, FSI2 and FSI3 by considering different physical parameters corresponding to Reynolds number Re=20, Re=100 and Re=200, respectively. FSI1 is “simple” and results in a

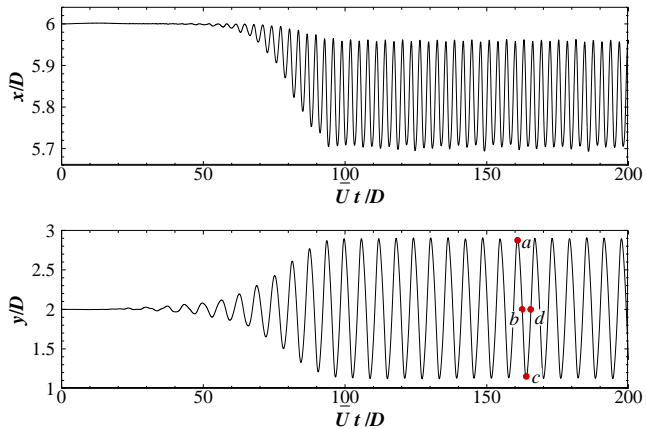


Figure 2. Temporal variation of \$x\$ and \$y\$ displacements of the point A

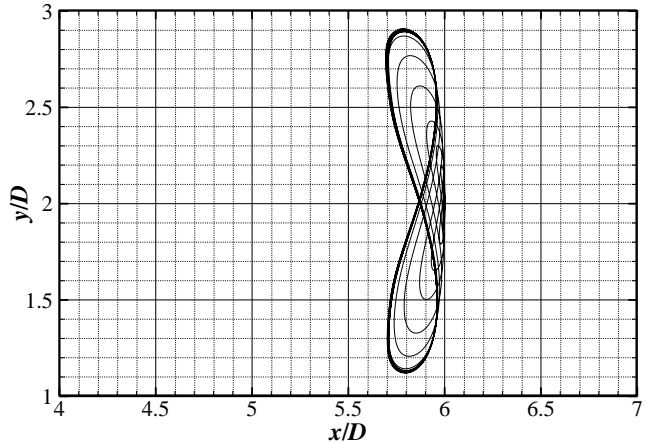


Figure 3. Trajectory of point A

steady state solution while the other two tests (FSI2, FSI3) result in periodic solutions. Because the shear modulus of the beam in FSI3 is four times larger than that in FSI2, the fluid structure interaction in FSI3 seems more like fluid interacting with rigid body. In contrast, FSI2 consists of a more flexible beam and is considered more suitable and challenging as the benchmark test case for the rigorous evaluation of different FSI approaches. Therefore, we just focus on the test of FSI2 in this work. Here, the dimensionless parameters are chosen as follows: density ratio of structure to fluid \$\rho_s / \rho_f = 10\$, Reynolds number \$\text{Re} = \rho_f \bar{U} D / \eta = 100\$, dimensionless Young's modulus \$E^* = E / (\rho_f \bar{U}^2) = 1.4 \times 10^3\$ and Poisson ratio \$\nu^* = 0.4\$. In our simulation, the initial particle spacing is set to be \$\Delta x = 0.05D\$, the artificial sound speed \$c_0 = 20\bar{U}\$, and a Wendland C2 [24] kernel function with a pre-set smoothing length \$h = 1.3 \times \Delta x\$ is used.

The time evolution of the x and y displacements of the free end of the beam (calculated at point A as marked in Fig.1) is shown in Fig.2. According to the y displacement, we can see the beam begins to exhibit small deformations after a dimensionless time of around 20, at which the starting procedure finishes in our simulation. As time goes on, the beam finally reaches a periodic self-sustained oscillation after a dimensionless time of 100. At this moment, an offset along the negative x direction can be clearly observed due to the effect of the beam's bending. Fig.3 presents the trajectory of point A during the simulation, which is a typical Lissajous curve with the frequency ratio of horizontal wave to vertical wave being 2:1.

TABLE I. COMPARISON OF RESULTS FOR FSI2 TEST CASE

Ref.	Amplitude in y direction (\$/D\$)	Frequency \$f_0\$
Turek and Hron [20]	0.83	0.19
Bhardwaj and Mittal [23]	0.92	0.19
Tian et al. [5]	0.784	0.19

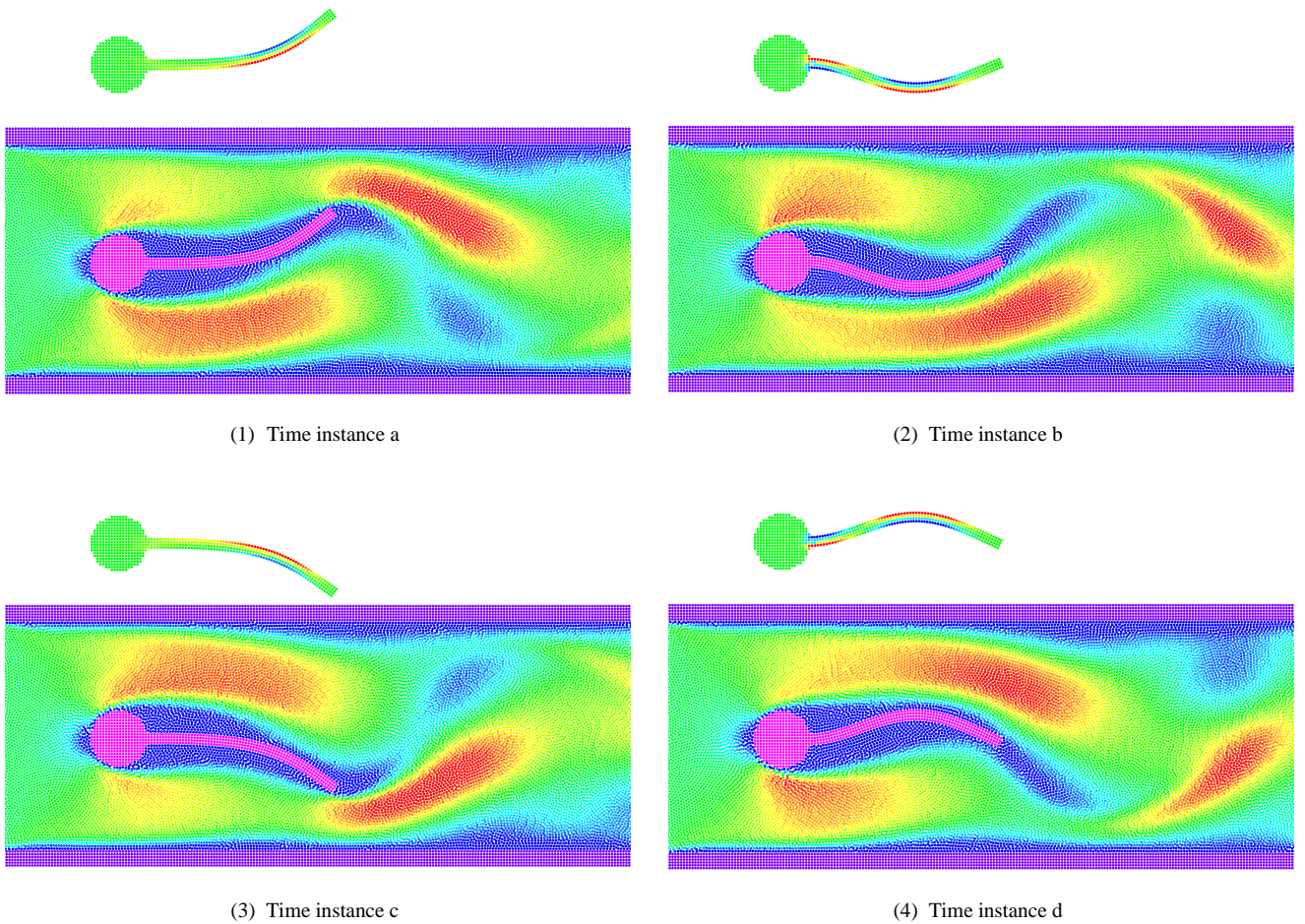


Figure 4. The fluid velocity field and beam deformation at different time instances marked in Fig.2. The top part of each subfigure shows the deformation of the beam with solid particles colored by contours of von Mises stress. The bottom part presents the distribution of axial velocity component of the fluid.

present	0.886	0.168
---------	-------	-------

Table I shows the quantitative comparison of the present results with those in references. The dimensionless amplitude of the oscillation in y direction from our simulation is 0.886, which is in good agreement with others. However, the dimensionless oscillation frequency obtained in this work cannot match well with them. To further validate the present frequency, we perform a resolution convergence study on this test case by decreasing the particle spacing Δx to $0.025D$. Almost the same frequency is observed. To analyse the apparent discrepancy with previous results, we resort to investigate the phenomenon of vortex shedding [25] behind circular cylinders. Based on Roshko's measurements [26], there is a fairly consistent unique linear relationship between the Roshko number and Reynolds number over the Reynolds number range 50~150, which can be formulated by

$$\text{Ro} = 0.212 \text{Re} - 4.5, \quad (40)$$

where Ro denotes Roshko number. According to Eq. (40), we know that the frequency of vortex shedding at $\text{Re}=100$ is 0.167. Since the beam is very flexible in this test case, the oscillation frequency can be mainly dominated by vortex

shedding, which means the oscillation frequency of the beam might also be close to this number. Besides, because our scheme is strictly momentum-conservative in contrast to those in the references, it is expected that the present result can be quite reasonable.

In Fig.4 we show the beam deformation at four different time instances in a typical oscillation cycle. Note that, since there is no elastic stress at the free end of the beam, particles in that region keep regular distribution all the time. This is not able to achieve by the SPH formulation based on Eulerian kernel in current configuration.

V. CONCLUSIONS

In this paper, we have proposed a numerical modelling approach for simulating FSI problems in a uniform SPH framework, where fluid governing equations are discretized with conventional Eulerian kernel in current configuration while solid governing equations with Lagrangian kernel in the reference configuration. To avoid tensile instability in fluid regions, a transport-velocity technique is employed to remedy the distribution of fluid particle. By using a total Lagrangian SPH formulation dealing with the structure

deformations, we also introduce a correction matrix to restore first order consistency and rotational invariance. It successfully avoids the occurrence of artificial strain and stress when a rigid coordinate transformation occurs on structures. Since both fluid and solid governing equations are solved in a uniform SPH framework, coupling becomes straightforward and meanwhile the momentum of an FSI system is strictly conservative. In order to validate the modelling and demonstrate its potential, a typical FSI benchmark test case is carried out.

ACKNOWLEDGEMENT

The authors gratefully acknowledge the financial support by Deutsche Forschungsgemeinschaft (DFG HU1527/6-1) for the present work.

REFERENCES

- [1] Bungartz Hans-Joachim, and Michael Schäfer, eds. Fluid-structure interaction: modelling, simulation, optimisation. Vol. 53. Springer Science & Business Media, 2006.
- [2] Sigmund, Jean-François. Fluid-structure interaction: an introduction to finite element coupling. John Wiley & Sons, 2015.
- [3] Tezduyar, Tayfun E., Sunil Sathe, Ryan Keedy, and Keith Stein. Space-time finite element techniques for computation of fluid-structure interactions. Computer methods in applied mechanics and engineering 195.17 (2006): 2002-2027.
- [4] Ahn, Hyung Taek, and Yannis Kallinderis. Strongly coupled flow/structure interactions with a geometrically conservative ALE scheme on general hybrid meshes. Journal of Computational Physics 219.2 (2006): 671-696.
- [5] Tian, Fang-Bao, Hu Dai, Haoxiang Luo, James F. Doyle, and Bernard Rousseau. Fluid-structure interaction involving large deformations: 3D simulations and applications to biological systems. Journal of computational physics 258 (2014): 451-469.
- [6] Wu, Ke, Dongmin Yang, and Nigel Wright. A coupled SPH-DEM model for fluid-structure interaction problems with free-surface flow and structural failure. Computers & Structures 177 (2016): 141-161.
- [7] Han K, Feng Y.T., Owen D.R. Numerical simulations of irregular particle transport in turbulent flows using coupled LBM-DEM. Computer Modeling in Engineering and Sciences. 2007 Mar;18(2):87.
- [8] Liu GR, Liu MB. Smoothed particle hydrodynamics: a meshfree particle method. World Scientific; 2003.
- [9] Lucy LB. A numerical approach to the testing of the fission hypothesis. Astron J 1977;82:1013–24.
- [10] Gingold RA, Monaghan JJ. Smoothed particle hydrodynamics: theory and application to non-spherical stars. Mon Not R Astron Soc 1977;181:375–89.
- [11] Antoci, Carla, Mario Gallati, and Stefano Sibilla. Numerical simulation of fluid-structure interaction by SPH. Computers & Structures 85.11 (2007): 879-890.
- [12] Gray, J. P., J. J. Monaghan, and R. P. Swift. SPH elastic dynamics. Computer methods in applied mechanics and engineering 190.49 (2001): 6641-6662.
- [13] Chi Zhang, Xiangyu Y. Hu, and Nikolaus A. Adams. A generalized transport-velocity formulation for smoothed particle hydrodynamics. Journal of Computational Physics 337 (2017): 216-232.
- [14] Libersky, Larry D., Albert G. Petschek, Theodore C. Carney, Jim R. Hipp, and Firooz A. Allahdadi. High strain Lagrangian hydrodynamics: a three-dimensional SPH code for dynamic material response. Journal of computational physics 109.1 (1993): 67-75.
- [15] Rade Vignjevic, Juan R. Reveles, and James Campbell. SPH in a total Lagrangian formalism. CMC-TECH SCIENCE PRESS- 4.3 (2006): 181.
- [16] Monaghan, Joseph J. SPH without a tensile instability. Journal of Computational Physics 159.2 (2000): 290-311.
- [17] S. Adami, X. Y. Hu, and Nikolaus A. Adams. A transport-velocity formulation for smoothed particle hydrodynamics. Journal of Computational Physics 241 (2013): 292-307. J.
- [18] Monaghan, Joe J. Simulating free surface flows with SPH. Journal of computational physics 110.2 (1994): 399-406.
- [19] Hu, Xiang Yu, and Nikolaus A. Adams. A multi-phase SPH method for macroscopic and mesoscopic flows. Journal of Computational Physics 213.2 (2006): 844-861.
- [20] S. Turek and J. Hron. Proposal for numerical benchmarking of fluid-structure interaction between an elastic object and laminar incompressible flow. In H.-J. Bungartz and M. Schäfer, editors, Fluid-Structure Interaction: Modelling, Simulation, Optimisation, LNCSE-53. Springer, 2006.
- [21] Adami, S., X. Y. Hu, and N. A. Adams. A generalized wall boundary condition for smoothed particle hydrodynamics. Journal of Computational Physics 231.21 (2012): 7057-7075.
- [22] Javier Bonet, and Sivakumar Kulasegaram. A simplified approach to enhance the performance of smooth particle hydrodynamics methods. Applied Mathematics and Computation 126.2 (2002): 133-155.
- [23] R. Bhardwaj, R. Mittal, Benchmarking a coupled immersed-boundary-finite-element solver for large-scale flow-induced deformation, AIAA J. 50 (2012) 1638–1642.
- [24] Wendland, Holger. Piecewise polynomial, positive definite and compactly supported radial functions of minimal degree. Advances in computational Mathematics 4.1 (1995): 389-396.
- [25] Gaster, Michael. Vortex shedding from circular cylinders at low Reynolds numbers. Journal of Fluid Mechanics 46.4 (1971): 749-756.
- [26] Roshko, Anatol. On the development of turbulent wakes from vortex streets. (1954).

Investigation of Interaction between Solitary Wave and Horizontal Plate based on MPS-FEM Coupled Method

Chengping Rao

State Key Laboratory of Ocean Engineering, School of Naval Architecture, Ocean and Civil Engineering, Shanghai Jiao Tong University, Collaborative Innovation Center for Advanced Ship and Deep-Sea Exploration
Shanghai 200240, China

Decheng Wan*

State Key Laboratory of Ocean Engineering, School of Naval Architecture, Ocean and Civil Engineering, Shanghai Jiao Tong University, Collaborative Innovation Center for Advanced Ship and Deep-Sea Exploration
Shanghai 200240, China

*Corresponding author: dcwan@sjtu.edu.cn

Abstract—This paper is mainly concerned with the problem of wave-plate interaction. To conduct the simulation of the solitary wave interacting with the horizontal plate, the moving particle semi-implicit and finite element coupled method (MPS-FEM) is employed. In this coupled approach, the MPS method is adopted to calculate the fluid domain while the structural domain is solved through the FEM method. In the simulation, the solitary wave with various amplitude is generated in the numerical wave tank and then be compared with the theoretical wave profile. Thereafter the interaction between the solitary wave and the rigid plate is simulated. The wave amplitude, as well as the elevation of the plate above the surface, varies from case to case in order to study its effects on the wave-induced force. The calculated results are compared with the available experimental data. Finally the interaction between the solitary wave and the flexible plate is simulated. The results are contrasted with the counterparts in the former rigid cases to investigate the contribution of the structural flexibility to the wave-induced force.

I. INTRODUCTION

The wave-structure interaction is a hot issue in the field of naval architecture and ocean engineering. The plate structure, such as the pier, jetty or very large floating structure (VLFS), is among the most common structures suffering from the impact of the wave. While encountering severe wave, these offshore or costal structures would produce considerable deformation which will exert a great influence on the flow field nearby, making the problem even more complex. Thus the research on the wave-plate interaction problem is crucial to the design of the offshore or costal structures.

With the development of the high-performance computer, the numerical method is playing a critical role in the research on wave-plate interaction. The numerical simulation can provide researchers with comprehensive information and consume much less resource than the experiment. Liu and Sakai [1] studied the hydroelastic responses of a 2D flexible plate exposed to waves based on

Boundary Element Method (BEM) for fluid and FEM for structure. Liao and Hu [2] combined the Finite Difference method (FDM) with the FEM method to investigate the interaction between surface flow and thin elastic plate. Despite the effectiveness, these mesh-based methods may suffer from the difficulties such as the adjustment or regeneration of mesh while coordinating the interface between fluid and solid domain. Some newly emerged mesh-free methods can exactly overcome the difficulties brought about by the mesh. The Smoothed Particle Hydrodynamics (SPH, Lucy [3]; Monaghan and Gingold [4]) and the MPS (Koshizuka and Oka [5]) are two typical particle-based mesh-free methods. These mesh-free methods display fair adaptation to the problems of large deformation and intense surface because there is no requirement for treatments of mesh or free surface. Although the SPH-FEM model was first proposed by Attaway et al. [6] to investigate the structure-structure interaction, it was subsequently applied into FSI problems by scholars (Antoci et al. [7]; Fourey et al. [8]; Yang et al. [9]). Different from the traditional SPH method, the pressure of the particle is obtained by solving the pressure Poisson equation (PPE) in the MPS method. Thus the obtained pressure field through MPS method is considered to be smoother. Till now, some preliminary researches on FSI have been conducted in the context of the MPS method. Sun et al. [10] proposed MPS-modal superposition method in which the elastic deformation of structure is computed through a mode superposition formulation. In contrast, more scholars chose to combine the MPS with the FEM method in order to address complicated FSI problem. Lee et al. [11] successfully simulated the interaction between dam-break and sloshing flow through the coupled MPS-FEM method. Some other researches performing the MPS-FEM model (Mitsume et al. [12]; Hwang et al. [13]; Zhang et al. [14]) also displayed fair agreement with available experimental results.

In the present paper, the interaction between solitary wave and the horizontal plate is mainly investigated. The performance of the numerical solitary wave generation is first examined to make sure that desired wave can be

generated. In the FSI analysis, the interaction between the solitary wave and rigid plate is simulated. The wave amplitude, as well as the vertical position of the plate, varies

in different cases in order to investigate their effects on the wave-induced force. Finally the solitary wave interacting with the flexible plate is investigated.

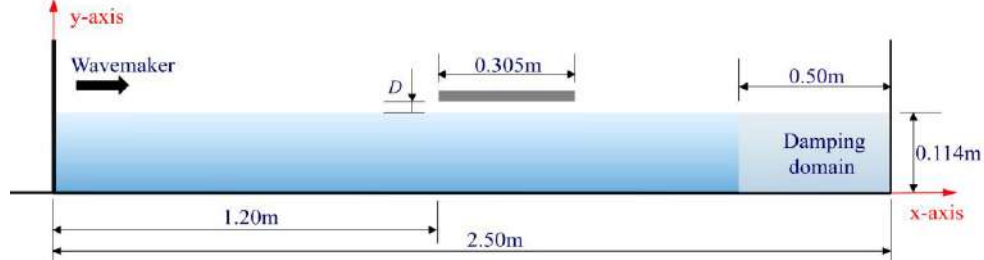


Figure 1. Geometric model of the numerical wave tank

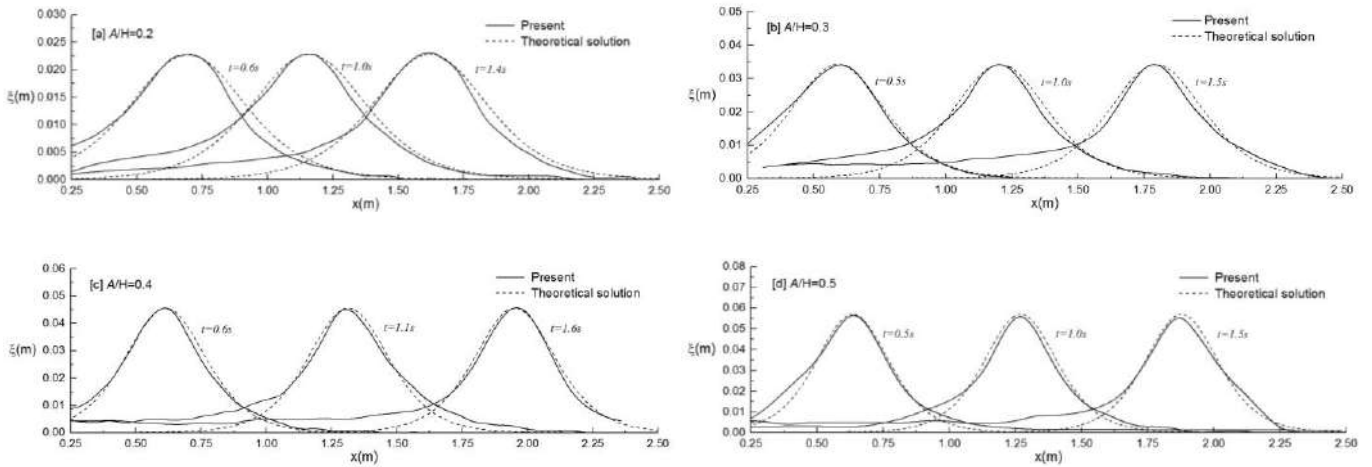


Figure 2. Comparison of the wave profiles between the calculated and theoretical solutions

II. NUMERICAL SIMULATIONS

The interaction between the solitary wave and a horizontal plate is simulated using the in-house solver in this section. The solver was developed based on the proposed MPS-FEM coupled method. The theory about the MPS, FEM method and the partitioned coupling strategy was introduced in our previous papers (Zhang et al. [15, 16]; Rao et al. [17]). The geometric model of the wave tank, as well as the horizontal plate, is depicted in Fig. 1. The length and water depth of the tank are 2.5 m and 0.114 m, respectively.

A. Numerical Wave Generation

The accuracy of the wave generation is crucial in the study of wave-structure interaction. In this sub-section, the wave generation is conducted in the numerical wave tank without the plate to validate the accuracy of the generated solitary wave. The piston-type wavemaker is employed to generate the solitary wave. Different wave amplitudes (A), including $A/H=0.2, 0.3, 0.4$ and 0.5 , are adopted in the simulations. The computational parameters are listed in Table I.

TABLE I. COMPUTATIONAL PARAMETERS FOR MPS

Parameter	Value
Water density	$1000(\text{kg}/\text{m}^3)$
Water depth	$0.114(\text{m})$
Kinematic viscosity	$1 \times 10^{-6}(\text{m}^2/\text{s})$
Gravitational acceleration	$9.81(\text{m}/\text{s}^2)$
Particle spacing	$0.002(\text{m})$
Fluid number	71193
Total number	75762

Figure 2 shows the comparison of the wave profiles between the numerical simulation and the theoretical solution. It can be seen that the wave crests of the simulation agree well with the theoretical solution presented by Goring [18]. However, there are still some slight distinctions, such as in the ascending portion of the curve, owing to the finite length and depth of the wave tank. It can be concluded that desired solitary wave can be generated based on the MPS method.

B. Interaction between Wave and Rigid Plate

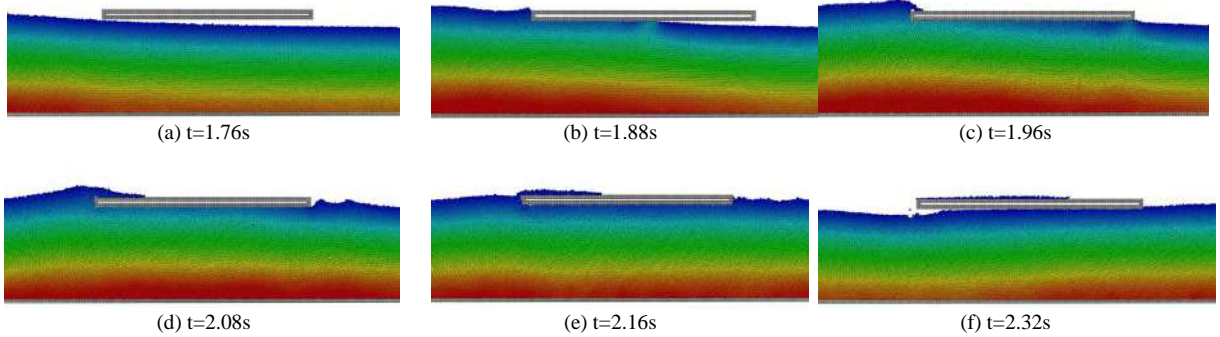
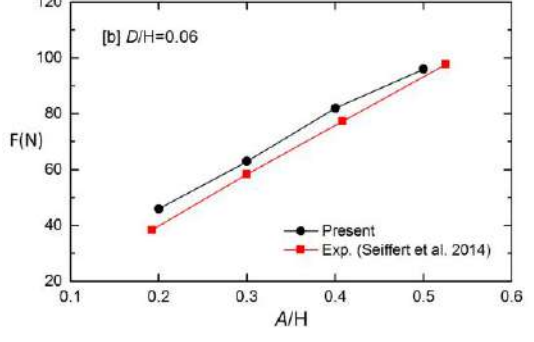
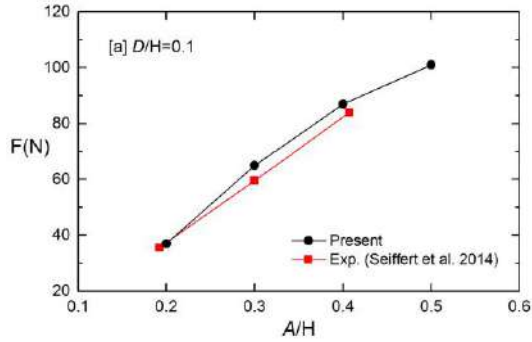
The interaction between the solitary wave and a rigid plate is simulated in this sub-section. The plate is placed at

the position of 1.2 meters from the wavemaker. And the distance between the bottom of the plate and the still water line (SWL) is defined as plate elevation (D), which can be altered by moving the plate vertically. In the simulations, the plate elevation (D) and wave amplitude (A) vary in different cases in order to investigate their effects on the wave-induced force on the plate. The dimensionless parameters of all the cases are shown in Table II.

TABLE II. CONFIGURATIONS OF THE CASES

Case No.	Amplitude (A/H)	Elevation (D/H)
1	0.2	0.03
2	0.2	0.06
3	0.2	0.1
4	0.3	0.03
5	0.3	0.06
6	0.3	0.1
7	0.4	0.03
8	0.4	0.06
9	0.4	0.1
10	0.5	0.03
11	0.5	0.06
12	0.5	0.1

The calculated vertical force on the plate of Case 6 ($A/H=0.3$, $D/H=0.1$) is shown in Fig. 3. Some snapshots of the simulation are presented in Fig. 4. It can be seen that the wave contacts the plate around $t=1.76$ s. Then the force starts

Figure 4. Snapshots of the simulation ($A/H=0.3$; $D/H=0.1$; Rigid plate).

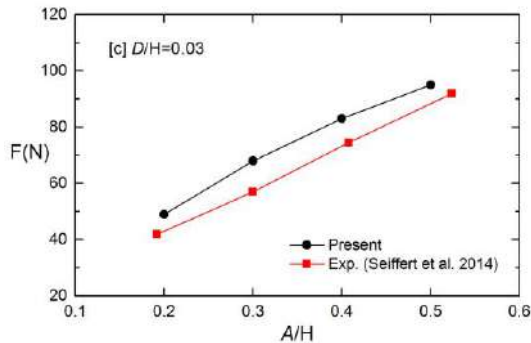
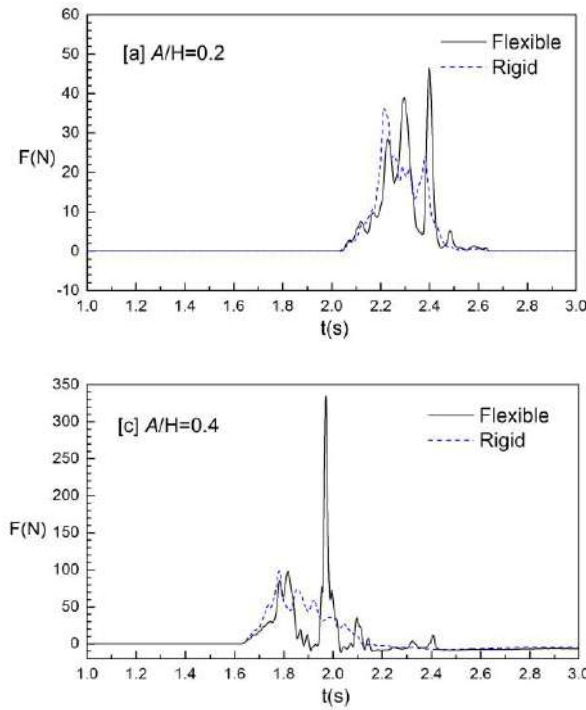


Figure 5. The maximum vertical force on the plate

To investigate the effects of the wave amplitude and plate elevation on the wave-induced force, the maximum value of the vertical force history in each case is collected. The comparison of the computed and experimental result is shown in Fig. 5. It can be seen that the vertical force on the plate is in proportion to the wave amplitude. However the maximum forces in the cases of different elevation are close to each other, which indicate that the maximum vertical force is not as sensitive to the plate elevation as to the wave amplitude. Although the comparison shows good agreement, the computed maximum force in each case is higher than the experimental result. It is partly due to the surface elevation resulting from the movement of the piston-type wavemaker. The length of the wave tank is relatively short compared with the experimental condition and the effects of the surface elevation cannot be neglected.

Figure 6. Comparison of the vertical forces on the plate ($D/H=0.1$)

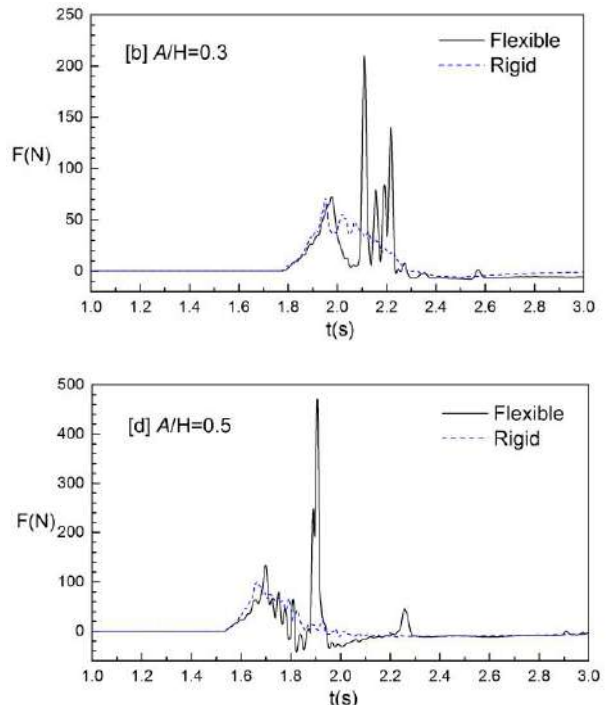
C. Interaction between Wave and Flexible Plate

To study the effects of structural flexibility on the interaction, the simulation of the solitary wave interacting with flexible plate is conducted in this sub-section. The FSI solver employed in this sub-section has proved to be reliable in our previous researches (Zhang et al. [14-16]; Rao et al. [17]). The setup of the wave amplitude and plate elevation is identical to that in the former sub-section, which is shown in Table II. However, the former rigid plate is replaced by a flexible plate with its ends clamped. The two-dimensional plate is divided into 152 planar beam elements in the structure analysis. The fluid parameter is the same as the one in the former simulations, which is shown in Table I. The structural parameter is shown in Table III.

TABLE III. COMPUTATIONAL PARAMETERS OF STRUCTURE

Parameters	Values
Structural density	1040 (kg/m ³)
Elastic modulus	1(MPa)
Cross area	2.5×10 ⁻⁵ (m ²)
Inertia moment	1×10 ⁻³ (m ⁴)
Damping coefficient α_1	1.6646
Damping coefficient α_2	0.00096
Element type	Planar beam element
Element number	152

Figure 6 shows the vertical wave-induced force on the flexible plate, which is compared with the counterpart in the rigid case in order to investigate the contribution of the structural flexibility to the wave-induced force. The case of $A/H=0.3$ and $D/H=0.1$ is selected specifically to be analyzed.



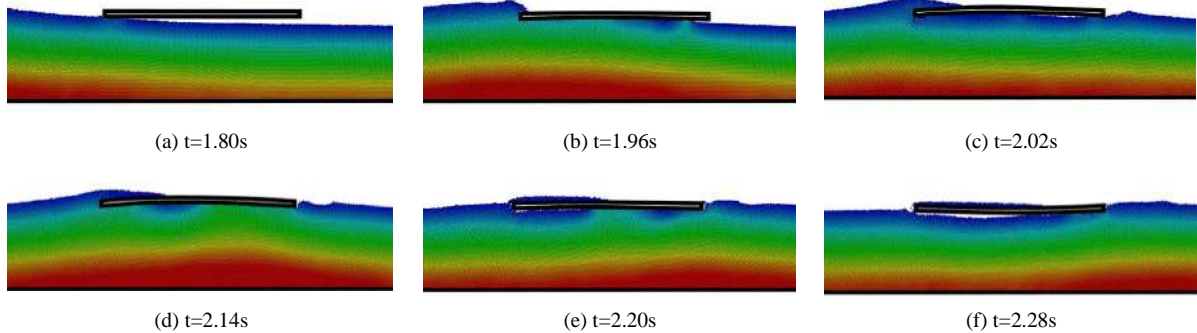


Figure 7. Snapshots of the wave-plate interaction ($A/H=0.3$; $D/H=0.1$; Flexible plate)

It can be observed in Fig. 6(b) that two curves agree well before the first peak ($t=1.96s$), during which the deformation of plate is not so obvious. After the peak, the curve of the flexible plate drops drastically while it goes through some slight oscillation in the rigid case. Around $t=2.14s$, the flexible plate encounters severe impacting force which is much greater than the first peak. To find out the reason of this phenomenon, some particular snapshots in the selected simulation are given in Fig. 7. It can be seen that the plate possess an upward velocity after being hit by the solitary wave. As the plate moves upward, it partially separates from the water surface around $t=2.02s$. After the deformation maximizes, the flexible plate starts to move downward and impacts onto the surface at 2.14 s, leading to an impacting force much greater than the first peak. And the value of the second peak is more than 3 times the value of the first peak.

Similar phenomenon can be observed in other cases. To quantitatively analyze the effects of the flexibility on the wave-induced force, the maximum wave-induced force (corresponds to second peak) in the flexible case is collected and then be contrasted with the maximum wave-induced force (correspond to the single peak) in the rigid case. The quantitative comparison is presented in Fig. 8. The enhancement of the maximum wave-induced force with regard to the wave amplitude displays strong nonlinearity. It can be inferred from the figures that the phenomenon of the second impact is not severe for cases of $A/H=0.2$. It is because the resulted deformation of the plate is so small that the impact is much milder. The magnification factor (MF), defined as ratio of the maximum value in flexible case to that in rigid case, in the cases of $A/H=0.2$ is 1.24, 1.87 and 1.35 respectively. For the cases of $A/H=0.3$, the MF (3.23, 5.28 and 3.66) increases as the impact onto the surface intensifies. However, the MF drops when the wave amplitude increases to $A/H=0.4$ in the cases of $D/H=0.06$ and 0.03. After checking the snapshots of the simulation, we find it is because the plate elevation is so small that the water always suffuses the bottom of the plate during the impact, which indicates that the slamming doesn't exist in these cases. As the wave amplitude increases further to $A/H=0.5$, the MF rises to 4.31, 6.25 and 5.89 as a result.

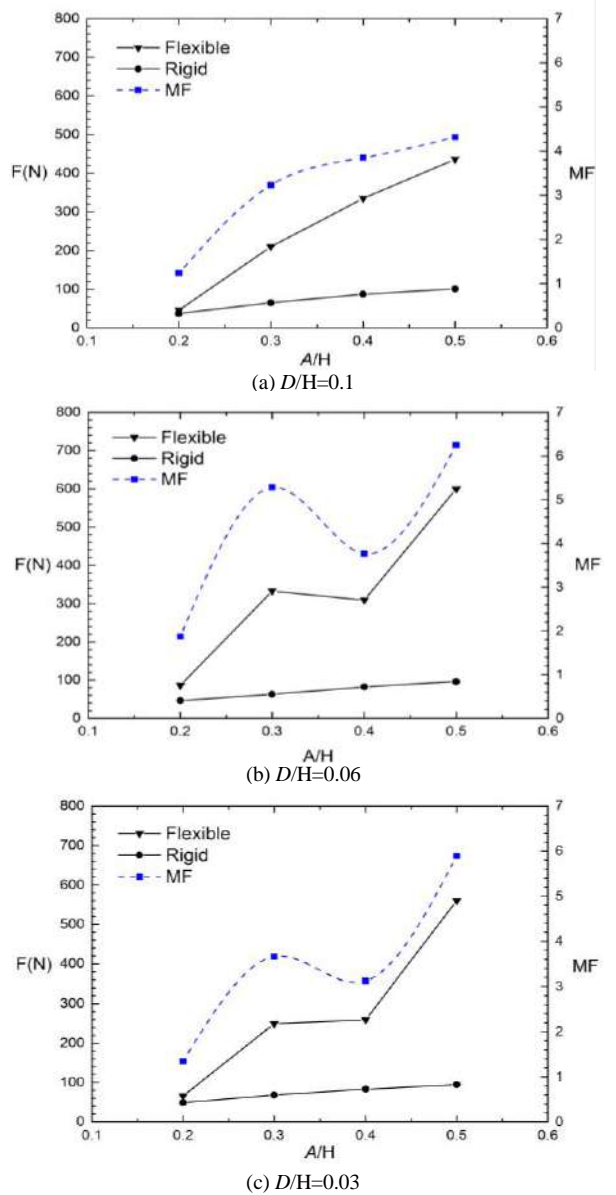


Figure 8. The maximum vertical force and the corresponding MF

III. CONCLUSIONS

In this paper, the interaction between the solitary wave and the horizontal plate is investigated using the proposed MPS-FEM coupled method. The numerical wave profile is contrasted with the theoretical solution, which shows a good agreement. In the simulation of the wave-plate interaction, both the rigid and flexible cases are considered. The wave amplitude ($A/H=0.2, 0.3, 0.4$ and 0.5) and plate elevation ($D/H=0.1, 0.06$ and 0.03) are altered to study their effects on the interaction. The results indicate that the maximum vertical force is in proportion to the wave amplitude, while it is not sensitive to the elevation within the $D/H=0.03\sim0.1$. The collected maximum vertical forces are also compared with the experimental results from Seiffert et al. [19]. Two curves show the same trend and the relative difference ranges from 1.8% to 19%.

In the flexible cases, the maximum vertical force increases at various levels compared with the result from rigid case. It can be observed that the maximum vertical force in the flexible case corresponds to the second peak of the curve. By analyzing the vertical force history and the snapshots from the case of $A/H=0.3$ and $D/H=0.1$, we find that the deformed plate possesses a downward velocity around the 2nd peak which intensifies its impact with the surface. The maximum vertical force in both the flexible and rigid case is collected in order to investigate the magnification effects of the flexibility. Compared with the relatively large-amplitude wave, the magnification effect ($MF=1.24, 1.87$ and 1.35) is not much evident for small-amplitude wave ($A/H=0.2$). Besides, in the cases of $D/H=0.06$ and 0.03 , the magnification factor drops as the wave amplitude increases from $A/H=0.3$ to 0.4 . It is found that in the low-elevation case ($D/H=0.03$) the water suffuses the plate bottom during the impact, which indicates that the slamming doesn't happen. In conclusion, the motion of the flexible plate exerts a complicated influence on the vertical wave-induced force.

ACKNOWLEDGEMENT

This work is supported by the National Natural Science Foundation of China (51379125, 51490675, 11432009, 51579145), Chang Jiang Scholars Program (T2014099), Shanghai Excellent Academic Leaders Program (17XD1402300), Program for Professor of Special Appointment (Eastern Scholar) at Shanghai Institutions of Higher Learning (2013022), Innovative Special Project of Numerical Tank of Ministry of Industry and Information Technology of China (2016-23/09) and Lloyd's Register Foundation for doctoral student, to which the authors are most grateful.

REFERENCES

- [1] X. Liu and S. Sakai, "Time domain analysis on the dynamic response of a flexible floating structure to waves," *Journal of Engineering Mechanics*, vol. 128(1), pp. 48-56, 2002.
- [2] K. P. Liao and C. H. Hu, "A coupled FDM-FEM method for free surface flow interaction with thin elastic plate," *Journal of marine science and technology*, vol. 18(1), pp. 1-11, 2013.
- [3] L. B. Lucy, "A numerical approach to the testing of the Fission Hypothesis," *The astronomical journal*, vol. 82, pp. 1013-1024, 1977.
- [4] R. A. Gingold and J. J. Monaghan, "Smoothed Particle Hydrodynamics: theory and application to non-spherical stars," *Monthly notices of the royal astronomical society*, vol. 181(3), pp. 375-389, 1977.
- [5] S. Koshizuka and Y. Oka, "Moving-particle Semi-implicit method for fragmentation of incompressible fluid," *Nuclear science and engineering*, vol. 123(3), pp. 421-434, 1996.
- [6] S. W. Attaway, M. W. Heinstein, and J. W. Swegle, "Coupling of Smooth Particle Hydrodynamics with the Finite Element Method," *Nuclear engineering and design*, vol. 150(2-3), pp. 199-205, 1994.
- [7] C. Antoci, M. Gallati, and S. Sibilla, "Numerical Simulation of Fluid-structure Interaction by SPH," *Computers and Structures*, vol. 85(11), pp. 879-890, 2007.
- [8] G. Fourey, G. Oger, D. L. Touzé, and B. Alessandrini, "Violent fluid-structure interaction simulations using a coupled SPH/FEM method," *Iop Conference Series Materials Science & Engineering*, 10, ID.012041, 2010.
- [9] Q. Yang, V. Jones, and L. McCue, "Free-surface flow interactions with deformable structures using an SPH-FEM model," *Ocean Engineering*, vol. 55, pp. 136-147, 2012.
- [10] Z. Sun, K. Djidjeli, J. T. Xing, and F. Cheng, "Coupled MPS-modal Superposition Method for 2D Nonlinear Fluid-structure Interaction Problems with Free Surface," *Journal of Fluids and Structures*, vol. 61, pp. 295-323, 2016.
- [11] C. J. K. Lee, H. Noguchi, and S. Koshizuka, "Fluid-shell structure interaction analysis by coupled Particle and Finite Element Method," *Computers and structures*, vol. 85(11), pp. 688-697, 2007.
- [12] N. Mitsume, S. Yoshimura, K. Murotani, and T. Yamada, "Improved MPS-FE fluid-structure interaction coupled method with MPS polygon wall boundary model," *Computer Modeling in Engineering & Sciences*, vol. 101(4), pp. 229-247, 2014.
- [13] S. C. Hwang, A. Khayyer, H. Gotoh, and J. C. Park, "Development of a fully Lagrangian MPS-based coupled method for simulation of fluid-structure interaction problems," *Journal of Fluids & Structures*, vol. 50(2), pp. 497-511, 2014.
- [14] Y. L. Zhang, X. Chen, and D. C. Wan, "An MPS-FEM coupled method for the comparative study of liquid sloshing flows interacting with rigid and elastic baffles," *Applied Mathematics and Mechanics*, vol. 37(12), pp. 1359-1377, 2016.
- [15] Y. L. Zhang, Z. Y. Tang, and D. C. Wan, "Numerical investigations of waves interacting with free rolling body by modified MPS method," *International Journal of Computational Methods*, vol. 13(4), pp. 1641013-1-1641013-14, 2016.
- [16] Y. L. Zhang, Z. Y. Tang, and D. C. Wan, "MPS-FEM coupled method for interaction between sloshing flow and elastic structure in rolling tanks," *Proceedings of the 7th International Conference on Computational Methods*, Berkeley, USA, paper No. ID 1493-6106-1-PB, 2016.
- [17] C. P. Rao, Y. L. Zhang, and D. C. Wan, "FSI analysis of solitary wave interacting with horizontal flexible plate by MPS-FEM Method," *The 27th International Ocean and Polar Engineering Conference*, San Francisco, California, USA, pp. 263-272, 2017.
- [18] D. G. Goring, "Tsunamis-the propagation of long waves onto a shelf," Ph.D. Thesis, California Institute of Technology, Pasadena, California, USA, 1978.
- [19] B. Seiffert, M. Hayatdavoodi, and R. C. Ertekin, "Experiments and computations of solitary-wave forces on a coastal-bridge deck. Part I: Flat Plate," *Coastal Engineering*, vol. 88, pp. 194-209, 2014.

Implement of the MPS-FEM Coupled Method for the FSI Simulation of the 3-D Dam-break Problem

Youlin Zhang

State Key Laboratory of Ocean Engineering, School of Naval Architecture, Ocean and Civil Engineering, Shanghai Jiao Tong University, Collaborative Innovation Center for Advanced Ship and Deep-Sea Exploration
Shanghai 200240, China

Decheng Wan*

State Key Laboratory of Ocean Engineering, School of Naval Architecture, Ocean and Civil Engineering, Shanghai Jiao Tong University, Collaborative Innovation Center for Advanced Ship and Deep-Sea Exploration
Shanghai 200240, China

*Corresponding author: dcwan@sjtu.edu.cn

Abstract—In the present study, the coupled moving particle semi-implicit (MPS) method and finite element method (FEM) is developed for the 3-D fluid structure interaction (FSI) problems. Herein, the MPS method is employed for the simulation of fluid domain while the FEM approach is used for the analysis of structural domain. For the implementation of the coupled approach, we proposed a mapping algorithm to transfer quantity values between the particles of flow field and the elements of structural field. In this mapping algorithm, the nonmatching refinement levels of both domains are permitted, which implies that the much larger size of element can be used in the FSI simulation and the computational efficiency can be improved. With the benefit of the proposed MPS-FEM coupled method, the 3-D FSI problem of dam-break flow impacting onto the flexible wall is numerically investigated. The evolutions of free surface and the impacting loads on the wall are compared against those regarding rigid tank. In addition, the deformation and the strength behaviors of the flexible wall are exhibited.

I. INTRODUCTION

The fluid structure interaction (FSI) problems with violent free surface have gained great attentions since they are often encountered in many engineering applications, such as the liquid sloshing in an oil tanker, very large floating structure interacting with waves, flexible structures experiencing dam-break flows, etc. In the past decades, the grid-based methods are much popular in the contributions regarding the simulation of FSI problems. However, it's quite a challenge for such methods to model phenomena that involve complex free surface flows, large deformations of flexible structures. By contrast, the mesh-less methods are free from these difficulties. Therefore, the mesh-less methods, cooperating with the finite element method (FEM), are promising for the FSI problems involving flexible structures and free surface flows.

In the recent decade, several representative mesh-less methods have been proposed for the FSI problems. For instance, the smoothed particle hydrodynamics (SPH) method has been extensively studied and extended to the FSI problems by coupling with the FEM method. Since the SPH method is flexible in describing the violent evolution of the fluid free surface, the movement and the deformation of elastic structures,

Rafiee and Thiagarajan [1] proposed a SPH-based solver for simulation of the dam-break flow interacting with an elastic gate. Liu et al. [2] employed an improved SPH method for modeling the hydro-elastic problems of the water impacting onto a forefront elastic plate. Besides, the particle finite element method (PFEM) is another good candidate for the FSI simulations. In this method, the same Lagrangian formulation is used for both the fluid and the solid analysis, which indicates that a monolithic system of equations could be created for the simultaneous solution of the fluid and structural response. Based on this monolithic approach, Zhu and Scott [3] simulated the process of sloshing wave interacting with a soft beam. In the recent few years, the moving particle semi-implicit (MPS) method, which is originally proposed by Koshizuka and Oka for incompressible flow [4], has also been introduced into the fluid domain analysis of the FSI problems. Hwang et al. [5] employed the MPS method to investigate the sloshing phenomenon in partially filled rectangular tanks with elastic baffles. Zha et al. [6] developed an improved MPS method to solve the hydro-elastic response of a wedge entering calm water. According to these results, the mesh-less methods are of great prospect in the simulation of 2-D FSI problems. However, there are very few works about the application of the mesh-less methods on the 3-D FSI problems.

In the present study, we devote to extend the mesh-less method for 3-D FSI problems. The MPS is employed for the simulation of fluid domain and the FEM method is used for the analysis of structural dynamic response. In the MPS-FEM coupled method, the spaces of fluid domain and structural domain will be dispersed by particles and grids, respectively. Hence, the interface between the fluid boundary particles and structural grids is isomeric and a special technique for the data communication crossing the interface is necessary. Here, a kernel function based interpolation (KFBI) technique is proposed to meet the requirement. The accuracy of the KFBI technique for the force and displacement interpolations between the fluid and the structural domains is validated. Then, the MPS-FEM coupled method is applied to the FSI problem of 3-D dam-break flow interacting with an elastic tank wall, and the influence of structural elasticity on the evolution of violent free surface is comparatively investigated.

II. NUMERICAL METHODS

In the present study, the MPS-FEM coupled method which is a partitioned coupled approach for the FSI problems is developed. Here, the formulas of MPS method, FEM method and the data interpolation on the interface between the fluid and structure domains are briefly introduced.

A. MPS Method for Fluid Analysis

In the MPS method for incompressible viscous flow, the governing equations which include the continuity equations and the Navier-Stokes equations, should be expressed by the particle interaction models based on the kernel function. Here, the kernel function presented by Zhang et al. [7] is employed.

$$W(r) = \begin{cases} \frac{r_e}{0.85r + 0.15r_e} - 1 & 0 \leq r < r_e \\ 0 & r_e \leq r \end{cases} \quad (1)$$

where r is distance between particles and r_e is the effect radius.

The particle interaction models, including the differential operators of gradient, divergence and Laplacian, are defined as

$$\langle \nabla \phi \rangle_i = \frac{\dim}{n^0} \sum_{j \neq i} \frac{\phi_j + \phi_i}{|\mathbf{r}_j - \mathbf{r}_i|^2} (\mathbf{r}_j - \mathbf{r}_i) \cdot W(|\mathbf{r}_j - \mathbf{r}_i|) \quad (2)$$

$$\langle \nabla \cdot \Phi \rangle_i = \frac{\dim}{n^0} \sum_{j \neq i} \frac{(\Phi_j - \Phi_i) \cdot (\mathbf{r}_j - \mathbf{r}_i)}{|\mathbf{r}_j - \mathbf{r}_i|^2} W(|\mathbf{r}_j - \mathbf{r}_i|) \quad (3)$$

$$\langle \nabla^2 \phi \rangle_i = \frac{2\dim}{n^0 \lambda} \sum_{j \neq i} (\phi_j - \phi_i) \cdot W(|\mathbf{r}_j - \mathbf{r}_i|) \quad (4)$$

where ϕ is an arbitrary scalar function, Φ is an arbitrary vector, \dim is the number of space dimensions, n^0 is the initial particle number density for incompressible flow, λ is a parameter defined as

$$\lambda = \frac{\sum_{j \neq i} W(|\mathbf{r}_j - \mathbf{r}_i|) \cdot |\mathbf{r}_j - \mathbf{r}_i|^2}{\sum_{j \neq i} W(|\mathbf{r}_j - \mathbf{r}_i|)} \quad (5)$$

which is introduced to keep the variance increase equal to that of the analytical solution [4].

In the present MPS method, the pressure Poisson equation (PPE) with the mixed source term is employed to satisfy the incompressible condition of fluid domain and defined as

$$\langle \nabla^2 P^{n+1} \rangle_i = (1 - \gamma) \frac{\rho}{\Delta t} \nabla \cdot \mathbf{V}_i^* - \gamma \frac{\rho}{\Delta t^2} \frac{\langle n^* \rangle_i - n^0}{n^0} \quad (6)$$

where γ is a blending parameter with a value between 0 and 1. The range of $0.01 \leq \gamma \leq 0.05$ is better according to numerical experiments conducted by Lee et al.[8] In this paper, $\gamma=0.01$ is adopted for all the simulations.

B. Structure Solver Based on the FEM Method

In the FEM method, the deformation of structure is governed by the dynamic equations expressed as

$$\mathbf{M} \ddot{\mathbf{y}} + \mathbf{C} \dot{\mathbf{y}} + \mathbf{K} \mathbf{y} = \mathbf{F}(t) \quad (7)$$

$$\mathbf{C} = \alpha_1 \mathbf{M} + \alpha_2 \mathbf{K} \quad (8)$$

where \mathbf{M} , \mathbf{C} , \mathbf{K} are the mass matrix, the Rayleigh damping matrix, the stiffness matrix of the structure, respectively. \mathbf{F} is the external force vector acting on structure, and varies with computational time. \mathbf{y} is the displacement vector of structure. α_1 and α_2 are coefficients which are related with natural frequencies and damping ratios of structure.

To solve the structural dynamic equations, another two group functions should be supplemented to set up a closed-form equation system. Here, Taylor's expansions of velocity and displacement developed by Newmark [9] are employed:

$$\dot{\mathbf{y}}_{t+\Delta t} = \dot{\mathbf{y}}_t + (1 - \gamma) \ddot{\mathbf{y}}_t \Delta t + \gamma \ddot{\mathbf{y}}_{t+\Delta t} \Delta t, 0 < \gamma < 1 \quad (9)$$

$$\mathbf{y}_{t+\Delta t} = \mathbf{y}_t + \dot{\mathbf{y}}_t \Delta t + \frac{1 - 2\beta}{2} \ddot{\mathbf{y}}_t \Delta t^2 + \beta \ddot{\mathbf{y}}_{t+\Delta t} \Delta t^2, 0 < \beta < 1 \quad (10)$$

where β and γ are important parameters of the Newmark method, and selected as $\beta=0.25$, $\gamma=0.5$ for all simulations in present paper. The nodal displacements at $t=t+\Delta t$ can be solved by the following formulas [10]:

$$\bar{\mathbf{K}} \mathbf{y}_{t+\Delta t} = \bar{\mathbf{F}}_{t+\Delta t} \quad (11)$$

$$\bar{\mathbf{K}} = \mathbf{K} + a_0 \mathbf{M} + a_1 \mathbf{C} \quad (12)$$

$$\begin{aligned} \bar{\mathbf{F}}_{t+\Delta t} = & \mathbf{F}_t + \mathbf{M}(a_0 \mathbf{y}_t + a_2 \dot{\mathbf{y}}_t + a_3 \ddot{\mathbf{y}}_t) \\ & + \mathbf{C}(a_1 \mathbf{y}_t + a_4 \dot{\mathbf{y}}_t + a_5 \ddot{\mathbf{y}}_t) \end{aligned} \quad (13)$$

$$\begin{aligned} a_0 &= \frac{1}{\beta \Delta t^2}, a_1 = \frac{\gamma}{\beta \Delta t}, a_2 = \frac{1}{\beta \Delta t}, \\ a_3 &= \frac{1}{2\beta} - 1, a_4 = \frac{\gamma}{\beta} - 1, \\ a_5 &= \frac{\Delta t}{2} \left(\frac{\gamma}{\beta} - 2 \right), a_6 = \Delta t(1 - \gamma), a_7 = \gamma \Delta t \end{aligned} \quad (14)$$

where $\bar{\mathbf{K}}$ and $\bar{\mathbf{F}}$ are the so-called effective stiffness matrix and effective force vector, respectively. Finally, the accelerations and velocities corresponding to the next time step are updated as follows.

$$\ddot{\mathbf{y}}_{t+\Delta t} = a_0(\mathbf{y}_{t+\Delta t} - \mathbf{y}_t) - a_2\dot{\mathbf{y}}_t - a_3\ddot{\mathbf{y}}_t \quad (15)$$

$$\dot{\mathbf{y}}_{t+\Delta t} = \dot{\mathbf{y}}_t + a_6\ddot{\mathbf{y}}_t + a_7\ddot{\mathbf{y}}_{t+\Delta t} \quad (16)$$

C. KFBI Technique for Data Interpolation

For the simulation of 3D FSI problems based on aforementioned MPS-FEM coupled method, the space of fluid domain will be dispersed by particles while the space of structural domain will be dispersed by grids. In general, the fine particles should be arranged within the fluid domain to keep a satisfactory precision for the fluid analysis. By contrast, the much coarser grids could be accurate enough for the structure analysis, which indicates that the fluid particles are usually not coincided with the structural nodes on the interface between the fluid and structure domain, as shown as Figure 1. Hence, the isomericous interface between the two domains may result in the challenge of data exchange in the process of FSI simulation. In the present study, the kernel function based interpolation technique is proposed to apply the external force carried by the fluid particles onto the structural nodes and update the positions of boundary particles corresponding to the displacements of structural nodes.

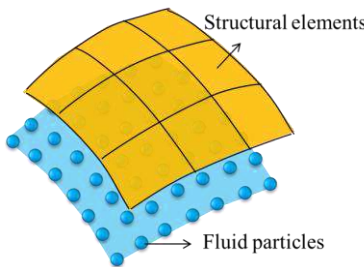


Figure 1. Interface between the fluid and structure domains

The schematic diagram of the KFBI technique for the force transformation from the fluid domain to the structural boundary is shown in Figure 2. In the KFBI technique, the boundary particle of the fluid domain will be denoted as the neighbour particle of the structure node while the distance between the particle and the node is smaller than the effect radius r_{ei} of interpolation. The weighted value of the fluid force of the neighbour particle $W(|\mathbf{r}_i - \mathbf{r}_n|)$ is calculated based on (1). Then, the equivalent nodal force F_n corresponding to the node n is obtained by the summation of force components regarding to the neighbour particles.

$$F_n = \frac{\sum_i P_i \cdot l_0^2 \cdot W(|\mathbf{r}_i - \mathbf{r}_n|)}{\sum_i W(|\mathbf{r}_i - \mathbf{r}_n|)} \quad (17)$$

where P_i is the pressure of the boundary particle obtained from the fluid domain, l_0 is the initial distance between the neighbour particles.

The schematic diagram of the technique for the deformation of the fluid structure interface is shown in Figure 3. The fluid boundary which is consisted of particles will deform corresponding to the deformation of structural boundary. The deflection value of boundary particle w_m can be obtained by the interpolation based on the kernel functions $W(|\mathbf{r}_i - \mathbf{r}_m|)$ and the nodal displacement δ_i .

$$w_m = \frac{\sum_i \delta_i \cdot W(|\mathbf{r}_i - \mathbf{r}_m|)}{\sum_i W(|\mathbf{r}_i - \mathbf{r}_m|)} \quad (18)$$

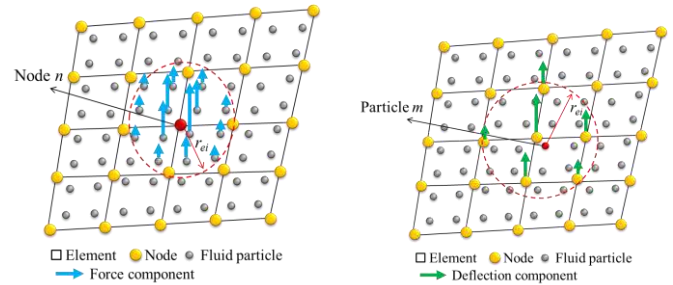


Figure 2. Schematic diagram of the force interpolation

Figure 3. Schematic diagram of the displacement interpolation

III. NUMERICAL VALIDATION

In this paper, a FSI solver, which includes the fluid domain calculation module, the structural domain calculation module and the interface data interpolation module, is developed based on the partitioned coupling strategy. For the fluid simulation, the accuracy of the fluid domain calculation module has been validated by a series of benchmarks in the previous works of our study group [7][11][12][13][14]. Here, the objective of the study in the present section is to validate the reliability of the other two modules.

A. Validation of Structural Domain Calculation Module

For the validation of the structural domain calculation module, the numerical test of the response of a square sheet is carried out. The schematic diagram of geometric dimensions of the square sheet is shown as the Figure 4. The side length and the thickness of the sheet are 2 m, 0.001 m, respectively. The sheet is clamped at all the four edges and dispersed by quadrilateral elements with size of 0.1 m. The concentrated force $F(t)=10$ N is applied at the geometric center A of the plate in the normal direction. The detailed calculation parameters can be found in the Table I.

TABLE I. PARAMETERS FOR STRUCTURAL RESPONSE TEST

Structural parameters	Values
Structure density (kg/m ³)	1800
Young's modulus (GPa)	40
Poisson's ratio	0.3
Element size (m)	0.1
Damping coefficients α_1	0.0
Damping coefficients α_2	0.0
Time step size (s)	1×10^{-3}

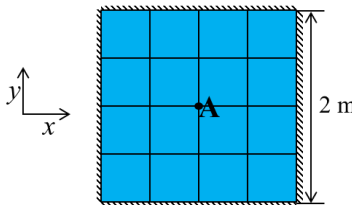


Figure 4. Schematic diagram of the square plane

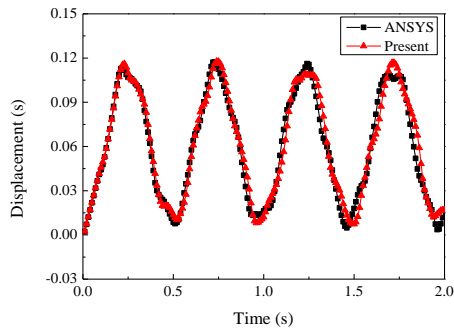


Figure 5. Time history of the displacement at the center of the square plane

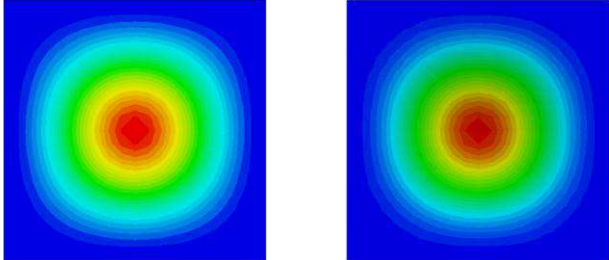
Figure 6. Deformations of the square plane at $t=0.75$ s (Left: ANSYS, right: present result)

Figure 5 shows the time histories of structural vibration at the geometric center A of the plate. Good agreement between the results from the present structural domain calculation module and the ANSYS software can be observed. Furthermore, the structural deformation contour at the time 0.75 s is compared against that calculated by the ANSYS software, as shown in the Figure 6. It can be noticed that the consistent deformation form is obtained by the two structure solver, which indicates that the structural domain calculation module of the present solver is reliable and can be applied to the structural dynamic response analysis of the FSI problems.

B. Validation of Data Interpolation Module

To validate the interpolation accuracy of the interface data transformation module, two numerical tests are carried out in the present section. The accuracy of the fluid force transformation from the fluid domain to the structural domain will be investigated by the first test. In this test, the rectangular sheet, which is with the length of 2 m and width of 0.6 m, is dispersed by the fluid particles and the structural elements, respectively. The distance between neighbour particles is 0.02 m and the size of element is 0.05 m. The triangular distributed force in the normal direction is applied onto the particle model of the rectangular sheet, as shown in the Figure 7. The value of force carried by the particles is calculated by

$$F = 1000 - 500x \quad (19)$$

With the help of the interface data interpolation module, the force on the particle model can be transferred to the nodes of the element model. Figure 8 shows the force distribution on the element model. It can be noticed that the present maximum 2.493 N approximates to the theoretical value 2.5 N.

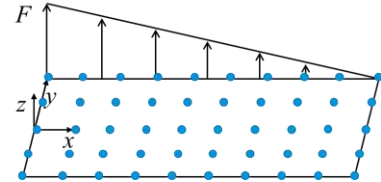


Figure 7. Diagrammatic sketch of force distribution on the particle model

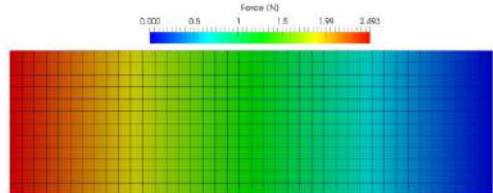


Figure 8. Force distribution on the element model

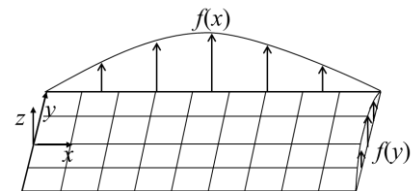


Figure 9. Diagrammatic sketch of deformation of the element model

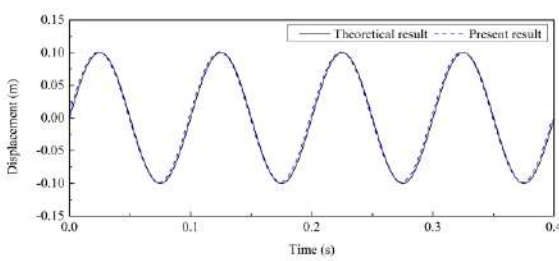


Figure 10. Displacement of the geometric center point of the particle model

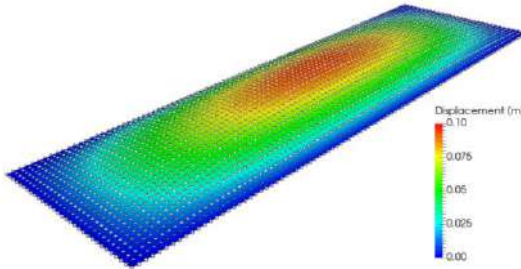


Figure 11. Deformation of the particle model ($t=0.12$ s)

In the second test, the accuracy of the deformation of the fluid boundary in accordance with that of the structural boundary is investigated. The rectangular sheet is dispersed to the same particle and element models. The structural boundary is forced to deform by setting the nodal velocity of the element model. As shown in Figure 9, the structural node will move in the normal direction and the distributed nodal velocity performs the parabolic shape in both x and y directions. The nodal velocity can be calculated by

$$V = 2\pi f(x)f(y)\cos(\omega t) \quad (20)$$

where $f(x) = 2x - x^2$, $f(y) = 1 - \frac{100}{9}y^2$

By the interface data interpolation module, the deformation values of the boundary particles can be obtained. Figure 10 shows the present interpolation value of the deflection on the geometric center point of the particle model and the theoretical value of the structure nodal displacement. Good agreement can be achieved between the two results. Furthermore, the deformed particle model and element model are compared at time 0.12 s, as shown in Figure 11. It can be found that the shapes of the two models are coincident with each other.

According to the results of the two tests, we deem that the interface data interpolation module is accurate in force and deformation value interpolation between the fluid and the structure domains.

IV. NUMERICAL SIMULATIONS

A. Numerical Setup

In this section, the numerical simulation of the fluid structure interaction between the dam-break slamming wave and the elastic wall is carried out. The applicability of the MPS-FEM coupled method in the 3-D fluid structure interaction problem is investigated. Figure 12 shows the schematic diagram of the computational model. All the walls of the tank are rigid except the right one. Elastic material is used for the right wall of the tank and the four edges of the wall are clamped on the adjacent walls. A pressure measuring point is mounted at the midpoint P of the bottom of the elastic wall, and five displacement measuring points (A-E) are arranged above the point P with the spacing of 0.1 m. Detailed parameters of the material property and the numerical condition are shown in Table II.

TABLE II. FLUID AND STRUCTURAL PARAMETERS OF SIMULATION

	Parameters	Values
Fluid	Fluid density (kg/m^3)	1000
	Kinematic viscosity (m^2/s)	1×10^{-6}
	Gravitational acceleration (s/m^2)	9.81
	Particle spacing (m)	0.03
	Number of fluid particles	15200
	Total number of particles	44371
	Time step size (s)	1×10^{-4}
Structure	Structure density (kg/m^3)	1800
	Young's modulus (GPa)	10
	Poisson's ratio	0.3
	Element size (m)	0.01
	Damping coefficients α_1	0.025
	Damping coefficients α_2	0.0005
	Time step size (s)	1×10^{-4}

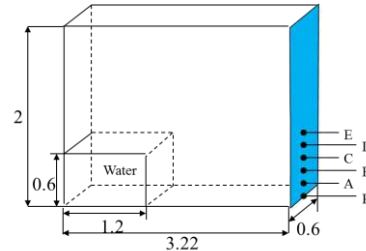


Figure 12. Schematic diagram of the computational model (Unit:m)

B. Numerical Results

To investigate the effect of structural elasticity to the evolution of free surface, the dam-break flows in both rigid tank and elastic tank are numerically simulated. Figure 13 shows the comparison of free surfaces in the rigid tank and the elastic tank at four instants. At the time 0.8 s, the upward jet flow is generated after the dam-break flow impacting onto the right wall of the tank. The height of jet flow in the elastic tank is slightly lower than that in the rigid tank. At the instant 1.4 s, the water front of jet flow falls down and the water surface with the rolling shape is formed. It can be noticed that the shape of rolling water surface approximates circular arc in the rigid tank, while that is closed to an

elliptical arc in the elastic tank. In addition, more the splashed water particles in the rigid tank are observed than those in the elastic tank. It may induced by the energy dissipation during the deformation of the lateral wall. At the instant 1.6 s, an air bubble is generated after the rolling of water front. As shown in the side view, the bubble in the elastic tank presents irregular three-dimensional shape while that in the rigid tank presents the two-dimensional characteristic. At the time 1.9 s, the water particles near the elastic wall are bounced back into the tank during the vibration of the structure, and the separation between the water and the wall is formed.

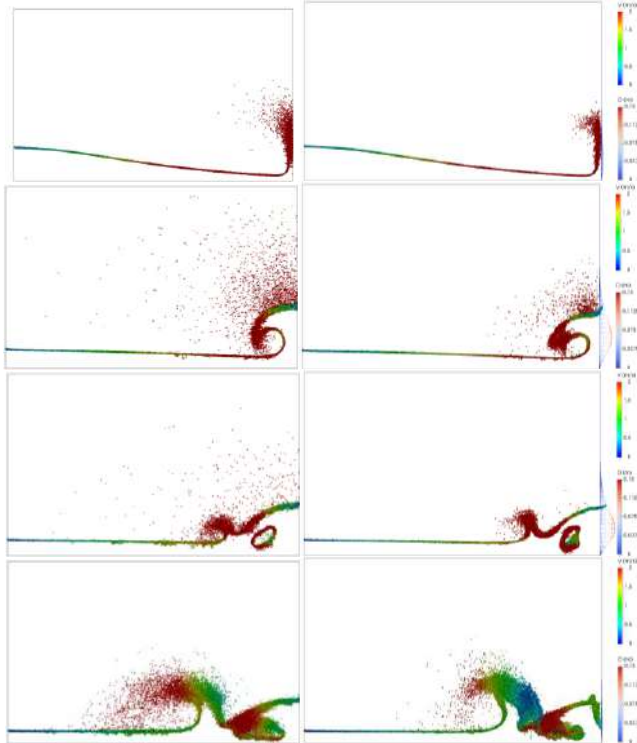


Figure 13. Evolution of free surface in side view (from top to bottom: $t=0.8, 1.4, 1.6, 1.9$ s)

Figure 14 shows the time histories of the structural vibration at the five measuring points on the elastic wall. It can be noticed that the trends of the curves are similar to each other except the peak values of the vibration. At the time 0.62 s, the dam-break wave reaches the right end of the tank and the elastic wall starts to deform due to the impact load. As more and more water particles acting onto the elastic wall, the amplitudes of the deformation increase and reach to the maximums at the instant 1.6 s. In the following stage, the elastic wall vibrates with the decreasing amplitudes since the combined action of the fluid load and the structural damping force. Besides, the elastic wall vibrates with the maximum amplitude in the transverse direction at the measuring point C which is 0.3 m above the bottom of the tank.

In the Figure 15, the time histories of impact loads at the measuring point P are compared between the elastic tank and the rigid tank. At the initial instant ($t=0.62$ s) of the

impact phenomenon, the first peak value of pressure on the lateral wall of the elastic tank is 9225 Pa, which is 21% smaller than that regarding the rigid tank (11673 Pa). And at the instant $t \approx 1.56$ s, which is close to the time that the largest amplitude of structural deformation occurs, the second peak of pressure is observed. In the following stage, the pressure history acting on the elastic wall presents significant fluctuation which is similar with the trend of structural vibration. It could be inferred that the varying of impact load acting on the wall is more complex since the vibration of the tank wall.

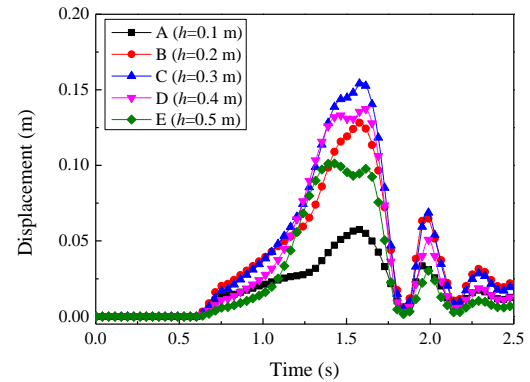


Figure 14. Time histories of vibrations on the elastic wall

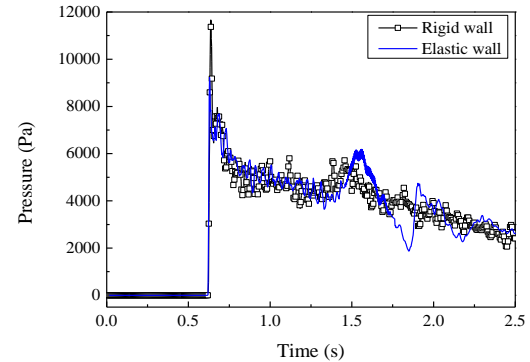


Figure 15. Time histories of impact loads at the measuring point P

V. CONCLUSIONS

In the present study, the MPS-FEM coupled method is developed for 3-D FSI problems. The kernel function based interpolation (KFBI) technique is proposed for the data transformation on the interface between the fluid and structural domains. To validate the reliability of the structural domain calculation module, the numerical test of the vibration response of a square sheet under the constant force is carried out. Both the time history of structural vibration and the deformation form of the sheet are in good agreements with the results calculated by the ANSYS software. Then, the interpolation accuracy of the KFBI technique is validated by two numerical tests. Coincident quantities of force and structural deformation can be achieved between the fluid boundary and the structural boundary. Finally, the MPS-FEM coupled solver is used to simulate the interaction between the dam-break flow and the

elastic wall. Different phenomena of the dam-break flow can be observed in the elastic tank. For instance, the qualitative results show that the evolutions of free surface in the elastic tank present obviously three dimensional characters in comparison with those of rigid tank. The quantitative results show that the impulse pressure induced by the dam-break wave impacting onto the elastic wall is 21% smaller than that regarding the rigid tank. In summary, as a preliminary attempt, present study develops a fully Lagrangian FSI approach and shows the capability of the in-house solver in simulation the 3-D FSI problems with violent free surface.

ACKNOWLEDGEMENT

This work is supported by the National Natural Science Foundation of China (51379125, 51490675, 11432009, 51579145), Chang Jiang Scholars Program (T2014099), Shanghai Excellent Academic Leaders Program (17XD1402300), Program for Professor of Special Appointment (Eastern Scholar) at Shanghai Institutions of Higher Learning (2013022), Innovative Special Project of Numerical Tank of Ministry of Industry and Information Technology of China (2016-23/09) and Lloyd's Register Foundation for doctoral student, to which the authors are most grateful.

REFERENCES

- [1] A. Rafiee and K. P. Thiagarajan, "An SPH projection method for simulating fluid–hypoelastic structure interaction," *Comput. Methods Appl. Mech. Eng.*, vol. 198, pp. 2785–2795, 2009.
- [2] M. B. Liu, J. R. Shao, and H. Q. Li., "Numerical simulation of hydro-elastic problems with smoothed particle hydrodynamics method," *Journal of Hydrodynamics, Ser. B*, vol. 25(5), pp.673–682, 2013.
- [3] M. J. Zhu and M. H. Scott, "Direct differentiation of the quasi-incompressible fluid formulation of fluid–structure interaction using the PFEM," *Computational Particle Mechanics*, vol. 4(3), pp. 1–13, 2016.
- [4] S. Koshizuka and Y. Oka, "Moving particle semi-implicit method for fragmentation of incompressible fluid," *Nuclear Science and Engineering*, vol. 123, pp. 421–434, 1996.
- [5] S. C. Hwang, J. C. Park, H. Gotoh, A. Khayyer, and K. J. Kang, "Numerical simulations of sloshing flows with elastic baffles by using a particle-based fluid–structure interaction analysis method," *Ocean Engineering*, vol. 118, pp. 227–241, 2016.
- [6] R. S. Zha, H. Peng, and W. Qiu, "Solving 2D coupled water entry problem by an improved MPS method," *The 32nd International Workshop on Water Waves and Floating Bodies*, Dalian, China, pp. 23–26, April, 2017.
- [7] Y. X. Zhang, D. C. Wan, and T. Hino, "Comparative study of MPS method and level-set method for sloshing flows," *Journal of hydrodynamics*, vol. 26(4), pp. 577–585, 2014.
- [8] B. H. Lee, J. C. Park, M. H. Kim, S. J. Jung, M. C. Ryu, and Y. S. Kim, "Numerical simulation of impact loads using a particle method," *Ocean Engineering*, vol. 37, pp. 164–173, 2010.
- [9] N. M. Newmark, "A method of computation for structural dynamics," *Journal of the engineering mechanics division*, vol. 85(3), pp. 67–94, 1959.
- [10] K. M. Hsiao, J. Y. Lin, and W. Y. Lin, "A consistent co-rotational finite element formulation for geometrically nonlinear dynamic analysis of 3-D beams," *Comput. Methods Appl. Mech. Engrg.*, vol. 169, pp. 1–18, 1999.
- [11] Y. L. Zhang, X. Chen, and D. C. Wan, "MPS-FEM coupled method for the comparison study of liquid sloshing flows interacting with rigid and elastic baffles," *Applied Mathematics and Mechanics*, vol. 37(12), pp. 1359–1377, 2016.
- [12] Y. L. Zhang, Z. Y. Tang, and D. C. Wan, "Numerical investigations of waves interacting with free rolling body by modified MPS method," *International Journal of Computational Methods*, vol. 13(4), pp. 1641013-1–1641013-14, 2016.
- [13] Z. Y. Tang, Y. L. Zhang, and D. C. Wan, "Multi-resolution MPS method for free surface flows," *International Journal of Computational Methods*, vol. 13 (4), pp. 1641018-1–1641018-17, 2016.
- [14] Y. L. Zhang and D. C. Wan, "Numerical study of interactions between waves and free rolling body by IMPS method," *Computers and Fluids*, vol. 155, pp.124–133, 2017.

A New Numerical Method For SPH Fluid-Solid Coupling Simulation And Its Preliminary Verification

MA Xiao-jing

College of Electrical Engineering
Xinjiang University
Urumqi, China
maxiaojing1983@163.com

Mamtimin Geni, JIN A-fang

College of Mechanical Engineering
Xinjiang University
Urumqi, China

Abstract—Based on the fundamental theory of Smoothed Particle Hydrodynamics (SPH), the constitutive relation of fluid and solid is introduced, and a feasible coupling algorithm for fluid-solid interface is proposed by utilizing continuum mechanics governing equations to describe fluid and solid dynamic behavior. The judgment is made that whether particles are involved in the governing equations calculation according to the motion direction and the stress of particles. Numerical simulation is conducted based on the SPH modeling and material interface coupling algorithm, and the good agreement is observed with the experiment results. It is shown in the results that the proposed SPH fluid-solid coupling algorithm is capable of effectively and accurately simulating the deformation of fluid with free surface and the elastic solid as well as the process of rebound during the fluid-solid impacting.

I. INTRODUCTION

Fluid-solid coupling is to investigate the behaviour during the interaction between fluid and solid, and is widely applied in various engineering domains such as draining process and impacting of dam break. During the process of draining, the fluid interacts with baffle and other obstacles that are solid. As a result, there are complicated phenomena of splash, merging and change of fluid-solid interface. Consequently, the solid structures lose stability, bend and rebound due to the impact of fluid. The interface and the interaction between two phases show substantial non-linear characteristics as a result of deformation in different scales on the interface. In early studies, the focus was intended to the free-surface deformation of fluid, treating solid as rigid wall boundary condition^[1,2]. However, in order to obtain simulation and prediction with high accuracy in the practical engineering problems, the deformation and damage of solid during the impacting as well as the reaction effect on the flow field should be analyzed.

Conventional meshing methods have been widely utilized in the related area whereas the quality of meshing has significant influence on the accuracy of numerical solution^[3-5]. When the free-surface of fluid with great deformation is dealt with, in order to maintain the stability of the solution, it is necessary to accurately capture the free-surface by continuously re-structuring the mesh or using the volume of fluid (VOF) method, which severely reduces the computation efficiency.

The hybrid method combining meshing method and meshless method is also developed by carefully selecting optimized contact points between node and interface to simulate the fluid-solid interaction^[6-9]. The accuracy of simulation is highly dependent on the computational errors of the intermediate variables between different methods of discretization.

In the last 1970s, Gingold^[10] and Lucy^[11] proposed a meshless numerical method based on Lagrange method, namely Smoothed Particle Hydrodynamics (SPH). It uses series of free-motion particles to solve integral simultaneous equations with different boundary conditions. Interface and its motion between different substances can be identified by tracking the movement and position of particles, therefore, motion of interface, deformation of boundaries and multi-phase interface real-time tracking and capturing can be achieved. It no longer requires conventional geometrical meshing, distortion and re-structure, these advantages advance SPH method into wide application in many fluid dynamic areas^[12-13]. In SPH method, the fluid and solid in the calculated domain are initially discretized into series of particles with corresponding physical properties; the field function will then be interpolated in the targeted particles domain for approximation. Any types of particles can interact within the governing domain, which enables the simplified realization of the two-way coupling of fluid and solid. Nevertheless, the special treatment on interface of different substances is needed due to the distinction in physical properties and dynamic characteristics^[14].

Several methods of interface coupling have been proposed by Antoci^[15], Rafiee^[16] and Shen^[17] when SPH method is applied to simulate the impact on the baffle during the draining.

In Antoci's study^[15], the coupling of fluid and solid is characterized as follow, the force from fluid particles to solid particles near the interface is calculated firstly, the reaction force from solid particles to fluid particles is then calculated based on the Newton's second law of motion.

In the improved SPH method proposed by Rafiee^[16], the viscosity force is accounted for firstly and pressure is omitted. The temporary predictive values of particles' position and velocity of are obtained, and then updated according to the pressure Poisson equation. The computation cost is greatly increased due to the prediction and updated of the intermediate variables.

A fluid-solid contacting algorithm proposed by Shen^[17] is constructing solid surface particles treated as virtual particles. These virtual particles are defined in initial particle configuration, containing both fluid and solid properties as well as producing repulsive force to prevent penetration. The properties of solid are manifested during the elastic-solid particle interpolation while the properties of rigid wall are applied when interpolated with fluid particles.

In order to broaden the future application of the SPH method in fluid-solid coupling, in this study, a new coupling method is proposed base on SPH method by introducing two-phase constitutive relation and status equations. A dynamic model characterized by uniform governing equation is established to describe the SPH fluid-solid coupling. A simplified and effective fluid-solid interface coupling treatment is developed. Typical examples of fluid impacting solid are simulated by this new method and results are compared with the references to test the reliability and accuracy of this fluid-solid coupling method.

II. INTRODUCTION OF THE SPH METHOD

A. Theoretical fundamentals of the SPH method

The essentials of SPH method is the interpolation theory, assuming any arbitrary field function and its derivative can be approximated as^[18]:

$$\langle f(x) \rangle = \sum_j^N \frac{m_j}{\rho_j} f(x_j) W \quad (1)$$

$$\langle \nabla \cdot f(x) \rangle = \sum_j^N \frac{m_j}{\rho_j} f(x_j) \nabla W \quad (2)$$

where, i and j are the index of different particles, respectively. N is the total number of particles in the calculated domain and W is the kernel function. In this study, cubic spline function is applied as commonly used in SPH method.

B. Governing equations

The governing equations of continuum mechanics are capable of characterizing both fluid dynamics when strength of fluid must be considered and solid dynamics. It is therefore reasonable to be applied in the modeling of fluid-solid coupling to uniformly written the dynamics for both fluid and solid. The governing equations are as follow in discretized form^[18]:

Conservation and continuity equation of mass:

$$\frac{d\rho_i}{dt} = \rho_i \sum_{j=1}^N \frac{m_j}{\rho_j} u_{ij}^\beta \cdot \frac{\partial W_{ij}}{\partial x_i^\beta} \quad (3)$$

Conservation equation of momentum:

$$\frac{du_i^\alpha}{dt} = \sum_{j=1}^N m_j \left(\frac{\sigma_i^{\alpha\beta}}{\rho_i \rho_j} + \frac{\sigma_j^{\alpha\beta}}{\rho_i \rho_j} \right) \frac{\partial W_{ij}}{\partial x_i^\beta} + F^\alpha \quad (4)$$

Equation of motion:

$$\frac{dx_i^\alpha}{dt} = u_i^\alpha \quad (5)$$

where, m is mass; ρ is density; x is displacement; α and β are coordinate, respectively; t is time; u^β is the velocity component in beta direction; F is volumetric force, which is gravity in this study as 9.81m/s^2 ; σ is stress tensor, comprised of isotropic pressure p and viscous stress $\tau^{\alpha\beta}$.

$$\sigma^{\alpha\beta} = -p \delta^{\alpha\beta} + \tau^{\alpha\beta} \quad (6)$$

In order to avoid the stress instability in conventional SPH method, the un-physical oscillation and particle penetration, the artificial stress K_{ij} and artificial viscosity Π_{ij} are applied in the solution, the momentum equation (4) is hence re-written as^[19,20]:

$$\frac{du_i^\alpha}{dt} = \sum_{j=1}^N m_j \left(\frac{\sigma_i^{\alpha\beta}}{\rho_i \rho_j} + \frac{\sigma_j^{\alpha\beta}}{\rho_i \rho_j} + K_{ij} + \Pi_{ij} \right) \frac{\partial W_{ij}}{\partial x_i^\beta} + F^\alpha \quad (7)$$

III. CONSTITUTIVE RELATION AND STATUS EQUATIONS

A. Constitutive relation and status equation of fluid

Fluid in this study is water, considered as Newtonian fluid, and the constitutive relation is as follow.

$$\tau^{\alpha\beta} = \mu \varepsilon^{\alpha\beta} \quad (8)$$

$$\varepsilon^{\alpha\beta} = \frac{\partial u^\beta}{\partial x^\alpha} + \frac{\partial u^\alpha}{\partial x^\beta} - \frac{2}{3} (\nabla \cdot u) \delta^{\alpha\beta} \quad (9)$$

where, μ is the dynamic viscosity coefficient, $\varepsilon^{\alpha\beta}$ is shear strain rate.

The minor density change can lead to severe fluctuation in pressure gradient when dealing with incompressible fluid or fluid close to incompressibility. In that case, the calculation becomes extremely unstable and the time step is required to be very small. By introduction artificial compressibility^[21], the fluid can be approximated as micro compressible fluid and the status equation is

$$p = c^2(\rho - \rho_0) \quad (10)$$

where, ρ_0 is the reference density, subtracted by to generate minor pressure difference and enhance density field stability; c is acoustic velocity, usually used as value 10 times greater than the maximum fluid velocity. The compressibility rate is maintained to 1% in this study.

B. Constitutive relation and status equation of solid

The draining impact experiment is adopted from [18] and simulated in this study, the material of the baffle is rubber, which is considered as homogeneously elastic, and the constitutive relation is

$$\tau^{\alpha\beta} = 2G(\varepsilon^{\alpha\beta} - \frac{1}{3}\delta^{\alpha\beta}\varepsilon^{\gamma\gamma}) + \tau^{\alpha\gamma}R^{\beta\gamma} + \tau^{\beta\gamma}R^{\alpha\gamma} \quad (11)$$

$$R^{\alpha\beta} = \frac{1}{2}\left(\frac{\partial u^\alpha}{\partial x^\beta} - \frac{\partial u^\beta}{\partial x^\alpha}\right) \quad (12)$$

where, $\tau^{\alpha\beta}$ is the strain rate; G is the shear modulus of the material.

In the study of solid deformation in the low velocity impact, the compressibility rate is approximately linear to the pressure^[15].

$$p = K\left(\frac{\rho}{\rho_0} - 1\right) \quad (13)$$

where, K is volume modulus; acoustic velocity in solid is $c = \sqrt{K / \rho_0}$, which holds the status equation in the same form as this of fluid.

IV. FLUID-SOLID COUPLING

A. Computation process of SPH

The SPH simulation method and calculation process in fluid-solid coupling is explained in Fig.1.

The fluid and solid in the calculated domain are firstly discretized as particles according to their own kinds and initialized with respective properties such as particle type, density, viscosity, elastic modulus, Poisson's ratio etc. Initial status parameters are also set for all particles such as position, velocity, acceleration and stress tensor. The governing equations based on the continuum mechanics are solved simultaneously in every time step. And then the parameters of every particle such as density, velocities and displacement are updated to bring into constitutive relation and status equations to calculate stress tensor and corresponding artificial stress and artificial viscosity. In this algorithm, the governing equations of fluid and solid particles are in the same form so that particles of different materials in the influence domain are regarded as neighboring particles. And the coupling between fluid and solid is eventually realized by iterating the updated parameters of all particles in governing equations.

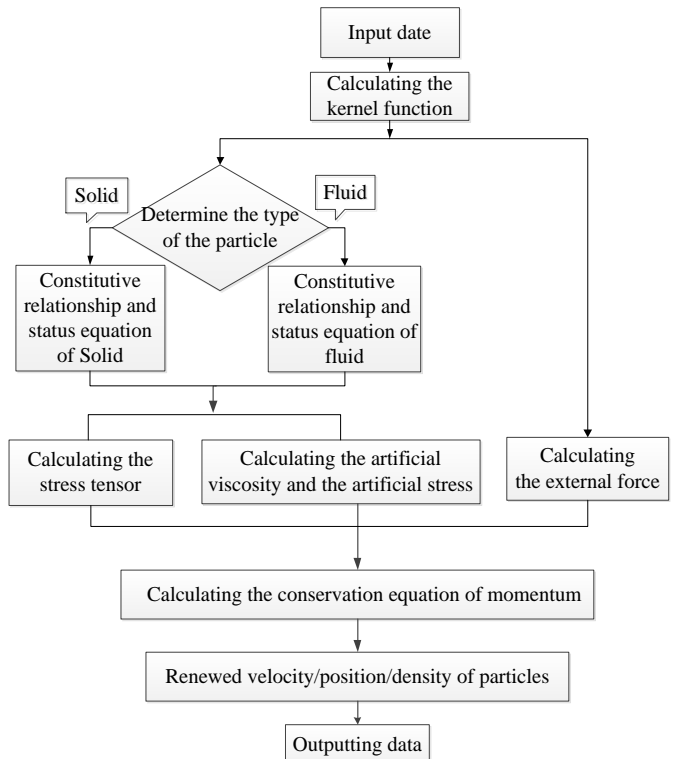


Figure 1. Fluid-solid interaction computation process in SPH

B. Coupling on the Fluid-solid interface

A simplified method of the coupling on the interface is proposed in this study by solving the governing equations in different domain with different types of particles. The coupling treatment is described in Fig.2.

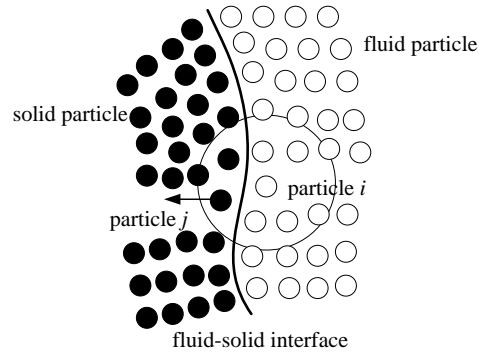


Figure 2. Coupling method for fluid-solid interface

In Fig.2 the hollow circle and solid circle stand for fluid particles and solid particles, respectively. The fluid particle i is the target particle, and the solid particle j is the neighboring particle in the support domain of particle i . The interaction on the interface stops when particle j departs from the fluid and is compressed in this direction. Which means particle j no longer has any influence on particle i and vice versa. In SPH method, the approximate derivative of the field function is obtained by the functions of all particles in the support domain weighted

by the derivative of kernel function. By doing this, it can be derived as

$$\text{When } x_{ji}^\alpha \cdot u_j^\alpha \geq 0 \text{ and } \sigma_j^{\alpha\alpha} \leq 0 \text{ then } \frac{\partial W_{ij}}{\partial x_i^\alpha} = 0 \quad (14)$$

where i and j represent particles of different materials, respectively.

In addition, due to the different dynamics of fluid and solid, the influences on the surrounding particles are also different. Different support domain and influential domain are considered for fluid and solid. Smooth length of fluid particles is slightly larger than that of solid particles because of its better fluidity.

C. Time integration

The Leap-Frog method is used in this study to deal with the time integration so that oscillation is avoided in the calculation. The length of the time step is constrained by following conditions [14, 22].

$$\Delta t_{fluid} \leq \min\left(\frac{h}{c}, \left(\frac{h}{f}\right)^{1/2}, \frac{0.5h^2}{\nu_0}\right) \quad (15)$$

$$\Delta t_{solid} \leq \min\left(\frac{0.3h}{c + |V_i^{\max}|}, \frac{0.3h}{|\nabla V_i^{\max}|}\right) \quad (16)$$

where, $\nu_0 = \eta_0 / \rho_0$ is viscosity coefficient; f is the force on the unit mass (acceleration). In the fluid-solid coupling simulation, time step should satisfy constraints for both fluid and solid as follow.

$$\Delta t \leq \min(\Delta t_{fluid}, \Delta t_{solid}) \quad (17)$$

V. NUMERICAL SIMULATION AND RESULT ANALYSIS

A computational code is developed based on SPH method with programming language C in this study to solve the fluid-solid impact in two-way coupling. Two iconic processes in fluid-solid coupling study are simulated and compared with experimental data.

A. Elastic baffle

The deformation of the baffle is investigated in [15], shown in Fig.3. A baffle is installed in the container with free elastic lower end. Deflection of the baffle occurs because of the gravity and the impact of the fluid. The experiment parameters are as below, $H=0.14m$, $A=0.1m$, $L=0.079m$, $\delta=0.005m$. The working fluid is water, with the density of $1000kg/m^3$, dynamic viscosity coefficient of $1Pa\ s$. The material of elastic baffle is rubber, with the density of

$1100kg/m^3$, Poisson ratio of 0.49, elastic modulus of 1.2×10^7Pa .

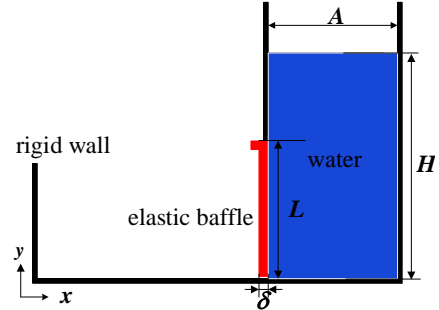


Figure 3. Configuration of the elastic baffle

A new SPH method is proposed in this study to simulate the baffle deformation during the draining process. The initial clearance between particles is $d_0=0.0015m$, total number of particles is 7145, the number of solid and fluid particles is 216 and 6424, respectively. And 505 static particles are used to simulate the rigid wall of the container. These static particles have fluid properties but are immobilized at their positions. The smooth length of fluid particles is $1.07d_0$, the smooth length of solid particles is $0.93d_0$, and the smooth length between fluid and solid particles is $0.65d_0$. The length of calculation time step is $8\times10^{-6}s$. Fig.4 and Fig.5 show the deformation of baffle lower end in the simulated results and the experiment.

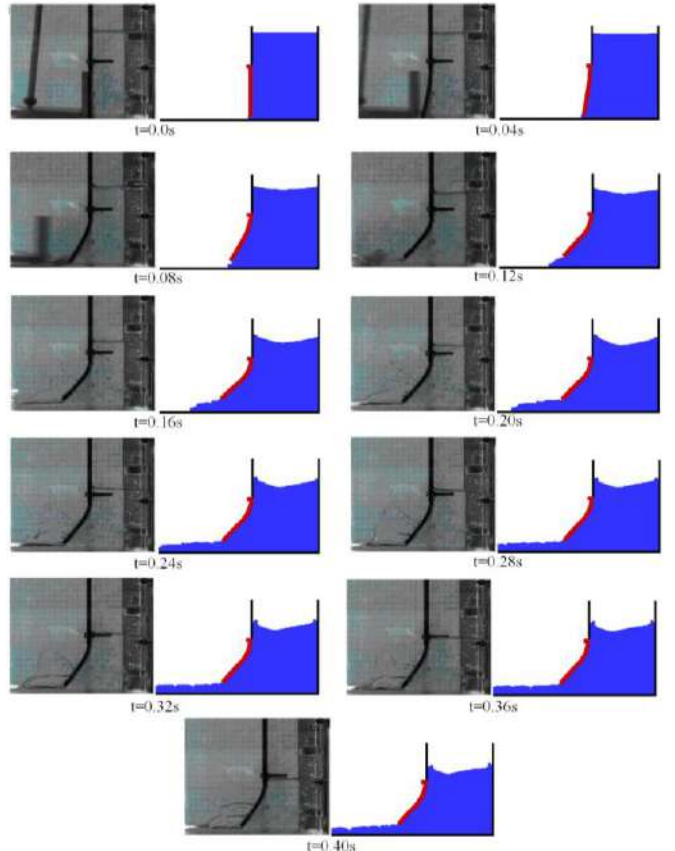


Figure 4. Comparison of experimental results with SPH simulation

Fig.4 shows the comparison between the numerical result and the experiment in 0.36s. Good agreement of baffle deformation caused by the fluid impact is observed. The distance from lower end of the baffle to the bottom of the container increases over time so that the outlet of the flow forms up, lowering the water level in the container. The deformation of the baffle is relieved because the pressure by the water level decreases. The gap between the free end of the baffle and the container bottom shrinks consequently.

It is also shown in Fig.4 that sunken surface of the fluid occurs close to the flow outlet. The reason for this phenomenon is that the static particle is used to simulate the rigid surface of the container and the position of these rigid particles stay immobilized. The fluid particles close to the rigid container surface tend to have lower flow velocity, adhesion is therefore observed. Nevertheless, fluid particles in the center region are not affected by that reason. They keep flowing towards the outlet at the bottom driven by gravity. The dip of the water surface therefore occurs in the position corresponding to the flow outlet. Rafiee^[16] and Shen^[17] simulated this experiment with improved SPH method. Stagnation of the flow next to the container inner surface is also observed in their studies.

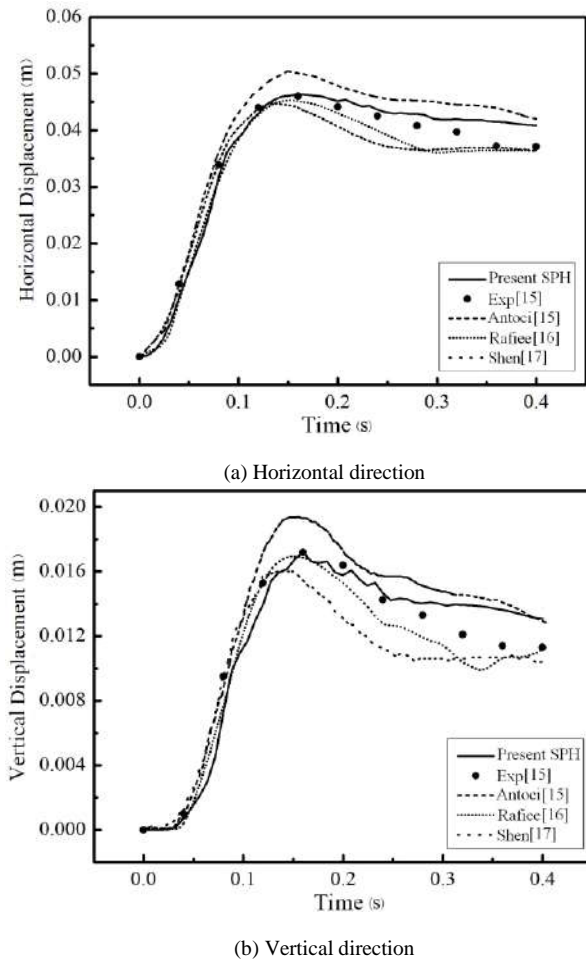


Figure 5. Horizontal and vertical displacement of the baffle's free end

Fig.5 shows the deflection trend of the baffle's free end over time, in both vertical and horizontal directions.

Simulation results in different studies show close trend to the experiment. The deformation caused by the fluid pressure exacerbates and maximizes near $t=0.16s$, then alleviates afterwards because of the decreased water level. The baffle will eventually go back to its original shape over a period of time due to its elasticity, which is not shown in Fig.5. Compared with the simulation results by Antoci^[15], Rafiee^[16] and Shen^[17], the result in this study shows better agreement with the experiment, particularly before $t=0.25s$. In Antoci's simulation, because viscous effect is omitted, water is treated as non-viscous micro compressible fluid which leads to the simulate result with larger deviation.

B. Dam-breaking impacted elastic baffle

In the simulation of fluid-solid coupling using continuum mechanics, the density field near the fluid-solid interface is relatively stable when the density of fluid and that of solid are very close as in the calculation. Nevertheless, the calculation will lose fidelity or even collapse when the density difference is larger between solid and fluid. This is because the particles of one type are involved in the density calculation of the other. Calculation instability is caused by large fluctuation of the density on the interface and pressure fluctuation in the solid due to large volumetric modulus.

In the SPH method proposed by Shen^[17], the governing equations of continuum mechanics is adopted to simulate the impact on the elastic baffle during dam-breaking process. The density ratio of solid to fluid is 1.1, but no larger density difference is investigated. However, in this study, a typical scenario of larger fluid-solid density ratio as 2.5 is calculated to verify the proposed SPH coupling method.

The configuration of the calculation is shown in Fig.6, where $L=0.146m$, $H=2L$, $b=0.08m$, $\delta=0.012m$, density of water is 1000kg/m^3 , dynamic viscosity coefficient is 1Pa s , elastic modulus is $1.0\times 10^6\text{Pa}$, the initial distance between particles is $d_0=0.0025\text{m}$. Total number of particles is 8222, in which 210 are solid elastic baffle particles, 7080 are fluid particles, and 932 are solid static particles to simulate the rigid container wall. The smooth length of both fluid particles and solid particles is $1.3d_0$, the smooth length between fluid and solid particles is $0.8d_0$, and length of calculation time step is $8\times 10^{-6}\text{s}$.

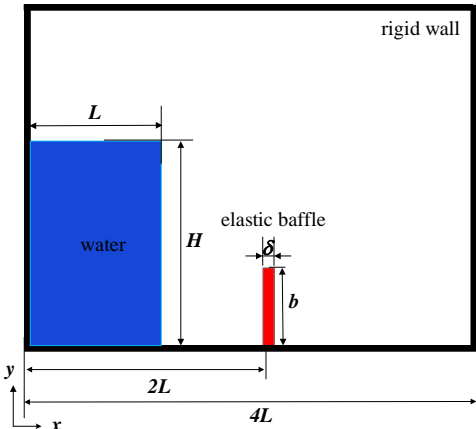


Figure 6. Configuration of dam-breaking with elastic plate

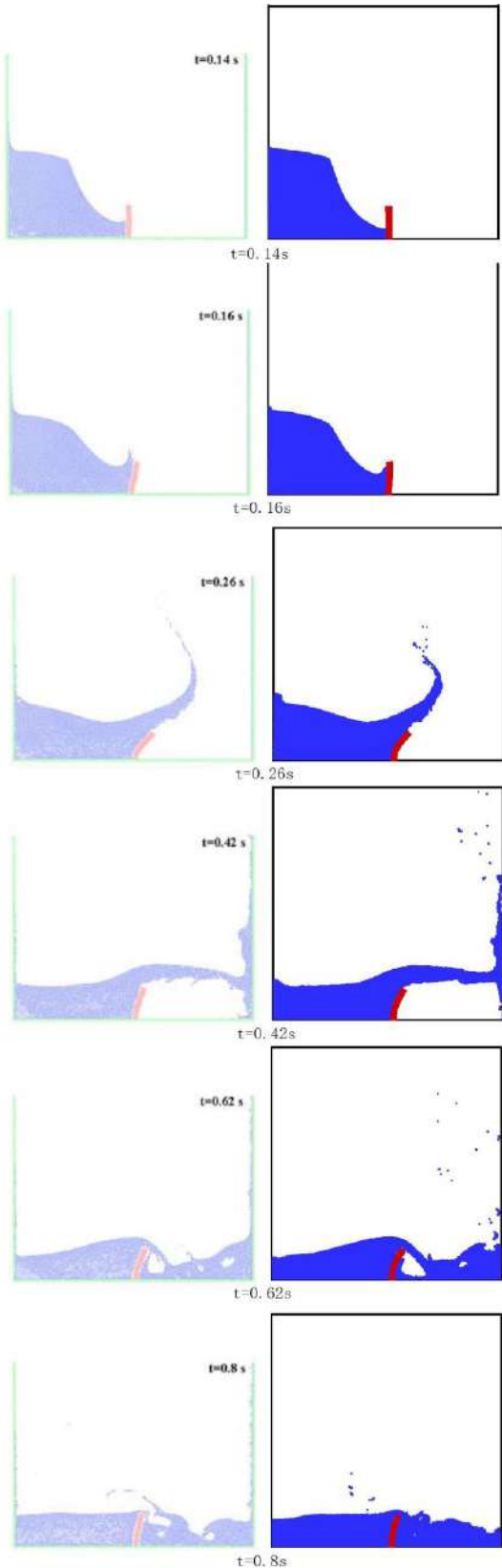


Figure 7. Comparison of the present SPH results with other available numerical results at different time

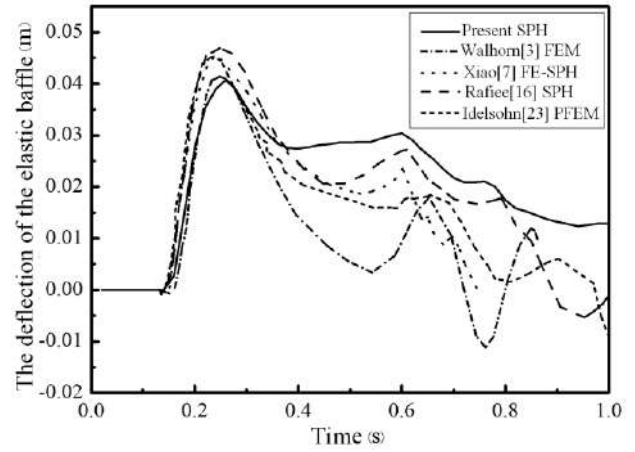


Figure 8. The deflection of the elastic baffle

Walhorn^[3], Xiao^[7], Rafiee^[16] and Idelsohn^[23] use the finite element method (FEM), FE-SPH, SPH and particle finite element method (PFEM) to simulate the same example, respectively. Fig.7 shows the results of this proposed method and results in [16]. Good agreement is observed in Fig.7 at different time. The baffle bends at the initial moment of impact while fluid rebounds and flow upwards obstructed by the baffle. Diversion and splash of the fluid occurs when the fluid hits the rigid wall of the container. The fluid eventually merges and calms due to gravity and the baffle's deflection vanishes.

The deformation of the baffle is depicted in Fig.8 for clear comparison between different methods. There is no difference in the results in the beginning of the impact. The deformation of the baffle commences at $t=0.13\text{ s}$ when the fluid contacts the baffle. The deformation maximizes at $t=0.23\text{ s}$ and starts to recover gradually. The rebounding process of the deformed baffle is not unanimous in different methods. The amplitude of the baffle is fierce when method with meshing is employed meanwhile meshless method gives relatively smaller amplitude of the baffle. In general, there are several fluctuations during the rebounding process and the fluctuation gradually tends to settle.

VI. CONCLUSION

Based on the fundamental principles of SPH method and fluid-solid two-phase mechanic characteristics, universal governing equations are proposed for continuum mechanics to describe the fluid-solid coupling dynamics. Two-way coupling of fluid and solid is realized by applying different types of particles in the support domain to solve the governing equations. No additional coupling terms are needed in the calculation in this proposed method.

A new coupling method is proposed for the fluid-solid interface coupling. The interaction is neglected when neighboring particles are departing and in the compressed condition. The derivative of corresponding kernel function can be assigned so that this numerical method is effectively simplified and more programmable by detecting the direction of particles motion and stress status. Different smooth length needs to be selected based on fluid and solid properties in order to solve the interaction and interference on the interface.

Numerical simulations of the fluid impacting elastic solid are conducted with this new SPH method. The deformation of the elastic baffle and the flow field of the fluid free surface are obtained, compared with experiments and reference. Good agreement is observed. Dam-breaking with great density difference is also simulated; results are compared with those of other numerical methods. It can be concluded from the results and comparison that the SPH method proposed in this study is capable of simulating the coupling during fluid impacting elastic solid effectively and accurately. It can be further investigated for the purpose of underwater structure force deflection and damage prognosis.

ACKNOWLEDGEMENT

This work was supported by the China National Natural Science Foundation (11762021), Xinjiang Natural Science Foundation (2017D01C085) and the Doctoral Starting up Foundation of Xinjiang University (BS160248).

REFERENCES

- [1] J. J. Monaghan, "Simulating free surface flow with SPH," *J. Comput. Phys.*, vol.110, pp.399-406, 1994.
- [2] B. Ataei-Ashtiani, G. Shobeyri, "Numerical simulation of landslide impulsive waves by incompressible smoothed particle hydrodynamics," *Int. J. Numer. Meth. Fl.*, vol.56, pp.209-232, 2008.
- [3] E. Walhorn, A. Kölke, B. Hübner, D. Dinkler, "Fluid-structure coupling within a monolithic model involving free surface flows," *Comput. Struct.*, vol.83, pp.2100-2111, 2005.
- [4] T. Nguyen-Thoi , P. Phung-Van, V. Ho-Huu , L. Le-Anh, "An edge-based smoothed finite element method (ES-FEM) for dynamic analysis of 2D Fluid-Solid interaction problems," *Ksce. J. Civ. Eng.*, vol.19, pp.641-650, 2015.
- [5] P. Sváček, "Numerical simulation of fluid-structure interactions with stabilized finite element method," *Adv. Eng. Softw.*, vol.114, pp.021181-021185, 2016.
- [6] J. Stasch, B. Avci, P. Wriggers, "Numerical simulation of fluid - structure interaction problems by a coupled SPH-FEM approach," *Pamm*, vol.16, pp.491-492, 2016.
- [7] Y. H. Xiao, X. Han, D. A. Hu, "Simulating fluid-structure interaction with FE-SPH method," *Chin. J. Comput.Phys.*, vol.28, pp.219-224, 2011.
- [8] F. Wang, R. Wang, W. Zhou, G. Chen, "Numerical simulation and experimental verification of the rock damage field under particle water jet impacting," *Int. J. Impact. Eng.*, vol.102, pp.169-179, 2017.
- [9] X. D. Lin, Y. Y. Lu, J. R. Tang, X. Ao, L. Zhang, "Numerical simulation of abrasive water jet breaking rock with SPH-FEM coupling algorithm," *J. Vib. Shock*, vol.33, pp.170-176, 2014.
- [10] R. A. Ginglad, J. J. Monaghan, "Smoothed particle hydrodynamics: theory and application to non-spherical stars," *Mon. Not. R. Astron. Soc.*, vol.181, pp.375-389, 1977.
- [11] L. B. Lucy, "A numerical approach to the testing of the fission hypothesis," *Astron. J.*, vol.88, pp.1013-1024, 1977.
- [12] G. Pahar, A. Dhar, "Robust boundary treatment for open-channel flows in divergence-free incompressible SPH," *J. Hydrol.*, vol.546, pp.464-475, 2017.
- [13] J. R. Shao, S. M. Li, M. B. Liu, "Numerical simulation of violent impinging jet flows with improved SPH Method," *Int. J. Comp. Meth-Sing.*, vol.13, pp.1641001(1-18), 2016.
- [14] M. B. Liu, Z. Zong, J. Z. Chang, "Developments and applications of smoothed particle hydrodynamics," *Advances in Mechanics*, vol.41, pp.217-234, 2011.
- [15] C. Antoci, M. Gallati, S. Sibilla, "Numerical simulation of fluid-structure interaction by SPH," *Comput. Struct.*, vol.85, pp.879-890, 2007.
- [16] A. Rafiee, K. P. Thiagarajan, "An SPH projection method for simulating fluid-hypoelastic structure interaction," *Comput. Method. Appl. M.*, vol.198, pp.2785-2795, 2009.
- [17] Y. M. Shen, K. He, J. Q. Chen, X.X.Yuan, "Numerical simulation of free surface flow impacting elastic structure with SPH uniform method," *J. Vib. Shock*, vol.34, pp.60-65, 2015.
- [18] G. R. Liu, M. B. Liu, "Smoothed particle hydrodynamics:A meshfree particle methods," *World Scientific Press*, Singapore, 2003.
- [19] J. J. Monaghan, "Smoothed particle hydrodynamics," *Annu. Rev. Astron. Astr.*, vol.30, pp.543-574, 1992.
- [20] J. J. Monaghan, "SPH without a tensile instability," *J. Comput. Phys.*, vol.159, pp.290-311, 2000.
- [21] J. P. Morris, P. J. Fox, Y. Zhu, "Modeling low Reynolds number incompressible flows using SPH," *J. Comput. Phys.*, vol.136, pp.214-226, 1997.
- [22] H. F. Qiang, L. J. Meng, "Computational simulation of hypervelocity penetration using adaptive SPH method," *J. Tianjin. Univ.*, vol.12, pp.75-78, 2006.
- [23] S. R. Idelsohn, J. Martí, A. Limache, E. Oñate, "Unified Lagrangian formulation for elastic solids and incompressible fluids: Application to fluid-structure interaction problems via the PFEM," *Comput. Method. Appl. M.*, vol. 197, pp.1762-1776, 2008.

Numerical Simulation of Rayleigh-Taylor Instability by Multiphase MPS Method

Xiao Wen

State Key Laboratory of Ocean Engineering, School of Naval Architecture, Ocean and Civil Engineering, Shanghai Jiao Tong University, Collaborative Innovation Center for Advanced Ship and Deep-Sea Exploration
Shanghai 200240, China

Decheng Wan*

State Key Laboratory of Ocean Engineering, School of Naval Architecture, Ocean and Civil Engineering, Shanghai Jiao Tong University, Collaborative Innovation Center for Advanced Ship and Deep-Sea Exploration
Shanghai 200240, China

*Corresponding author: dcwan@sjtu.edu.cn

Abstract—The Rayleigh-Taylor instability problem is one of the classic hydrodynamic instability cases in natural scenarios and industrial applications. For the numerical simulation of the Rayleigh-Taylor instability problem, this paper presents a multiphase method based on the moving particle semi-implicit (MPS) method. Herein, the incompressibility of the fluids is satisfied by solving a Poisson Pressure Equation and the pressure fluctuation is suppressed. A single set of equations is utilized for fluids with different densities, making the method relatively simple. To deal with the mathematical discontinuity of density in the two-phase interface, a transitional region is introduced into this method. For particles in the transitional region, a density smoothing scheme is applied to improve the numerical stability. The simulation results show that the present MPS multiphase method is capable of capturing the evolutionary features of the Rayleigh-Taylor instability, even in the later stage when the two-phase interface is quite distorted. The unphysical penetration in the interface is limited, proving the stability and accuracy of the proposed method.

I. INTRODUCTION

The Rayleigh-Taylor instability (RTI) is one of the most common instability phenomena existing in multi-fluid flows. Due to the density difference of different fluids, the two-phase interface is sensitive to various perturbation. Even a very small perturbation may induce a fingering RTI in which the light fluid violently pushes the heavy fluid against gravity. The RTI can be observed in a wide range of natural scenarios and industrial applications, including astrophysics, nuclear engineering, turbulent mixing, and inertial confinement fusion (ICF).

Due to the strong nonlinearity of the RTI, theoretical investigations have difficulties in obtaining correct results beyond the early linear regime. And experimental investigations are easily influenced by the perturbation introduced in the experimental process itself. In recent decades, the huge progress of Computational Fluid Dynamics (CFD) facilitates the application of a variety of numerical methods to the simulations of the RTI.

In the RTI simulations, the tracing of the two-phase interface is the most important technology. Compared with grid-based methods, the gridless particle methods is more advantageous for solving multiphase problems with large deformation of the two -phase interface. However, stable multiphase simulations is difficult to be conducted due to the discontinuity of density in the interface and the phenomenon of pressure fluctuation commonly existing in particle method. Therefore, a stable and accurate multiphase model in particle methods is necessary to be studied.

The moving particle semi-implicit (MPS) which is originally proposed by Koshizuka and Oka [1], is an important kind of particle method. By solving the Poisson Pressure Equation (PPE), the MPS method is suitable for the simulations of fully incompressible flow. The first MPS multiphase method is developed by Gotoh and Fredsøe [2] for solid-liquid two-phase flows. Liu et al. [3] proposed a hybrid MPS-FVM method for the viscous, incompressible, multiphase flows, in which the heavier fluid is represented by moving particles while the lighter fluid is defined on the mesh. Shakibaeinia and Jin [4] studied a straightforward multiphase method based on the weakly compressible MPS (WCMPS) method, by treating the multiphase system as a multi-viscosity and multi-density system, but the unphysical penetration is observed due to the weakly compressibility of their method. Khayyer and Gotoh [5] firstly developed four schemes which are more accurate and consistent than the schemes of the original MPS method, then a first order density smoothing scheme [6] is derived for multiphase flows characterized by high density ratios. Although experiencing a much shorter development time than the grid-based methods, the MPS method has shown the advantages in multiphase simulations, especially when the large deformation of interface exists, such as the simulation of RTI.

In this paper, a MPS multiphase solver is developed and applied to the simulation of RTI. The multiphase solver is based on our in-house single phase particle method solver MLParticle-SJTU, and a density smoothing scheme is included for the treatment of two-phase interface. The MLParticle-SJTU solver adopts the modified MPS method and has been commonly applied to a variety of violent hydrodynamic problems, such as liquid sloshing flows [7-9], dam-breaking flows [10-12], wave-floating body interaction [13,14], water entry problems [15,16], fluid-structure interaction [17,18]. The

density smoothing scheme here is similar with the scheme adopted by Shakibaeinia and Jin [4], in which the density discontinuity in the interface is avoided through setting a transitional region. In the next parts of this paper, the MPS multiphase method is firstly introduced in detail. Then, the simulation of RTI is conducted and the stability and accuracy of the MPS multiphase method is validated.

II. NUMERICAL SCHEME

A. Governing Equations

In the present method, the multiphase system is treated as a multi-density system. The form of governing equations for different fluids is identical, written as:

$$\frac{1}{\rho} \frac{D\rho}{Dt} = -\nabla \cdot \mathbf{V} = 0 \quad (1)$$

$$\frac{D\mathbf{V}}{Dt} = -\frac{1}{\rho} \nabla \cdot \mathbf{P} + \nu \nabla^2 \cdot \mathbf{V} + \mathbf{g} \quad (2)$$

where \mathbf{V} is the flow velocity vector, P is the pressure, ρ is the fluid density, ν is the kinematic viscosity, \mathbf{g} is the gravitational acceleration vector. For different fluids, the ρ and ν in above equations are different. Differing from the governing equations in grid-based methods, the convective acceleration term in the left hand side of momentum conservation equation is included in the material derivative, thus the numerical diffusion is eliminated.

B. Kernel Function

The spatial derivatives in the governing equation need to be approximated by the particles interaction. A particle interacts with all particles within a specified domain. The size of this domain is defined as the radius of the interaction area of each particle. To weight the interaction of each pair of particles, a kernel function is introduced in the MPS method. This article adopts a modified kernel function proposed by Zhang and Wan [13], which can be written as:

$$W(r_{ij}) = \begin{cases} \frac{r_e}{0.85r_{ij} + 0.15r_e} - 1 & (0 \leq r_{ij} < r_e) \\ 0 & (r_e \leq r_{ij}) \end{cases} \quad (3)$$

where r_{ij} is the distance between particle i and particle j , r_e is the maximum radius of support region. Compared with the original kernel function proposed by Koshizuka [1], the modified kernel function prevents the existence of singular point by making the value of $W(r_{ij})$ finite when the r_{ij} is equal to zero. Thus the numerical instability of the MPS method can be improved.

C. Gradient Model

In the MPS method, the gradient operator is discretized into a local weighted average of radial function. In this paper, an anti-symmetric gradient model is adopted, written as:

$$\langle \nabla P \rangle_i = \frac{d}{n^0} \sum_{j \neq i} \left[\frac{P_j - P_{i_min}}{|\mathbf{r}_j - \mathbf{r}_i|^2} (\mathbf{r}_j - \mathbf{r}_i) \cdot \mathbf{W}(r_{ij}) \right] \quad (4)$$

where $\langle \cdot \rangle_i$ represents the kernel approximation in particle i , n^0 represents the initial particle number density, d is the number of space dimension, P_{i_min} refers to the minimum pressure within the support domain of particle i . This model is proposed by Koshizuka [19], to overcome the tensile instability of original model by ensuring repulsive force between particles.

D. Laplacian Model

The Laplacian model used here is derived by Koshizuka [1] from the physical concept of diffusion, written as:

$$\langle \nabla^2 \phi \rangle_i = \frac{2d}{n^0 \lambda} \sum_{j \neq i} (\phi_j - \phi_i) \cdot \mathbf{W}(r_{ij}) \quad (5)$$

$$\lambda = \frac{\sum_{j \neq i} W(r_{ij}) \cdot |\mathbf{r}_j - \mathbf{r}_i|^2}{\sum_{j \neq i} W(r_{ij})} \quad (6)$$

where λ is a parameter introduced to keep the increase of variance equal to analytical solution.

E. Model of Incompressibility

In order to keep the fluids incompressible, a semi-implicit algorithm is employed in the MPS method. The main characteristic of this algorithm is the prediction-correction process in each iteration. In the prediction step, a temporal velocity is explicitly predicted based on the gravity term and viscosity term as follow:

$$\mathbf{V}_i^* = \mathbf{V}_i^k + \Delta t (\nu \nabla^2 \cdot \mathbf{V} + \mathbf{g}) \quad (7)$$

Since the temporal velocity field doesn't satisfy the divergence-free condition, a second correction step is required to project the velocity field into a divergence-free space. The velocity is corrected based on the pressure gradient as follow:

$$\mathbf{V}_i^{k+1} = \mathbf{V}_i^* - \frac{\Delta t}{\rho} \nabla P^{k+1} \quad (8)$$

In the MPS method, the pressure field is obtained by solving the Poisson Pressure Equation (PPE). To suppress the pressure oscillation, we employ the PPE with the mixed source term of constant particle number density condition and divergence-free condition. This is developed by Tanaka and Masunaga [20] and rewritten by Lee [21] as:

$$\langle \nabla^2 P^{k+1} \rangle_i = (1-\gamma) \frac{\rho}{\Delta t} \nabla \cdot \mathbf{V}_i^* - \gamma \frac{\rho}{\Delta t^2} \frac{\langle n^k \rangle_i - n^0}{n^0} \quad (9)$$

where γ is a parameter suggested to be 0.01, the superscripts k and $k+1$ indicate the current time step, $\langle n^k \rangle_i$ represents the particle number density at k^{th} time step.

F. Density Smoothing

When the particle methods are employed to simulate the multiphase flows, a major challenge is the density discontinuity in the two-phase interface, which would result in an unsmooth pressure gradient field. This is the main reason of the interface disorder and the blow-up of simulation.

To overcome this problem, we adopt a density smoothing method similar with the one used by Shakibaeinia and Jin [4]. In this method, a transitional region is introduced to smooth the densities of particles within a certain distance (the width of density smoothing) from the interface. The densities of these particles are re-evaluated according to a spatial averaging of the densities of all neighbouring particles. The spatial averaging follows the formula below:

$$\langle \rho \rangle_i = \frac{\sum_{j \neq i} \rho_j \cdot W(r_{ij})}{\sum_{j \neq i} W(r_{ij})} \quad (10)$$

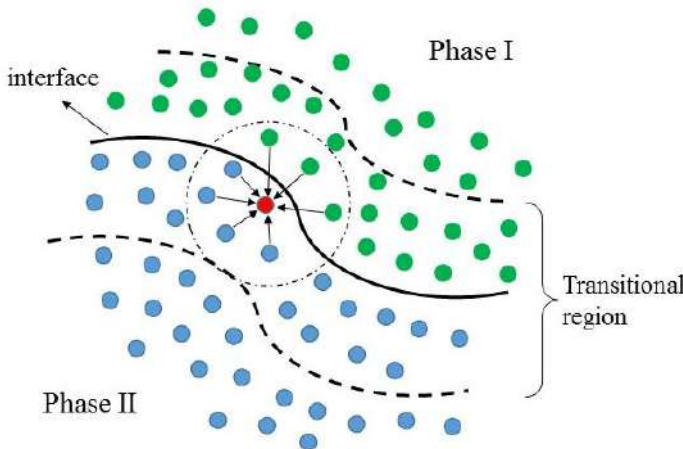


Figure 1. Sketch of density smoothing

The results obtained by Shakibaeinia and Jin [4] have validated the reliability of the density smoothing scheme. However, there still be some unphysical penetration being observed in the interface, even in the early stage when the motion of particles is not violent. This may be induced by the weakly compressibility of the WCMPS method used in their study. In this paper, we employ a fully incompressible MPS, which has been proven to be effective to suppress the pressure fluctuation. Therefore, the density smoothing scheme is believed to be enough to deal with the density discontinuity in the two-phase interface.

III. NUMERICAL SIMULATION

A. Numerical Setup

In this part, we consider the RTI problem in a rectangular container with the dimension of 0.5 m (width) \times 1 m (height), as illustrated in Fig. 2. The origin of coordinates is fixed in the middle point of this container. The heavier fluid is identified by the Green color, with a density of 3000 kg/m³. The lighter fluid is identified by the blue color, with a density of 1000 kg/m³. The interface of these two fluids is given an initial single mode perturbation, $y_{\text{interface}} = 0.025 \cos(4\pi x)$. The gravity acceleration in this simulation is set to be $g=10$ m/s and points downwards. To better test the stability of this method, the viscous effect is ignored in our simulation. The initial particle distance r_0 is 0.005 m, meaning that totally 100×200 fluid particles are used in our simulation. In the MPS method, the radiiuses of the interaction area for different models don't need to be quite the same. For the purpose of saving computational cost, the radius of the interaction area for gradient model and the width of density smoothing is $4.1r_0$, the radius of the interaction area for Laplacian model is $8.1r_0$ in our simulation.

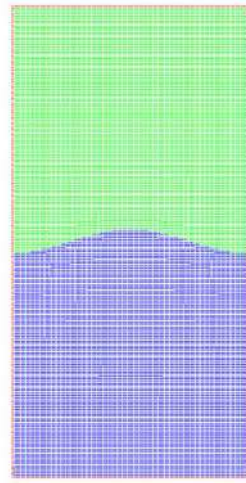


Figure 2. Initial distribution of particles

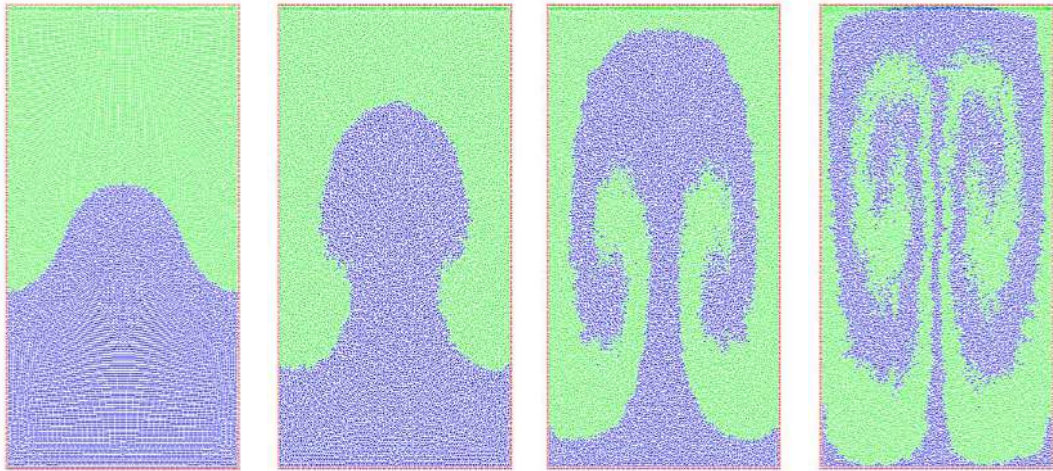


Figure 3. Evolution of RTI with a density ratio of 3:1, at $t = 0.5$ s, 1 s, 1.5 s, 2 s.

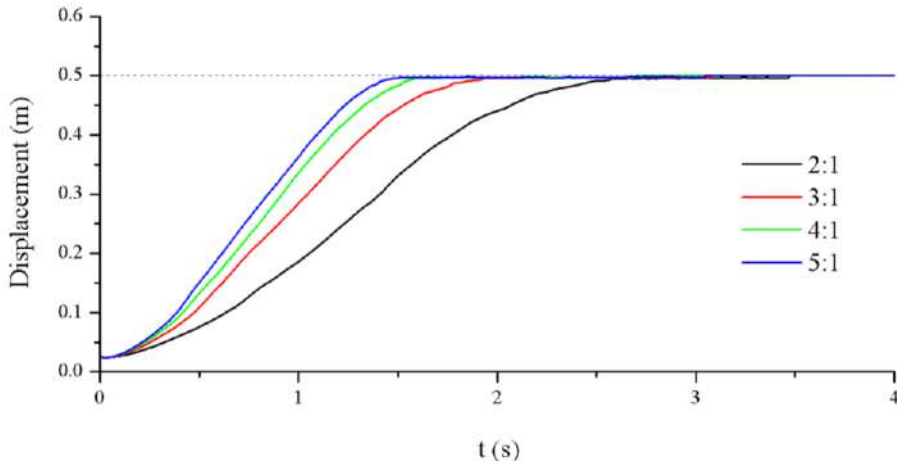


Figure 4. Displacement of the peak of the lighter fluid with different density ratios.

B. Results

Fig. 3 shows the evolution of the RTI problem with a density ratio of 3:1 at 0.5 s, 1 s, 1.5 s, 2 s. The simulation snapshot of the simulation demonstrates the ability of the present MPS multiphase method to capture the complex interface between two different fluids. Under the effect of initial perturbation, the lighter fluid moves upward and pushes the heavier fluid upon, then a bubble is formed at 0.5 s. After about 1 s, the upside part of the lighter fluid starts to form a mushroom shape. At 1.5 s, due to the influence of the neighbouring heavier fluid moving downward, two streams of the lighter fluid are separated from the rising part and strong vortex roll can be observed. At 2 s, the vortex roll becomes stronger and the light fluid reaches the top of the container. The evolution of RTI is similar with the results obtained by Shakibaenia and Jin [4] at early stage, but due to ignorance of viscous effects in our simulation, more of the lighter fluid are able to move upward, resulting in a

more complex vortex structure. And the unphysical penetrations in our simulation are much less compared with the results obtained by Shakibaenia and Jin [4] with a large kinematic viscosity of 0.01.

Fig. 4 compared the growth rate of RTI with different density ratios. When the density ratio increasing from 2:1 to 5:1, the time needed for the lighter fluid to reach the top of the container is largely reduced, indicating the importance of the density ratio for RTI problems. This also illustrates the applicability of the present MPS multiphase method for multiphase flows with different density ratios.

Fig. 5 shows the velocity vector of all particles in the RTI simulation. An obvious symmetry property can be observed during the whole RTI evolution process. Two vortexes appear respectively at the two balanced positions of the initial perturbation at 0.5 s, which is induced by the interaction of upward motion of the lighter fluid and downward motion of the heavier fluid. Then these vortexes

keep developing fast and forms multilayer vortex with clear two-phase interface at 2 s. Moreover, another two vortexes appear near the corner in the bottom of the container at 2 s, complicating the flow field structure.

Fig. 6 and Fig. 7 demonstrate the y-velocity and x-velocity during the simulation, respectively. In y-direction, the velocity of middle part of the fluid field points upside, just the reverse for the fluid near two side walls. In x-direction, the fluid near the bottom converges toward the middle of the tank, while the fluid near the top separately flows to two side walls.

IV. CONCLUSION

The paper proposes a MPS multiphase method and develops corresponding solver based on our in-house single phase particle method solver MLParticle-SJTU. When the multiphase solver is applied to the simulation of Rayleigh-Taylor instability, stable and accurate results can be obtained. The density smoothing scheme used in this paper can greatly reduce the unphysical penetrations appearing in other multiphase methods and keep the two-phase interface clear and natural, even when the interface is quite distorted. The results show that the complete evolution of Rayleigh-Taylor instability when an initial perturbation is given to the interface position. At the beginning, the lighter fluid pushes upon the heavier fluid and forms a mush-like shape. Two vortexes appear and develop fast to become the main flow characteristic in the container. Another two vortexes appear in the later time, indicating the complexity of the RTI problems. The simulations of RTI with different density ratios demonstrate the important role of the high density ratio in improving the growth rate of RTI, and validate the applicability of the MPS multiphase method in different conditions.

ACKNOWLEDGEMENT

This work is supported by the National Natural Science Foundation of China (51379125, 51490675, 11432009, 51579145), Chang Jiang Scholars Program (T2014099), Shanghai Excellent Academic Leaders Program (17XD1402300), Program for Professor of Special Appointment (Eastern Scholar) at Shanghai Institutions of Higher Learning (2013022), Innovative Special Project of Numerical Tank of Ministry of Industry and Information Technology of China (2016-23/09) and Lloyd's Register Foundation for doctoral student, to which the authors are most grateful.

REFERENCES

- [1] S. Koshizuka and Y. Oka, "Moving-particle semi-implicit method for fragmentation of incompressible fluid," Nuclear Science & Engineering, vol. 123(3), pp. 421-434, 1996.
- [2] H. Gotoh and J. Fredsøe, "Lagrangian two-phase flow model of the settling behavior of fine sediment dumped into water," Proc. ICCE, Sydney, pp. 3906-3919, 2000.

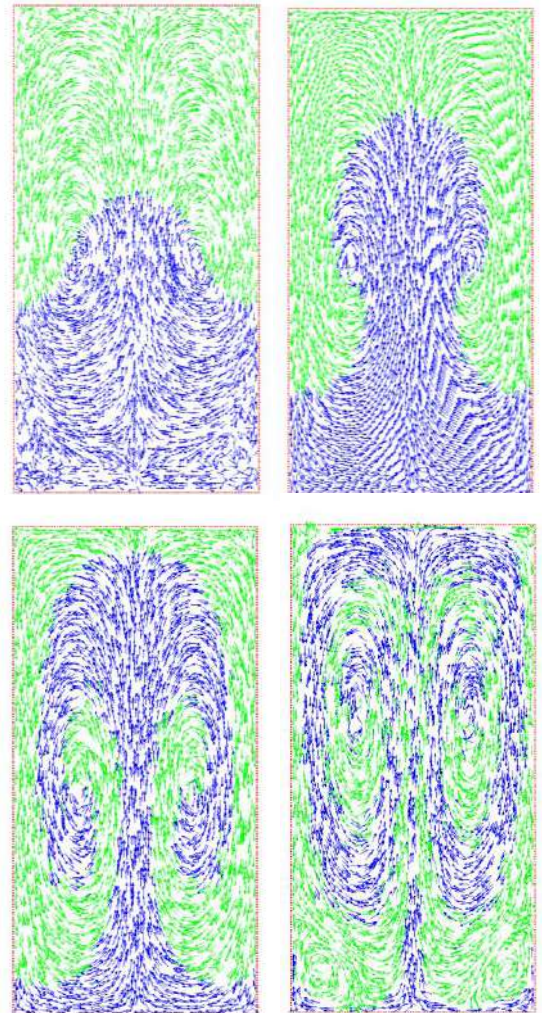


Figure 5. Velocity vector of RTI with a density ratio of 3:1, at $t = 0.5$ s, 1 s, 1.5 s, 2 s

- [3] J. Liu, S. Koshizuka, and Y. Oka, "A hybrid particle-mesh method for viscous, incompressible, multiphase flows," Journal of Computational Physics, vol. 202(1), pp. 65-93, 2005.
- [4] A. Shakibaenia and Y. C. Jin, "MPS mesh-free particle method for multiphase flows," Computer Methods in Applied Mechanics & Engineering, vol. 229, pp. 13-26, 2012.
- [5] A. Khayyer and H. Gotoh, "Enhancement of stability and accuracy of the moving particle semi-implicit method," Journal of Computational Physics, vol. 230, pp. 3093-3118, 2011.
- [6] A. Khayyer and H. Gotoh, "Enhancement of performance and stability of MPS mesh-free particle method for multiphase flows characterized by high density ratios," Journal of Computational Physics, vol. 242, pp. 211-233, 2013.
- [7] X. Wen, X. Chen, and D. C. Wan, "MPS simulation of sloshing flows in a tuned liquid damper," Proceedings of the Twenty-seven International Ocean and Polar Engineering Conference, San Francisco, USA, pp. 1009-1016, 2017.
- [8] Y. X. Zhang and D. C. Wan, "Comparative study of MPS method and Level-Set method for sloshing flows," Journal of Hydrodynamics, vol. 26(4), pp. 577-585, 2014.

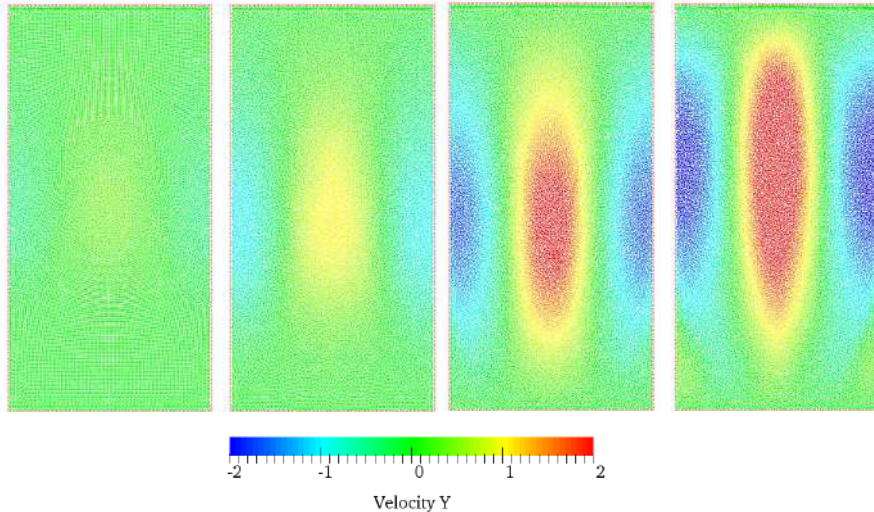


Figure 6. Y-velocity of RTI with a density ratio of 3:1 , at $t = 0.5$ s, 1 s, 1.5 s, 2 s.

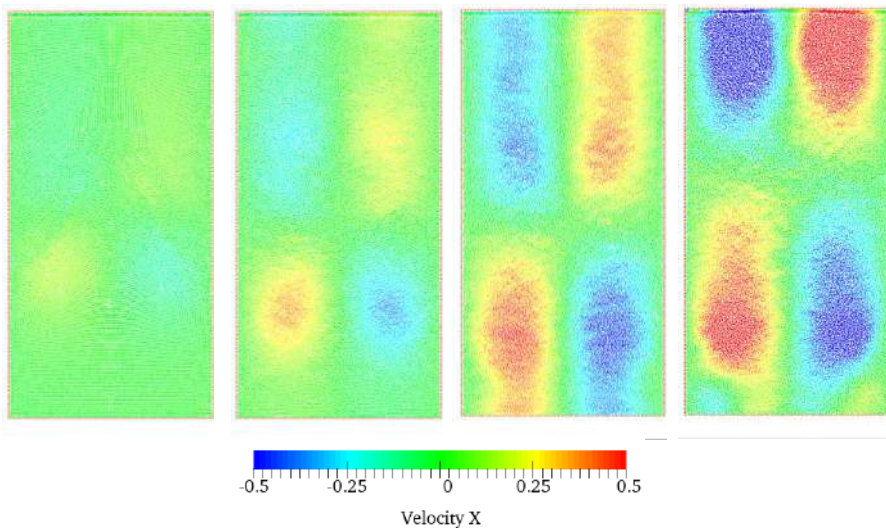


Figure 7. X-velocity of RTI with a density ratio of 3:1 , at $t = 0.5$ s, 1 s, 1.5 s, 2

- [9] X. Chen, Z. Y. Tang, and D. C. Wan, "The effects of T type baffle on liquid sloshing by MPS method, Proceedings of 3rd International Conference on Violent Flows, Osaka, Japan, No. 25, 2016.
- [10] Y. X. Zhang, "Application of MPS in 3D dam breaking flows," Scientia Sinica, vol. 41, pp. 140-151, 2011. (in Chinese)
- [11] Z. Y. Tang, Y. L. Zhang, and D. C. Wan, "Multi-resolution MPS method for free surface flows," International Journal of Computational Methods, vol. 13(04), No. 1641018, 2016.
- [12] Z. Y. Tang, Y. L. Zhang, and D. C. Wan, "Numerical simulation of 3-D free surface flows by overlapping MPS," Journal of Hydrodynamics, vol. 28(2), pp. 306-312, 2016.
- [13] Y. L. Zhang and D. C. Wan, "Numerical study of interactions between waves and free rolling body by IMPS method," Computers and Fluids, vol. 155, pp. 124-133, 2016.
- [14] Y. L. Zhang, Z. Y. Tang, and D. C. Wan, "Numerical investigations of waves interacting with free rolling body by modified MPS method," International Journal of Computational Methods, vol. 13(04), No. 1641013, 2016.
- [15] X. Chen, C. P. Rao, and D. C. Wan, "Numerical simulation of water entry of two-dimensional wedge by MPS," Chinese Journal of Computational Mechanics, vol. 34(3), pp. 356-362, 2017.
- [16] Y. L. Zhang, Z. Y. Tang, and D. C. Wan, "Simulation of water entry of a free-falling wedge by improved MPS method," Proceedings of the Twenty-sixth International Ocean and Polar Engineering Conference, Rhodes, Greece, pp. 220-227, 2016.
- [17] Y. L. Zhang, X. Chen, and D. C. Wan, "MPS-FEM coupled method for the comparison study of liquid sloshing flows interacting with rigid and elastic baffles," Applied Mathematics and Mechanics, vol. 37(12), pp. 1359-1377, 2016.
- [18] Y. L. Zhang, X. Chen, and D. C. Wan, "Sloshing flows in an elastic tank with high filling liquid by MPS-FEM coupled method," Proceedings of the Twenty-seven International Ocean and Polar Engineering Conference, San Francisco, USA, pp. 1077-1084, 2017.
- [19] S. Koshizuka, A. Nobe, and Y. Oka, "Numerical analysis of breaking waves using the moving particle semi - implicit method," International Journal for Numerical Methods in Fluids, vol. 26(7), pp. 751-769, 1998.
- [20] M. Tanaka and T. Masunaga, "Stabilization and smoothing of pressure in MPS method by quasi-compressibility," Journal of Computational Physics, vol. 229(11), pp. 4279-4290, 2010.
- [21] B. H. Lee, J. C. Park, M. H. Kim, and S. C. Hwang, "Step-by-step improvement of MPS method in simulating violent free-surface motions and impact-loads," Computer Methods in Applied Mechanics and Engineering, vol. 200(9), pp. 1113-1125, 2011.

Modeling of single film bubble and numerical study of the Plateau structure in foam system

Zhongguo SUN

School of Energy and Power Engineering
Xi'an Jiaotong University
Xi'an, China
sun.zg@xjtu.edu.cn

Yijie SUN

School of Energy and Power Engineering
Xi'an Jiaotong University
Xi'an, China

Ni NI

School of Energy and Power Engineering
Xi'an Jiaotong University
Xi'an, China

Guang XI

School of Energy and Power Engineering
Xi'an Jiaotong University
Xi'an, China
xiguang@xjtu.edu.cn

Abstract—The single-film bubble has a special geometry that a certain amount of gas is shrouded by a layer of liquid film under the surface tension, which acts both on the inside and outside surfaces of the bubble. Based on the mesh-less Moving Particle Semi-implicit method (MPS), a single-film double-gas-liquid-interface surface tension model (SDST) was established for the single-film bubble which has double gas-liquid interfaces. Then the complex interface movement in the oscillation process of the single-film bubble was captured. Typical flow phenomena and deformation characteristics of the liquid film were obtained by simulating and analyzing the coalescence and connection process of two single-film bubbles. In addition, a concave tangent method was proposed to calculate the angle of the liquid film of the connected bubbles, which could help describe the shape quantitatively. Furthermore, the classic Plateau structure in foam system was simulated and numerically proved to be the steady status for multi-bubble connections.

I. INTRODUCTION

Single film bubble is the basic unit of foam, and it has a special structure and mechanical characteristics that a bulk of gas is enfolded by a very thin liquid film, and surface tension force acts both on the inside and outside of the liquid film. It is quite common that one single this kind of bubble will stay in sphere shape because of the pressure difference between the two sides and the shrink tendency of the surface tension. In the case of two single film bubbles act with each other, coalescence or connection would happen. When coalescence happens, only one larger bubble would remain, and the volume of the gas inside the new bubble is the summation of the two original bubbles. When connection happens, a stable new interface between the two connected bubbles is generated.

Many scholars interested in the study of gas-liquid interface and the action of surface tension on the free surface. In the theoretical analysis aspect, Chan et al proposed a two-

stage model for bubble generating^[1], Yang analyzed the volume of the bubbles in the liquid based on the two-phase fluid dynamics theory, he found the equation to calculate the bubble volume and could estimate the size of the bubble^[2].

In the experimental aspect, Zhang used high speed camera to investigate the bubble movement in the water^[1]. Chan described the study on the film drainage process of the droplet and bubble by using atomic force microscope, optical interference stripes image and coalescence timing. Gu used double parallel probe and camera to study the single bubble flow inside a horizontal straight tube^[4].

In the numerical simulation aspect, conventional CFD methods contain the Front-tracking^[5], VOF^[6], Level-set^[7] and LBM^[8] etc. Chen et al employed VOF method to investigate the influence of the surface tension coefficient and viscosity coefficient on the rising bubble movement^[9]. Zhang et al used interface reproducing technology in VOF to discuss the interaction between the bubbles with different position settings in the liquid^[10]. Sussman combined the VOF and Level-set methods and simulated the bubble rising without viscosity and sphere bubble breaking near the wall^[11]. LBM method was also applied in the research fields of single bubble or several bubbles deformation.

However, most researches mentioned above were all about the bubble's shape and deformations in liquid or tube based on the single-gas-liquid-interface surface tension model, the study about the behavior of single film bubble in the air, which means double-gas-liquid-interfaces were seldom reported according to the best of the author's knowledge. That's because the single film bubble has double-interface structure and the liquid film is very thin, furthermore, the coalescence and connection process come with large deformation and complex interface change, which means high request on the interface tracing and computational stability for the numerical method.

The Moving Particle Semi-implicit, (MPS) [14] was employed in this study which has advantage on dealing with the flow cases with large deformation. So far, the MPS method has been successfully used in the study of engineering and science researches, such as the simulation of bubble rising and deforming process in water [15], free surface movement driven by surface tension force etc [16-19]. This paper will study the coalescence and connection process for single film bubble, and simulate the Plateau structure by using meshless MPS method.

II. NUMERICAL METHOD

The MPS method is a kind of meshless method and basically has the same theory as SPH method but with different equation solving process. In MPS the pressure field is calculated implicitly by solving a pressure Poisson equation. The skeleton of the method was introduced briefly as follow.

A. Governing Equations

The governing equations of fluid mechanics include the conservation equations of the mass and momentum. For an incompressible flow, they can be written in a Lagrangian form as:

$$\frac{D\rho}{Dt} + \rho \frac{\partial u_i}{\partial x_i} = 0 \quad (1)$$

$$\rho \frac{Du_i}{Dt} = -\frac{\partial p}{\partial x_i} + \frac{\partial \tau_{ij}}{\partial x_j} + \rho f_i + \gamma \quad (2)$$

Where ρ is the fluid density, u_i is the fluid velocity, τ_{ij} is the shear stress, f_i is the mass of external force in the unit, p is the fluid pressure, γ is the surface tension.

B. Kernel Function

MPS method uses the kernel function to form the particle action model to discrete control equations. The kernel function used in this paper is:

$$w(r) = \begin{cases} \frac{r_e}{r} - 1 & (r < r_e) \\ 0 & (r \geq r_e) \end{cases} \quad (3)$$

Where r is the distance between the two particles, r_e is the radius of the particle scopes, and the kernel function is only valid within the radius of influence of the particles.

C. Gradient Operator and Laplacian Operator

The gradient operator and the Laplacian operator in the control equation can be discretized based on the kernel function:

$$\langle \nabla \varphi \rangle_i = \frac{d}{n^0} \sum_{j \neq i} \frac{p_j - p_i}{|r_j - r_i|^2} (\varphi_j - \varphi_i) w(|r_j - r_i|) \quad (4)$$

$$\langle \nabla^2 \varphi \rangle_i = \frac{2d}{\lambda n^0} \sum_{j \neq i} (\varphi_j - \varphi_i) w(|r_j - r_i|) \quad (5)$$

The MPS method calls this discrete method based on the kernel function as the model of interaction between particles.

III. SURFACE TENSION MODEL

A. Basic Theory for Single Film Bubble

According to its geometry character (as shown in Fig. 1), the single film bubble in the air could be considered as a liquid film shell which enfolds amount of gas inside. There is gas on both side of the liquid film, and we consider the gas outside of the bubble is atmosphere which has the constant pressure ($P=0.0$) and very limit influence on the bubble. In other words, the gas outside of the bubble is setting as no viscosity and has nothing to do with the movement of liquid film. The gas inside the bubble is taken as incompressible fluid and has even density and the same pressure. Though the single liquid film is very thin, it has two gas-liquid interfaces as shown in the cross section in Fig. 1.

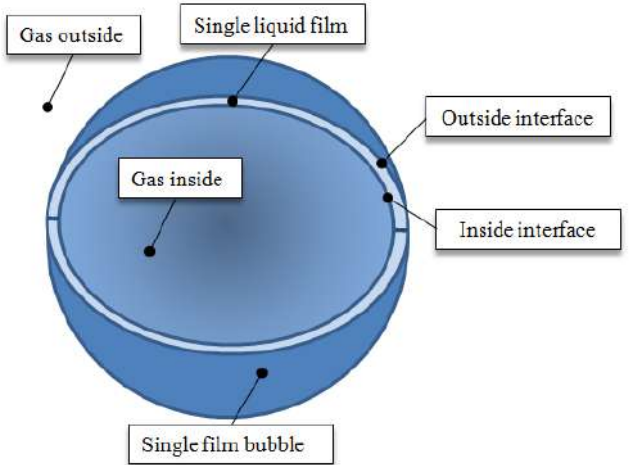


Figure 1. Sketch-map of the structure of single film bubble

B. Surface Tension Model for Single Film Bubble

Based on the theory, a single-film double-gas-liquid-interface surface tension model (SDST) for single film bubble was proposed (shown in Fig. 2). Within the framework of the MPS method, the surface tension forces on the two interfaces will be calculated separately using the surface free energy surface tension model, which will be discussed in the later chapter.

The influence of the outside gas on bubble will be totally ignored except the atmosphere pressure, because the

flow of the liquid film and the deformation of the bubble all happen in very low Reynolds Number with very small flow velocity. In the algorithm of MPS, there will be no fluid particles discrete for the gas phase outside the bubble, and the outside free surface open in the air is set zero pressure constantly.

On the other hand, the gas inside the bubble is considered incompressible with even density and pressure. Incompressible viscosity fluid particles were discrete for

them with physical parameters of gas, and the pressure of these particles on the inside interface is set the same as the gas inside the bubble.

In order to accurately calculate the surface tension force for both sides, an interlayer of viscosity fluid particles were employed to stand for the liquid between the two interfaces, and their flow parameters such as the velocity, position and pressure were all integrated calculated.

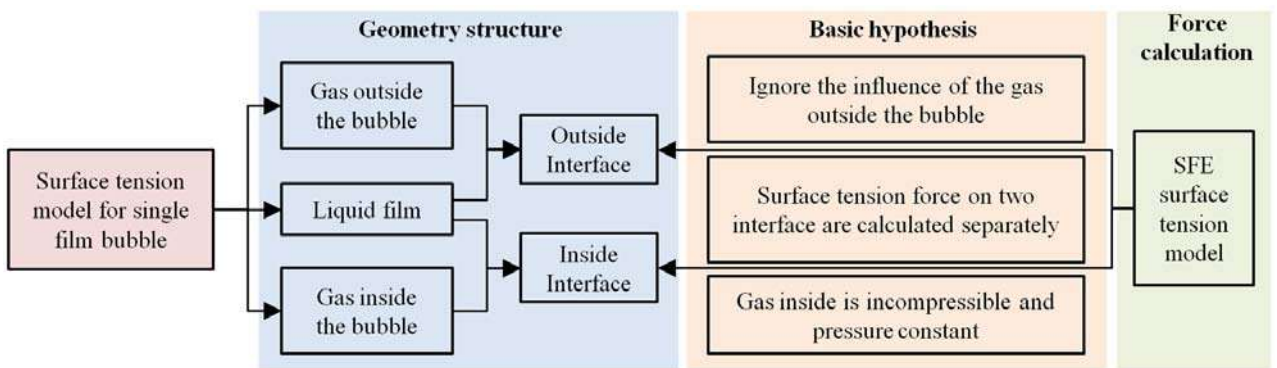


Figure 2. Surface tension model for single film bubble

C. Surface Tension Force Calculation

At present, the MPS method has two main methods to simulate the surface tension: one is the CST (Continuum Surface Tension) model [20], which is widely used in the Euler method and the other is the surface free energy model [21]. In this paper, the surface free energy (SFE) model is used to simulate the surface tension of the particles by constructing the interaction force between particles. The potential energy between two particles is defined as $P(r)$, and then the force f between the particles is:

$$f = \frac{\partial P}{\partial r} n \quad (6)$$

The force between the particles can be chosen using different formulas [21], but when the distance between the particles is less than the critical value, the repulsion between the particles; greater than the critical value, the particles between the gravitational; other particles around the particle distribution uniform force and symmetry, the force of the resultant force is 0; when the particles for the surface or adjacent to the free surface of the particles, the resultant force is not 0, that is, the performance of the surface tension. Therefore, the formula for calculating the potential energy between particles is:

$$P(r) = \begin{cases} \frac{C}{3} \left(r - \frac{3}{2} r_{min} + \frac{1}{2} r_e \right) (r - r_e)^2 & (r < r_e) \\ 0 & (r \geq r_e) \end{cases} \quad (7)$$

(6), (7): n is the unit vector between the two particles, r_{min} is the gravitational force between the particles, the demarcation of the demarcation point, taken as $1.5l_0$ [19]; r_e is the affect the domain, taken as $3.1l_0$; r is the distance between the two particles; C is the correction factor, according to the physical properties of the fluid, C is the greater, the stronger the role of surface tension.

From the formula (6), we could get the surface tension calculation equation (8).

$$f = \begin{cases} C'(r - r_e)(r - r_{min}) & (r < r_e) \\ 0 & (r \geq r_e) \end{cases} \quad (8)$$

D. Improvement of Surface Tension Model

In this paper, in order to increase the accuracy of the model, we improve the equation of potential energy from 1st order derivable to 2nd order derivable; the equation (7) could be rewritten as:

$$p = \begin{cases} \frac{C}{3} \left(r - \frac{3}{2}r_m + \frac{1}{2}r_e \right) (r - r_e)^2 & \left(0 \leq r \leq \frac{r_m + 3r_e}{4} \right) \\ C(r - r_e)^3 (ar^2 + br + c) & \left(\frac{r_m + 3r_e}{4} < r < r_e \right) \\ 0 & (r \geq r_e) \end{cases} \quad (9)$$

where $a = \frac{-32}{(r_e - r_m)^2}$, $b = \frac{8(3r_m + 5r_e)}{(r_e - r_m)^2}$,

and $c = -\frac{5}{3} - \frac{4(r_m + 3r_e)(r_m + r_e)}{(r_e - r_m)^2}$.

The new potential energy model is smoother (see in Fig. 3(a)) than the original one especially when the x -coordinate is larger than 2.70 (the dash line is the result from Kondo and the real line is the result of this model), and has higher order which would more close to the reality with increased calculation accuracy and also better stableness and convergence of the model.

With the new potential energy model, the surface tension force is calculated using Eq.(10), and the division between the traction force and repulsion force is set $r_{min}=1.5l_0$. As shown in the Fig. 3(b), the surface tension force is modified mostly for the repulsion force part (around $r=2.7-3.1 l_0$). The changing trend of the repulsion force is smoother when it is decreasing to zero.

$$f = \begin{cases} C(r - r_e)(r - r_m) & \left(0 \leq r \leq \frac{r_m + 3r_e}{4} \right) \\ C[3(r - r_e)^2(ar^2 + br + c) + (r - r_e)^3(2ar + b)] & \left(\frac{r_m + 3r_e}{4} < r < r_e \right) \\ 0 & (r \geq r_e) \end{cases} \quad (10)$$

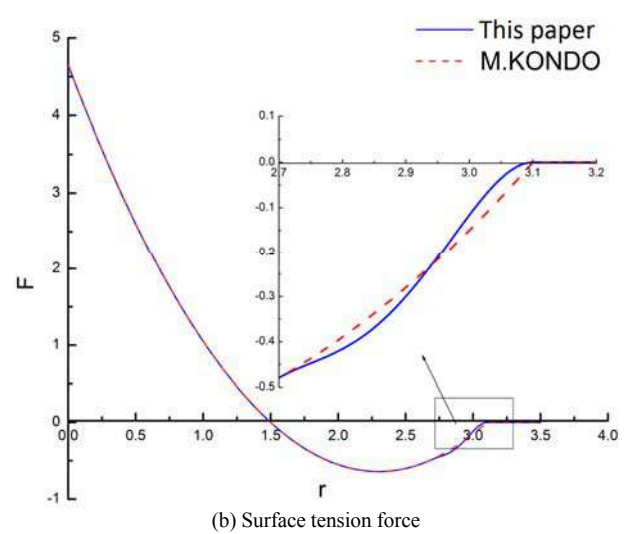
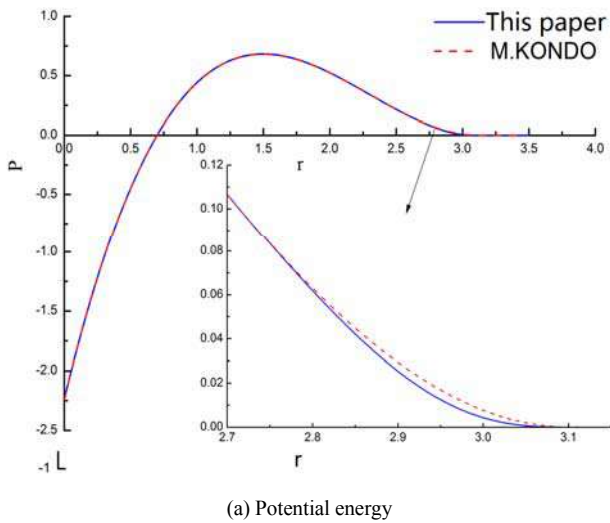


Figure 3. Comparison bewtween the original and modified surface tension model

We take the numerical case Kondo used in his article as the validation example [21], the results were shown in Fig. 4. The original model we used in this paper can get the droplet closer to a standard circle with the circular degree of 0.908, and the modified model could bring this value to 0.920 with better round shape, better symmetry and smoother boundary.

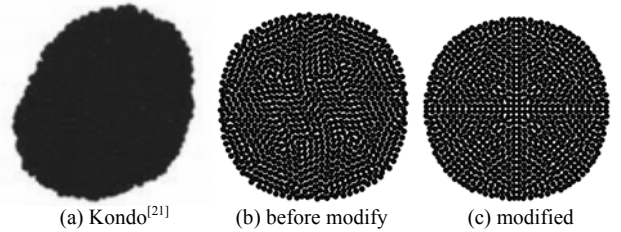


Figure 4. Results of square droplet coalescence and comparison between different models ($t=1.3$ s)

E. Oscillation of square single film bubble

The square single film bubble oscillation process was calculated with the modified single film bubble surface tension model. The results with time advance were shown in Figure 5. The single film was discrete into three layers of particles including the outside layer, inside layer and the inter layer between them. The gas outside the bubble is ignored, and the gas inside the bubble were incompressible and even which was not shown in the figures.

The side length of the square bubble was 18mm and it was discrete by 60×60 fluid particles with size of 0.3mm. The time step was $\Delta t=1 \times 10^{-5}$ s and the physical parameters were shown in the captions of the figure 5. The square bubble was firstly shrinking from the four corners which have large curvatures, and the films on four sides were project out until it deformed into a diamond shape.

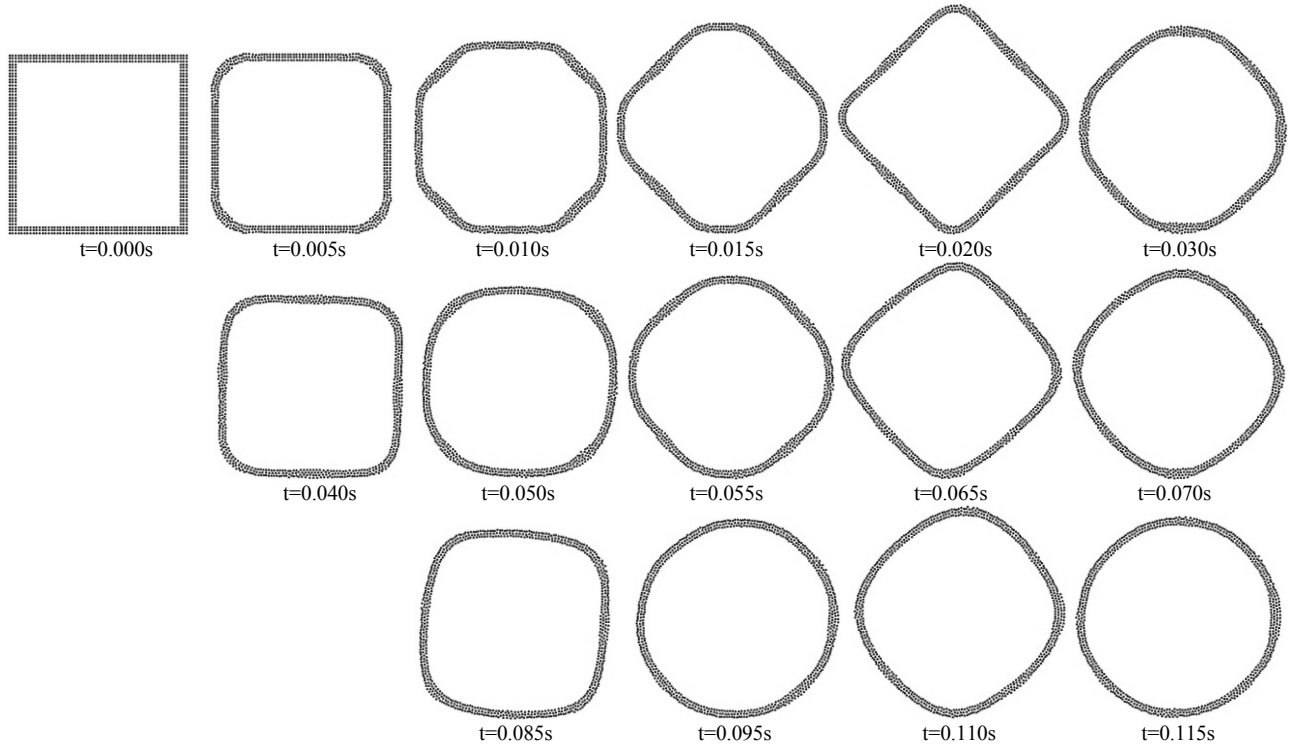


Figure 5. Oscillation process of square single film bubble under surface tension force.

$$(\rho = 1000 \text{ kg/m}^3, \rho_g = 1.5 \text{ kg/m}^3, \mu_f = 1.01 \times 10^{-3} \text{ N}\cdot\text{S/m}^2, \mu_g = 1.79 \times 10^{-5} \text{ N}\cdot\text{S/m}^2, \sigma = 0.0725 \text{ N/m})$$

Then the similar deforming process was repeat, the square shape and diamond shape appeared alternately, however, the curvature of the corner was decreasing all the time (see in column direction) because the viscous dissipation of the liquid and gas and their interaction. The oscillation amplitude was reduced with time, and the deformation will ended when the amplitude was approaching zero, as a result, a perfect round shape was generated.

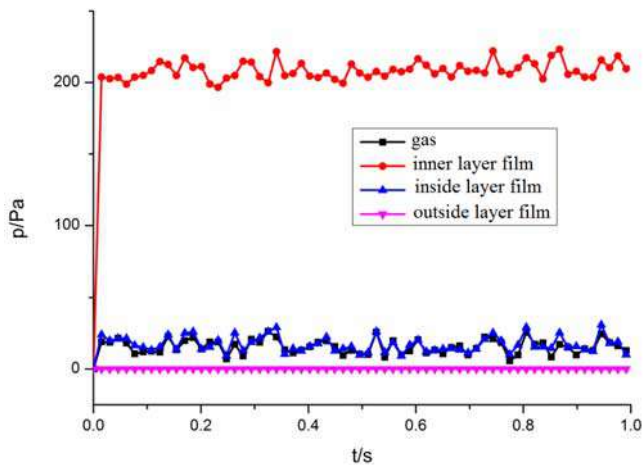


Figure 6. Pressure of the film and gas inside the bubble

The pressure of the bubble film and gas inside were shown in Fig. 6. The results showed that pressure of the outside liquid film (line with down triangle) was zero for reasons of opening in the atmosphere. The inside layer of liquid film (line with up triangle) had the same pressure as the gas inside (line with square), and the pressure was about 13 Pa which was slightly higher than the pressure of atomshpere. The pressure for inter layer was higher than others', because the surface tension force shrink the film on the gas sphere and also the film was squeezed by the two layers of liquid films.

IV. NUMERICAL SIMULATION AND DISCUSSION

In this part, the essential and basic behaviours of single film bubbles, such as the coalescence and connection phenomenon were simulated and analyzed.

A. Coalescence of single film bubbles

The coalescence of two single film bubbles with different sizes was simulated, and the results were shown in Fig. 7. The diameter of the big bubble was 9.0 mm, and the small one was 3mm. Other parameters were shown in the captions of figure. When two bubbles contacted with each other, the films merged with each other rapidly since the contact angle was small which lead to very large curvature. A connected film between two bubbles appeared ($t=0.02\text{s}$) until it broke and merged into the film nearby ($t=0.05\text{s}$).

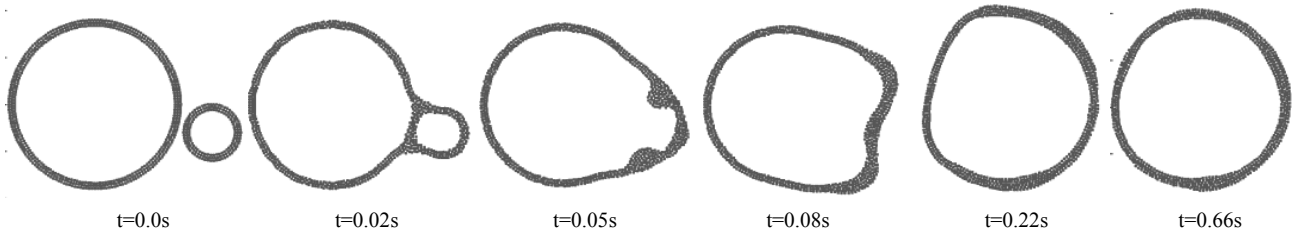


Figure 7. Coalescence of two single film bubbles with different sizes.
 $(\rho_l=1000 \text{ kg/m}^3, \rho_g=1.5 \text{ kg/m}^3, \mu_l=1.01 \times 10^{-3} \text{ N}\cdot\text{S/m}^2, \mu_g=1.79 \times 10^{-5} \text{ N}\cdot\text{S/m}^2, \sigma=0.0725 \text{ N/m})$

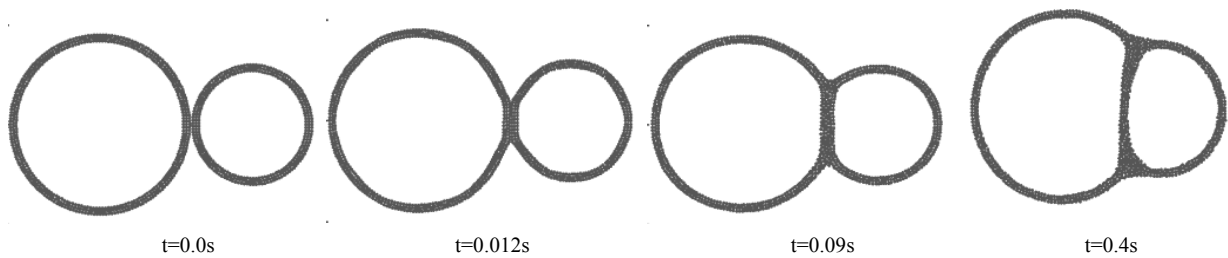


Figure 8. Connection of two single film bubbles with different sizes.
 $(\rho_l=1000 \text{ kg/m}^3, \rho_g=1.5 \text{ kg/m}^3, \mu_l=7.0 \times 10^{-3} \text{ N}\cdot\text{S/m}^2, \mu_g=1.79 \times 10^{-5} \text{ N}\cdot\text{S/m}^2, \sigma=0.032 \text{ N/m})$

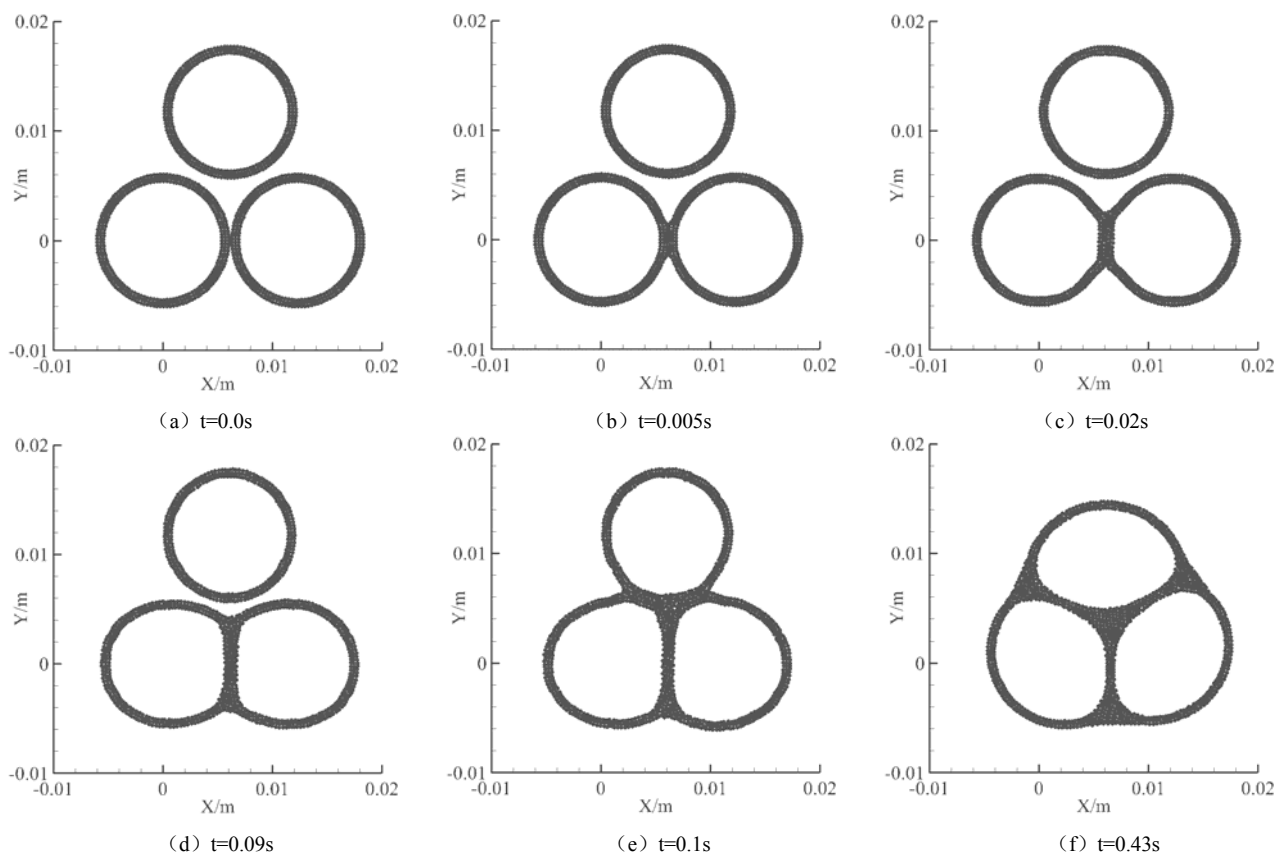


Figure 9. Connection of three single film bubbles with the same sizes
 $(\rho_l=1000 \text{ kg/m}^3, \rho_g=1.5 \text{ kg/m}^3, \mu_l=1.01 \times 10^{-3} \text{ N}\cdot\text{S/m}^2, \mu_g=1.79 \times 10^{-5} \text{ N}\cdot\text{S/m}^2, \sigma=0.0725 \text{ N/m})$

The diameter of the small bubble is very small, so when the connect film was broken, the local curvature where the small bubble located was large which lead to large surface tension force. The force made this segment of film moving rapidly towards the big bubble and generated a concave shape ($t=0.08s$). Another two large local curvature parts were generated and they became two waves transmitted to the downstream. After several times oscillations, the newly bigger bubble was stable in a round shape.

B. Connection of single film bubbles

The process of two single film bubbles with different sizes connected with each other was calculated and the results were shown in Fig. 8. In this simulation, the viscosity coefficient was set larger and the surface tension coefficient was set smaller than those in last numerical cases shown in Fig. 7. The adjustment of these two parameters was in order to keep the connected film stable.

As shown in Fig. 8, the length of the connected film between the two bubbles was growing with time, and when the length grew to its largest value, the connecting bubble system reached stable status.

Two connected bubble all showed as scallop shape, and the connecting film was not straight because the pressures of the inside gas for two bubbles were not the same. It is obviously that the gas inside the small bubble got larger pressure and the connected film was curve and project to the side of large bubble.

It is notable that two single film bubbles connected with each other did not result in a new single round shape as the droplet did, but a tandem style that the whole outline of the assembly was decided by the locale distribution of surface tension force.

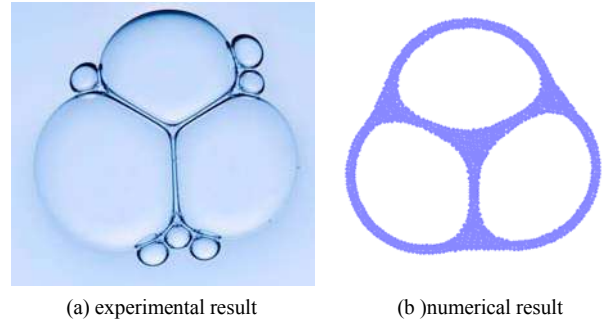
C. Plateau structure in foam system

When the connection process happened between three single film bubbles with the same size, the numerical results were shown in Fig. 9. Three single film bubbles were located in three vertexes of an equilateral triangle, and slightly adjustment was made to let two of them connected first before the third one.

The figures showed that two single film bubbles underneath connected with each other and a straight connecting film was generated since the bubbles were in the same size ($t=0.05s - 0.09s$). Then they connected with the upside bubble ($t=0.1s$) and the position pattern of ‘tandem + single’ deformed into a new equilateral triangle shape with round angles ($t=0.43s$).

The juncture area of three bubbles generated a liquid trident shape, in other words, the liquid full fill the gaps between the bubbles. These liquid bridges or tunnels were called Plateau structures, and they were the most common structures in a foam system.

The calculation result of tri-bubble connection and the Plateau structure were compared qualitatively with the experimental result in Fig. 10. The angle between the branches of Plateau structure of calculation agreed well with that of experimental.



(a) experimental result

(b) numerical result

Figure 10. Pattern of three connected single film bubbles

However, the sides, corners and their transitions between the Plateau structure branches of experimental were apparently clearer than those of numerical results. That's because when the bubbles connected to each other, the surface area decreased significantly, and also the sharing of film boundaries make the liquid more than needed. Therefore, a liquor drainage process would happen in the reality, however, in the simulations of this study was not considered yet. In the authers' opinion the liquor drainage process was one of the factors influencing the detail shape of foam system.

V. CONCLUSIONS

Within the framework of the meshless moving particle semi-implicit method, a single-film double-gas-liquid-interface surface tension model (SDST) was proposed for single film bubble, which was the basic unit of foam system. Considering the special structure of single thin film wrapping within amount of gas inside, hypotheses as ignoring the gas outside, gas inside has incompressible and even physical character were proposed. The surface tension force on two sides of the film was calculated separately using an improved surface free energy surface tension model which was more accurate and stable.

Typical behaviours as the coalescence and connection, and feature structure as Plateau structure of the single film bubbles were simulated, and the unsteady process with time under surface tension showed characters and deformation details of single film bubble. The numerical result of basic interactions between two or three bubbles provided fundamental information for relative studies, and the SDST model would propose an efficient method to study the performance of the complex foam system.

ACKNOWLEDGEMENT

This work is supported by the Natural Science Foundation of China (NSFC) Project (No. 51576154) and Project (No. 51236006), and supported by “the Fundamental Research Funds for the Central Universities”.

REFERENCES

- [1] D.Y.C. Chan, E Klaseber, R Manica, “Film drainage and coalescence between deformable drops and bubbles” *Soft Matter*, vol.7, pp. 2235-2264, 2011.
- [2] LT Yang, JQ Lv, YH Sun, et al. “Theoretical analysis of leakage during the bubble size” *Machine design and manufacturing engineering* vol. 39, pp.78-79, 2010.
- [3] JS Zhang, Q Lv, CD Sun, et al. “High speed photography to motion of bubbles in water” *Photonics Journal*, vol.29, pp.952-955, 2000.
- [4] HY Gu, LJ Guo, XM Zhang, et al. “Single bubbles in gas-liquid two-phase flow in a horizontal tube shape characteristics” *Journal of Engineering Thermo-physics*, vol.27, pp.433-436, 2006.
- [5] HL Lu, ZH Shen, JM Ding, et al. “Numerical simulation of bubble and particles motions in a bubbling fluidized bed using direct simulation Monte-Carlo method” *Powder Technology*, vol. 169, pp.159-171, 2006.
- [6] E Olmos, C Gentric, C Vial, et al. “Numerical simulation of multiphase flow in bubble column reactors Influence of bubble coalescence and break-up”. *Chemical Engineering Science*, vol.56, pp.6359-6365, 2001.
- [7] H Liu, MZ Xie, K Li, et al. “Liquid metal bath numerical simulation of bubble-liquid two-phase turbulent flow” *Chinese Journal of Computational Mechanics*, vol.24, pp.669-673, 2007.
- [8] R Sungkorn, J.J. Derksen, J.G. Khinast. “Modeling of turbulent gas-liquid bubbly flows using stochastic Lagrangian model and lattice-Boltzmann scheme”. *Chemical Engineering Science*, vol. 66. Pp. 2745-2757, 2011.
- [9] L Chen, S.V. Garimella, J.A. Reizes, et al. “The development of a bubble rising in a viscous liquid” *Journal of Fluid Mechanics*, vol. 387. Pp61-96, 1999.
- [10] SJ Zhang, CJ Wu. “Numerical simulation of the interaction between bubbles” *Hydrodynamic Research and Progress*, vol. 23, pp.89-94, 2008.
- [11] M Sussman, A.S. Almgren, J.B. Bell, et al. “An Adaptive Level Set Approach for Incompressible Two-Phase Flows” *Office of Scientific & Technical Information Technical Reports*, vol. 148, pp.81-124, 1999.
- [12] L Anaya-bower, T Lee. “Single bubble rising dynamics for moderate Reynolds number using Lattice Boltzmann Method”. *Computers & Fluids*, vol. 39, pp.1911, 2010.
- [13] Z Yu, H Yang, LS Fan. “Numerical simulation of bubble interactions using an adaptive lattice Boltzmann method” *Chemical Engineering Science*, vol. 66, pp. 3441-3451, 2011.
- [14] S Koshizuka. “Moving-particle semi-implicit method for fragmentation of incompressible fluid” *Nuclear Science & Engineering*, vol. 123, pp. 421-434, 1996.
- [15] ZG Sun, G Xi, LF Xiang. “Simulation on rising bubble in water with meshfree method” *Journal of Engineering thermophysics*, vol. 28, pp. 771-774, 2007.
- [16] ZG Sun, G Xi, X Chen. “A numerical study of stir mixing of liquids with particle method” *Chemical Engineering Science*, vol. 64, pp.341-250, 2009.
- [17] ZG Sun, G Xi, Xi Chen. “Mechanism study of deformation and mass transfer for binary droplet collisions with particle method” *Physics of Fluids*, vol.21, pp. 032106, 2009.
- [18] X Chen, G Xi, ZG Sun. “Improving stability of MPS method by a computational scheme based on conceptual particles” *Computer Methods in Applied Mechanics & Engineering*, vol. 278, pp. 254-271, 2014.
- [19] X Chen, ZG Sun, G Xi. “Improvement of the surface free energy model and numerical study on the infiltration of droplets” *Journal of Xian Jiao Tong University*, vol. 46, pp. 115-121, 2012.
- [20] S Zhang, K Morita, K Fukuda, N Shirakawa, “A new algorithm for surface tension model in moving particle methods” *International Journal for Numerical Methods in Fluids*, vol. 55, pp. 225-240, 2010.
- [21] M Kondo, S Koshizuka, K Suzuki, et al. “Surface Tension Model Using Inter-Particle Force in Particle Method” *ASME/JSME Joint Fluids Engineering Conference*, vol. 81, pp. 82, 2007.
- [22] Y Bahoba, TK Yang. “Physical and chemical properties of the soap solution”. *Daily Chemical Science*, vol. 4, pp.31-32, 1985.
- [23] A. Tartakovsky, P. Meakin, “Modeling of surface tension and contact angles with smoothed particle hydrodynamics”, *Physical Review E*, vol. 72, pp. 2m 54-271, 2005.

A two-phase SPH model for sediment transport in free surface flows

Huabin Shi, Xiping Yu

Department of Hydraulic Engineering

Tsinghua University

Beijing, China

shihuabin@tsinghua.edu.cn

Abstract—A SPH model based on a general two-phase formulation for solid-liquid mixtures is proposed for sediment transport in free surface flows. The water and the sediment are treated as two miscible fluids, and the miscible-fluid system is discretized by a single set of SPH mixture particles, which move with water velocity and carry properties of the two phases. Large eddy simulation (LES) is introduced to deal with the turbulence, and the standard Smagorinsky model is modified to take into account the effect of solid particles on turbulence. In the model, the water is assumed to be weakly compressible while the sediment phase is incompressible. A novel equation of state is proposed for the hydrodynamic pressure in the sediment-water mixture and a matching strategy of Shepard filtering is adopted to damp the oscillation in pressure. A constitutive law based on the rheology of granular flows is utilized to formulate the sediment stress. The model is validated and applied to 2D bed erosion under dam break flows and 3D sand dumping into a water tank. The computed results are in good agreement with the experimental data, and thus it is shown that the proposed model promises to be an effective tool for sediment transport in free surface flows.

I. INTRODUCTION

Sediment transport by free surface flows is a classical but not yet fully understood subject of river and coastal engineering. Over the past few decades, numerous mesh-based two-phase models have been developed for sediment transport [1-3]. However, the mesh-based models perform poorly in tracking the complicate deformation of free water surface and lose the advantage of two-phase formulation when applied to sediment transport in free surface flows [4]. In the present paper, the meshless smoothed particle hydrodynamics (SPH) method is extended to a general continuum two-phase model for simulations of sediment transport by free surface flows.

SPH, which is well-known for its flexibility in dealing with extremely large deformation or even breaking of free surface, has been widely applied to hydrodynamic problems [5-6]. In recent years, it has also been increasingly used to study multi-phase flows [7-9]. Specifically, as SPH has good capability in tracking the interface between different phases, it has been particularly applied to immiscible fluid flows, such as air bubble rising in pure water [10] and Rayleigh-Taylor instability [11], which are characterized by the complex deformation of

interfaces between fluids. In these studies, different fluids are represented by different sets of SPH particles, and the particles carry individual fluid properties. There is no overlap between different sets of particles, and the clear interface between fluids moves with the particles. The SPH models for immiscible fluid flows have also been applied to problems of sediment transport [8, 12]. However, usually there is no clear macroscopic interface between the sediment and the water phases, and it seems more reasonable to treat the solid and the liquid phases in sediment laden flows as miscible. Hence, a SPH model for miscible fluids is preferred for sediment transport. References [13-15] employed continuum two-phase models based on a two-SPH-particle-layer approach [8] for miscible solid-liquid flows. In their two-SPH-particle-layer approach, each of the two phases is represented by a different set of SPH particles, and the particles of different sets move on individual layer, overlapping and interacting with each other according to the inter-phase forces. As reviewed in [8], this technique tends to be cumbersome and memory intensive. References [16] treated the two-phase system as a mixture and represented it by a single set of SPH particles, which moved with mixture velocity and carried properties of the mixture and volume fraction of each component. The two-phase formulation was replaced by the single-phase modeling of mixture, which might reduce the accuracy of the model.

The present study aims to establish a SPH model based on a general two-phase formulation of solid-liquid mixtures for sediment transport in free surface flows. The two phases are treated as two miscible fluids and described using the continuum approach. To avoid variable smoothing length scales, non-conservation of momentum, and intensive memory usage [8, 17], the multi-fluid system is discretized by a single set of SPH particles, rather than by two layers of particles as in [13-15]. The particles move with water velocity and carry properties of both the two phases. Large eddy simulation (LES) along with a modified sub-particle scale Smagorinsky model is introduced to take into account the turbulence. A constitutive law based on the rheology of granular flows is employed to formulate the sediment stress. The proposed model is validated and applied to problems of 2D bed erosion by dam break flows and 3D sand dumping into a water tank.

The rest of the paper is organized as follows. The governing equations of the model and their SPH formulations are described in Section II. Validation and application of the model are given in Section III. Finally, conclusions are summarized in Section IV.

II. A CONTINUUM TWO-PHASE SPH MODEL

A. Governing Equations for Solid-Liquid Flows

In a continuum system, both the solid and liquid phases are governed by the conservation laws for mass and momentum. The general two-fluid form of continuity and momentum equations for two-phase flows originally derived by [18] are employed here for sediment-water mixtures. To deal with turbulence in two-phase flows, LES is introduced to the model and the conservation equations are spatially filtered. In the present study, the two-phase system is discretized into a single set of SPH particles, which move with water velocity and carry properties of the two phases. Rewrite the Eulerian form of conservation equations in Lagrangian form, and hence the governing equations for water density, water velocity, sediment concentration, and sediment velocity carried by a SPH particle can be expressed as [19]

$$\frac{d(\alpha_f \rho_f)}{dt} = -(\alpha_f \rho_f) \frac{\partial u_{fj}}{\partial x_j}, \quad (1)$$

$$\begin{aligned} \frac{du_{f,i}}{dt} &= -\frac{1}{\rho_{f0}} \frac{\partial p}{\partial x_i} + \frac{1}{\alpha_f \rho_f} \frac{\partial (\alpha_f \rho_f T_{f,ij})}{\partial x_j} + g_i \\ &\quad - \frac{\gamma \alpha_s}{\alpha_f \rho_f} (u_{f,i} - u_{s,i}) + \frac{\gamma \alpha_s}{\alpha_f \rho_f} \frac{\nu'_f}{\alpha_f \text{Sc}} \frac{\partial \ln \alpha_s}{\partial x_i}, \end{aligned} \quad (2)$$

$$\frac{d\alpha_s}{dt} = -\alpha_s \frac{\partial u_{f,j}}{\partial x_j} - \frac{\partial [\alpha_s (u_{s,j} - u_{f,j})]}{\partial x_j}, \quad (3)$$

$$\begin{aligned} \frac{du_{s,i}}{dt} &= -(u_{s,j} - u_{f,j}) \frac{\partial u_{s,i}}{\partial x_j} - \frac{1}{\rho_s} \frac{\partial p}{\partial x_i} + \frac{1}{\alpha_s} \frac{\partial (\alpha_s T_{s,ij})}{\partial x_j} \\ &\quad + g_i + \frac{\gamma}{\rho_s} (u_{f,i} - u_{s,i}) - \frac{\gamma}{\rho_s} \frac{\nu'_f}{\alpha_f \text{Sc}} \frac{\partial \ln \alpha_s}{\partial x_i}. \end{aligned} \quad (4)$$

In the equations, the subscript f and s represent the water phase and the sediment phase, respectively; the indices $i, j = 1, 2, 3$ represent the coordinate directions and follow the summation convention; x is the coordinate; t is the time; u is the velocity; ρ is the density; α is the volume fraction; p is the hydrodynamic pressure; g is the gravitational acceleration; γ is a coefficient correlated with the inter-phase drag force; Sc is the Schmidt number; T is related to the viscous stress and subscale turbulence stress, formulated by

$$T_{f,ij} = (\nu_f^0 + \nu'_f) \left(\frac{\partial u_{f,i}}{\partial x_j} + \frac{\partial u_{f,j}}{\partial x_i} \right), \quad (5)$$

$$T_{s,ij} = (\nu_s^0 + \nu'_s) \left(\frac{\partial u_{s,i}}{\partial x_j} + \frac{\partial u_{s,j}}{\partial x_i} \right) - \frac{p_s}{\rho_s} \delta_{ij}; \quad (6)$$

ν_k^0 ($k = f, s$) are the kinematic viscosities of the two phases, and ν'_k are the eddy viscosities due to subscale turbulence; p_s is the pressure of sediment phase, resulting from enduring contact, collisions, and frictions between the solid particulates.

It should be noted that in the present study the water is assumed to be weakly compressible, while the sediment phase is incompressible. Thus, the water density ρ_f is an unknown, but the sediment density ρ_s is a constant with $d\rho_s/dt = 0$. It also have to be emphasized that as the velocities of the two phases are different, there are mass and momentum fluxes of sediment among SPH interpolating particles, resulting in the second term on the right side of (3) and the first term on the right side of (4).

The last two terms on the right side of both (2) and (4) represent the inter-phase momentum transfer, and in the present study only the drag force is included. Note that the coefficient γ in practical applications may be expressed as

$$\gamma = \frac{1}{(1-\alpha_s)^{1.65}} \frac{3C_D \rho_f}{4d_s} \|\mathbf{u}_f - \mathbf{u}_s\|, \quad (7)$$

where, d_s is the diameter of sand particles; $\|\mathbf{u}_k\|$ is the norm of the velocity vector; C_D is the drag coefficient for a sediment particulate in an infinite fluid, and correction factor $1/(1-\alpha_s)^{1.65}$ is introduced for the hindered settling effect. C_D is a function of the particle Reynolds number $\text{Re}_s = \|\mathbf{u}_f - \mathbf{u}_s\| d_s / \nu_f^0$, and can be determined by the well-known formula [20]

$$C_D = \begin{cases} \frac{24}{\text{Re}_s} (1.0 + 0.15 \text{Re}_s^{0.687}) & \text{Re}_s < 1000 \\ 0.44 & \text{Re}_s \geq 1000 \end{cases}. \quad (8)$$

To consider turbulence in the two phases, the widely used Smagorinsky model is utilized to compute the eddy viscosities but modified to take into account the effect of solid particles on the turbulence [21]

$$\nu'_f = (C_f \Delta)^2 \|\mathbf{S}_f\| (1 - \alpha_s / \alpha_{sm})^n, \quad (9)$$

$$\nu'_s = (C_s \Delta)^2 \|\mathbf{S}_s\| (1 - \alpha_s / \alpha_{sm})^n. \quad (10)$$

in which, Δ is the filtering length in LES and set to be equal to the initial particle spacing in a SPH model; \mathbf{S}_k is the rate-of-strain tensor, with its element defined as

$$S_{k,ij} = \frac{1}{2} \left(\frac{\partial u_{k,i}}{\partial x_j} + \frac{\partial u_{k,j}}{\partial x_i} \right), \quad (11)$$

while $\|\mathbf{S}_k\| = \sqrt{2S_{k,ij}S_{k,ij}}$; $n = 5$ is a coefficient; C_f and C_s are Smagorinsky constants.

To estimate the viscosity ν_s^0 and pressure p_s of sediment phase, a constitutive law based on the rheology of dense granular flows is adopted [22-23]. The pressure of sediment phase can be divided into two components, i.e. enduring-contact component p_{se} for the effect of enduring elastic contact between particulates and rheology component p_{sr} for the inertia and collision effects. The following formulations which have been successfully applied to sediment transport [22-23] can be employed to estimate the pressure of sediment phase, expressed as

$$p_s = p_{se} + p_{sr} \quad (12)$$

$$p_{se} = \begin{cases} 0 & \alpha_s < \alpha_* \\ K(\alpha_s - \alpha_*)^\chi \left[1 + \sin \left(\pi \frac{\alpha_s - \alpha_*}{\alpha^* - \alpha_*} - \frac{\pi}{2} \right) \right] & \alpha_s \geq \alpha_* \end{cases} \quad (13)$$

$$p_{sr} = \left(\frac{c_1 \alpha_s}{\alpha_{s0} - \alpha_s} \right)^2 (\rho_f \nu_f^0 + c_2 \rho_s d_s^2 \|\mathbf{S}_s\|) \|\mathbf{S}_s\| \quad (14)$$

where, K is a coefficient related to solid material's Young's modulus; χ , c_1 , c_2 are model parameters; α_{s0} is the jamming volume fraction; α_* is the random loose packing fraction and α^* is the random close packing fraction. Relating the kinematic viscous stress of sediment phase to the pressure according to granular flow rheology, we obtain the expression for the viscosity

$$\nu_s^0 = \frac{\eta p_s}{\rho_s \|\mathbf{S}_s\|}, \quad (15)$$

in which, η is the friction coefficient, which depends on the inertia number I and can be estimated by

$$\eta = \eta_1 + \frac{\eta_2 - \eta_1}{1 + \sqrt{I_0/I}}. \quad (16)$$

$\eta_1 = \tan \phi$ (ϕ is the angle of repose) is the friction coefficient when $I = 0$ and η_2 is the value when I approaches infinite. I_0 is a model parameter. Based on the rheology of granular flow [24], values of the inertia number can be obtained by

$$I = \left(\frac{\alpha_{s0} - \alpha_s}{c_1 \alpha_s} \right)^2. \quad (17)$$

B. Equation of State (EOS) for Sediment-Water Mixture

As described in the above section, weakly compressible SPH (WCSPH) approach is utilized, and we assume the water phase is weakly compressible but the sediment phase is incompressible. In such case, the commonly used equation of state for single-phase flows may be not appropriate. Here, we propose a novel equation of state for sediment-water mixture [19].

Use the Macdonald-Tait formula [25] to correlate the hydrodynamic pressure with the density of mixture, and consider the conservation of the mass of the two phases. Adopt the relation between the bulk modulus of the mixture and sediment concentration in [26], and we finally obtain the following expression for the hydrodynamic pressure in sediment-water mixture,

$$p = \frac{\rho_{f0} c_0^2}{\xi} \frac{\alpha_f \rho_f + \alpha_s \rho_{f0}}{\alpha_f \rho_f} \left[\left(\frac{\alpha_f \rho_f + \alpha_s \rho_{f0}}{\rho_{f0}} \right)^\xi - 1 \right]. \quad (18)$$

C. SPH Formulations

A detailed description of SPH formulations can be referred to [27-28]. In a SPH model, the value of a physical variable f carried by SPH particle a (f_a) is approximated by the summation over all neighbouring particles in the supporting domain of the quintic kernel function W ,

$$f_a = \sum_b V_b f_b W_{ab}, \quad (19)$$

in which, f_b is the value of f carried by the neighbouring particle b ; $W_{ab} = W(|\mathbf{x}_a - \mathbf{x}_b|, h)$; V_b is the volume of particle b defined by

$$V_b = \left(\frac{m_f}{\alpha_f \rho_f} \right)_b \quad (20)$$

with m_f being the water mass carried by the particle which remains to be constant during the simulations.

The standard SPH formulation for the divergence of the water velocity is utilized, and the symmetric scheme which conserves momentum is used to discretize the gradient of the pressure and the stresses. A modified upwind scheme is proposed for the formulations of the mass and momentum flux terms in (3) and (4). Finally, the discretized SPH equations for sediment-water mixture are obtained as

$$\frac{d(X_i)_a}{dt} = (u_{f,i})_a \quad (21)$$

$$\frac{d(\alpha_f \rho_f)_a}{dt} = (\alpha_f \rho_f)_a \sum_b V_b [(u_{f,j})_a - (u_{f,j})_b] (\nabla_a W_{ab})_j \quad (22)$$

$$\begin{aligned} \frac{d(u_{f,i})_a}{dt} &= -\frac{1}{\rho_{f0}} \sum_b V_b (p_a + p_b) (\nabla_a W_{ab})_i \\ &+ \sum_b V_b \frac{(\alpha_f \rho_f)_a (T_{f,ij})_a + (\alpha_f \rho_f)_b (T_{f,ij})_b}{(\alpha_f \rho_f)_a} (\nabla_a W_{ab})_j \\ &+ g_i - \frac{\gamma_a (\alpha_s)_a}{(\alpha_f \rho_f)_a} (u_{f,i} - u_{s,i})_a \\ &+ \frac{\gamma_a (\alpha_s)_a}{(\alpha_f \rho_f)_a} \frac{(\nu_f^t)_a}{(\alpha_f)_a} \sum_b V_b \ln \frac{(\alpha_s)_b}{(\alpha_s)_a} (\nabla_a W_{ab})_i \\ \frac{d(\alpha_s)_a}{dt} &= (\alpha_s)_a \sum_b V_b [(u_{f,j})_a - (u_{f,j})_b] (\nabla_a W_{ab})_j \\ &- \sum_b V_b \left\{ (\alpha_s)_a \max \left[(u_{s,j} - u_{f,j})_a (\nabla_a W_{ab})_j, 0 \right] \right. \\ &\left. + (\alpha_s)_b \min \left[(u_{s,j} - u_{f,j})_b (\nabla_a W_{ab})_j, 0 \right] \right\} \end{aligned} \quad (23)$$

$$\begin{aligned} \frac{d(u_{s,i})_a}{dt} &= -\frac{1}{\rho_s} \sum_b V_b (p_a + p_b) (\nabla_a W_{ab})_i + g_i \\ &+ \sum_b V_b \min \left[(u_{s,j} - u_{f,j})_b (\nabla_a W_{ab})_j, 0 \right] \left[(u_{s,i})_a - (u_{s,i})_b \right] \\ &+ \sum_b V_b \left[(T_{s,ij})_a + (T_{s,ij})_b \right] \left(1 + \frac{1}{2} \ln \frac{(\alpha_s)_b}{(\alpha_s)_a} \right) (\nabla_a W_{ab})_j \\ &+ \frac{\gamma_a}{\rho_s} (u_{f,i} - u_{s,i})_a - \frac{\gamma_a}{\rho_s} \frac{(\nu_f^t)_a}{(\alpha_f)_a} \sum_b V_b \ln \frac{(\alpha_s)_b}{(\alpha_s)_a} (\nabla_a W_{ab})_i \end{aligned} \quad (25)$$

Note that (21) is for the evolution of the position of the SPH interpolating particle.

D. Time Integration

The predictor-corrector scheme is utilized to numerically integrate (21) – (25) with respect to time. A variable time step is adopted, and it is restricted by the numerical sound

speed c_s , the maximum inertia forces, and the viscous forces of the two phases through the CFL conditions,

$$\Delta t = \min(\Delta t_c, \Delta t_F, \Delta t_v) \quad (26)$$

$$\Delta t_c = 0.3 h / \max(c_s)_a \quad (27)$$

$$\Delta t_F = 0.3 \min \left(\sqrt{h / \max \| \mathbf{a}_f \|_a}, \sqrt{h / \max \| \mathbf{a}_s \|_a} \right) \quad (28)$$

$$\Delta t_v = 0.125 \min \left(h^2 / \max(v_f)_a, h^2 / \max(v_s)_a \right) \quad (29)$$

where, $\mathbf{a}_f = d\mathbf{u}_f / dt$ and $\mathbf{a}_s = d\mathbf{u}_s / dt$; $v_f = v_f^0 + v_f^t$ and $v_s = v_s^0 + v_s^t$ are the total viscosities of the two phases, respectively.

E. Boundary Conditions and Shepard Filtering

The dynamic boundary condition proposed by [29] is used for the solid wall boundaries to avoid the kernel truncation. Free water surfaces can be naturally tracked by the SPH approach.

A new strategy of Shepard filtering is proposed to damp the oscillation of hydrodynamic pressure. The filtering is preformed every 20 time steps by reinitializing the water density of each particle according to

$$(\bar{\rho}_f)_a = \frac{\sum_b V_b (\rho_f)_b W_{ab}}{\sum_b V_b W_{ab}} = \frac{\sum_b \frac{(m_f)_b}{1 - (\alpha_s)_b} W_{ab}}{\sum_b \frac{(m_f)_b}{(\alpha_f \rho_f)_b} W_{ab}} \quad (30)$$

In the filtering, the mass of the water and the sediment carried by a SPH particle should be conserved, resulting in

$$(\overline{\alpha_f \rho_f})_a = \frac{(\alpha_f \rho_f)_a}{(\alpha_f \rho_f)_a + \alpha_s (\bar{\rho}_f)_a} (\bar{\rho}_f)_a \quad (31)$$

$$(\bar{\alpha}_s)_a = \frac{(\alpha_s)_a}{(\alpha_f \rho_f)_a + (\alpha_s)_a (\bar{\rho}_f)_a} (\bar{\rho}_f)_a \quad (32)$$

III. APPLICATIONS TO SEDIMENT TRANSPORT

The proposed model is validated and applied to the cases of 2D bed erosion by dam break flows and 3D sand dumping into a water tank. The model is implemented on the basis of the open-source free surface flow SPH-package GPUSPH originally developed by [30], programmed with CUDA and C++. The computations are carried out on an Nvidia Tesla K40c GPU, which has 2880 processor cores.

A. 2D Bed Erosion by Dam Break Flows

The laboratory experiments of 2D bed erosion by dam break flows carried by [31] are employed to validate the proposed model. The geometry of the experiment includes a water tank blocked by a gate over an erodible bed. Both the bottom of the tank and that of the downstream channel are covered with fully saturated particle materials. Reference [31] had adjusted the upstream and downstream sediment depths and tried two different bed materials. Due to space limitation, in the present paper only the case of flat bed (where the upstream sediment depth equals to the downstream sediment depth) covered by PVC pellets is simulated by the proposed SPH two-phase model, as shown in Fig. 1. The PVC pellets are slightly cylindrical in shape with an equivalent spherical diameter of 0.0039m and a density of 1580 kg/m³. The friction angle of the PVC pellets is 38°, and the initial volume fraction of the bed material is 0.58. The total length of the channel L is 6 m, with the length of the water tank being 3 m. The depth of the movable bed is 0.12 m, and the water depth in the tank is 0.35 m. The gate is removed instantaneously downward, and the dam-break flow erodes the downstream bed. The free water surface and the bed profile are measured at the instants of 0.25s, 0.50s, 0.75s, 1.00s, 1.25s, and 1.50s.

In the SPH simulation, periodic boundary condition is applied to the transverse direction of the channel for the two-dimensional simulations. In GPUSPH, at least four layers of interpolating particles should be set for the periodic boundary condition. The initial size of SPH particles is set to be 0.01 m, and a total number of 79272 SPH interpolating particles are used to represent the water, the sand bed, and the solid boundaries. It requires about 2 hours of computational time to simulate 1.50 s of the physical experiment.

Fig. 2 show the comparisons between the computed and the measured free water surfaces and bed profiles. In each figure, the upper picture shows the snapshots of the experiments, and the bottom figure shows the computed configurations of SPH particles and the distribution of sediment concentration. It is shown that the computed erosion heights of the sand bed and the frontal positions of the flow are in reasonable agreement with the experimental results. However, it should be noted that the computed elevations of the water surface seem to be a little higher than the measured values, especially at the front of the flow.

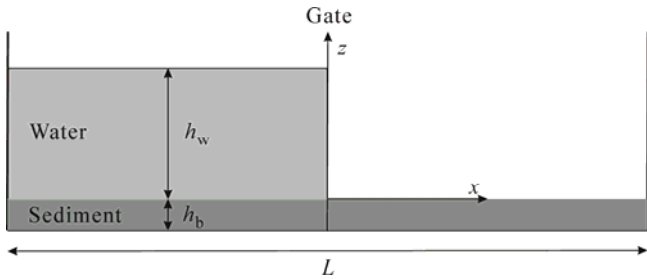


Figure 1. Schematic of the experiment of bed erosion by dam break flows.

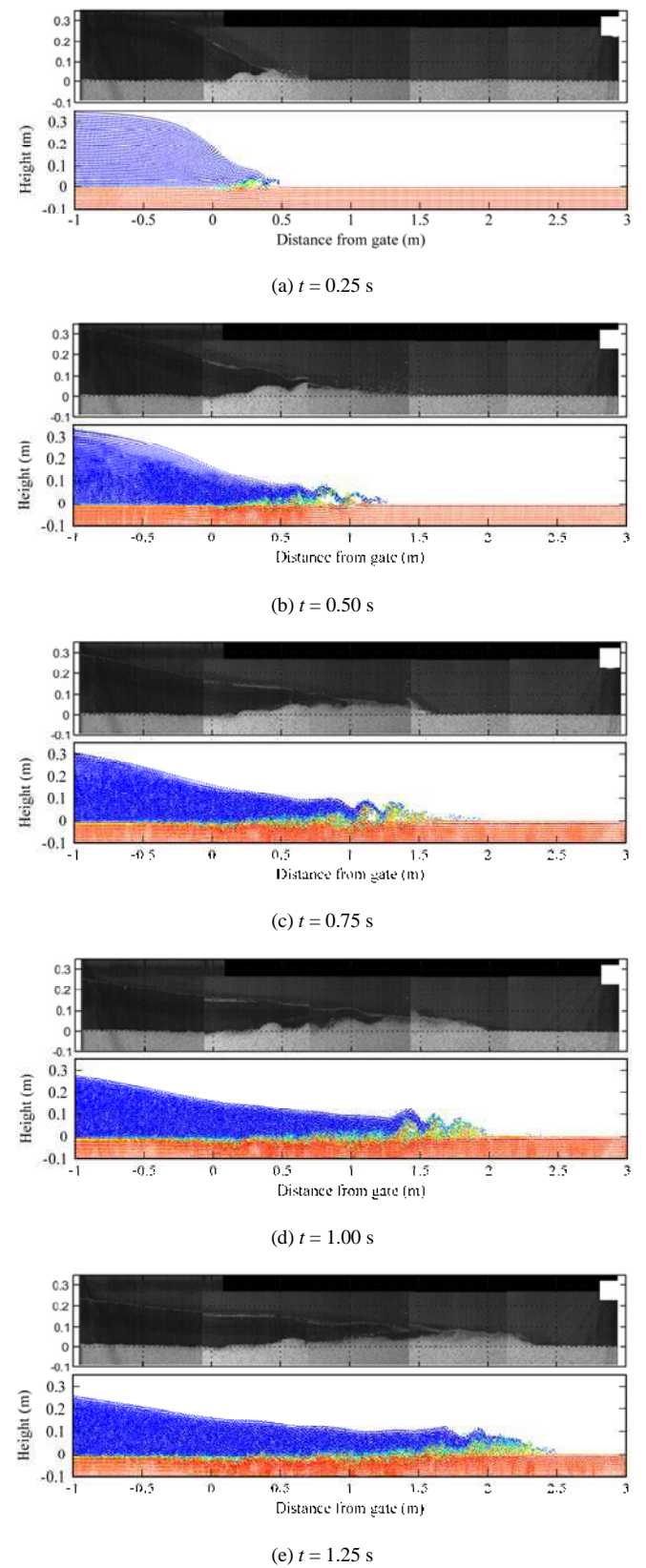


Figure 2. Comparisons between the computed and the measured free water surfaces and bed profiles.

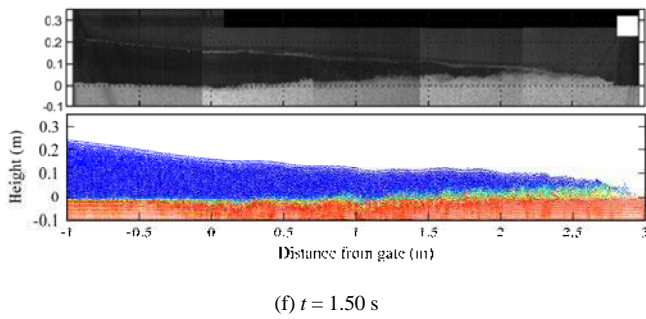
(f) $t = 1.50$ s

Figure 2 (continued). Comparisons between the computed and the measured free water surfaces and bed profiles.

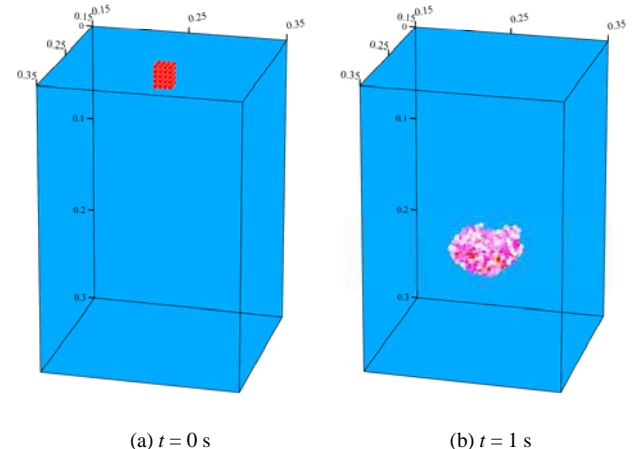
B. 3D Sand Dumping into a Water Tank

Sand dumping is a common practice in construction of breakwaters and dredging of navigation channels. A comprehensive understanding of the settling process of sand cloud is important to the management of estuarine and coastal zones. In this section, the proposed two-phase SPH model is applied to the sudden dumping of sediment from a point source into a wide water tank, where the sand cloud settles with a response of the free water surface.

The initial size of the sand cloud is $2 \text{ cm} \times 2 \text{ cm} \times 2 \text{ cm}$, with the diameter and the density of the sand particles being 1.3 mm and 2650 kg/m^3 , respectively. The water tank is 0.50 m wide, 0.50 m long, and 1.00 m high, which is taken to be large enough so that constraints of the walls on the evolution of sand cloud can be neglected. The initial sediment volume fraction in the sand cloud is 0.606 . In the simulations, the computational domain is discretized into a set of SPH interpolating particles with an initial size of 0.005 m . The fluid domain is discretized by 2 million particles, including $4 \times 4 \times 4$ particles representing the initial sand cloud as shown in Fig. 3(a). In addition, 293267 particles are employed for the dynamic boundary conditions. Hence, a total number of 2293267 interpolating particles are used in the simulations. It requires about 3 h of computational time to simulate 1 s of the physical process. Fig. 3(b) shows the configuration of the interpolating particles representing the sand cloud. It can be shown that the sand cloud has a shape of bowl with the maximum sediment concentration locating in the centre of the bowl. The results are consistent with that of [32], verifying the applicability of the present two-phase SPH model to problems of sand dumping.

IV. CONCLUSIONS

A SPH model based on a general continuum two-phase formulation for solid-liquid mixtures is developed for sediment transport in free surface flows. The solid and the liquid phases are treated as two miscible fluids, and the two-fluid system is discretized into a set single of SPH interpolating particles. The particles move with water velocity and carry properties of the two phases. The WCSPh assumption is utilized, i.e., the water in the solid-liquid mixtures is assumed to be weakly compressible while



(a) $t = 0$ s (b) $t = 1$ s

Figure 3. Configurations of SPH particles representing the sand cloud

the sediment is incompressible. Accordingly, a novel equation of state is proposed for the hydrodynamic pressure in the sediment-water mixture. Large eddy simulation (LES) is employed for the turbulence in the two phases, and the well-known Smagorinsky model is modified to consider the effect of solid particulates on turbulence. A constitutive law based on the rheology of granular flows is used to estimate the sediment stress. The proposed continuum two-phase SPH model is validated and applied to the problems of 2D bed erosion by dam break flows and 3D sand dumping into water tank. In the simulation of bed erosion under dam break flows, the computed bed erosion height and the position of the leading edge of the flow are in reasonable agreement with the experimental data, though the computed elevations of the water surface is a little higher than the measured results. For sand dumping into a wide water tank, the model successfully simulates the formation of a bowl-like sand cloud.

ACKNOWLEDGEMENT

The first author would like to thank Professor Robert A. Dalrymple for the help and discussions associated with the work. This research is supported by National Natural Science Foundation of China (NSFC) under grant No. 11472156.

REFERENCES

- [1] P. Dong, K. F. Zhang, "Two-phase flow modeling of sediment motions in oscillatory sheet flows," *Coast. Eng.*, vol. 36, no. 2, pp. 87-109, 1999.
- [2] X. Chen, Y. Li, X. Niu, D. Chen, X. Yu, "A two-phase approach to wave-induced sediment transport under sheet flow conditions," *Coast. Eng.*, vol. 58, no. 11, pp. 1072-1088, 2011.
- [3] H. Shi, X. Yu, "An effective Euler-Lagrange model for suspended sediment transport by open channel flows," *Int. J. Sediment Res.*, vol. 30, pp. 361-370, 2015.
- [4] L. Fu, Y. C. Jin, "Improved multiphase Lagrangian method for simulating sediment transport in dam-break flows," *J. Hydraul. Eng., ASCE*, vol. 142, no. 6, pp. 04016005, 2016.
- [5] R. A. Dalrymple, B. D. Rogers, "Numerical modeling of water waves with the SPH method," *Coast. Eng.*, vol. 53, no. 2, pp. 141-147, 2006.

- [6] M. Gomez-Gesteira, B. D. Rogers, R. A. Dalrymple, A. J. Crespo, "State-of-the-art of classical SPH for free-surface flows," *J. Hydraul. Res.*, vol. 48, no. S1, pp. 6-27, 2010.
- [7] C. Ulrich, M. Leonardi, T. Rung, "Multi-physics SPH simulation of complex marine-engineering hydrodynamic problems", *Ocean Eng.*, vol. 64, pp. 109-121, 2013.
- [8] G. Fourtakas, B. D. Rogers, "Modeling multi-phase liquid-sediment scour and resuspension induced by rapid flows using Smoothed Particle Hydrodynamic (SPH) accelerated with a Graphics Processing Unit (GPU)," *Adv. Water Resour.*, vol. 92, pp. 186-199, 2016.
- [9] Z. Wei, H. Shi, C. Shi, J. Katz, R. A. Dalrymple, G. Bilotta, "Behavior of oil under breaking waves by a two-phase SPH model," *Proceeding of 11th International SPHERIC Workshop*, Munich, Germany, June 14-16, 2016.
- [10] A. Colagrossi, M. Landrini, "Numerical simulation of interfacial flows by smoothed particle hydrodynamics," *J. Comput. Phys.*, vol. 191, no. 2, pp. 448-475, 2003.
- [11] Z. Chen, Z. Zong, M. B. Liu, L. Zou, H. T. Li, C. Shu, "An SPH model for multiphase flows with complex interfaces and large density differentiates," *J. Comput. Phys.*, vol. 283, pp. 169-188, 2015.
- [12] A. Shakibaeinia, Y. C. Jin, "A mesh-free particle method for simulation of mobile-deb dam break," *Adv. Water Resour.*, vol. 34, pp. 794-807, 2011.
- [13] H. H. Bui, K. Sako, R. Fukagawa, "Numerical simulation of soil-water interaction using smooth particle hydrodynamics (SPH) method", *J. Terramechanics*, vol. 44, no. 5, pp. 339-346, 2007.
- [14] H. Sakai, K. Maeda, T. Imase, "Erosion and seepage failure analysis of ground with evolution of bubbles using SPH ,," *Prediction and Simulation Methods for Geohazard Mitigation*, CRC press, Kyoto.
- [15] G. Pahar, A. Dhar, "Coupled incompressible Smoothed Particle Hydrodynamics model for continuum-based modeling sediment transport," *Adv. Water Resour.*, vol. 102, pp. 84-98, 2017.
- [16] B. Ren, C. Li, X. Yan, M. C. Lin, J. Bonet, S. M. Hu, "Multiple-fluid SPH simulation using a mixture model," *ACM T. Graphic.*, vol. 33, no. 5, pp. 171:1-11, 2014.
- [17] G. Lai, D. J. Price, "Dusty gas with one fluid in smoothed particle hydrodynamics," *Monthly Notices of the Royal Astronomical Society*, vol. 440, no. 3, pp. 2147-2163, 2014.
- [18] D. A. Drew, "Mathematical modeling of two-phase flow," *Annu. Rev. Fluid Mech.*, vol. 15, no. 1, pp. 261-291, 1983.
- [19] H. Shi, X. Yu, R. A. Dalrymple, "Development of a two-phase SPH model for sediment laden flows," *Comput. Phys. Commun.*, in press.
- [20] L. Schiller, Z. Naumann, "A drag coefficient correlation," *V. D. I. Zeitung*, vol. 77, pp. 318-320, 1935.
- [21] X. Chen, Y. Li, X. Niu, D. Chen, X. Yu, "A general two-phase turbulent flow model applied to the study of sediment transport in open channels," *Int. J. Multiphas. Flow*, vol. 37, no. 9, pp. 1099-1108, 2011.
- [22] C. H. Lee, Y. M. Low, Y. M. Chiew, "Multi-dimensional rheology-based two-phase model for sediment transport and applications to sheet flow and pipeline scour," *Phys. Fluids*, vol. 28, pp. 053305, 2016.
- [23] J. Chauchat, "A comprehensive two-phase flow model for unidirectional sheet flows," *J. Hydraul. Res.*, 2017.
- [24] M. Trulsson, B. Andreotti, P. Claudin, "Transition from the viscous to inertial regime in dense suspensions," *Phys. Rev. Lett.*, vol. 109, no. 11, pp. 118305, 2012.
- [25] J. R. Macdonald, "Some simple isothermal equations of state," *Rev. Mod. Phys.*, vol. 38, no. 4, pp. 669-679, 1966.
- [26] J. E. Nafe, C. I. Drake, "Variation with depth in shallow and deep water marine sediments of porosity, density and velocities of compressional and shear waves," *Grophysics*, vol. 22, no. 3, pp. 523-552, 1957.
- [27] M. Liu, G. Liu, "Smoothed particle hydrodynamics (SPH): an overview and recent developments," *Arch. Comput. Method E.*, vol. 17, no. 1, pp. 25-76, 2010.
- [28] D. Violeau, B. D. Rogers, "Smoothed particle hydrodynamics (SPH) for free-surface flows: past, present, and future," *J. Hydraul. Res.*, vol. 54, no. 1, pp. 1-26, 2016.
- [29] A. J. C. Crespo, M. Gomez-Gesteira, R. A. Dalrymple, "Boundary conditions generated by dynamic particles in SPH methods," *Cmc – Tech Science Press*, vol. 3, no. 3, pp. 173-184, 2007.
- [30] A. Herault, G. Bilotta, R. A. Dalrymple, "SPH on GPU with CUDA," *J. Hydraul. Res.*, vol. 48, pp. 74-79, 2010.
- [31] B. Spingwine, Two-layer flow behaviour and the effects of granular dilatancy in dam break induced sheet-flow. PhD thesis, Universitite de Louvain, 2005.
- [32] P. Lin, D. Wang, "Numerical modeling of 3D stratified free surface flows: a case study of sediment dumping," *Int. J. Numer. Meth. Fl.*, vol. 50, no. 12, pp. 1425-1444, 2006.

Numerical simulation of water-entry problems using an improved multiphase SPH method

H. Cheng

College of Shipbuilding Engineering
Harbin Engineering University
Harbin, China
18346194802@163.com

F.R. Ming

College of Shipbuilding Engineering
Harbin Engineering University
Harbin, China
Mingfuren2006@126.com

A.M Zhang

College of Shipbuilding Engineering
Harbin Engineering University
Harbin, China
zhangaman@hrbeu.edu.cn

Abstract—Water entry is a complex fluid-solid interaction problems that be focused in many aspects, i.e., the shipbuilding and aerospace. The impacting loads are hard to be predicted especially for the solid with a small deadrise angle, because the effect of the air should be taken into account. In the paper, an improved multiphase SPH model is established to simulate the water entry of wedge with different deadrise angles. The Sub-Grid Scale (SGS) model with a multiphase form is adopted in the SPH scheme to represent the effect of the turbulence. What's more, the traditional shifting algorithm is improved for multiphase problems. Based on this, firstly, the water entry of the wedge are simulated and compared to the experimental data to validate the feasibility and accuracy of the SPH model in the paper. Then, the numerical simulations with small deadrise angle are carried out, and the results are compared to the single-phase SPH model to investigate the effect of the air. It is found that the slamming forces for the water entry of the plate without air is bigger and has smaller pulse width, and the value of the Mach number of the water can significantly influence the slamming forces.

I. INTRODUCTION

The prediction of the hydrodynamics loads acting on an impacting body is very important in many aspects, i.e., the shipbuilding and aerospace. The water-entry problem is a transient process during which the extreme loads can cause the damage of the structure. Thus, the determination of the impact load plays a crucial role in the evaluation of the safety standards. However, due to the nonlinearity and complexity of the water entry, the impacting loads are hard to be predicted. Besides, the effect of the air should not be ignored when the deadrise angle of the structure is small enough, especially in the initial stage of the impact. According to the Wagner's theory [1], for the water entry of the structure with the small deadrise angle, an air cushion can be formed reducing the impacting loads significantly. In summary, based on the deadrise angle of the structure, the water-entry problems can be divided into three types [2]: the Wagner type, the trapped-air type and the intermediate type.

In the past, the water entry has been extensively studied by many scholars based on the theoretical and experimental methods. As a pioneer, Karman [3] investigated the problem of the ditching of the sea plane on the water based on theoretical method without considering the effect of the air.

Besides, the water are assumed to be incompressible and inviscid and the gravity is ignored, which limits its application. In Wagner's theory [1], he noted that the air cushion can absorb the impact and deform the water surface before the structure contacts with the water. Then, it was verified in the experiment carried out by Chuang et al. [4] that the impact loads generated by the water entry of the wedge is smaller than the theoretical value. In Sumi's experiments [2], it was found that the loads acted on the plate are more well-distributed due to the existence of the air cushion. In general, for the water entry of the structure with the small deadrise angle, the theoretical method is not applicable any more due to the ignoring of the air.

In the recent years, with the developing of the computers, the numerical simulation has been an optional scheme in settling the water-entry problem. Nonetheless, the extreme characteristics of the impact bring many difficulties for the simulation. Thus as yet, more attentions are focused on the dynamics characteristics of the flow field after entering the water. Ng et al. [5] simulated the water entry of the plate based on the volume of fluid method (VOF) considering the effect of the air. It is also found that the air can deform the water surface before impact. Similar works has been carried out by Iwanowski et al. [6] where the effect of the compressible air cushion is investigated. In his work, the air and the water are assumed to be compressible and incompressible respectively, and the VOF method is solved in the time domain. Recently, the CIP method has been employed by yang et al. [7] to simulate the water impact for 2D and 3D bodies including the wedge and plate. Good agreement has been found between the numerical results and the related experimental data. However, in the CIP scheme which is a grid-based method, the interface between the air and the water need to be captured using the density functions specially.

In the paper, the multiphase smoothed particle hydrodynamics (SPH) method is employed to simulate the whole process of the water entry of the structure with different deadrise angles. As a meshfree particle method, the SPH method is originally applied to the astronomical problem [8]. Soon, due to its meshless and Lagrangian characteristics, the SPH method is proved to have great advantages in dealing with free surface flow problem [9, 10] including the structure

water entry. Oger et al. [11] studied the two-dimensional wedge water entries based on the SPH method with variant smoothing lengths. The numerical results agree well with the experimental data, but the effect of the air is ignored. In [12], the incompressible SPH method combined with LES turbulence model was adopted to investigate the free-falling wedge water entry. Good results were also achieved without considering the air. Recently, the two-phase SPH method was employed by Gong et al. in [13] to simulate the water entry of the wedge. It has been found that both the water and air phases are reasonably predicted including the closure of the cavity. However, Gong's study is focused on the later stage of the water entry and the deadrise angle of the structure is large. In [14], a two-phase incompressible-compressible smoothed particle hydrodynamics (SPH) method for water and air, respectively, is applied where the water phase imposes kinematics on the air at the air-water phase and the air phase imposes pressures in the water at the interface. The hydrodynamics loads acted on the plate when impact are compared with the relevant experimental data where acceptable agreements are achieved. But it must be admitted that the interface treatment in the coupled SPH method is very complex. In the paper, the weakly compressible SPH method is improved for solving the water-air problems with a large density difference. Three key points are focused in the SPH scheme, i.e., the stability of the air, the interface between the air and the water and the compressibility of the water. For the stability of the air, we employ the continuity and momentum equation adopted in the [12] combined with a LES turbulence model with a multiphase form. Then, the shifting algorithm [15] is improved to avoid the interface instability. At last, the effect of the Mach number of the water on the impact loads is investigated. On this basis, the water entry of the wedge is firstly simulated where good agreements are achieved between the numerical results and experimental data. However, for the water entry of the plate, the impact load accords with experimental results until the Mach number of the water is set to be 0.02. In general, the air flow during the water entry is stable which validates the feasibility of the SPH model in the paper.

This paper is arranged as follows: in Section II, the multiphase SPH scheme employed in the paper is briefly introduced; in section III, the results of the water entry of the wedge and the plate are presented respectively. At last, conclusions and further development are described.

II. MULTIPHASE SPH MODEL

A. SPH approximation formulae

In the SPH method, the Navier-Stokes equations including the continuity equation and the momentum equation are employed to move the particle as follows:

$$\frac{d\rho}{dt} = -\rho \nabla \cdot \vec{v} \quad (1)$$

$$\frac{d\vec{v}}{dt} = -\frac{1}{\rho} \nabla p + \vec{g} + \vec{Q} + \frac{1}{\rho} \nabla \cdot \vec{\tau} \quad (2)$$

where ρ, p, \vec{v} refer to the density, pressure and velocity of the particle, \vec{g} the acceleration of gravity, \vec{Q} the diffusion term and $\vec{\tau}$ the turbulent stress which is modelled using a large eddy simulation approach as:

$$\frac{\tau_{ab}}{\rho} = 2\nu_t S_{ab} - \frac{2}{3}k\delta_{ab} \quad (3)$$

where S_{ab} is the strain rate of the mean flow, k the turbulence kinetic energy, δ_{ab} the Kronecker delta and ν_t the turbulence eddy viscosity which is modelled using the Smagorinsky model as [16]:

$$\nu_t = C_s^2 \zeta^2 |\bar{S}| \quad (4)$$

where C_s is the Smagorinsky constant which is set to be 0.12 in the paper, ζ the particle space and $|\bar{S}| = (2S_{ab}S_{ab})^{1/2}$.

Based on the discretization method, the continuity and momentum equations can be discretized into the SPH form. There are various forms of the SPH formulation which possess respective merits. For the water entry problem existing the complex interfaces and large density differences, the form in [17] is adopted due to its efficiency and stability, and the turbulence stress in equation (2) is discretized in the same form as the pressure. Besides, the artificial viscosity [8] is also added to the momentum equation to reduce the pressure noise. The present SPH system is as follows:

$$\frac{d\rho_i}{dt} = \rho_i \sum_{j=1}^N \frac{m_j \vec{v}_{ij} \cdot \nabla_i W_{ij}}{\rho_j} \quad (5)$$

$$\begin{aligned} \frac{d\vec{v}_i}{dt} = & -\sum_{j=1}^N m_j \left(\frac{p_i + p_j}{\rho_i \rho_j} + \Pi_{ij} \right) \nabla_i W_{ij} \\ & + \sum_{j=1}^N m_j \left(\frac{\vec{\tau}_i + \vec{\tau}_j}{\rho_i \rho_j} \right) \nabla_i W_{ij} + \vec{g} \end{aligned} \quad (6)$$

$$\Pi_{ij} = \begin{cases} -\frac{\alpha c_{i0} \mu_{ij}}{\rho_j} & \vec{v}_{ij} \cdot \vec{r}_{ij} < 0 \\ 0 & \vec{v}_{ij} \cdot \vec{r}_{ij} > 0 \end{cases} \quad (7)$$

$$\mu_{ij} = \frac{h \vec{v}_{ij} \cdot \vec{r}_{ij}}{\vec{r}_{ij} + 0.01h^2} \quad (8)$$

where m, h refer to the mass and smoothing length of the particle, $\vec{v}_{ij} = \vec{v}_i - \vec{v}_j$, $\vec{r}_{ij} = \vec{r}_i - \vec{r}_j$, α the artificial viscosity coefficient which is set to be 0.05 and W the kernel function. In the paper, the improved Gaussian kernel function is adopted.

B. Boundary condition

The structure is deemed to be rigid body in the paper and the dummy boundary [18] is adopted. The core idea of the boundary treatment is to arrange enough particles beyond the boundary to satisfy the impenetrable condition and the information of the dummy particles is interpolated from the fluid particles near the boundary, taking the pressure for example, that is:

$$p_w = \frac{\sum_f p_f W_{wf} + \sum_f (\vec{g} - \vec{a}_w) \cdot \vec{r}_{wf} \rho_f W_{wf}}{\sum_f W_{wf}} \quad (9)$$

where the subscripts w, f refer to the boundary particle and fluid particle respectively. When solving the continuity equation (5) and the momentum equation (6), the dummy particles above are treated as fluid particles.

C. Equation of state

In the paper, the air and the water are both deemed to be weakly compressible, and the linear state equation is adopted as follow [19]:

$$p = c^2(\rho - \rho_0) + p_b \quad (10)$$

where c refers to the artificial sound speed, ρ_0 the reference density of the fluid and p_b the background pressure which is 1000Pa in the paper. One key issue is the value of the sound speed since it can influence the impact process. Generally, the artificial sound speed is about 10 times of the largest speed of all the particles, that is $c = 10v_{\max}$, to guarantee the fluctuation of the density less than 1%. In other words, the Mach number $Ma = v/c < 0.1$. In the paper, the sound speed of the air is set to be 340m/s as the velocity of the jet airflow when impact is big. The choice of the sound speed of the water will be discussed in the later section.

D. Shifting algorithm

During the calculation of the violent fluid-structure interactions, some instability phenomena may happen within the flow field especially for the air. Thus, the shifting algorithm is adopted in the paper to correct the velocity as [15]:

$$v' = -D\nabla C_i \quad (11)$$

where D is the diffusion coefficient which can be obtained as follow [20]:

$$D = A_s h |\mathbf{v}_i| \quad (12)$$

The gradient of the parameter C in equation (11) can be obtained as follow [21]:

$$\nabla C_i = \sum_j (C_j - C_i) \frac{m_j}{\rho_j} \nabla W_{ij} \quad (13)$$

where C can be estimated using the sum of the smoothing kernel:

$$C_i = \sum_j \frac{m_j}{\rho_j} W_{ij} \quad (14)$$

It is worth noting that the interface instability will happen when applying the shifting algorithm to the water and the air [22]. Thus, the particles around the interface do not participate the calculation of the equation (11). To identify the interface, the following algorithm is adopted:

$$\mathbb{Q} = \sum_j \frac{m_j}{\rho_j} \mathbf{r}_{ij} \cdot \nabla_i W_{ij} \quad (15)$$

where subscripts i, j refer to the particles that belong to the same phase as shown in Figure 1.

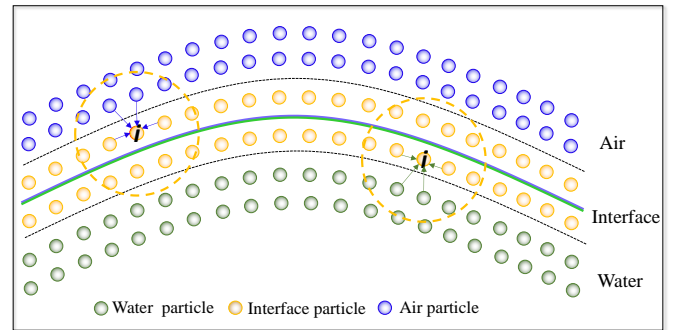


Figure 1. The interface treatment in the multiphase SPH method.

III. NUMERICAL RESULTS

A. Water entry of the wedges

The first numerical validation is the water entry of a wedge tested by Zhao et al. [23]. The length of the wedge is 1.0m and the width is 0.5m. The dead-rise angle of the wedge is 30 degrees. In the experiment, a free falling rig is used to drop the wedge, and the total weight of the drop rig is 241kg. The vertical velocity of the wedge is measured through an optical sensor, and the contact force between solid and fluid is measured using two force transducer connected to the drop rig. In the experiment, the vertical motion is the only degree of freedom that allowed to the wedge, and the impact velocity is 6.15m/s. In the numerical simulation, the 2D SPH model is established to reduce the computation complexity. As shown in Figure 2, the total length of the water tank is 2.5m and the depth is 1.5m. A sponge layer proposed by Gong et al. [24] is implemented inside the fluid domain to eliminate the affection of the wave reflected from the boundary particles. The artificial sound speed of the water is set to be 60m/s which is about 10 times of the impact velocity of the wedge. The initial particle spacing is set to be 0.005m and about 0.18 million particles are used in the simulation. The wedge is initially located at 1.92m away from the free surface of the water.

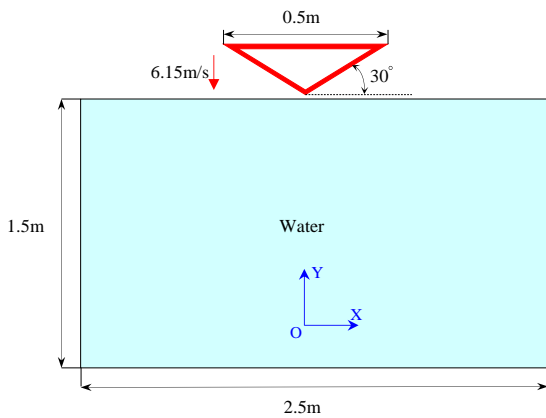


Figure 2. Sketch of the 2-D wedge water entry.

Figure 3 shows the snapshots of the evolution of the 2-D wedge water entry. To distinguish the water and the air, they are presented using the velocity and pressure field with different colour systems. The paper focuses on the early stage of the impact where the violent fluid-structure interactions happen. It can be seen clearly from Figure 3 (a) that the airflow behind the wedge has a big velocity. Since the lower end of the wedge is far away from the free surface of the water, there is no pressure disturbance that can be observed within the water domain. At $t=0.62$ s, the wedge is going to contact with water and the airflow between the structure and the water moves faster. To investigate the effect of the air on the water domain more clearly, the velocity vector of the air when impact is shown in Figure 4. It can be seen that the air in the middle moves to the sides and the free surface of the water has little distortion. At the moment, the pressure of the water domain close to the free surface is larger than the hydrostatic pressure, which means the airflow has non-negligible influence on the impact.

As shown in the Figure 3 (c) and (d), an impact zone with high pressure is generated when the wedge falls into the water domain. Meanwhile, the airflow between the wedge and the water has been pressed and gets thin forming a jet flow with a large velocity. Note that the high pressure area moves from the bottom of the wedge to its sides over time. At $t=0.65$ s and $t=0.67$ s, as most of the wedge has been submerged under the water, the pressure field of the water domain is getting stable and two sprayes have been formed. In general, the interface between the air and the water is stable throughout the impacting process which verified the viability of the multiphase SPH model in the paper.

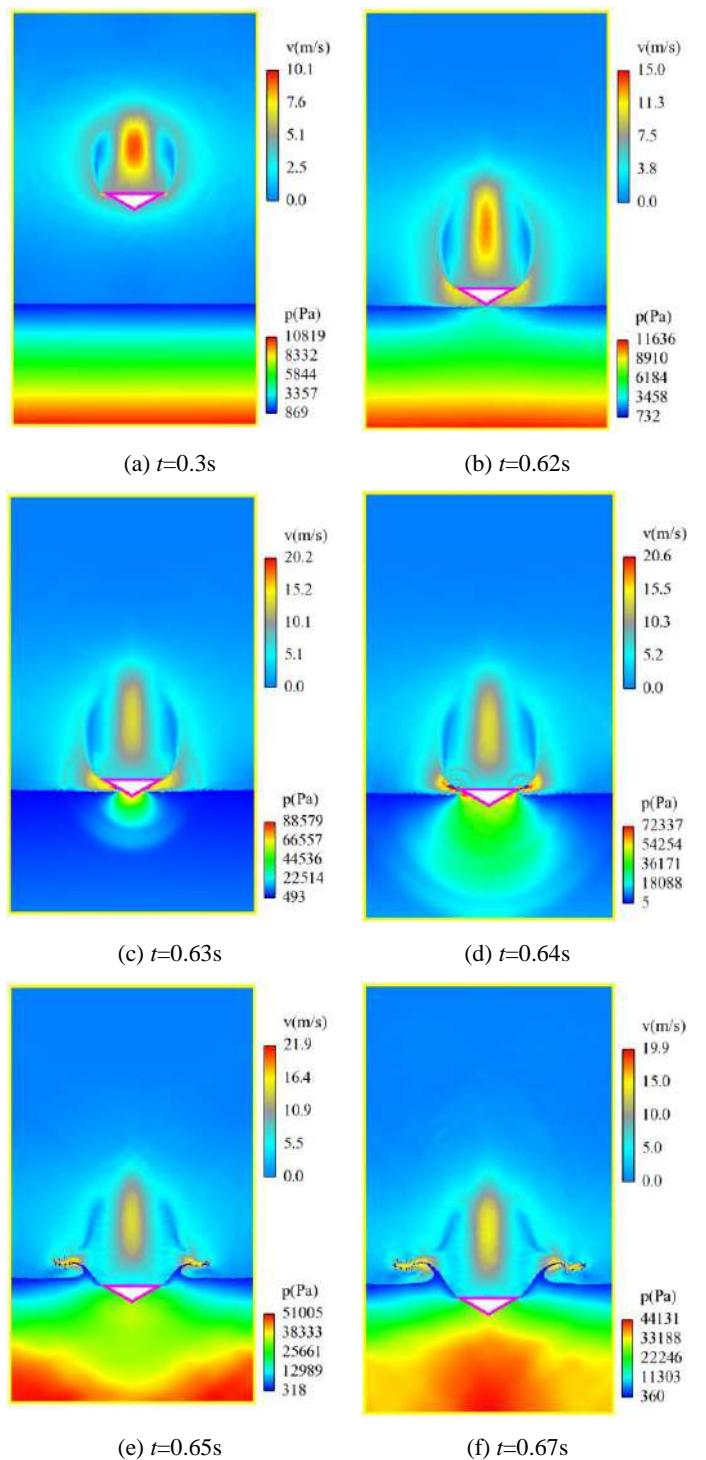


Figure 3. Snapshots of the evolution of the 2-D wedge water entry in a water tank. The air and the water are presented using the velocity and pressure field respectively.

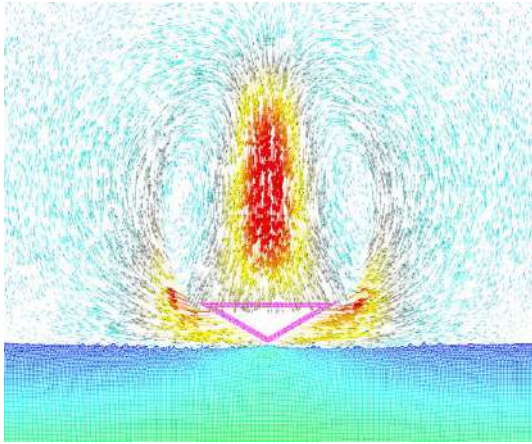


Figure 4. The velocity vectors of the air when impact.

The time history of the contact force and the falling velocity compared with experimental data [23] are presented in Figure 4 and Figure 5. It can be seen that in spite of some deviations in the vertical velocities, the results calculated by the two-phase SPH model agree well with the experimental data in general, which validated the accuracy of the numerical model adopted in the paper. It is worth nothing that for the water entry of the wedge, the effect of the air can be ignored since there is almost no difference between the results of the single phase and two phase. In this section, the Mach number of the water is set to be 0.1 and good results have been achieved, which illustrates that the compressibility of the water has less effect on the impact when the deadrise angle of the wedge is big. After all, it has been demonstrated the impacting loads are well predicted based on ISPH method even the water are deemed to be completely incompressible. So we will not talk about the effect of the Mach number on the impact loads any more in this case.

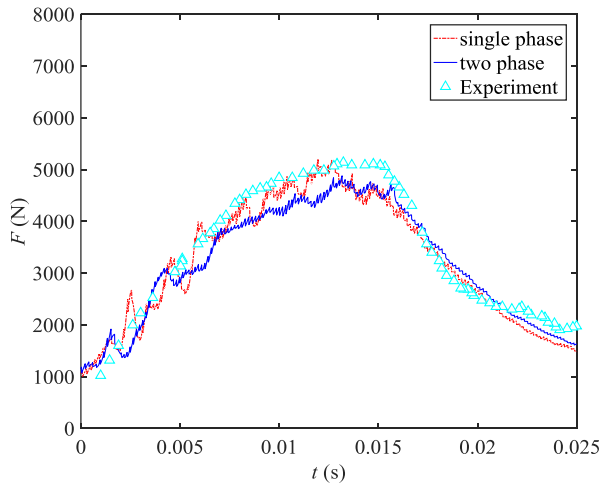


Figure 5. Time history of the contact forces during the impacting process compared with the experimental data in [23].

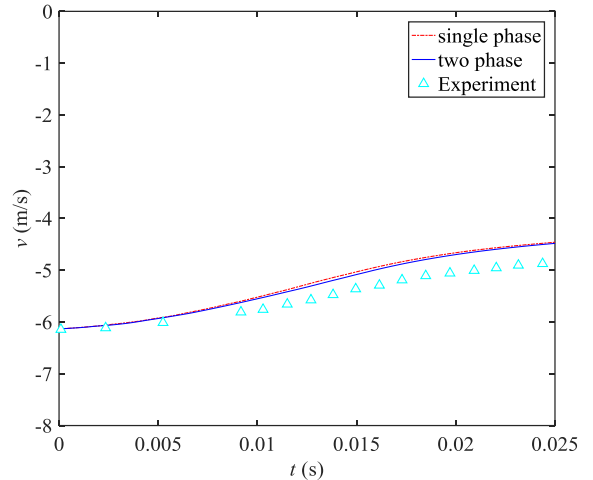


Figure 6. Time history of the vertical velocities during the impacting process compared with the experimental data in [23].

B. Water entry of the plate

In this section, the water entry of the structure with the small deadrise angle, i.e., the plate, is investigated. The sketch of the 2-D plate water entry is shown in Figure 7. The experimental studies was carried out by Ma et al. [25] where attention is focused on the measurement of the slamming loads on the plate during the impact. The plate is 0.25 m wide with a 5.5 m/s impact velocity. The mass of the plate is 32kg. In the experiment, the plate is accelerated through a free-fall period. As shown in Figure 3, the airflow can influence the water domain until the wedge has gotten close enough to the free surface. Thus, in this section, in order to reduce the computing burden of the numerical calculation, the plate is released with an initial velocity. Nonetheless, there is still enough space left between the plate and the water domain to avoid unphysical effect. In the numerical calculation, the particle spacing is set to be 0.002m. The lengths of the water domain in x and y direction are 1.2m and 0.8m respectively and about 0.24 million particles are used in the case. Up to now, very few studies has been focused on the impact loads of the plate water entry based on the SPH method, expect the numerical investigation carried by Rogers where the water is deemed to be incompressible. In the paper, the linear state equation is applied to both of the water and the air, where the compressibility of the fluid depends on the choice of the sound speed. The Mach number of the fluid around the plate can be calculated as:

$$\text{Ma} = \frac{v_i}{c_0} \quad (16)$$

Where v_i refer to the impact velocity of the plate. In the case, the sound speed of the air is still set to be 340m/s. But the Mach number of the water will be adjusted to study its effect on the impact.

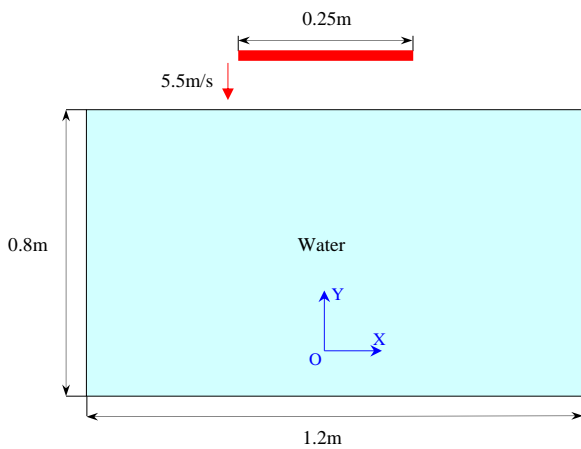


Figure 7. Sketch of the 2-D plate water entry.

In this case, attention is focused on the dynamics characteristic of the airflow. As shown in Figure 8, the air and the water are presented using the velocity and pressure filed with different colour systems. When $t=48\text{ms}$ and $t=78\text{ms}$, the air behind the plate has a large velocity. Meanwhile the air domain between the plate and the water is stable since the plate is far away from the free surface. And there is no obvious disturbance of pressure that can be observed within the water domain. It is worth noting that the there are two isolated domains in which the airflow velocity is far less than their surroundings. The cause of this phenomenon can be found out in Figure 9 where the velocity vectors of the air are presented. It can be clearly seen that the circulation behind the plate is formed when the velocity of the plate is big. And the air at the centre of the circulation is almost static.

At $t=97\text{ms}$, as the plate is getting close to the free surface, the air flow between the plate and the water is moving faster. At $t=106\text{ms}$ as shown in Figure 8 (d), two jet flows with a large velocity are generated before the plate contacts with water. It can be clearly seen from Figure 9 that only the air around the edge of the plate is moving fast. The air in the middle cannot be exhausted in time and the free surface of the water has been pressed. Thus despite the large velocity of the exhaust air, there are still some gases observed which are trapped between the plate and the free surface. Although the plate has not yet contact with the water completely at $t=106\text{ms}$, there is a high pressure domain close to the free surface that is generated due to the compress of the air cushion. As mentioned earlier, the air cushion can help absorbing the impact and make the slamming loads acted on the plate well distributed. Thus the effect of the air for the water entry of the plate cannot be ignored. One thing that should be mainly considered is the compressibility of the air and water since it can influence the slamming loads.

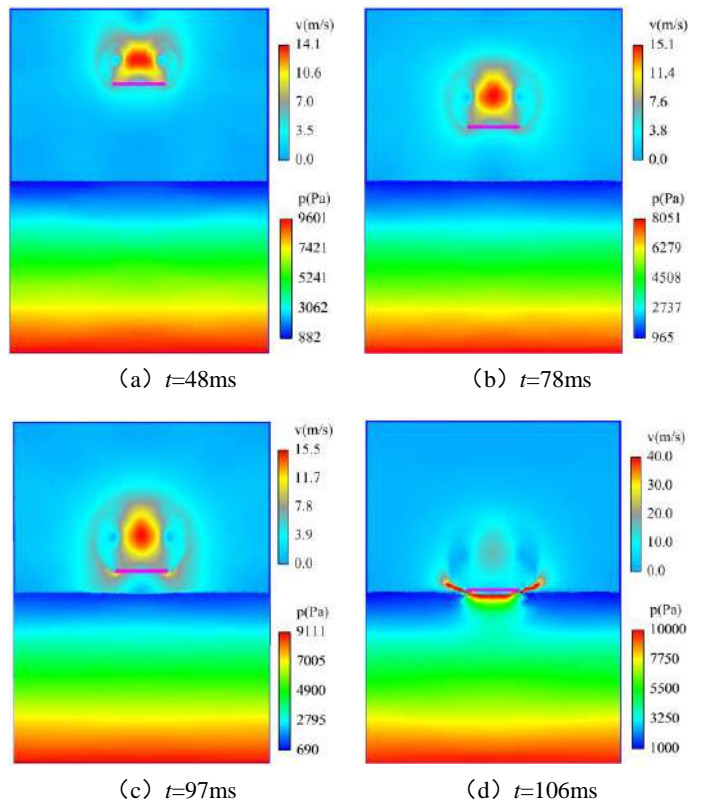


Figure 8. Snapshots of the evolution of the 2-D plate water entry in a water tank. The air and the water are presented using the velocity and pressure filed respectively.

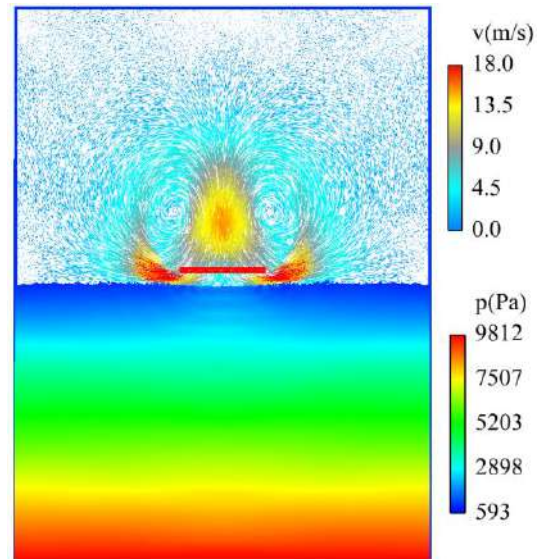


Figure 9. The velocity vectors of the air when impact.

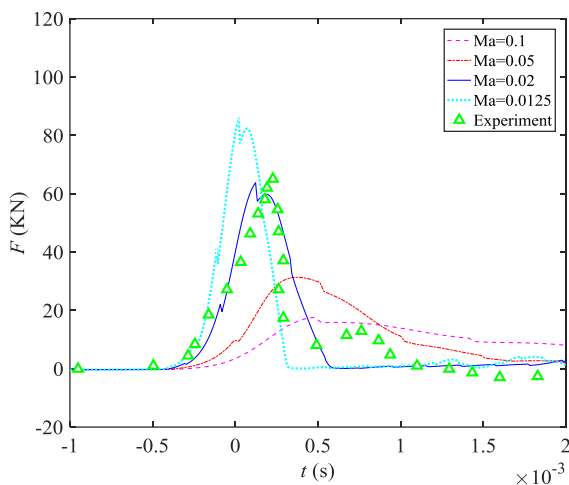


Figure 10. Time history of the contact forces during the impacting process with different Mach number compared with the experimental data in [25].

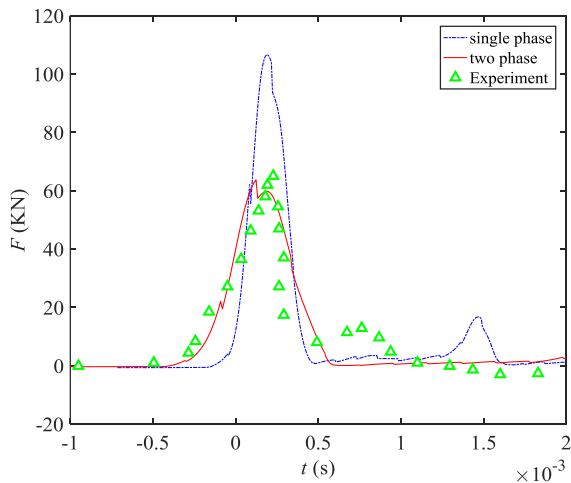


Figure 11. Time history of the contact forces during the impacting process with and without air compared with the experimental data in [25].

Time history of the contact forces during the impacting process with different Mach number is shown in Figure 10. It is found that the slamming loads vary with the Mach number. The numerical results agree with the experimental data until the Mach number is adjusted to 0.02. Note that with the decrease of the Mach number, the peak value of the slamming loads increase and the pulse width decrease. As shown in Figure 11, when the Mach number is set to be 0.02, the water entry of the plate with and without air is respectively simulated and compared with experimental data. It can be seen that the slamming forces when impact without air is bigger and has smaller pulse width. Besides, the existence of the air can delay the impacting process. In general, the air plays an important role in the water entry of the structure with small deadrise angle.

IV. CONCLUSION

In the paper, the multiphase SPH model is established to simulate the water entry of wedge and plate. In the SPH scheme, the SGS model which can deal with the turbulent flows are adopted with a multiphase form. The shifting algorithm is used within the fluid domain expect the particles around the interface to avoid the unphysical penetration. As the linear state equation is adopted in the paper, the choice of the sound speed of the water is discussed in detail. The water entry of the wedge is firstly simulated using the multiphase SPH model where good agreements have been achieved between the numerical results and the experimental data. And the velocity and pressure fields of the air and the water are presented during the impact process where the interface is stable. Then, the simulation of the water entry of the plate is carried out. It is found that an air cushion can be formed during the impact process. The slamming forces when impact without air is bigger and has smaller pulse width. Besides, the value of the Mach number of the water can significantly influence the slamming forces. In general, the multiphase SPH model established in the paper is suitable for solving the water entry problem. But for the water entry of the structure with small deadrise angle, the Mach number of the water should be taken into account emphatically.

ACKNOWLEDGEMENT

This paper is supported by the National Natural Science Foundations of China (51609049), the Natural Science Foundation of Heilongjiang Province (QC2016061).

REFERENCES

- [1] H. Wagner, Über Stoß- und Gleitvorgänge an der Oberfläche von Flüssigkeiten. ZAMM - Journal of Applied Mathematics and Mechanics/Zeitschrift für Angewandte Mathematik und Mechanik,12 (1932) 193-215.
- [2] S. Okada, Y. Sumi, On the water impact and elastic response of a flat plate at small impact angles. Journal of marine science and technology,5 (2000) 31-39.
- [3] T. Von Karman, The impact on seaplane floats during landing. (1929)
- [4] S.-L. Chuang, Experiments on flat-bottom slamming. Journal of Ship Research,10 (1966) 10-27.
- [5] C. Ng, S. Kot, Computations of water impact on a two-dimensional flat-bottomed body with a volume-of-fluid method. Ocean Engineering,19 (1992) 377-393.
- [6] B. Iwanowski, M. Fujikubo, T. Yao, Analysis of horizontal water impact of a rigid body with the air cushion effect. Journal of the Society of Naval Architects of Japan,1993 (1993) 293-302.
- [7] Q. Yang, W. Qiu, Numerical simulation of water impact for 2D and 3D bodies. Ocean Engineering,43 (2012) 82-89.
- [8] J. Monaghan, R. Gingold, Shock simulation by the particle method SPH. Journal of computational physics,52 (1983) 374-389.
- [9] J. J. Monaghan, Simulating free surface flows with SPH. Journal of computational physics,110 (1994) 399-406.
- [10] M. Liu, G. Liu, Smoothed particle hydrodynamics (SPH): an overview and recent developments. Archives of computational methods in engineering,17 (2010) 25-76.
- [11] G. Oger, M. Doring, B. Alessandrini, P. Ferrant, Two-dimensional SPH simulations of wedge water entries. Journal of computational physics,213 (2006) 803-822.
- [12] S. Shao, Incompressible SPH simulation of water entry of a free - falling object. International Journal for numerical methods in fluids,59 (2009) 91-115.

- [13] K. Gong, S. Shao, H. Liu, B. Wang, S.-K. Tan, Two-phase SPH simulation of fluid–structure interactions. *Journal of Fluids and Structures*,65 (2016) 155-179.
- [14] S. Lind, P. Stansby, B. Rogers, P. Lloyd, Numerical predictions of water-air wave slam using incompressible-compressible smoothed particle hydrodynamics. *Applied Ocean Research*,49 (2015) 57-71.
- [15] R. Xu, P. Stansby, D. Laurence, Accuracy and stability in incompressible SPH (ISPH) based on the projection method and a new approach. *Journal of Computational Physics*,228 (2009) 6703-6725.
- [16] J. Smagorinsky, General circulation experiments with the primitive equations: I. The basic experiment. *Monthly weather review*,91 (1963) 99-164.
- [17] A. Colagrossi, M. Landrini, Numerical simulation of interfacial flows by smoothed particle hydrodynamics. *Journal of computational physics*,191 (2003) 448-475.
- [18] S. Adami, X. Hu, N. Adams, A generalized wall boundary condition for smoothed particle hydrodynamics. *Journal of Computational Physics*,231 (2012) 7057-7075.
- [19] M. Antuono, A. Colagrossi, S. Marrone, Numerical diffusive terms in weakly-compressible SPH schemes. *Computer Physics Communications*,183 (2012) 2570-2580.
- [20] A. Skillen, S. Lind, P. K. Stansby, B. D. Rogers, Incompressible smoothed particle hydrodynamics (SPH) with reduced temporal noise and generalised Fickian smoothing applied to body–water slam and efficient wave–body interaction. *Computer Methods in Applied Mechanics and Engineering*,265 (2013) 163-173.
- [21] J. J. Monaghan, Smoothed particle hydrodynamics. *Reports on progress in physics*,68 (2005) 1703.
- [22] A. Mokos, B. D. Rogers, P. K. Stansby, A multi-phase particle shifting algorithm for SPH simulations of violent hydrodynamics with a large number of particles. *Journal of Hydraulic Research*,55 (2017) 143-162.
- [23] R. Zhao, O. Faltinsen, J. Aarsnes, in *Proceedings of the 21st symposium on naval hydrodynamics*. (Trondheim, Norway, National Academy Press, Washington, DC, USA, 1996), pp. 408-423.
- [24] K. Gong, B. Wang, H. Liu, Modelling water entry of a wedge by multiphase SPH method. *Coastal Engineering Proceedings*,1 (2011) 10.
- [25] Z. Ma, D. Causon, L. Qian, C. Mingham, T. Mai, D. Greaves, A. Raby, Pure and aerated water entry of a flat plate. *Physics of Fluids*,28 (2016) 016104.

SPH numerical simulation of lift-off by impact of sand particles on flat sand bed

Jie Zhao, Afang Jin, Maimtimin Geni, Xiaojing Ma

College of Mechanical Engineering

Xinjiang University

Urumqi Xinjiang, China

Abstract—The study of Aeolian processes (which pertain to wind activity in the study of geology and weather) can offer insights into past and present geographies and climatic conditions. Previous studies on collisions between sand particles have used models which are complex and require enormous amounts of calculation. In this light, we use the smoothed particle hydrodynamics (SPH) method to simulate the lift-off phenomenon of sand particles in air flows which impact the surface of a grain bed. The colliding process between the incident sand particles and grain bed is dynamically shown. Using the SPH method, the whole computational domain is broken down into discrete particles using control equations. These discrete particles are consistent with natural sand particles in terms of shape. Therefore, using the SPH method has particular advantages in processing collision problems of sand particles. We carry out statistical analyses and compare our results with previous studies, and our simulated results show that the collision effect is very important for the take-off of sand particles in wind-blown sand movement and that it dictates the entire process of sand movement. The collision effect of sand particles can stir up several bigger and heavier sand particles. The simulated results demonstrate the micro-collision process more dynamically and precisely. Our study provides a better simulation method for research on the micro-movements of wind-blown sand. We believe that our simulation method can significantly contribute to the study of wind-blown sand transport.

I. INTRODUCTION

The wind-blown sand flow begins with the lift-off of sand particles from the stationary state into a state of motion (Ding 2008, Shi & Huang 2012, Kang & Liu 2010). The lift-off mechanism of sand is one of the focal problems of physics research on wind-blown sand. The lift-off mechanism of sand has thus far been attributed to two types of particle motion: direct lift-off by a fluid and impact lift-off. (1) Direct lift-off: The first type of particle transport is the direct lift-off of sand particles by wind, and this is further classified into two types of theories. As regards the first set of theories, particle transport has been discussed by Von Karman in terms of turbulence pulsation and vibration theory. This class of theories proposes that sand lift-off is due to the pulsation of turbulence on the vertical velocity of sand particles; when the wind velocity equals the sand lift-off velocity, particles begin to vibrate under the action of vertical pulsation power. This vibration increases with the increase in wind velocity until particles are lifted off from the ground. The second class of theories involves differential pressure lift. This set of theories explains sand lift-

off movement using the lift theory and the Magnus effect, and they describe in detail the effects of various types of sand lift-off; however, the various types of forces involved are not classified, and only qualitative analysis is performed. (2) Impact collision theory: This theory attributes sand lift-off mainly to the force of impact by other particles. In this regard, Bagnold (1941) has experimentally proved that the high-speed movement of sand in the saltation process can lead to the lift-off of particles which are two hundred times heavier than the particles impacting the sand bed. In this study, we use the smoothed-particle hydrodynamics method to carry out modelling and simulation analysis of the sand lift-off phenomenon of wind-blown sand transport. We focus on the impact lift-off mechanism, and we numerically simulate sand lift-off by the impact of other sand particles. Further, we dynamically demonstrate the process of sand collision with a sand bed, and we perform statistical analysis and compare our simulation results with previously reported results. The SPH method is a kind of meshless particle method, and it uses a discrete calculation domain to represent a series of random distributions of particles. In the study, the weighted average of neighbouring particles is used to solve integral equations under different boundary conditions or partial differential equations. There is no need for grid connections between the particles, and the approach avoids dealing with large deformation problems and the complexities of generating grids with complicated shapes and areas. This method provides several advantages (Liu & Liu 2003); it is highly suitable for addressing large deformation, the calculation area can be divided into discrete partitions, and sand movement can be dictated by control equations.

II. MATHEMATICAL MODEL

A. Control equations of atmospheric boundary layer flow

The flow of wind forms the root cause of all wind-blown sand activities. Wind-blown sand flow is due to air which causes sand to move near the ground surface, and this type of movement can be represented by a gas–solid two-phase flow. The wind-blown sand flow can be treated as an incompressible Newtonian fluid (Zheng 2009). Because changes in the longitudinal velocity of the wind field on the earth's surface are negligible, in this study, the atmospheric boundary layer is simply considered as a two-dimensional space. The atmospheric boundary layer flow can be completely described by the wind's density ρ , humidity q , temperature T , concentration of sand in the wind c , velocity field, and pressure field values over time. The control equation includes the

equations of motion, state equations, and continuity equations. For convenience, we use the Boussinesq assumptions to simplify the control equation (Bagnold 1941). We consider the following equations:

1) Continuity equation used to describe the conservation of mass, given by:

$$\frac{\partial \rho}{\partial t} = -\rho \frac{\partial u^\beta}{\partial x^\beta}. \quad (1)$$

Here, u^β denotes the fluid velocity of the β -direction component and ρ denotes the density.

2) The equations of motion can be represented as:

$$\frac{\partial u^\alpha}{\partial t} + u^\alpha \frac{\partial u^\alpha}{\partial x^\alpha} = -\frac{1}{\rho} \frac{\partial p}{\partial x^\alpha} + v \frac{\partial^2 u^\alpha}{\partial (x^\alpha)^2}. \quad (2)$$

Here, $v = u / \rho$ denotes the dynamic viscosity ratio, and for atmospheric boundary layer flow, its value can be taken to be approximately $1.5 \times 10^{-5} \text{ m}^2 / \text{s}$. The term P denotes the pressure, ρ the gas density, and u the air velocity.

3) The state equation of the air phase, which is represented by the pressure, temperature, and density, and their relationship, is given by:

$$p = \rho R_a T. \quad (3)$$

Here, R_a denotes the molar gas constant, and for dry gas, this value is $R_a = 287 \text{ J/(kg} \cdot \text{K)}$.

The pressure on the sand particles can be considered as the sum of the pressures generated by the kinetic energy and the collision:

$$\begin{aligned} p_s &= p_s^k + p_s^I \\ p_s^k &= \rho_s T_s \\ p_s^I &= 2\rho g (1+e) T_s \end{aligned} \quad (4)$$

Here, T_s denotes the virtual temperature of sand, representing the fluctuation intensity of the sand phase, and e denotes the coefficient of restitution for sand.

B. SPH discretization of control equations

Here, we consider the SPH discretization of the control equations as follows:

1) The continuous density method is applied to obtain the transformed continuity equation:

$$\frac{d\rho_i}{dt} = \rho_i \sum_{j=1}^N \frac{m_j}{\rho_j} u_{ij}^\beta \bullet \frac{\partial W_{ij}}{\partial x_i^\beta} \quad (5)$$

Here $u_{ij} = u_i - u_j$, $\frac{\partial W_{ij}}{\partial x_i} = \frac{x_i - x_j}{r_{ij}} \frac{\partial W_{ij}}{\partial r_{ij}}$, and r_{ij} denotes the distance between particle i and particle j . m_j denotes the mass of particle j . W_{ij} denotes the kernel function.

In the formula considering the relative velocity of particles in the support domain, the antisymmetric relative velocity can effectively reduce the error produced by the discontinuity of the particles. This formula is suitable for processing large density flows, and it is particularly suitable for numerical calculations of the two-phase flow of wind-blown sand.

2) Momentum equation: Eq. (2) is transformed as below via the SPH particle approximation method.

$$\begin{aligned} \frac{du_i^\alpha}{dt} &= -\sum_{j=1}^N m_j \left(\frac{p_i + p_j}{\rho_i \rho_j} \right) \frac{\partial W_{ij}}{\partial x_i^\alpha} \\ &\quad + v \sum_{j=1}^N \frac{m_j}{\rho_j} (u_i^\beta + u_j^\beta) \frac{\partial^2 W_{ij}}{\partial x_i^{\beta^2}} \end{aligned} \quad (6)$$

III. NUMERICAL SIMULATION METHOD AND SIMULATION CONDITIONS

In numerical simulations, we assume that the sand grains consist of homogeneous rigid discs, the collision point is the contact point between two grains of sand, and that collision occurs along the centre-of-mass plane. Further, the collision force between sand grains is mainly considered to be the instantaneous impact force, and it can change the momentum and energy of sand. We ignore other external forces.

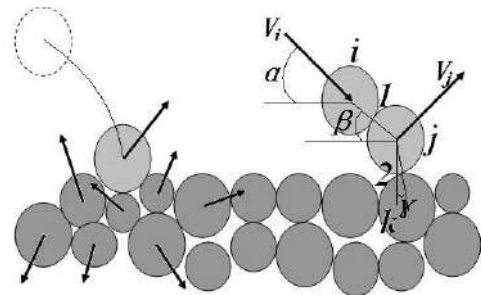


Figure 1. Collision of sand particles with those in sand bed.

In Fig. 1, sand particles i , j , and k impact the sand in a successive manner. Particle i represents a descending particle via saltation, j represents a particle creeping in the sand bed, and k denotes a stochastic (random) sand particle in the bed. We assume that i impacts j at velocity v_i at a horizontal angle α , and particle j at velocity v_j impacts the static sand particle k in the bed. The collision points are identified as 1 and 2 in the figure. The angle of collision between i and j is equal to β (measured between the centre-of-mass plane of particles i and j)

and the horizontal), and the collision angle between particles j and k is given by γ (measured between the centre-of-mass plane of particles j and k and the vertical direction).

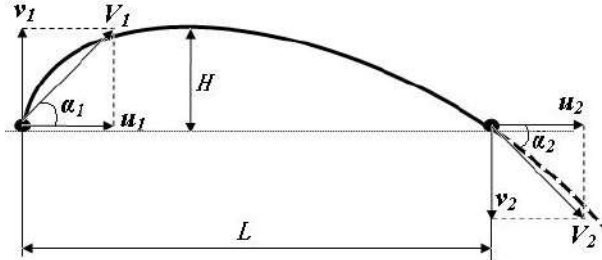


Figure 2. Parameters used to describe the process of collision.

Fig. 2 shows the lift-off trajectory of sand particles from the bed. The parameters u and v denote the horizontal and vertical velocities, respectively, of a given sand particle, α denotes the representative angle, the subscript 1 indicates parameter values when the sand particle is in lift-off, and the subscript 2 indicates parameter values when the sand particle is falling back to the bed surface. Subsequent to falling back on the bed surface, the sand particle will impact other sand particles in the bed surface, and therefore, we also consider the secondary impact velocity and impact angle; we denote these as the rebound velocity and rebound angle after collision. If particle impact on the bed surface causes other sand particles to lift off, then the corresponding velocity and angle of the subsequently rising sand particles are denoted as the sputtering velocity and sputtering angle, respectively.

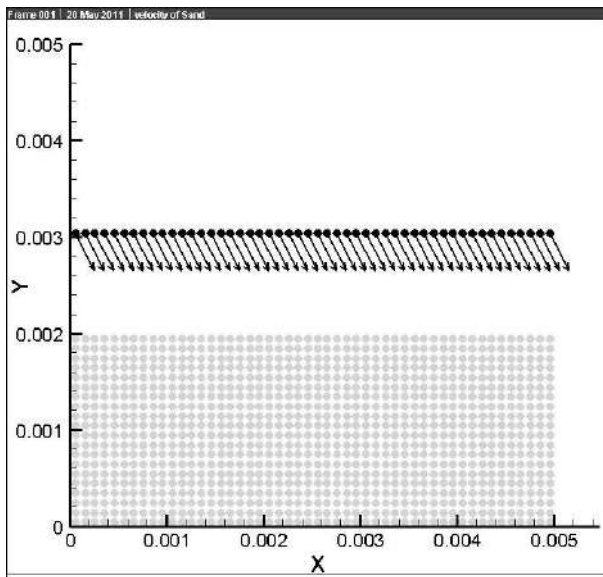


Figure 3. Initial distribution of sand particles before collision.

The process of sand particles impacting the bed and causing other sand particles to lift off ('splashing') is one of the primary mechanisms of wind-blown sand transport. When particles transported by saltation fall back onto the bed surface, they impact other sand particles, causing the primary particles

to rebound while the bed particles undergo 'sputtering'. This cycle describes the complete process of sand movement. Natural sand beds usually consist of particles with different sizes and shapes, and impacting sand particles also have varied shapes and sizes. Thus, an accurate and complete simulation of the transport process from particles lifting off via saltation and impacting back down on the bed surface to cause other sand particles to lift off by splashing is nearly impossible. Here, we consider an example of the simulation process of sand movement after collision for different incident angles and incidence rates, and we analyse the process. In this example, we initially set the incident angle and velocity of particles transported by saltation.

The simulation procedure is described below.

1) Calculation of regional settings: In fig. 3, the incident sand layer is represented by solid black circles. The size of the incident sand particles is set to 0.25 mm. The grey circles indicate sand particles on the sand bed. The particle sizes in the bed range between 0.1 mm and 0.25 mm. The grey circles indicate sand particles on the sand bed. The particle sizes in the bed range between 0.1 mm and 0.25 mm. The initial distance between the incident sand layer and the bed surface is around 10 layers of sand.

2) Boundary conditions and initial conditions: The geometric boundary conditions are derived using periodic boundary conditions. The initial velocity of particles in the bed surface is zero, and the air velocity is described by the wind-speed logarithmic profile. The velocity and direction of the incident sand particles are listed in table 1.

3) Simulation results and analysis: Fig. 4 shows the dynamic process of sand particles impacting the bed surface. In fig. 4(a), we note that as the incident sand layer descends to impact the bed, the top layers of sand on the bed are also in motion under the effect of air flow. These upper layers of sand do not experience lift-off; they are considered to exist in a quasi-dynamic state caused by the slightly undulating terrain surface of the sand bed. Consequently, we note that the incident sand does not impact stationary particles on the bed.

Most of the incoming sand particles collide with the top-layer sand of the bed at step number 4500, as shown in fig. 4(b) (the open circles indicate particles in the bed while the solid circles indicate incident sand). However, a small portion of the incident sand does not reach the sand bed in the process of downward movement because the local change in the airflow field causes these particles to change velocity and direction.

Most of the incident sand particles impact the sand particles on the top of bed and then rebound. Some incident sand particles do not exhibit any movement after reaching the sand bed. Some of the particles in the bed lift-off via splashing due to incident particles, and these particles exhibit large velocities. The 'splashing height' can also increase the rebound height of the incident sand. The rebounding particles fall back to the bed after the collision and again impact with the top layers of the sand bed fall back to the bed after impact.

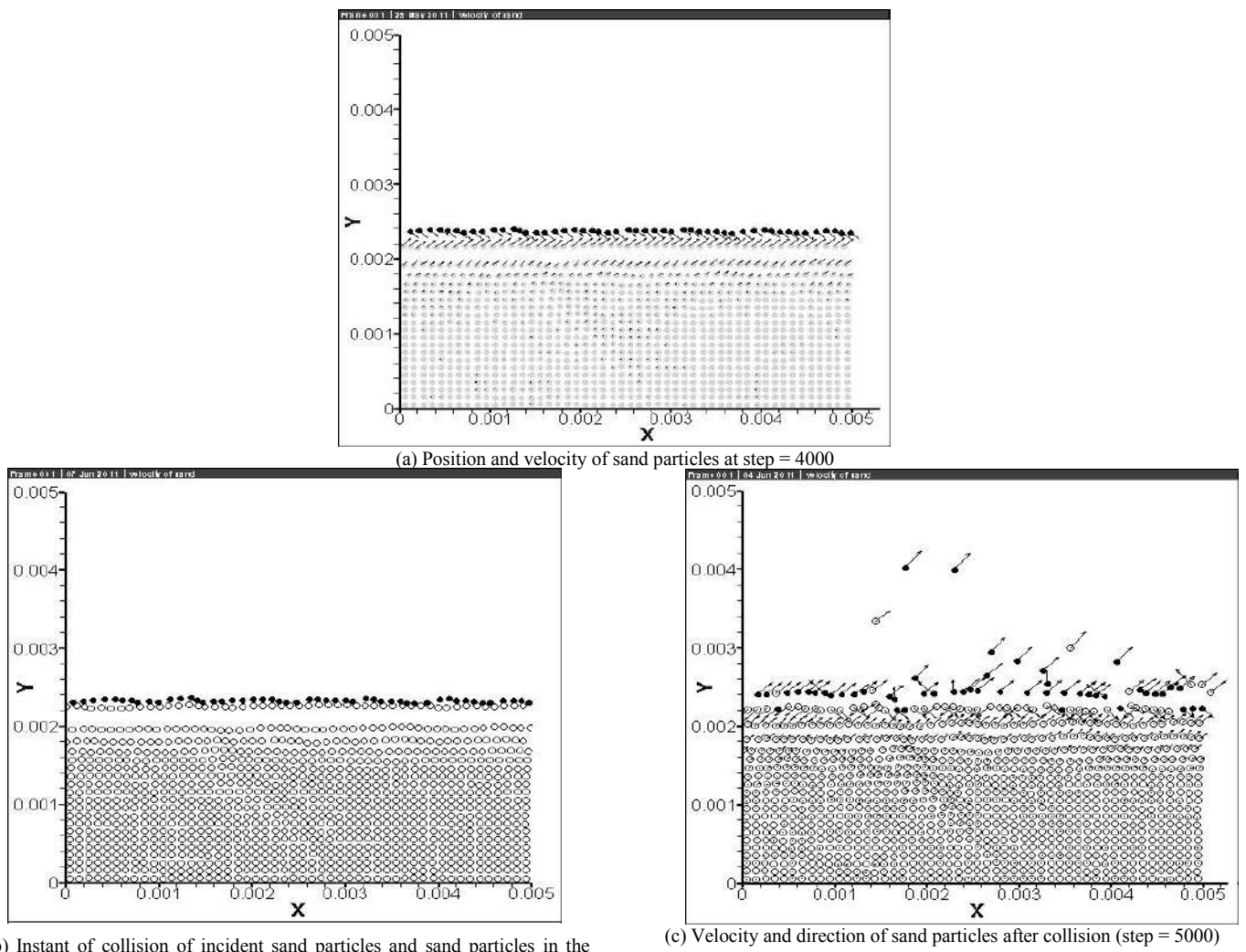


Figure 4. Dynamic process of sand impacting bed surface

IV. RESULTS AND DISCUSSION

From fig. 4, we observe that the most of the incident sand particles rebound after collision with sand in the bed surface. The rebound angle and velocity are closely related to the collision angle and velocity of the incident sand particles. Table 1 lists the chosen initial velocities and angles of the incident sand particles. The rebound velocity and angle of the incident sand particles are compared with the corresponding results of previous studies. We note that the rebound angles obtained in our study are similar to previous results. From the results, we note that the velocity and direction of incident sand particles exhibit a large change after collision. The rebound velocity is obviously less than the incident velocity before collision because collisions make the particles lose energy.

We have previously noted that sand on the bed splashes because of incident sand particles impacting the bed. Table 2 lists the sputtering velocity of the splashing sand obtained for various studies including our study. From the table, we note that the calculation results of our study exhibit noticeably larger values. The incident angle largely influences the

sputtering velocity. In fact, the chosen incident angle in this study is identical to the falling angle of saltation sand. From figure 2, we note that saltation sand particles with smaller incident angles are more likely to impact the bed. Rice et al. (1995) have reported that the incident angle negligibly affects the sputtering parameters; this result contradicts the results obtained in our study. Our results indicate that both the incident angle and velocity significantly affect sputtering. Thus, the effect of the incident angle parameters on sputtering cannot be neglected.

Table 3 lists the sputtering angles of the splashing sand for various studies including this one. Our results exhibit a larger range because some simulation trajectories were obviously not parabolic; a few sand particles lifted off nearly perpendicular to the bed surface. Some sand particles also lifted off with small sputtering angles because the sputtering velocity was small compared to the incident particle velocity.

TABLE I. COMPARISON OF INCIDENT VELOCITIES, INCIDENT ANGLES, REBOUND VELOCITIES, AND REBOUND ANGLE BETWEEN OUR STUDY AND PREVIOUS STUDIES

Study	Incident sand particle size (mm)	Incident velocity (m/s)	Incident angle (°)	Rebound velocity (m/s)	Rebound angle (°)	Rebound/incident (velocity)
Rice et al. 1995	0.425-0.6	2.73	13.94	1.58	20.95	0.58
		1.70	14.75	1.50	23.03	0.56
		2.71	14.73	1.52	22.55	0.56
		2.80	15.04	1.59	25.63	0.58
		3.16	11.82	1.77	29.95	0.57
	0.3-0.355	3.36	11.47	1.81	30.331	0.54
		3.36	11.53	1.96	31.06	0.59
		3.30	11.36	1.88	29.58	0.58
		3.85	10.85	1.99	44.63	0.52
		0.15-0.25	3.78	10.24	2.13	0.58
Anderson & Haff 1991	0.32 (same size)	3.74	10.45	2.16	37.85	0.58
		1-8	8	0.5-4.4	40-45	
Li 2007	0.32 (mix size)	1-8	11.5	0.6-4.9	42-48	
		2.24	8	0.6-5.0	47	0.6-0.65
Our study	0.25	1.41	45	0.8-1.1	26-49	0.6-0.8
		2.07	15	1.2-1.7		

TABLE II. COMPARISON OF SPUTTERING VELOCITIES BETWEEN VARIOUS STUDIES

Study	Incident sand particle size (mm)	Sputtering velocity (m/s)				Sputtering/incident (velocity)
		0.425-0.6	0.3-0.355	0.15-0.25	all	
Rice et al. 1995	0.425-0.6	0.2134	0.2537	0.2335	0.243	0.09
		0.2574	0.2402	0.2418	0.2422	0.09
		0.2381	0.2548	0.2521	0.2522	0.09
		0.2708	0.2878	0.2398	0.2637	0.09
		0.2253	0.2839	0.2268	0.2544	0.08
	0.3-0.355	0.2051	0.2686	0.2416	0.2520	0.08
		0.2584	0.2716	0.2506	0.2607	0.08
		0.2730	0.3117	0.2848	0.2950	0.09
		0.2011	0.2669	0.2914	0.2757	0.07
		0.1736	0.2299	0.2946	0.2566	0.07
Anderson & Haff 1991	0.32 (same size)	0.1956	0.2905	0.2736	0.2773	0.07
		Incident angle	8 11.5	Incident velocity	1-8	0.27-0.47
Li 2007	0.32 (mix size)	Incident angle	8 11.5	Incident velocity	<3 ≥3	0.18-0.26 0.26-0.38
		30	8 11.5	2.24 Incident velocity	0.35-0.43 0.46-0.52	0.1-0.2 0.05-0.1
Our study	0.25	45	30 45 15	1.41 2.07	0.28-0.36	0.17-0.3

TABLE III. COMPARISON OF SPUTTERING ANGLES BETWEEN VARIOUS STUDIES

Study	Incident sand particle size (mm)	Sputtering angle (°)			
		0.425-0.6	0.3-0.355	0.15-0.25	all
Rice et al. 1995	0.425-0.6	48.32	50.39	50.58	50.36
		44.76	51.83	47.36	49.27
		46.86	54.37	54.31	53.77
		37.41	48.82	51.49	49.34
		47.75	54.05	66.41	59.03
	0.3-0.355	52.89	52.74	54.35	53.57
		36.31	59.09	62.09	59.47
		47.40	52.56	53.02	52.50
		32.28	56.14	60.07	56.57
		41.21	55.07	56.13	54.58
Our study	0.15-0.25	42.88	55.47	55.73	55.00

Anderson & Haff 1991	0.32 (same size)	Incident velocity	1-8	Incident angle	8 11.5	67-76
Li 2007	0.32 (mix size)	Incident velocity	1-8	Incident angle	8 11.5	63-69 mean=66
Our study	0.25	Incident velocity	2.24 1.41 2.07	Incident angle	30 45 15	35-89

V. CONCLUSION

The impact of sand particles on a sand bed is a very important and commonly studied phenomenon in the two-phase flow of wind-blown sand. The accurate simulation of the collision of sand particles is the key to refining and developing the theory of the two-phase flow of wind-blown sand. In previous studies, models for the collision of sand required the calculation of the collision probability (Rice et al. 1996). The SPH method used in this study provides unique advantages in terms of modelling sand collision; there is no need to calculate the collision probability. The smoothed length can be directly set to determine the collision effect between two sand particles. Further, this method is simple and convenient. The simulation results of the microscopic process of sand particle–sand bed collision is more detailed and accurate. This more accurate simulation method can further aid in the microscopic study of wind-blown sand flow. Simulation results show that the collision of sand particles plays a very important role in the lift-off of sand particles. Further, the collision dictates the entire process of wind-blown sand flow. Collision between an incident particle and stationary particles can cause the movement of one or more particles which are considerably heavier than the incident particle. This shows that the fluid lift-off and impact lift-off of sand particles are complementary processes. Fluid lift-off causes the sand to change its initial static state into that of motion. Impact lift-off conditions are formed only after the occurrence of fluid lift-off. Therefore, the mechanism underlying impact lift-off is hypothesized to be fluid lift-off. In conclusion, from our simulation results, we note that the SPH method is very suitable for solving the problem of sand-particle collision under conditions of wind-blown sand flow. We believe that this method can significantly contribute to the development of the physics of sandstorms.

ACKNOWLEDGEMENT

The authors wish to acknowledge the support of the China Natural Science Foundation (No. 11102178)

REFERENCES

- [1] ANDERSON, R. S. & HAFF, P. K. 1991 Wind modification and bed response during saltation of sand in air. *Acta Mechanica* (suppl.) 1, 21-52.
- [2] BAGNOLD R. A. 1941 The Physics of Blown Sand and Desert Dunes [M]. London, Methuen & Co. Ltd.
- [3] DING, G.D. 2008 Status and prospect of study on two focuses in Aeolian physics. *Journal of Desert Research* 28(3), 395 - 398 (in Chinese).
- [4] KANG, L.Q. & LIU, D. Y. 2010 Numerical Investigation of Particle Velocity Distributions in Aeolian Sand Transport [J]. *Geomorphology* 115, 156-171.
- [5] LI, W.Q. 2007 Numerical simulation of stochastic collision between grain and bed in Aeolian sand saltation [D]. Lanzhou: PhD dissertation, Lanzhou University (in Chinese).
- [6] LIU, G. R. & LIU, M. B. 2003 Smoothed Particle Hydrodynamics: A Meshfree Particle Method [M]. Singapore: World Scientific. pp. 25-34 (in Chinese).
- [7] RICE, M. A., WILLETTS, B. B. & MCEWAN, I. K. 1995 An experimental study of multiple grain-size ejecta produced by collisions of saltating grains with a flat bed [J]. *Sedimentology* 42, 695-706.
- [8] RICE, M. A., WILLETTS, B. B. & MCEWAN, I. K. 1996 Observations of collisions of saltating grains with a granular bed from high-speed cine-film. *Sedimentology* 43, 21-31.
- [9] SHI, F. & HUANG, N. 2012 Measurement and simulation of sand saltation movement under fluctuating wind in a natural field environment. *Physica A* 391, 474-484.
- [10] ZHENG, X. 2009 Mechanics of wind-blown sand movement [M]. New York: Verlag Berlin Heidelberg, pp. 205-219.

Multiphase Godunov-typed Smoothed Particle Hydrodynamics Method with Approximate Riemann Solvers

Z.W.Cai

Department of Offshore Structures
China Ship Scientific Research Center
Wuxi, China
caizhiwen0904@163.com

Z. Zong^a, L. Zhou^a, Z. Chen^b, C.Tiao^c

^aSchool of Naval Architecture
Dalian University of Technology
Dalian, China

^bDepartment of Mechanical Engineering
National University of Singapore
Singapore, Singapore

^cChina Ship Scientific Research Center
Department of Offshore Structures
Wuxi, China

Abstract—In this paper, we propose a Multiphase Godunov-typed Smoothed Particle Hydrodynamics (MGSPH) method for simulating multi-fluid Riemann problems. In this method, different EOSs are applied on different materials; and interfacial approximate Riemann solvers are introduced on the interfacial particle pairs to deal with the transition between different EOSs. Various combinations of five kinds of single-phase approximate Riemann solvers (LLXF, ROE, HLLE, HLLC, DUCO) and three types of interface approximation Riemann solvers (ROE, LRS, RRS) are comparatively studied in three numerical tests. It turns out that LLXF and HLLE give worse results than other approximate Riemann solvers; and pressure instabilities are observed when applying RRS on interfacial particle pairs. In general, the combinations of DUCO+ROE and DUCO+LRS may be the suitable choices for MGSPH in simulating multiphase Riemann problems. (*Abstract*)

I. Introduction

Multiphase Riemann problems are widely observed in engineering and natural, such as the shock tube problems and underwater explosion problems[1]. The Riemann problem is defined as the Initial Value Problems (IVP) with discontinuous initial conditions for Euler equations. And the multiphase Riemann problem

involves different materials that are described by different Equations of State (EOSs), which makes the problem more complex. Numerical simulations of multiphase Riemann problems are very challenging and attract extensive attentions [1-3].

In recent decades, various types of Godunov-typed SPH have been developed [4-8]. Which makes SPH an optional solution to the Riemann problems. On the other hand, the particles in SPH move with the fluid flows, in which way the interfaces can be naturally formed without extra tracking algorithms. Such characteristic makes SPH an ideal solution to the multiphase problems [9-15].

Although, it is still challenging to deal with multiphase Riemann problems. The reason is that different fluids may have distinct physical characteristics; due to which different EOSs are need. To tackle this problem, in this paper we present a multiphase Godunov-typed SPH (MGSPH) method which combines the single-phase approximate Riemann solver and the interfacial approximate Riemann solver and incorporates multiple equations of states. In MGSPH, the Godunov-typed SPH (GSPH) proposed by Sirothian and Yoh [4] is applied globally to solve the governing equations with distinct EOSs used for particles belonging to different fluids. The intermediate pressure and velocity involved in GSPH calculations

are evaluated either by single-phase approximate Riemann solver if two particles in the pair belong to the same fluid, or by interfacial approximate Riemann solver when two particles in the pair are in different fluids. Specifically, various combinations of five kinds of single-phase approximate Riemann solvers (LLXF, ROE, HLLE, HLLC and DUCO) and three types of interfacial approximate Riemann solvers (ROE, LRS and RRS) [16, 17] are compared comprehensively in five numerical examples.

Three examples, including gas-water shock tube, underwater explosion and 2D radially symmetric problems, are presented for the comparative study of various combinations of single-phase and interfacial approximate Riemann solvers.

II. Godunov-typed SPH model

A. Godunov-typed SPH model

As its name says, SPH is a smoothing method. When dealing with Riemann problems, all discontinuities are smoothed by SPH. Therefore, special treatment is necessary to obtain sharp and accurate solutions. Godunov-typed SPH (GSPH) model is one of the most popular models in recent years. And in our work, the GSPH model developed by Sirothi and Yoh[4] is adopted as the global flow solver. Specifically, the density summation method is applied to update the density; and by enforcing the principle “one particle’s loss is another cell’s gain”, the momentum and the energy equation can be further simplified. In general, the discretized governing equations of the present GSPH model can be written as:

$$\rho_a = \sum_b m_b \cdot W_{ab} \quad (1)$$

$$\frac{dv_a}{dt} = -2 \sum_b m_b \frac{P^*}{\rho_a \rho_b} \nabla_a W(r_{ab}, h_{ab}) \quad (2)$$

$$\frac{dE_a}{dt} = 2 \sum_b m_b \frac{P^* u^*}{\rho_a \rho_b} \cdot \mathbf{e}_{ab} \cdot \nabla_a W(r_{ab}, h_{ab}) \quad (3)$$

where P^* and u^* are the intermediate pressure and velocity of Riemann solvers or approximate Riemann solvers, respectively. And $\mathbf{e}_{ab} = \mathbf{r}_{ab}/|\mathbf{r}_{ab}|$ represents

the unit vector.

B. Multiphase Godunov-typed SPH (MGSPH) method with approximate Riemann solvers

Multiphase Riemann problem is a very challenging academic topic. In this kind of problem, discontinuities of fluid properties as well as physical characteristic (equation of state) need to be considered. In this section, we propose a novel multiphase Godunov-typed SPH (MGSPH) method with approximate Riemann solvers to simulate multi-fluid Riemann problems with multiple equations of states.

In MGSPH, regular formulations in GSPH, i.e. Eqs.(1)-(3), is applied as the global flow solver. As mentioned in the previous section, the intermediate pressure and velocity involved in GSPH calculations need to be evaluated by Riemann solvers. However, obtaining exact Riemann solver is tedious, time-consuming and even mathematically impractical. Therefore, approximate Riemann solvers gradually become preferable due to its simplicity and explicitness [6]. Another issue is that typical single-phase approximate Riemann solvers require single equation of state; therefore directly applying them into the multiphase problems may lead to numerical instability on phase interfaces. Inspired by Fechter et al’s[16] work which adopted interfacial approximate Riemann solvers to deal with the discontinuities of the EOSs in multiphase problems, we offer the following criteria in determining the intermediate pressure and velocity in MGSPH, as shown in Figure 1. Assume particle a and particle b are the two particles under consideration

1) If a and b belong to the same fluid, single-phase approximate Riemann solver is implemented to calculate the intermediate pressure and velocity.

2) If a and b belong to different fluids, interfacial approximate Riemann solver is adopted to determine the intermediate pressure and velocity.

In this paper, five approximate Riemann solvers are introduced: a) The local Lax–Friedrichs Riemann solver(LLXF); b) Roe’s approximate Riemann solver(ROE); c) Harten, Lax, van Leer and Einfeldt

approximate Riemann solver (HLLE); d) Harten, Lax and van Leer scheme with contact (HLLC); e) Ducowicz approximate Riemann solver (DUCO). These approximate Riemann had been incorporated into GSPH by Puri et al. [6] in numerical simulations of single-phase Riemann problems.

Meanwhile, three types of interface approximation Riemann solvers including ROE and the solvers presented by Fechter et. al. [16] (Linearized wave curves (LRS) and Relaxation approach (RRS)).

Comprehensive comparisons will be conducted on various combinations of five types of single-phase approximate Riemann solvers and three kinds of interfacial approximate Riemann solvers.

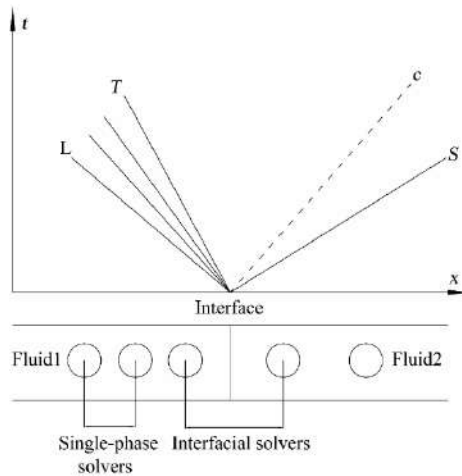


Figure 1 Illustration of MGSPH

III. Numerical results

In this section, three numerical tests of multiphase Riemann problems, including gas-water shock tube, underwater explosion and 2D radially symmetric problems, are presented. Various combinations of the five single-phase approximate Riemann solvers and three interface approximate Riemann solvers are comparatively studied through these three examples. Through these tests, comprehensive validations of our multiphase Godunov-typed SPH (MGSPH) method are conducted, which considers the following situations

- a) Multiphase flow with EOSs in the same form but with different parameters.
- b) Multiphase flow with different EOSs.

A. Gas-water shock tube

The first test is the gas-water shock tube, This problem is quite challenging since the EOSs of air and water are drastically different[18]:

$$P = (\gamma - 1)\rho e - \gamma P_c \quad (4)$$

The parameters are presented in Table 1. Initial conditions of this problem are given as:

$$(\rho, u, P)$$

$$= \begin{cases} (1.271, 0, 9.119252 \times 10^9), & 0 \leq x < 50 \text{ (air)} \\ (0.999983, 0, 1.01325 \times 10^6), & 50 \leq x < 100 \text{ (water)} \end{cases} \quad (5)$$

With initial particle spacing of 0.08 and 0.1 for the air and the water phases, respectively.

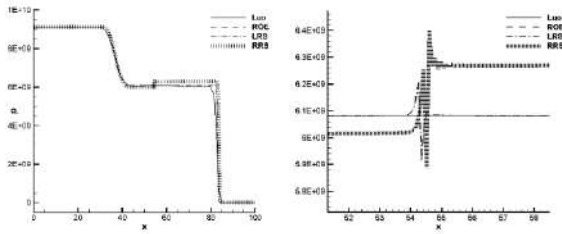
Figure 2 shows the results obtained by all combinations of the approximate Riemann solvers discussed in this paper. The results are compared with the data reported by Luo et al. [18] who adopted the second-order Godunov scheme. Broken features are observed in the pressure curves of all combinations, with the cases with LLXF+RRS and HLLE+RRS suffering the most. The reason is that when applying RRS on the interfacial particle pairs, relaxed pressure, instead of the physical pressure, is substituted into the interface conditions, in which process certain errors are introduced. In cases obtained by the single-phase solvers of ROE, HLLC and DUCO, to different extents, density oscillations are found in the density distribution contours; and it is noted that the oscillations in cases with DUCO are relatively smaller.

In summary, among all single-phase approximate Riemann solvers, the DUCO solver maintains the best sharpness and consistency with various interface approximate Riemann solvers. And due to the error introduced by the relaxed pressure, RRS performs worse than the other two interface approximate Riemann solvers (ROE and LRS).

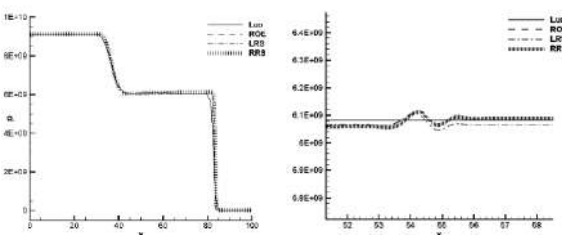
Table 1 The parameters of gas-water shock tube problem

Fluid	Parameters in EOS
Gas	$\gamma = 1.4, P_c = 0$
Water	$\gamma = 7, P_c = 3.03975E + 9$

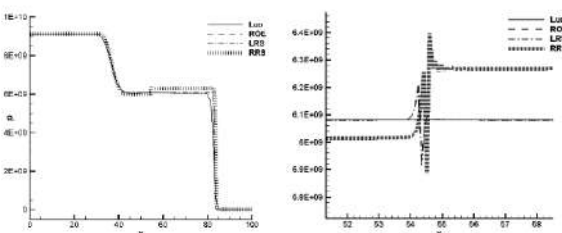
LLXF:



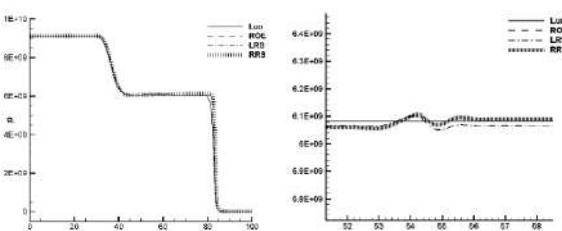
ROE:



HLLE:



HLLC:



DUKO:

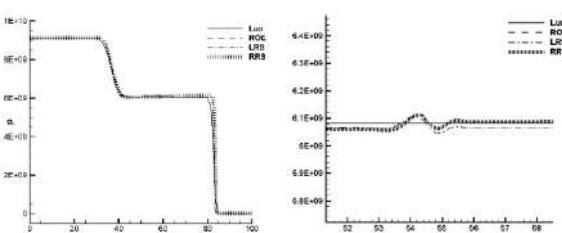


Figure 2 Gas-water shock tube problem. The solutions of $t=0.000156$. Left: pressure; right: broken features

B. Underwater explosion

In this section, a more difficult test of one-dimensional underwater explosion is presented, in which two materials are governed by different forms of equations of state. This problem was initially proposed in [19], and has been numerically studied using other mesh-based methods[20, 21]. The initial condition adopted is:

$$(\rho, u, P, e)$$

$$= \begin{cases} (1.63, 0, 7.81 \times 10^{10}, 4.2814 \times 10^{10}), & 0 \leq x < 200 \text{ (gas)} \\ (1.0, 0, 1 \times 10^6, \text{N/A}), & 200 \leq x < 400 \text{ (water)} \end{cases}$$

Different EOSs are used to describe distinguished physical characteristics of gas and water. Specifically, the EOS for the gas is the following JWL equation:

$$\begin{aligned} P = A & \left(1 - \frac{\omega \rho}{R_1 \rho_0} \right) e^{-\frac{R_1 \rho_0}{\rho}} \\ & + B \left(1 - \frac{\omega \rho}{R_2 \rho_0} \right) e^{-\frac{R_2 \rho_0}{\rho}} \quad (7) \\ & + \omega \rho e \end{aligned}$$

And Tait's EOS is used for water:

$$P = B \left[\left(\frac{\rho}{\rho_0} \right)^Y - 1 \right] + A \quad (8)$$

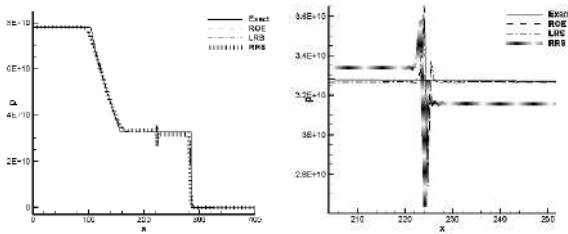
All parameters involved in EOSs are tabulated in Table 2. The initial particle spacing of the left state is $1/1.63$, while the initial spacing of the right state is 1.

Our numerical results are presented in Figure 3. Similar to the gas-water shock tube problem, broken features are observed in the pressure curves, with the cases of LLXF+RRS and HLLE+RRS suffering the most. Generally speaking, cases with the single phase solvers of ROE, HLLC and DUCO and interface solvers of ROE and LRS give similar and appealing results in this problem.

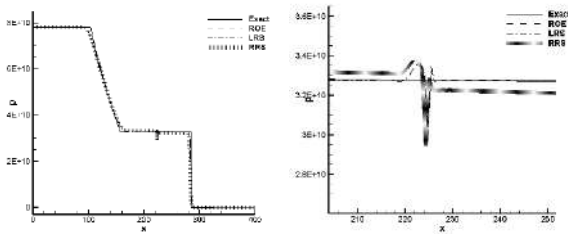
Table 2 Parameters of JWL EOS and Tait's EOS [19]

JWL	A	B	R_1	R_2	ω	ρ_0
	5.484E+12	0.09375E+12	4.94	1.21	0.28	1.63
Tait	A	B			γ	
	1.E+6	3.31E+9			7.15	

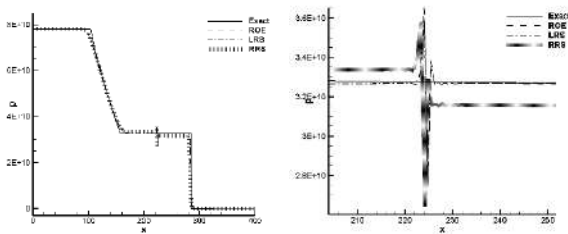
LLXF:



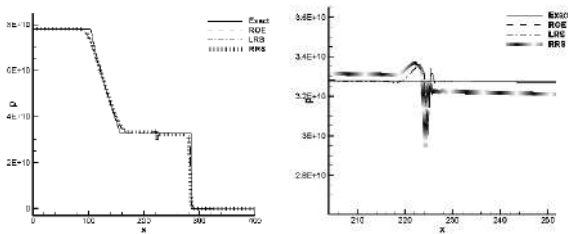
ROE:



HLLE:



HLLC:



DUKO:

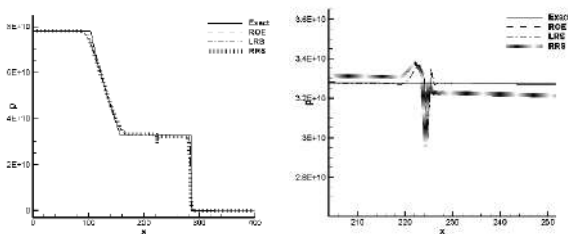


Figure 3 Underwater explosion problem. The solutions of $t=0.00025$. Left: pressure; right: broken features

C. 2D radially symmetric problem

Finally, a typical 2D radially symmetric problem[22, 23]is studied to evaluate the performance of the present method in two-dimensional simulations. The physical configuration of this problem is the underwater explosion initiated by a high pressure air bubble inside the water. In numerical simulation, an air bubble with the initial radius of $r_0 = 0.2$ is surrounded by water in a rectangular region of $[0,1] \times [0,1]$, with uniform initial particle spacing of 0.0025. The initial conditions of this case are:

$$(\rho, u, v, P)$$

$$= \begin{cases} (1.241, 0, 0, 2.753), & (x - 0.5)^2 + (y - 0.5)^2 \leq 0.04 \text{ (bubble)} \\ (0.991, 0, 0, 3.059 \times 10^{-4}), & \text{rest (water)} \end{cases}$$

The EOS is the same with Eq. (5), and the parameters are presented in Table 3.

Pressure contours obtained by different combinations of solvers are given in Figure 6. As can be seen, the symmetry of the profiles are well maintained, which indicates the good accuracy of the present method. In addition, flow details, e.g., the outgoing circular shock wave and the rarefaction wave propagating towards the center, are well captured. The remaining parts of the pressure fields are generally smooth. Such phenomenon indicates the nice ability of the present method in both retaining the sharpness of the solution and maintaining the stability of computation. However, broken features are so severe in observed occasionally, e.g., in the cases of LLXF+RRS and HLLE+RRS.

For the purpose of quantitative comparison, the distributions of density and pressure along the centerline of $y=0.5$ are depicted in Figure 5 and compared with those obtained by Leveque and Shyue[23]. Corresponding to our observations in the pressure contours, broken features are more obvious in solutions obtained by the interface approximate solver of RRS. And density oscillations are also induced accordingly in these cases. Comparatively, solutions obtained by single-phase approximate Riemann solvers of ROE, HLLC and DUCO and interface approximate solvers of ROE and LRS are similar to each other and

perform better in numerical accuracy and stability.

Table 3 The EOSs and their parameters of 2D underwater explosion problem

Fluid	Parameters
Bubble	$\gamma = 1.4, P_c = 0$
Water	$\gamma = 5.5, P_c = 1.505$

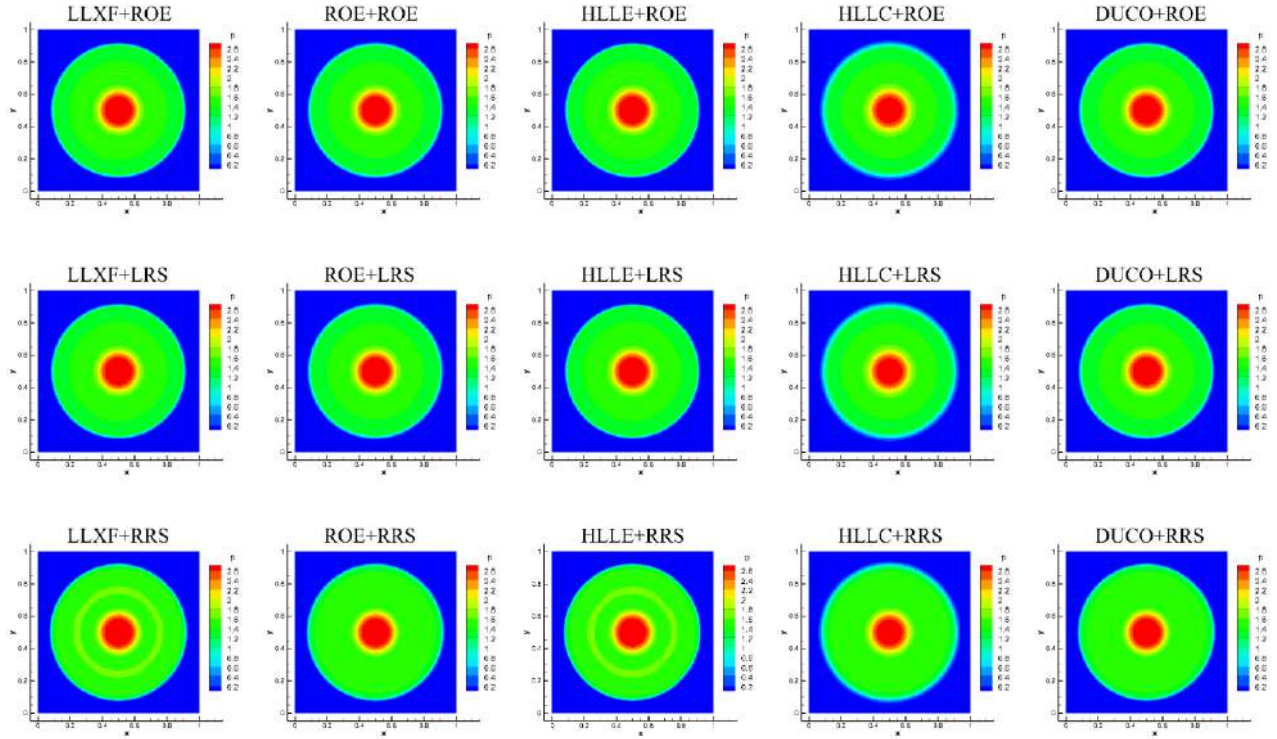
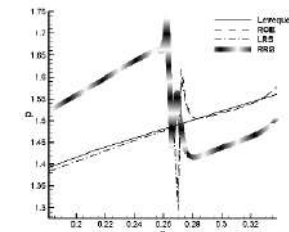
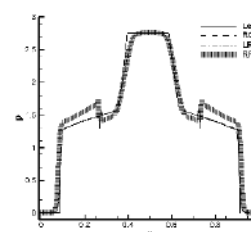
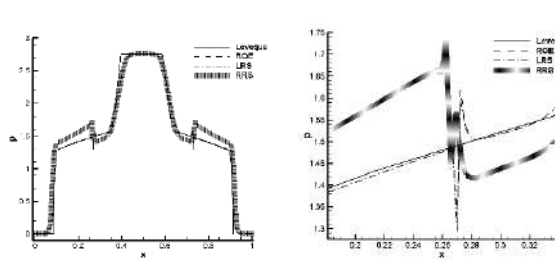


Figure 4 Pressure contours when $t = 0.058$ for radially symmetric problem

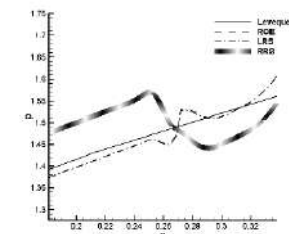
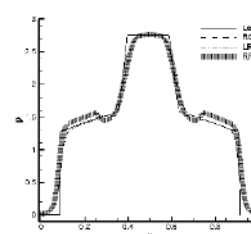
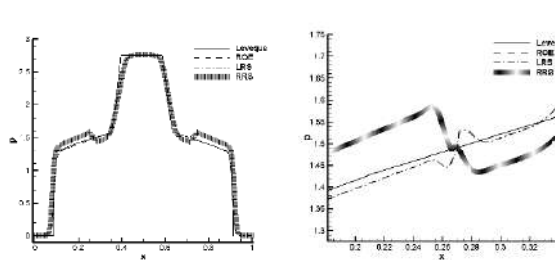
HLLE:

LLXF:



HLLC:

ROE:



DUCO:

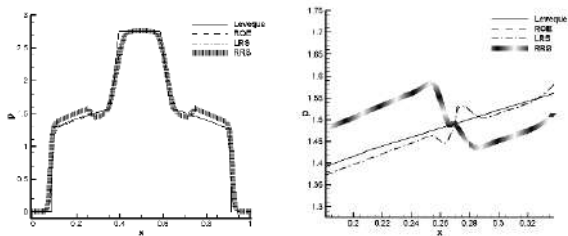


Figure 5 Radially symmetric problem. The solutions of $t=0.00025$. Left: pressure; right: broken features

IV. Conclusion

In this paper, a Multiphase Godunov-typed Smoothed Particle Hydrodynamics (MGSPH) method with approximate Riemann solvers is developed for multiphase Riemann problems with multiple Equations of States (EOSs). In this method, the Godunov-typed SPH model proposed by Sirothian and Yoh[4] acts as the global flow solver and is combined with single-phase approximate Riemann solvers and interfacial approximate Riemann solvers. Specifically, the single-phase approximate Riemann solvers are adopted when the particles in pair belong to the same fluid, while the interfacial approximate Riemann solvers are employed when the particles in pair belong to different fluids. And to describe the distinct physical characteristics of different fluids, multiple Equations of States (EOSs) can be incorporated into MGSPH computations, which makes it more general and flexible compared to either single-phase GSPH or multiphase SPH with uniform Equation of State.

To validate the proposed MGSPH method and to provide suggestions in choosing single-phase and interfacial approximation Riemann solvers, various combinations of five kinds of single-phase approximate Riemann solvers (LLXF, ROE, HLLE, HLLC, DUCO) and three kinds of interfacial approximate Riemann solvers (ROE, LRS, RRS) are incorporated into MGSPH to conduct three numerical tests: gas-water shock tube, underwater explosion and two-dimensional radially symmetric problems. It is observed in these tests that all combinations of solvers generally reproduce the analytical solution or reference data,

which validate the robustness of the theoretical foundation of the present MGSPH method. It is also noted that, due to the contact discontinuity, broken features occur in pressure distribution curves. Comparatively, among all single-phase approximate Riemann solvers, LLXF and HLLE show more severe broken features; and DUCO generally performs well in all tests and show the best consistency in single-phase test. And among all interfacial approximate Riemann solvers, much larger oscillations are found in the solutions obtained by RRS, which is due to the error introduced by using the relaxed pressure.

In summary, MGSPH is a robust solver for multiphase Riemann problems with multiple EOSs. By incorporating approximate Riemann solvers, MGSPH shows advantages in explicitness and flexibility. Through evaluating the numerical results obtained various combinations of single-phase and interfacial approximate Riemann solvers in five typical tests, it is found that the combinations of DUCO+ROE and DUCO+LRS give both accurate and stable results and are preferable choices of approximate Riemann solvers for MGSPH.

Acknowledgements

This research was supported by 973 Program (Grant No. 2013CB036101), the Nature Science Foundation of China, under Grant number 51639003 and 516779037.

References

- [1] B. Einfeldt, On Godunov-type methods for gas dynamics, *SIAM Journal on Numerical Analysis*, 25 (1988) 294-318.
- [2] I. Toumi, A. Kumbaro, H. Paillere, *Approximate Riemann solvers and flux vector splitting schemes for two-phase flow*, CEA Saclay, Direction de l'information scientifique et technique, 1999.
- [3] R. Abgrall, S. Karni, Computations of compressible multifluids, *Journal of computational physics*, 169 (2001) 594-623.
- [4] F.V. Sirotkin, J.J. Yoh, A Smoothed Particle Hydrodynamics method with approximate Riemann solvers for simulation of strong explosions, *Comput*

- Fluids*, 88 (2013) 418-429.
- [5] S. Inutsuka, Reformulation of smoothed particle hydrodynamics with Riemann solver, *Journal of Computational Physics*, 179 (2002) 238-267.
- [6] K. Puri, P. Ramachandran, Approximate Riemann solvers for the Godunov SPH (GSPH), *Journal of Computational Physics*, 270 (2014) 432-458.
- [7] A.N. Parshikov, S.A. Medin, Smoothed particle hydrodynamics using interparticle contact algorithms, *Journal of Computational Physics*, 180 (2002) 358-382.
- [8] S.H. Cha, A.P. Whitworth, Implementations and tests of Godunov-type particle hydrodynamics, *Mon Not R Astron Soc*, 340 (2003) 73-90.
- [9] X. Hu, N.A. Adams, A multi-phase SPH method for macroscopic and mesoscopic flows, *Journal of Computational Physics*, 213 (2006) 844-861.
- [10] X. Hu, N.A. Adams, An incompressible multi-phase SPH method, *Journal of Computational Physics*, 227 (2007) 264-278.
- [11] J. Monaghan, A. Rafiee, A simple SPH algorithm for multi - fluid flow with high density ratios, *International Journal for Numerical Methods in Fluids*, 71 (2013) 537-561.
- [12] Z. Chen, Z. Zong, M. Liu, L. Zou, H. Li, C. Shu, An SPH model for multiphase flows with complex interfaces and large density differences, *Journal of Computational Physics*, 283 (2014) 169-188.
- [13] A. Colagrossi, M. Landrini, Numerical simulation of interfacial flows by smoothed particle hydrodynamics, *Journal of Computational Physics*, 191 (2003) 448-475.
- [14] X. Yang, M. Liu, Numerical modeling of oil spill containment by boom using SPH, *Science China Physics, Mechanics and Astronomy*, 56 (2013) 315-321.
- [15] J.P. Vila, On particle weighted methods and SPH, *Mathematical Models & Methods in Applied Sciences*, 09 (1999) 161-209.
- [16] S. Fechter, F. Jaegle, V. Schleper, Exact and approximate Riemann solvers at phase boundaries, *Computers and Fluids Fluids*, 75 (2013) 112–126.
- [17] P.L. Roe, Approximate Riemann solvers, parameter vectors, and difference schemes, *Journal of computational physics*, 43 (1981) 357-372.
- [18] H. Luo, J.D. Baum, R. Lohner, On the computation of multi-material flows using ALE formulation, *Journal of Computational Physics*, 194 (2004) 304-328.
- [19] A.B. Wardlaw Jr, *Underwater explosion test cases*, in, DTIC Document, 1998.
- [20] R.P. Fedkiw, T. Aslam, B. Merriman, S. Osher, A non-oscillatory Eulerian approach to interfaces in multimaterial flows (the ghost fluid method), *Journal of computational physics*, 152 (1999) 457-492.
- [21] T. Liu, B. Khoo, K. Yeo, Ghost fluid method for strong shock impacting on material interface, *Journal of Computational Physics*, 190 (2003) 651-681.
- [22] K.-M. Shyue, An efficient shock-capturing algorithm for compressible multicomponent problems, *Journal of Computational Physics*, 142 (1998) 208-242.
- [23] R.J. Leveque, K.-M. Shyue, One-dimensional front tracking based on high resolution wave propagation methods, *SIAM Journal on Scientific Computing*, 16 (1995) 348-377.

SPH energy balance during the generation and propagation of gravity waves

Domenico Davide Meringolo^a, Yong Liu^a, Andrea Colagrossi^b

^a Shandong Provincial Key Laboratory of Ocean Engineering, Ocean University of China, Qingdao, 266100, China
davide.m86@gmail.com, liuyong@ouc.edu.cn.

^b CNR-INSEAN, Marine Technology Research Institute, Rome, 00128, Italy
andrea.colagrossi@cnr.it

Abstract— This work presents an energy analysis of the time behaviours of mechanical and internal fluid energies during generation and propagation of gravity waves. The analyses are performed through the δ -SPH model, which is a Smoothed Particles Hydrodynamic (SPH) variant based on a weakly-compressible fluid approximation. The solid boundary techniques adopted are: the ghost and the fixed ghost particles. A first problem in which the dynamic is generated by a water patch falling into a still water tank is analyzed. In this case, the dissipation processes due to the diffusive and viscous numerical corrections are investigated. Then, a problem of relevant interest in coastal engineering field, concerning the wave generation and propagation in a wave flume, is studied. Particular attention is given to the analysis of the energy introduced in the fluid domain as the work made by the moving solid boundary on the fluid mass. Then, a comparison of the time evolution of the energy components is presented for a wave reflecting case, characterized by a flat bottom flume with a vertical wall, and a wave absorbing case, characterized by a flume with a sloping bottom end.

I. INTRODUCTION

Recent studies have shown that the SPH method is able to accurately describe the energy conservation of the flow evolution. Specifically, a first analysis on the modelling of dissipation mechanisms has been presented by Colagrossi et al. [1] in the context of small-amplitude gravity waves. A successive extension to large-amplitude waves with wave breaking has been given by Colagrossi et al. [2], in which it is shown that in presence of a free surface, the viscous dissipation for a Newtonian liquid can be decomposed into two terms: an enstrophy component and a free-surface deformation component. In the work presented by Antuono et al. [3], the energy decomposition analysis has been extended to the so called “diffusive” formulations (see e.g., [4, 5, 6]). In the SPH framework is an established practice to add a numerical correction in the continuity equation in order to enhance the numerical stability of the method. This correction presents the form of a density diffusion process, which induces an additional numerical dissipation that has to be taken into account when performing an energy balance analysis. The extension of the energy balance in the context of solid-fluid interaction has been presented by Cercos-Pita et al.

[7] with the analysis of the power released by a moving solid body immersed into water.

In this work, we present a further study on the energy balance for the δ -SPH model. Specifically, a first problem in which the solid boundaries are fixed in time and the wave dynamic is induced by a water patch falling into a still water tank is analyzed. Successively, the analysis is applied to waves generated by a moving solid boundary. The analysis of the solid-fluid work exchange is studied following the approach presented by [7]. A test case characterized by a wave reflecting condition, obtained by a wave canal with a vertical wall positioned at the end of the flume, is studied. A second test regards a wave absorbing condition. In this case the waves propagate on an inclined beach inducing a breaking wave phenomenon which dissipates the mechanical energy of the wave group.

II. THE NUMERICAL METHOD

A. δ -SPH model

In the problems analyzed in this work, the continuity and momentum equations are discretized according with the δ -SPH formulation [6]:

$$\left\{ \begin{array}{l} \frac{D\rho_i}{Dt} = -\rho_i \sum_j (\mathbf{u}_j - \mathbf{u}_i) \cdot \nabla_i W_{ij} V_j + \delta h c_0 D_i \\ \frac{D\mathbf{u}_i}{Dt} = -\frac{1}{\rho_i} \sum_j (p_j + p_i) \nabla_i W_{ij} V_j + \mathbf{g}_i \\ \quad + \delta h c_0 \frac{\rho_0}{\rho_i} \sum_j \pi_{ij} \nabla_i W_{ij} V_j \\ \frac{D\mathbf{r}_i}{Dt} = \mathbf{u}_i, \quad p_i = c_0^2 (\rho_i - \rho_0) \end{array} \right. \quad (1)$$

In (1) the sub-indexes indicate the quantities associated with the generic i -th or j -th particles, while the symbol ∇_i denotes the gradient taken with respect to the coordinates of particle i . The term r_i represents the position vector and $r_{ij} = r_i - r_j$. The viscous term π_{ij} in (1) is given by:

$$\pi_{ij} = 2(2+n) \frac{(\mathbf{u}_j - \mathbf{u}_i) \cdot \mathbf{r}_{ji}}{|\mathbf{r}_{ij}|^2} \quad (2)$$

while α is a coefficient that is chosen in the range [0.01 – 0.05]. Differently from the Standard SPH formulation, the δ -SPH formulation presents a diffusive correction, D_i , in the continuity equation of system (1), defined as:

$$D_i = 2 \sum_j \psi_{ji} \frac{\mathbf{r}_{ji} \cdot \nabla_i W_{ij}}{|\mathbf{r}_{ji}|^2} V_j \quad (3)$$

in which:

$$\psi_{ji} = (\rho_j - \rho_i) - 0.5 \left[\langle \nabla \rho \rangle_i^L + \langle \nabla \rho \rangle_j^L \right] \cdot \mathbf{r}_{ji} \quad (4)$$

and the quantities $\langle \nabla \rho \rangle_i^L$ and $\langle \nabla \rho \rangle_j^L$ represent the renormalized density gradients, defined in [6]. Conversely to the artificial viscosity, the δ coefficient for the diffusive term presents a range of variation that is very narrow (see Antuono et al. [8]) and therefore is usually considered constant and equal to 0.1. In the numerical simulations, the solid boundaries are modelled through Ghost Particles (GP) [9] and Fixed Ghost Particles (FGP) [10] approaches.

B. Equations for the solid/fluid power exchange

In the present work, for an accurate study of the power exchange between solid and fluid particles, we follow the approach presented by [3] and [7], in which the contribution accounting for the solid/fluid interaction is isolated from that representing the fluid/fluid interaction. In this way, the actual power exchanged between solid and fluid particles can be written as the sum of three contributions $P_S = P_S^V + P_S^p + P_S^C$, in which:

$$\begin{cases} P_S^V = \alpha h c_0 \rho_0 \sum_j^{\text{solid fluid}} \sum_i V_i V_j \pi_{ij} \mathbf{u}_i \cdot \nabla_i W_{ij} \\ P_S^p = - \sum_j^{\text{solid fluid}} \sum_i V_i V_j (p_i + p_j) \mathbf{u}_i \cdot \nabla_i W_{ij} \\ P_S^C = - \sum_j^{\text{solid fluid}} \sum_i V_i V_j p_i (\mathbf{u}_j^C - \mathbf{u}_i) \cdot \nabla_i W_{ij} \end{cases} \quad (5)$$

In (5), P_S^V and P_S^p represent the power transferred from the solid to the liquid particles through viscous diffusion and pressure forces respectively, while P_S^C is the power transferred as a consequence of the compressibility of the fluid and is therefore dependent on the extended velocity field used for the calculation of the continuity equation \mathbf{u}^C (for more details see De Leffe et al. [11]).

In the case of a moving solid boundary, the power delivered from the solid particles to the fluid particles can be also written as:

$$P_{\text{solid}/\text{fluid}} = - \sum_j^{\text{solid fluid}} \sum_i V_i V_j (p_i + p_j - \alpha h c_0 \rho_0 \pi_{ij}) \nabla_i W_{ij} \cdot \mathbf{u}_{Bj} \quad (6)$$

in which \mathbf{u}_{Bj} represents the nominal velocity of the solid boundary. The nominal work presented in (6) represents the ideal work made by a moving boundary on the fluid domain, being exactly equal to zero for a fixed boundary. As presented in [7], when a fixed ghost particles approach is used, the

power exchanged between fluid and solid particles, P_S , may not be exactly equivalent to the nominal power, $P_{\text{solid}/\text{fluid}}$. Indeed, the term P_S is the result of the field values associated to the ghost particles representing the solid boundary, that may differ from the nominal velocity of the boundary \mathbf{u}_{Bj} . Comparing (5) with (6) it is possible to write the following relationship between these two components [7]:

$$P_S^V + P_S^p + P_S^C = P_{\text{solid}/\text{fluid}} + \Delta P^V + \Delta P^p + \Delta P^C, \quad (7)$$

in which:

$$\begin{cases} \Delta P^V = \alpha h c_0 \rho_0 \sum_j^{\text{solid fluid}} \sum_i V_i V_j \pi_{ij} (\mathbf{u}_i - \mathbf{u}_{Bj}) \cdot \nabla_i W_{ij} \\ \Delta P^p = - \sum_j^{\text{solid fluid}} \sum_i V_i V_j (p_i + p_j) (\mathbf{u}_i - \mathbf{u}_{Bj}) \cdot \nabla_i W_{ij} \\ \Delta P^C = \sum_j^{\text{solid fluid}} \sum_i V_i V_j p_i (\mathbf{u}_i - \mathbf{u}_j^C) \cdot \nabla_i W_{ij} \end{cases} \quad (8)$$

The power equations presented in this section can be expressed in their integral form, as the work done by the solid boundaries on the fluid mass:

$$\int_{t_0}^t P_S d\tau = W_S, \quad \int_{t_0}^t P_{\text{solid}/\text{fluid}} d\tau = W_{\text{solid}/\text{fluid}} \quad (9)$$

$$\int_{t_0}^t (\Delta P^V + \Delta P^p + \Delta P^C) d\tau = W_S - W_{\text{solid}/\text{fluid}} \quad (10)$$

in which W_S and $W_{\text{solid}/\text{fluid}}$ are the effective mechanical and nominal work done in the interval $[t_0, t]$, according with the previous definitions. A positive sign for these terms means that the body is doing work on the fluid.

C. Equations for the energy conservation

According with the second law of thermodynamics, the external power delivered by a solid boundary equals the rate of change of the total energy of the system. In integral form it is possible to write:

$$\Delta \mathcal{E}_I + \Delta \mathcal{E}_M = W_S \quad (11)$$

in which $\Delta \mathcal{E}_M = \mathcal{E}_M - \mathcal{E}_{M0}$ and $\Delta \mathcal{E}_I = \mathcal{E}_I - \mathcal{E}_{I0}$, are the variation of mechanical and internal energies in the interval $[t_0, t]$, while W_S is the work done by the solid boundaries on the fluid mass on the same time interval. The mechanical energy of the system is:

$$\mathcal{E}_M = \mathcal{E}_K + \mathcal{E}_P \quad (12)$$

In which:

$$\mathcal{E}_K = \sum_j^{\text{fluid}} \frac{1}{2} m \|\mathbf{u}_j\|^2 \quad \text{and} \quad \mathcal{E}_P = \sum_j^{\text{fluid}} m g z_j \quad (13)$$

The internal energy of the system can be also written as the sum of two components:

$$\mathcal{E}_I = \mathcal{E}_C + Q \quad (14)$$

in which \mathcal{E}_C is the compressible energy, due to the fact that the fluid is modelled as a weakly-compressible medium and is a

purely reversible term, meaning that it can be re-transferred into mechanical energy. When a linear state equation is taken into account the compressible energy is given by:

$$\varepsilon_c = \varepsilon_c(\rho_0) + c_0^2 \sum_j^{\text{fluid}} m \left[\log\left(\frac{\rho_j}{\rho_0}\right) + \frac{\rho_0}{\rho_j} - 1 \right] \quad (15)$$

in which ε_{c0} is the elastic energy of the fluid at rest conditions. In (14), Q represents instead the dissipated energy (energy transformed into heat) and is therefore an irreversible term. As analyzed by Antuono et al. [3], the dissipated energy in the δ -SPH solver can be written as the sum of two contributions:

$$Q = Q_V + Q_\delta = - \int_{t_0}^t P_V d\tau - \int_{t_0}^t P_\delta d\tau \quad (16)$$

in which P_V is the power dissipated by the viscosity:

$$P_V = \frac{\mu}{2} \sum_j^{\text{fluid}} V_j \sum_i^{\text{fluid}} V_i \pi_{ij} (\mathbf{u}_j - \mathbf{u}_i) \cdot \nabla_j W_{ij} \quad (17)$$

and P_δ is the power dissipated by the diffusive term:

$$P_\delta = \partial h C_0 \sum_j^{\text{fluid}} \frac{p_j}{\rho_j} D_j V_j \quad (18)$$

For the derivation of these formulas we address the reader to [3].

III. NUMERICAL RESULTS

In this section, the numerical results are presented for two problems. A first problem regards the wave dynamic induced by a water patch entering into a still water tank. In this case no external energy, due to the action of a moving solid boundary, is introduced into the fluid domain. A second problem regards the analysis of waves generated by a moving solid boundary. The propagation and reflection processes are studied for a flat bottom flume with a vertical wall and a wave flume with a sloping bottom end.

A. Water patch entering a still water tank

The initial configuration of the problem is presented in Fig. 1, in which the length of the water tank is $L_c = 4$ m, while $d = 0.4$ m. The water tank is initialized with a hydrostatic pressure distribution, while the water patch presents null initial pressure and an initial downwards vertical velocity $U_0 = 0.1$ m/s. For this problem, the solid boundaries are modelled through GP. In this case we found from the numerical results that the corrective terms in (8) result to be null or very small, because of the mirroring between the fluid-solid domains. Therefore in this case, for sake of brevity, we only present the results of the dissipation due to the viscosity and the diffusive terms and leave the analysis of the terms in (8) to the next section, where FGP are implemented to model the solid boundary.

The energy quantities here presented are normalized with respect to $\varepsilon_{M\text{tot}} = \varepsilon_{M0} - \varepsilon_{M\infty}$, in which ε_{M0} is the initial mechanical energy, while $\varepsilon_{M\infty}$ is the mechanical energy

obtained after the kinetic energy has been completely dissipated and the system assumes a static configuration.

The water dynamic generated in this problem is that of a “quasi” standing wave and the different stages of its evolution are accurately described, through the analysis of the energy conservation, in the next section.

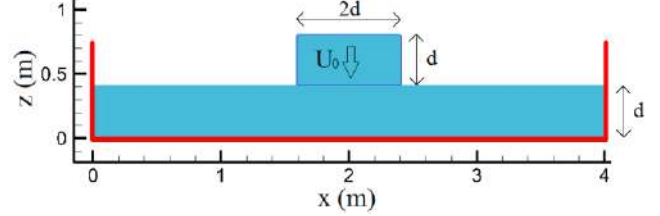


Fig. 1: Fluid domain with boundaries for the water patch and the still water tank.

A1. Energy components evolution

Here, the results for the evolution of the single components of energy for the case $\alpha = 0.01$ and $d/\Delta x = 100$, are analyzed. In Fig. 2 the first 7 seconds of the time evolution of potential, kinetic, compressible and dissipated energies are presented. Specifically, ε_{p0} is the initial potential energy evaluated from the bottom of the tank, ε_{k0} is the initial kinetic energy due to the initial velocity of the patch U_0 , while ε_{c0} is the energy due to the initial compression of the fluid particles.

As it is possible to observe, a continuous transfer between the potential and kinetic energy occurs. Significant time instants are highlighted in Fig. 2 and the correspondent frames of the flow evolution, with the velocity field, are represented in Figs. 3 and 4. Specifically, Fig. 3 presents the time instants in which the kinetic energy is at its maximum (highlighted by the higher magnitude of velocities), corresponding to the minimum in the potential energy. Conversely, Fig. 4 represents the time instant in which the kinetic energy is at its minimum and the potential energy at its maximum (energy manifested as wave elevation above the still water level).

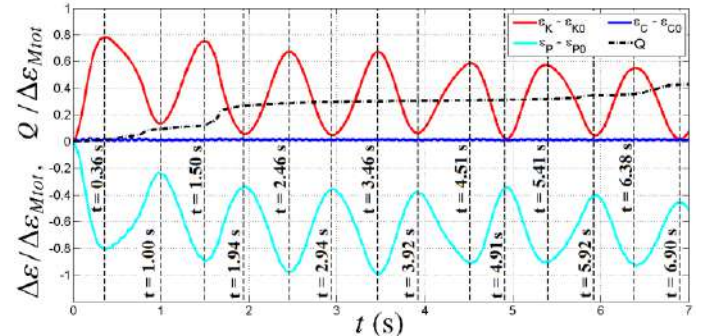


Fig. 2: Time evolution of kinetic, ε_K , potential, ε_p , compressible, ε_c , and dissipated, Q , energies for the water patch entering into the still water tank.

As the wave evolves the amplitudes of the oscillations progressively decrease since the energy is dissipated, resulting in an increase of Q , as further analysed in the next section. Regarding the compressible energy only very small oscillations around zero can be observed, in accordance with the weakly-compressibility assumption.

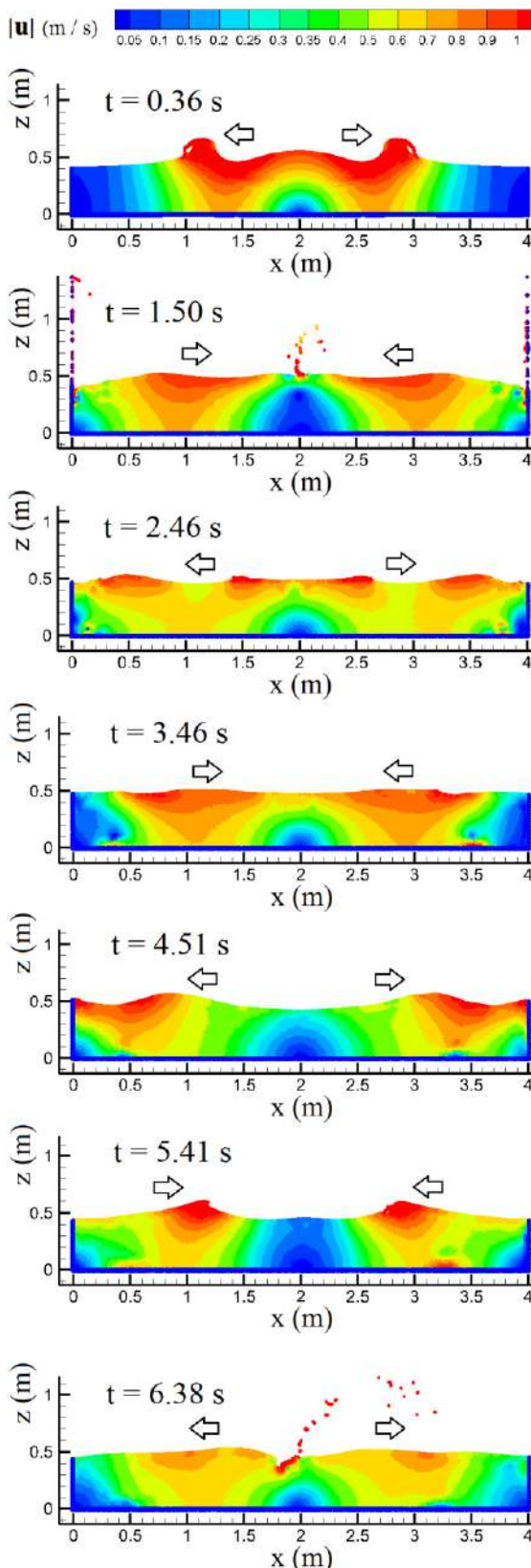


Fig. 3: Frames of the simulation with velocity magnitudes for the time instant highlighted in Fig. 2, corresponding to the maximum in the kinetic energy.

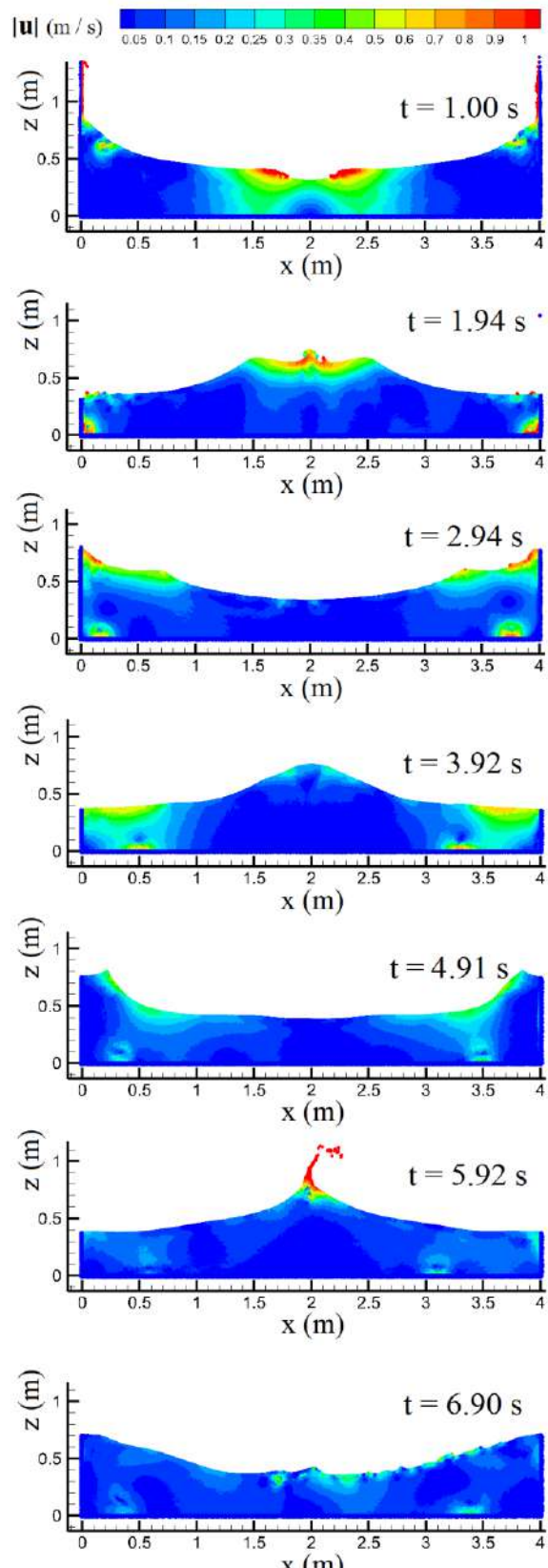


Fig. 4: Frames of the simulation with velocity magnitudes for the time instant highlighted in Fig. 2, corresponding to the maximum in the potential energy.

In Fig. 5 the time evolution of mechanical and internal energies is presented. As it is possible to see, the mechanical energy lost during the flow evolution is converted into internal energy. According with (11), the energy transfer from the mechanical energy to the internal one is conserved, being the variation of total energy of the fluid mass $\Delta\epsilon_{tot} = \Delta\epsilon_M + \Delta\epsilon_I$ constant during the flow evolution or, in other words, $W_S = 0$. It is interesting to observe that the higher amount of energy is dissipated at the initial stage of the flow evolution, in which a more violent dynamic with breaking and splashing phenomena and cavities collapses, is encountered (this is further analysed in the next section). After this initial part in which the wave is attenuated at a very fast rate, the dissipation becomes smaller and a long time is required to completely dissipate the mechanical energy and reach a final static configuration.

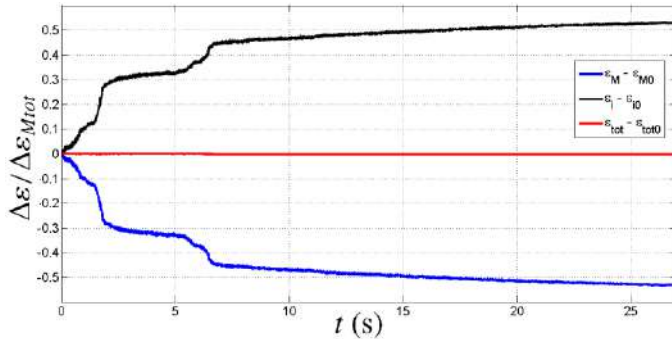


Fig. 5: Time evolution of mechanical, ϵ_M , internal, ϵ_I , and total, ϵ_{tot} , energies for the water patch entering into the still water tank.

A2. Analysis of the dissipative components

In this section, an analysis of the energy dissipated, Q , by inspecting the contribution due to the artificial viscosity, Q_V , and the contribution due to the diffusive term, Q_δ is presented. The analysis is carried out considering different values for the parameters which determine the magnitude of the dissipation. Specifically, since the energy dissipation is a function of the spatial resolution adopted, three resolutions $d/\Delta x = 50, 100$ and 200 , are analyzed. Moreover, two values of the artificial viscosity coefficient $\alpha = 0.01$ and 0.03 are taken into account for these analyses. Conversely to the artificial viscosity, the diffusive term does not need for tuning, therefore a value for the coefficient $\delta = 0.1$ is implemented for all the test cases. The energy dissipated by the viscous contribution is presented in Fig. 6, for the case $\alpha = 0.01$, while in Fig. 7, for the case $\alpha = 0.03$. As expected, the energy dissipated by the viscosity for $\alpha = 0.03$ is higher than that dissipated for $\alpha = 0.01$.

The energy dissipated by the diffusive term is presented instead in Fig. 8, for the case $\alpha = 0.01$, while in Fig. 9, for the case $\alpha = 0.03$. In this case, it is interesting to notice that, nonetheless the diffusive coefficient is constant in the various cases, different results are obtained when the artificial viscosity coefficient is changed.

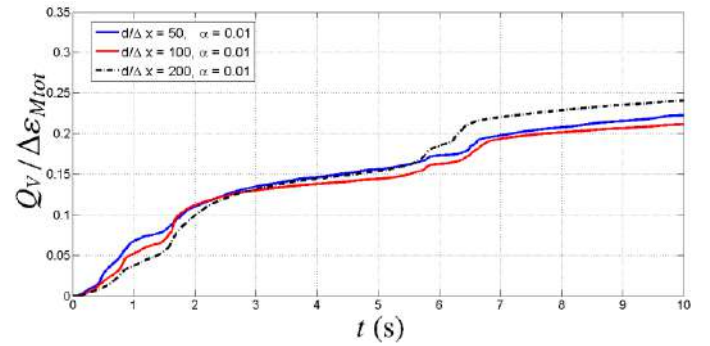


Fig. 6: Time evolution of the energy dissipated by the artificial viscosity, Q_V , for the spatial resolutions $d/\Delta x = 50, 100$ and 200 with $\alpha = 0.01$.

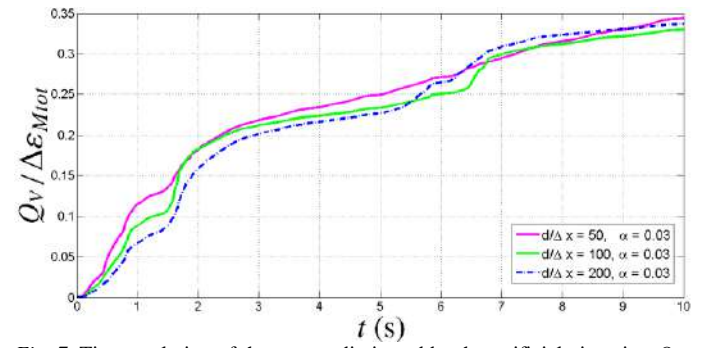


Fig. 7: Time evolution of the energy dissipated by the artificial viscosity, Q_V , for the spatial resolutions $d/\Delta x = 50, 100$ and 200 with $\alpha = 0.03$.

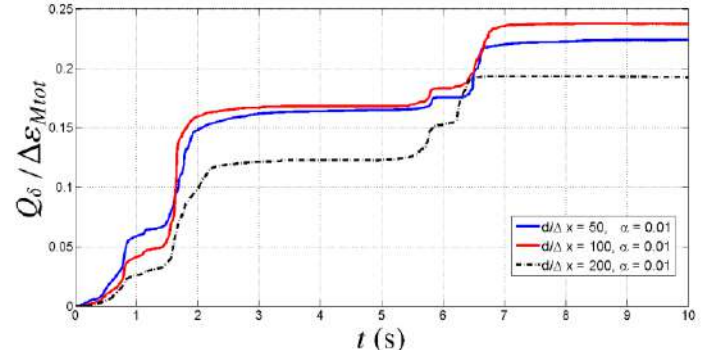


Fig. 8: Time evolution of the energy dissipated by the diffusive term, Q_δ , for the spatial resolutions $d/\Delta x = 50, 100$ and 200 with $\alpha = 0.01$.

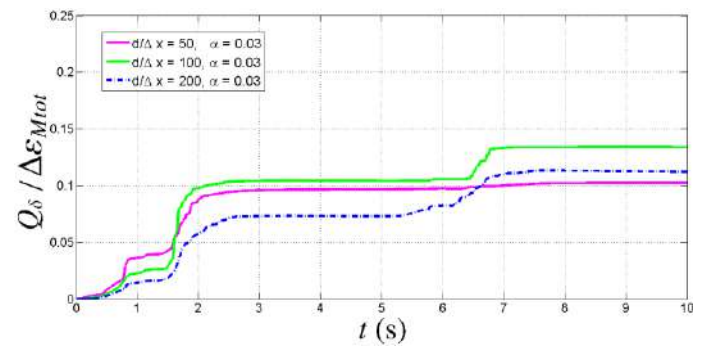


Fig. 9: Time evolution of the energy dissipated by the diffusive term, Q_δ , for the spatial resolutions $d/\Delta x = 50, 100$ and 200 with $\alpha = 0.03$.

Indeed, for the lower viscous dissipation case $\alpha = 0.01$ a higher diffusive dissipation is observed, while the case of a higher viscous dissipation $\alpha = 0.03$ results in a smaller dissipation by the diffusive term. The energies dissipated by the two components compensate each other, resulting in a overall dissipation that is not too different in the various cases. Different considerations regarding the influence of the spatial resolution on the energy dissipated can be drawn. According with the theory, the dissipation is dependent on the adopted spatial resolution and is expected to vanish when refining, that is when $d/\Delta x$ is increased. This fact can be observed in the initial stage of the flow evolution, in which the dissipations result to converge as the spatial resolution is increased (lower dissipation for higher resolution). However, when the splashing phenomena occur with the consequent higher rate of energy dissipation, this result is no longer exactly respected. In this case indeed, the use of a higher resolution allows to better describe the splashing phenomena and the loss of energy due to the water particles hitting the free surface after the splashing becomes more relevant compared with that obtained at a lower resolution. These results are in accordance with the ones found by [12], in which in presence of a fluid impact even the use of a very high resolution do not ensure the condition of vanishing dissipation. From these results another insight about nature of the diffusive dissipation can be observed. The energy dissipated by the diffusive term (Figs. 8 and 9) presents a stair-like behavior in which, in presence of an impact it suddenly increase, but when no impact occurs the power dissipated by the diffusive term is very close to zero. A similar results has been obtained by [3], in which, as they observed, in presence of fluid impacts the high frequency oscillation of the pressure field (that are essentially acoustic waves generated after the impact) are smoothed by the action of the diffusive term, leading to an increasing of Q_δ . When not violent impacts take place in the fluid domain the diffusive term is not dissipating anymore. The diffusive term therefore mainly acts against the high frequency oscillations caused after impact events.

B. Waves generation and propagation: analysis of reflective and non-reflective cases

In this section, the results about the energy decomposition for regular waves are presented. A water tank is initialized with a hydrostatic pressure distribution of the fluid particles and the wave generation is obtained by a piston-type wavemaker implemented at the left side of the tank. The action of the wavemaker on the fluid mass is therefore the source of energy that propagates along the flume.

Two conditions are studied for this test: the first one is characterized by constant water depth and a vertical wall at the right end of the tank, representative of a fully reflective condition (i.e. $R_C \approx 1$), while the second one is a bottom flume characterized by a slope 1:13.125 and is representative therefore of a wave absorbing condition (i.e. $R_C \rightarrow 0$). In Fig. 10 the sketch of the flat-bottom flume with a vertical right wall is presented, in which the water depth is $d = 0.4$ m while

the length of the flume is $L_c = 4$ m. Fig. 11 represents instead the configuration of the sloping bottom flume in which, for an initial length $L_{c1} = 0.5$ m, the water depth is constant with $d = 0.4$ m while in the second part, for a length $L_{c2} = 5.25$ m, the bottom flume linearly varies from zero to d .

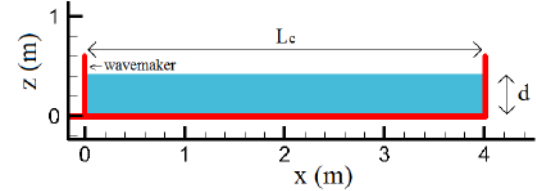


Fig. 10: Fluid domain with boundaries for the wave flume with constant water depth and vertical right wall.

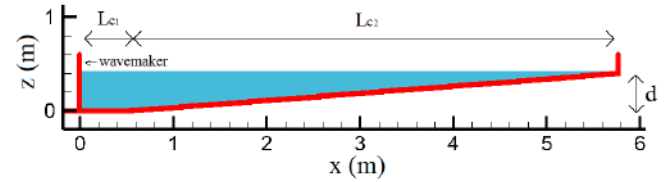


Fig. 11: Fluid domain with boundaries for the wave flume with sloping bottom.

The regular wave train generated by the wavemaker is characterized by wave height $H = 0.12$ m and period $T = 0.85$ s for both flat and sloping bottom flumes, guaranteeing in this way the introduction of the same amount of energy for the two configurations. For the easy of comparison of the results, the quantities here presented are normalized with the respect of W_{sf} , that represents the work made by the solid boundary on the fluid mass, W_s , calculated for the flat bottom flume case, at $t = 11.9$ s (time instant that corresponds to 14 wavemaker strokes, including the ramp period). The analizes are performed considering different values of the spatial resolution.

B1. Analysis of the solid-fluid work exchange

In this section, the work done by the solid boundary on the water mass is analysed. In Fig. 12 the numerical results of the nominal work, $W_{solid/fluid}$, and the effective work, W_s , made by the solid boundaries on the fluid mass, are compared with the variation of total energy evaluated inside the fluid domain, $\Delta\epsilon_{tot} = \Delta\epsilon_M + \Delta\epsilon_I$.

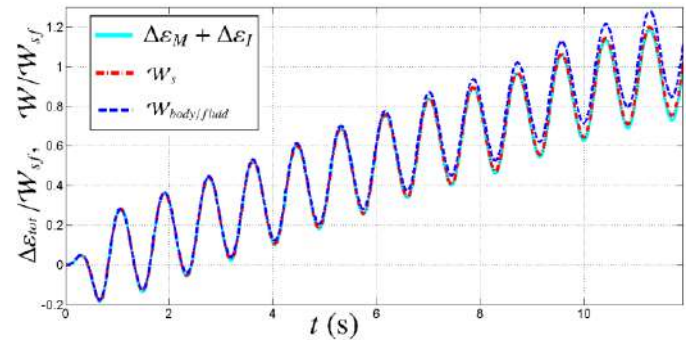


Fig. 12: Time evolution of the nominal work, $W_{solid/fluid}$, and effective work, W_s , made by the solid boundaries on the fluid mass in comparison with the variation of total energy evaluated inside the fluid domain, $\Delta\epsilon_{tot}$. The results refers to the flat bottom flume case, $d/\Delta x = 100$.

The result represents a very good approximation of the global energy conservation expressed in (11), since W_s is practically superimposed to $\Delta\epsilon_{tot}$. The nominal work made by the solid boundary results to be greater than the effective work and the difference between these two quantities, expressed by (10), is given in Fig. 13, for different values of the spatial resolution. As it is possible to see, this quantity decreases when the spatial resolution is increased, allowing for the work made by the solid boundary to converge to the nominal work.

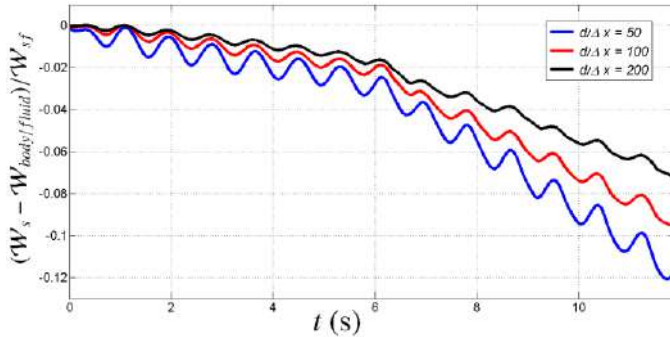


Fig. 13: Time evolution of the difference between effective and nominal work made by the solid boundary on the fluid domain, $W_s - W_{solid/fluid}$, for the flat bottom flume case and spatial resolutions $d/\Delta x = 50, 100$ and 200 .

In Fig. 14, the time evolution of the total energy for the flat and sloping bottom cases, $\Delta\epsilon_{tot} = \Delta\epsilon_M + \Delta\epsilon_I$, is displayed for the case $d/\Delta x = 100$. As it is possible to see, since the wavemakers are implemented with the same time law for the two cases, the same energy evolution is also observed. Indeed, only in the final part of the simulation a slight difference between the two cases is encountered. At that stage, in fact, the reflected wave in the flat bottom flume case reaches the wavemaker and it influence the wave height at the interface solid-fluid and therefore also the power released by the wavemaker.

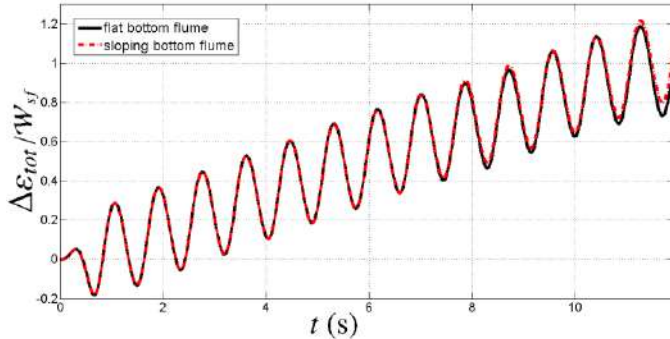


Fig. 14: Comparison of the time evolution of the total energy for waves traveling in the flat and sloping bottom flumes, for the case $d/\Delta x = 100$.

B2. Energy components evolutions for reflective and non reflective cases

In this section the time evolution of the single energy components are compared for the reflective and non-reflective case, for the resolution $d/\Delta x = 100$. Proven that the time evolution of the total energy is the same for the two configurations (see Fig. 14), a different behaviour is instead

observed when inspecting the single energy components and interesting insights can be found regarding the water dynamics for the two cases. To this aim, in Fig. 15 the evolution of kinetic energy and potential energy for the two analyzed cases is presented. As it is possible to see, for the initial part of the flow evolution, for both flat and sloping bottom flumes, the kinetic energy gradually increases with time since, as the waves travel in the flume, a higher amount of fluid mass is set into motion. Moreover, small oscillations in the kinetic energy are also observed. The potential energy, for the same reason, presents a similar evolution with a higher amplitude of the oscillations. It is interesting to notice that in this initial part of the simulation the time evolution of the energies for the two configurations is practically superimposed. This condition is no longer conserved after the first wave reaches the vertical wall of the flat-bottom flume and the effect of the reflected wave can be observed in the kinetic and potential energies evolutions. As it is possible to see in Fig. 15, as the reflected wave travels back in the flume its effect results in an increasing of the amplitude of the oscillations of kinetic and potential energies. A different situation is instead observed for the sloping bottom case, in which as the waves reach the end of the flume no reflection effects are encountered. In this case indeed, a steady condition is reached and the potential and kinetic energies attain an oscillating behavior around a constant value.

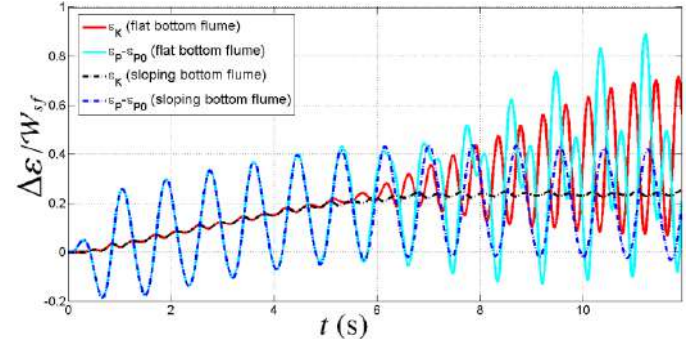


Fig. 15: Comparison of kinetic, ϵ_K , and potential, ϵ_P , energies for waves traveling in the flat and sloping bottom flumes.

A further insight of the waves dynamic is given in Fig. 16, in which the evolution of mechanical and internal energies is presented. According with the weakly-compressible assumption, the energy due to the compression of the fluid particles is very small and the internal energy is essentially due to the dissipated one. Also in this case the time evolution of the energies for the two configurations result to be the same for the initial part of the simulation in which the waves propagate towards the right end of the flume. After the time instant $t = 5.1$ s the two cases start to diverge since, as shown in the frames of the simulations in Fig. 17, the first wave reaches the end of the vertical wall flume. The wave reflection in the case of the flat-bottom flume results indeed in an increasing of the mechanical energy at a similar rate of change as in the initial part of the simulation. As a consequence, also the rate of change of the internal energy (i.e. power dissipated) it results to be similar as in the initial part. At $t = 7.7$ s, as

shown in Fig. 17, the first wave reaches the end of the sloping bottom flume while for the vertical wall the effect of the reflected wave can be observed on the height of the last wave. In this phase of the evolution, the mechanical energy for the sloping bottom configuration, attains a steady oscillating behavior while the internal energy presents a high rate of change.

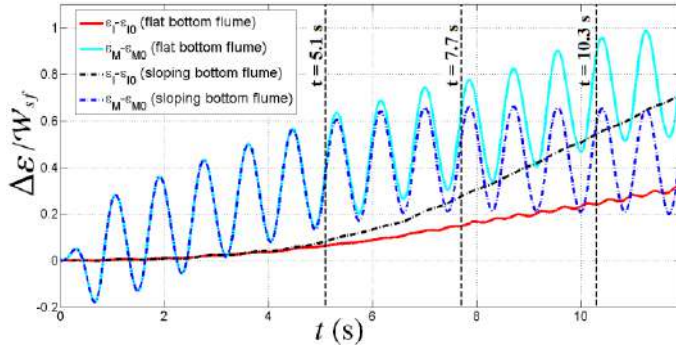


Fig. 16: Comparison of mechanical, ϵ_M , and internal, ϵ_I , energies for waves traveling in the flat and sloping bottom flumes. The frames of the simulations at the time instants highlighted by the vertical dashed lines are represented in Fig. 17.

In this case indeed the system do not accumulate more mechanical energy, since the successive energy given by the wavemaker is dissipated in the breaking process of the waves on the slope. Finally, at $t = 10.3$ s, the reflected waves in the flat-bottom flume reaches back the wavemaker.

IV. CONCLUSIONS

An in-detail analysis of the energy decomposition for problems regarding waves generation and propagation has been presented. A first case, regarding the wave dynamic generated by a water patch falling into a still water tank has been studied. In this case particular attention has been given to the analysis of the dissipation processes, due to the viscous component and to the use of the diffusive numerical correction. The results have shown that, for this problem, the energy dissipation is not too different when the viscosity coefficients and the spatial resolution are changed.

The energy analysis has been then applied to waves generated by a moving solid boundary. A study of the solid/fluid work exchange has been presented, showing the equivalence between the external work made by the solid boundary and the total energy evaluated inside the flume. The energy decomposition has been then presented for waves traveling in a flat bottom (reflective condition) and a sloping bottom (absorbing condition) wave flumes. This methodology has been proven to be a valuable instrument for studying the wave energy balance occurring when waves interact with structures and can be used for analysing the dissipation induced by more complex configurations.

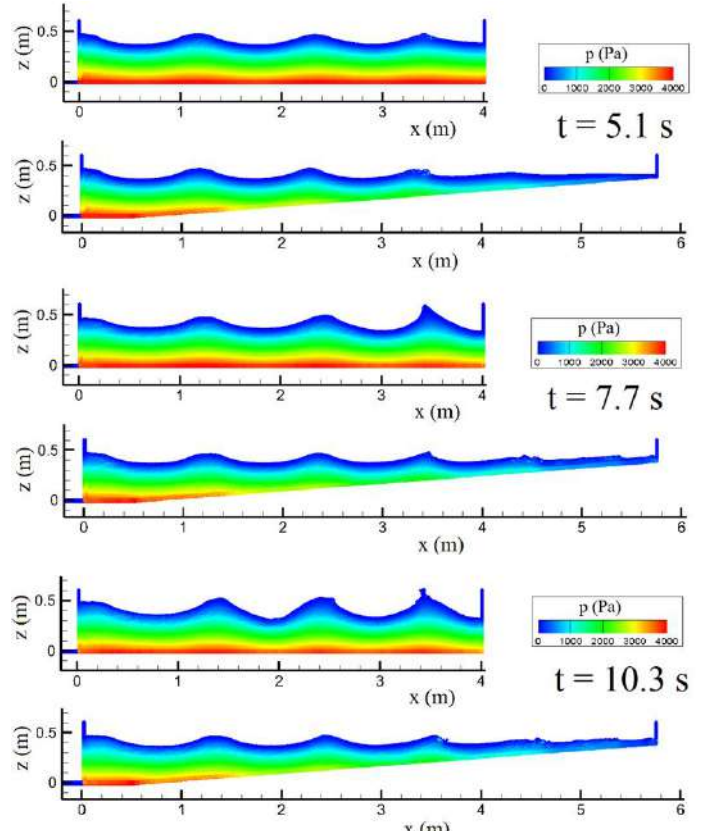


Fig. 17: Frames of the simulations with pressure distributions for significant time instants of the flow evolution.

REFERENCES

- [1] Colagrossi A., Souto-Iglesias, A., Antuono, M., Marrone, S., 2013. Smoothed-particle-hydrodynamics modeling of dissipation mechanisms in gravity waves. *Phys. Rev. E* 87, 023302.
- [2] Colagrossi, A., Bouscasse, B., Marrone, S., 2015. Energy-decomposition analysis for viscous free-surface flows. *Phys. Rev. E* 92, 053003.
- [3] Antuono, M., Marrone, S., Colagrossi, A., Bouscasse, B., 2015. Energy balance in the δ -SPH scheme. *Comp. Meth. in Appl. Mech. Eng.* 289.
- [4] Molteni, D., Colagrossi, A., 2009. A simple procedure to improve the pressure evaluation in hydrodynamic context using the SPH. *Computer Physics Comm.* 180, 861–872.
- [5] Ferrari, A., Dumbser, M., Toro, E.F., Armanini, A., 2009. A new 3D parallel SPH scheme for free surface flows. *Comp. & Fluids* 38, 1203–1217.
- [6] Antuono, M., Colagrossi, A., Marrone, S., Molteni, D., 2010. Free-surface flows solved by means of SPH schemes with numerical diffusive terms. *Comp. Physics Comm.* 181, 532–549.
- [7] Cercos-Pita, J., Antuono, M., Colagrossi, A., Souto-Iglesias, A., 2017. SPH Energy Conservation for Fluid-Solid Interactions. *Comput. Methods Appl. Mech. Engineering*.
- [8] Antuono, M., Colagrossi, A., Marrone, S., 2012. Numerical diffusive terms in weakly-compressible SPH schemes. *Comp. Physics Comm.* 183, 2570–2580.
- [9] Colagrossi, A., Landrini, M., 2003. Numerical Simulation of Interfacial flows by SPH. *J. Comp. Phys.* 191, 448–475.
- [10] Marrone, S., Antuono, M., Colagrossi, A., Colicchio, G., Le Touzé, D., Graziani, G., 2011. Delta-SPH model for simulating violent impact flows. *Computer Methods in Applied Mechanics and Engineering* 200, 1526–1542.
- [11] De Leffe, M., Le Touzé, D., Alessandrini, B., 2011. A modified noslip condition in weakly-compressible SPH, in: 6th ERCOFTAC SPHERIC workshop on SPH applications, pp. 291–297.
- [12] Marrone, S., Colagrossi, A., Di Mascio, A., Le Touzé, D., 2016. Analysis of free-surface flows through energy considerations: Single-phase versus twophase modeling. *Physical Review E* 93, 1–13.

Particle Trajectory Calculation in SPH

Jiayuan SHEN, Whenhuan LU

School of Computer Software
Tianjin University
Tianjin 300350, China
shenjiayuan@tju.edu.cn

Yaxuan XING

School of Mathematics
Tianjin University
Tianjin 300350, China

Darcy Q. HOU*

School of Computer Science and Technology
Tianjin University
Tianjin 300350, China

*Corresponding to: ghou@tju.edu.cn

Arris S. TIJSELING

Department of Mathematics and Computer Science
Eindhoven University of Technology
Eindhoven 5600 MB, The Netherlands

Abstract—Smoothed particle hydrodynamics (SPH) method is a Lagrangian meshless approach for modelling fluid dynamics problems. Due to the Lagrangian property, particles change their positions at every time step and hence the calculation of particle trajectories plays an important role in SPH and may largely affect the overall accuracy. Many explicit time integration algorithms have been used in SPH, but the effect of these time stepping schemes on the calculation of particle trajectories has not been well studied. With specially designed examples, this paper compares the performance of six commonly used time stepping schemes for particle trajectory calculation, including the Euler forward method, modified Euler, second-order Runge-Kutta (RK2), fourth-order Runge-Kutta (RK4), velocity Verlet and leap-frog. Numerical analysis indicates that for problems with (nearly) uniform velocity fields, all schemes can give solutions with adequate accuracy, but the Euler method, modified Euler and RK2 may not predict accurate particle trajectories in certain highly non-uniform velocity fields. These methods may also introduce varying degrees of artificial dispersion that could lead to overestimation of spill area of particle clouds. On the other hand, the algorithms of RK4, velocity Verlet and leap frog can accurately calculate the particle trajectories without artificial dispersion. In order to find the most efficient scheme with acceptable accuracy, the computational costs of these schemes have also been compared. In addition, by analyzing the accuracy and convergence, we conclude that convergence rate can be different from the accuracy order for a given method.

I. INTRODUCTION

Smoothed Smoothed particle hydrodynamics (SPH) method is a Lagrangian, meshless, particle approach for modelling fluid dynamics problems [1,2], which offers significant advantages over conventional mesh-based methods, particularly when coupled with moving free surface and interface, and large deformations at the material boundary region. During its early development (1980s), SPH was mainly applied to compressible astrophysical and cosmological flows. At the beginning of the 1990s, Libersky and Petschek [3] extended SPH to solid dynamics, especially to high velocity impact problems. Monaghan (1994) [4] applied a concept of artificial compressibility and used an equation of state for

liquids with artificially low speed of sound to model incompressible free-surface flows. Monaghan (1997) [5] used SPH to simulate dust–gas mixtures. After that, SPH was used to model a vast range of fluid dynamics problems. The applications of SPH in the fluid dynamics field include low Reynolds number flows [6], viscous and heat conducting flows [7,8], multiphase flows [9,10,11], coastal hydrodynamics [12] and so on.

In particle methods, continuous media is firstly discretized into a finite number of points known as particles, which carry different field variables depending on the specific problems. Then field functions and/or their spatial derivatives in the governing equations are approximated based on these discrete particles. The SPH method consists of two steps of approximations, i.e. kernel approximation and particle approximation [1], after which semi-discrete SPH equations are obtained. Furthermore, together with a proper time integration algorithm (time stepping), a full discretization of the governing equations can be derived. Finally, with numerically enforced boundary conditions, simulation is marched on with increasing time.

The choice of different time stepping directly affects the accuracy of the numerical solution and many explicit and implicit time stepping methods have been used in the SPH community. Rook et al. [13] solved a two-dimensional transient heat conduction problem using SPH with a Crank-Nicolson implicit time integration technique. Monaghan (1995) [14] focused on the dusty gas problem, using predictor-corrector time stepping scheme, where the time step is controlled by gravity, CFL condition, viscosity and drag terms. Monaghan (1997) [15] considered the application of two implicit schemes (the first-order backward-Euler and the second-order Tischer schemes) to SPH dust–gas mixtures. Laibe and Price (2012) [16] simulated two-fluid gas and dust mixtures in smoothed particle hydrodynamics (SPH), using implicit leap frog time stepping scheme. Although implicit time stepping schemes can be used, the mostly applied ones in the SPH community are the explicit methods due to many advantages such as simplicity, clearness and easy implementation. Theoretically explicit multi-step integration

methods can be used, but various one-step ones are most popular in SPH. They are the Euler forward method, modified Euler, second-order Runge-Kutta (RK2), fourth-order Runge-Kutta (RK4), velocity Verlet and leap-frog.

In SPH, particle trajectory equation describes the relation between the position and time about each particle. Apart from computed velocity field, the solution of trajectory equation highly depends on the applied time integration algorithms. In fact, as the calculation of other field variables depends on the particle distribution through kernel and kernel gradient, the computation of particle trajectory directly affects the whole computational process. This paper studies the effect of the above six explicit time stepping schemes on the evolution of particle trajectories. Numerical analysis indicates that for problems with (nearly) uniform velocity fields, all schemes can give solutions with adequate accuracy, but the Euler method, modified Euler and RK2 may not predict accurate particle trajectories in certain highly non-uniform velocity fields. These methods may also introduce varying degrees of artificial dispersion that could lead to overestimation of spill area of particle clouds. On the other hand, the algorithms of RK4, velocity Verlet and leap frog can accurately calculate the particle trajectories without artificial dispersion. In order to find the most efficient scheme with acceptable accuracy, the computational costs of these schemes have also been compared.

The structure of this paper: Section 2 the trajectory equation is briefly introduced. Section 3 six time stepping schemes are presented. Section 4 analyzes algorithms time-accuracy, and compares the numerical results with exact solution. Section 5 gives computational cost and draws convergence rate curve. Section 6 makes conclusion about six methods to solve trajectory equation.

II. TRAJECTORY EQUATION

In SPH fluid dynamics, many equations need to be solved, and one of them is the particle trajectory equation due to the Lagrangian property of the SPH method. This is one of the fundamental differences from Eulerian mesh-based methods. It is also different from the particle trajectory calculation in arbitrary Lagrangian Eulerian methods (or semi-Lagrangian), where interpolation is necessary to obtain the particle velocity field. The calculation of particle trajectories can significantly affect the overall accuracy of SPH simulations, and here needs more attention and detailed study. The particle trajectory equation can be simply written as

$$\frac{d\vec{x}_i}{dt} = \vec{v}_i(t, \vec{x}_i) \quad (1)$$

where \vec{x}_i is the i particle coordinate, \vec{v}_i is the local velocity and it is often dependent on the particle position.

III. TIME STEPPING SCHEMES

Equation (1) is a fully ordinary differential equation (ODE) and its integration only depends on the applied time integration algorithms (time stepping). For solving equation (1), six most often used explicit time stepping methods are reviewed and

their performances are systematically compared. They are the Euler method, modified Euler, second-order Runge-Kutta (RK2), fourth-order Runge-Kutta (RK4), velocity Verlet and leap frog. Define Δt as the time step size, and n as the time step index such that $t^n = n\Delta t$. The above methods are presented below.

Euler Method. The method frequently used to solve the system of equation (1) is the Euler forward time stepping. It is first-order accurate and simple to program. It is implemented in the following way:

$$\vec{x}_i^{n+1} = \vec{x}_i^n + \Delta t \vec{v}_i(t^n, \vec{x}_i^n) \quad (2)$$

Modified Euler. To improve the accuracy of Euler time stepping, the modified Euler is often used, which includes two steps, the predictor step

$$\vec{x}_i^{n+1,p} = \vec{x}_i^n + \Delta t \vec{v}_i^n \quad (3)$$

where $\vec{v}_i^n := \vec{v}_i(t^n, \vec{x}_i^n)$, and the corrector step

$$\vec{x}_i^{n+1} = \vec{x}_i^n + \Delta t \frac{\vec{v}_i^n + \vec{v}_i^{n+1,p}}{2} \quad (4)$$

The modified Euler (also known as trapezoid method) is second-order accurate.

Except Euler and modified Euler, Runge-Kutta family schemes are popular in SPH too. They are the second-order Runge-Kutta (RK2) and fourth-order Runge-Kutta (RK4).

Second-Order Runge-Kutta (RK2). Similar as the modified Euler, RK2 is also a predictor-corrector method as given below.

Predictor step:

$$\vec{x}_i^{n+1/2} = \vec{x}_i^n + \frac{\Delta t}{2} \vec{v}_i^n \quad (5)$$

Corrector step:

$$\vec{x}_i^* = \vec{x}_i^n + \frac{\Delta t}{2} \vec{v}_i^{n+1/2} \quad (6)$$

$$\vec{x}_i^{n+1} = 2\vec{x}_i^* - \vec{x}_i^n \quad (7)$$

where $\vec{v}_i^{n+1/2} := \vec{v}_i(t^{n+1/2}, \vec{x}_i^{n+1/2})$. The RK2 scheme can be casted in the standard form:

$$\Rightarrow \begin{cases} k_1 = \Delta t \vec{v}_i(t^n, \vec{x}_i^n) \\ k_2 = \Delta t \vec{v}_i\left(t^n + \frac{\Delta t}{2}, \vec{x}_i^n + \frac{k_1}{2}\right) \\ \vec{x}_i^{n+1} = \vec{x}_i^n + k_2 \end{cases} \quad (8)$$

Fourth-Order Runge-Kutta. The RK4 scheme in the standard form is:

$$\vec{x}_i^{n+1} = \vec{x}_i^n + \frac{1}{6} (k_1 + 2k_2 + 2k_3 + k_4) \quad (9)$$

where the coefficients k_1 , k_2 , k_3 and k_4 are defined as follows:

$$\Rightarrow \begin{cases} k_1 = \Delta t \vec{v}_i \left(t^n, \vec{x}_i^n \right) \\ k_2 = \Delta t \vec{v}_i \left(t^n + \frac{\Delta t}{2}, \vec{x}_i^n + \frac{k_1}{2} \right) \\ k_3 = \Delta t \vec{v}_i \left(t^n + \frac{\Delta t}{2}, \vec{x}_i^n + \frac{k_2}{2} \right) \\ k_4 = \Delta t \vec{v}_i \left(t^n + \Delta t, \vec{x}_i^n + k_3 \right) \end{cases} \quad (10)$$

Velocity Verlet. As representatives of the symplectic time stepping algorithms, velocity Verlet and its counterpart leapfrog have gained much attention due to their excellent conservation property and exact time reversibility [10,11].

Suppose the acceleration of particle i is $\vec{a}_i = d\vec{x}_i / dt$. The calculation steps in the Verlet scheme follows:

$$\vec{v}_i^{n+1/2} = \vec{v}_i^n + \frac{1}{2} \vec{a}_i \Delta t \quad (11)$$

$$\vec{x}_i^{n+1} = \vec{x}_i^n + \vec{v}_i^{n+1/2} \Delta t \quad (12)$$

$$\vec{v}_i^{n+1} = \vec{v}_i^{n+1/2} + \frac{1}{2} \vec{a}_i^{n+1} \Delta t \quad (13)$$

They can be simply derived by Taylor series expansion of the position and velocity:

$$\vec{x}_i^{n+1} = \vec{x}_i^n + \vec{v}_i^n \Delta t + \frac{1}{2} \vec{a}_i^n \Delta t^2 \quad (14)$$

$$\vec{v}_i^{n+1} = \vec{v}_i^n + \frac{1}{2} \Delta t \left(\vec{a}_i^{n+1} + \vec{a}_i^n \right) \quad (15)$$

Leap Frog. For the leap frog algorithm [12], the calculation procedure follows

$$\vec{v}_i^{n+1/2} = \vec{v}_i^{n-1/2} + \vec{a}_i^n \Delta t \quad (16)$$

$$\vec{x}_i^{n+1} = \vec{x}_i^n + \vec{v}_i^{n+1/2} \Delta t \quad (17)$$

$$\vec{v}_i^n = \frac{1}{2} \left(\vec{v}_i^{n+1/2} + \vec{v}_i^{n-1/2} \right) \quad (18)$$

with velocity at the first half step updated by

$$\vec{v}_i^{1/2} = \vec{v}_i^0 + \frac{1}{2} \vec{a}_i^0 \Delta t \quad (19)$$

The leapfrog algorithm is an economical version of the basic algorithms as it needs to store only one set of positions and one set of velocities.

IV. NUMERICAL EXPERIMENT

The purpose of these experiments is to compare the numerical behaviour of different time stepping algorithms presented in Section III for calculating the trajectories with a given velocity field. Not only the accuracy, but also the numerical dispersion and computational cost will be studied.

Numerical analysis An arbitrary smooth function $f(t)$ can be expanded into Taylor series in the neighbourhood of point t_i as

$$f(t) = f(t_i) + \Delta t \cdot f'(t_i) + \frac{\Delta t^2}{2} f''(t_i) + \frac{\Delta t^3}{6} f'''(t_i) + \dots \quad (20)$$

where $\Delta t = t - t_i$.

According to formulation (22), all time stepping schemes can be derived by finite terms in Taylor series expansion, and truncation error (TE) will be caused.

In Euler forward time stepping,

$$f'(t_i) = \frac{f(t_{i+1}) - f(t_i)}{\Delta t} \quad (21)$$

It neglects the second and higher-order derivative terms in (20). In fact,

$$f'(t_i) = \frac{f(t_{i+1}) - f(t_i)}{\Delta t} + \frac{\Delta t}{2} f''(t_i) + \frac{\Delta t^2}{6} f'''(t_i) + \dots \quad (22)$$

Then the truncation error for Euler forward time stepping is obtained as

$$TE = -\frac{\Delta t}{2} f''(t_i) - \frac{\Delta t^2}{6} f'''(t_i) + \dots \quad (23)$$

Particularly, if $f''(t_i)$, i.e. particle acceleration in trajectory calculation, equals to zero, Euler forward time stepping can also achieve second-order accuracy. In that way, other time integral algorithms mentioned above will also have higher accuracy.

Two-dimensional example. In a two-dimensional domain, for the flow field given by

$$\begin{aligned} v_x &= ax - by \\ v_y &= ay + bx \end{aligned} \quad (24)$$

where x and y are the cartesian coordinates and a and b are constants, we can obtain the exact solution of particle trajectories in this velocity field as

$$\begin{aligned} x(t) &= \exp(at) [x_0 \cos bt - y_0 \sin bt] \\ y(t) &= \exp(at) [x_0 \sin bt + y_0 \cos bt] \end{aligned} \quad (25)$$

where $x(t)$ and $y(t)$ are the exact coordinates at time t . In this paper, we assume $(x_0, y_0) = (1000, 0)$, $a = 0$, and $b = 0.001$.

It is noted that varying a and b , we may generate non-uniform divergent, convergent or circular velocity fields for testing purposes.

We will calculate the trajectories of $N=100$ particles in this velocity field and compare the six explicit time stepping schemes results with the analytical solution (25).

The N particles variance is a measure of the dispersion of the particle cluster. As shown in Fig. 1, the distribution of $N=100$ random particles is obtained.

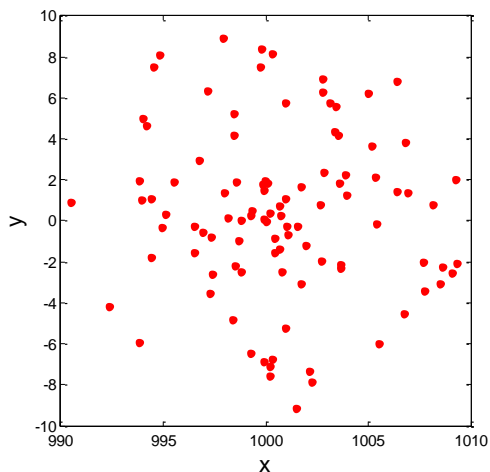


Figure 1. The distribution of $N = 100$ random particle

Fig. 2 presents the analytical solution corresponding to the complete circular trajectory of the particle cluster during 4000π h. The figure also shows the exact trajectory of a particle starting from the point $(1000, 0)$.

Fig. 3 depicts the numerical solution with Euler method using $\Delta t = 60$ s. Particle clusters are shown at 60 s intervals. A total run 4000π h. It is clear that Euler method has a large numerical dissipation compared to the exact solution.

Fig. 4 shows the numerical solution with modified Euler method using $\Delta t = 60$ s. Particle clusters are shown at 60 s intervals. A total run 4000π h. It is clear that the result of modified Euler is better than Euler forward method, but it is far from the exact solution.

Fig. 5 shows the numerical solution with RK2 method using $\Delta t = 60$ s. Particle clusters are shown at 60 s intervals. A total run 4000π h. It is clear that the result of RK2 is better than modified Euler method, but it is far from the exact solution.

Fig. 6 shows the numerical solution with RK4 method using $\Delta t = 60$ s. Particle clusters are shown at 60 s intervals. A total run 4000π h. It is clear that the result of RK4 is better than RK2 method, and the result of RK4 is same as exact solution, it has high accuracy.

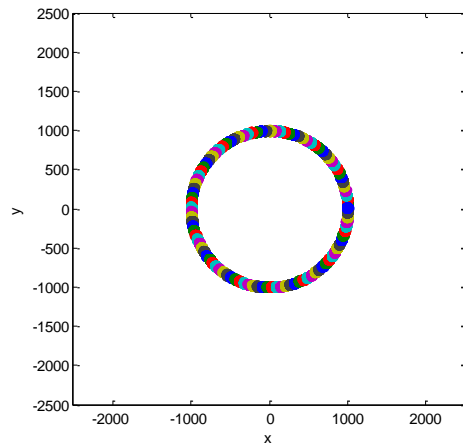


Figure 2. Exact trajectories. $N = 100$ particles

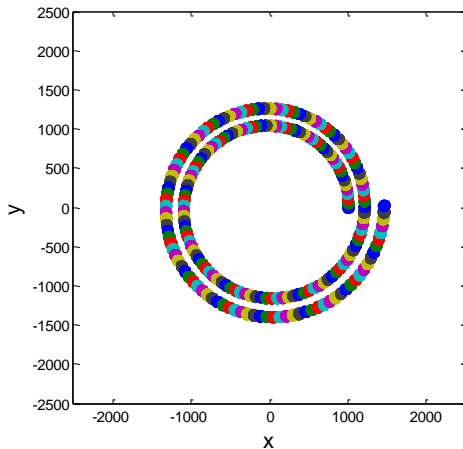


Figure 3. Numerical solution with Euler forward method

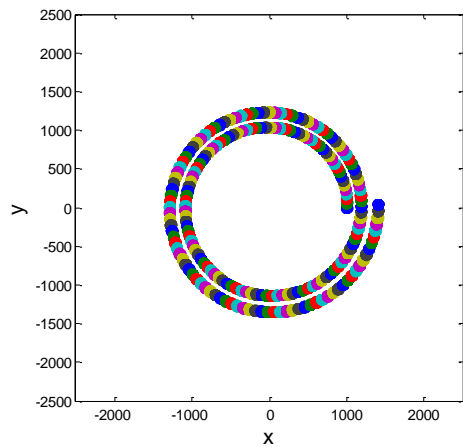


Figure 4. Numerical solution with modified Euler method

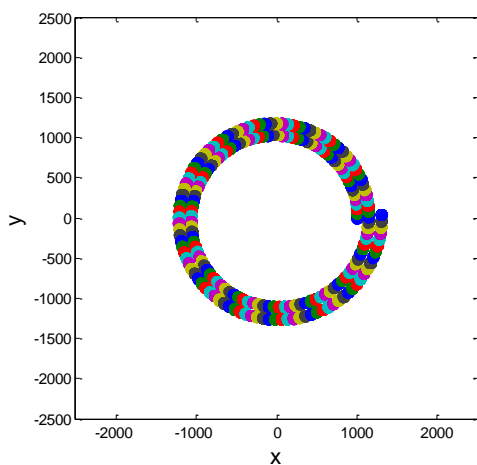


Figure 5. Numerical solution with RK2 method

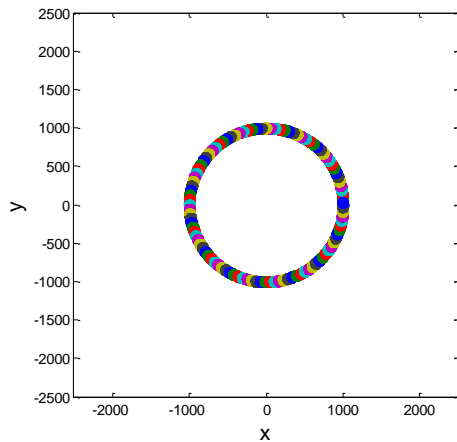


Figure 6. Numerical solution with RK4 method

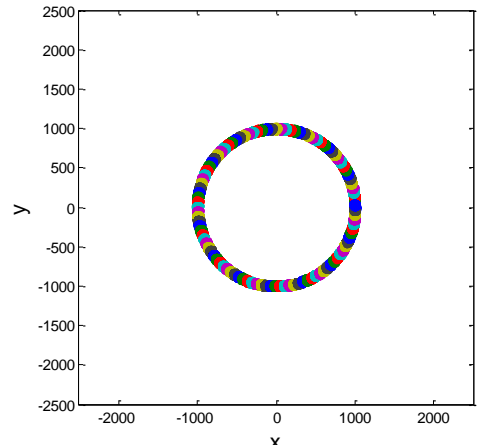


Figure 7. Numerical solution with velocity Verlet method

Fig. 7 shows the numerical solution with velocity Verlet method using $\Delta t=60$ s. Particle clusters are shown at 60 s intervals. A total run 4000π h. The result of velocity Verlet is same as exact solution, it has high accuracy.

Fig. 8 shows the numerical solution with leap frog method using $\Delta t=60$ s. Particle clusters are shown at 60 s intervals. A total run 4000π h. The result of leap frog is same as exact solution, it has high accuracy.

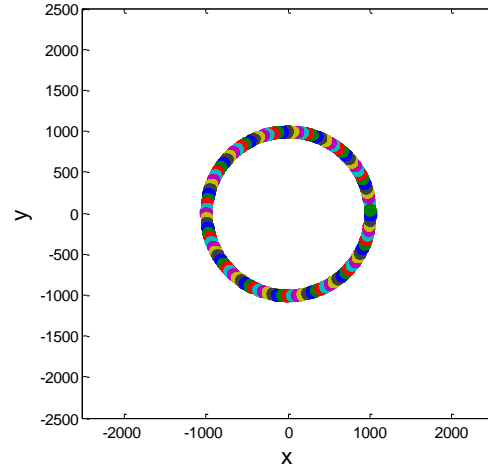


Figure 8. Numerical solution with leap frog method

V. ERROR ANALYSIS

Computational cost Table 1 represents the computational CPU cost of six time integral schemes. Comparing the results, it is seen that RK4 CPU cost is larger than both velocity Verlet and leap frog, although all these three time stepping algorithms possess higher accuracy.

TABLE I. COMPARISON SIX METHODS OF CPU TIME COST

Method	CPU time
Euler forward	0.039
Modified Euler	0.079
RK2	0.076
RK4	0.159
Velocity Verlet	0.069
Leap Frog	0.063

Computational convergence rate We will use the following error measure in the L norm:

$$\text{error} = \sqrt{\frac{[\text{Var}(x_n) - \text{Var}(x_{\text{exact}})]^2}{\text{Var}(x_{\text{exact}})^2} + \frac{[\text{Var}(y_n) - \text{Var}(y_{\text{exact}})]^2}{\text{Var}(y_{\text{exact}})^2}}$$
(26)

where $Var(x)$ is the variance of the x particle coordinates; $Var(y)$ the variance of the y particle coordinates; (x_n, y_n) are the coordinates obtained numerically and (x_{exact}, y_{exact}) are the exact coordinates.

The N particles variance is a measure of the dispersion of the particle cluster and therefore, the error takes into account the artificial dispersion that the numerical method may generate.

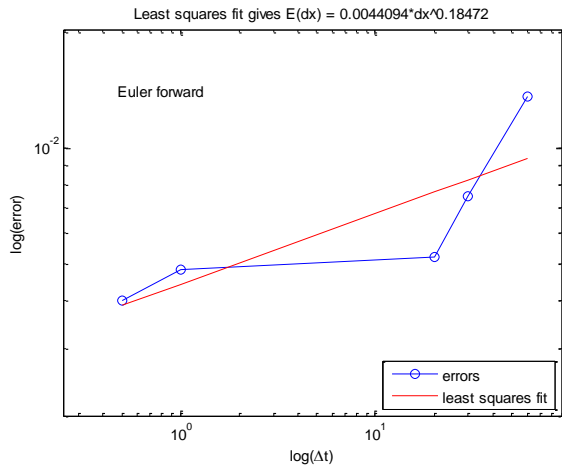
First, the paper calculates the error in different Δt for different time stepping schemes, by using loglog function draws convergence curve.

TABLE II. EULER ERROR VALUE FOR DIFFERENT TIME STEP

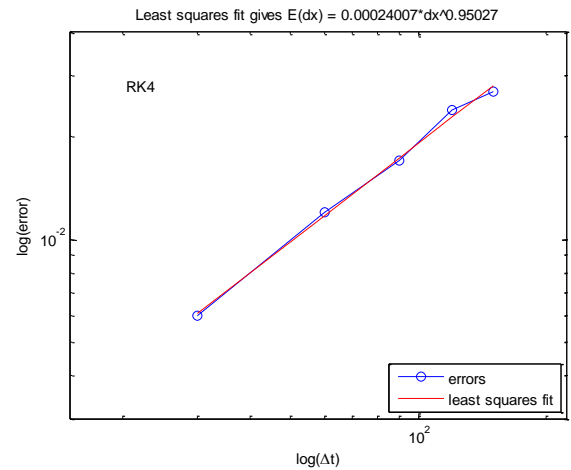
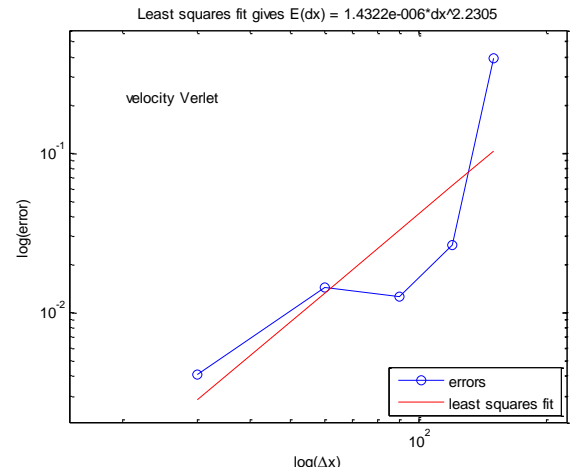
Δt (s) error	0.5	1	20	30	60
Euler	0.004	0.0048	0.0052	0.0075	0.0136

TABLE III. RK4 ERROR VALUE FOR DIFFERENT TIME STEP

Δt (s) error	30	60	90	120	150
RK4	0.006	0.012	0.017	0.0238	0.027
Velocity Verlet	0.0041	0.0144	0.0126	0.0266	0.3933

Figure 9. Euler method error curve for different Δt

Above tables give Euler, RK4 and velocity Verlet error value in different time step, and draw corresponding convergence rate curves, while results of other three methods are not represented herein for convenience. From Fig. 9, we see that convergence rate of Euler method is less than first-order, even if the time-accuracy of which can achieve two-order in theory. Similarly, according to Fig. 10 and Fig. 11, we can make the conclusion that convergence rate does not exactly equal to time-accuracy for the same method.

Figure 10. RK4 method error curve for different Δt Figure 11. Velocity Verlet method error curve for different Δt

VI. CONCLUSION

This paper compares the performance of six commonly used time stepping schemes for particle trajectory calculation, including the Euler forward method, modified Euler, second-order Runge-Kutta (RK2), fourth-order Runge-Kutta (RK4), velocity Verlet and leap-frog. Numerical analysis indicates that for problems with (nearly) uniform velocity fields, all schemes can give solutions with adequate accuracy, but the Euler method, modified Euler and RK2 may not predict accurate particle trajectories in certain highly non-uniform velocity fields. These methods may also introduce varying degrees of artificial dispersion that could lead to overestimation of spill area of particle clouds. On the other hand, the algorithms of RK4, velocity Verlet and leap frog can accurately calculate the particle trajectories without artificial dispersion. By analyzing the time-accuracy in theory and drawing convergence rate curves, we can make the conclusion that convergence rate does not exactly equal to time-accuracy for the same method.

ACKNOWLEDGEMENT

The work is supported by the National Natural Science Foundation of China (No. 51478305), SKL of HESS (No. HESS-1408) and Scientific Research Foundation for the Returned Overseas Chinese Scholars, State Education Ministry.

REFERENCES

- [1] G. R. Liu, M. B. Liu, *Smoothed Particle Hydrodynamics: A Meshfree Particle Method*, World Scientific, Singapore, 2003.
- [2] D. Violeau, *Fluid Mechanics and the SPH Method: Theory and Applications*, Oxford University Press, UK, 2012.
- [3] L. D. Libersky, A. G. Petschek, T. C. Carney, J. R. Hipp and F. A. Allardadi. High strain Lagrangian hydrodynamics: A three dimensional SPH code for dynamic material response. *J. Comput. Phys.*, 1993, 109: 67–75.
- [4] J. J. Monaghan. Simulating free surface flows with SPH[J]. *J. Comput. Phys.*, 1994, 110: 399–406.
- [5] Monaghan J J. Implicit SPH drag and dusty gas dynamics[J]. *J. Comput. Phys.*, 1997, 138(2): 801–820.
- [6] J. P. Morris. Analysis of Smoothed Particle Hydrodynamics with Applications. Ph.D. Thesis, Monash University, Melbourne, Australia, 1996.
- [7] P. W. Cleary and J. J. Monaghan. Conduction modelling using smoothed particle hydrodynamics. *J. Comput. Phys.*, 1999, 148: 227–264.
- [8] J. J. Monaghan. Smoothed particle hydrodynamic simulation of shear flow. *Mon. Not. R. Astron. Soc.*, 2006, 365: 199–213.
- [9] X. Y. Hu and N. A. Adams. A multi-phase SPH method for macroscopic and mesoscopic flows. *J. Comput. Phys.*, 2006, 213: 844–861.
- [10] X. Y. Hu and N. A. Adams. An incompressible multi-phase SPH method. *J. Comput. Phys.*, 2007, 227: 264–278.
- [11] J. J. Monaghan and A. Kocharyan. SPH simulation of multi-phase flow. *Comput. Phys. Commun.*, 1995, 87: 225–235.
- [12] M. G ómez-Gesteira, B. D. Rogers, R. A. Dalrymple and A. J. C. Crespo. State-of-the-art of classical SPH for free-surface flows. *J. Hydraul. Res.*, 2010, 48: 6–27.
- [13] R. Rook, M. Yıldız, S. Dost. Modeling transient heat transfer using SPH and implicit time integration[J]. *Numer. Heat Tr. B Fund.*, 2007, 51(1): 1-23.
- [14] Monaghan J J, Kocharyan A. SPH simulation of multi-phase flow[J]. *Comput. Phys. Commun.*, 1995, 87(1-2): 225-235.
- [15] Sun P., Ming F., Zhang A. Numerical simulation of interactions between free surface and rigid body using a robust SPH method[J]. *Ocean Eng.*, 2015, 98: 32-49.
- [16] Laibe G, Price D J. Dusty gas with smoothed particle hydrodynamics-II. Implicit timestepping and astrophysical drag regimes[J]. *Mon. Not. R. Astron. Soc.*, 2012, 420(3): 2365-2376.
- [17] Lucy L. B. A numerical approach to the testing of fission process. *Astron. J.*, 1977, 88: 1013–1024.
- [18] Gingold R. A. and Monaghan J. J. Smoothed particle hydrodynamics: Theory and application to non-spherical stars. *Mon. Not. R. Astron. Soc.*, 1977, 181: 375–389.
- [19] Benson A. J., Pearce F. R., Frenk C. S., Baugh C. M., Jenkins A. Comparison of semi-analytic and smoothed particle hydrodynamics for galaxy formation. *Mon. Not. R. Astron. Soc.*, 320 (2001), 261–280.
- [20] Couchman H. M. P., Thomas P. A., Pearce F. R. HYDRA: An adaptive mesh implementation of P3M-SPH. *Astrophys. J.*, 452 (1995), 797–813.
- [21] Pearce F. R., Jenkins C. S., Frenk J. M., Colberg J. M., Thomas P. A., White S. D. M., Couchman H. M. P., Peacock J. A., Efstathiou G. P. A simulation of galaxy formation and clustering. *Astrophys. J.*, 1999, 521(2): 99–102.
- [22] Rosswog S. Astrophysical smooth particle hydrodynamics. *New Astron. Rev.*, 2009, 53: 78–104.

Adaptive particle splitting in the Finite Volume Particle Method

Nathan J. Quinlan
 Mechanical Engineering
 National University of Ireland Galway
 nathan.quinlan@nuigalway.ie

Abstract—Adaptive or dynamic resolution in particle methods is a vital capability for reduction of computational cost. This paper presents a simple particle splitting scheme for the finite volume particle method (FVPM). The scheme is tested on a 2D dambreak flow, where the initial particle column is coarsely discretised, and particles are split to improve resolution as they approach the downstream wall. Results for pressure, overall flow structure and total energy show improvements over the baseline coarse static resolution, and in some cases show progress approach results obtained on a finer static discretisation. This work indicates that there is potential for FVPM to achieve particle simulations with dynamic resolution, which can lead to large reductions in particle numbers and computation time.

I. INTRODUCTION

The Finite Volume Particle Method (FVPM) is based on overlapping compactly supported particles, like standard SPH. It employs interparticle area analogous to intercell area in the classical mesh-based finite volume method. Since particle interactions are defined in terms of interparticle flux, the method maintains exact conservation in all circumstances, including and zero-order consistency in non-uniform particle size distribution. This property makes it a strong candidate for implementation of adaptive particle distribution by particle splitting, which has the potential to reduce computational costs by orders of magnitude in complex problems. Adaptive particle splitting has previously been developed in SPH by several authors [1, 2, 3]. Particle splitting in FVPM was first described by Jahanbakhsh *et al.* [1]. In this paper, some issues of adaptive particle refinement specific to FVPM are discussed. A simple splitting algorithm is presented and evaluated for a benchmark dambreak problem.

II. THE FINITE VOLUME PARTICLE METHOD

A. Principles

FVPM was first developed independently by Hietel *et al.* [2] and Ismagilov [3], and further analysed by Keck and Hietel [4] and Junk [5]. It is applied to equations written in the conservative form

$$\frac{\partial \mathbf{U}}{\partial t} + \nabla \cdot \mathbf{F}(\mathbf{U}) = 0, \quad (1)$$

where \mathbf{U} is the vector of conserved variables and \mathbf{F} is the flux. As in SPH, the domain is discretised by a set of particles, each associated with a compactly supported kernel-like particle

weight function $W_i(\mathbf{x}, t)$, which is used to define a test function

$$\psi_i(\mathbf{x}, t) = \frac{W_i(\mathbf{x}(t))}{\sum_j W_j(\mathbf{x}(t))}. \quad (2)$$

This function represents the fraction of an infinitesimal volume element at \mathbf{x} assigned to particle i . The total volume assigned to particle i is

$$V_i = \int \psi_i(\mathbf{x}, t) d\mathbf{x}. \quad (3)$$

The FVPM discrete version of Eq. (1) is

$$\frac{d}{dt}(\mathbf{U}_i V_i) + \sum_j \beta_{ij} \cdot \mathcal{G}(\mathbf{U}_i, \mathbf{U}_j, \dot{\mathbf{x}}_i, \dot{\mathbf{x}}_j) = 0, \quad (4)$$

where $\dot{\mathbf{x}}_i$ is the transport velocity of particle i , the flux function \mathcal{G} is a numerical approximation to \mathbf{F} , and β_{ij} denotes $\gamma_{ij} - \gamma_{ji}$, where

$$\gamma_{ij} = \int_{\Omega} \frac{W_i(\mathbf{x}) \nabla W_j(\mathbf{x})}{(\sum_k W_k(\mathbf{x}))^2} d\mathbf{x}. \quad (5)$$

(Boundary terms are omitted for brevity.)

FVPM is closely related to the mesh-based finite volume method, and the interparticle area β_{ij} , is strictly analogous to the cell-cell interface area. Formulation (5) ensures the properties $\beta_{ij} = -\beta_{ji}$, which ensures conservative particle-particle exchanges, and $\sum_j \beta_{ij} = 0$, which ensures that a uniform field remains steady (zero-order consistency). These properties are independent of any variation in particle size or smoothing length.

In original versions of FVPM, $W_i(\mathbf{x})$ was constructed using smooth polynomials. Equation 5 was integrated by Gaussian quadrature, introducing numerical errors and costly computation. Instead, $W_i(\mathbf{x})$ can be defined as a top-hat function, 1 inside the support of particle i and 0 elsewhere. This enable fast exact computation of β_{ij} , and facilitates modelling of free surfaces [6]. This approach was extended to 3D by Jahanbakhsh *et al.* [1], [7]. The normalising denominator of Eq. 5, $\sum_k W_k(\mathbf{x})$, also known as $\sigma(\mathbf{x})$, is then simply the number of particles that cover \mathbf{x} .

III. PARTICLE SPLITTING

Once a particle is selected for splitting, the basic problems are to position the new particles, determine their size, and initialise them with values of field variables.

Particle splitting in SPH was proposed by Lastiwka *et al.* [8]. Most recent work has followed the approach developed by Feldman and Bonet [9] and Lopez *et al.* [10]. These authors distributed the mass of the parent particle among the children, conserving mass, and copied the parents velocity to the children, thus conserving momentum and kinetic energy. By analysing error in the SPH approximations for density [9] and gradient [10] they optimised the distributions of position, size and mass of child particles.

In FVPM, there is less freedom to define the child particles. A particle's properties are approximations to weighted averages over the particle's support,

$$\phi_i V_i = \int_{\Omega_i} \psi_i(\mathbf{x}) \psi_i(\mathbf{x}) d\mathbf{x}. \quad (6)$$

In principle, therefore, the child particles should cover the same region as the parent. If the size of the child particles is chosen, their volume is determined by their geometric interaction with their neighbours. If the density is then set by some interpolation from the parent particles and other neighbours, the mass $m = \rho V$ is determined. Thus the mass of child particles is a function of their position and size and the local density field. This contrasts with SPH, where mass can be chosen independently of position and size. Fundamentally, this is because the size of the compact support is directly connected to particle volume in FVPM. In SPH, in contrast, the compact support defines only the numerical stencil, and has no physical meaning.

To examine conservation in particle splitting operations, three sets of particles are defined. The parent particles I are replaced with a set J of child particles by splitting. The neighbours of I and J constitute the set K . The total volume of the particles is unaffected by the splitting operation, since the volume of space they cover is unchanged. This can be expressed as

$$\sum_{j \in J} V'_j + \sum_{k \in K} V'_k = \sum_{i \in I} V_i + \sum_{k \in K} V_k, \quad (7)$$

where the prime denotes values after splitting. The mass of particle i is simply $\rho_i V_i$. Therefore the change in total mass due to splitting is

$$m' - m = \left(\sum_{i \in I} \rho_i V_i + \sum_{k \in K} \rho_k V_k \right) - \left(\sum_{j \in J} \rho'_j V'_j + \sum_{k \in K} \rho'_k V'_k \right) \quad (8)$$

This result is general. Now, specific details of a simple splitting procedure are introduced. Only one particle in the neighbourhood, i , is split at a time. The density of the daughter particles is set equal to that of the parent, and the density of other neighbours is unchanged ($\rho'_k = \rho_k$). Accounting for volume conservation according to Eq. (7), the change in mass then simplifies to:

$$m' - m = \sum_{k \in K} (\rho_k - \rho_i)(V'_k - V_k). \quad (9)$$

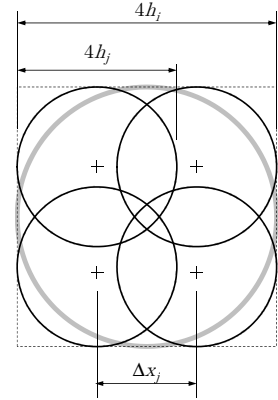


Fig. 1. A particle of smoothing length h_i replaced with 4 particles of smoothing length h_j at spacing Δx_j .

This shows that in general, mass is not conserved in splitting operations, and this is connected with the change in volume of each neighbouring particle, caused by change in the configuration of its neighbours. This suggests that conservation errors should be minimised by preserving the distribution of volume in the neighbourhood of a split.

Ideally, therefore, new particles should cover exactly the same volume as the original ones. For circular particles, it is impossible in general for multiple child particles to cover exactly the same support region, or have the same total particle volume, as the parent particle. In the present work, circular particles are split into 4 new particles, distributed as shown in Fig. 1, so that they approximately cover the support of the original particle.

For square particles, new particles can easily be aligned on the support of the original particle to ensure they cover its support exactly. Even then, however, it is not possible to preserve the particle volume (as distinct from support volume). There is a necessary overlap between the child particles, as illustrated in Fig. 2. A region originally covered by the parent and one neighbour, for example, may now be covered by two children and the neighbour. While volume of that region was originally shared between the parent and neighbour, $2/3$ of it is now assigned to the children and $1/3$ to the neighbour k . Consequently, even if the support region of the children is identical to that of the parent (impossible for circular particles), volume would effectively be reassigned from the original neighbours to the children, resulting in $\sum_{j \in J} V'_j > V_i$.

Overlap must be maintained between the newly generated particles to ensure that every point in the domain is covered by at least one particle. It is not possible, for example, to halve the particle size ($h_j/h_i = 1/2$) in a splitting operation, while approximating the original support volume with the new particles. As shown by Jahanbakhsh *et al.* [1], the relationship between particle size and overlap is

$$\frac{h_j}{h_i} = \frac{1}{1 + \frac{1}{4} \frac{\Delta x_j}{h_j}}, \quad (10)$$

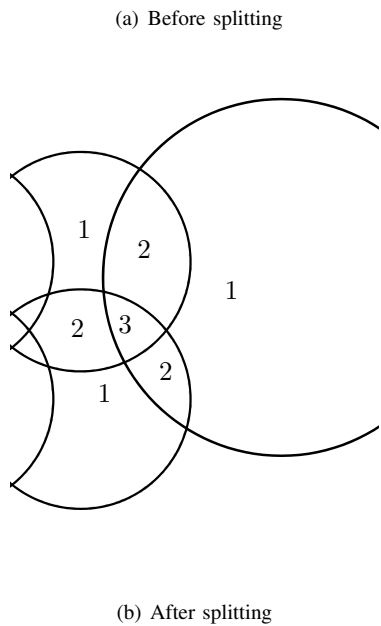
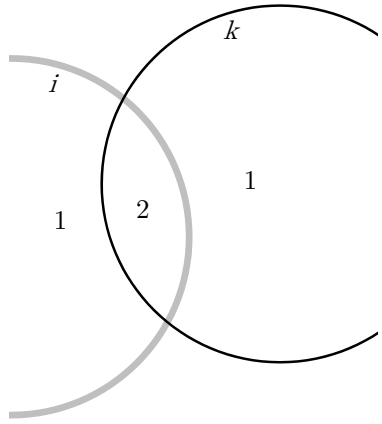


Fig. 2. A particle i with a lone neighbour j , showing values of σ (number of covering particles) (a) before and (b) after particle i is split into 4 child particles.

where the subscripts i and j denote original and new particles, respectively.

IV. APPLICATION TO DAMBREACK FLOW

Adaptive particle splitting has been applied in 2D simulations of the dambreak experiment of Lobovský *et al.* [11]. Water of depth H is retained behind a gate which is removed quickly. The initial length of the water column is $2H$ and the length of the tank is $5.366H$ (Fig. 3). Kinematics of the gate opening were found to have a significant effect. Gate motion was determined from a video provided by Lobovský *et al.* [11], and scaled to fit the median gate velocity reported over multiple experiments. The water is discretised with particles at initial spacing $\Delta x/H$ of 1/15, 1/30 or 1/60. Smoothing

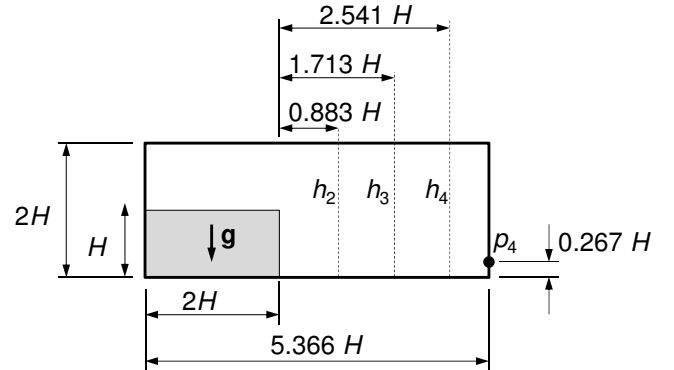


Fig. 3. Schematic diagram of the model of the dambreak experiment of Lobovský *et al.* [11], showing the location of pressure measurement p_4 .

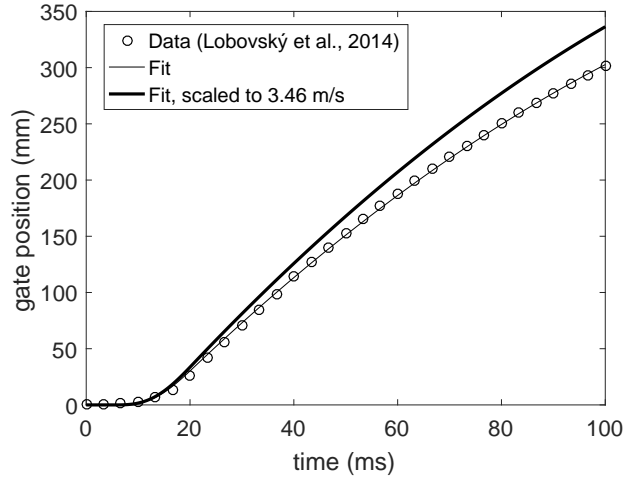


Fig. 4. Data from one experiment of Lobovský *et al.* [11] for gate removal, with fitted model, and the same model scaled to give the reported median gate velocity.

length is specified as $h/\Delta x = 0.48$, giving 9 neighbours per particle in the initial Cartesian distribution. In cases of static resolution, h remains constant throughout each simulation, with $H/h = 31.25, 62.5, 125$ corresponding to the three values above.

Adaptive refinement was tested in two configurations of an approach similar to that of Barcarolo *et al.* [12] in SPH simulations. The initial water column is modelled at the resolution of the coarsest static case considered, $H/\Delta x = 15$. Particles are split as they approach the downstream wall, where there is complex flow and high resolution is desirable. Refined particles are created with the same overlap ratio as the original particles, $h/\Delta x = 0.48$. According to Eq. (10), the child-to-parent particle size ratio is then $h_j/h_i = 0.643$. This splitting is applied as particles pass $x = 4H$, yielding particles with $H/h = 48.6$. In the second configuration, particles are split again at $x = 4.33H$, resulting in a final $H/h = 75.78$ near the wall. This particle size is intermediate between the medium ($H/h = 62.5$) and fine ($H/h = 125$) static resolution

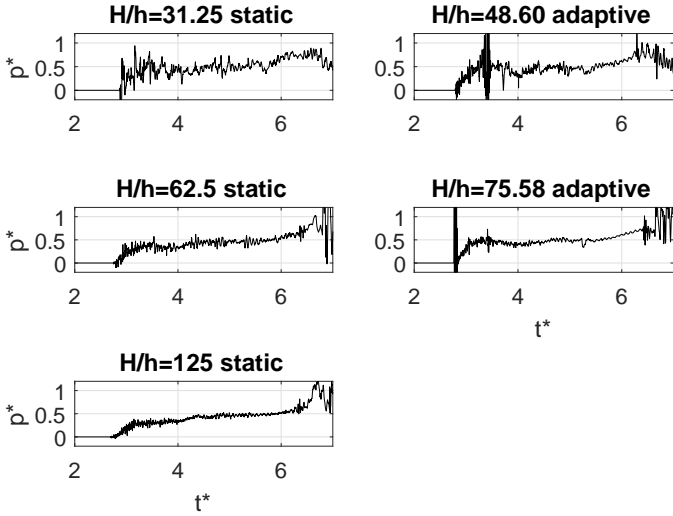


Fig. 6. Pressure at sensor p_4 on the downstream wall for various resolution configurations.

conditions.

In the results that follow, non-dimensionalised pressure and time are $p^* = p/(p_0 g H)$ and $t^* = t \sqrt{g/H}$, respectively. Energy is non-dimensionalised with respect to initial potential energy, $\rho_0 g H^3$.

Sample results are shown in Fig. 5. The coarsest static resolution under-resolves the splashing and wave-breaking structure predicted with the finest resolution. The adaptive simulation, however, predicts the structure correctly. It agrees with results of the fine static-resolution case on position of the wave tip, shape of the cavity under the plunging wave, and formation of a cavity on the downstream wall.

Pressure history at sensor p_4 (as defined in Fig. 3) is shown in Fig. 6. Adaptive cases include strong pressure transients at $t \simeq 3.5$ in single splitting and $t \simeq 2.5$ in the two-level splitting case. This requires further investigation. Otherwise, the computed pressure using adaptive distribution with final $H/h = 75.58$ is similar to results from the static distribution with $H/h = 62.5$. Adaptive refinement gives a marked reduction in high-frequency noise, relative to the coarse static case.

Quantitative results for potential energy are shown in Fig. 7 for the three static and two adaptive resolution tests. Late in the simulation, at $t^* \simeq 8$, resolution has a significant effect, and the result appears not to have converged fully at static resolution of $H/h = 125$. The adaptive cases, with initial H/h of 31.25 leading to final values of 48.60 and 75.58, follow the same trend. Significantly, the adaptive simulation with final $H/h = 75.58$ appears to perform slightly better than the case of static $H/h = 62.5$. Judged against convergence of cases with static resolution, simulations with adaptive refinement achieve satisfactory results using fine resolution in a restricted area.

Kinetic energy is plotted in Fig. 8. According to these results, adaptive simulations show a spurious spike in kinetic

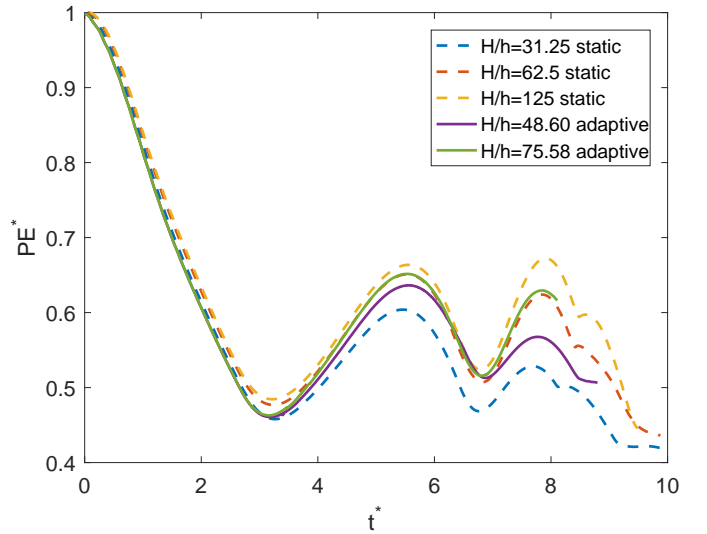


Fig. 7. Evolution of potential energy in the dambreak, for static and dynamic resolution.

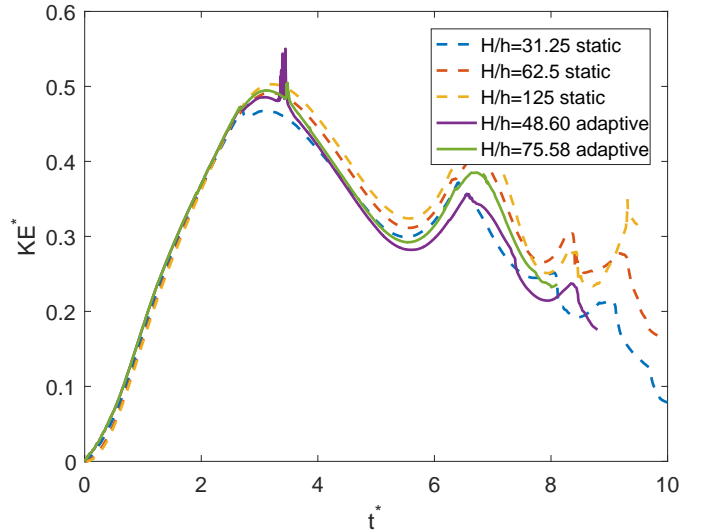


Fig. 8. Evolution of kinetic energy in the dambreak, for static and dynamic resolution.

energy at $t^* \simeq 3.5$, corresponding to a pressure spike. After that, results for adaptive resolution are similar to those for the coarsest static resolution. Later, around the second kinetic energy peak at $t \simeq 6.5$, the case with 2 splitting levels, final $H/h = 75.58$, is significantly more accurate than the simulation with static $H/h = 31.25$.

Mass conservation error is plotted in Fig. 9 for static and adaptive cases. With fine static resolution, there is a maximum global mass error of approximately 3×10^{-4} or 0.03%. This is due to the advection of free surface particles, which is determined by the momentum equation, without regard for mass conservation. Free-surface particles change the total volume of fluid when they move. (Fully immersed FVPM particles do not change the total volume as they move.) In addition to this mass error at the free surface, particle

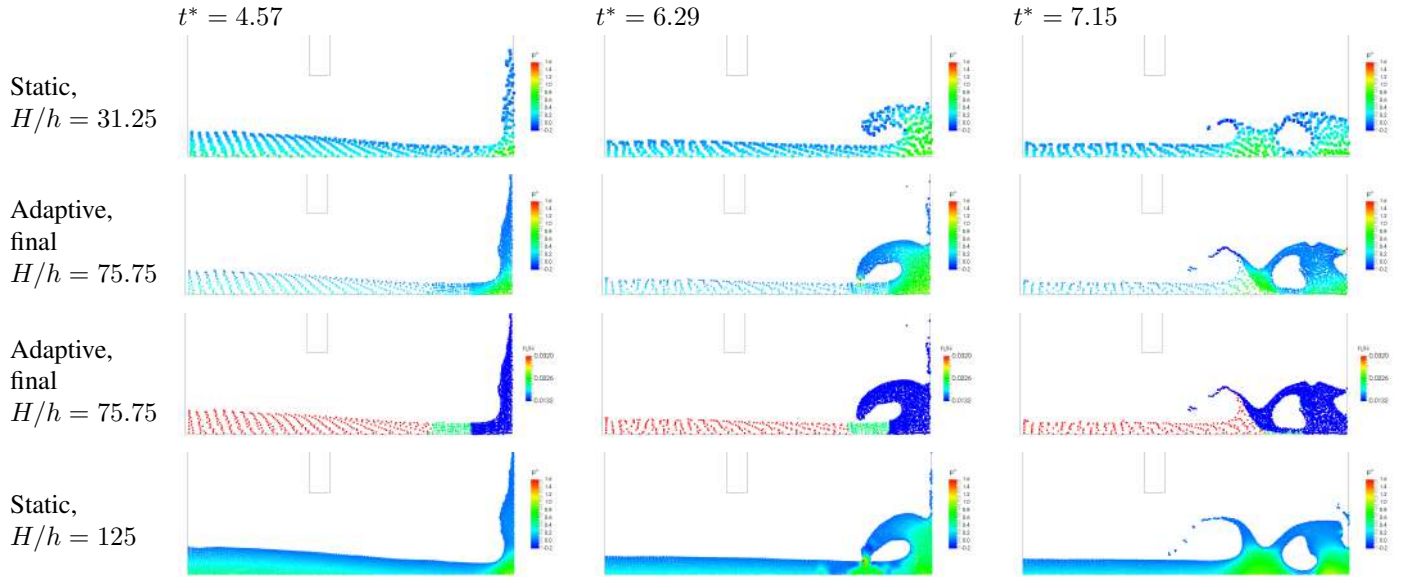


Fig. 5. Pressure distribution in dambreak simulations at various times for coarse ($H/\Delta x = 15, H/h = 31.25$) and fine ($H/\Delta x = 60, H/h = 125$) static resolution; pressure and smoothing length for adaptive resolution with initial $H/\Delta x = 15, H/h = 31.25$ and final $H/h = 75.58$. Smoothing length in the adaptive case is shown in the third row.

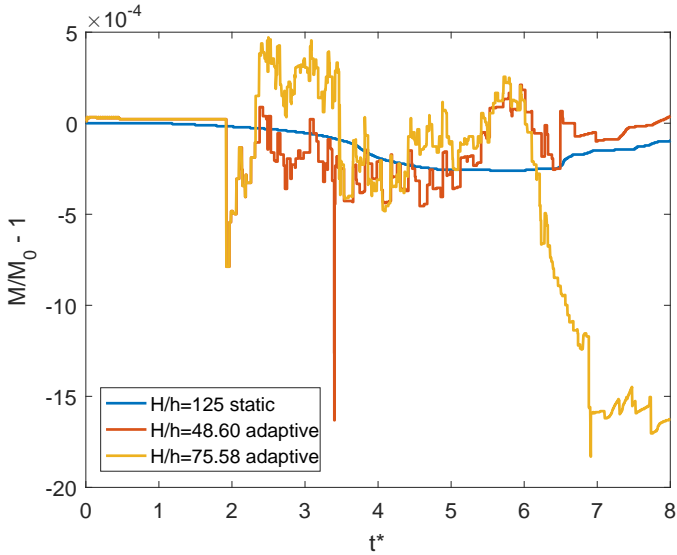


Fig. 9. Variation of system mass M , where M_0 is the initial mass.

splitting adds a further error. This is evident in the results for the two-level splitting simulation, where mass decreases by almost 20×10^{-4} . Arguably, this level of non-conservation is acceptable, particularly in this challenging test case in which more than half of all particles are split.

V. DISCUSSION AND CONCLUSIONS

In principle, FVPM is well placed to take advantage of adaptive particle resolution, because of its strong properties of conservation and consistency. A simple particle splitting scheme has been presented and tested for FVPM. Tests on a dambreak flow have shown that the method performs well

in terms of global quantities and structure. It approximates the results of static fine particle distributions while using a smaller total number of particles. In prediction of pressure in a downstream impact, the method can approach the results predicted by fine particle distributions, although some spurious transients are produced.

It has been shown theoretically that exact conservation cannot be maintained in particle-splitting operations. The effect on global mass conservation is small, but the effect of these errors on accuracy is not yet well understood. Further work is required to optimise the positioning of newly created child particles and interpolation from parent to child particles.

REFERENCES

- [1] E. Jahanbakhsh, C. Vessaz, A. Maertens, and F. Avellan, "Development of a finite volume particle method for 3-D fluid flow simulations," *Computer Methods in Applied Mechanics and Engineering*, vol. 298, pp. 80–107, 2016.
- [2] D. Hietel, K. Steiner, and J. Struckmeier, "A finite volume particle method for compressible flows," *Mathematical Models and Methods in Applied Science*, vol. 10, pp. 1363–1382, 2000.
- [3] T. Ismagilov, "Smooth volume integral conservation law and method for problems in Lagrangian coordinates," *Computational Mathematics and Mathematical Physics*, vol. 46, pp. 453–464, 2006.
- [4] R. Keck and D. Hietel, "A projection technique for incompressible flow in the meshless finite volume particle method," *Advances in Computational Mathematics*, vol. 23, pp. 143–169, 2005.
- [5] M. Junk, "Do finite volume methods need a mesh?" in *Meshfree Methods for Partial Differential Equations*, M. Griebel, Ed. Springer, 2003, pp. 223–238.
- [6] N. J. Quinlan and R. M. Nestor, "Fast exact evaluation of particle interaction vectors in the finite volume particle method," in *Meshfree Methods for Partial Differential Equations V*, ser. Lecture Notes in Computational Science and Engineering, M. Griebel and M. A. Schweitzer, Eds. Springer Berlin Heidelberg, 2011, vol. 79, pp. 219–234. [Online]. Available: http://dx.doi.org/10.1007/978-3-642-16229-9_14

- [7] E. Jahanbakhsh, A. Maertens, N. Quinlan, C. Vessaz, and F. Avellan, "Exact finite volume particle method with spherical-support kernels," *Computer Methods in Applied Mechanics and Engineering*, 2016.
- [8] M. Lastiwka, N. Quinlan, and M. Basa, "Adaptive particle distribution for smoothed particle hydrodynamics," *International Journal for Numerical Methods in Fluids*, vol. 47, pp. 1403–1409, 2005.
- [9] J. Feldman and J. Bonet, "Dynamic refinement and boundary contact forces in sph with applications in fluid flow problems," *International Journal for Numerical Methods in Engineering*, vol. 72, no. 3, pp. 295–324, 2007. [Online]. Available: <http://dx.doi.org/10.1002/nme.2010>
- [10] Y. Reyes López, D. Roose, and C. Recarey Morfa, "Dynamic particle refinement in sph: application to free surface flow and non-cohesive soil simulations," *Computational Mechanics*, vol. 51, no. 5, pp. 731–741, Jun. 2013. [Online]. Available: <http://dx.doi.org/10.1007/s00466-012-0748-0>
- [11] L. Lobovský, E. Botia-Vera, F. Castellana, J. Mas-Soler, and A. Souto-Iglesias, "Experimental investigation of dynamic pressure loads during dam break," *Journal of Fluids and Structures*, vol. 48, pp. 407–434, 2014.
- [12] D. A. Barcarolo, D. Le Touzé, G. Oger, and F. de Vuyst, "Adaptive particle refinement and derefinement applied to the smoothed particle hydrodynamics method," *Journal of Computational Physics*, vol. 273, pp. 640–657, Sep. 2014. [Online]. Available: <http://dx.doi.org/10.1016/j.jcp.2014.05.040>

The study on SPH method with space variable smoothing length and its applications to multi-phase flow

Wenkui Shi Yanming Shen Jianqiang Chen*

Computational Aerodynamics Institute

China Aerodynamics Research and Development Center

Mianyang, China

621000

Abstract—The smoothed particle method has unique advantages in simulating interfacial deformation. However, a constant smoothing length in whole flow field is widely used in early SPH simulations, leading to a defect of low computational efficiency. In order to improve the computational efficiency and space resolution, particle diffusion distribution models are proposed in this paper. Then each particle is assigned to an independent smoothing length and mass, and the SPH method with the space variable smoothing length is used to solve the problems. In addition, because linked-list search algorithm is not suitable for dealing with variable smoothing length problems, a more robust and effective balanced ADT (alternating digital tree) search algorithm was established. The methods and models were validated by three cases about two-dimensional air bubble rising problem, asymmetric wedge water entry problem and three-dimensional space capsule's water recovery problem. The results showed that, with a reasonable particle distribution model, the calculated results are consistent with the experimental results. It's worth noting that the particle numbers of both two-dimensional cases are decreased by about 1/4 compared to uniform particle distribution, and the total computational times are reduced by about 25%. For three-dimensional space capsule water entry case, the particle number is decreased by about 3/5, and the total computational time is reduced by about 60%. This indicates that the SPH method with space variable smoothing length can improve the computational efficiency obviously while ensuring the computational accuracy, which is suitable to simulate the problems of complex engineering such as three-dimensional multi-phase flow and water impact.

I. INTRODUCTION

Smoothed particle hydrodynamics [1,2] is a flexible Lagrangian and meshless technique for CFD simulations initially designed for astrophysics problems. This method has been then adapted in order to include the presence of a free surface in fluid flow simulations [3], and finally turned out to be an interesting tool for describing fluid mechanics and solid mechanics problems. Thanks to its meshless and Lagrangian characteristics, simulations of multi-media, multiphase, unsteady, fluid-solid interaction, interfacial deformation and strong nonlinearity can be easily handled.

However, the computational cost is a disadvantage of SPH. In this method, smoothing length h is one of the important variables of the kernel function, which directly

affects the computational efficiency and precision when solving engineering problems. A fixed h [4] was widely adopted in early SPH simulations, consequently a uniform particle distribution model used in whole flow field, and would furthermore not take full advantages of the particle local distribution. With the computational problem becoming more and more complex, the number of particles is becoming larger and larger, which results in a serious reduction in computational efficiency and a huge computational cost.

To reduce the number of particles and consequently the CPU cost, the density of particle distribution should be targeted according to the importance of position in the flow field. Similar to the grid-based numerical method, dense particles are distributed in the region of concern, such as impact location, while relatively sparse particles are distributed in other regions. Besides, each particle is assigned to an independent smoothing length^[5] and mass^[6].

SPH method with variable smoothing length mainly consists of two forms of smoothing length varying with time and space. Considering both the consistency and accuracy, an SPH method with local variable smoothing length algorithms was presented by Benz [7], which adapts h according to the density of particles. The resulting equations can be discretized by the SPH approximation or can be computed by other parallel differential equations. Evard [8] also proposed the local variable smoothing length algorithms in SPH when solving the three-dimensional universe aerodynamic problems. In his study, he pointed out the ∇h effects and this kind of effects can be ignored safely if the smoothing length varies slowly in space. Springel [9] and Monaghan [10] adopted similar idea to treat the inconsistent problems of varying smoothing length, which improves the relationship between the smoothing length and density. In addition, SPH equations including fully variable smoothing length was proposed by Qiang [11]. Compared to reference [9] and [10], the adaptive symmetrical kernel estimation algorithm was adopted in his study.

In the above studies, the smoothing length changes mainly with time, and consequently changes with space. And their main purpose was to improve the accuracy of calculation. Then in order to improve the calculation efficiency by using irregular particle distribution, a framework for adaptively inserting and removing particles

with SPH was proposed by Martin^[12], which was used to solve shock tube problem. Besides, Barcarolo^[13] developed a more specific adaptive particle refinement and derefinement method for SPH. In his study, he also gave the global kernel gradient refinement error for the kernel gradient. However, for particle adaptive method, how to guarantee the conservation of physical quantities is still a difficult problem.

This paper focuses on improving the computational efficiency and space resolution. Firstly, proper particle distribution models are proposed, then independent smoothing length and mass are assigned to each particle. Some techniques are also adopted to ensure the symmetry of particle interaction. Besides, a balanced ADT (alternating digital tree) search algorithm is proposed to deal with variable smoothing length problems. Finally, this method is successfully applied to simulate multiphase flow problems such as gas-liquid and fluid-solid interaction.

II. SPH EQUATIONS WITH VARIABLE SMOOTHING LENGTH

As in SPH method, for a given particle i and located at the point \mathbf{x}_i , the interpolated value of the quantity f can be written as

$$\langle f(x_i) \rangle = \sum_{j=1}^N \frac{m_j}{\rho_j} f(x_j) W_{ij} \quad (1)$$

Where $W_{ij} = W(x_i - x_j, h)$ is the weighting interpolation formula or smoothing kernel with h . The differentiable form of the interpolant of the function f according to (1) allows us to express a gradient as

$$\langle \nabla \bullet f(x_i) \rangle = \sum_{j=1}^N m_j \frac{f(x_j)}{\rho_j} \nabla_i W_{ij} \quad (2)$$

A. Initial Parameters Assignment for Particles and Symmetrize interactions

Initial particle distribution is determined according to the importance degree of position in the flow field. Then the density of same type particle remains the same, and the water particle pressure satisfies the hydrostatic equilibrium state. It's noteworthy that particle mass is proportional to its own area or volume^[14] (Fig. 1). Besides, typical interparticle distance Δx is nonuniform, so the ratio of the smoothing length of each particle to its own Δx is determined so that the particle number in interpolation circle almost remains same, that is $h = 1.23\Delta x$ ^[15].

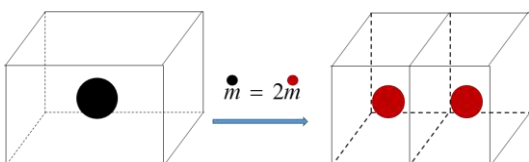


Figure 1. initial mass distribution

When the particles are not uniformly distributed, the smoothing length of particle i and particle j may not be equal. This refers to that the influence domain of particle i may include particle j , but the influence domain of particle j may not include particle i . Consequently, particles do not conserve linear momentum since $\vec{F}_{ij} \neq -\vec{F}_{ji}$. So some technologies are needed to ensure the symmetry of interactions between particles.

Firstly, the average value of smoothing length is used to determine the particle interaction pairs in nearest neighbour particle search,

$$h_{ij} = \frac{h_i + h_j}{2} \quad (3)$$

Then the kernel and its derivatives can be obtained by substituting (3) into the kernel after the particle pairs are determined,

$$\begin{aligned} W_{ij} &= W(r_{ij}, h_{ij}) \\ \nabla_i W_{ij} &= \frac{\mathbf{x}_{ij}}{r_{ij}} \frac{\partial W(r_{ij}, h_{ij})}{r_{ij}} \end{aligned} \quad (4)$$

Finally, the SPH equations with space variable smoothing length can be obtained by substituting (4) into SPH system,

$$\left\{ \begin{array}{l} \frac{d\rho_i}{dt} = \sum_{j=1}^N \frac{m_j \rho_i}{\rho_j} v_{ij}^\beta \cdot \frac{\partial W(r_{ij}, h_{ij})}{\partial x_i^\beta} \\ \frac{dv_i^\alpha}{dt} = \sum_{j=1}^N m_j \left(\frac{\sigma_i^{\alpha\beta} + \sigma_j^{\alpha\beta}}{\rho_i \rho_j} + \Pi_{ij} \right) \frac{\partial W(r_{ij}, h_{ij})}{\partial x_i^\beta} \\ \frac{de_i}{dt} = \frac{1}{2} \sum_{j=1}^N m_j \left(\frac{\sigma_i^{\alpha\beta} + \sigma_j^{\alpha\beta}}{\rho_i \rho_j} + \Pi_{ij} \right) v_{ij}^\beta \cdot \frac{\partial W(r_{ij}, h_{ij})}{\partial x_i^\beta} + H_i \end{array} \right. \quad (5)$$

With $\sigma_i^{\alpha\beta}$ total stress tensor. Π_{ij} artificial viscosity, it not only provides the necessary dissipation of the shockwave surface, but also prevents the non-physical penetration when the particles are close to each other. H_i artificial heat, v_{ij} Velocity difference between particles. The density, momentum and energy of the particles are interpolated by all particles in the supporting domain.

One of the main SPH features consists in considering any fluid flow as compressible, resulting in the use of an equation of state. In this paper, the following equation^[3] was used:

$$p = B \left(\left(\frac{\rho}{\rho_0} \right)^r - 1 \right) \quad (6)$$

called Tait's equation, linking the pressure to the density and allowing the above system of equations to be closed.

The constant B refers to the sound speed in the fluid medium and comes from $c_0^2 = \frac{dp}{d\rho} \Big|_{\rho=\rho_0}$, that is $B = \frac{c_0^2 \rho_0}{\gamma}$, where c_0 is the nominal value of the chosen sound speed, ρ_0 the nominal density value and γ the polytropic constant.

B. Balanced ADT Search Algorithm

There are three nearest neighbour particle search algorithm commonly used in SPH method. All-pair search algorithm is very simple, but its efficiency is too low. Linked-list search algorithm is the most widely used method at present, and it's effective when the smoothing length is spatial constant. However, its robustness is low, especially not suitable for dealing with variable smoothing length problems.

For space variable smoothing length algorithm, a balanced ADT method is proposed in this paper. Its main idea is to establish a balanced tree structure. In the original form, partitions for the ADT were chosen by geometrically bisecting the point set and the resulting sub-regions [16]. However, since the particles are non-uniformly distributed in the search space, the partition is located at a position that corresponds to the median location in the sorted list, assigning half of the list to each child. Then, on the above basis, the maximum problem domain is recursively divided into cells, until each cell contains only one particle (Fig. 2).

After the tree structure is completed, the nearest neighbour particle search can be carried out. For the given particle i , take the particle i as the center and surround it with a cube with a length of $2K h_i$. Then according to the traversal algorithm, the points that lie inside the searching cube can be found. Finally, check whether these points are in interpolation circle of point I . Its order of complexity is $O(N \lg N)$.

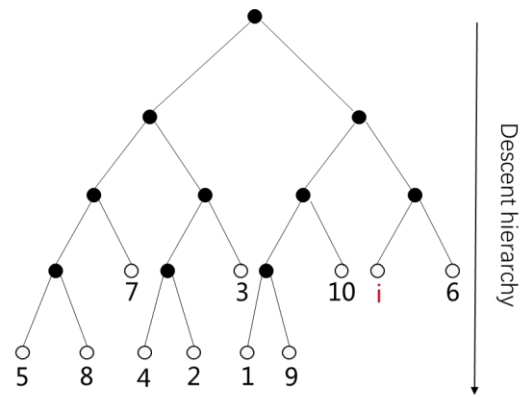
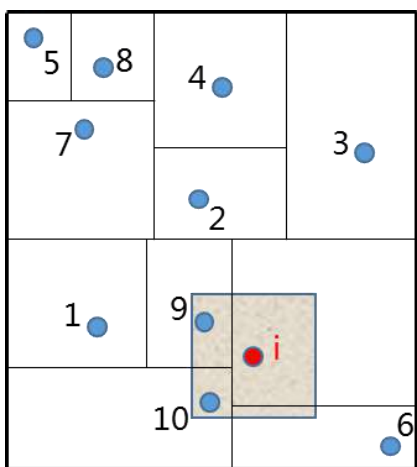
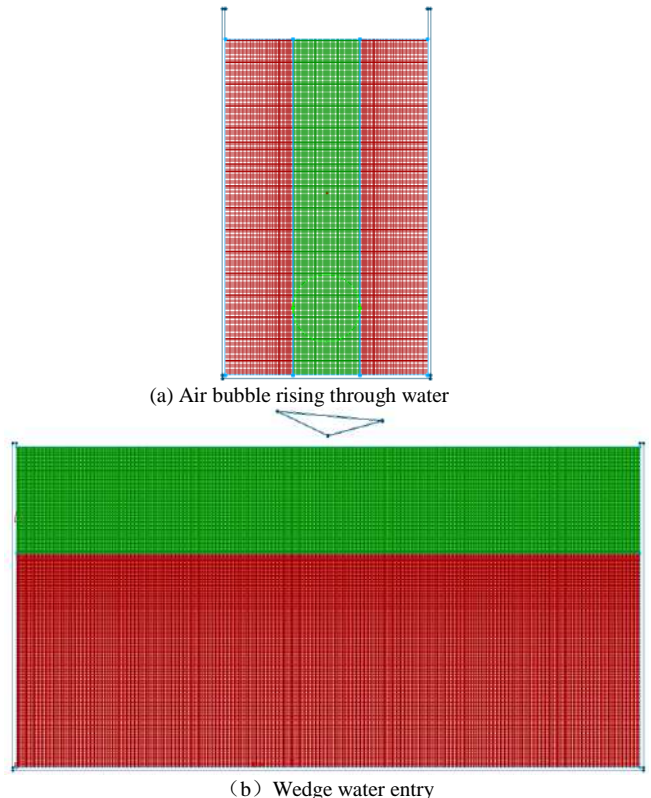
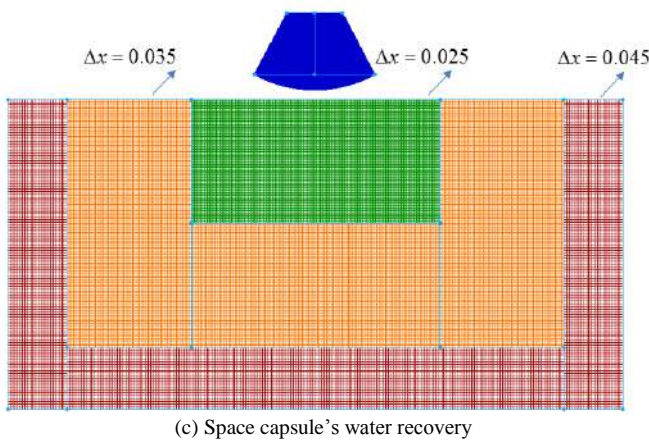


Figure 2 Construction of a balanced ADT and tree search algorithm

C. Particle Diffusion Distribution Model

In the past, SPH with constant smoothing length were widely used, which leading to a uniform particle distribution model used for the whole flow field. In this paper, a particle diffusion distribution model is adopted. That's to say, dense particles are distributed in the region of concern, while relatively sparse particles are distributed in other regions. Particle diffusion distribution models of several cases throughout this study are show in Fig. 3.





(c) Space capsule's water recovery

Figure 3 Particle diffusion distribution models

In two-dimensional air bubble rising case, the bubble with a radius of R rises vertically and symmetrically. The shapes and positions are the key information we need to focus on when bubble rising. Thus when designing the initial particle distribution of particle, the flow field is divided into three parts. The particles in the middle section are uniformly distributed ($\Delta x / R = 0.05$), while lateral spacing between two particles on both sides increase gradually from the middle. Then the maximum lateral space is $\Delta x / R = 0.144$, and the particle number are reduced by 25% compared to uniform particle distribution.

In asymmetric wedge water entry case, the peak value of impact load and the maximum angular acceleration are the information that we pay close attention to. When designing the initial distribution of particles, the flow field is divided into two parts. The upper particles are regular distributed ($\Delta x = 0.005$), while the vertical inter-particle distance of the lower particles gradually increases from the dividing line. Then the maximum vertical inter-particle distance is 0.015, and the particle number are reduced by 25% compared to uniform particle distribution.

In three-dimensional space capsule water entry case, the depth of water is 5m, while length and width are 10m. The peak value of the impact load directly threatens the structural safety and astronaut personal safety, which is the focus of our attention. Therefore, the flow field is divided into three parts when designing initial particle distribution, and the inter-particle distance is 0.025, 0.035 and 0.045 respectively. Consequently, the particle number is reduced from more than 30 million to more than 13 million compared to uniform particle distribution.

III. RESULTS AND ANALYSIS

In order to verify the capabilities of the present method, several problems including two-dimensional and three-dimensional multiphase flow were tested. The following simulations were updated using a standard leapfrog integrator. And the first kind of particle model proposed by Liu^[17] was adopted to be the treatment of boundary conditions.

A. Two-dimensional air bubble rising

Air bubble rising is a typical gas-liquid two-phase free surface flow. The circular bubble rises gradually under the action of floatation, accompanied by bubble deforming and even breaking. In the process, the pressure drag and surface tension are complicated. The test case sketched in Fig. 4: a circular bubble of fluid Y is free to rise through the initially quiescent heavier fluid X. The considered density ratio is $\rho_X : \rho_Y = 1000 : 1$.

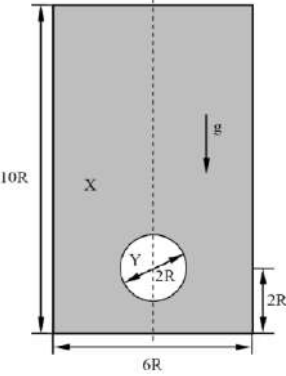
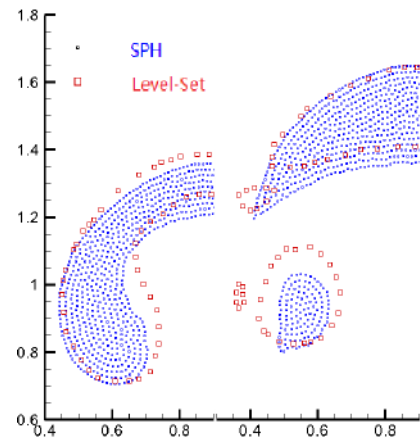


Figure 4 Two-dimensional air bubble rising

Firstly, the uniform particle distribution model was adopted to simulate this case with traditional SPH method. The ratio of the uniform particle spacing to radius R is $\Delta x / R = 0.05$. Then the number of particles used in this simulation is $N=24940$. For interfacial flow, the pressure needed to be continuous across the interface. So in the state equation, we selected $c_X / (gR)^{1/2} = 14$, $\gamma_X = 7$, resulting in $c_Y / (gR)^{1/2} = 198$, $\gamma_Y = 1.4$. Surface tension term is presented in the form of reference^[18]. Fig. 5 shows the comparison between the calculated results and the Level-Set results^[19]. It can be seen that the shapes and positions of the bubble match well at different times. So the program is effective for simulating gas-liquid two-phase flow problems.

Figure 5 Comparison of calculation results between SPH and Level-Set
(left to right: $t \sqrt{g / R} = 3.2, 4.8$)

On the basis of the above, in order to improve the computational efficiency, the particle diffusion distribution

model (Fig. 3(a)) was adopted. Then the particle number is 19120, decreases by about 1/4 compared to uniform distribution model. Other parameters are consistent with above. Fig. 6 shows how space variable smoothing length algorithm improves the precision of results when using the particle diffusion distribution model. The red dots are the result calculated by uniform particle distribution model in Fig. 5. If we still use traditional SPH method when adopting particle diffusion distribution model (green points), then a bad result will be got. However, if the space variable smoothing length algorithm is added to SPH method (black dots), then it can be seen that bubble positions and shapes match well with the results obtained by uniform particle distribution model.

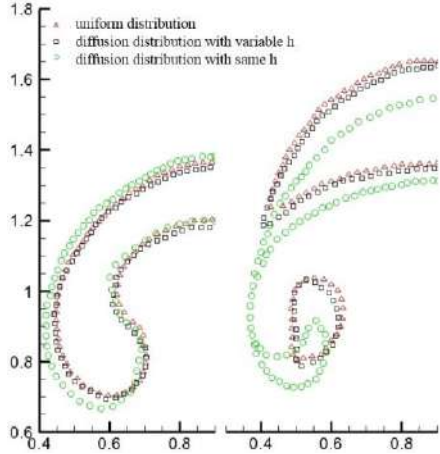


Figure 6 Effects of particle diffusion distribution model and space variable smoothing length algorithm

Table 1 shows the computational efficiency comparison between two distribution models. In order to avoid the interference caused by multicore parallel, single core is used for testing. Besides, the balanced ADT search algorithm mentioned in section 2 was used to test searching time. Computing time equals total time minus searching time. The result shows that total time decreases by almost 1/4, and the computational efficiency is greatly improved.

Table 1 Computational efficiency comparison between uniform and diffusion distribution models

models 1000 steps \	Diffusion model (19120 particles)	Uniform model (24940 particles)	Time ratio
Computing time	36.27s	49.06s	73.9%
Searching time	62.28s	79.32s	78.5%
Total time	98.55s	128.38s	76.8%

B. Asymmetric wedge water entry

Wedge water entry impact is a typical fluid-solid interaction problem. The water impact problem with initial heel angle is coupled with large deformation and multi-degree of freedom, so it is more difficult to simulate. The wedge initial position and some inertia properties of the

wedge is provided in Fig. 7. More details on this experiment can be found in [20].

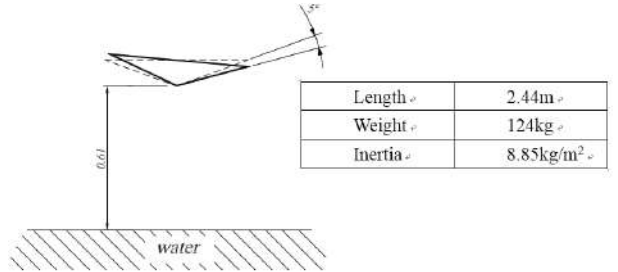


Figure 7 Test section description

Firstly, the uniform particle distribution model was used to simulate this case with traditional SPH method. The inter-particle distance is 0.005, and the number of particles is 265277. Time step is 10⁻⁵ second, and simulation was performed using 4 cores for parallel computation. The solid boundary pressure is obtained by SPH approximation method. Besides, the effects of a completely free solid in interaction with water are calculated by using the method proposed by Oger [21]. Fig. 8 shows the comparison of vertical, angular acceleration and impact velocity time histories between SPH and experimental results. It can be seen that the program is valid for simulating fluid-solid interaction and interfacial deformation.

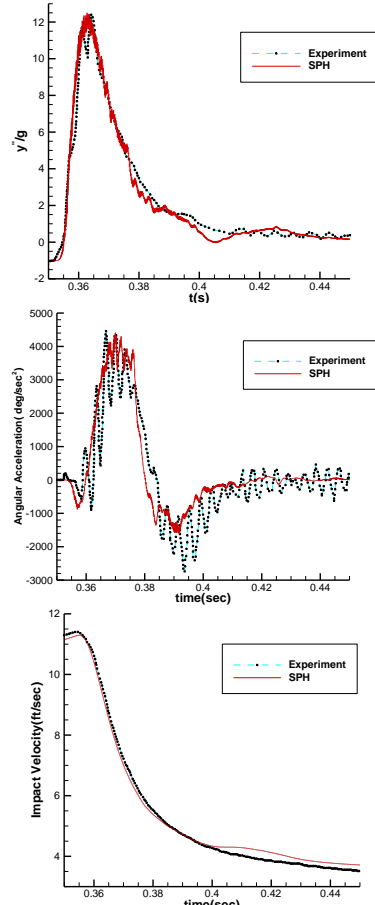


Figure 8 Vertical acceleration, angular acceleration and impact velocity validation

On the basis of above, the particle diffusion distribution model (Fig. 3(b)) was used to improve the computational efficiency. Then, the particle number is 199029, reducing by 25% compared to uniform particle distribution. The choice of other parameters is consistent with that above. Fig. 9 shows the improvement effects of space variable smoothing length algorithm on the result when using the particle diffusion distribution model. The calculation results obtained by traditional SPH method (green line) are poor, which is due to the strong instability caused by the nonuniform distribution of the particles. However, when adopting the space variable smoothing length algorithm (black line), its acceleration and angular acceleration are well matched with the results obtained by uniform distribution particle model (red line). Besides, the disturbance of flow field is well inhibited (Fig. 10). This is because the particle number in the support domain of every particle can be guaranteed to be basically consistent after each particle is assigned with an independent smoothing length. On the other hand, the symmetry of particle interaction is realized, satisfying Newton's third law.

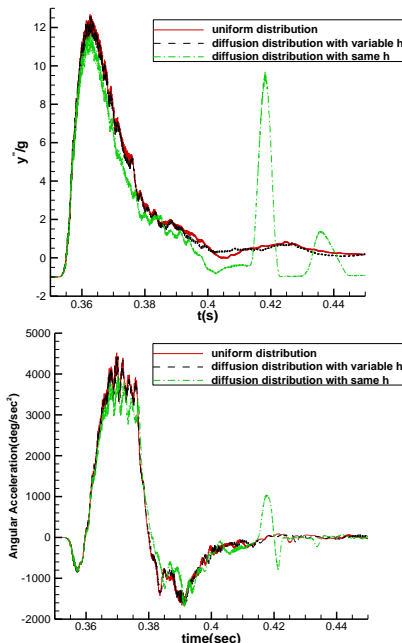


Figure 9 Effects of particle diffused distribution model and space variable smoothing length algorithm

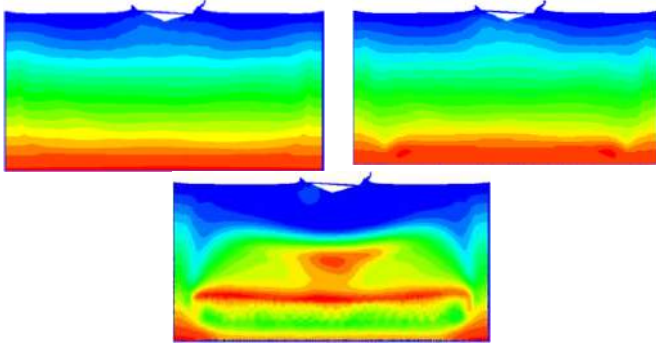


Figure 10 State of motion at 0.407s (upper left, right and lower down: uniform distribution; diffusion distribution with variable h, with same h)

Table 2 shows the computational efficiency comparison between two different distribution models. Similar to air bubble rising case, single core is used for testing. And the parameters in this table are the same as in air bubble rising case too. The result shows that total time decreases by almost 1/4, and the computational efficiency is greatly improved.

Table 2 Computational efficiency comparison between uniform and diffusion distribution models

models 2000 steps	Diffusion model (199029 particles)	Uniform model (265277 particles)	Time ratio
Computing time	832. 6s	1122. 1s	74. 2%
Searching time	1395. 7s	1846. 3s	75. 6%
Total time	2228. 3s	2968. 4s	75. 1%

C. Three-dimensional space capsule water entry

Through the above two two-dimensional cases, it can be seen that it is effective to improve the computational efficiency and spatial resolution by using SPH with space variable smoothing length method. Next, the computational model was extended to three dimensions. The re-entry capsule will suffer huge impact loads in the early stage of entering water, which will directly threaten the structural safety and astronaut safety. The calculation model is shown in Fig. 11. It needs to be explained that this example is mainly to investigate the validity of space variable smoothing length algorithm, so it does not focus on practical engineering. Considering the computational complexity, the geometry of the re-entry capsule is reduced by 2 times in all directions compared to NASA capsule model [22]. The depth of water is 5m, while length and width are 10m.

Mass	3330.0kg
Pitch deg	0
Vertical velocity	9.5m/s

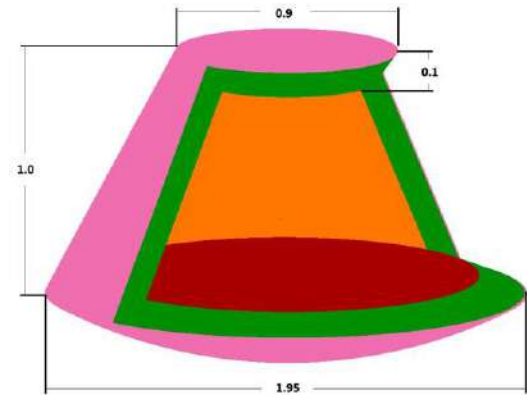


Figure 11 Test section description of space capsule

Firstly, the uniform particle distribution model was used to simulate this case with traditional SPH method. The

inter-particle distance is 0.025, and the particle number is 32678720. Time step is 10^{-5} second, and simulation was performed using 16 cores for parallel computation. The method of calculating solid boundary pressure and fluid-solid coupling module are the same as wedge water entry case. Then in order to improve computational efficiency, the particle diffusion distribution model (Fig. 3(c)) was adopted to simulate this case. And then the particle number is decreased to 13788282. The choice of other calculation parameters is consistent with uniform particle distribution model. Fig. 12 gives a comparison between the results of vertical acceleration obtained by two different distribution models. If the particle diffusion distribution model is calculated by traditional SPH method, the result (green line) is poor. However, if the space variable smoothing length algorithm is adopted (black line), the results are in good agreement with the uniform particle distribution model (red line) in both the peak load and the trend of vertical acceleration. This case verifies the effectiveness of the SPH method with space variable smoothing length in simulating 3D problems.

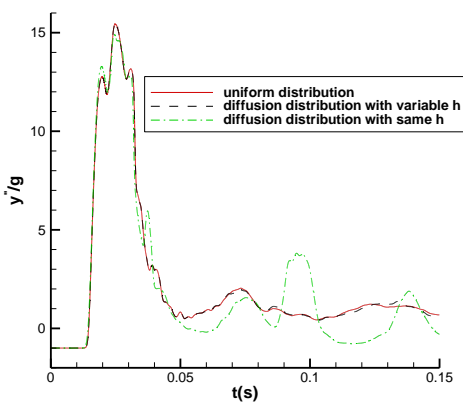


Figure 12 Effects of particle diffusion distribution model and space variable smoothing length algorithm on vertical acceleration

Table 3 shows the computational efficiency comparison between two distribution models. Because the number of particles is too large, single-core computing can't meet virtual memory requirement. Therefore, 16 cores are used for efficiency test. And the parameters in this table are the same as in air bubble rising case too. The result shows that total time decreases by almost 3/5, and the computational efficiency is greatly improved.

Table 3 Computational efficiency comparison between two models

models \ 500 steps	Diffusion model (13788282 particles)	Uniform model (32678720 particles)	Time ratio
Computing time	4832.0s	14768.0s	32.7%
Searching time	7968.0s	16720.0s	47.7%
Total time	12800.0s	31488.0s	40.7%

IV. CONCLUSION

In order to improve the computational efficiency and space resolution, Similar to the grid-based numerical method, a particle diffusion distribution model is proposed. This means dense particles are distributed in the desired accurate area or the region where physical quantities vary dramatically. Then each particle is assigned to an independent smoothing length and mass. Finally, the average value of smoothing length is used in the SPH formulation, therefore ensures the symmetry of particle interactions. Besides, a balanced ADT search algorithm was established to deal with the variable smoothing length program. The study shows that:

1. The particle diffusion model can effectively reduce the number of particles under the premise of keeping the calculation accuracy. But it also causes strong instability, which results in errors. Fortunately, the space smoothing length algorithm can restrain the strong instability that caused by the nonuniform distribution of particles. Good results are obtained both in bubble shape, location, or the peak value of impact load, and angular acceleration.

2. Under the reasonable particle distribution mode, computational cost can be greatly reduced by using space variable smoothing length algorithm, while the numerical accuracy is still held. This lays the foundation for solving three-dimensional complex engineering problem. However, further research is needed to optimize and standardize the particle distribution model, to suppress the instability caused by the variable smoothing length.

REFERENCES

- [1] Antoci C, Gallati M, Sibilla S. Numerical simulation of fluid-structure interaction by SPH [J]. Computers and Structures, 2007, 85:879-90.
- [2] Violeau D, Rogers B D. Smoothed particle hydrodynamics (SPH) for free-surface flows: past, present and future [J]. Journal of Hydraulic Research, 2016, 54(1): 1-26.
- [3] Monaghan J J. Simulating free surface flows with SPH [J]. Journal of computational physics, 1994, 110(2): 399-406.
- [4] Shen, Y M, Chen, J Q. Numerical tracking of interface in multifluid flow with smoothed particle hydrodynamics. Acta Aerodynamica Sinica, 2012, 30(2):157-161.
沈雁鸣, 陈坚强. SPH 方法对气液两相流自由界面运动的追踪模拟[J]. 空气动力学学报, 2012, 30(2):157-161.
- [5] Monaghan J J. Smoothed particle hydrodynamics [J]. Annual review of astronomy and astrophysics, 1992, 30 : 543-74.
- [6] Omidvar P, Stansby P K, Rogers B D. Wave body interaction in 2D using smoothed particle hydrodynamics (SPH) with variable particle mass[J]. International Journal for Numerical Methods in Fluids, 2012, 68(6): 686-705.
- [7] Benz W. Smooth particle hydrodynamics: A review. Numerical Modeling of Stellar Pulsation: Problems and Prospects; proceedings of the Proceedings of NATO Workshop, Les Arcs, France, F, 1989 [C].
- [8] Evrard AE. Beyond n-body: 3D cosmological gas dynamics. Mon. Not. R. astr. Soc., 1988; 235:911-934.
- [9] Springel V, Hernquist L. Cosmological smoothed particle hydrodynamics simulations the entropy equation [J]. Mon Not R Astron Soc, 2002, 333:649-64.

- [10] Monaghan J J. SPH compressible turbulence [J]. Monthly Notices of the Royal Astronomical Society, 2002, 335(3): 843-52.
- [11] Qiang H, Gao W. A new SPH equation including variable smoothing lengths aspects and its implementation[M]/Computational Mechanics. Springer, Berlin, Heidelberg, 2007: 343-343.
- [12] Martin L, Nathan Q, Basa M. Adaptive particle distribution for Smoothed Particle [J]. INTERNATIONAL JOURNAL FOR NUMERICAL METHODS IN FLUIDS, 2005, 47:1403-9.
- [13] Barcarolo, D. A., Le Touzé D., Oger, G., & De Vuyst, F. Adaptive particle refinement and derefinement applied to the smoothed particle hydrodynamics method [J]. Journal of Computational Physics, 2014, 273:640-57.
- [14] Omidvar P, Stansby P K, Rogers B D. SPH for 3D floating bodies using variable mass particle distribution[J]. International Journal for Numerical Methods in Fluids, 2013, 72(4): 427-452.
- [15] Shen, Y M, He K, Chen, J Q, & Yuan, X X. Numerical simulation of free surface flow impacting elastic structure with SPH uniform method [J]. JOURNAL OF VIBRATION AND SHOCK, 2015, 16: 60-5.
- [16] Bonet J, Peraire J. An alternating digital tree (ADT) algorithm for 3D geometric searching and intersection problems[J]. International Journal for Numerical Methods in Engineering, 1991, 31(1): 1-17.
- [17] Liu, M. B., Liu, G. R., Zong, Z., & Lam, K. Y. (2001, March). Numerical simulation of incompressible flows by SPH. In International Conference on Scientific & Engineering Computational, Beijing.
- [18] Morris J P. Simulating surface tension with smoothed particle hydrodynamics [J]. International journal for numerical methods in fluids, 2000, 33(3): 333-53.
- [19] Szewc, K., Taniere, A., Pozorski, J., & Minier, J. P. (2012). A study on application of smoothed particle hydrodynamics to multi-phase flows. International Journal of Nonlinear Sciences and Numerical Simulation, 13(6), 383-395.
- [20] Xu L, Troesch A W, Peterson R. Asymmetric hydrodynamic impact and dynamic response of vessels[J]. Journal of Offshore Mechanics and Arctic Engineering. Transactions of the ASME, 1999, 121(2): 83-89.
- [21] Oger, G., Doring, M., Alessandrini, B., & Ferrant, P. Two-dimensional SPH simulations of wedge water entries [J]. Journal of Computational Physics, 2006, 213:803-22.
- [22] Stubbs S M. Dynamic model investigation of water pressures and accelerations encountered during landings of the Apollo spacecraft [C]. National Aeronautics and Space Administration, Washington D. C., 1967.

A dynamic refinement strategy in SPH for simulating the water entry of an elastomer

Lu Wang Fei Xu Yang Yang

School of Aeronautics

Northwestern Polytechnical University

Xi'an, China

xufei@nwpu.edu.cn

Abstract—When we simulate a FSI problem by SPH method, the structure is generally treated as a rigid body rather than an elastomer. There is not much research on interaction between elastomers and fluid in SPH because the movable and deformable interface between two phases is difficult to be captured and handled. To describe the interface precisely, extensive particles are usually used which would cause great computational cost. Achieving variable resolution has been an important step in the development of the SPH method. Therefore, we apply the dynamic refinement strategy to achieve variable resolution in the water entry of an elastic beam. In this paper, we provide a general dynamic refinement strategy including the refinement pattern and the determination of relevant parameters. A new refinement criterion aiming at the FSI problems is proposed to describe the interface exactly. By comparisons of the slamming force, the surface pressure of elastic beam and the computational time, the results indicate that this new strategy can obtain remarkable accuracy and efficiency.

I. INTRODUCTION

Achieving variable resolution is an important step in the development of the SPH method. The method of refining particles is a general and effective access to obtain varied resolution. Different from the static refinement, dynamic refinement is performed locally with the evolution of the physical field. It can adaptively improve the spatial resolution and reduce the computational cost to some extent. The crucial factor for accuracy and efficiency in dynamic refinement is the criterion that decides whether the particle should be refined. Initially, the dynamic refinement in SPH was performed for an astrophysical simulation [1] using density as the criterion to change the resolution. With the expansion of this application for SPH, various refinement criteria and forms have appeared. In 2005, Martin Lastiwka [2] et al. used the velocity gradient to realize the adaptive refining/removal of particles when simulating a shock tube. When the velocity gradient of a particle is greater than a threshold value, additional particles would be added. In contrast, when the velocity gradient is less than a threshold value, the particle would be deleted. In 2007, J. Feldman [3] et al. considered the position of the particle as the criterion to complete the refinement for a Couette flow simulation. To define the adaptive conditions in a more accurate way, In 2009, He Yan [4] et al. presented a special function as the criterion that considered the distance to the free surface, the isotropic pressure and the number of particles

within the supported domain of the representative fluid particle. The strain of the particle usually is the refinement standard when the structure particle is involved in the refinement implementation [5]. Presently, only single-phase material has been considered for dynamic refinement, which is not enough for FSI two-phase problems.

With the employment of various materials in aviation, spaceflight and ship, the elastic effect of the entry of the structure into water becomes more and more prominent. Because of the nonlinearity and complex coupling process, there is no exact theory solution about the entry of an elastomer into water. As a fully Lagrangian particle method, SPH's major advantage for the FSI (Fluid-Structure Interaction) issue is that the highly nonlinear behaviour of the motion of the interface can be implicitly captured with a complex interface. In 2009, Oger et al. [6] studied the wedge which slammed into the water free surface by the FEM / SPH coupling method. In 2012, Campbell and Vignjevic [7] applied the FEM / SPH coupling method to simulate the damage of the helicopter metal floor when it slammed the water, as well as the response of the life buoy in the wave. In the same year, Panciroli [8] simulated the deformable wedge using FEM / SPH coupling method. In all of above studies, the deformable structures are dispersed by FEM elements, and the fluid is scattered by SPH particles. Nevertheless, FEM and SPH methods are completely different numerical methods. In the calculation process, it is necessary to exploit two solvers and provide additional management to connect two solvers, which complicates the computational process. Therefore, in this paper, SPH method is employed to simulate the deformable structure and fluid. In SPH simulation, as a carrier to transmit the interaction, the deformable interface between the fluid and elastic body needs to be caught in each time step, and a large number of particles need to be involved in the catch of the interface. Therefore, this paper intends to apply variable resolution SPH method to water entry of an elastomer.

II. SPH METHOD FOR WATER ENTRY OF AN ELASTOMER

A. SPH formulas for water

Assuming that the water is a weakly compressible viscous fluid, the control equations in Lagrangian form are:

$$\begin{cases} \frac{D\rho}{dt} = -\rho \operatorname{div}(\mathbf{u}) \\ \rho \frac{D\mathbf{u}}{Dt} = -\nabla P + \mathbf{F}_v + \mathbf{F}_s + \mathbf{F}_b \\ P = \frac{\rho_0 c_0^2}{\gamma} \left(\left(\frac{\rho_0}{\rho} \right)^\gamma - 1 \right) \\ \frac{D\mathbf{x}}{Dt} = \mathbf{u} \end{cases} \quad (1)$$

Where, ρ , P , \mathbf{x} and \mathbf{u} are density, pressure, displacement and velocity of the water, respectively. ρ_0 , c_0 and γ in state equation are reference density ($\rho_0 = 1000 \text{ kg/m}^3$), reference sound velocity and state constant of the water. \mathbf{F}_v , \mathbf{F}_s and \mathbf{F}_b are viscous forces, surface tension and volume force, respectively. Because the surface tension does not dominate in momentum equation, it is neglected.

The discrete control equations for water by using SPH method can be given by

$$\begin{cases} \frac{D\rho_i}{dt} = \rho_i \sum_j \frac{m_j}{\rho_j} (\mathbf{u}_i - \mathbf{u}_j) \nabla_i W_{ij} \\ \frac{D\mathbf{u}_i}{dt} = -\sum_j m_i \left(\frac{P_i}{\rho_i^2} + \frac{P_j}{\rho_j^2} + \Pi_{ij} \right) \nabla_i W_{ij} + \sum_s m_s \mathbf{x}_{is} f(|\mathbf{x}_{is}|) + \mathbf{g} \\ P_i = \frac{\rho_0 c_0^2}{\gamma} \left(\left(\frac{\rho_0}{\rho_i} \right)^\gamma - 1 \right) \\ \frac{D\mathbf{x}_i}{Dt} = \mathbf{u}_i \end{cases} \quad (2)$$

Where, j represents the particle within the supported domain of the particle i , s represents the structure particle within the supported domain of the particle i . ρ_i , m_i , \mathbf{u}_i , P_i and \mathbf{x}_i are density, mass, velocity, pressure, and displacement of the particle i , respectively. \mathbf{g} is the gravity, $\nabla_i W_{ij}$ is the gradient of kernel function. The viscosity Π_{ij} is artificial viscosity proposed by Monaghan[9]. It not only provides the essential dissipation, and can prevent particles from penetrating.

$$\begin{aligned} \Pi_{ij} &= \begin{cases} -\alpha_\Pi \bar{c}_{ij} \phi_{ij} + \beta_\Pi \phi_{ij}^2 \\ \bar{\rho}_{ij} \end{cases}, \mathbf{v}_{ij} \cdot \mathbf{x}_{ij} < 0 \\ \phi_{ij} &= \frac{h_{ij} \mathbf{v}_{ij} \cdot \mathbf{x}_{ij}}{|\mathbf{x}_{ij}|^2 + \varphi^2}, \mathbf{v}_{ij} = \mathbf{v}_i - \mathbf{v}_j, \mathbf{x}_{ij} = \mathbf{x}_i - \mathbf{x}_j \\ \bar{c}_{ij} &= \frac{1}{2}(c_i + c_j), \bar{\rho}_{ij} = \frac{1}{2}(\rho_i + \rho_j), h_{ij} = \frac{1}{2}(h_i + h_j) \end{aligned} \quad (3)$$

$f(|\mathbf{x}_{is}|)$ is the interaction force between water and structure, which is proposed by Monaghan[10] in 2009. It reflects the interaction between water and structure and prevents the penetration between fluid and structure. Expression of $f(|\mathbf{x}_{is}|)$ is

$$f(|\mathbf{x}_{is}|) = \begin{cases} \frac{B_{is} W(\mathbf{x}_{is})}{r_{is}^2}, & r_{is} \leq 2h \\ 0, & r_{is} > 2h \end{cases} \quad (4)$$

where $B_{is} = 0.02 c_i^2 / (m_i + m_s)$, and c_i is the sound speed of particle i .

B. SPH formulas for an elastomer

Similar to the water, the discrete control equation for elastomer can be given by:

$$\begin{cases} \frac{D\rho_i}{dt} = \rho_i \sum_j \frac{m_j}{\rho_j} (\mathbf{u}_i - \mathbf{u}_j) \nabla_i W_{ij} \\ \frac{D\mathbf{u}_i}{dt} = -\sum_j m_i \left(\frac{\sigma_i^{\alpha\beta}}{\rho_i^2} + \frac{\sigma_j^{\alpha\beta}}{\rho_j^2} + \Pi_{ij} \right) \nabla_i W_{ij} + \sum_f m_f \mathbf{x}_{if} f(|\mathbf{x}_{if}|) + \mathbf{g} \\ P_i = c^2 (\rho_i - \rho_{0i}) \\ \frac{D\mathbf{x}_i}{Dt} = \mathbf{u}_i \end{cases} \quad (5)$$

where, f represents the water particle within the supported domain of the particle i , $\sigma^{\alpha\beta}$ is the total stress tensor, it contains deviatoric stress $S^{\alpha\beta}$ and isotropic pressure P , which is given by (6).

$$\sigma^{\alpha\beta} = S^{\alpha\beta} - \delta^{\alpha\beta} P \quad (6)$$

The rate of deviatoric stress $S^{\alpha\beta}$ is

$$\frac{dS^{\alpha\beta}}{dt} = 2\mu(\dot{\epsilon}^{\alpha\beta} - \frac{1}{3}\delta^{\alpha\beta}\dot{\epsilon}^{\alpha\beta}) + S^{\alpha\gamma}\Omega^{\beta\gamma} + \Omega^{\alpha\gamma}S^{\gamma\beta} \quad (7)$$

Where μ is shear modulus, $\dot{\epsilon}^{\alpha\beta}$ is the rate of strain tensor, $\Omega^{\alpha\beta}$ is the rate of rotation tensor. By continuous medium mechanics, we can obtain:

$$\dot{\epsilon}^{\alpha\beta} = \frac{1}{2} \left(\frac{\partial v^\alpha}{\partial x^\beta} + \frac{\partial v^\beta}{\partial x^\alpha} \right) \quad (8)$$

$$\Omega^{\alpha\beta} = \frac{1}{2} \left(\frac{\partial v^\alpha}{\partial x^\beta} - \frac{\partial v^\beta}{\partial x^\alpha} \right) \quad (9)$$

The gradient of velocity is discretized and can be given by:

$$\left(\frac{\partial v^\alpha}{\partial x^\beta} \right)_i = \sum_{j=1}^N \frac{m_j}{\rho_j} (v_j^\alpha - v_i^\alpha) \nabla_i^\beta W_{ij} \quad (10)$$

The state equation in (5) can be used when the density and temperature change little for the structure.

III. DYNAMIC REFINEMENT IN SPH

The dynamic refinement in SPH usually is carried on locally with the evolution of the physical field. It could change the spatial resolution adaptively and decrease the computational cost under a certain accuracy. In order to implement dynamic refinement into the SPH framework, four main considerations need to be dealt with:

- Firstly, an appropriate criterion is very necessary, which efficiently identifies the candidate particles for refinement.
- Secondly, the refinement algorithm should preserve the basic properties of the entire system.
- Thirdly, the interaction between the coarse particles and fine particles must be consistent.
- Fourthly, a better computational accuracy and efficiency are required.

Based on above considerations, we would like to provide a general dynamic refinement strategy including the criterion, algorithm, interaction between the coarse particle and fine particle and other issues.

A. Criterion for refinement

The candidate particles for refinement should be identified depending on the type of problem. For water entry problem, as the reflection of the interaction between water and structure, $f(|\mathbf{x}_{if}|)$ and $f(|\mathbf{x}_{is}|)$ play a dominant role in the external force for water and structure. So there we select the interaction force as the criterion. That is:

$$f(|\mathbf{x}_{if}|) \neq 0 \text{ or } f(|\mathbf{x}_{is}|) \neq 0 \quad (11)$$

When $f(|\mathbf{x}_{if}|) \neq 0$ or $f(|\mathbf{x}_{is}|) \neq 0$, the particle i is translated into a candidate particle for refinement. From (4), we can know when the fluid and the structure particles close to each other until they enter mutual support domain, the fluid and structure particles are split. Since this criterion splits the particles at the nearby interface, application of the adaptive refinement will describe the fluid-solid interaction minutely.

B. Refinement algorithm

We assume the candidate refinement coarse particle as A , and its mass, position, velocity, and smoothing length are defined as m_A , \mathbf{x}_A , \mathbf{v}_A and h_A , respectively. The “daughter” fine particle of A is denoted as a , and its mass, position,

velocity, and smoothing length are defined as m_a , \mathbf{x}_a , \mathbf{v}_a and h_a , respectively. Particle refinement needs to meet the system conservation, such as: quality, angular momentum, line momentum, kinetic energy and potential energy conservation. A splitting algorithm satisfying the above properties is given: 1. The mass is evenly distributed among the fine particles after splitting; 2. The velocity remains unchanged; 3. The position of the “daughter” particle is symmetrical about the coarse particles. Generally, m_a , \mathbf{x}_a , \mathbf{v}_a and h_a could be determined by:

$$\begin{cases} m_a = \frac{1}{M} m_A \\ \mathbf{u}_a = \mathbf{u}_A \\ h_a = \alpha h_A \\ d_a = \varepsilon d_A \end{cases} \quad (12)$$

Where M is the number of fine particles generated from one coarse particle, and ε and α are the parameters to decide the spacing and smoothing length of the fine particles, whose range is $(0,1)$.

In this paper, square split form is employed, as shown in Fig.1.

C. Interaction between the coarse particle and fine particle

It is apparent that the smoothing lengths of the fine particle and the coarse particle are different. In the mutual searching region, it is possible to violate Newton's third law, so the smoothing length is forced to be taken as the average of h_A and h_a . This average implementation of the different smoothing lengths could conserve the interactions between the coarse and fine particles.

For the four considerations that need to be addressed and resolved in dynamic refinement, the first three have been described, and the fourth point would be verified in the simulation case.

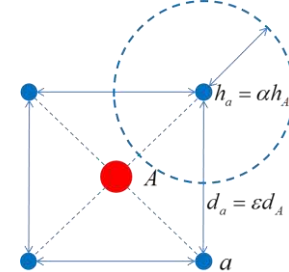


Figure 1. Splitting pattern in dynamic refinement strategy

D. other issues in dynamic refinement

Adjustment of the fine particle position. To avoid the position coincidence of the fine particles after the refinement implementation, the position will be adjusted by rotating iteration arithmetic.

Refinement level. For the constant accuracy, a lower refinement level is always recommended since it could decrease the cost and improve the stability of calculation.

IV. SIMULATION OF THE ENTRY OF AN ELASTIC BEAM INTO WATER

The process of the entry of an elastic structure into water, the interaction between the water and structure becomes more complicated due to the deformation of the elastomer when compared with the rigid body. In this section, the particle dynamic refinement strategy is applied to the entry of an elastic beam into water.

A. Numerical simulation models

This section studies the entry of an elastic aluminium beam at both ends with a constant speed into water, to explore the slamming force of the overall beam and the surface pressure of some special points. The size of the beam is shown in Fig.2, where $L = 1.2m$, $d = 0.04m$. Elastic modulus of material $E = 67.5GPa$, Poisson's ratio $\nu = 0.34$, density $\rho = 2700kg/m^3$. Both ends of the beam always be compelled with a constant downward speed $u = 30m/s$.

The numerical model is based on the following two assumptions: (1) the water is weakly compressible and the free surface is initially stationary. (2) The air isn't be considered in the model, and the surface tension, cavitation and air cushion effect are ignored. The size of the water region is $3m \times 2m$, and it could guarantee the reflection wave doesn't interfere with the structure during the period of impact. Both the beam and water are dispersed by SPH particles, and the particle spacing is $0.01m$, the smoothing length is $0.015m$. In addition, the water density is $1000kg/m^3$, the speeds of sound for water and beam are $1480m/s$ and $6305m/s$, respectively.

In SPH numerical model, as shown in Fig.3, there are solid walls around the water. The repulsive force exists between the wall particles and water particles to prevent penetration. To state the effect of the dynamic refinement strategy, we designed two models (no refinement and dynamic refinement) in SPH simulation as shown in Fig.4.

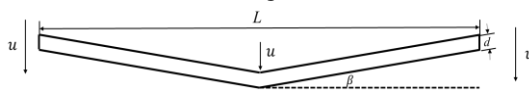


Figure 2. Model of beam

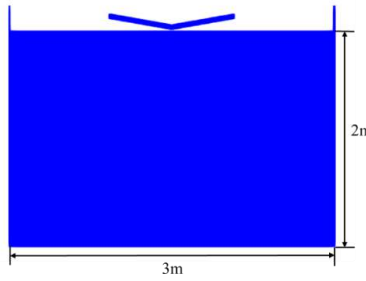
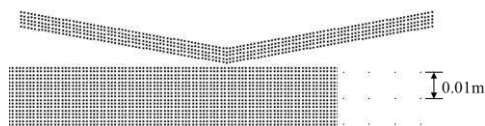
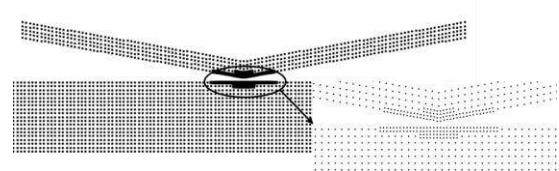


Figure 3. SPH model of the entry of an elastic beam into water



(a) No refinement model



(b) Dynamic refinement model
Figure 4. Two models for SPH simulation

B. Dynamic refinement strategy for water entry of an elastomer

According to the description for the implementation of dynamic refinement strategy in Section 3, when water and beam two-phase particles enter into the supported domain of each other, the two-phase particles are split, respectively. The split form of the elastomer particle is different from that of the rigid. As shown in Fig.5, the split degree α_0 for the rigid particle is constant while for the elastomer particle, the split degree α_i are required to be updated at each time step because of the deformation of the elastomer. The split degree α_i needs to guarantee the connection between two fine "daughter" particles is always parallel to the tangential τ of the coarse particle position.

C. Results and discussion

1) Slamming force

The slamming forces of the no refinement in SPH simulation, dynamic refinement in SPH simulation, SPH / FEM simulation in literature [11] and the analytical solution [12] are shown in the Fig.6. It is shown that: (1) In general, the trends of slamming forces in SPH simulation are almost consistent with the result of the literature [11], which shows that the SPH method could simulate the elastomer well. (2) The results of SPH simulation is smaller than that of the SPH / FEM simulation. This may be due to the different discrete ways for elastic beam in FEM and SPH methods. (3) When comparing the slamming forces of the dynamic refinement and no refinement in SPH simulation, it can be seen that the refinement of water and solid particles at the interface makes the peak value of the slamming force of the beam bigger, which is closer to the SPH / FEM and the theoretical value. This result is coincident with the rigid result that the force is overestimated in the dynamic refinement model. On one hand, that the smaller particle spacing leads to the bigger external force. On the other hand, the average length of the smoothing lengths between the coarse particles and fine particles makes the smoothing length of the fine particles larger, and the supported domain contains more particles.

If we just change the elastic beam into the rigid body, Fig.7 gives the slamming force of the water entry of a rigid and elastic beam. We can see that the peak value of the slamming force for elastic beam is smaller than rigid, and the trend of the force change is slower than rigid beam. This is because the elastic effect makes the kinetic energy transformed into the strain energy stored in the elastic body, which mitigates the water entry slamming force.

The comparison of the total stresses at X direction of the elastic between SPH simulation and the literature [11] when

its slamming force reached its peak value(at 2.5ms) are given in Fig.8. We can see that the tensile force effects on the upper part of the beam while compression force effects on the bottom part of the beam at that moment, which is consistent

with the results of the literature. From the value of the total stress, it can be seen that the strain could reach 10^{-3} order of magnitude, and the beam belongs to the small deformation.

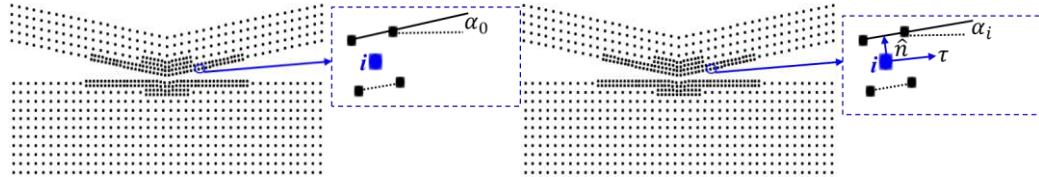


Figure 5. Particle split form of the dynamic refinement model in the entry of an rigid(Left)/elastic(Right) beam into water

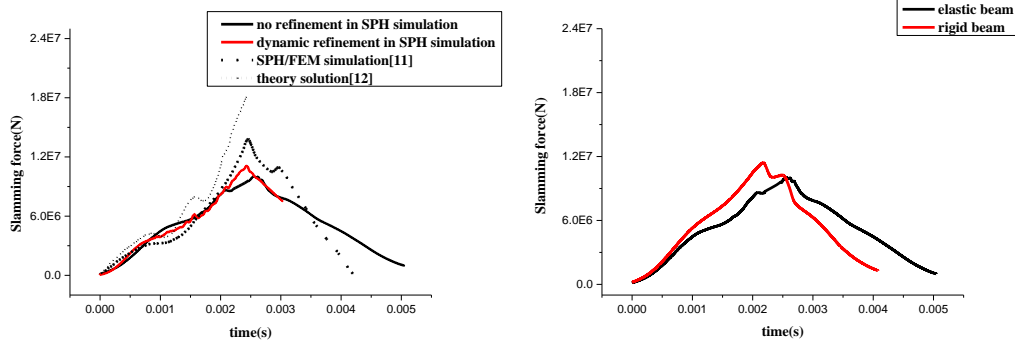


Figure 6. (Left)Slamming force of the elastic beam in no refinement simulation, dynamic refinement simulation, SPH / FEM simulation [11], the analytical solution [12]

Figure 7. (Right)Comparison of the slamming force between the water entry of a rigid and elastic beam

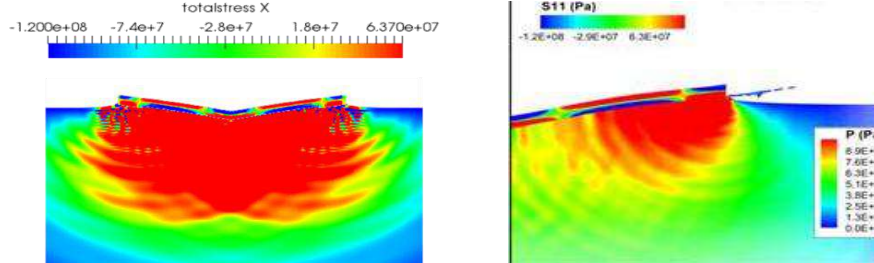


Figure 7. (Right)Comparison of the slamming force between the water entry of a rigid and elastic beam

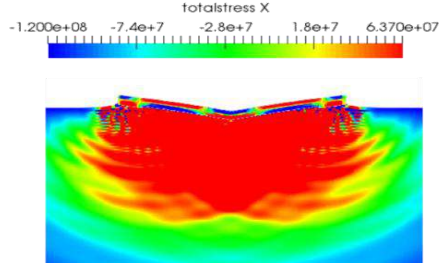


Figure 8. Total stress (X direction) of the elastic beam between SPH simulation(Left) and the literature [11] (Right)at $t=2.5$

2) Surface pressure

Because of the movable and deformable interface in water entry of an elastic beam, when extracting the surface pressure, the normal direction $\hat{\mathbf{n}}$ of the interface must be confirmed firstly at each time step[13]. To get the surface pressure at the point i of the beam, the repulsive force of the beam particles in the range of d length is superimposed and projected into the normal direction $\hat{\mathbf{n}}$ of particle i , and then divided by d to obtain the surface pressure of point i . Specific expression is given by (13), where s represents the solid particles within the range of d length.

$$P_i = \frac{F_i}{d} = \frac{\sum_s f_s \cdot \hat{\mathbf{n}}}{d} \quad (13)$$

The Fig.10 shows the pressure change curves at three points of A, B and C on the beam (see Fig.9). The comparison of

SPH simulation, SPH / FEM simulation[11] and the theoretical value[11] shows that (1) the trends of the pressure change are the same, which shows that the rationality of the method to extract the surface pressure for the elastic body. The pressure peak at point B is the smallest, and A, C two points are nearly same. This is because point B is located at the midpoint of the beam, and A, C two points are close to the fixed speed sides. (2) The surface pressures in SPH simulation are lower than SPH / FEM simulation and theory, which is also due to the different discrete ways.

Fig. 11 shows the comparison of the surface pressure distribution at different times between the dynamic refinement and no refinement models. It is can be seen that the surface pressure of dynamic refinement is larger than that of the no refinement, and the reasons have been explained in Section C.1). So the results of dynamic refinement are more consistent with the theoretical and SPH / FEM simulation results.

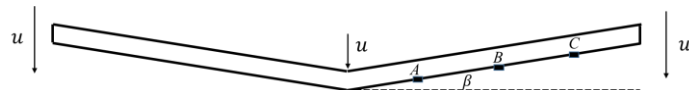


Figure 9. Three pressure measurement points on beam

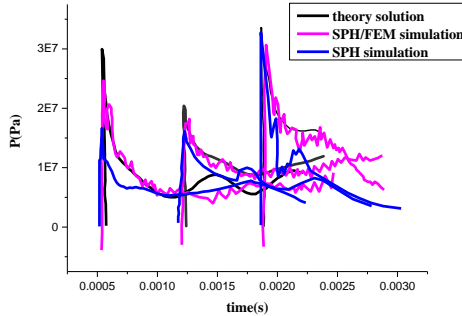


Figure 10. Pressure change curves at three points of A, B and C

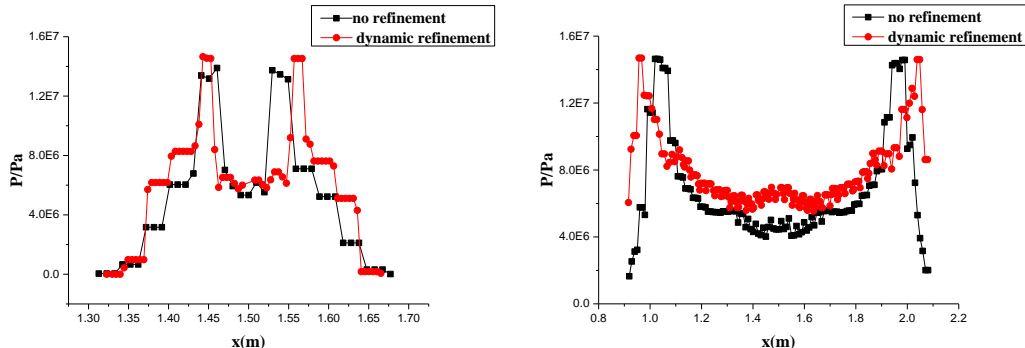


Figure 11. Comparison of the surface pressure distribution at different times(Left:0.05ms,Right:0.25ms) between the dynamic refinement and no refinement simulations

3) Computational efficiency

To explain the efficiency of the dynamic refinement strategy, we designed the total refinement model, which is identical to the no refinement model, while just the initial particle spacing is halved to match the “daughter” fine particles spacing in the dynamic refinement model. The computational time among no refinement, dynamic refinement and total refinement models in SPH simulations are compared. Table I gives the peak values of the slamming forces of elastic beam and the computational time for three conditions, which indicates that with an equivalent computational accuracy between the dynamic refinement and total refinement, the computation time for the dynamic refinement is much shorter. This result is coincident with the rigid result, demonstrating the efficiency of the dynamic refinement strategy.

TABLE I. COMPARISON OF PEAK VALUE OF SLAMMING FORCE AND CALCULATION TIME AMONG NO REFINEMENT, DYNAMIC REFINEMENT AND TOTAL REFINEMENT IN SPH SIMULATIONS

	peak value of slamming force(E7)	computational time (/no refinement)
No refinement	1.004	—
Dynamic refinement	1.111	1.059
Total refinement	1.108	3.891

V. CONCLUSION

Simulating the elastomer by SPH method is an extension application of SPH. In this paper, we use SPH method to simulate the water entry of an elastomer. Moreover, to deal with the interface more finely, the particle dynamic refinement is applied to the entry of the elastomer into water. This is also an important improvement for the dynamic refinement applied in SPH method. In this paper, a refinement strategy aiming at the elastic structure is proposed and the effectiveness of the strategy is illustrated. The results show that the slamming force and the surface pressure in the dynamic refinement simulation are remarkable, and the dynamic refinement reflects its high efficiency with an equivalent accuracy.

REFERENCES

- [1] Monaghan J.J., Varnas S. The dynamics of interstellar cloud complexes. Monthly Notices of the Royal Astronomical Society, 1988; 231(2):515-534.
- [2] Martin Lastiwka, Nathan Quinlan. Adaptive particle distribution for Smoothed Particle Hydrodynamics. International Journal for Numerical Methods in Fluids, 2005; 47:1403–1409.
- [3] J. Feldman, J. Bonet. Dynamic refinement and boundary contact forces in SPH with applications in fluid flow problems. International Journal for Numerical Methods in Engineering, 2007; 72:295–324.
- [4] He Yan, Zhangye Wang. Real-time fluid simulation with adaptive SPH. Computer Animation and Virtual Worlds, 2009; 20: 417–426.

- [5] Yaidel R. L., Disk Roose. Dynamic particle refinement in SPH: Application to free surface flow and non-cohesive soil simulations. *Computational Mechanics*, 2013; 51:731-741.
- [6] Oger G, Ferrant P, Alessandrini B. Free surface impact in a biphasic SPH simulation. Longyearbyen, France: 20th International Workshop on Water Waves and Floating Bodies, 2005: 1-4.
- [7] Campbell J C, Vignjevic R. Simulating structural response to water impact. *International Journal of Impact Engineering*, 2012, 49: 1-10.
- [8] Panciroli, R., et al., Hydroelasticity in water-entry problems: Comparison between experimental and SPH results. *Composite Structures*, 2012. 94(2): 532-539.
- [9] Monaghan J. J.. Smoothed Particle Hydrodynamics and Its Diverse Applications. *Annual Review of Fluid Mechanics*, 2012; 44:323-46.
- [10] Monaghan J. J., Kajtar J.. SPH particle boundary forces for arbitrary boundaries. *Computer Physics Communications*, 2009; 180(10): 1811–1820.
- [11] Fourey G, Oger G, Le Touz éD, et al. Violent fluid-structure interaction simulations using a coupled SPH/FEM method[C]. IOP Conference Series: Materials Science and Engineering. IOP Publishing, 2010, 10(1): 012041.
- [12] Scolan Y M. Hydroelastic behaviour of a conical shell impacting on a quiescent-free surface of an incompressible liquid[J]. *Journal of Sound and Vibration*, 2004, 277(1): 163-203.
- [13] S. Adami, X. Hu, N. Adams, A new surface-tension formulation for multi-phase SPH using a reproducing divergence approximation. *J. Comput. Phys.* 229 (2010) 5011–5021.

Simulating shock waves with corrective smoothed particle method (CSPM)

Chunying HUANG & Jie DENG
School of Computer Software,
Tianjin University,
Tianjin 300350, China
cyhuang416@163.com

Yaxuan XING,
School of Mathematics,
Tianjin University,
Tianjin 300350, China

Darcy Q.HOU*,
School of Computer Science and Technology,
Tianjin University,
Tianjin 300350, China
Corresponding author: qhou@tju.edu.cn

Arris S. TIJSSELING,
Department of Mathematics and Computer Science
Eindhoven University of Technology,
Eindhoven MB5600, The Netherlands

Abstract—Numerically solving the compressible Euler equations plays a vital role in many science and engineering problems, among which the shock wave is one of the benchmark tests providing a valuable evaluation for numerical methods. To identify prototypical meshless particle methods for simulating shock waves, the current state-of-the-art smoothed particle hydrodynamics (SPH) schemes with kernel corrections are reviewed. Among others, the corrective smoothed particle method (CSPM) is an early version of the traditional SPH with corrected kernel and has achieved many successes in both solid and fluid dynamics problems. It solves the boundary deficiency and tensile instability problems in traditional SPH. However, there are some drawbacks to deal with huge shocks problems due to the denominator normalization in CSPM. In this paper, together with the SPH summation form of the continuity equation, the CSPM is applied to simulate shock waves and good results were obtained. To enhance the performance, a variable smoothing length was also employed, together with virtual particle method for boundaries.

I. INTRODUCTION

The fluid flow and their applications have a huge impact on our daily life. For example, the brothers Wright successfully achieved the first flight by the principle of lift on a wing at beginning of 20th century. Edward Lorentz published the famous chaos theory to introduce the research on the air flow in the atmosphere. One can firmly believe that the research results about fluid flow are of utmost importance for our real life.

Compressible, inviscid, one-dimensional, unsteady flow can be described by using the Euler equations. Considering allowing discontinuities in the solution, one-dimensional Euler equations are used to describe the shock tube problem, a typical problem in gas dynamics. It is also known as Riemann problem.

Different numerical methods have been used to solve the one-dimensional Euler equations, including the meshless smoothed particle hydrodynamics (SPH) method [1]. In order to improve the accuracy, the corrective particle method (CSPM) proposed by Chen [2, 3], is a generalization of the standard SPH [4], and has achieved many successes in both solid [5, 6] and fluid dynamics problems [7]. It is quite straightforward compared with

other modifications of SPH, and it can solve the boundary deficiency and tensile instability problems [3]. However, as shown by Liu and Liu [8], CSPM cannot give the corrective results for the shock tube problem. Based on Taylor series expansion borrowed from CSPM, Liu and Liu [8] developed the discontinuous SPH (DSPH) for shock waves. However, an effective discontinuity detection algorithm has to be used, which would be rather challenging in multi-dimensional problems.

In this paper, considering the defect of CSPM caused by denominator largely departing from unity in the shock tube problem, we change the approximation of the continuity equation with the SPH density summation form. It is found that CSPM leads to reasonable results. Sect. II is devoted to the governing equations. Sect. III introduces the basics of CSPM, variable smoothing length and numerical boundary conditions. Sect. IV presents the discrete Euler equations. Sect. V gives some numerical results and discussion. Finally, conclusion is listed in Sect. VI.

II. GOVERNING EQUATIONS

The governing equations for one-dimensional shock wave comprise the following continuity equation, momentum equation and energy equation [9] :

$$\frac{d\rho}{dt} = -\rho \frac{\partial V}{\partial x} \quad (1)$$

$$\frac{dV}{dt} = -\frac{1}{\rho} \frac{\partial P}{\partial x} \quad (2)$$

$$\frac{de}{dt} = -\frac{P}{\rho} \frac{\partial V}{\partial x} \quad (3)$$

where P is pressure, V is velocity, ρ is density, and e is thermal energy. These three equations need to be closed with an equation of state (EOS). For shock tube problem, usually we use the ideal gas EOS:

$$P = (\gamma - 1)\rho e \quad (4)$$

in which γ is the adiabatic index.

Discrete Euler equations derived by using meshless particle methods are given in section IV. In the next section, as theoretical basis, there is a brief description of the corrective smoothed particle method (CSPM).

III. NUMERICAL METHOD

A. Corrective Smoothed Particle Method

The CSPM is a generalization of the standard SPH. Considering the key idea of CSPM is to expand the kernel estimate into the Taylor series, the CSPM is quite easy to be understood and applied. Moreover, CSPM remedies the two drawbacks of SPH method, i.e. boundary deficiency and tensile instability [5,6].

Since shock wave is modelled herein as a one-dimensional problem, only those formulations that are required in the current work are briefly presented. For the basic theory of CSPM in multi-space dimensions, see e.g. [5, 6].

An arbitrary smooth function $f(x)$ can be expanded into a Taylor series in the neighbourhood of point x_i as

$$f(x) = f(x_i) + f'(x_i)(x - x_i) + \frac{1}{2} f''(x_i)(x - x_i)^2 + \dots \quad (5)$$

Multiplying a smoothing function or kernel function $W_i(x)$ at both sides of the expansion yields

$$\begin{aligned} f(x)W_i(x) &= f(x_i)W_i(x) + f'(x_i)(x - x_i)W_i(x) \\ &+ \frac{1}{2} f''(x_i)(x - x_i)^2 W_i(x) + \dots \end{aligned} \quad (6)$$

where $W_i(x) = W(x_i - x, h)$ and h is the smoothing length.

Integrating over the whole computational domain Ω gives

$$\begin{aligned} \int_{\Omega} f(x)W_i(x)dx &= f(x_i) \int_{\Omega} W_i(x)dx \\ &+ f'(x_i) \int_{\Omega} (x - x_i)W_i(x)dx + \frac{1}{2} f''(x_i) \int_{\Omega} (x - x_i)^2 W_i(x)dx + \dots \end{aligned} \quad (7)$$

Neglecting all the derivative terms, we can get the corrective kernel estimate of the function $f(x)$ at point x_i ,

$$f(x_i) = \frac{\int_{\Omega} f(x)W_i(x)dx}{\int_{\Omega} W_i(x)dx} \quad (8)$$

Particularly, for formulation (8), due to the normalization condition of the kernel, we get

$$f(x_i) = \int_{\Omega} f(x)W_i(x)dx \quad (9)$$

In meshless methods, continuous media are divided into a finite number of parts that are called as particles. Each particle carries a mass, density, velocity, pressure and other

properties depending on the specific problem. During motion, a particle is allowed to change its density and volume, but the mass keeps constant. Representing the spatial domain Ω by particles in formulation (8) and (9), we obtain

$$f(x_i) = \frac{\sum_{j=1}^N f(x_j)W_i(x_j)m_j/\rho_j}{\sum_{j=1}^N W_i(x_j)m_j/\rho_j} \quad (10)$$

$$f(x_i) = \sum_{j=1}^N f(x_j)W_i(x_j)m_j/\rho_j \quad (11)$$

Formulations (10) and (11) are the discrete forms of the function approximation in CSPM and SPH method.

The CSPM estimate of the first derivative of $f(x)$ at a point x_i can be obtained as [5]

$$f'(x_i) = \frac{\int_{\Omega} f(x)W'_i(x)dx}{\int_{\Omega} (x - x_i)W'_i(x)dx} \quad (12)$$

or in discrete form as

$$f'(x_i) = \frac{\sum_{j=1}^N f(x_j)W'_i(x_j)m_j/\rho_j}{\sum_{j=1}^N (x_j - x_i)W'_i(x_j)m_j/\rho_j} \quad (13)$$

in which $W'_i(x_j) = W'(x_i - x_j, h)$ and N is the total number of particles in the domain.

Particularly, due to the normalization condition of the kernel gradient, we get the SPH approximation of the first derivative of $f(x)$ in discrete form as

$$f'(x_i) = \sum_{j=1}^N f(x_j)W'_i(x_j)m_j/\rho_j \quad (14)$$

To get higher accuracy for the first derivative approximation, the following form is obtained by using the identity $\rho f' = (\rho f)' - f \rho'$,

$$f'(x_i) = \frac{\frac{1}{\rho_i} \sum_{j=1}^N m_j(f(x_j) - f(x_i))W'_i(x_j)}{\sum_{j=1}^N (x_j - x_i)W'_i(x_j)m_j/\rho_j} \quad (15)$$

In this form, first derivative will be exactly reproduced when the function $f(x)$ is a constant. Moreover, it is difficult to build a consistent representation for energy equation. Therefore, it is a common practice in CSPM form to employ the symmetrized representation

$$f'(x_i) = \frac{\rho_i \sum_{j=1}^N m_j \left(\frac{f(x_i)}{\rho_i^2} + \frac{f(x_j)}{\rho_j^2} \right) W'_i(x_j)}{\sum_{j=1}^N (x_j - x_i) W'_i(x_j) m_j / \rho_j} \quad (16)$$

The first derivative of the function in CSPM is second-order accurate for the interior points and first-order accurate for the points near or on the boundary [5]

Similarly, due to the normalization condition of the kernel gradient, we get the SPH approximation of the first derivative in two forms as

$$f'(x_i) = \frac{1}{\rho_i} \sum_{j=1}^N m_j (f(x_j) - f(x_i)) W'_i(x_j) \quad (17)$$

$$f'(x_i) = \rho_i \sum_{j=1}^N m_j \left(\frac{f_i}{\rho_i^2} + \frac{f_j}{\rho_j^2} \right) W'_i(x_j) \quad (18)$$

B. Variable Smoothing Length

In this paper, variable smoothing length technique is applied, and the smoothing length evolves according to

$$h_i = \zeta \left(\frac{m_i}{\rho_i} \right)^{1/d} \quad (19)$$

or its time change rate

$$\frac{dh_i}{dt} = -\frac{1}{d} \frac{h_i}{\rho_i} \frac{d\rho_i}{dt} = -\frac{1}{d} \frac{h_i}{\rho_i} \sum_j^N m_j (V_i - V_j) W'_i(x_j) \quad (20)$$

where ζ is a constant scaling factor and d is the number of dimension.

Due to the different of all smoothing lengths, in order to satisfy the Newton's law, the situation that particles can interact each other have to be judged again according to the relation between the distance and the new smoothing length, and which can be set as the average of two smoothing lengths:

$$h_{ij} = \frac{h_i + h_j}{2} \quad (21)$$

C. Boundary Conditions

Although CSPM does not suffer from boundary deficiency problem, if we properly handle the boundary condition, the accuracy of the results will be higher. To enforce boundary conditions, the virtual particle technique is usually employed in meshless methods. In general, field variables on virtual particles are explicitly given or obtained by interpolation. For the shock tube problem considered herein, the virtual particle method is applied. It should be noted that the number of the virtual particles may change due to the variable smoothing length.

IV. DISCRETE EULER EQUATIONS

The momentum and energy equations discrete forms can be written as:

$$\frac{dV_i}{dt} = \frac{\sum_{j=1}^N m_j \left(\frac{P_i}{\rho_i^2} + \frac{P_j}{\rho_j^2} + \Pi_{ij} \right) W'_i(x_j)}{\sum_{j=1}^N (x_j - x_i) W'_i(x_j) m_j / \rho_j} \quad (22)$$

$$\frac{de_i}{dt} = \frac{\frac{1}{2} \sum_{j=1}^N m_j \left(\frac{P_i}{\rho_i^2} + \frac{P_j}{\rho_j^2} + \Pi_{ij} \right) (V_i - V_j) W'_i(x_j)}{\sum_{j=1}^N (x_j - x_i) W'_i(x_j) m_j / \rho_j} \quad (23)$$

where the artificial viscosity term Π_{ij} used to model the dissipation term for the CSPM simulation of shock waves [10] is given by

$$\Pi_{ij} = \begin{cases} \frac{(\alpha \bar{c}_{ij} \mu_{ij} - \beta \mu_{ij}^2)}{\bar{\rho}_{ij}}, & (V_i - V_j)(x_i - x_j) < 0, \\ 0, & (V_i - V_j)(x_i - x_j) \geq 0, \end{cases} \quad (24)$$

$$\mu_{ij} = \frac{\bar{h}_{ij}(V_i - V_j)(x_i - x_j)}{|x_i - x_j|^2}, \quad (25)$$

where $\bar{h}_{ij} = (h_i + h_j)/2$, $\bar{c}_{ij} = (c_i + c_j)/2$, $\bar{\rho}_{ij} = (\rho_i + \rho_j)/2$

The constant coefficients $\alpha = 1$, $\beta = 2$ are typical values for shocks [8]. The speed of the sound can be obtained by

$$c_i^2 = e_i \cdot \gamma \cdot (\gamma - 1) \quad (26)$$

and $\gamma = 1.4$ for ideal gas.

As described above, in this problem, we assume the mass of the particle is constant, so the volume will change during the calculation. For saving the computing resources and improving the efficiency, the variable smoothing length is employed in numerical simulation. At the beginning of the problem, the volume of the particles is different between the two parts of particles. We set the initial smoothing length of all particles according to the distance of the lower density particles initially. The update of the smoothing length of all particles should be considered during the computational process.

The continuity equation is approximated in two different forms,

A. Density Summation Form

The density of particle i is obtained as

$$\rho_i = \sum_j m_j W_i(x_j) \quad (27)$$

or according to formulation (10), the density is obtained as

$$\rho_i = \frac{\sum_j m_j W_i(x_j)}{\sum_j W_i(x_j) m_j / \rho_j} \quad (28)$$

B. Discrete Continuity Equation

The approximated continuity equations by SPH and CSPM are

$$\frac{d\rho_i}{dt} = \sum_j^N m_j (V_j - V_i) W'_i(x_j) \quad (29)$$

and

$$\frac{d\rho_i}{dt} = \frac{\sum_j^N m_j (V_j - V_i) W'_i(x_j)}{\sum_{j=1}^N (x_j - x_i) W'_i(x_j) m_j / \rho_j} \quad (30)$$

V. NUMERICAL EXPERIMENTS

In this section, numerical experiments are performed to assess the methods discussed previously. For shock tube problem, Sod shock tube problem is well-known and it is a particular case of the Riemann problem [11]. In the Sod shock tube problem, a high density and high pressure gas is separated by a membrane from a low density and low pressure gas. Once the membrane is removed instantly, a shock wave occurred and it moves into the original low density region. Meanwhile, a rarefaction wave travels into the original high density region. The initial states of the problem are given as $P_L = 1$, $V_L = 0$, $\rho_L = 1$, $P_R = 0.1$, $V_R = 0$, $\rho_R = 0.125$.

In this paper, the effect of the approximated continuity equation in different forms and the smoothing length are the main concerns. The energy equation and the momentum equation are discretized by Eqs. (22) and (23) in all experimental cases. Initially, there are 400 fluid particles with the same mass evenly distributed in the domain. The simulation time is 1 s with the time increment of 0.0001 s.

Fig. 1 shows the results with density and smoothing length calculated by formulation (28) and (20), respectively. It can be seen that the shock wave was not captured at all. If we calculate the smoothing length with formulation (19), the results do not change much, which are shown in Fig. 2. The results are similar to those shown in [8] with the same method.

Then we calculate the continuity equation with formulation (29) and (30). The results are shown in Fig. 3 and Fig. 4 respectively. Compared with the results shown in Figs. 1 and 2, these results are more reasonable, although there are still some oscillations at the shock front. In those two cases, the smoothing length is obtained by (19). We also tried formulation (20) to calculate the smoothing length, but the results show no difference.

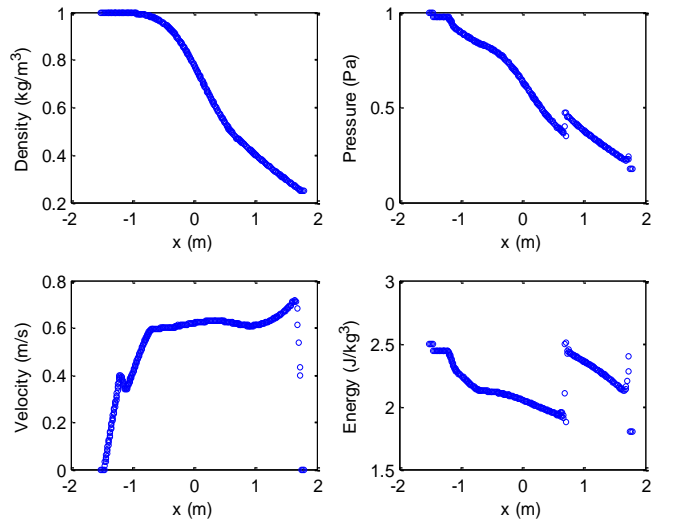


Fig. 1 Results of the original CSPM with Eqs. (20) and (28)

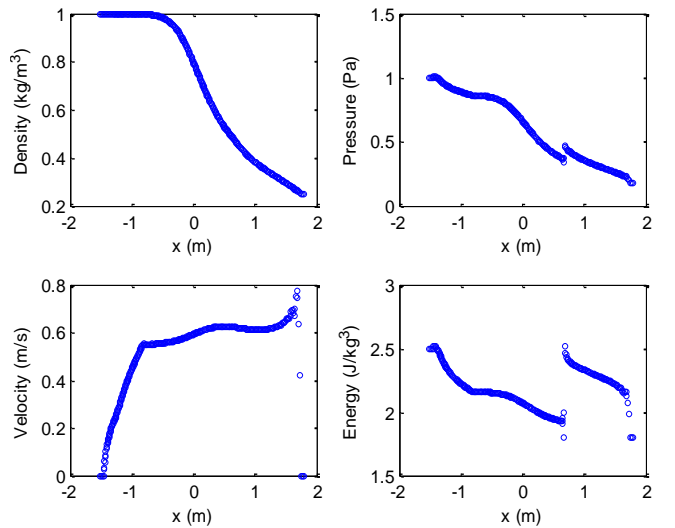


Fig. 2 Results of original CSPM with Eqs. (19) and (28)

With formulation (27) for mass conservation, the results are shown in Fig. 5. It is seen that the SPH summation form of the continuity equation can lead to better solutions.

Together with the exact solution, the results of SPH and CSPM are shown in Fig. 6. The solid line is the exact Riemann solution, the hollow circle is the SPH solution, and the square is the result of CSPM. It is seen that the difference between solutions of SPH and CSPM is not distinguishable and both of them have good agreement with the exact solution.

VI. CONCLUSION

In this paper, the shock tube problem is successfully simulated by the corrective smoothed particle method (CSPM). The main reason why the original CSPM cannot give correct solution to this problem is that in the region close to the discontinuity the denominator in density

approximation highly departs from unity as it should not be. Together with SPH summation form of the density, CSPM can capture the shock very well. To improve the performance, the variable smoothing length was also employed in CSPM.

ACKNOWLEDGEMENT (HEADING 5)

The work is supported by the National Natural Science Foundation of China (No. 51478305), SKL of HESS (No. HESS-1408) and Scientific Research Foundation for the Returned Overseas Chinese Scholars, State Education Ministry.

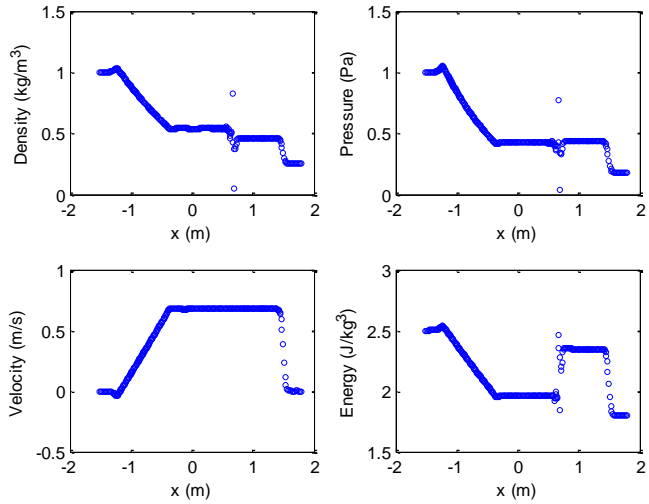


Fig. 3 Results of original CSPM with Eqs. (19) and (29)

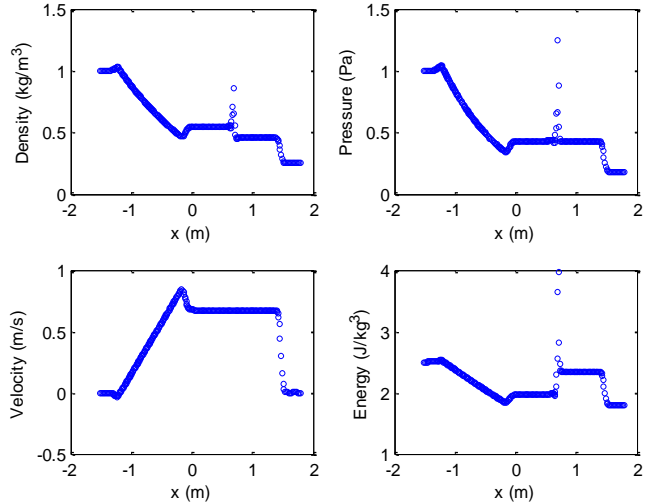


Fig. 4 Results of original CSPM with Eqs. (19) and (30)

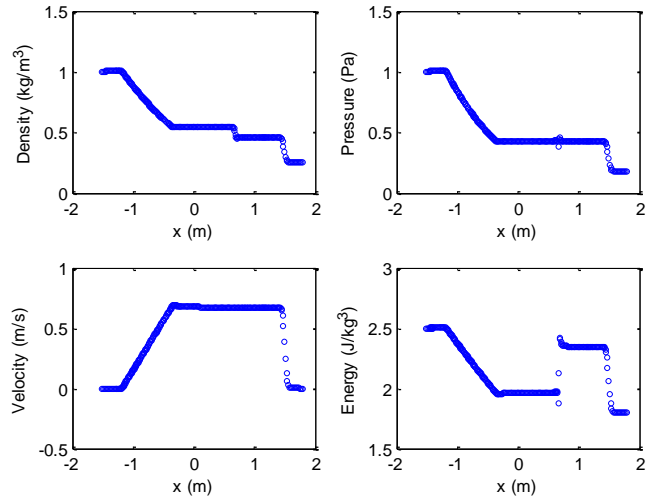
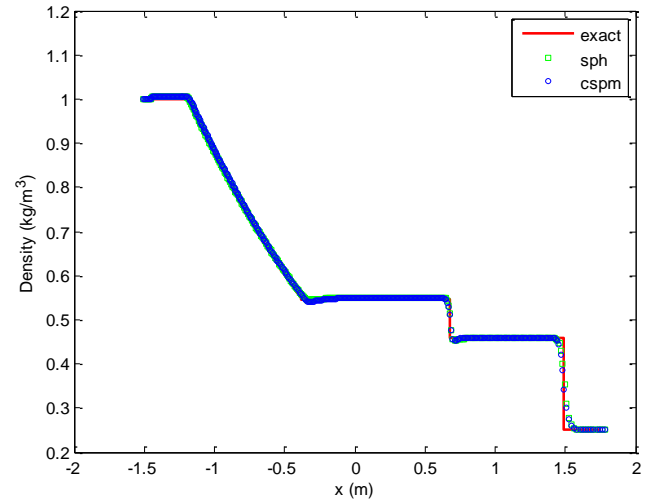
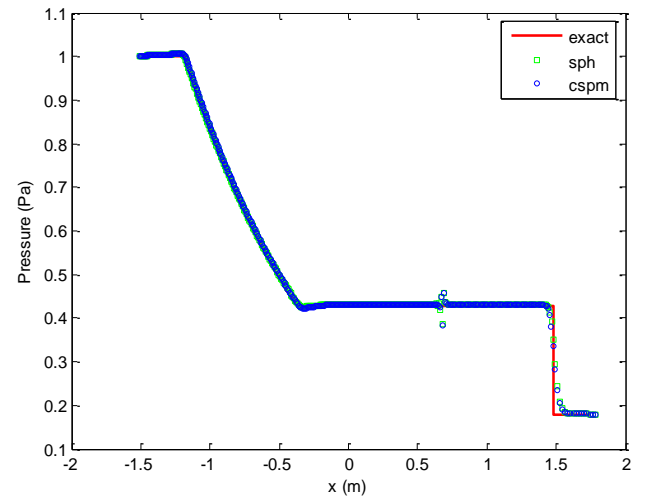


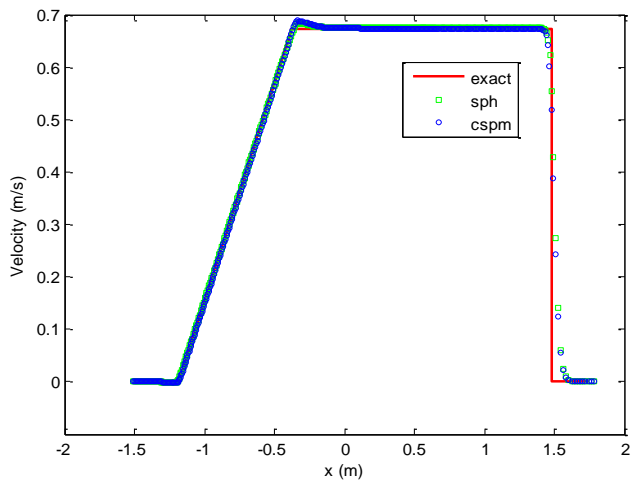
Fig. 5 Results of original CSPM with Eqs. (19) and (27)



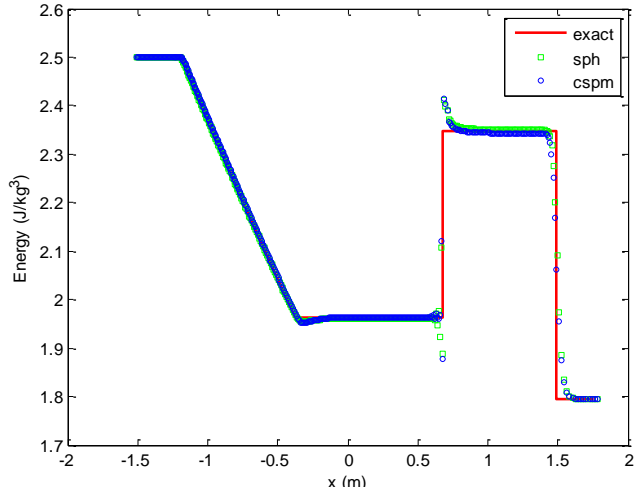
(a)



(b)



(c)



(d)

Fig. 6 Numerical solution of SPH and CSPM for the shock tube problem

REFERENCES

- [1] Nejad-Asghar M (2006). Simulation of shock waves by smoothed particle hydrodynamics[J]. *Astrophys. & Space Sci.*, 313(4): 425-430.
- [2] Chen, J. K., Beraun, J. E. and Carney, T. C. (1999). A corrective smoothed particle method for boundary value problems in heat conduction. *Int. J. Numer. Meth. Eng.*, 46:231–252.
- [3] Chen, J. K., Beraun, J. E. and Jih, C. J. (1999). An improvement for tensile instability in smoothed particle hydrodynamics. *Comput. Mech.*, 23: 279–287.
- [4] Monaghan, J. J. (2005). Smoothed particle hydrodynamics. *Rep. Prog. Phys.*, 68: 1703–1759.
- [5] Chen J. K., Beraun, J. E. and Carney T. C. (1999). A corrective smoothed particle method for boundary value problems in heat conduction, *Int. J. Numer. Methods Eng.*, 46: 231–252.
- [6] Chen J. K., Beraun J. E. and Jih C. J. (2001). A corrective smoothed particle method for transient elastoplastic dynamics, *Comput. Mech.*, 27: 177–187.
- [7] Fang J., Parriaux A., Rentschler M. and Ancey C. (2009). Improved SPH methods for simulating free surface flows of viscous fluids. *Appl. Numer. Math.*, 59: 251–271.
- [8] Liu G. R. and Liu M. B. (2003). *Smoothed Particle Hydrodynamics: A Mesh Free Particle Method* [M]. World Scientific, Singapore. Chapter 5.
- [9] Puri K. and Ramachandran P. (2014). A comparison of SPH schemes for the compressible Euler equations[J]. *J. Comput. Phys.*, 256: 308–333.
- [10] Monaghan J. J. and Gingold R. A. (1983). Shock simulation by the particle method SPH[J]. *J. Comput. Phys.*, 52(2): 374-389.
- [11] Naber J. (2005). Building your own shock tube [R]. *Modelling, Analysis and Simulation* [MAS], No. E 0502, 1-88.

Developing an Extensible, Portable, Scalable Toolkit for Massively Parallel Incompressible Smoothed Particle Hydrodynamics (ISPH)

Xiaohu Guo^a, Benedict D. Rogers^b, Steven Lind^b, Rebecca Fair^a, Peter K. Stansby^b

^aHartree Centre, STFC, Daresbury Laboratory, WA4 4AD, UK.

^bSchool of Mechanical, Aerospace and Civil Engineering, University of Manchester, M13 9PL, UK

Abstract—This paper presents our ISPH3D toolkit for massively parallel simulations which aims to resolve the challenges arising from solving the large-scale, highly complex, nonlinear and distorted flow applications and facilitate the projection-based particle-methods software development. The data structures are specifically designed to organise multiple kinds of fluid particles together with different boundary particles to maximise data locality and cache reuse. This enables software extensibility and communication between highly irregular subdomains. We have implemented all the major performance critical ‘software kernels’ and described them in detail, these kernels contains the nearest neighbour list searching kernel using cell linked list approach, the domain decomposition, dynamic load balancing and particles ordering kernels using Hilbert Space Filling Curve and the PPE solver using the open-source high-performance computing (HPC) library PETSc. The final benchmark results showed the promising efficiency with more than 12 thousand cores.

I. INTRODUCTION

The stability, accuracy, energy conservation, boundary conditions of the projection based particle method such as incompressible smoothed particle hydrodynamics ISPH [1] have been greatly improved [2]–[4]. However, for applications requiring hundreds of millions of particles from the perspective of computation and high performance software implementation [5], there are still many challenges compared with other particle based methods. These may potentially hinder the use and exploitation of these methods for the large-scale real engineering applications which generally involve highly complex, nonlinear and distorted flow. Solving such applications requires a large number of particles and this in turn demands distributed computing with accelerating paradigms. The domain decomposition and dynamic load balancing using the message passing interface (MPI) for irregular particles distribution and computational domains with complex geometries are extremely challenging to implement. An appropriate assignment of particles to processors and grouping physically-close particles within a single processor can greatly reduce communication overhead and improve the software scalability. The additional distinct challenge for projection-based particle methods is solving pressure Poisson equations (PPE). The added complexity for solving sparse linear equations for projection-based particle methods such as ISPH is that the sparsity of the matrix is changing every time step due to the particle movement at each time step.

In order to facilitate the scientific development using ISPH, we have developed an ISPH software toolkit to provide the major performance kernels to address challenges in terms of large-scale computing with large number particles, domain decomposition and dynamic load balancing with Hilbert Space Filling Curve (HSFC), optimised data mapping using unstructured communication, optimised data structure for nearest neighbour list searching and software extensibility for solving complex physics.

II. BASIC INCOMPRESSIBLE SMOOTHED PARTICLE HYDRODYNAMICS (ISPH) METHODOLOGY AND ITS IMPLEMENTATION

In the ISPH method, the NavierStokes equations are solved in Lagrangian form to simulate the flow.

$$\nabla \cdot \mathbf{u} = 0 \quad (1)$$

$$\frac{d\mathbf{u}}{dt} = -\frac{1}{\rho}\nabla p + \nu\nabla^2\mathbf{u} + \mathbf{f} \quad (2)$$

where \mathbf{u} is the velocity vector, p is pressure, ν is kinematic viscosity, \mathbf{f} is a body force and t is time. Incompressibility is enforced in the projection method by means of a pressure Poisson equation [6].

The position of the particles \mathbf{r} is integrated through time by using the velocity (3)

$$\frac{d\mathbf{r}}{dt} = \mathbf{u} \quad (3)$$

SPH is based on an approximation of the integral interpolation of a variable A at location \mathbf{r}

$$\langle A(\mathbf{r}) \rangle \approx \int_{\Omega} \mathbf{A}(\mathbf{r}') \omega_h(|\mathbf{r} - \mathbf{r}'|) d\mathbf{r}' \quad (4)$$

where $\langle \rangle$ denotes an interpolated value, $\omega_h(|\mathbf{r} - \mathbf{r}'|)$ is the weighting function or smoothing kernel function with a smoothing length h , and Ω is the supporting domain. In a discrete format, the interpolation is approximated as:

$$A(\mathbf{r}_i) \approx \sum V_j A_j \omega_h(r_{ij}), \quad (5)$$

where V is the volume of a particle and \mathbf{r}_{ij} is a distance vector between particle i and j . Hereafter $\omega_h(r_{ij}) = \omega_h(|\mathbf{r}_i - \mathbf{r}_j|)$ is written as ω_{ij} . In this work a quintic spline kernel, continuous to the fifth derivative is used for all cases. The smoothing length $h = 1.3\Delta x$ is used, where Δx is the initial inter-particle spacing.

The gradient operator for a general variable ϕ is given by:

$$\nabla \phi_i \simeq - \sum_j V_j (\phi_i - \phi_j) \nabla \omega_{ij} \quad (6)$$

This gradient operator has been chosen thanks to its superior accuracy when used in combination with the kernel gradient normalisation [7]:

$$\nabla W_{ij} = \mathbf{L}(\mathbf{r}) \nabla \omega_{ij}, \quad (7)$$

where the correction matrix is

$$\mathbf{L}(\mathbf{r}) = \begin{pmatrix} \sum V_j (x_j - x) \frac{\partial \omega_{ij}}{\partial x} & \sum V_j (x_j - x) \frac{\partial \omega_{ij}}{\partial y} \\ \sum V_j (y_j - y) \frac{\partial \omega_{ij}}{\partial x} & \sum V_j (y_j - y) \frac{\partial \omega_{ij}}{\partial y} \end{pmatrix}^{-1} \quad (8)$$

Using these SPH spatial discretisations, the conservation of mass equation (1) in discrete form is:

$$\sum_j V_j (\mathbf{u}_i - \mathbf{u}_j) \cdot \nabla W_{ij} = 0 \quad (9)$$

The SPH discretised conservation of momentum equation (2) is

$$\frac{d\mathbf{u}_i}{dt} = \frac{1}{\rho} \sum_j V_j (p_j - p_i) \nabla W_{ij} + \sum_j V_j \frac{2\mu \mathbf{r}_{ij} \cdot \nabla \omega_{ij}}{(\mathbf{r}_{ij}^2 + \eta^2)} \mathbf{u}_{ij} + \mathbf{f}_i \quad (10)$$

The pressure can be obtained from the pressure Poisson equation (PPE), written as:

$$\nabla \cdot \left(\frac{1}{\rho} \nabla p^{n+1} \right)_i = \frac{1}{\delta t} \nabla \cdot \mathbf{u}_i^* \quad (11)$$

Due to the truncated kernel, the ISPH3D code employs the Schwaiger operator [8] for viscous and Laplacian operators

$$(\nabla \cdot \mu \nabla f)_i = \frac{\text{tr}(\Gamma)^{-1}}{n} \left\{ \sum_j V_j (\mu_i + \mu_j) (f_i - f_j) \frac{\mathbf{r}_{ij} \cdot \nabla \omega_{ij}}{\mathbf{r}_{ij}^2} - [\nabla(\mu_i f_i) - f_i \nabla \mu_i + \mu_i \nabla f_i] \cdot \left(\sum_j V_j \nabla \omega_{ij} \right) \right\} \quad (12)$$

where Γ is a tensor defined as:

$$\Gamma_{\beta\gamma} = \sum \frac{\mathbf{r}_{ij} \cdot \nabla \omega_{ij}}{\mathbf{r}_{ij}^2} \Delta x_\beta \Delta x_\gamma$$

where β and γ are coordinate directions, f is general variable (for example can be velocity and pressure), and μ is a diffusion coefficient.

To prevent particles themselves from bunching up in highly distorting flows, after each time step, particles are shifted slightly to maintain a uniform arrangement. The particle shifting algorithm is based on Fick's law of diffusion [1].

$$\delta \mathbf{r}_s = -D' \nabla C \quad (13)$$

where C is the concentration, D' is a diffusion coefficient. $\delta \mathbf{r}_s$ is the particle's shifting distance. The gradient of concentration ∇C can be calculated with the following formula:

$$\nabla C_i \approx \sum_j V_j (1 + f_{ij}) \nabla \omega_{ij} \quad (14)$$

The hydrodynamic variables are corrected by the Taylor series approximation,

$$\phi_{i'} = \phi_i + (\nabla \phi)_i \cdot \delta \mathbf{r}_{ii'} + O(\delta \mathbf{r}_{ii'}^2) \quad (15)$$

The basic algorithm of ISPH can be summarised in the Algorithm 1:

Algorithm 1 ISPH Basic Algorithm Description

Read in the particles data, calculate the domain size
Distribute particles with HSFC method.
In each partition
for $t = 1 \rightarrow \text{total_number_of_timesteps}$ **do**
 Step 1: calculate viscosity term: $\nu \nabla^2 \mathbf{u}_i^n$ **{Loop 1}**
 Step 2: $\mathbf{u}_i^* = \mathbf{u}_i^n + (\nu \nabla^2 \mathbf{u}_i^n + \mathbf{f}_i^n) \delta t$, Calculate \mathbf{u}_i^* without pressure gradient.
 Step 3: $\nabla \cdot \left(\frac{1}{\rho} \nabla p^{n+1} \right)_i = \frac{1}{\Delta t} \nabla \cdot \mathbf{u}_i^*$, Solve pressure Poisson equation to get pressure P_i^{n+1} **{Loop 2}**
 Step 4: Get pressure gradient ∇p_i^{n+1} **{Loop 3}**
 Step 5: $\mathbf{u}_i^{n+1} = \mathbf{u}_i^* - \frac{\delta t}{\rho} \nabla p_i^{n+1}$, Calculate velocity \mathbf{u}_i^{n+1}
 Step 6: $\mathbf{r}_i^{n+1} = \mathbf{r}_i^n + \delta t \left(\frac{\mathbf{u}_i^{n+1} + \mathbf{u}_i^n}{2} \right)$, Particles' positions are centred in time
 Step 7: $\delta \mathbf{r}_s = -D' \nabla C$. Shift the particle by Fick's law **{Loop 4}**
end for

There are four major loops that involve using particle neighbour lists (see Algorithm 1 Loop 1-4), where Loop 1, Loop 2 and Loop 3 use the same neighbour lists. Due to data dependencies, these loops cannot be merged together into one loop. These loops all involve nearest neighbour search operations. In order to avoid redundant calculation of smoothing kernel gradients and other expensive floating point operations, we rearranged these four loops to be performed as a sweep over the neighbour list outside of these functions, so that each function is called once for each pair of neighbours. Now, values such as the smoothing kernel gradients can be calculated once in each loop for each pair of neighbours and passed to the functions as arguments. This helps to reduce the number of redundant calculations without increasing the memory footprint. Furthermore, this restructuring enable calculations to be performed without saving the neighbour

list. Furthermore, looping over cells improves the pattern of data accesses when particle ordering. Resulting performance improvements, from not saving the neighbour list, are shown in section VII.

III. DATA PRECONDITIONING FOR EXTENSIBILITY AND EFFICIENT NEAREST NEIGHBOUR LIST SEARCHING

For simulations with real flow applications often involve different types of the particles. For example, In the Fig. 1(a), there are fluid particles which can have different sub-types of particles if simulating multi-phase flow, the floating rigid body particles, and the boundary particles. The particles representing the boundaries and the floating rigid body particles can be further divided according to different SPH boundary techniques. When solving these applications at large scales, managing data locality is particularly challenging due to particles moving over time. Here we are using data preconditioning techniques to explore data locality and manage particle indices with various types of particles

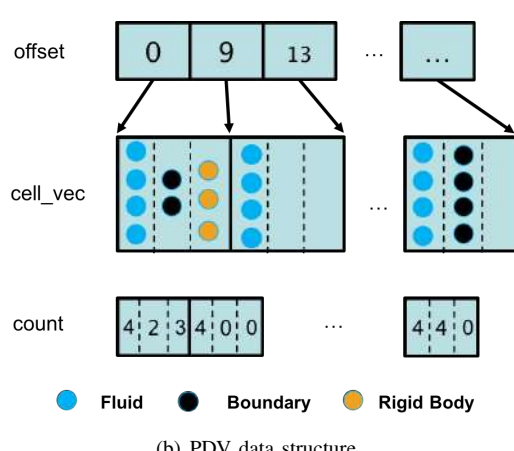
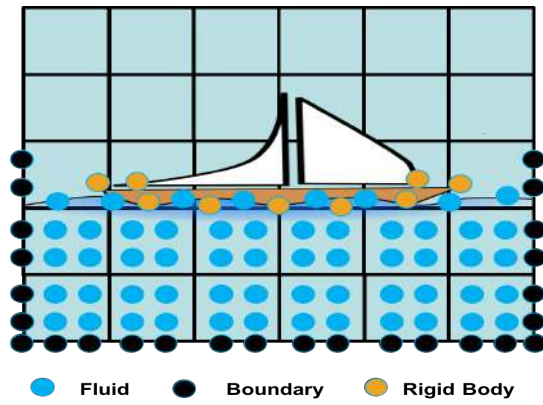


Fig. 1. Diagram (a) is to show the different types of particles interaction in the same cell, in this case, fluid particles, boundary particles and rigid body particles, (b) is to show using PDV with consideration of different types of particles

Considering extensibility, the ISPH3D provides a choice of either a linked list or newly implemented preconditioned

dynamic vector (PDV) [9] is enabled for the nearest neighbour searching operation. Fig. 1(b) shows how we use PDV with consideration of different types of particles. Similar to PDV [9], an array **offset** contains an index pointing to the beginning of each cell, **cell_vec** contains the particle indices, each cell has fluid, boundary and rigid body particles arranged in sequence. Array **count** is used to count the number of fluid, boundary and rigid body particles in each cell. this new structure-of-array-of-structures(SOAOS) showed in Fig. 1(b) requires new implementations of both the nearest neighbour list searching kernel and the MPI halo exchange kernels for send buffer packing and receive buffer unpacking with consideration of different types of particles comparing with our previous approach [10]. Internally, the data layout/arrangement of types of particles are fixed for PDV data structures, but the sequence of generating the different types of particles in the preprocessing stage and then in input file can be any order according to the users' request.

IV. DOMAIN DECOMPOSITION AND DYNAMIC LOAD BALANCING WITH UNSTRUCTURED COMMUNICATION TOOLKIT

We have developed a Hilbert Space Filling Curve (HSFC) method based toolkit for particles domain decomposition and dynamic load balancing [10]. The basic idea of domain decomposition along SFCs is to reduce a multidimensional domain decomposition problem to a one-dimensional splitting problem. Fig. 2 shows the advantage of using an SFC-based method to perform domain decomposition for 3-D complex fluid, the method we use here does not require extra effort to deal with trade-off between dynamic load balancing and data locality.

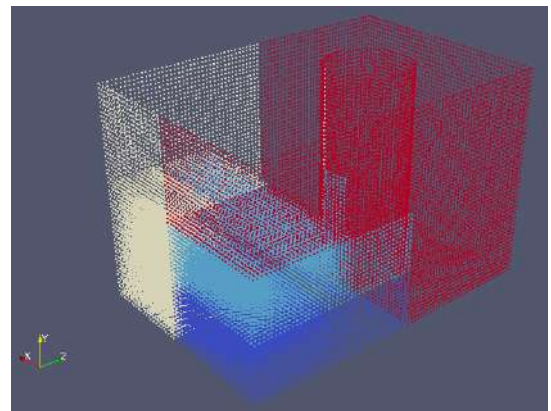


Fig. 2. 3D domain decomposition with HSFC with 4 MPI partitions for dam break cylinder post test case, different colours represent different partitions. There are no need special treatment for rigid cylinder and fluid during domain decomposition and dynamic load balncing

For simulations where the number of cells have the same order magnitude with the number of particles, keeping and updating such a global mapping is very expensive. A minimal memory footprint approach is required for such a mapping. Hence, we employ a bounding box approach to manage the

cells locations after data migrations or to make information globally accessible. Alternatively, this bounding box approach can further reduce the memory footprint and improve MPI efficiency of mapping kernels. The number of bounding boxes will be determined by number of cells and number of partitions, hence, the size of bounding box should be small comparing with number of cells. Once the number of bounding boxes is fixed, we then use the number of particles in each bounding box as its weight function, and using SFC to decompose bounding box. This should be able to balance automatically the number of particles in each partition and also reduce the memory footprint of mapping kernels. The extra benefit keeps the run-time cost of the SFC domain decomposition kernel to a minimum and Fig. 3 shows the comparison between using a bounding box and cell as domain decomposition object. The shape of the domain with bounding box are much less complex comparing with using cell(size of the smoothing length) which will be benefit for communication setup.

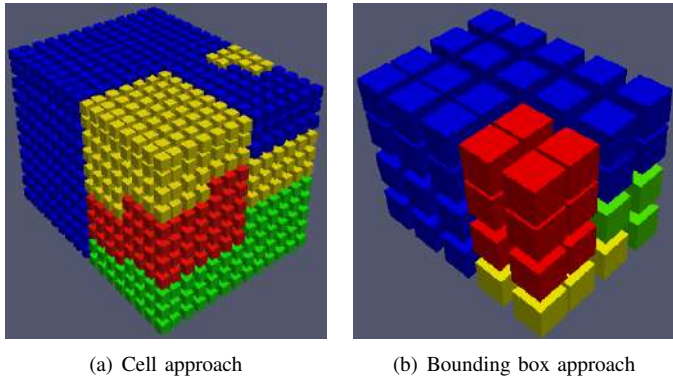


Fig. 3. Use the BOUNDING BOX as Domain Decomposition object with the HSFC, visually improves domain decomposition quality

In the ISPH3D parallel toolkit, two main computing kernel operations were carefully designed and implemented. The first computing kernel is **particles_migration** which is used to maintain particles belonging to a partition. This kernel involves two operations, the first operation is compressing the resident particles and the second operation is copying the entering particles. The particles exiting will be copied into the send buffer. As the number of particles leaving and/or entering changes during the simulation, it is not appropriate to preallocate the memory for this situation, the linked-list data structures are used here to deal with such situations. This computing kernel will be automatically called at the beginning of each time step.

The second computing kernel is **halo_update** which is used to resolve data dependencies due to neighbour list searching. Considering that future developers may need solve extra equations which may require new variables for halo update, the halo update kernel has been designed in such a way that users only need to tell kernel which variable or block of variables need to do halo update. As shown in

Algorithm 2, field variable **Var** can be integer, real, double or multi-block of real and double. We have used interface overloading to automatically halo update for integer type, real type, and real/double precision vector type variables. During each time step, we keep the communication stack **halo_sends** and **halo_recvs** implelnted with linked list data structure and only destroy them when the partition has changed.

Algorithm 2 The Syntax for halo update in ISPH

```

for  $t = 1 \rightarrow T_{total}$  do
    call halo_plan_setup(halo_sends, halo_recvs)
    performing local calculation for Var
    call call halo_update(halo_sends, halo_recvs, Var)
    if change then
        call halo_plan_destroy(halo_sends, halo_recvs)
    end if
end for

```

V. PARTICLES ORDERING

Due to the Lagrangian nature of the particle methods, such as smoothed particle hydrodynamics (SPH) or incompressible SPH, the pattern of data access and computation are unknown until the applications run time. This often leads to poor temporal and spatial data accesses and insufficient usage of a memory hierarchy. As multi-level memory hierarchies are still going to be deployed in computing architectures for the foreseeable future, ordering algorithms are critical techniques to increase applications data locality.

It has already been shown that reordering particles such that ensuring particles in physical space are close in memory space can produce up to 20% performance improvement in weakly compressible SPH (WCSPH) applications [9]. ISPH3D provide natural ordering, space filling curve ordering including Hilbert SFC and Morton SFC. Besides general computing time improvement for typical SPH kernels [11], improvement for the pressure Poisson equation matrix bandwidth was also observed. Fig. 4 gives the matrix spare pattern using the natural ordering with 1 MPI partition and 24 MPI partitions. With 1 MPI partition, the matrix bandwidth are greatly reduced using ordering methods with natural and space filling curve ordering. However, with 24 MPI partitions, the matrix bandwidth are not obviously reduced due to not using global ordering which is generally expensive. Further investigations for ordering with multiple MPI partitions are need to be done in the future.

VI. FLEXIBLE IMPLEMENTATION OF SPARSE LINEAR SOLVER PETSC

In ISPH3D, the PETSc software [12] is used to solve the sparse linear system. PETSc offers great flexibility to choose the preconditioners and Krylov Subspace methods that available in the PETSc. In the mean time, PETSc also provide a interface to call other established sparse linear solvers like HYPRE [13]. The HYPRE BoomerAMG algebraic multigrid has been used as the default preconditioner. The PETSc Shell

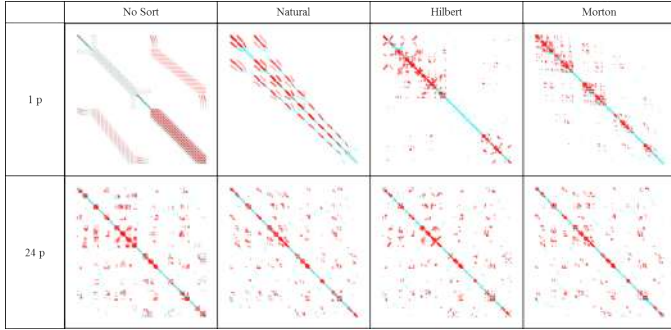


Fig. 4. The structure of the PPE sparse matrix when the water hits the wall in 3D, using 1 and 24 MPI partitions

matrix is used to provide user an interface to define user own preconditioner to allow further sparse linear solver study for incompressible SPH.

The code has been restructured to reduce accesses to PETSc memory spaces. For example, the boundary conditions for the free surface flow of pressure Poisson equation, this has to be done before the left hand side matrix and right hand side vector are assembled.

PETSc partitions matrices by continuous rows in parallel. While in the ISPH code, each row represents all neighbouring particles of a specific particle, a renumbering matrix has to be employed so that each partition can assemble its own matrix. The assembly matrix has therefore been implemented row by row, such that the accesses to PETSc memory spaces are reduced to minimal to reduce the overhead of matrix assembly stage.

VII. PERFORMANCE AND SCALABILITY EVALUATION

The 3-D dam break with a dry bed has been used in this paper as the benchmark test case. The total number of particles used for the benchmark is approximately 100 million. The sparse linear solver is using multigrid preconditioner HYPRE BoomerAMG [13] and Krylov subspace method GMRES. The multigrid preconditioner HYPRE BoomerAMG has two phases, the first phase is setup phase including selection of coarse grids, creation for the interpolation operators, and the representation of the fine grid matrix operator on each coarse grid. The second phase is the solving phase containing matrix-vector multiply and the smoothing operators.

For the performance results presented herein, the ISPH3D code has been run on the the UK National HPC platform ARCHER, which is Cray XC30 system. ARCHER compute nodes contain two 2.7 GHz, 12-core E5-2697 v2 (Ivy Bridge) series processors. Each of the cores in these processors can support 2 hardware threads (Hyper-threads). Within the node, the two processors are connected by two QuickPath Interconnect (QPI) links. Standard compute nodes on ARCHER have 64 GB of memory shared between the two processors. There are a smaller number of high-memory nodes with 128 GB of memory shared between the two processors. The memory is arranged in a non-uniform access (NUMA) form: each 12-core

processor is a single NUMA region with local memory of 32 GB (or 64 GB for high-memory nodes). Access to the local memory by cores within a NUMA region has a lower latency than accessing memory on the other NUMA region. There are 4544 standard memory nodes (12 groups, 109,056 cores) and 376 high memory nodes (1 group, 9,024 cores) on ARCHER giving a total of 4920 compute nodes (13 groups, 118,080 cores), providing a total of 2.55 petaflops of theoretical peak performance.

The efficiency is obtained with the following formula:

$$S_p = \frac{T_1}{T_p * p} * 100\% \quad (16)$$

where T_1 is the wall time with 1 node, each node comprises 24 Intel E5-2697 cores, T_p is the wall time with p nodes ($p \geq 1$). S_p is the measure generally used to show the code scalability.

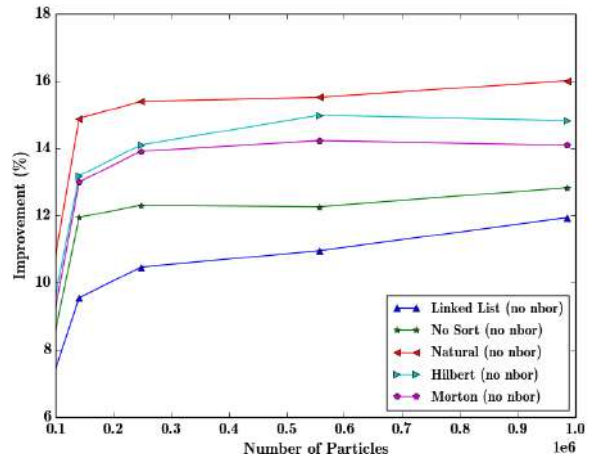


Fig. 5. The improvement in time without the solver when reordering owned particles without saving the neighbour list compared with the original linked list in serial

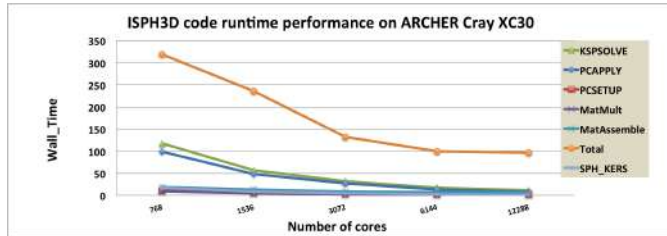
The resulting improvement in time when not saving the neighbour list calculation for different ordering methods is shown in Fig 5. Not saving the neighbour list implementation has resulted in time improvements up to 16% comparing with saving the neighbour list approach. This is largely due to the reduction of redundant calculations of smoothing gradients and other floating point operations, and providing a more favourable pattern of data accesses by looping over cells. Details of implementation can be seen in section V

Fig. 6 shows the overall performance of the ISPH3D running 10 time steps, Fig. 6(a) gives the wall time of each components/kernels in the ISPH3D. Fig. 6(b) gives the efficiency of each components/kernels. The efficiency defined in Equation 16. The KSPSOLVE gives performance of GMRES, PCSETUP and PCAPPLY gives statistics of BoomerAMG's setup phase and solve phase, MatMult is matrix vector multiplication, MatAssemble is the cost of calculation of pressure Poisson equation matrix coefficients, right hand side and

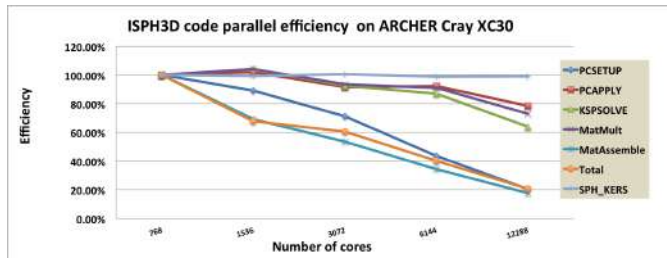
assembly them to the PETSc memory space for later solving. SPH_KERS are those kernels mentioned in Algorithm 1 from step 1 to step 7 except step 3 (pressure solver).

In the Fig. 6(a), we can see the majority of the walltime is now spent solving the pressure Poisson equation. The main costs in the solver are KSPSOLVE(using GMRES) and PCAPPLY which is BoomerAMG's solver phase. The other SPH related kernels account for very small percentage comparing with pressure solver.

In the Fig. 6(b) shows the scalabilities of each kernel. Firstly, we can see the ISPH kernels are now able to scale linearly. With up to 12288 cores, it can still achieve 99.04% efficiency. In the PPE solver part, With 12288 cores, KSPSOLVE and PCAPPLY can still reach more than 60% efficiency. However, the scalability of those relatively low cost parts, like PCSETUP, MatAssemble becomes worse (only 20% efficiency with 12K cores) when using large number of cores. They are now become the bottleneck for the scalability of ISPH3D. These issues need to be further investigated.



(a) ISPH3D Walltime Analysis



(b) ISPH3D Efficiency Analysis

Fig. 6. Strong scaling results for the whole ISPH3D using up to 512 XC30 nodes (12288 cores) [14]

VIII. DISCUSSION AND CONCLUSION

For the purpose of software scalability and extensibility, We have investigated the nearest neighbour searching data structure concerning multiple types of particles using data preconditioning technique. In order to reduce memory footprint for mapping particles into different MPI partitions, we have replaced cells with bounding box as partition objects. And this also result a better partition quality. In the mean time, the capability to deal with irregular distributed particles is demonstrated with HSFC partition method.

As a ISPH3D toolkit, the key performance computing kernels have been presented including the neighbour list

searching, particles ordering, sparse linear solver of pressure Poisson equation, particles migration and halo update etc parallel data management kernels. This ISPH3D toolkit has been benchmarked on the UK National Super-computing Platform ARCHER, where we have presented the results of memory efficient implementation for 3-D incompressible SPH, using more than 10,000 cores with around 100 million particles. The results showed the promising efficiency with more than 12K cores.

Good program design stresses modularity and encapsulation with each software component having a clear, modulized interface. Applied naively, these ideas can lead to many more redundant floating point operations and cache misses/memory accesses than necessary. For example, a standard high-level program design for an ISPH code would probably separate sorting, linked-list-building, force calculation, diagnostic accumulation and time integration into separate, independent modules. Each of these modules requires a complete scan of the list of particles, so the entire data set would have memory access many times and redundant floating point calculations. To recover performance, the time integration, diagnostic accumulation and force calculation are combined together in a single loop. This may result in a significant speedup if the program is memory bandwidth limited or computation limited, but the optimised codes modularity is far less apparent. How to find a tradoff between modularity and efficiency will be a interesting topic in the future development.

ACKNOWLEDGEMENT

The work was partially funded by the EPSRC Grant "SERT: Scale-free, Energy-aware, Resilient and Transparent Adaptation of CSE Applications to Mega-core Systems ". Grant Number:EP/M01147X/1.

The authors would also like to acknowledge the funding support under the embedded CSE programme of the ARCHER UK National Supercomputing Service (<http://www.archer.ac.uk>). The authors would also like to thank the EPCC eCSE support team for their help throughout this work.

The work was carried out on ISPH software which was original funded by the EPSRC Grant "An incompressible smoothed particle hydrodynamics (ISPH) wave basin with structure interaction for fully nonlinear and extreme coastal waves". Grant Number: EP/H018603/1, EP/H018638/1.

REFERENCES

- [1] S. Lind, R. Xu, P. Stansby, and B. Rogers, "Incompressible smoothed particle hydrodynamics for free-surface flows: A generalised diffusion-based algorithm for stability and validations for impulsive flows and propagating waves," *Journal of Computational Physics*, vol. 231, no. 4, pp. 1499 – 1523, 2012. [Online]. Available: <http://www.sciencedirect.com/science/article/pii/S0021999111006279>
- [2] H. Gotoh and A. Khayyer, "Current achievements and future perspectives for projection-based particle methods with applications in ocean engineering," *Journal of Ocean Engineering and Marine Energy*, vol. 2, no. 3, pp. 251–278, 2016. [Online]. Available: <http://dx.doi.org/10.1007/s40722-016-0049-3>

- [3] S. Yeylaghi, B. Moa, P. Oshkai, B. Buckham, and C. Crawford, "ISPH modelling for hydrodynamic applications using a new MPI-based parallel approach," *Journal of Ocean Engineering and Marine Energy*, vol. 3, no. 1, pp. 35–50, 2017. [Online]. Available: <http://dx.doi.org/10.1007/s40722-016-0070-6>
- [4] A. Khayyer, H. Gotoh, and Y. Shimizu, "Comparative study on accuracy and conservation properties of two particle regularization schemes and proposal of an optimized particle shifting scheme in ISPH context," *Journal of Computational Physics*, vol. 332, pp. 236 – 256, 2017. [Online]. Available: <http://www.sciencedirect.com/science/article/pii/S0021999116306465>
- [5] J. M. Dominguez, A. J. Crespo, and M. Gmez-Gesteira, "Optimization strategies for CPU and GPU implementations of a smoothed particle hydrodynamics method," *Computer Physics Communications*, vol. 184, no. 3, pp. 617 – 627, 2013. [Online]. Available: <http://www.sciencedirect.com/science/article/pii/S001046551200358X>
- [6] A. Chorin, "Numerical solution of the navier stokes equations," *J. Math. Comput.*, vol. 22, pp. 745 – 762, 1968.
- [7] G. Oger, M. Doring, B. Alessandrini, and P. Ferrant, "An improved SPH method: Towards higher order convergence," *Journal of Computational Physics*, vol. 225, no. 2, pp. 1472 – 1492, 2007. [Online]. Available: <http://www.sciencedirect.com/science/article/pii/S0021999107000630>
- [8] H. F. Schwaiger, "An implicit corrected SPH formulation for thermal diffusion with linear free surface boundary conditions," *International Journal for Numerical Methods in Engineering*, vol. 75, no. 6, pp. 647–671, 2008. [Online]. Available: <http://dx.doi.org/10.1002/nme.2266>
- [9] J. M. Domnguez, A. J. C. Crespo, M. Gomez-Gesteira, and J. C. Marongiu, "Neighbour lists in smoothed particle hydrodynamics," *International Journal for Numerical Methods in Fluids*, vol. 67, no. 12, pp. 2026–2042, 2011. [Online]. Available: <http://dx.doi.org/10.1002/fld.2481>
- [10] X. Guo, S. Lind, B. D. Rogers, P. K. Stansby, and M. Ashworth, "Efficient massive parallelisation for incompressible smoothed particle hydrodynamics (isph) with 10^8 particles," in *The 8th SPHERIC Workshop*, vol. 1, 2013, pp. 397–402.
- [11] F. Rebecca, G. Xiaohu, and C. Tao, "Efficient particle ordering with space-filling curves for incompressible smoothed particle hydrodynamics," in *The 12th SPHERIC Workshop*, vol. 1, 2017, pp. 322–329.
- [12] S. Balay, S. Abhyankar, M. F. Adams, J. Brown, P. Brune, K. Buschelman, V. Eijkhout, W. D. Gropp, D. Kaushik, M. G. Knepley, L. C. McInnes, K. Rupp, B. F. Smith, and H. Zhang, "PETSc users manual," Argonne National Laboratory, Tech. Rep. ANL-95/11 - Revision 3.5, 2014. [Online]. Available: <http://www.mcs.anl.gov/petsc>
- [13] A. Baker, M. Schulz, and U. M. Yang, "On the performance of an algebraic multigrid solver on multicore clusters," in *VECPAR 2010, J.M.L.M. Palma et al., eds., vol. 6449 of Lecture Notes in Computer Science*. Springer-Verlag, 2011, pp. 102–115.
- [14] X. Guo, B. D. Rogers, S. Lind, P. K. Stansby, and M. Ashworth, "Exploring an efficient parallel implementation model for 3-d incompressible smoothed particle hydrodynamics," in *The 10th SPHERIC Workshop*, 2015.

The Simulation of Three-Dimensional Flow by Using GPU-based MPS Method

Xiang Chen

State Key Laboratory of Ocean Engineering, School of Naval Architecture, Ocean and Civil Engineering, Shanghai Jiao Tong University, Collaborative Innovation Center for Advanced Ship and Deep-Sea Exploration
Shanghai 200240, China

Abstract—A modified moving particle semi-implicit (MPS) method based on GPU acceleration technique is applied to simulate three-dimensional (3-D) free surface flow by using our in-house solver MPSGPU-SJTU in this work. In order to validate MPSGPU-SJTU solver, 3-D dam break and sloshing, two typical violent flows with large deformation and nonlinear fragmentation of free surface are simulated. For dam break case, the results of fluid field, water front, wave height and impact pressure by GPU simulation are compared to CPU calculation, experiment, smooth particle hydrodynamics (SPH) and boundary element method (BEM). The comparison of fluid field and impact pressure among GPU, CPU and experiment is made in sloshing case. The accuracy of GPU solver is verified by these comparisons. Moreover, the computation time of every part in each calculation step is compared between GPU and CPU solvers. The results show that computational efficiency is improved dramatically by employing GPU acceleration technique.

I. INTRODUCTION

Moving particle semi-implicit method is one Lagrangian meshless method for incompressible fluid field, which was introduced by Koshizuka and Oka in 1996 [1]. Similar to other meshless methods like SPH, many randomly distributed particles are used to represent the fluid domain in MPS. These particles contain the information of mass, momentum, pressure and so on. The pattern of solving Navier-Stokes equation is semi-implicit, which is distinctive feature of MPS. The stable pressure field of fluid can be obtained from solving pressure Poisson equation. Because of the particles representation, MPS can easily track free surfaces and moving boundaries and remove many numerical difficulties due to the nonlinear surface. In the recent years, more and more researchers have used MPS to simulate the problems of violent flow with large deformation or nonlinear fragmentation of free surface, such as dam break (Zhang et al. (2011) [2]), sloshing (Yang et al. (2015) [3]), water entry (Chen et al. (2017) [4]), fluid-structure interaction (Zhang et al. (2016) [5]) and so on.

In order to obtain more accuracy and stable results, many researchers devoted themselves to improving the calculation accuracy and suppressing the pressure oscillation. Many numerical models of MPS are modified such as kernel function (Koshizuka et al. (1998) [6], Ataie-Ashtiani and Farhadi (2006)

Decheng Wan*

State Key Laboratory of Ocean Engineering, School of Naval Architecture, Ocean and Civil Engineering, Shanghai Jiao Tong University, Collaborative Innovation Center for Advanced Ship and Deep-Sea Exploration
Shanghai 200240, China

*Corresponding author: dcwan@sjtu.edu.cn

[7]), gradient model (Koshizuka et al. (1998) [6], Khayyer and Gotoh (2008) [8], Tsuruta et al.(2013) [9]), Laplacian model (Khayyer and Gotoh (2012) [10], Ikari et al. (2015) [11]), pressure Poisson equation (Khayyer and Gotoh (2009) [12], Tanaka and Masunaga (2010) [13], Kondo and Koshizuka (2011) [14]) and free surface detection (Khayyer and Gotoh (2009) [12], Tanaka and Masunaga (2010) [13]). In the past years, MPS is usually applied to simulate the two-dimensional problems because of the low computational efficiency. The refined particles methods like multi-resolution (Tang et al. (2016) [15-16]) and overlapping (Shibata et al. (2012) [17], Tang et al. (2016) [18]) are typical numerical acceleration technologies to reduce the calculation amount. In addition, many researchers use CPU parallel technique to accelerate the calculation of MPS (Ikari and Gotoh (2008) [19], Iribi et al. (2010) [20]).

By using CPU parallel technique, it is found that the computation time of MPS is reduced with the increase of calculation cores. The graphics processing unit (GPU) whose remarkable feature is multi cores have been produced with the development of industry. Based on GPU acceleration technique, many meshless methods are applied to simulate massive problems. The application of GPU technique in SPH is more mature than MPS. Harada et al. (2007) developed one search method for neighboring particles in order to implement the SPH entirely on GPU. By the limit of GPU card capacity, the maximum particle number is four million and the maximum speedup is 28 [21]. Crespo et al. (2011) developed DualSPHysics solver based on GPU acceleration technique. They used this solver to simulate 3-D dam break problem with one million particles and achieved a speedup of 64 by comparing to one CPU core [22]. Then Domínguez et al. (2013) optimized DualSPHysics solver based on the characters of GPU and accelerated the SPH codes with a maximum speedup of 56.2 [23]. Mokos et al. (2015) developed two-phase GPU code to simulate 3-D dam break with obstacle and obtain high acceleration ratio on different GPU card [24]. Because pressure Poisson equation is solved implicitly, the acceleration effect of GPU for MPS is not remarkable and the research of this field is rare. Zhu et al. (2011) developed different versions of MPS code based on different GPU memories [25]. Hori et al. (2011) used CUDA (Compute Unified Device Architecture) language to develop a GPU-accelerated MPS code and only acquired about 3-7 acceleration ratio by simulating two-dimensional (2-D) dam break [26]. Li et al. (2015) applied GPU acceleration technique to two parts of MPS, neighbor

particle list and pressure Poisson equation. By simulating 3-D dam break and sloshing, the speedup of these two parts is about 1.5 and 10, respectively [27]. Gou et al. (2016) used GPU accelerated MPS to simulate the isothermal multi-phase fuel-coolant interaction [28].

In this work, the GPU acceleration technique is applied to simulate 3-D free surface flows based on modified MPS. The brief introduction of modified MPS and GPU implementation in this paper is presented. Then the GPU solver is used to simulate 3-D dam break and sloshing problems. The numerical results of GPU code such as fluid field, impact pressure, wave height and water front are compared to the results of CPU solver, experiment and other methods. In addition, the comparison of computation time between GPU solver and CPU solver is conducted.

II. NUMERICAL METHOD

In this paper, the simulation of flow is calculated by our in-house particle solver MPSGPU-SJTU based on modified MPS method. The applied numerical models are introduced briefly in this section.

A. Governing Equations

The governing equations for viscous incompressible fluid contain continuity equation and Navier-Stokes equation.

$$\frac{1}{\rho} \frac{D\rho}{Dt} = \nabla \cdot \vec{V} = 0 \quad (1)$$

$$\frac{D\vec{V}}{Dt} = -\frac{1}{\rho} \nabla P + \nu \nabla^2 \vec{V} + \vec{g} \quad (2)$$

where ρ is the fluid density, t is the time, \vec{V} is the velocity vector, P is the pressure, ν is the kinematic viscosity and \vec{g} is the gravitational acceleration vector.

B. Kernel Function

In MPS method, the particle interaction is described by a kernel function. Zhang and Wan (2012) developed a modified kernel function in order to avoid the singularity at $r=0$ in original version [29].

$$W(r) = \begin{cases} \frac{r_e}{0.85r + 0.15r_e} - 1 & 0 \leq r < r_e \\ 0 & r_e \leq r \end{cases} \quad (3)$$

where r is the distance between two particles and r_e is the radius of the particle interaction.

C. Particle Interaction Models

The models of particle interaction include gradient model, divergence model and Laplacian model for MPS. These models can be written as:

$$\langle \nabla \phi \rangle_i = \frac{D}{n^0} \sum_{j \neq i} \frac{\phi_j + \phi_i}{|\vec{r}_j - \vec{r}_i|^2} (\vec{r}_j - \vec{r}_i) \cdot W(|\vec{r}_j - \vec{r}_i|) \quad (4)$$

$$\langle \nabla \vec{V} \rangle_i = \frac{D}{n^0} \sum_{j \neq i} \frac{(\vec{V}_j - \vec{V}_i) \cdot (\vec{r}_j - \vec{r}_i)}{|\vec{r}_j - \vec{r}_i|^2} \cdot W(|\vec{r}_j - \vec{r}_i|) \quad (5)$$

$$\langle \nabla^2 \phi \rangle_i = \frac{2D}{n^0 \lambda} \sum_{j \neq i} (\phi_j - \phi_i) \cdot W(|\vec{r}_j - \vec{r}_i|) \quad (6)$$

$$\lambda = \frac{\sum_{j \neq i} W(|\vec{r}_j - \vec{r}_i|) \cdot |\vec{r}_j - \vec{r}_i|^2}{\sum_{j \neq i} W(|\vec{r}_j - \vec{r}_i|)} \quad (7)$$

where D is the space dimension, n^0 is the initial particle number density, \vec{r} is coordinate vector of particle, ϕ is any physical quantity and λ is applied to make sure that the increase of variance is equal to the analytical solution..

D. Model of Incompressibility

Lee et al. (2015) improved a mixed source term method (Tanaka and Masunaga(2010) [13]) combined with the velocity divergence-free condition and constant particle number density condition [30].

$$\langle \nabla^2 P^{k+1} \rangle_i = (1-\gamma) \frac{\rho}{\Delta t} \nabla \cdot \vec{V}_i^* - \gamma \frac{\rho}{\Delta t^2} \frac{\langle n^* \rangle_i - n^0}{n^0} \quad (8)$$

where γ is a variable parameter from 0 to 1, Δt is the time step, n^* is the temporal particle number density and defined as:

$$\langle n \rangle_i = \sum_{j \neq i} W(|\vec{r}_j - \vec{r}_i|) \quad (9)$$

E. Free Surface Detection

In MPS method, the Dirichlet boundary condition is imposed by assigning zero pressure for surface particles. Zhang and Wan (2012) developed a modified surface particle detection method, which is based on the asymmetry arrangement of neighboring particles [29].

$$\langle \bar{F} \rangle_i = \frac{D}{n^0} \sum_{j \neq i} \frac{1}{|\bar{r}_i - \bar{r}_j|} (\bar{r}_i - \bar{r}_j) W(r_{ij}) \quad (10)$$

$$\langle |\bar{F}| \rangle_i > \alpha \quad (11)$$

$$\alpha = 0.9 |\bar{F}|^0 \quad (12)$$

where \bar{F} is a vector which represents the asymmetry of arrangements of neighbor particles, $|\bar{F}|^0$ is the initial value of $|\bar{F}|$.

F. Boundary Condition

In this work, multilayer particles are used to present the wall boundary. The wall particles are arranged at the boundary and the pressures of them are solved by PPE. Two layers of ghost particles are configured to fulfill the particle number density near the boundary so that the particle interaction can be properly simulated near the boundary. The pressure of ghost particle is obtained by interpolation.

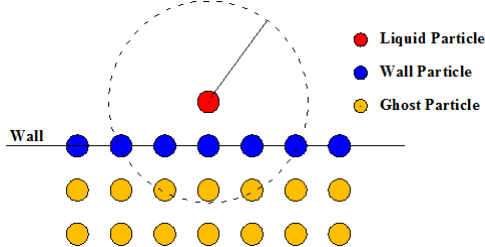


Figure 1. Schematic of boundary particles

III. GPU ACCELERATION

Based on the above brief introduction, one feature of MPS method can be found that the calculation of each particle is independent of the synchronous results of other particles except solving pressure Poisson equation. This feature determines that the calculation flow of MPS can be effectively parallelized. Comparing to CPU, GPU is designed possess more arithmetic logic units (ALU) in the same chip area. This hardware design makes GPU to own high floating point operations per second (FLOPS) and ability to process multi objects simultaneously.

CUDA is a parallel computing platform and programming model created by NVIDIA and implemented by GPU [31]. A CUDA program is divided into a host part and a device part. The host part runs on CPU while the device part runs on GPU. The host code includes instructions for setting parallelism and communicating data between host and device.

In order to accelerate the iteration of pressure Poisson equation, the open source library CUSP is applied in GPU

solver. Cusp is a library for sparse linear algebra and graph computations based on Thrust. Cusp provides a flexible, high-level interface for manipulating sparse matrices and solving sparse linear systems [32].

The computational flow chart of MPS method is shown in Fig. 2. One time integration of MPS method is mainly composed of two steps. The first step corresponds to an explicit calculation considering the gravity and viscosity terms. The second step is an implicit calculation accounting for the pressure term. The pressure field of particles is obtained by solving pressure Poisson equation which is discretized into a linear system. The GPU implementation mainly consists of eight steps except the data exchange between GPU and CPU.

- Step 1: Neighbor particle searching
- Step 2: Explicit calculation of gravity and viscous force
- Step 3: Updating for temporary velocity of particles
- Step 4: Calculation of particle number density
- Step 5: Free surface detection
- Step 6: Solving the pressure Poisson equation implicitly
- Step 7: Calculation of pressure gradient
- Step 8: Updating for velocity and position of particles finally

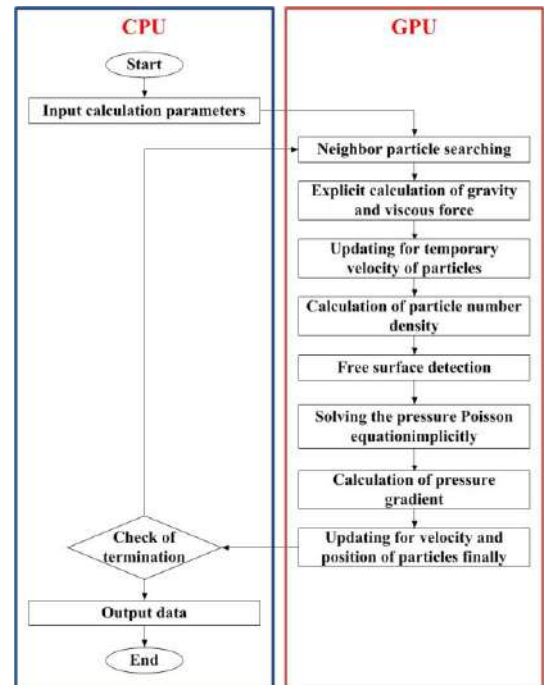


Figure 2. The flow chart of GPU implementation

IV. NUMERICAL SIMULATION

In this section, the results of GPU simulations are obtained by running MPSGPU-SJTU solver. In addition, another in-house CPU solver MLParticle-SJTU is used to

compare with GPU solver. The reliability of MLParticle-SJTU solver was validated by many violent flow cases in previous articles [2-5]. The comparisons between CPU and GPU include fluid field, monitoring data, computation time and so on. In this paper, all simulations are performed on parallel high performance computing (HPC) with multi cores of Intel(R) Xeon(R) E5-2680 v2, 2.80 GHz. The GPU card is NVIDIA Tesla K40M, which has 2880 CUDA cores with 12GB graphics memory. Table 1 shows the parameters of computing devices. All data are saved by double precision floating point in both CPU and GPU solvers.

TABLE I. COMPUTATIONAL ENVIRONMENT OF CPU AND GPU

	HPC	GPU
Card	Intel(R) Xeon(R) E5-2680 v2, 2.80 GHz	Tesla K40M
Memory	DDR3 1600, 16GB	12GB
Max Cores	10	2880
Programming Language	C++	CUDA C/C++
Compiler	gcc, MVAPICH	CUDA 7.0, Cusp v0.5.1

A. Dam Break Flow

Dam break flow is a typical violent free surface flow with complex phenomena such as the overturning of free surface, splashing and jet flow. In this sub-section, a 3-D dam break flow is numerically simulated by MPSGPU-SJTU solver and MLParticle-SJTU solver, respectively. The numerical model is the same as the experimental facility given by Colicchio (2001). Fig. 3 shows the sketch of computational domain. For fluid domain, the height of water column (H) is 0.6 m and the length is 1.2 m. One pressure probe and one wave gauge are placed in the tank to measure the impact pressure on lateral wall and wave height. The arrangements of monitoring points are listed in Table 2. In this case, the initial particle space is 0.01 m. In total, 1199205 particles with 712800 fluid particles are used to model. The time step is 2.5×10^{-4} s and the density of liquid is 1000 kg/m^3 .

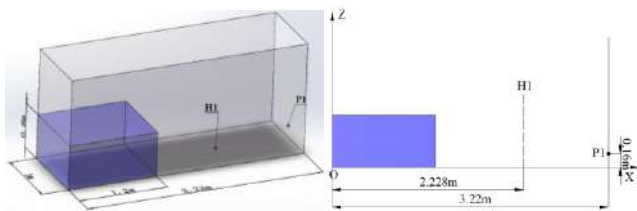


Figure 3. The sketch of model

TABLE II. ARRANGEMENTS OF PROBES

	X/m	Y/m	Z/m
H1	2.228	0	0
P1	3.22	0.5	0.16

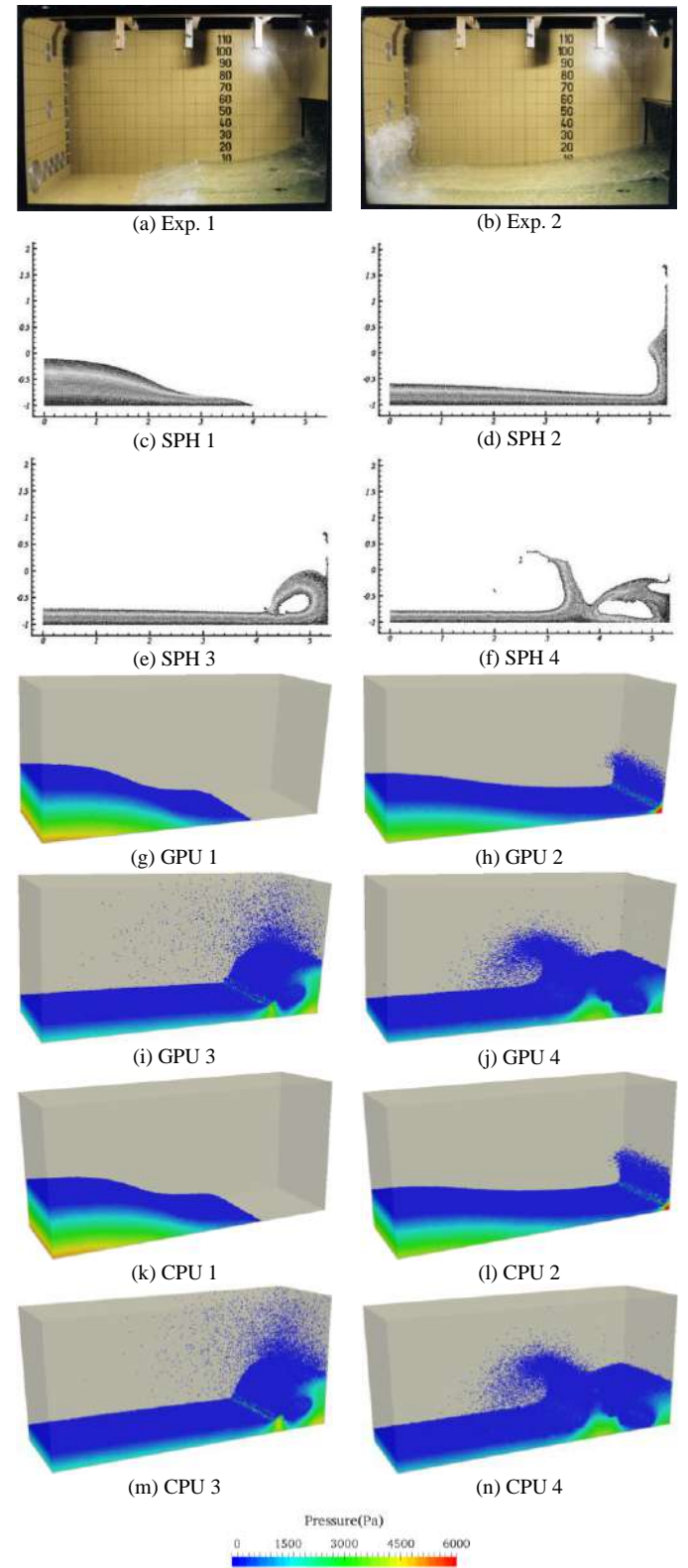


Figure 4. The flow fields of experiment, SPH, GPU and CPU

Fig. 4 shows some snapshots of numerical and experimental flow fields. After the water column is released, the water front firstly moves along the dry bottom of tank. The free surface is smooth and the pressure of fluid field is equal to hydrostatic pressure. Then the water front impacts the corner of tank and the pressure around the corner increases suddenly. The water front runs up along the lateral wall and a part of fluid splashes. Under the action of gravity, the subsequent fluid forms the overturning of free surface and falls into the lower fluid domain. The fallen water against the surface generates the second successive curling wave. From these figures, the numerical flow field of GPU simulation is in good agreement with CPU, SPH, BEM and experimental results.

In addition, some simulated results of GPU are also compared to the results of GPU, SPH, BEM and the data of experiment. Fig. 5 gives the propagation of water front. All the results show that the fluid accelerates smoothly and reaches to a stable velocity. The wave front propagation along the dry bottom of tank by GPU simulation is similar to the result of CPU and also in agreement with SPH and BEM. However, the experimental propagation speed of water front is slower than the results of numerical simulation.

Fig. 6 shows the comparison of impact pressure on the right wall among numerical methods and experiment. The overall tendency of pressure history by MPSGPU-SJTU solver shows a good agreement with CPU solver, SPH, BEM and experimental data. There are two peak values in the pressure history. After the process of water front moves along the bottom of tank, the first peak value of pressure is suddenly caused by the impact of fluid on the side wall. And the second pressure peak results from the impact of fallen overturning water on the free surface of lower fluid domain. There is a clear phase difference and value difference of the second pressure peak between numerical results and experimental data.

The variation of wave height by many numerical simulations and experiment is shown in Fig. 7. Because of the transition from dry-deck condition to wet-deck condition, the wave height increases suddenly. Then the wave height rises slowly with the process of fluid movement. Due to the overturning of water front, the wave height reaches to the maximum value in whole process. The peak value of wave height by numerical simulations is obviously higher than that of experiment. For these differences between numerical methods and experiment, one or two phase model is the possible reason mentioned by Colagrossi and Landrini (2003). In addition, BEM can not capture the phenomena of nonlinear stage such as overturning of free surface and splashing from recorded pressure and wave height. However, these phenomena can be qualitatively simulated by MPS and SPH.

Fig. 8 shows the computation time of every part in one step by GPU and CPU simulations. For MPS, solving pressure Poisson equation has the most amount of time which limits the computational efficiency. The computation

time of every part decreases with the increase of CPU cores. The computational efficiency of GPU is remarkable and the speedup is up to 18 by comparing to one CPU core in Fig. 9.

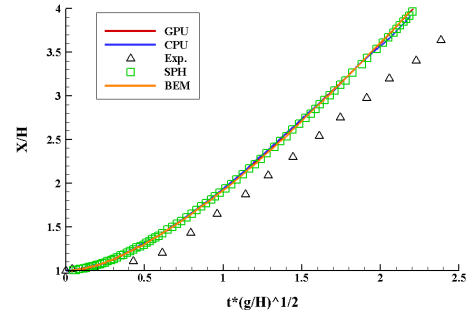


Figure 5. The water-front of GPU, CPU experiment, SPH and BEM

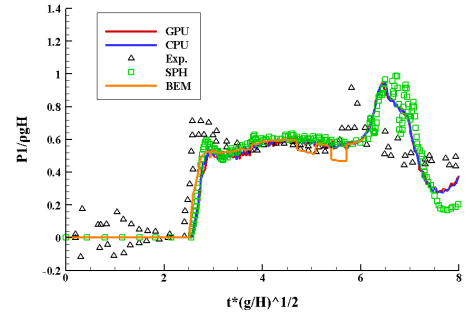


Figure 6. The impact pressure of GPU, CPU experiment, SPH and BEM

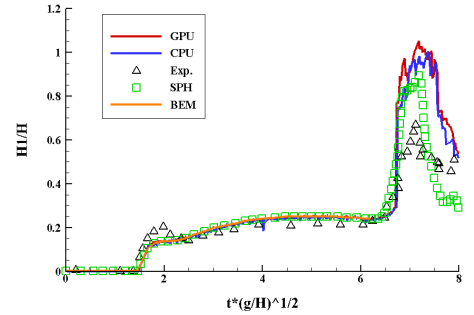


Figure 7. The wave height of GPU, CPU experiment, SPH and BEM

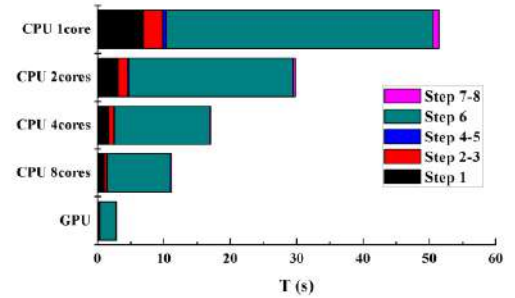


Figure 8. The computation times of GPU and CPU

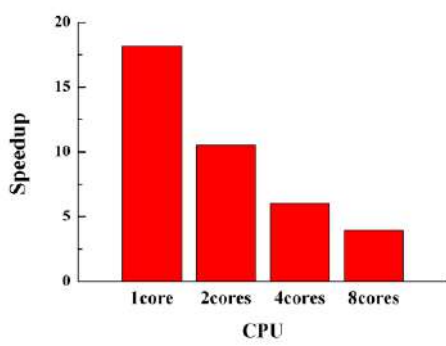


Figure 9. The speedup by GPU

B. Sloshing Flow

A 3-D liquid tank under horizontal excitation which is the same as the experimental model given by Song et al. (2013) is selected as numerical model to simulate in this sub-section. The sketch and geometric parameters of the liquid tank are shown in Fig. 10. The length of tank is 0.79 m, the width and the height are 0.48 m. The filling level is 30% and the corresponding depth of water is 0.144 m. Two pressure probes are placed at the lateral wall to measure the variation of impact pressure. The whole sloshing system is subject to move by the external surge excitation:

$$x = A \cdot \sin(\omega \cdot t) \quad (13)$$

where A is the amplitude of excitation with the value of 0.0575 m and ω is the excitation frequency which is set to 4.49 rad/s. The initial particle space is 0.005 m, the time step is 2×10^{-4} s and the density of liquid is 1000 kg/m³. In this case, total 678373 particles including 432535 fluid particles are used to simulate this model.

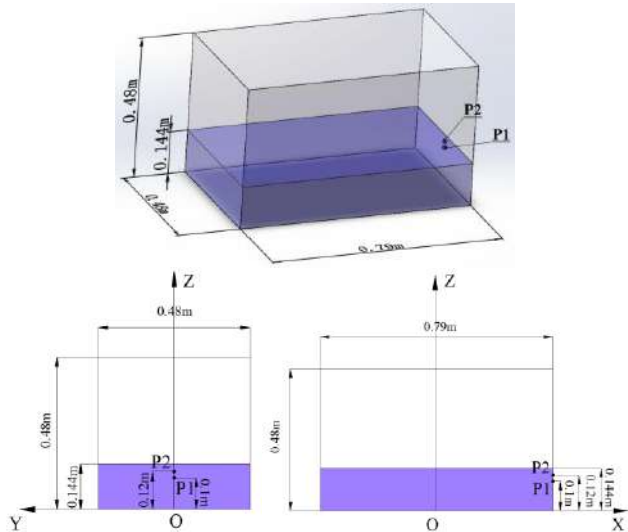


Figure 10. The sketch of model

TABLE III. ARRANGEMENTS OF TWO PRESSURE PROBES

	X/m	Y/m	Z/m
P1	0.395	0	0.1
P2	0.395	0	0.12

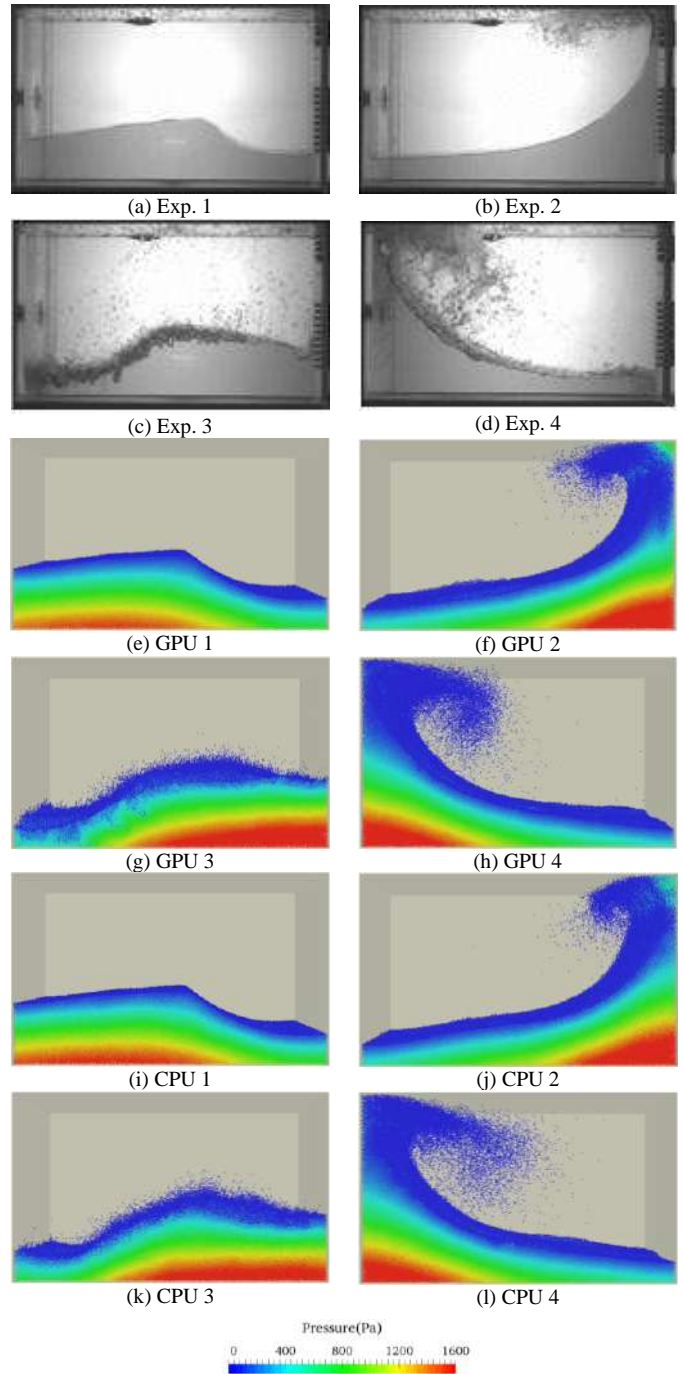


Figure 11. The flow fields of experiment, GPU and CPU

Some snapshots of experimental and numerical flow fields are shown in Fig. 11. The GPU simulation is in good agreement with the flow fields of CPU simulation and experiment. The fluid field is forced to move by the

movement of tank. The sloshing wave travels to the right walls when the tank moves right. Then the water front impacts and climbs along the lateral wall. And the front of fluid hits the corner and forms jet flow which still spreads along the ceiling of tank. Under the action of gravity, the jet flow falls into the lower fluid field and moves to the left wall. From Fig. 11, the obvious nonlinear phenomena such as overturning of water and liquid splash can be observed. These large deformation and nonlinear fragmentation of free surface are simulated by both MLParticl-SJTU solver and MPSGPU-SJTU solver.

In addition, Fig. 12 shows the numerical pressure histories of CPU and GPU by comparing to the experimental data. A typical impact pressure pattern “church roof” can be observed in the figure. When the liquid tank reaches its maximum position on the right and starts to move left, the fluid field still moves to and impinges the right wall, which results in an instant pressure peak. The sloshing flow runs up along the right wall with the decrease of pressure. The fallen fluid which drops down on the free surface due to the gravity causes the second pressure peak. Finally, the pressure is less than zero, because the depth of water near right-side wall is below pressure probes while the fluid field moves to the left side wall.

Fig. 13 also gives the comparison of computation time between GPU and CPU. The performance of GPU is outstanding in the conditions of guaranteeing the accuracy. The GPU solver can reduce the computation time of every part up to one order. In addition, the acceleration ratio between GPU and one CPU core is up to 35 from Fig. 14.

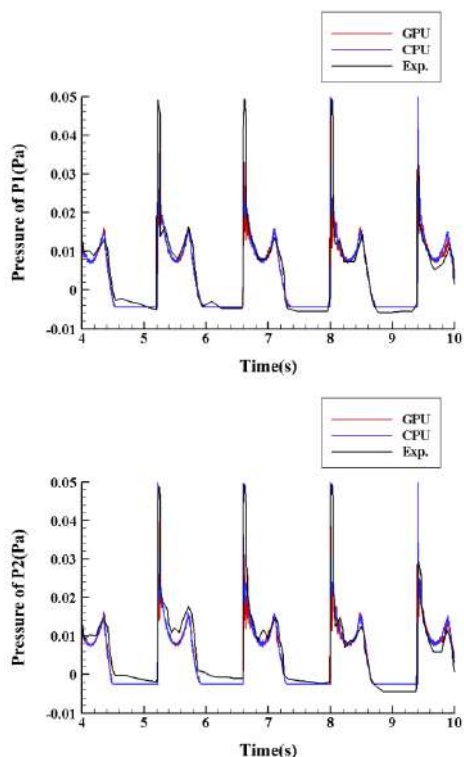


Figure 12. The impact of experiment, GPU and CPU

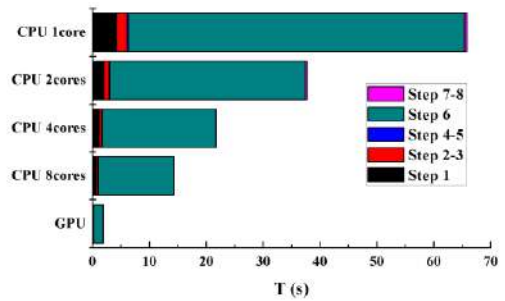


Figure 13. The computation times of GPU and CPU

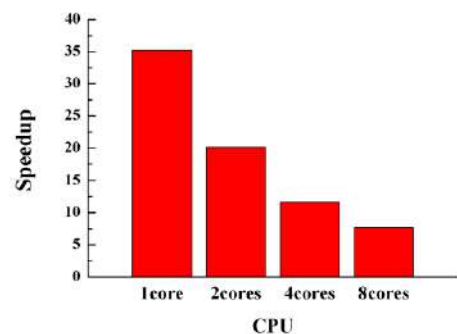


Figure 14. The speedup by GPU

V. CONCLUSIONS

In this work, the in-house solver MPSGPU-SJTU based on modified MPS method is developed to simulate the three-dimensional violent flows such as dam break and sloshing. The large deformation and nonlinear fragmentation of free surface, like overturning wave, jet flow, splashing and so on, can be observed clearly in these numerical simulations. The numerical results such as impact pressure on the lateral wall, wave height and water front of GPU simulation shows a good agreement with CPU calculation, SPH, BEM and experiment. These comparisons demonstrate the validity of MPSGPU-SJTU solver. In addition, the GPU solver can dramatically reduce the computation time and improve the computational efficiency. The speedup of every calculation step between GPU and CPU solvers is up to 35.

ACKNOWLEDGEMENTS

This work is supported by the National Natural Science Foundation of China (51379125, 51490675, 11432009, 51579145), Chang Jiang Scholars Program (T2014099), Shanghai Excellent Academic Leaders Program (17XD1402300), Program for Professor of Special Appointment (Eastern Scholar) at Shanghai Institutions of Higher Learning (2013022), Innovative Special Project of Numerical Tank of Ministry of Industry and Information Technology of China (2016-23/09) and Lloyd's Register Foundation for doctoral student, to which the authors are most grateful.

REFERENCE

- [1] S. Koshizuka and Y. Oka. "Moving-particle semi-implicit method for fragmentation of incompressible fluid," Nuclear Science and Engineering, vol. 123(3), pp.421–434, July 1996.
- [2] C. Zhang, Y. X. Zhang, and D. C. Wan. "Comparative study of SPH and MPS methods for numerical simulations of dam breaking problems," Chinese Journal of Hydrodynamics, vol. 26, pp.736–746, June 2011.
- [3] Y. Q. Yang, Z. Y. Tang, Y. L. Zhang, and Wan, DC. "Investigation of Excitation Period Effects on 2D Liquid Sloshing by MPS Method," Proceedings of the Twenty-fifth (2015) International Ocean and Polar Engineering Conference, Hawaii, USA, 937–944, June 2015.
- [4] X. Chen, C. P. Rao, and D. C. Wan. "Numerical simulation of water entry for two-dimensional wedge by MPS," Chinese Journal of Computational Mechanics, vol. 34, pp.356–362, June 2017.
- [5] Y. L. Zhang, Z. Y. Tang, and D. C. Wan. "Numerical Investigations of Waves Interacting with Free Rolling Body by Modified MPS Method," International Journal of Computational Methods, vol. 13: 1641013–1–1641013–14, August 2016.
- [6] B. Ataie-Ashtiani and L. Farhadi. "A stable moving-particle semi-implicit method for free surface flows," Fluid Dynamics Research, vol. 38, pp.241–256, April 2006.
- [7] S. Koshizuka, A. Nobe, and Y. Oka. "Numerical analysis of breaking waves using the moving particle semi-implicit method," International Journal for Numerical Methods in Fluids, vol. 26, pp.751–769, April 1998.
- [8] A. Khayyer and H. Gotoh. "Development of CMPS method for accurate water-surface tracking in breaking waves," Coastal Engineering Journal, vol. 50, pp.179–207, June 2008.
- [9] N. Tsuruta, A. Khayyer, and H. Gotoh . "A short note on dynamic stabilization of moving particle semi-implicit method," Computers & Fluids, vol. 82, pp.158–164, August 2013.
- [10] A. Khayyer and H. Gotoh. "A 3D higher order Laplacian model for enhancement and stabilization of pressure calculation in 3D MPS-based simulations," Applied Ocean Research, vol. 37, pp.120–126, August 2012.
- [11] H. Ikari, A. Khayyer and H. Gotoh. "Corrected higher order Laplacian for enhancement of pressure calculation by projection-based particle methods with applications in ocean engineering," Journal of Ocean Engineering and Marine Energy, vol. 1, pp.361–376, November 2015.
- [12] A. Khayyer and H. Gotoh. "Modified moving particle semi-implicit methods for the prediction of 2D wave impact pressure," Coastal Engineering, vol. 56, pp.419–440, April 2009.
- [13] M. Tanaka, and T. Masunaga. "Stabilization and smoothing of pressure in MPS method by quasi-compressibility," Journal of Computational Physics, vol. 229, pp.4279–4290, June 2010.
- [14] M. Kondo, and S. Koshizuka. "Improvement of stability in moving particle semi-implicit method," International Journal for Numerical Methods in Fluids, vol. 65, pp.638–654, February 2011.
- [15] Z. Y. Tang, Y. L. Zhang, and D. C. Wan. "Multi-resolution MPS method for free surface flows," International Journal of Computational Methods, vol. 13: 1641018, August 2016.
- [16] Z. Y. Tang, D. C. Wan, G. Chen, and Q. Xiao. "Numerical Simulation of 3D Violent Free-Surface Flows by Multi-Resolution MPS Method," Journal of Ocean Engineering and Marine Energy, vol. 2, pp.355–364, July 2016.
- [17] K. Shibata, S. Koshizuka, M. Sakai, and K. Tanizawa. "Lagrangian simulations of ship-wave interactions in rough seas," Ocean Engineering, vol. 42, pp.13–25, March 2012.
- [18] Z. Y. Tang, Y. L. Zhang, and D. C. Wan. "Numerical simulation of 3D free surface flows by overlapping MPS," Journal of Hydrodynamics, vol. 28, pp.306–312, July 2016.
- [19] H. Ikari, and H. Gotoh. "Parallelization of MPS method for 3D wave analysis," Advances in Hydro-science and Engineering, 8th International Conference on Hydro-science and Engineering (ICHE), Nagoya, Japan, September 2008.
- [20] T. Iribe, T. Fujisawa, and S. Koshizuka. "Reduction of communication in parallel computing of particle method for flow simulation of seaside areas," Coastal Engineering Journal, vol. 52, pp.287–304, December 2010.
- [21] T. Harada, S. Koshizuka, and Y. Kawaguchi. "Smoothed Particle Hydrodynamics on GPUs," Structure, vol. 4, pp.671–691, January 2007.
- [22] A. J. C. Crespo, J. M. Domínguez, A. Barreiro, M. Gómez-Gesteira, and B. D. Rogers. "GPUs, a new tool of acceleration in CFD: efficiency and reliability on smoothed particle hydrodynamics methods," PLoS One, vol. 6: e20685, June 2011.
- [23] J. M. Domínguez, A. J. C. Crespo, and M. Gómez-Gesteira. "Optimization strategies for CPU and GPU implementations of a smoothed particle hydrodynamics method," Computer Physics Communications, vol. 184, pp.617–627, March 2013.
- [24] A. Mokos, B. D. Rogers, P. K. Stansby, and J. M. Domínguez. "Multi-phase SPH modelling of violent hydrodynamics on GPUs," Computer Physics Communications, vol. 196, pp.304–316, November 2015.
- [25] X. S. Zhu, L. Cheng, L. Lu, and B. Teng. "Implementation of the moving particle semi-implicit method on GPU," Science China, vol. 54, pp.523–532, March 2011.
- [26] C. Hori, H. Gotoh, H. Ikari, and A. Khayyer. "GPU-acceleration for moving particle semi-implicit method," Computers & Fluids, vol. 51, 174–183, December 2011.
- [27] H. Z. Li, Y. L. Zhang, and D. C. Wan. "GPU Based Acceleration of MPS for 3D Free Surface Flows," Proceedings of the 9th International Workshop on Ship and Marine Hydrodynamics, Glasgow, UK, August 2015.
- [28] W. Gou, S. Zhang, and Y. Zheng. "Simulation of isothermal multi-phase fuel-coolant interaction using MPS method with GPU acceleration," Kerntechnik, vol. 81, pp.330–336, June 2016.
- [29] Y. X. Zhang, and D. C. Wan. "Numerical simulation of liquid sloshing in low-filling tank by MPS," Journal of Hydrodynamics, vol. 27, pp.101–107, January 2012.
- [30] B. H. Lee, J. C. Park, M. H. Kim, and S. C. Hwang. "Step-by-step improvement of MPS method in simulating violent free-surface motions and impact-loads," Computer Methods in Applied Mechanics and Engineering, vol. 200, pp.1113–1125, February 2011.
- [31] CUDA Toolkit Documentation v8.0.61. <http://docs.nvidia.com/cuda/>. 2017.
- [32] CUSP. <https://developer.nvidia.com/cusp>. 2017.
- [33] G. Colicchio, A. Colagrossi, M. Greco, and M. Landrini. "Free surface flow after a dam break a comparative study," 4th Numerical Towing Tank Symposium, Germany, September 2001.
- [34] Y. K. Song, K. A. Chang, Y. Ryu, and S. H. Kwon. "Experimental study on flow kinematics and impact pressure in liquid sloshing," Experiments in Fluids, vol. 54, pp.1–20, September 2013.

GPU-based SPH modeling of flood with floating bodies in urban underground spaces

Jiansong Wu*, Na Li, Wenyu Liu

School of Resources and Safety Engineering
China University of Mining & Technology
Beijing 100083, China
jiansongwu@hotmail.com

Hui Zhang

Institute for Public Safety Research
Tsinghua University
Beijing 10084, China
zhhui@tsinghua.edu.cn

Abstract—Due to the “innate” low-lying weakness, underground facilities in urban areas are prone to flood. The underground inundation may cause loss of life and very serious damage to properties particularly in the case of the flooding flow involving in floating objects. In this paper, the mesh-free Smoothed Particle Hydrodynamics (SPH) method with the Graphic Processing Unit (GPU) parallel computing technique employed (GPUSPH) is employed to simulate dam-break flooding in complex urban underground spaces. Taking advantage of powerful GPU parallel computing ability, the dam-break flooding immersed three floating objects into an underground basement through staircases that involves in millions of particles (computational nodes) are simulated. Numerical results fairly reproduce the complex inundation process, and reasonably present complicated underground flooding flow features involving in interactions of flooding flow with floating objects and staircases, which indicates that SPH method is an alternative tool for the modelling of flooding in complex urban underground spaces.

I. INTRODUCTION

Due to the “innate” low-lying weakness, underground facilities in urban areas are prone to flooding caused by the breaking of a dam or a levee, or a flash flood after an exceptional rainfall [1]. The underground inundation may cause loss of life and very serious damage to properties, particularly in the case of the flooding flow involving floating objects. Therefore, it is very important to study the urban underground inundation in terms of hydraulic analysis and disaster prevention. An important way of clarifying the physical phenomena and determining the risk of the underground flooding flow is to numerically simulate the inundation process.

With respect to the numerical modeling of urban underground flooding, Japanese scientists first started the research work and have made much progress on grid-based two dimensional (2D) models for simulating underground flooding. Toda et al. proposed a storage pond model and runoff model to implement the flood propagation between underground spaces, and used the empirical step flow formula to model the flood inflow and outflow through the gates, passages and stairs [2, 3]. Additionally, Han et al. presented a model using link-node mode to implement the flood propagation between underground spaces, and assumed the tunnel for the subway and the pavement as links and the station and underground malls as nodes [4].

Ishigaki et al. improved Toda’s model, and successfully modeled pluvial flooding of 10 to 100 year scale and tsunami flooding of 1000 year scale [5]. These 2D models based on solving Shallow Water Equations (SWEs) could achieve reasonable results for simulating simple underground inundation subject to some simplified assumptions or empirical parameters, or will have significant oscillations in geometrically complex underground spaces involving complex layouts of staircases and basements due to computationally grid distortion issues. Furthermore, these SWEs models have great difficulty in handling floating objects.

In this paper, in order to enhance the quality and accelerate the computation speed of numerical modeling of complex underground inundation, especially simulating underground flood with floating bodies, we apply GPU-based SPH method (GPUSPH) to simulate dam-break flood with floating objects in a three dimensional (3D) geometrically complex underground facility.

II. METHODOLOGY

A. SPH formulations

SPH is a purely Lagrangian mesh-free method, which was originally developed to solve astrophysical problems and has been widely used to simulate free surface flow these years [6]. The key feature of SPH is to use moving interpolating particles or nodes to discretize computational domain. Each particle has individual mass and associated physical properties. These attractive features make it explicitly conserve mass and linear momentum and not require explicit interface tracking treatment, and therefore geometrically complex and moving boundaries can be handled without undue difficulty.

The SPH formulations of Navier-Stokes equations are based on integral and interpolation theory, and are generally derived through two steps: kernel approximation and particle approximation. The first step, kernel approximation, describes the integral representation of field functions and their derivatives, which is given as follows:

$$f(\mathbf{x}) = \int_{\Omega} f(\mathbf{x}') W(\mathbf{x} - \mathbf{x}', h) d\mathbf{x}' \quad (1)$$

$$\nabla \cdot f(\mathbf{x}) = - \int_{\Omega} f(\mathbf{x}') \cdot \nabla W(\mathbf{x} - \mathbf{x}', h) d\mathbf{x}' \quad (2)$$

where $f(\mathbf{x})$ is a function of the position vector \mathbf{x} , $W(\mathbf{x} - \mathbf{x}', h)$ is the smoothing function which is approximated to the Dirac delta function $\delta(\mathbf{x} - \mathbf{x}')$ when h is close to zero, h is the smoothing length determining the influence area of the smoothing function, and $\nabla \cdot f(\mathbf{x})$ is the spatial derivative of field function. Further, the integral field variables and their derivatives can be replaced by discretized forms of summations with all the corresponding values at the neighbouring particles of the influence domain. This scheme is named as particle approximation, which is described in Eqs. (3) and (4).

$$f(\mathbf{x}_i) = \sum_{j=1}^N \frac{m_j}{\rho_j} f(\mathbf{x}_j) \cdot W_{ij} \quad (3)$$

$$\nabla \cdot f(\mathbf{x}_i) = \sum_{j=1}^N \frac{m_j}{\rho_j} f(\mathbf{x}_j) \cdot \nabla_i W_{ij} \quad (4)$$

with $W_{ij} = W(\mathbf{x}_i - \mathbf{x}_j, h) = W(|\mathbf{x}_i - \mathbf{x}_j|, h)$,

$$\nabla_i W_{ij} = \frac{\mathbf{x}_i - \mathbf{x}_j}{r_{ij}} \frac{\partial W_{ij}}{\partial r_{ij}} = \frac{\mathbf{x}_{ij}}{r_{ij}} \frac{\partial W_{ij}}{\partial r_{ij}}, \text{ where } N \text{ is the number of}$$

particles in the support domain of particle i , r_{ij} is the distance between particle i and j , ρ_j is the density associated with particle j , and m_j is the mass associated with particle j . W_{ij} is the smoothing function of particle i evaluated at particle j , and is closely related to the smoothing length h .

For Newtonian fluid flows, the viscous shear stress should be proportional to the shear strain rate. The governing Navier-Stokes equations with laminar viscous stresses can be written in Lagrangian description as follows:

$$\frac{D\rho}{Dt} = -\rho \nabla \cdot \mathbf{v} \quad (5)$$

$$\frac{D\mathbf{v}}{Dt} = -\frac{1}{\rho} \nabla p + \mathbf{g} + \nu_0 \nabla^2 \mathbf{v} \quad (6)$$

where \mathbf{v} is the velocity vector, p is the pressure, \mathbf{g} is the gravitational acceleration. While in order to handle and capture the turbulence effects in the flow, the Large Eddy Simulation turbulence scheme for the sub-particle scale(SPS) flow is obtained by adding a flattop spatial filter on equations (5) and (6) by Lo and Shao [7].

$$\frac{D\rho}{Dt} = -\rho \nabla \cdot \bar{\mathbf{v}} \quad (7)$$

$$\frac{D\bar{\mathbf{v}}}{Dt} = -\frac{1}{\rho} \nabla \bar{p} + \mathbf{g} + \nu_0 \nabla^2 \bar{\mathbf{v}} + \frac{1}{\rho} \nabla \cdot \boldsymbol{\tau} \quad (8)$$

The SPS approach above to model turbulence was originally presented by Lo and Shao in their incompressible SPH scheme [7]. Dalrymple and Rogers firstly introduced SPS model to the weakly compressible SPH scheme with the derived discretized forms based on the SPH approximations mentioned in the above section as follows

[8]:

$$\frac{d\rho_i}{dt} = \sum_{j=1}^N m_j (\mathbf{v}_i - \mathbf{v}_j) \cdot \nabla_i W_{ij} \quad (9)$$

$$\begin{aligned} \frac{d\mathbf{v}_i}{dt} = & -\sum_{j=1}^N m_j \left(\frac{p_i}{\rho_i^2} + \frac{p_j}{\rho_j^2} \right) \nabla_i W_{ij} + \mathbf{g} + \\ & \sum_{j=1}^N m_j \left(\frac{4\nu_0 \mathbf{x}_{ij} \cdot \nabla_i W_{ij}}{(\rho_i + \rho_j)r_{ij}} \right) \mathbf{v}_{ij} + \sum_{j=1}^N m_j \left(\frac{\boldsymbol{\tau}_i}{\rho_i^2} + \frac{\boldsymbol{\tau}_j}{\rho_j^2} \right) \nabla_i W_{ij} \end{aligned} \quad (10)$$

In the SPH simulation, the artificial compressibility is introduced by using a quasi-incompressible equation of state to model the incompressible flow. The following equation of state for water to model free surface flows has been widely used [9].

$$p = B \left\{ \left(\frac{\rho}{\rho_0} \right)^{\gamma} - 1 \right\} \quad (11)$$

where $\gamma = 7$ is used in most circumstances, ρ_0 is the reference density. B is a problem dependent parameter, which is always taken as the initial pressure p_0 .

In terms of the rate of change of particle position, the following XSPH correction equation is often to simulate free surface problems,

$$\frac{d\mathbf{x}_i}{dt} = \mathbf{v}_i - \varepsilon \sum_{j=1}^N \frac{m_j}{\rho_j} \mathbf{v}_{ij} \cdot W_{ij} \quad (12)$$

where ε is a constant in the range of $0 < \varepsilon < 1.0$, in most circumstances $\varepsilon = 0.5$ is a good choice [10].

B. Motion of floating objects in SPH

The scheme to implement the floating objects in underground flooding is referred to the motion equations of moving rigid bodies proposed by Monaghan et al. (2003) [11] and Monaghan (2005) [12]. The motion of rigid objects is determined through the motion and the rotation of the centre of mass. The equations of the motion and rotation of the centre of mass is given by:

$$M \frac{d\mathbf{V}}{dt} = \mathbf{F} \quad (13)$$

$$I \frac{d\boldsymbol{\Omega}}{dt} = \mathbf{T} \quad (14)$$

where M is the mass of rigid objects, \mathbf{V} is the velocity of the center of mass, \mathbf{F} is the total force adding on the rigid bodies, I is the moment of inertia, $\boldsymbol{\Omega}$ is the angular velocity of the center of mass, \mathbf{T} is the total torque about the center of mass.

The rigid object is represented by a number of boundary particles, and thus the movement of each boundary particle is part of the motion of the rigid object. These boundary particles interact with fluid particles, and the summation of the forces adding on each boundary particle by fluid particles is the total forces adding on the rigid object, so equations (13) and (14) become

$$M \frac{d\mathbf{V}}{dt} = \sum_{k=1}^{N_{BP}} m_k \mathbf{f}_k \quad (15)$$

$$I \frac{d\Omega}{dt} = \sum_{k=1}^{N_{BP}} m_k (\mathbf{x}_k - \mathbf{x}_0) \times \mathbf{f}_k \quad (16)$$

where N_{BP} is the total boundary particles of the rigid body, \mathbf{f}_k is the force per unit mass on boundary particle k , m_k is the mass of boundary particle k , \mathbf{x}_0 is the displacement of the center of mass. The velocity of boundary particles is given by

$$\mathbf{v}_k = \frac{d\mathbf{x}_k}{dt} = \mathbf{V} + \Omega \times (\mathbf{x}_k - \mathbf{x}_0) \quad (17)$$

The force adding on each boundary particle is calculated by summing up the contribution from all the surrounding fluid particles within the support kernel, which is given by

$$\mathbf{f}_k = \sum_{i=1}^{N_{WP}} \mathbf{f}_{ki} \quad (18)$$

where N_{WP} is the total surrounding fluid particles of boundary particle k , \mathbf{f}_{ki} is the force per unit mass exerted by fluid particle i on boundary particle k . To ensure that linear and angular momentum conservation of the entire particle system in the absence of external forces, the force on boundary particle k due to fluid particle i must be equal and opposite to the force on i due to k , so

$$m_k \mathbf{f}_{ki} = -m_i \mathbf{f}_{ik} \quad (19)$$

This is very useful as during the computation we only actually compute repulsive force, which is calculated based on the modified version of boundary repulsive force by Monaghan and Kos (1999) [13]. The integrations of equations (15) ~ (17) with time can track and predict the motion of floating bodies.

III. GPUSPH MODEL

GPUSPH (or called GPUSPHysics), originally developed by Herault et al [14], is programmed using Compute Unified Device Architecture (CUDA), which is a programming language introduced by NVIDIA corporation for engineers and scientists to readily use the GPU by extending the C++ language to handle the computing operations of the GPU and its interfacing with the CPU host. Furthermore, it also employs C++ and OpenGL. In the spring of 2007, GPUSPH totally implements all the SPH computing segments (neighbour search, force computation and time integration) on GPU, and has many options for SPH numerical techniques, such as interpolation kernels, density smoothing, variable time step, wall boundary treatments, free surface tracking, “XSPH” technique, SPS turbulence mode, etc. With OpenGL, GPUSPH can display computing results real-time. It is an open source code and updated to Version 4.1 with multi-node parallelism at present [15]. For more details you can download the GPUSPH code and the guide from this link:

www.gpusph.org or www.ce.jhu/dalrymple/GPUSPH. The typical features of GPUSPH used in this paper are briefly introduced as follows.

A. Smoothing kernel

There have been three kernel functions implemented in GPUSPH model: quadratic, cubic spline and Wendland quintic. The accuracy of the SPH interpolation generally increases with the order of the polynomial employed in the smoothing function. In this paper, we use the Wendland quintic function, which can constitute a good choice in terms of computational accuracy and effectiveness, since it provides a higher order of interpolation with a computational cost comparable to the quadratic kernel [16]. The Wendland quintic smoothing function is given by

$$W(\mathbf{x} - \mathbf{x}', h) = \alpha_d (1 - \frac{q}{2})^4 (2q+1), \quad 0 \leq q \leq 2 \quad (20)$$

where α_d is taken as $7/(4\pi h^2)$ and $7/(8\pi h^3)$ in 2D and 3D space, respectively.

B. Virtual geometric boundary treatment

In the GPUSPH model, a virtual geometric boundary treatment (VGBT) is developed. Instead of establishing the fixed boundaries with particles, VGBT construct the fixed solid wall by using virtual mathematical planes [17]. This can be a considerable saving in memory as particle boundaries require a great amount of particles for large-scale problems, especially for GPU computing it could save much video memory. The first step of VGBT is to calculate the distance between water particle and the virtual plane, and then compute the repulsive force exerted on the corresponding water particle by the virtual plane according to ‘‘Lennard Jones’’-like repulsive force equation proposed by Monaghan[12].

The plane is defined by a linear equation as follows:

$$ax + by + cz = d \quad (21)$$

The distance of a particle located at (x_1, y_1, z_1) from the plane is calculated by:

$$r = \frac{|ax_1 + by_1 + cz_1 + d|}{\sqrt{a^2 + b^2 + c^2}} \quad (22)$$

where d is to determine the distance between the plane and the coordinate axis and the (a, b, c) correspond to the components of the normal vector of the plane, which is generally made as an unit vector so that the denominator in Eq. (22) is 1.0. With the distance of a particle located from the plane, we can calculate the repulsive force exerted by the virtual plane according to ‘‘Lennard Jones’’-like force equation [12].

In this paper, we apply VGBT to construct the outmost wall boundary and underground bottom of the city layout, and use the fixed boundary treatment for complex underground facilities and staircases.

C. Basic problem modules

In the GPUSPH model, there are a variety of basic objects that can be used to generate problem domain or complex structures. In 2D cases, the basic objects (in C++ terms, classes) include Point, Vector, Segment, Rect (rectangle) and Circle. In 3D cases, there are additional objects: Cone, Cube, Cylinder, Sphere and TopoCube. The TopoCube object is used to input the bottom (bathymetry) of the 3-D problem domain via a Digital Elevation Model (DEM) file. Using these basic objects, many types of problem scenarios and complex structures can be constructed.

In this paper, we use the basic Rect object to construct staircases, and use the Cube object, Sphere object, Cylinder object and Cone object together with the Rect object to establish intricate buildings, infrastructural foundations, and underground basements which will be presented in next section.

IV. RESULTS AND DISCUSSION

A. Computing platform

Our numerical testing platform is a workstation rack mounting 4×Tesla C2075 cards on as many 2nd generation PCI-Express slots. The system is based on a 2×Intel Xeon X5675 processor with 12 total cores totally (3.06 GHz, 12 MB cache) and 96 GB RAM. Each Tesla C2075 has 480 CUDA cores grouped in 15 multiprocessors, 48KB shared memory per MP, 6.0 GB global memory. The operating system is CentOS 6.3 with CUDA runtime 4.2 installed.

With many GPUs coordinated in a GPU cluster, the simulation of large-scale city flooding can be realized, however, at present GPUSPH is limited by the maximum number of GPUs on a single PCIe bus. Therefore, this paper investigates the small-scale underground flooding with one or couples of GPUs. This small section of complex underground spaces can illustrate the effects of underground facilities, staircases and floating objects on the underground flooding propagation.

B. Simulation set-ups

The complex city layout is consisted of several kinds of buildings, infrastructural constructions, three floating objects and two building basements (see Figure. 1). The flooding district is in a channel which is horizontally 12.0 m long and 5.4 m wide. We arrange a dam column locating at the origin of the channel with a size of 1.0 m × 5.4 m × 1.0 m to model flooding water. The first row of the urban layout is 2.0 m away from the dam. The distance between the first two rows of buildings is 0.8 m. The width of the central street is 0.6 m. The height of the buildings in the first row is 2.0 m, and the heights of buildings in the second row are between 2.5 m and 3.0 m. The tallest tower downstream is high of 5.4 m. The floating objects of cone, cube and sphere shape locate upstream in red colour as shown in Figure. 1. There are two building basements, whose entrances locate at (2.6m, 1.134m, 2.5m) and (4.3m, 3.24m, 2.5m) respectively

in the city layout. Each basement has an entrance of 0.6 m×0.4 m in size and has stairs down to the ground floor. The stair size is 0.30 m×0.10 m×0.15 m.

Our numerical simulation uses only one GPU. The particle spacing that we initialize the intricate urban flooding layout with is 0.02 m, and total particles is up to 1,348,488. We use the variable time step in SPH scheme with an initial time step ($dt = 0.00003$ s). With the acceleration of GPU parallel computing technique, it just takes 1047.43 s to finish computing a period of physical time 4.0 s.

C. Results analysis

Figure 1~9 show the propagation of the dam-break flooding in the intricate urban layout with two basements, which is evaluated by the displacement of particles by SPH method at $t = 0, 0.5$ s, 1.0 s, 1.5 s, 2.0 s, 2.5 s, 3.5 s, 4.0 s after the dam break.

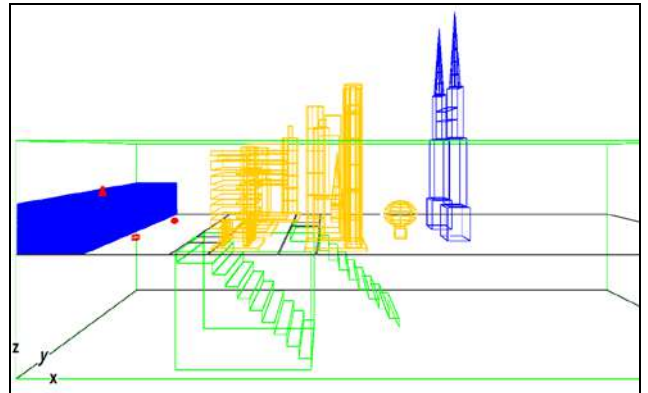


Figure 1. Displacement of underground flooding flow and floating objects ($t=0$)

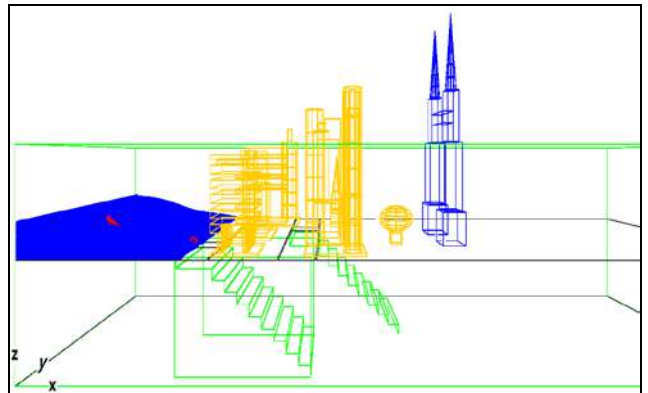


Figure 2. Displacement of underground flooding flow and floating objects ($t=0.5$ s)

From Figure 2~9, we can observe that all three floating objects move downstream with the flooding flow, and the floating objects of cone and sphere shape enter into the basement through the staircases. At $t=0.5$ s, the moving cube object reaches the first basement entrance with the flooding flow, but doesn't move down to the basement (see Fig. 2). Because the velocity of flooding head at this instant

is so big that it strongly pushes the cube object to move fast across the basement entrance, so does the rapid flooding flow itself. At $t = 2.0$ s, we can see plenty of flooding water move down to the first basement due to the decrease of flooding velocity. At this instant, the cone object floating in the slower flooding flow enters into the first basement. Also, the sphere object moves into the basement through the other entrance and staircase (see Fig. 5). Later, the objects move on the ground of the basement with the flooding flow.

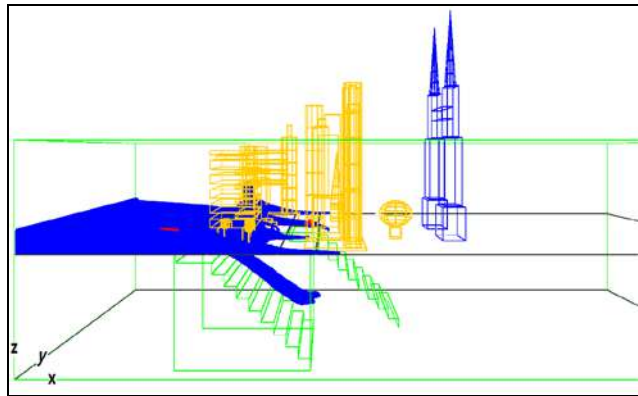


Figure 3. Displacement of underground flooding flow and floating objects ($t = 1.0$ s)

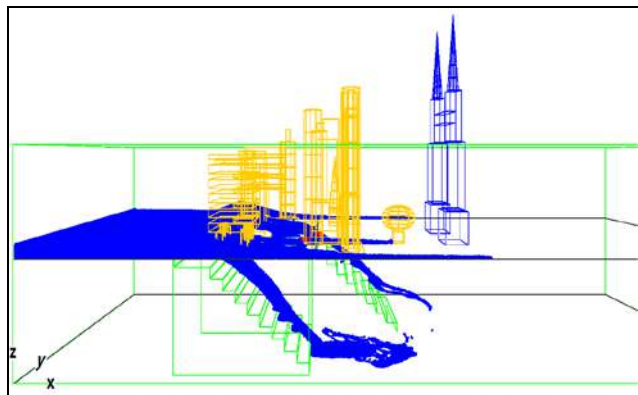


Figure 4. Displacement of underground flooding flow and floating objects ($t = 1.5$ s)

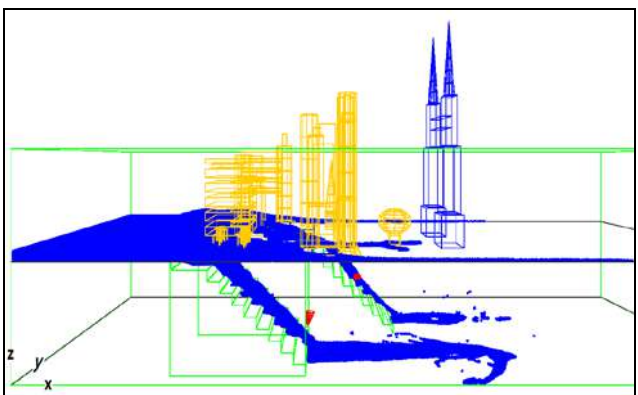


Figure 5. Displacement of underground flooding flow and floating objects ($t = 2.0$ s)

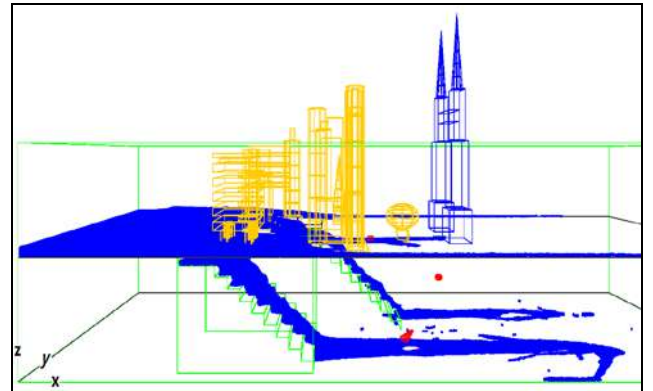


Figure 6. Displacement of underground flooding flow and floating objects ($t = 2.5$ s)

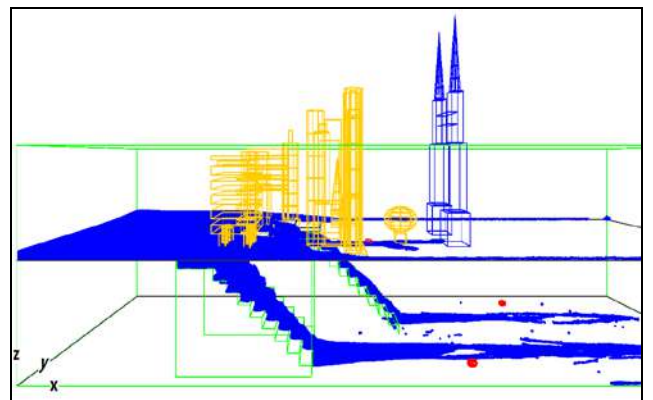


Figure 7. Displacement of underground flooding flow and floating objects ($t = 3.0$ s)

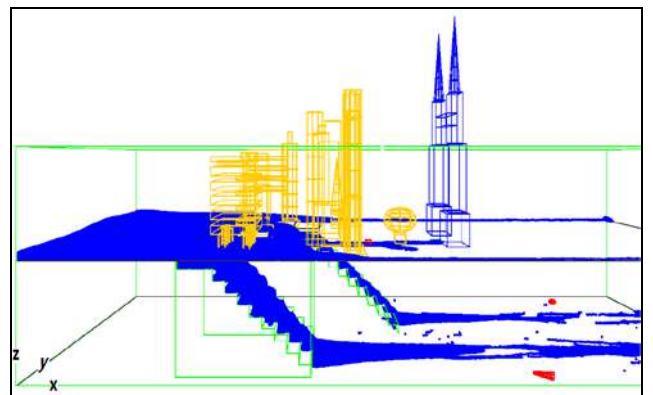


Figure 8. Displacement of underground flooding flow and floating objects ($t = 3.5$ s)

From the underground inundation process shown in Figure 2~9, we also observe that the flooding flow on the staircase presents a good skimming flow and the floating objects move with violent impacts against the staircases and the ground of the basement (see Fig. 5~8), which is close to practice. This indicates that GPUSPH model can well handle the fluid-structure interactions between flooding flow and moving objects, and the interactions between floating objects and staircases, building walls and ground floor as well.

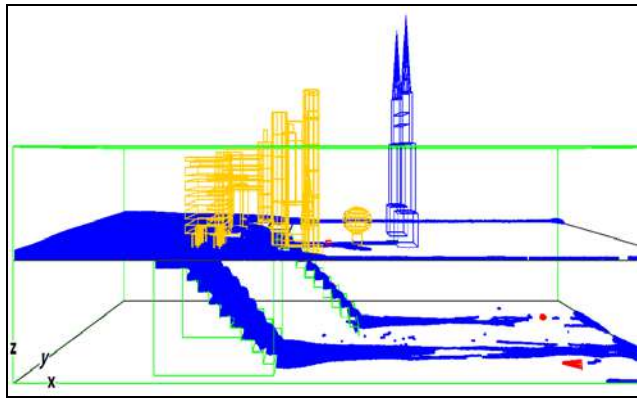


Figure 9. Displacement of underground flooding flow and floating objects ($t=4.0\text{ s}$)

Incorporating the floating objects in the underground flooding modeling is useful for investigating flow characteristics and flow propagation paths, which is important to enhance the quality of urbanized underground flood hazard assessment and well forecast the underground inundation mapping.

V. CONCLUSION

In this paper, A 3D model based on SPH method with GPUs parallel computing technique employed, GPUSPH, is used to investigate the flooding in geometrically complex underground spaces. Indeed, the proposed SPH-based underground flooding model offers some advantages over traditional grid-based models:

(a) SPH model can feasibly and directly compute the inundation process in complex underground spaces.

(b) SPH model can well handle the collision and confluence of flooding flow, and also the interactions between the flooding flow and fixed walls.

(c) SPH model can easily incorporate the floating objects in underground flooding simulation and reasonably model the fluid-structure interactions between flooding flow and moving objects, and the interactions between floating objects and the staircases, building walls and ground floor as well.

Although some preliminary reasonable results have been achieved, the SPH model for handling flooding in geometrically complex urban underground facilities requires further improvements. More quantitative comparison with other numerical methods, experimental data or underground inundation events will be conducted.

ACKNOWLEDGEMENT

This work was supported by the National Natural Science Foundation of China (Grant No. 11502283).

REFERENCES

- [1] J. S. Wu, S. D. Xu, H. Zhang, "A review of experimental and numerical simulation studies on flooding in urban underground spaces," *China Safety Science Journal*, vol. 26, pp. 1-6, September, 2016,
- [2] K. Toda, K. Kuriyama, R. Oyagi, K. Inoue, "Inundation analysis of complicated underground space," *Journal of Hydroscience and Hydraulic Engineering(JSCE)*, vol. 22, pp. 47-58, 2004.
- [3] K. Toda, N. Kawaike, S. Yoneyama, S. Fukakusa, D. Yamamoto, "Underground inundation analysis by integrated urban flood model," *Advances in Water Resources and Hydraulic Engineering*, 2009, pp. 166-171.
- [4] K. Y. Han, G. Kim, C. H. Lee, "Modeling of flood inundation in urban areas including underground space," *4th International Symposium on Flood Defense*, Toronto, Ontario, Canada, 2008.
- [5] T. Ishigaki, N. Asano, M. Morikane, T. Ozaki, K. Toda, "Extreme Hazard of Pluvial and Tsunami Floods in a Densely Urbanized Area," *International Conference on Flood Resilience: Experiences in Asia and Europe*, Exeter, United Kingdom, 2013.
- [6] M. B. Liu, G. R. Liu, "Smoothed Particle Hydrodynamics (SPH): an overview and recent developments," *Arch. Comput. Methods Eng.*, vol. 17, pp. 25-76, March, 2010.
- [7] E. Lo, S. Shao, "Simulation of near-shore solitary wave mechanics by an incompressible SPH method," *Applied Ocean Research*, vol. 24, pp. 275-286, October, 2002.
- [8] R. A. Dalrymple, B. D. Rogers, "Numerical modeling of water waves with the SPH method," *Journal of Coastal Engineering, ASCE*, vol. 53, pp. 141-147, February, 2006.
- [9] J.J. Monaghan, "Simulating free surface flow with SPH," *Journal of Computational Physics*, vol. 110, pp. 399-406, February, 1994.
- [10] J. J. Monaghan, "Smoothed Particle Hydrodynamics and its diverse applications," *Annual Review Fluid Mechanics*, vol. 44, pp. 323-346, January, 2012.
- [11] J. J. Monaghan, A. Kos, and N. Issa, "Fluid Motion Generated by Impact," *J. Waterway, Port, Coastal, Ocean Eng.*, vol. 129, pp. 250-259, November, 2003
- [12] J.J. Monaghan, "Smoothed Particle Hydrodynamics," *Rep. Prog. Phys.*, vol. 68, pp. 1703-1759, July, 2005.
- [13] J.J. Monaghan, A. Kos, "Solitary waves on a Cretan Beach," *J. Waterway, Port, Coastal, Ocean Eng.*, vol. 125, no. 3, pp. 145-154, June, 1999.
- [14] A. Héault, G. Bilotta, R. A. Dalrymple, "SPH on GPU with CUDA," *Journal of Hydraulic Research*, vol. 48(extra issue), pp. 74-79, June, 2010.
- [15] E. Rustico, G. Bilotta, A. Herault, C. D.Negro, G. Gallo, "Advances in multi-GPU smoothed particle hydrodynamics simulations," *IEEE Transactions on Parallel and Distributed Systems*, vol. 25, pp. 43-52, 2014.
- [16] M. Gomez-Gesteira, B. D. Rogers, R. A. Dalrymple, A. J. C. Crespo, "State-of-the-art of classical SPH for free-surface flows," *Journal of Hydraulic Research*, vol. 48(extra issue), pp. 6-27, June, 2010,
- [17] A. Héault, G. Bilotta, A. Vicari E. Rustico, "Numerical simulation of lava flow using a GPU SPH model," *Annals of Geophysics*, vol. 54, pp. 600-620, December, 2011.

Image processing with the SPH method

Chunying HUANG & Wenhuan LU
School of Computer Software,
Tianjin University,
Tianjin China

Yaxuan XING,
School of Mathematics,
Tianjin University,
Tianjin, China

Darcy Q. HOU* & Xin CHENG
School of Computer Science and Technology,
Tianjin University,
Tianjin China
Corresponding author: qhou@tju.edu.cn

Abstract—One of the most significant research fields in computer graphics is digital image processing. Scaling, rotating and repairing are the fundamental components in image processing which are all based on interpolation. There are many grid-based interpolation algorithms for image processing such as the nearest neighbor interpolation, bilinear interpolation, polynomial interpolation, B-spline interpolation and cubic convolution interpolation. Although these algorithms have achieved great success, their dependence on the grids might introduce difficulties and disadvantages for advanced image processing. On the other hand, the meshless methods only use the image information in the support domain to compensate the missing parts without the limit of grids. In this paper, the meshless smoothed particle hydrodynamics (SPH) method and the corrective smoothed particle method (CSPM) are used to deal with scaling, rotating and repairing of three typical images including Lenna, Pepper and Stanford Dragon. The numerical results indicate that the meshless methods can obtain better results according to the Peak Signal to Noise Ratio (PSNR). Moreover, dissipation of moving images has also been successfully achieved by modelling it with a convection-diffusion process.

I. INTRODUCTION

Image processing is one of the basic operations in computer graphics and is widely used in many applications. Simple image processing usually includes the scaling, rotating and repairing. All these processing technologies need interpolation and the quality of processed image is directly affected by the interpolation algorithms.

Several commonly used interpolation algorithms have been suggested such as the nearest neighbor interpolation, bilinear interpolation, polynomial interpolation, B-spline interpolation and cubic convolution interpolation [1-3]. The simplest is the nearest neighbor interpolation algorithm, which is fast, but the interpolation results are not satisfactory because the target image will appear the phenomenon of contour jaggies. Bilinear interpolation algorithm can maintain continuity of the internal pixel information, but the edges and details will be seriously blurred. The cubic convolution method is more complex and the results can meet the subjective visual requirements in the aspect of image background smoothness. With this method, the values of the pixel information remain continuous and even differentiable. However, there is some ambiguity sense in the details of image edges. Polynomial interpolation is another algorithm

with good effect. By increasing the order number of polynomials, we can get a smooth image background with no jagged edges. However, the numerical calculation is too complicated, and the rounding error accumulates. All these interpolation schemes are grid-based algorithms and may introduce difficulties and some disadvantages for advanced image processing. For handling the image more convenient, meshless methods have the natural advantages. It is not important whether the particles are uniformly distributed or not. By representing image pixels with particles, we can get rid of the limit of grids and get better results. With these meshless methods, advanced image processing results can be obtained such as dissipation and transformation of moving images.

One of the earliest meshless methods is the smoothed particle hydrodynamics (SPH) [4-5], which initially was used for modelling astrophysical phenomena. SPH can be considered as an interpolation method based on kernel estimation and particles estimation. The accuracy of this interpolation method has been analyzed by Monaghan [6-7]. Since then, many researchers have further developed the SPH with further improvements. The applications of SPH have been extended to a variety of engineering problems with very promising results [8].

In this paper, the SPH method and the corrective smoothed particle method (CSPM) are used to deal with scaling, rotating and repairing of three typical images, and the numerical results indicate that the meshless methods can obtain better results according to the Peak Signal to Noise Ratio (PSNR). In addition, the dissipation of moving images has also been successfully achieved by modelling it with a convection-diffusion process, which also proves the advantage of meshless method. This is a new idea for advanced image processing.

II. SMOOTHED PARTICLE HYDRODYNAMICS

Interpolation methods play an important role in calculating the information of pixels during image processing. With the development of the meshless methods, SPH method and its corrective schemes can replace the traditional grid-based interpolation method in image processing. The basic SPH and CSPM formulations used in this paper are presented below. For advanced information, the readers are referred to the recent reviews paper [9].

An arbitrary smooth function $f(x)$ can be expanded into

a Taylor series at the neighborhood of point x_i as

$$f(x) = f(x_i) + f'(x_i)(x - x_i) + \frac{1}{2} f''(x_i)(x - x_i)^2 + \dots \quad (1)$$

Multiplying a smoothing function or kernel function $W_i(x)$ at both sides of the expansion yields

$$\begin{aligned} f(x)W_i(x) &= f(x_i)W_i(x) + f'(x_i)(x - x_i)W_i(x) \\ &+ \frac{1}{2} f''(x_i)(x - x_i)^2 W_i(x) + \dots \end{aligned} \quad (2)$$

where $W_i(x) = W(x_i - x, h)$, h is smoothing length.

Integrating over the whole computational domain Ω gives

$$\begin{aligned} \int_{\Omega} f(x)W_i(x)dx &= f(x_i) \int_{\Omega} W_i(x)dx \\ &+ f'(x_i) \int_{\Omega} (x - x_i)W_i(x)dx + \frac{1}{2} f''(x_i) \int_{\Omega} (x - x_i)^2 W_i(x)dx + \dots \end{aligned} \quad (3)$$

Neglecting all the derivative terms, we can get the corrective kernel estimate of the function $f(x)$ at point x_i ,

$$f(x_i) = \frac{\int_{\Omega} f(x)W_i(x)dx}{\int_{\Omega} W_i(x)dx} \quad (4)$$

which is known as shaped function [10].

In formulation (4), due to the normalization condition of the kernel function, the denominator is 1. Then we can get

$$f(x_i) = \int_{\Omega} f(x)W_i(x)dx \quad (5)$$

This is the SPH kernel approximation of a function.

Formulation (4) and (5) is enough to deal with sample function interpolation problems. However, for advanced image processing, such as the dissipation of the moving images, we need to simulate the first derivative of function which is obtained as following processing.

In formulation (2), if the kernel $W_i(x)$ is replaced by its derivative $W'_i(x) = \frac{dW_i(x)}{dx}$ and neglecting the second and higher derivative terms, a corrective kernel estimate of the first-derivative $f'(x_i)$ is generated as

$$f'(x_i) = \frac{\int_{\Omega} (f(x) - f(x_i))W'_i(x)dx}{\int_{\Omega} (x - x_i)W'_i(x)dx} \quad (6)$$

Representing the spatial domain Ω by particles [11], we have

$$f'(x_i) = \frac{\sum_{j=1}^N (f(x_j) - f(x_i))W'_i(x_j)m_j/\rho_j}{\sum_{j=1}^N (x_j - x_i)W'_i(x_j)m_j/\rho_j} \quad (7)$$

in which $W'_i(x_j) = W'(x_i - x_j, h)$, N is the total number of the particles in the domain.

III. EXPERIMENT RESULTS

A. Image Scaling

In order to test the performance of the SPH method and CSPM method for image processing, three typical images including Lenna, Pepper and Stanford Dragon with a resolution of 512 * 512 as shown in Fig. 1

At first, we shrink image to half of the original size. And then the shrunken image was expanded to its original size by using different interpolation algorithms. At last, the qualities of the enlarged images are compared using Peak Signal to Noise Ratio (PSNR) which is quantitative baseline of image quality and used to evaluate image expansion performance of different algorithms.

PSNR is defined as

$$\text{PSNR} = 10 \log_{10} \frac{(2^n - 1)^2}{\text{MSE}} \quad (8)$$

where $n = 8$, MSE is the mean square error between original image and target image, which can be written as

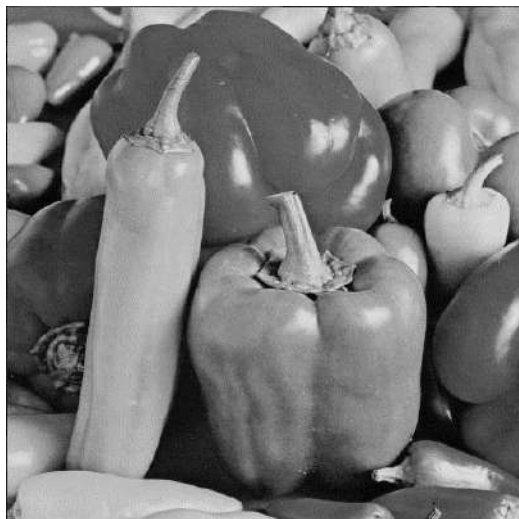
$$\text{MSE} = \frac{1}{2N * 2M} \sum_{i=1}^{2N} \sum_{j=1}^{2M} (f(i, j) - f^*(i, j))^2 \quad (9)$$

where $f(i, j)$ is the original image information, $f^*(i, j)$ is information of the target image, and the size of those two images is $2N * 2M$.

In general, the value of PSNR is higher, the processing effects of image are better in the subjective sense.



(a) Lenna



(b) Pepper



(b) Target image with bilinear interpolation



(c) Dragon

Fig 1. Typical images for processing



(c) Target image with SPH method



(a) Target image with nearest neighbor interpolation



(d) Target image with CSPM method

Fig. 2 Image scaling results with different interpolation methods

Fig. 2 is the image results in different interpolation methods. In this paper, we just show one example image results to save space. TABLE I shows the PSNRs for different image interpolation methods.

The values of PSNR with SPH method and CSPM method are higher than other interpolation methods, which indicates that SPH and CSPM can be used in image scaling and can get reasonable results. It should be noted that the CSPM can get better results at image edges due to the boundary problems were neglected.

TABLE I. PSNRs in scaling for different image interpolation methods

Case name	Interpolation methods			
	Nearest neighbor	Bilinear	SPH	CSPM
Lenna	28.1987	28.1984	29.7391	31.1865
Pepper	27.1608	28.3115	30.7758	28.9502
Standford Dragon	28.5788	30.5884	31.7239	31.8727

B. Image Rotating

Image rotating is also a common image operation in computer graphics. It is known that digital image is stored in computer by the information of all pixels. So the image rotating can be considered as the calculation of the pixels of the image.

In image rotating, we assume that the coordinate of the pixel is (x, y) , and the new coordinate of the pixel is (x', y') . If a two-dimensional image rotates θ degrees clockwise, the new coordinate will be

$$\begin{bmatrix} x' \\ y' \\ 1 \end{bmatrix} = \begin{bmatrix} \cos \theta & \sin \theta & 0 \\ -\sin \theta & \cos \theta & 0 \\ 0 & 0 & 1 \end{bmatrix} \begin{bmatrix} x \\ y \\ 1 \end{bmatrix} \quad (10)$$

Due to position change, new image information cannot completely match the original one. Therefore, we usually find the original image pixels according to the target image in image rotation. The relation of the pixels can be got as following:

$$\begin{bmatrix} x \\ y \\ 1 \end{bmatrix} = \begin{bmatrix} \cos \theta & -\sin \theta & 0 \\ \sin \theta & \cos \theta & 0 \\ 0 & 0 & 1 \end{bmatrix} \begin{bmatrix} x' \\ y' \\ 1 \end{bmatrix} \quad (11)$$

In this paper, the image is rotated by the image center, and the center of the image will change. We set the center of the original image is (a, b) , and the center of the target image is (c, d) , the height of the original image is H , the width of the original image is W , the height of the target image is H' , the width of the target image is W' . The formulation of the rotating can be obtained as:

$$\begin{bmatrix} x \\ y \\ 1 \end{bmatrix} = \begin{bmatrix} 1 & 0 & a \\ 0 & -1 & b \\ 0 & 0 & 1 \end{bmatrix} \begin{bmatrix} \cos \theta & -\sin \theta & 0 \\ \sin \theta & \cos \theta & 0 \\ 0 & 0 & 1 \end{bmatrix} \begin{bmatrix} 1 & 0 & -c \\ 0 & -1 & d \\ 0 & 0 & 1 \end{bmatrix} \begin{bmatrix} x' \\ y' \\ 1 \end{bmatrix} \quad (12)$$

Then we can get the original position as:

$$\begin{cases} x = x' \cos \theta + y' \sin \theta - c \cos \theta - d \sin \theta + a \\ y = -x' \sin \theta + y' \cos \theta + c \sin \theta - d \cos \theta + b \end{cases} \quad (13)$$

The height and width of target image are

$$W' = \max(|-(H-1) \sin \theta - (W-1) \cos \theta|, |-(H-1) \sin \theta + (W-1) \cos \theta|) \quad (14)$$

and

$$H' = \max(|-(H-1) \cos \theta + (W-1) \sin \theta|, |-(H-1) \cos \theta - (W-1) \sin \theta|) \quad (15)$$

With formulation (13), we can get the target image position from the original image. It means that the pixel information can be applied. As the target image position may not have information, we need to interpolate the pixel information according to other pixels. It is considered as the main error source in the rotating operation. In order to reduce the error, the interpolation methods play a critical role.

All mesh-based methods discussed above can be used in image rotating, such as the nearest neighbor interpolation, bilinear, cubic convolution method. In this paper, we used the bilinear interpolation method and the result is shown in Fig. 3(a). The results of SPH and CSPM are shown in Fig. 3(b) and Fig. 3(c), respectively. It is seen that the SPH method and CSPM method can also get reasonable results, and the CSPM result is better at image edges.



(a) Rotating image with bilinear interpolation



(b) Rotating image with SPH method



(c) Rotating image with CSPM method

Fig. 3 Rotating image results with different interpolation methods

C. Image Repairing

Reconstruction of missing or damaged portions of images is a basic technique in practice, which is used extensively from restoration of photographs, films and paintings to removal of occlusions, such as text, subtitles and publicity, from images. Image repairing is usually based on the principle that missing part of an image can be well synthetized by suitably sampling and copying uncorrupted patches [12-13]. In this paper, by using SPH and CSPM method, simple image repairing can also be realized and the results are shown in Figs. 5 and 6, respectively. As seen, SPH result is not satisfactory but the CSPM result is much feasible.



Fig. 4 Damaged image



Fig. 5 Recovering image with SPH method



Fig. 6 Recovering image with CSPM method

D. Dissipation of Moving Images

Dissipation of moving images play a vital role in animation, rendering or other graphic fields. In this part, by solving the two-dimensional convection-diffusion equations with SPH method [14], image dissipation and movement are handle easily. The detail results at different time is shown as Fig. 7 (a) – 7(d).

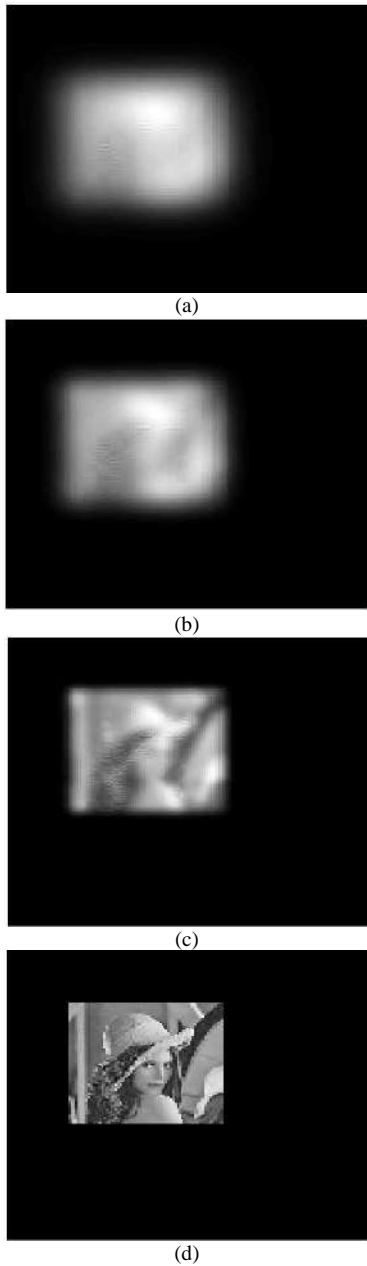


Fig. 7 Dissipation of image with SPH method in different time

IV. CONCLUSION

The SPH method and CSPM method have been successfully applied to process digital images, such as image scaling, rotating, and repairing. The most appearing advantage of these meshless methods is that they do not depend on the grid. Moreover, the effect of dissipation moving images can

also be achieved. Further studies on boundary processing and animation generation with meshless methods are needed.

ACKNOWLEDGEMENT (HEADING 5)

The work is supported by the National Natural Science Foundation of China (No. 51478305), SKL of HESS (No. HESS-1408) and Scientific Research Foundation for the Returned Overseas Chinese Scholars, State Education Ministry.

REFERENCES

- [1] Parker J A, Kenyon R V, Troxel D E. Comparison of interpolating methods for image resampling. *IEEE Transactions on Medical Imaging*, 1983, 2(1): 31-39.
- [2] Carey W K, Chuang D B, Hemami S S. Regularity-preserving image interpolation. *IEEE Transactions on Image Processing*, 1999, 8(9): 1293-1297.
- [3] Han D. Comparison of commonly used image interpolation methods[C] Proceedings of the 2nd International Conference on Computer Science and Electronics Engineering (ICCSEE). 2013: 1556-1559.
- [4] Lucy LB. A numerical approach to the testing of the fission hypothesis. *J Astron* 1977; 82: 1013-24.
- [5] Gingold RA, Monaghan J. J. Smoothed particle hydrodynamics: theory and allocation to non-spherical stars. *Mon Not Roy Astron Soc* 1977; 181: 375-89.
- [6] Monaghan J. J. An introduction to SPH. *Comput Phys Commun* 1988; 48:89-96.
- [7] Monaghan J. J. Why particle methods work. *SIAM J Sci Stat Comput* 1982; 3: 422-33
- [8] G. R. Liu, M. B. Liu. Smoothed Particle Hydrodynamics: A Mesh Free Particle Method. World Scientific, 2003.
- [9] J. K. Chen, J. E. Beraun, T. C. Carney, A corrective smoothed particle method for boundary value problems in heat conduction, *Int. J. Numer. Methods Eng.* 46 (1999) 231-252.
- [10] Wang J G, Liu G R. On the optimal shape parameters of radial basis functions used for 2-D meshless methods[J]. *Computer Methods in Applied Mechanics & Engineering*, 2002, 191(23-24):2611-2630.
- [11] Hou Q, Kruisbrink A C H, Tijsseling A S, et al. Simulating water hammer with corrective smoothed particle method[C] 11th International Conference on Pressure Surges, Lisbon, Portugal. 2012.
- [12] Bertalmio M, Sapiro G, Caselles V, et al. Image inpainting[C] Proceedings of the 27th annual conference on Computer graphics and interactive techniques. ACM Press/Addison-Wesley Publishing Co., 2000: 417-424.
- [13] Richard M M O B B, Chang M K Y S. Fast digital image inpainting[C] Appeared in the Proceedings of the International Conference on Visualization, Imaging and Image Processing (VIIP 2001), Marbella, Spain. 2001: 106-107.
- [14] Wang, Z., Delestre, O., Hou, D. Q., Wei, J., and Dang, J.. SPH Simulation of Pollutant Transport in Rivers. International Conference on Civil, Transportation and Environment. 2016.

On the efficacy of augmenting SPH simulations of mixed-mode failure with the Material Point Method

S. Raymond, B. Jones, R. Pramanik, K. Pan, T. Douillet-Grellier, J. Williams

Geonumerics Group
Civil and Environmental Engineering
Massachusetts Institute of Technology

Abstract

A study of mixed-mode failure in rocks was conducted using SPH and MPM. These two meshless methods possess many similar qualities as numerical techniques. A simple coupling algorithm between the two methods can be used and was shown to be effective for an example solid mechanics loading problem. A common issue in meshless simulations is the application of exact boundary conditions. Since these arise naturally from the derivation of the MPM technique, it is an ideal candidate to couple with SPH simulations where such boundary conditions are required. As MPM is still a relatively unknown method, a comparison with SPH in modeling failure in solids presents a useful benchmark. A simulation of rock failure using the 2D Brazilian test shows that SPH and MPM produce similar results that agree well with analytical solutions to the stress field and both methods are shown to produce the same failure patterns.

1 Introduction

Meshless methods such as Smoothed Particle Hydrodynamics (SPH) and the Material Point Method (MPM) have been applied in recent years to study complex geomechanics problems. SPH, first developed in the late 1970s to study problems in astrodynamics by Gingold and Monaghan [1] has since been successfully applied to a broad range of problems. These include, but are not limited to, elastic flow [19], fluid flow [3; 4], impact problems [5], heat transfer problems [6], multi-phase flow [7; 8], geophysical flow [9], fluid–structure interaction [10; 11] and post-failure of cohesive and non-cohesive soils. MPM, in its current form was first introduced in 1990s to study a variety of solid mechanics problems [12–15]. MPM is a derivative of an earlier method, known as the Particle-In-Cell (PIC) technique from the 1950s. As PIC and its further developed form, FLIP, dealt entirely with fluids, MPM was spawned

as a method to handle solid mechanics. SPH too was initially created for fluid mechanics problems, the first application of SPH to solid mechanics was carried out by Libersky and Petschek [16]. Their work was subsequently extended to simulation of the fracture process in brittle solids by Benz and Asphaug [17]. Randles and Libersky[18] and then Gray et al.[19] have since made significant improvements in extending SPH to elastic dynamics. More recently, Douillet-Grellier et al.[20] proposed a new approach for stress based boundary conditions in SPH, which has been validated for elastic problems in solid mechanics. Particle methods like SPH and MPM are based upon a formulation where multiple crack initiations and propagations may emerge naturally from a well formulated constitutive model. Due to the meshless nature of these methods, no remeshing is required to simulate large deformations. Similar to more traditional methods such as the finite element method, material properties may be specified a priori, requiring no calibration. The challenge of accurate fracture modeling therefore lies in the choice and implementation of suitable constitutive models to capture both shear and tensile failure. A number of authors using both techniques have pursued the Drucker–Prager plasticity model in order to capture plasticity and shear failure in geomechanics problems [11; 21]. For tensile failure, the Grady Kipp damage model has been incorporated into the SPH framework as proposed by Benz and Asphaugh[17] and validated for failure in solid bars loaded in tension. To date, Grady Kipp has not been implemented in MPM simulations. Use of the Grady Kipp damage model has proved successful for simulation of high speed impacts[5]. Previously, a study by Douillet-Grellier et al. [20] showed that combining the Drucker Prager plasticity model and the Grady Kipp model yielded very good results when comparing simulations of a uniaxial test of a rock specimen with a predefined flaw to the experimental results of Wong [22]. Additionally, a new approach to boundary conditions was presented by Raymond et al.[23] that used

a boundary region of MPM particles and coupled this to an inner SPH domain. Since boundary conditions can be applied with more completeness in the MPM framework, this allowed for more flexibility when choosing different boundary conditions. In this work the similarities between SPH and MPM are discussed as well as the applicability of MPM to be used in place of SPH when modeling particular systems that may pose difficulties for SPH. MPM and SPH are described, briefly and to highlight their similarities, the coupling is explained in the following section. Additionally, in this work, a comparison of SPH and MPM is carried in order to understand better the differences and similarities of these two methods when modeling mixed-mode failure using a Drucker Prager plasticity model and a Grady Kipp damage model.

2 A brief overview of SPH and MPM

The focus of this work lies in the application of a coupled set of constitutive models therefore only a cursory coverage of the underlying methods will be presented. Hence, the full derivations of SPH are not included in this paper but the interested reader is suggested to read Monaghan and Liu's reviews. Due to its lack of widespread use, an overview of MPM will be given with useful references.

2.1 Solid Mechanics in SPH

Since the majority of SPH research does not involve solid mechanics, the SPH solid mechanics equations will be briefly revisited. For solids, an SPH discretization begins with governing equations for mass and momentum conservation equations. For shorthand in the following equations, the subscript " v_{ab} " refers to $v_a - v_b$. In this work, the following approximation of the momentum equation is used as per Gray and Monaghan [19].

$$\frac{D\mathbf{v}_a}{Dt} = \sum_{b \in \Lambda_a} m_b \left(\frac{\boldsymbol{\sigma}_a}{\rho_a^2} + \frac{\boldsymbol{\sigma}_b}{\rho_b^2} + \Pi_{ab} \right) \nabla_a W_{ab} \quad (2.1)$$

where, $\boldsymbol{\sigma}_a$ is the stress tensor of particle a , and Π_{ab} is the artificial viscosity, which is included to resolve any non-physical oscillation in the solution. The form of the artificial viscosity is the same in the work as used by Cleary in [24].

$$\Pi_{ab} = \begin{cases} \frac{-\alpha c_0 \eta_{ab} + \beta \eta_{ab}^2}{\bar{\rho}_{ab}} & \mathbf{v}_{ab} \cdot \mathbf{x}_{ab} < 0 \\ 0 & \mathbf{v}_{ab} \cdot \mathbf{x}_{ab} \geq 0, \end{cases} \quad (2.2)$$

where

$$\eta_{ab} = \frac{h_{ab} \mathbf{v}_{ab} \cdot \mathbf{x}_{ab}}{|\mathbf{r}_{ab}|^2} \quad (2.3)$$

c_0 denotes the speed of sound of the material. To calculate the stress rate from the generalized Hooke's law, the strain rate tensor is approximated into the SPH form.

$$\dot{\boldsymbol{\epsilon}}_a = \frac{1}{2} \left[\sum_{b \in \Lambda_a} \frac{m_b}{\rho_b} \mathbf{v}_{ba} \otimes \nabla_a W_{ab} \right. \\ \left. + \sum_{b \in \Lambda_a} \left(\frac{m_b}{\rho_b} \mathbf{v}_{ba} \otimes \nabla_a W_{ab} \right)^T \right]$$

To close the set of equations a constitutive model is introduced to transform the strains into stresses. For this work a simple elastic, small strains approach is followed.

2.2 An Overview of MPM

The Material Point Method (MPM) discretizes a body in a similar manner to SPH. A geometry is divided into small mass elements, Fig. 1, referred to as material points, and assigned all the variables required to describe the state of the material: stress, strain, position, velocity, mass, etc. Where this method differs from

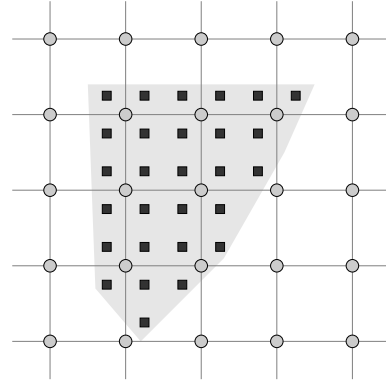


Figure 1: A body discretized using material points and the surrounding mesh nodes.

SPH is that these particles are then embedded in a background mesh that uses the same nodal shape functions found in FEM. Instead of the kernel function used on each SPH particle, during a time-step, information is transmitted from the material points to the nodes. Equations of motion are solved on the nodes, and the updated variables are sent to the material points in order to update their state variables. Once the material points have been updated, the grid is reset back to its original position, or updated for some specific purpose if the user so desires. MPM was largely developed in the Los Alamos National Labs[12] in the second half of the last century. Today MPM has been applied in a number of fields including geomechanics [25–27], manufacturing [14; 28], sea ice dynamics [29; 30], and many more. A key advantage of MPM is that since the grid is reset at

the end of each timestep, mesh tangling and distortions that can plague a typical Lagrangian FEM code under large deformation is entirely avoided [12; 13; 31]. Additionally, since MPM, like FEM, can be derived from the weak form of the variational principal, boundary conditions can be represented exactly on surfaces of nodes or material points [12]. This differs from SPH where boundaries are smoothed and cannot be exactly enforced without special treatments.

The MPM Timestep

The basic algorithm for an MPM time-step begins with extrapolating the mass, momenta, and stresses to the grid nodes so that the internal force equation can be formed. Extrapolation is made possible by use of nodal shape functions, $N_i(x)$, such that for node i the relevant shape function is:

$$N_i(x) = \begin{cases} 0 & x - x_i \geq -L, \\ 1 + \frac{(x-x_i)}{L} & -L < x - x_i \leq 0, \\ 1 - \frac{(x-x_i)}{L} & 0 < x - x_i \leq L, \\ 0 & L < x - x_i \end{cases} \quad (2.4)$$

with L being the cell-size of the MPM grid cell. The above 1-D formula can be extended to 3-D elements by simple multiplication: $N_i(x, y, z) = N_i(x)N_i(y)N_i(z)$. To extrapolate the required quantities to solve the equations of motion, the mass, momenta and internal forces are ascribed to the grid as presented in general MPM literature (for example see [32]).

$$M_i = \sum_{p=1}^{N_p} m_p N_{ip} \quad (2.5)$$

$$M_i v_i = \sum_{p=1}^{N_p} m_p v_p N_{ip} \quad (2.6)$$

$$f_i^{int} = -\sum_{p=1}^{N_p} \boldsymbol{\sigma}_p G_{ip} V_p \quad (G_{ip} \equiv \nabla N_{ip}) \quad (2.7)$$

$$f_i^{ext} = \sum_{p=1}^{N_p} m_p \mathbf{b} N_{ip} \quad (2.8)$$

In the above equations, M_i and m_p refer to the nodal and material point masses, respectively, N_{ip} and G_{ip} are the shape and gradient shape functions of node i with respect to material point p , v_i and v_p are the nodal and material point velocities respectively, f_i^{int} and f_i^{ext} are the internal and external nodal forces respectively, $\boldsymbol{\sigma}_p$ is the stress tensor for material point p , V_p is the volume of material point p and \mathbf{b} is a body force, such as gravity, that acts as an external force. Using the quantities from (2.5 - 2.8), Newton's second law of motion can be stated and the new acceleration for the current time step evaluated.

$$M_i a_i = f_i^{int} + f_i^{ext} \quad (2.9)$$

The acceleration of node i , a_i , can now be found and the grid velocity, v_i can be updated to v_i^* using the computational timestep Δt :

$$v_i^* = v_i + a_i \Delta t \quad (2.10)$$

In theory the grid positions would be updated too, however in practice this step is rarely explicitly performed and the grid is reset instead. Now that the grid is in its updated state, the material points must be updated. Nodal acceleration and velocity gradients are sent to the material points to update their kinematic and constitutive variables. This process requires a reverse operation to the extrapolation performed at the beginning of the timestep. Instead of all the material points contributing to the relevant nodes, the nodes contribute to all material points within their vicinity. In a typical simulation the number of material points is larger than the number of nodes resulting in non-square matrices for node-material point relationships [12; 14]. This prevents, in a general simulation, the inversion of a "shape function matrix" and requires a summation procedure instead of the contributing nodes.

$$v_p^* = v_p + \sum_{i=1}^{N_i} a_i \Delta t \quad (2.11)$$

$$x_p^* = x_p + v_p \Delta t \quad (2.12)$$

In equation 2.12, the material point position, x_p , is updated to a new position x_p^* using the material point velocity. In some instances it is better to use the updated grid velocity, or a contribution of each. More details of this can be found in [33]. To update the constitutive variables, for small strain theory, the velocity gradient, ∇v is used:

$$\varepsilon_p^* = \varepsilon_p + \frac{\Delta t}{2} \sum_{i=1}^{N_i} [v_i G_{ip} + G_{ip} v_i] \quad (2.13)$$

Using the strain, stresses can be updated using any constitutive law. Once the material point state variables have all been updated to the current values, the grid no longer carries any required information to describe the material and can be reset for the next timestep.

2.3 Similarities between SPH and MPM

The two methods described above, SPH and MPM, are both meshless numerical methods. While MPM uses a background grid to calculate the gradient terms like acceleration and strain rate, the entire state of the material is stored and tracked on the material points, in exactly the same way as SPH. This Lagrangian particle nature that the two methods share allows for a very

simple coupling between the two. As the only key difference lies between the different interpolation methodologies, constitutive models and time updates of the particles can be used for either MPM or SPH.

3 Coupling Strategy

In the last section MPM was outlined as a way of particle information to be transferred to a background grid and back again. For SPH, as the method only consists of particles, a coupling between MPM and SPH would allow SPH to communicate with the nodes of MPM if they were within the domain of the nodal shape functions. This then provides a neat and simple manner in which to couple these two methods. Essentially the domain is discretized as shown in Fig.2. A more de-

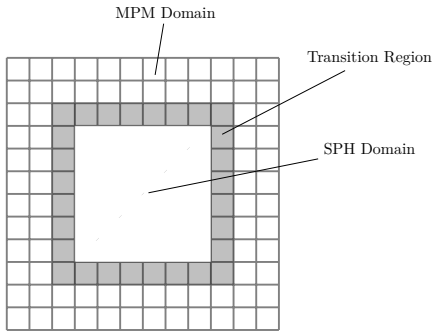


Figure 2: Schematic of SPH-MPM geometry showing the different regions discretised as either MPM, SPH or transitional regions.

tailed description and validation of the coupling was presented in Raymond2016. Here we look at the use of MPM as a means to overcome some of the difficulties associated with SPH in 2D stress problems.

3.1 Hole in a uniaxially loaded plate

To test the smoothness of the coupling in regions of high stress gradients, a 2D plate containing a hole was discretized as in Fig.3. The top and bottom two layers of particles were assigned a constant velocity of 1mm/s so as to produce a tensile load in the material. To better resolve the stress concentration about the hole the resolution for this simulation was increased and the von Mises stresses were calculated for Fig. 4. As expected there is a large stress concentration around the hole, contour lines also show the stress gradients. It is also apparent that the transition from SPH to MPM creates no noticeable disturbance in the stress field. Fig. 5 shows the comparison of the stresses along the horizontal mid line simulated and predicted by theory. While the high stress gradient area is well reproduced, there

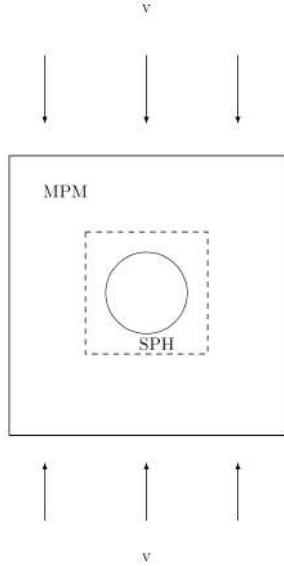


Figure 3: 2D schematic of a plate with a hole under uniaxial loading simulated by the coupled MPM-SPH model.

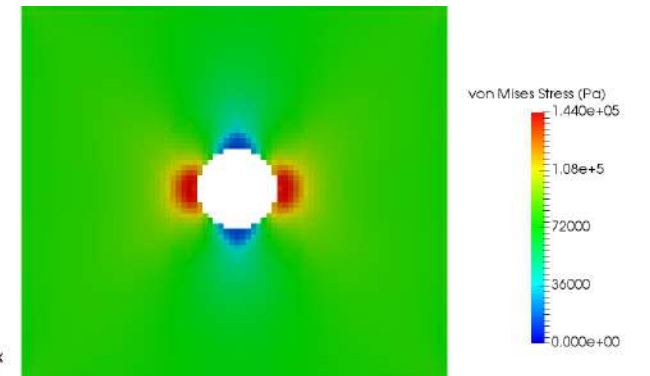


Figure 4: von Mises stress field of the material during loading.

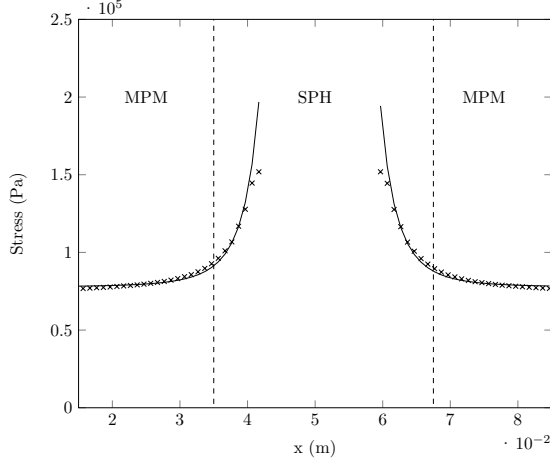


Figure 5: Comparison of the equivalent stresses along the horizontal center line from the simulation (crosses) and the analytical solution (line).

are some oscillations further away from the stress concentration. This is most likely due to the limited extent of the material and the transient response of the material under this loading. These results show that a smooth transition between SPH and MPM can be obtained even in dynamic systems where large stress gradients are present, highlighting the efficacy of this coupling and use of MPM. As MPM is still in its infancy relative to SPH and with their numerous similarities in terms of meshless modeling, it is worthwhile comparing the two methods side-by-side to see the extent to which MPM can be a possible substitute method, where appropriate.

4 Modeling Mixed Mode Failure

Due to its handling of large deformation and its foundation in hydrodynamics, SPH research has largely focused on fluid mechanics with fewer works relating to solid mechanics. As the derivation of SPH doesn't account naturally for exact boundary conditions and the presence of the tensile instability, solids modeling normally requires more numerical augmentations than fluid modeling. It is possible that a similar but alternative method, like MPM, could prove preferable when modeling particular systems. This would allow for more flexible solution procedures while still preserving many, if not all, of the best aspects that SPH posses. To see if MPM can be a suitable alternative, this work focuses on the modeling of rock failure using a Drucker Prager plasticity and Grady Kipp damage coupled constitutive model.

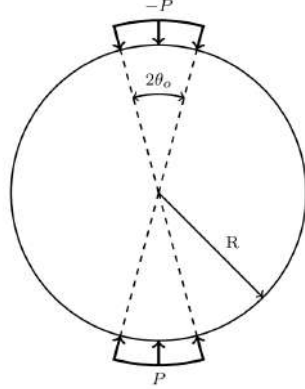


Figure 6: Schematic of the Brazilian test.

4.1 The Brazilian Test

The 2D Brazilian test was chosen to compare SPH and MPM in modeling damage and plasticity because this model separates the failure due to each process into different areas of the material and has analytical results (in the elastic regime). The Brazilian test problem is a well-known experiment that allows an indirect measure of the tensile strength of a material. It consists of a cylindrical disk subjected to a normal pressure along a short arc at opposing ends of the cylinder surface as illustrated in Fig.6. This applied pressure will result in a positive horizontal stress which causes the sample to break along the vertical diameter if the induced tensile stress is greater than the tensile strength of the material. For the elastic equilibrium of a homogeneous, continuous, isotropic circular disc with diameter D = 2R subjected to an uniform vertical radial pressure P over finite arcs which corresponds to a loading angle 2θ₀, the stresses along the vertical diameter are given by Hondros [16].

$$\sigma_x(0, y) = \frac{2p}{\pi} \left[\frac{(1 - \frac{y^2}{R^2}) \sin 2\theta_0}{1 - \frac{2y^2}{R^2} \cos 2\theta_0 + \frac{y^4}{R^4}} - \tan^{-1} \left(\frac{1 + \frac{y^2}{R^2} \tan \theta_0}{1 - \frac{y^2}{R^2}} \right) \right] \quad (4.1)$$

4.2 Results

Two models were created with SPH and MPM to be as similar as possible. In SPH since the resolution is governed by the smoothing length, which also controls the amount of particles, in MPM there is some ambiguity. This is because the cellsize controls the spatial resolution of the gradient calculations, like acceleration and strainrate, but the number of particles per cell controls the number of particles in the simulation. For these models, the spatial resolution was matched since plasticity and damage are sensitive to spatial resolution. Using the parameters in Table. 1 two simulations were run using, for SPH, a smoothing length of

Parameter	Value
Bulk Modulus (GPa)	20.38
Shear Modulus (GPa)	22.73
Density (kg/m^3)	2500.0
Platen Speed (m/s)	0.5
Cohesion (MPa)	34.94
Critical Strain	0.1
Friction Angle	51.48
Damage Parameter: m	8.0
Damage Parameter: k	1.14×10^{34}
Crack Speed (m/s)	1154.61

Table 1: Table of simulation parameters

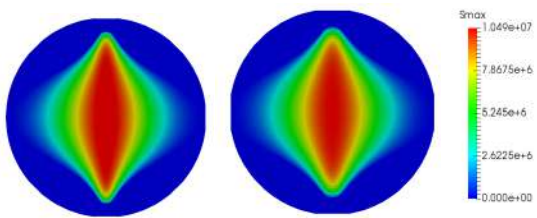


Figure 7: Maximum tensile stresses in the rock during compression.

0.004m and, for MPM, a cellsize of 0.004m for MPM. The simulations were run over a 5ms timespan, or until the specimens had failed completely. A schematic of the relevant dimensions is shown in Fig.6. As both of the simulations were run using second order explicit solvers, the loading on the top and bottom edges was achieved with a fixed velocity condition. The angle of loading, θ_0 was chosen to be 7° . Prior to the onset of damage or plasticity, the elastic loading of a circular specimen has an analytical solution, described by Hondros [1]. Fig.7 shows a side-by-side comparison of the tensile stresses of two simulations at the same point in

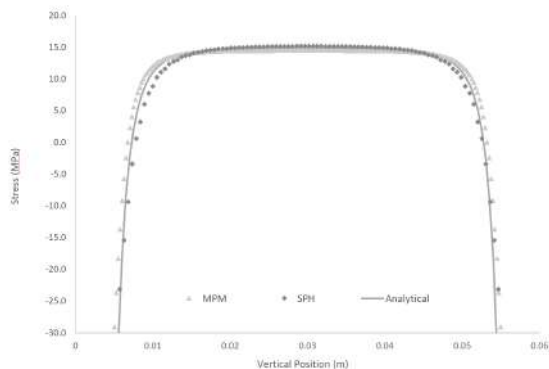


Figure 8: Comparison of SPH and MPM results to the analytical solution for maximum tensile stresses for the Brazilian test.

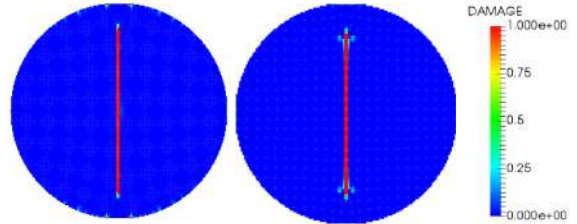


Figure 9: Damage state of the material at failure (left MPM, right SPH).

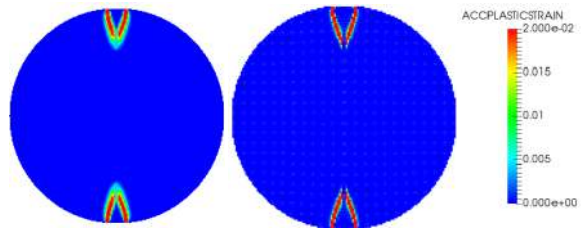


Figure 10: Accumulated plastic strain in the material at failure (left MPM, right SPH).

time, Fig.8 shows the stresses along the vertical centerline as compared to the analytical solution. Both the SPH and MPM results agree well with the static solution, with some deviation towards the edges of the specimen. Due to the dynamic state of the simulations, it is possible that there are still some stress waves in the explicit solution that are causing the values to over-under estimate the analytical solution. A possible solution to this would be to run an implicit solver, but this would cause difficulties in tracking the evolution of damage later on as the crack speed requires a small timestep. The failure behavior for this model is a single line of damage along the vertical center line extending to almost the upper and lower edges. Due to the finite width of the platens used to load the rock, a region of shear is encountered near the top and bottom surfaces, leading to shear failure by plasticity. Fig.9 shows the damage pattern for both SPH and MPM once the rock had failed. The extent to which the damage propagates along the centerline is matched very well by both techniques. SPH shows a slight amount of branching at the furthermost edges of the failure line and MPM shows some small damage in the vicinity of the contact with the loading platens. These variations are minor and can be attributed to slight differences in interpolation, symmetry and stress wave behavior. As there are no true analytical solutions to this point of material response it is difficult to ascertain which features should be expected. Nevertheless, the main failure pattern is captured well by both methods. Some variation in the results is found when examining the plastic strains Fig. 10. While the overall shape and lengths of the two shear bands is represented well by both methods,

SPH shows a much wider zone of higher plasticity with very little plasticity leading away from the shear band. The MPM results, on the other hand, show a thinner zone of higher plasticity with a wider zone of decreasing plasticity away from the shear bands. The overall goal of this work was to determine if MPM could be used in place of SPH for simulations where the weaknesses of the SPH method are accentuated, mainly solid mechanics and exact boundary conditions. As MPM requires essentially no artificial corrections in order to achieve the same results and exact boundary conditions are inherent in its derivation, it makes sense that it could be used in place of SPH where appropriate. The results presented here show that MPM is capable of reproducing the same behavior as SPH for solid mechanics and modeling failure.

5 Conclusion

A study of mixed-mode failure in rocks was conducted using SPH and MPM. These two meshless methods possess many similar qualities as numerical techniques and as such, a simple coupling algorithm between the two methods can be used and was shown to be effective for an example solid mechanics loading problem. Exact boundary conditions arise naturally from the derivation of the MPM technique making it an ideal candidate to couple with SPH simulations where such boundary conditions are required. As MPM is still a relatively unknown method, a comparison with SPH in modeling failure in solids presented a useful benchmark. Two simulations using MPM and SPH were run on the 2D Brazilian test to compare the solutions of stresses, damage, and plasticity by utilizing a combined Drucker Prager and Grady Kipp plasticity and damage model which has been shown in previous work to model mixed-mode failure. Both results agree well with the analytical solution of the stress field and the main failure patterns are reproduced in MPM and SPH.

References

- [1] R.a Gingold and Joseph J. Monaghan. Smoothed Particle Hydrodynamics: Theory and Application to non-spherical stars. *J. Chem. Inf. Model.*, 53(9):1689–1699, 1977.
- [2] Donald D Gray. *A first course in fluid mechanics for civil engineers*, volume 28. 2001.
- [3] Joseph J. Monaghan and R.a Gingold. Shock simulation by the particle method SPH. *J. Comput. Phys.*, 52(2):374–389, 1983.
- [4] Joseph P. Morris, Patrick J. Fox, and Yi Zhu. Modeling Low Reynolds Number Incompressible Flows Using SPH. *J. Comput. Phys.*, 136:214–226, 1997.
- [5] S. Raymond, V. Lemiale, R. Ibrahim, and R. Lau. A meshfree study of the Kalthoff–Winkler experiment in 3D at room and low temperatures under dynamic loading using viscoplastic modelling. *Eng. Anal. Bound. Elem.*, 42:20–25, may 2014.
- [6] P. W. Cleary. Modelling confined multi-material heat and mass flows using SPH. *Appl. Math. Model.*, 22(12):981–993, 1998.
- [7] J J Monaghan and a Kocharyan. SPH simulation of mulpi-phase flow. *Comput. Phys. Commun.*, 87:225, 1995.
- [8] A. M. Tartakovsky, N. Trask, K. Pan, B. Jones, W. Pan, and John R. Williams. Smoothed particle hydrodynamics and its applications for multiphase flow and reactive transport in porous media. *Comput. Geosci.*, 2015.
- [9] P. W. Cleary, Gerald G. Pereira, Vincent Lemiale, Claudio Delle Piane, and M. Ben Clennell. Multiscale model for predicting shear zone structure and permeability in deforming rock. *Comput. Part. Mech.*, 2015.
- [10] K Pan, B D Jones, and B W H Van Beest. Application of the SPH Method to Solitary Wave Impact on an Off-shore Platform. pages 1–21.
- [11] R. Pramanik and D. Deb. Implementation of Smoothed Particle Hydrodynamics for Detonation of Explosive with Application to Rock Fragmentation. *Rock Mech. Rock Eng.*, 48(4):1683–1698, 2015.
- [12] D. Sulsky, Z. Chen, and H. L. Schreyer. A particle method for history-dependent materials. *Comput. Methods Appl. Mech. Eng.*, 118:179–196, 1994.
- [13] D. Sulsky, S. Zhou, and H. L. Schreyer. Application of a particle-in-cell method to solid mechanics. *Comput. Phys. Commun.*, 87:236–252, 1995.
- [14] D. Sulsky and A. Kaul. Implicit dynamics in the material-point method. *Comput. Methods Appl. Mech. Eng.*, 193(12-14):1137–1170, 2004.
- [15] James E. Guilkey and Jeffrey A. Weiss. Implicit time integration for the material point method: Quantitative and algorithmic comparisons with the finite element method. *Int. J. Numer. Methods Eng.*, 57(October 2002):1323–1338, 2003.

- [16] Larry D. Libersky, Albert G. Petschek, Theodore C. Carney, Jim R. Hipp, and Firooz a. Allahdadi. High Strain Lagrangian Hydrodynamics, 1993.
- [17] W. Benz and E. Asphaug. Simulations of brittle solids using smooth particle hydrodynamics. *Comput. Phys. Commun.*, 87:253–265, 1995.
- [18] P. W. Randles and Larry D. Libersky. Smoothed Particle Hydrodynamics: Some recent improvements and applications. *Comput. Methods Appl. Mech. Eng.*, 139(1-4):375–408, 1996.
- [19] J. P. Gray, J. J. Monaghan, and R. P. Swift. SPH elastic dynamics. *Comput. Methods Appl. Mech. Eng.*, 190(49-50):6641–6662, 2001.
- [20] T. Douillet-grellier, R. Pramanik, K. Pan, A. Albaiz, B. D. Jones, and J. R. Williams. Development of stress boundary conditions in Smoothed Particle Hydrodynamics (SPH) for the modeling of solids deformation. *Comput. Part. Mech.*, pages 1–28, 2016.
- [21] R Pramanik and D Deb. SPH approach to rock failure with embedded discontinuity. pages 185–191, 2013.
- [22] N. Y. Wong. Crack coalescence in molded gypsum and carrara marble. *PhD Thesis, Massachusetts Institute of Technology*, 2008.
- [23] S. Raymond, B. Jones, and J. R. Williams. A strategy to couple the material point method (mpm) and smoothed particle hydrodynamics (sph) computational techniques. *Computational Particle Mechanics*, Dec 2016.
- [24] P. W. Cleary. Elastoplastic deformation during projectile-wall collision. *Appl. Math. Model.*, 34(2):266–283, 2010.
- [25] K. Abe, K. Soga, and S. Bandara. Material Point Method for Coupled Hydromechanical Problems. *J. Geotech. ...*, pages 1–16, 2013.
- [26] K. Abe and K Konagai. Numerical simulation of a series of flume tests with dry and wet sands by using depth averaged material point method. In *Geomech. from Micro to Macro*, pages 971–976, 2015.
- [27] S. Raymond, Y.E Aimene, J Nairn, and A Ouene. Coupled Fluid-Solid Geomechanical Modeling of Multiple Hydraulic Fractures Interacting with Natural Fractures and the Resulting Proppant Modeling Proppant Distribution in the Presence of Natural Fractures using the Material Point Method (MPM). In *SPE Unconv. Resour. Conf.*, 2015.
- [28] V. Lemiale, J. Nairn, and A. Hurmane. Material Point Method Simulation of Equal Channel Angular Pressing Involving Large Plastic Strain and Contact Through Sharp Corners. *C. - Comput. Model. Eng. Sci.*, 70(1):41–66, 2010.
- [29] D. Sulsky, H. L. Schreyer, K. Peterson, R. Kwok, and M. Coon. Using the material-point method to model sea ice dynamics. *J. Geophys. Res. Ocean.*, 112(August 2006):1–18, 2007.
- [30] D. Sulsky and K. Peterson. Toward a new elastic-decohesive model of Arctic sea ice. *Phys. D Nonlinear Phenom.*, 240(20):1674–1683, 2011.
- [31] J. Nairn. Material point method calculations with explicit cracks. *C. - Comput. Model. Eng. Sci.*, 4(6):649–663, 2003.
- [32] S.G. Bardenhagen, J.U. J. U. Brackbill, and D. Sulsky. The material-point method for granular materials. *Comput. Methods Appl. Mech. Eng.*, 187(99):529–541, 2000.
- [33] J. A Nairn. Numerical Modeling of Orthogonal Cutting : Application to Woodworking with a Bench Plane. pages 1–17, 2015.

Suppression of non-physical voids in the finite volume particle method

Mohsen H. Moghimi and Nathan J. Quinlan

Department of Mechanical Engineering
National University of Ireland Galway
Galway, Ireland

M.HASSANZADEHMOGHIMI1@nuigalway.ie

Abstract— The Finite Volume Particle Method (FVPM) is used to simulate the fluid flow in 2D. The solver includes conservative equations of mass and momentum, temporal evolution of volume, and an equation of state to calculate the pressure. In this work, we present an innovative simple algorithm to differentiate non-physical voids from physical free surfaces in the FVPM, which facilitates the suppression of spurious voids due to the unfavourable distribution of the particles in the domain. Applying the new particle detection method along imposing the background pressure is investigated and it is proved that implementing the new algorithm is necessary for realistic simulation of the flow fields.

I. INTRODUCTION

The finite volume particle method (FVPM) is a relatively novel numerical technique in computational fluid dynamics, introduced by Hietel *et al.* in 2000 [1]. The basic idea is to preserve the computational model of numerical flux developed in finite volume method (FVM) and use the advantages of mesh-free particle method, in this case smoothed particle hydrodynamics, in simulation of moving boundary and free-surface problems.

The FVPM is a meshless method in which particles behave like cells in the classical-finite volume method, but are allowed to overlap each other and move arbitrarily. Particles with overlapping supports are considered to be neighbouring particles. The values of the particle's variables are calculated through the exchange of the numerical flux from the neighboring particles in overlapping area and by interpolating through the kernel function.

FVPM has been used and tested for different areas of fluid dynamics. The method has been developed to higher order of accuracy by Nestor [2] and Kadrnka [3]. It was extended to solve viscous flow by Nestor [2] and Nestor *et al.* [4]. The capability of FVPM has been extended to simulate moving-boundary problems ([2, 5, 6]), and developed for 3-D by Jahanbakhsh [7]. In addition, the interaction between fluid-silt, fluid-solid, and impinging jet in the FVPM successfully modeled ([7, 8]). The method has been tested for some improvement of interparticle area calculation [9], a new 3-D formulation for spherical support [10], and rectangular top-hat kernel for computation of interaction vectors [8].

Despite the de facto potential of the method and the developments to date, Like Smoothed Particle Hydrodynamics (SPH), FVPM may suffer from poor particle distribution as a result of fully Lagrangian particle motion, and the formation of unphysical voids in regions of negative pressure. This is closely related to tensile instability in SPH. Increasing the background pressure throughout the numerical domain has positive effect to suppress the voids ([11, 12]) but without correct detection of free surfaces it cannot work perfectly for the reason that it should be applied only on the physical free surfaces to maintain the absolute pressure high enough everywhere. But, the FVPM still lacks the correct detection of the physical free surfaces. Determination of physical free surfaces is necessary in order to impose the correct boundary condition to prevent the creation of unphysical voids and non-physical behavior of the numerical method. In this paper, a new method is proposed to overcome this deficiency.

This paper is organized as follows. Section II summarizes the FVPM formulation for fluid flow computations. In section III, the common problem between SPH and FVPM which is the unfavorable particle distribution in the numerical domain is described. In section IV, the general free-surface detection and the innovative particle detection method is presented. Finally section V presents the numerical results of different test cases.

II. GOVERNING EQUATIONS AND NUMERICAL MODEL

A. Governing Equations

The basic governing equations of fluid dynamics based on physical laws of conservation are Navier-Stokes equations. The differential form of these equations without source terms is written in the compact form as the following:

$$\frac{\partial \Phi(t, x)}{\partial t} + \nabla \cdot F(\Phi(t, x)) = 0 \quad (1)$$

where $\Phi(t, x)$, F , t , x represent the vector of conservative quantities, flux functions, time, and position. The conservative quantities and flux functions are $\{\rho\}$ and $\{\rho u\}$, where ρ , u , p , I , τ are fluid density, velocity vector, pressure, identity tensor, and viscous stress tensor of

the fluid, respectively. Equation (2) is used for pressure calculation.

$$p = P_a + \frac{\rho_0 a_0^2}{\gamma} \left[\left(\frac{\rho}{\rho_0} \right)^\gamma - 1 \right] \quad (2)$$

where P_a , ρ_0 , a_0 , γ are background pressure, reference density of the fluid, reference sound speed, and a constant, respectively. The value of γ is chosen as 7 for most circumstances.

B. Numerical Model

The FVPM formulation of (1) for particle i , is shown as the following:

$$\begin{aligned} \frac{d}{dt} (\Phi_i(t) V_i(t)) &= - \sum_{j=1}^N \beta_{ij} \cdot [\mathbf{F}(\Phi_{ij})(t, \mathbf{x}) - \Phi_{ij}(t, \mathbf{x}) \dot{\mathbf{x}}_{ij}(t)] \\ &\quad - \int \Psi_i(t, \mathbf{x}) \mathbf{F}(\Phi_{ij})(t, \mathbf{x}) \cdot d\mathbf{S} \end{aligned} \quad (3)$$

where V_i , β_{ij} , $\Phi_{ij}(t)$, $\dot{\mathbf{x}}_{ij}$, Ψ_i , and $d\mathbf{S}$ are particle's volume, interparticle area vector between particles i and j , vector of conservative quantities at the interface of particles i and j , velocity of the interface, test function of the particle, and the surface vector of particle i , respectively. The interaction vector is defined as:

$$\beta_{ij} = \gamma_{ij} - \gamma_{ji} \quad (4)$$

where γ_{ij} is $\int \Psi_i(t, \mathbf{x}) \frac{\nabla W_j(t, \mathbf{x})}{\sigma(t, \mathbf{x})} d\mathbf{x}$ in which W_j and σ are the kernel function of particle j and kernel summation. The kernel function, kernel summation, and the test function of the particle i , are defined as the following, respectively:

$$W_i(t, \mathbf{x}) = m_i W(\mathbf{x} - \mathbf{x}_i(t), h) \quad (5)$$

$$\sigma(t, \mathbf{x}) = \sum_{j=1}^N W_j(t, \mathbf{x}) \quad (6)$$

$$\Psi_i(t, \mathbf{x}) = \frac{W_i(t, \mathbf{x})}{\sigma(t, \mathbf{x})} \quad (7)$$

In (5), m_i and h are particle's mass and smoothing length of the compactly supported kernel function. The radius of the base of the kernel function is assumed as kh , and in the current research selected as $2h$. The kernel function, W_i , is defined as zero outside particle i . As it is clear, summation of Ψ_i that is equal to 1, describes that all particles at time t and position \mathbf{x} are showing an integrated computational domain.

It is worth mentioning that, indeed Ψ_i provides a unit criterion to check the status of each particle in comparison to the other particles throughout the computational domain at the same time and position or in other word, it shows the share of the particle of interest at time t and position \mathbf{x} .

To close the system of equations, the evolution of the volume of the particle is presented in below:

$$\frac{d}{dt} V_i(t) = \sum_{i=1}^N \left(\gamma_{ij} \cdot \dot{\mathbf{x}}_j(t) - \gamma_{ji} \cdot \dot{\mathbf{x}}_i(t) \right) \quad (8)$$

where the particle's volume $V_i(t)$ is defined as $V_i(t) = \int \Psi_i(t, \mathbf{x}) d\mathbf{x}$. For the detailed derivation of the FVPM formulation the readers are referred to [1] and [2].

III. UNFAVORABLE PARTICLE DISTRIBUTIONS IN FVPM

Fully Lagrangian particle motion can provide better prediction of the flows with free surfaces and moving boundaries, because of particles transportation throughout the computational domain with local fluid velocity. Despite this capability, it can lead to inappropriate particle distribution like particle clumping and creation of unphysical voids. It is for the reason that the position of the particles is only prescribed at the initial condition and then by marching in time, the fluid flow determines their next positions.

There is not a robust solution to achieve a particle distribution which can cover the flow domain completely and physically. But in order to maintain good particle distribution, there is a mechanism in which a small correction added to the Lagrangian particle transport velocity (similar to particle shifting), taking advantage of the Arbitrary Lagrangian-Eulerian (ALE) nature of FVPM [4]. However, for different applications and physics a special velocity correction formulation should be used. The magnitude of the velocity added to the Lagrangian velocity is determined by considering the velocity of the neighbouring particles of the particle of interest.

IV. INNOVATIVE FREE-SURFACE DETECTION METHOD AND VOID SUPPRESSION

As it is seen from (3), like classical FVM, in FVPM the time evolution of the conservative variables is related to the numerical fluxes between particles. In addition, in FVPM magnitude of the passing fluxes through boundaries are weighting by the interaction vectors of each particle, which has the same role as surface vectors of each cell in FVM; implies their great influence on the accuracy of the numerical calculations in finite volume particle method.

A. General Free-Surface Detection in FVPM

Two points which constitute the calculation of the interaction vectors are non-zero kernel function only in the overlapping area of interacting particles, and presence of the number of the neighbouring particles through σ . As illustrated in Fig. 1, particles j, k, m, n, and p are considered as the neighbours of particle i, because their compact support overlap the compact support of the particle of interest. The interface of the interacting particles is the side which connects the intersections of their compact supports. The interaction vectors are calculated on these interfaces, but their directions are dependent on the direction of the gradients of the kernels as can be seen in (4). If the boundary of a particle's support is fully covered by neighbouring particles, it means that its area vectors sum to zero. Then this particle is considered as a particle not

positioned on the free surface (Fig. 1). In contrast, if the summation of the interaction vectors between the particle of interest and its neighbours is not equal to zero (Fig. 2) it means that the particle is on the free surface which can be a physical or non-physical due to the poor particle distribution as a result of fully Lagrangian particle motion.

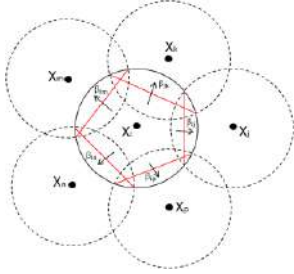


Fig. 1. Summation of interaction vectors of particle i and its neighbours is zero.

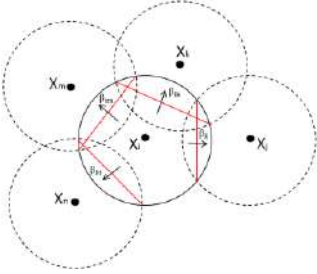


Fig. 2. Summation of interaction vectors of particle i and its neighbours is non-zero.

B. Innovative Method for Detection of Physical Free Surfaces

Unlike SPH in which a particle is considered as a neighbour of the particle i , if its centre positioned in the compact support of the particle of interest, in the FVPM if the compact support of two particles overlap each other they are considered as the neighbouring particles. Because the radius of the compact support is $2h$ then it means that the maximum distance between the particle of interest and each of its neighbours is $4h$. On the other side, the time step determined by a Courant-Friedrichs-Lowy (CFL) criterion for the FVPM is as the following:

$$\Delta t = C \frac{V_i}{\sum_j \left(\left(\frac{\mathbf{u}_i + \mathbf{u}_j}{2} \right) \cdot \boldsymbol{\beta}_{ij} + \left(\frac{a_i + a_j}{2} \right) |\boldsymbol{\beta}_{ij}| \right)} \quad (9)$$

where C is the Courant number, a is the local speed of the sound, and V_i is the particle volume.

It appears clearly from (12) that each particle can have a displacement about the ratio of its volume to its surface area, which is about its diameter in each time step for circular particle. It implies that the particle of interest can only replace its position with its neighbours at most. If due to the Lagrangian motion of the particle of interest, the particle cannot be covered completely, it can be considered as physical or non-physical free surface, but if the particle of interest does not have any free-surface neighbour at time $t - \Delta t$, then it is unlikely for this particle to reach to the free surface in time t , determined as non-physical free surface.

C. Background Pressure and Void Suppression

References [11] and [12] show that increasing the background pressure throughout the computational field can have considerable effect to suppress the unphysical cavitation with generation of voids in SPH.

However, increasing the background pressure cannot lead to favourable results in all cases completely without correct detection of physical free surfaces, because in order to apply background pressure at free surfaces, the force $P_a \boldsymbol{\beta}_{ij}$ should be added to the RHS of momentum equation, then if free surfaces (physical or non-physical) are not distinguished accurately, it is not only applied at physical free surfaces but also at unphysical free surfaces that leads to the growth of the voids.

On the other side, the bigger the background pressure the higher the error in the computations is [13]. Therefore, implementing the new free-surface detection method is considerably important to apply the background pressure on the right particles accurately.

V. NUMERICAL RESULTS

The importance of the novel particle detection method is shown in the following. The new numerical algorithm has been tested for different fluid flows including the immersed stationary cylinder with physical free surface, translating rotating cylinder, translating rotating square, translating trapezoid, and oscillating liquid in rectangular tank. In all test cases, general descriptions of the flow field and the significant effect of the new physical free surface detection method are presented.

A. Immersed Stationary Cylinder with Physical Free Surface

The first test case is a stationary cylinder immersed in the water with physical free surface, as shown in Fig. 3. The Reynolds number based on the diameter of the cylinder is 96×10^4 . The non-dimensional time is defined as $t^* = \frac{t V_{in}}{D}$, where V_{in} and D are inlet velocity and diameter of the cylinder, respectively. The ratio of $\frac{D}{\Delta x}$ equals 11, where Δx is the initial particle spacing. For inlet and outlet velocities the value of $\frac{V}{V_{in}}$ is prescribed as 1.

For brevity, only for this test case the effect of low and high background pressure is compared. The results were obtained for $\frac{P_a}{2\rho V_{in}^2}$ as 5.6 and 280 for low and high background pressures, respectively (Figs. 4 and 5). As it is seen from Fig. 5, the stronger the background pressure has positive effect to reduce the unphysical void region, but it is not capable to suppress them at the back of the cylinder completely which is due to the lack of free-surface detection in this simulation. In these cases the background pressure is applied not only on the physical free surfaces but also on the unphysical free surfaces which prevents the non-physical voids to be suppressed completely. However, it is seen in Fig. 9, applying the innovative free-surface detection method makes it possible to suppress the voids at the same background pressure as in Fig. 4, without using higher background pressure which can increase the numerical errors. In this test case regions without particles are seen in Figs. 6, 8, and 10. The voids can be treated if correct free-surface particle detection is implemented by the new method (Figs. 7, 9, and 11).

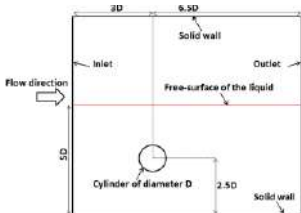


Fig. 3. Stationary cylinder immersed in the water with physical free surface.

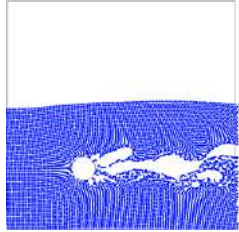


Fig. 4. Pressure distribution with basic Lagrangian FVPM and $\frac{P_a}{2\rho V_{in}^2} = 5.6$, $t^* = 13.7$, $\frac{D}{\Delta x} = 11$.

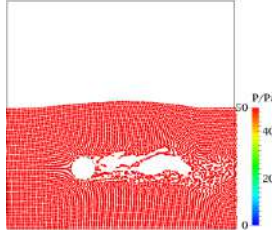


Fig. 5. Pressure distribution with basic Lagrangian FVPM and $\frac{P_a}{2\rho V_{in}^2} = 280$, $t^* = 13.7$, $\frac{D}{\Delta x} = 11$.

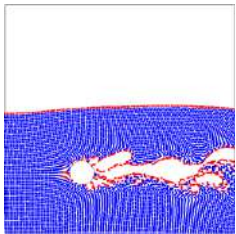


Fig. 6. Particle distribution with basic Lagrangian FVPM (Red points are free surface), $t^* = 13.7$, $\frac{D}{\Delta x} = 11$.

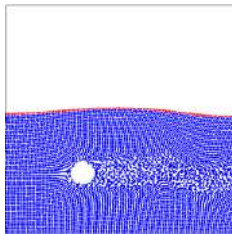


Fig. 7. Particle distribution with basic Lagrangian FVPM and free-surface detection (Red points are free surface), $t^* = 13.7$, $\frac{D}{\Delta x} = 11$.

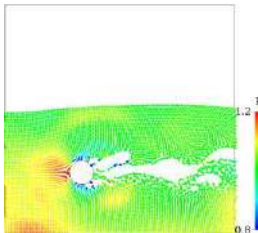


Fig. 8. Pressure distribution with basic Lagrangian FVPM, $t^* = 13.7$, $\frac{D}{\Delta x} = 11$.

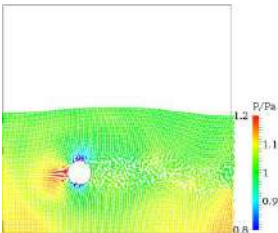


Fig. 9. Pressure distribution with basic Lagrangian FVPM and free-surface detection, $t^* = 13.7$, $\frac{D}{\Delta x} = 11$.

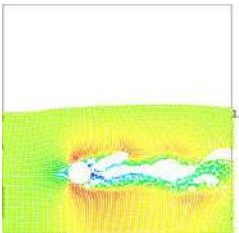


Fig. 10. Velocity field with basic Lagrangian FVPM, $t^* = 13.7$, $\frac{D}{\Delta x} = 11$.

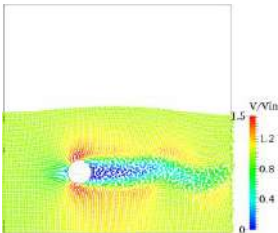


Fig. 11. Velocity field with basic Lagrangian FVPM and free-surface detection, $t^* = 13.7$, $\frac{D}{\Delta x} = 11$.

B. Translating Rotating Cylinder

The second test case is a translating rotating cylinder. Fig. 12 shows a sketch of the geometry. The Reynolds number based on the diameter of the cylinder and horizontal velocity is 18×10^5 . The non-dimensional time is defined as $t^* = \frac{tV_c}{D}$, where V_c and D are translational velocity and diameter of the cylinder. For vertical and horizontal velocities of the cylinder, the values of $\frac{V}{V_c}$ are prescribed as 0.07 and 0.99, respectively. The non-dimensional angular velocity $\frac{\omega_c}{(V_c/D)}$ equals 0.11, where ω_c is the angular velocity of the cylinder. The results were obtained for $\frac{P_a}{2\rho V_c^2} = 2.4$, and $\frac{D}{\Delta x} = 7$. In this test case the regions without particles are seen in Figs. 13, 15, and 17. The voids can be treated if correct free-surface particle detection is implemented by the new method (Figs. 14, 16, and 18).

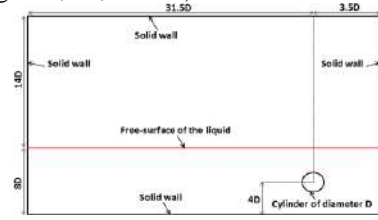


Fig. 12. Translating rotating cylinder immersed in the water with physical free surface.

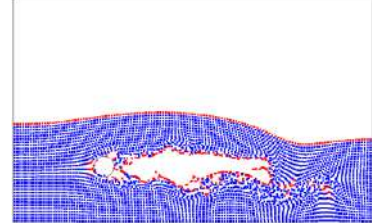


Fig. 13. Particle distribution with basic Lagrangian FVPM (Red points are free surface), $t^* = 10.8$, $\frac{D}{\Delta x} = 7$.

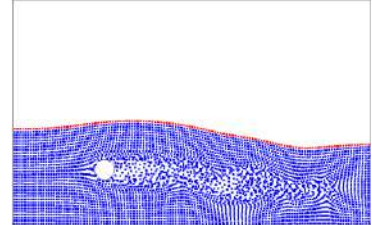


Fig. 14. Particle distribution with basic Lagrangian FVPM and free-surface detection (Red points are free surface), $t^* = 10.8$, $\frac{D}{\Delta x} = 7$.

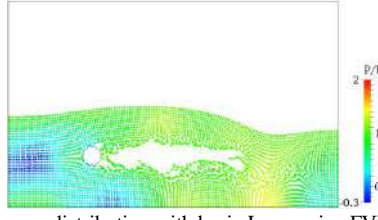


Fig. 15. Pressure distribution with basic Lagrangian FVPM, $t^* = 10.8$, $\frac{D}{\Delta x} = 7$.

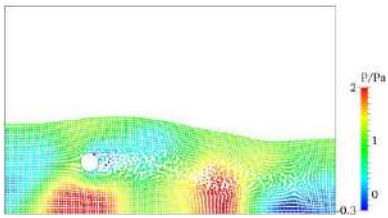


Fig. 16. Pressure distribution with basic Lagrangian FVPM and free-surface detection, $t^* = 10.8$, $\frac{D}{\Delta x} = 7$.

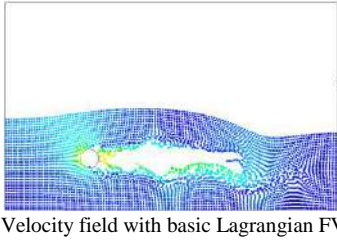


Fig. 17. Velocity field with basic Lagrangian FVPM, $t^* = 10.8$, $\frac{D}{\Delta x} = 7$.

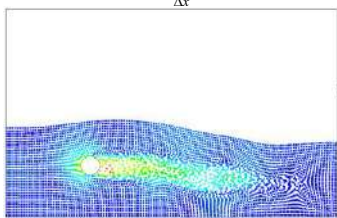


Fig. 18. Velocity field with basic Lagrangian FVPM and free-surface detection, $t^* = 10.8$, $\frac{D}{\Delta x} = 7$.

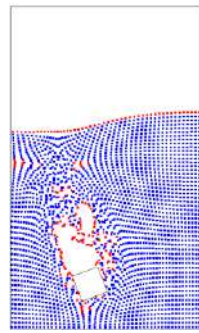


Fig. 20. Particle distribution with basic Lagrangian FVPM (Red points are free surface), $t^* = 4.4$, $\frac{L}{\Delta x} = 7$.

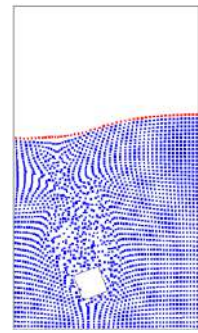


Fig. 21. Particle distribution with basic Lagrangian FVPM and free-surface detection (Red points are free surface), $t^* = 4.4$, $\frac{L}{\Delta x} = 7$.

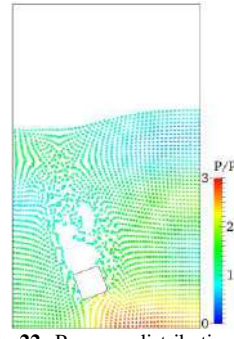


Fig. 22. Pressure distribution with basic Lagrangian FVPM, $t^* = 4.4$, $\frac{L}{\Delta x} = 7$.

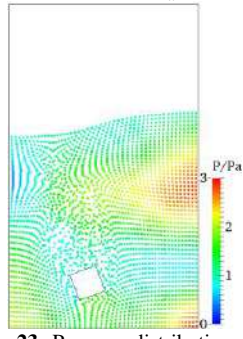


Fig. 23. Pressure distribution with basic Lagrangian FVPM and free-surface detection, $t^* = 4.4$, $\frac{L}{\Delta x} = 7$.

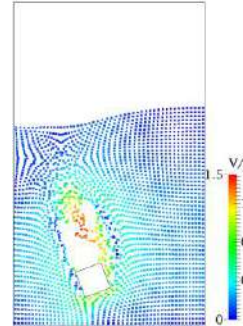


Fig. 24. Velocity field with basic Lagrangian FVPM, $t^* = 4.4$, $\frac{L}{\Delta x} = 7$.

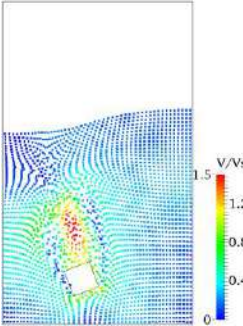


Fig. 25. Velocity field with basic Lagrangian FVPM and free-surface detection, $t^* = 4.4$, $\frac{L}{\Delta x} = 7$.

C. Translating Rotating Square

The third test case is a translating rotating square. Fig. 19 shows a sketch of the geometry. The Reynolds number based on the length of the side of the square and vertical velocity is 7×10^6 . The non-dimensional time is defined as $t^* = \frac{t V_s}{L}$, where V_s and L are translational velocity and length of the side of the square. For vertical and horizontal velocities of the square the values of $\frac{V}{V_s}$ are prescribed as 0.96 and 0.27, respectively. The non-dimensional angular velocity $\frac{\omega_s}{(\frac{V_s}{D})}$ is equal to 0.27, where ω_s is the angular velocity of the square. The results were obtained for $\frac{P_a}{\rho V_s^2} = 3.8$ and $\frac{L}{\Delta x} = 7$. The regions without particles are seen in Figs. 20, 22, and 24. The voids can be treated if correct free-surface particle detection is implemented by the new method (Figs. 21, 23, and 25).

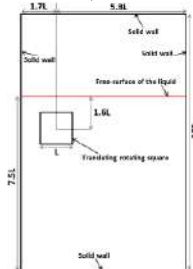


Fig. 19. Translating rotating square immersed in the water with physical free surface.

D. Translating Trapezoid

The fourth test case is a translating rotating square. Fig. 26 shows a sketch of the geometry. The Reynolds number based on the height of the trapezoid and vertical velocity is 6×10^6 . The non-dimensional time is defined as $t^* = \frac{t V_t}{H}$, where V_t and H are translational velocity and height of the trapezoid (in this case $0.15L$). For vertical velocity of the trapezoid the value of $\frac{V}{V_t}$ is prescribed as 1. The results were obtained for $\frac{P_a}{\rho V_s^2} = 3.1$ and $\frac{H}{\Delta x} = 11$.

The regions without particles are seen in Figs. 27, 29, and 31. The voids can be treated if correct free-surface particle detection is implemented by the new method (Figs. 28, 30, and 32).

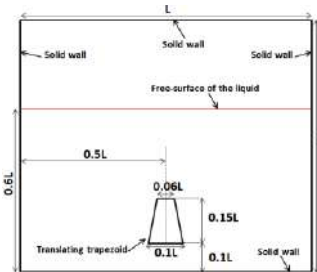


Fig. 26. Translating trapezoid immersed in the water with physical free surface.

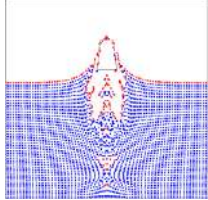


Fig. 27. Particle distribution with basic Lagrangian FVPM (Red points are free surface), $t^* = 3.6$, $\frac{H}{\Delta x} = 11$.

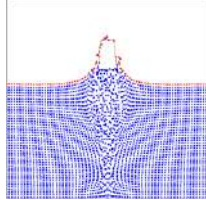


Fig. 28. Particle distribution with basic Lagrangian FVPM and free-surface detection (Red points are free surface), $t^* = 3.6$, $\frac{H}{\Delta x} = 11$.

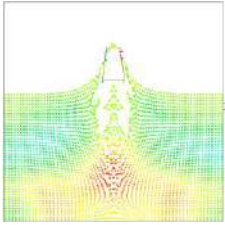


Fig. 29. Pressure distribution with basic Lagrangian FVPM, $t^* = 3.6$, $\frac{H}{\Delta x} = 11$.

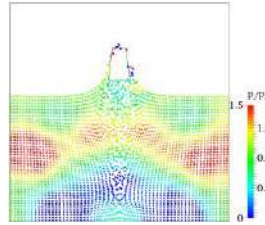


Fig. 30. Pressure distribution with basic Lagrangian FVPM and free-surface detection, $t^* = 3.6$, $\frac{H}{\Delta x} = 11$.

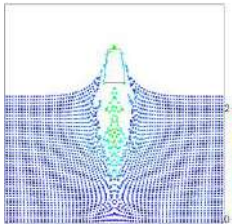


Fig. 31. Velocity field with basic Lagrangian FVPM, $t^* = 3.6$, $\frac{H}{\Delta x} = 11$.

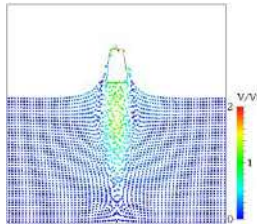


Fig. 32. Velocity field with basic Lagrangian FVPM and free-surface detection, $t^* = 3.6$, $\frac{H}{\Delta x} = 11$.

E. Oscillating Liquid in Rectangular Tank

The last test case is a simple tank oscillating vertically with displacement $y = A \sin(2\pi f t)$, where A , f , and t are amplitude, frequency, and time, respectively.

Instead of defining a moving aperture plate, the acceleration due to oscillation has been added to the RHS of the Navier-Stokes momentum equation as a momentum source. To do so, the term $\Phi_i(t)$ in (3) can be substituted for the ρu to form the equation of momentum conservation. By doing dimensional analysis it is clear that the LHS of (3)

has the unit of force, then in the FVPM the intended momentum source is indeed a force which is due to the oscillation and should be added to the RHS of (3). The oscillating force is written in the form of the following:

$$F_{\text{Osc}} = \rho_i V_i (-A(2\pi f)^2 \sin(2\pi f t)) \quad (10)$$

As it is seen from Fig. 33, the oscillation results in negative pressure, which causes the growth of regions without particles.

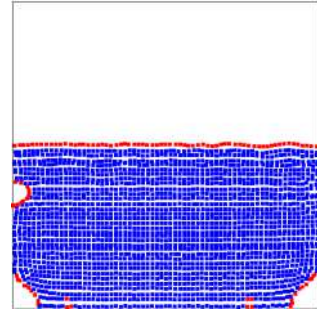


Fig. 33. Particle distribution with basic Lagrangian FVPM (Red points are free surface), $\frac{L}{A} = 200$, $\frac{t}{T} = 26$, $\frac{L}{\Delta x} = 35$.

The voids can be remedied if correct free surface particle detection is implemented by the new method, because zero absolute pressure is applied on non-physical free surfaces, and no voids grow (Fig. 34); but still there are some small voids which can be treated by applying the particle transport correction on the flow domain (Fig. 35).

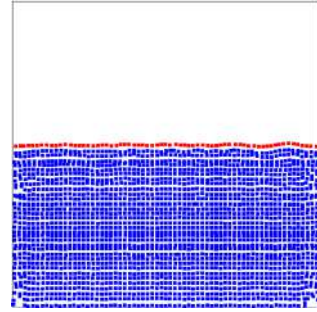


Fig. 34. Particle distribution with Lagrangian particle motion and free-surface detection (Red points are free surface), $\frac{L}{A} = 200$, $\frac{t}{T} = 26$, $\frac{L}{\Delta x} = 35$.

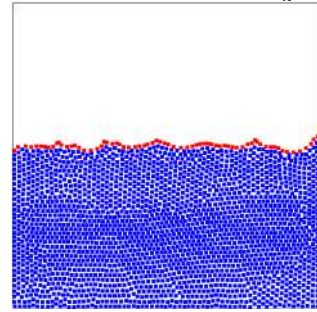


Fig. 35. Particle distribution with particle transport correction and free-surface detection (Red points are free surface), $\frac{L}{A} = 200$, $\frac{t}{T} = 26$, $\frac{L}{\Delta x} = 35$.

These results were obtained for Reynolds number 2011 (based on the length of the tank and the amplitude of oscillating velocity $2\pi f A$), $\frac{P_a}{\rho(2\pi f A)^2} = 40$, $\frac{L}{A} = 200$, $\frac{t}{T} = 26$, and $\frac{L}{\Delta x} = 35$, where L and T are liquid depth and period of oscillation, respectively.

VI. CONCLUSION

The finite volume particle method (FVPM) has a rigorous capability to use the advantageous of the classical finite volume method (FVM) and the smoothed particle hydrodynamics (SPH) to simulate different flow fields due to its properties including consistency, conservation, and Arbitrary Lagrangian-Eulerian (ALE) motion of the particles.

To date, the FVPM was not able to differentiate between physical and non-physical free surfaces accurately which was preventing the implementation of accurate boundary condition on different particles and suppression of the non-physical voids in the regions of negative pressures.

However, the innovative particle detection method, provided in this paper, added a strong capability to the FVPM to detect the spurious voids with high accuracy which makes it possible to impose the correct boundary condition only on the physical free surfaces to prevent the non-physical behavior of the numerical method. The obtained results show the obvious effectiveness and power of the proposed particle detection algorithm.

ACKNOWLEDGEMENT

This publication has emanated from research conducted with the financial support of Science Foundation Ireland (SFI) and Aerogen, and is co-funded under the European Regional Development Fund under Grant Number 13/RC/2073.

REFERENCES

- [1] D. Hietel, K. Steiner, and J. Struckmeier, "A finite volume particle method for compressible flows," *Mathematical Models and Methods in Applied Sciences*, vol. 10, no. 9, pp. 1363-1382, 2000.
- [2] R. Nestor, "Development of a finite volume particle method for incompressible flow with moving boundaries," PhD thesis, National University of Ireland Galway, 2008.
- [3] L. Kadnka, "The finite volume particle method - A meshfree method of second order for the numerical solution of hyperbolic conservation laws," PhD thesis, Hamburg University, 2014.
- [4] R. Nestor, M. Basa, M. Lastiwka, and N. Quinlan, "Extension of the finite volume particle method to viscous flow," *Journal of Computational Physics*, vol. 228, no. 5, pp. 1733-1749, 2009.
- [5] R. Nestor and N. Quinlan, "Incompressible moving boundary flows with the finite volume particle method," *Computer Methods in Applied Mechanics and Engineering*, vol. 199, no. 3336, pp. 2249-2260, 2010.
- [6] R. Nestor and N. Quinlan, "Application of the meshless finite volume particle method to flow-induced motion of a rigid body," *Computers and Fluids*, vol. 88, pp. 386-399, 2013.
- [7] E. Jahanbakhsh, "Simulation of silt erosion using particle-based methods," Ph.D. thesis, Swiss Federal Institute of Technology in Lausanne, 2014.
- [8] E. Jahanbakhsh, C. Vessaz, A. Maertens, and F. Avellan, "Development of a Finite Volume Particle Method for 3-D fluid flow simulations," *Computer Methods in Applied Mechanics and Engineering*, vol. 298, pp. 80-107, 2016.
- [9] N. Quinlan, L. Lobovsky, and R. Nestor, "Development of the meshless finite volume particle method with exact and efficient calculation of interparticle area," *Computer Physics Communications*, vol. 185, no. 6, pp. 1554-1562, 2014.
- [10] E. Jahanbakhsh, A. Maertens, N. Quinlan, C. Vessaz, and F. Avellan, "Exact finite volume particle method with spherical-support kernels," *Computer Methods in Applied Mechanics and Engineering*, vol. 317, pp. 102-127, 2017.
- [11] S. Marrone, A. Colagrossi, M. Antuono, G. Colicchio and G. Graziani, "An accurate SPH modeling of viscous flows around bodies at low and moderate Reynolds numbers," *Journal of Computational Physics*, vol. 245, pp. 456-475, 2013.
- [12] J.P. Morris, "Analysis of smoothed particle hydrodynamics with applications," PhD Thesis, Monash University, 1996.
- [13] A. Colagrossi, B. Bouscasse, M. Antuono, and S. Marrone, "Particle packing algorithm for SPH schemes," *Computer Physics Communications*, vol. 183, no. 2, pp. 1641-1683, 2012.

The Hermit-type Radial Reproducing Kernel Particle Method for Piezoelectric Materials

Ma Jichao

School of Mechanical and Automotive Engineering,
Qilu University of Technology
Jinan, China, 250353
Majichao0110@126.com

Wei Gaofeng

School of Mechanical and Automotive Engineering,
Qilu University of Technology
Jinan, China, 250353
weigaofeng@126.com

Abstract—In this paper, the radial basis function (RBF) and its normal derivative are introduced into the reproducing kernel particle method (RKPM), and the Hermit-type radial reproducing kernel particle method (Hermit-type RRKPM) is proposed. The method can reduce the adverse effect of the kernel function on the calculation precision. The errors can be decreased on the boundary, and the accuracy and stability of the algorithm are improved. Then the proposed method is applied to the numerical simulation of piezoelectric materials and the corresponding governing equations are derived. The numerical results show that the Hermit-type RRKPM is more stable and accurate than the RKPM.

I. INTRODUCTION

Intelligent control system, which is used in the detection of cracks and defects within structures, can adapt to the environment by self-regulation. The sensor is an important part of the intelligent control system [1,2]. Its accuracy, sensitivity and stability have a great effect on the performance of the intelligent control system. Therefore, it is important to select the material to manufacture sensor. Due to the unique characteristics of piezoelectric materials, such as ease of integration into existing structures, and easily controlled by voltage, they are suitable candidates to be implemented as sensors.

At present, there are three main methods to research piezoelectric materials, which are theoretical derivation, numerical simulation and experimental analysis. The numerical simulation has become the main method to analyze piezoelectric materials because it can quickly and efficiently solve the domain. Numerical simulation methods mainly include finite element method (FEM) [3], boundary element method, and meshless method [4], etc. When FEM is used to accurately solve the local domain, work of mesh refinement is heavy, which results in costing a lot of computing time and low precision. Boundary element method needs to integrate the domain to solve the problem, which shows strong singularity near the singular point, making it difficult to calculate. Meshless method has the advantages of quick calculation and high precision when it is used to solve the local domain. So it has been developed in recent years.

There are a variety of meshless methods, such as reproducing kernel particle method [5], polynomial point interpolation method [6], boundary integral equation method [7], element-free Galerkin method [8], moving least-squares method [9], smooth particle hydrodynamics [10], radial basis function method [11], the partition of unity method [12], local Petrov-Galerkin method [13], finite point method [14], Hermite radial point interpolation method [15], and meshless manifold method [16].

The RKPM has a fast convergence speed and high accuracy, so it is mainly used to solve displacements and electric potential of piezoelectric materials. But in the process of solving the domain, the influence domain of kernel function has great influence on calculation precision. In this paper, the Hermit-type RRKPM is proposed to improve the RKPM, which adds the RBFs and the derivative of the RBFs. In the process of solving approximate function, the RKPMs are constructed by internal nodes in the domain; the derivatives of the RBFs are constructed by nodes on the boundary; the RBFs are constructed by all nodes in the domain. The method can decrease the adverse effect of the kernel function on the calculation accuracy, and cuts down the errors on the boundary. The accuracy and stability of the proposed method are demonstrated by the piezoelectric strip and the cantilever piezoelectric bimorph beam.

II. THE GOVERNING EQUATIONS OF PIEZOELECTRIC MATERIAL

In the x - z plane, the constitutive equations of piezoelectric material can be expressed as

$$\sigma_p = c_{pq}^E \epsilon_q - e_{pk} E_k \quad (1)$$

$$D_i = e_{iq} \epsilon_q + \xi_{ik}^e E_k \quad (2)$$

where σ , ϵ , E_k and D_i are the stress tensor, the strain tensor, the electric field vector and the electric displacement vector, respectively. c^E , e and ξ^e are the elastic stiffness, piezoelectric constant, and dielectric constant, respectively.

Superscript ε and E represent coefficients measured at constant strain and electric field, respectively.

The relation between strain and displacement is

$$\varepsilon_{ij} = \frac{1}{2}(u_{i,j} + u_{j,i}) \quad (3)$$

The condensed matrix can be given as

$$\varepsilon_x = \varepsilon_{xx} = u_{,x} \quad (4)$$

$$\varepsilon_z = \varepsilon_{zz} = w_{,z} \quad (5)$$

$$\gamma_{xz} = 2\varepsilon_{xz} = u_{,z} + w_{,x} \quad (6)$$

where u and w represent the displacement functions in the x and z directions, respectively. Commas followed by indices represent partial differentiation with respect to that index.

The relationship between electric field and electric potential is

$$E_i = -\varphi_i \quad (7)$$

The mechanical constitutive equation of piezoelectric material is expressed as two-dimensional matrix form given in

$$\begin{bmatrix} \sigma_x \\ \sigma_z \\ \tau_{xz} \end{bmatrix} = \begin{bmatrix} c_{11} & c_{13} & 0 \\ c_{13} & c_{33} & 0 \\ 0 & 0 & c_{55} \end{bmatrix} \begin{bmatrix} \varepsilon_x \\ \varepsilon_z \\ \gamma_{xz} \end{bmatrix} - \begin{bmatrix} 0 & e_{31} \\ 0 & e_{33} \\ e_{15} & 0 \end{bmatrix} \begin{bmatrix} E_x \\ E_z \end{bmatrix} \quad (8)$$

The two-dimensional matrix form of electrostatic constitutive equation is

$$\begin{bmatrix} D_x \\ D_z \end{bmatrix} = \begin{bmatrix} 0 & 0 & e_{15} \\ e_{31} & e_{33} & 0 \end{bmatrix} \begin{bmatrix} \varepsilon_x \\ \varepsilon_z \\ \gamma_{xz} \end{bmatrix} + \begin{bmatrix} \xi_{11}^\varepsilon & 0 \\ 0 & \xi_{33}^\varepsilon \end{bmatrix} \begin{bmatrix} E_x \\ E_z \end{bmatrix} \quad (9)$$

The mechanical and electrostatic constitutive equations can be rewritten as

$$\begin{bmatrix} \varepsilon_x \\ \varepsilon_z \\ \gamma_{xz} \end{bmatrix} = \begin{bmatrix} s_{11} & s_{13} & 0 \\ s_{13} & s_{33} & 0 \\ 0 & 0 & s_{55} \end{bmatrix} \begin{bmatrix} \sigma_x \\ \sigma_z \\ \tau_{xz} \end{bmatrix} + \begin{bmatrix} 0 & d_{31} \\ 0 & d_{33} \\ d_{15} & 0 \end{bmatrix} \begin{bmatrix} E_x \\ E_z \end{bmatrix} \quad (10)$$

$$\begin{bmatrix} D_x \\ D_z \end{bmatrix} = \begin{bmatrix} 0 & 0 & d_{15} \\ d_{31} & d_{33} & 0 \end{bmatrix} \begin{bmatrix} \sigma_x \\ \sigma_z \\ \tau_{xz} \end{bmatrix} + \begin{bmatrix} \xi_{11}^\sigma & 0 \\ 0 & \xi_{33}^\sigma \end{bmatrix} \begin{bmatrix} E_x \\ E_z \end{bmatrix} \quad (11)$$

where d_{ij} is the piezoelectric constant, s_{ij} is the elastic compliance constant, and ξ_{ij}^σ is the dielectric constant. The superscript σ represents quantities measured at constant stress, respectively.

In $x-z$ plane, the governing mechanical equilibrium equation is

$$\sigma_{jj,j} = 0 \quad (12)$$

The electrostatic equilibrium equations is

$$D_{i,i} = 0 \quad (13)$$

Substituting Eqs. (1), (2), (4)-(6) and (7) into equilibrium Eqs. (12) and (13), the equilibrium equations can be rewritten in following forms

The governing mechanical equilibrium equations are

$$c_{11}u_{,xx} + c_{55}u_{,zz} + (c_{13} + c_{55})w_{,xz} + (e_{31} + e_{15})\varphi_{,xz} = 0 \quad (14)$$

$$(c_{13} + c_{55})u_{,xz} + c_{33}w_{,zz} + c_{55}w_{,xx} + e_{33}\varphi_{,zz} + e_{15}\varphi_{,xx} = 0 \quad (15)$$

The governing electrostatic equilibrium equation is

$$(e_{31} + e_{15})u_{,xz} + e_{15}w_{,xx} + e_{33}w_{,zz} - \xi_{11}^\varepsilon\varphi_{,xz} - \xi_{33}^\varepsilon\varphi_{,zz} = 0 \quad (16)$$

III. THE APPROXIMATE DISPLACEMENT FUNCTION CONSTRUCTED BY HERMIT-TYPE RRKPM

In the z -direction, the approximate displacement function $w^h(x, z)$ can be expressed as the linear combination of RBFs (Radial Basis Function, constructed by n nodes), normal derivative of RBFs (constructed by n_{DB} nodes on the boundary) and RKPMs (constructed by n_m nodes) in local influence domain.

$$w^h(x, z) = \sum_{i=1}^n R_i(x, z)a_i + \sum_{j=1}^{n_{DB}} \frac{\partial R_j^{DB}(x, z)}{\partial n} b_j + \sum_{k=1}^{n_m} R_k^m(x, z)c_k \quad (17)$$

where a_i , b_j and c_k are undetermined coefficients; n is the number of all nodes in the local influence domain; n_{DB} is the number of nodes on the boundary; n_m are RKPM items; R_i , R_j are RBFs constructed by nodes; R_k^m is RKPM constructed by nodes.

In Eq. (17), $R_i(x, z)$ expresses a class of functions whose values depend only on the distance between evaluation nodes (x, z) and the nodes (x_i, z_i) , $r_i = \sqrt{(x - x_i)^2 + (z - z_i)^2}$

$$R_i(x, z) = (1 - \frac{r_i}{\delta})^5 (8 + 40\frac{r_i}{\delta} + 48\frac{r_i^2}{\delta^2} + 25\frac{r_i^3}{\delta^3} + 5\frac{r_i^4}{\delta^4}) \quad (18)$$

In the normal derivative term of RBF,

$$r_j = \sqrt{(x - x_j)^2 + (z - z_j)^2}$$

$$R_j^{DB}(x, z) = (1 - \frac{r_j}{\delta})^8 (1 + 8 \frac{r_j}{\delta} + 25 \frac{r_j^2}{\delta^2} + 32 \frac{r_j^3}{\delta^3}) \quad (19)$$

$$\frac{\partial R_j^{DB}(x, z)}{\partial n} = l_{nj} \frac{\partial R_j^{DB}(x, z)}{\partial x} + l_{nj} \frac{\partial R_j^{DB}(x, z)}{\partial z} \quad (20)$$

where δ is shape parameter; $l_{nj} = \cos(n, x_j)$ and

$l_{nj} = \cos(n, z_j)$ is direction cosine

The derivative term of RKPM is

$$R_k^m(x, z) = c_k^m(x - x_i, z - z_i) w(r_k) R_k^m(x_i, z_i) \Delta V_i \quad (21)$$

where x_i, z_i are coordinates of node I, $R_k^m(x_i, z_i)$ is the unknown nodal parameter at node I, and ΔV_i is a measure of domain surrounding node I.

$$c_k^m(x - x_i, z - z_i) = \mathbf{b}_k^T(x, z) \mathbf{p}_k(x - x_i, z - z_i) \quad (22)$$

Coefficient matrix is

$$\mathbf{b}_k(x, z) = [b_1(x, z) \ b_2(x, z) \ \dots \ b_6(x, z)]^T \quad (23)$$

where $\mathbf{b}_k(x, z)$ can be obtained by the reproducing conditions of kernel approximation.

And a quadratic basis function in two-dimension is provided by

$$\begin{aligned} \mathbf{p}_k^T(x - x_i, z - z_i) \\ = [1, x - x_i, z - z_i, (x - x_i)^2, (x - x_i)(z - z_i), (z - z_i)^2] \end{aligned} \quad (24)$$

In Eq. (21), $r_k = d_k / d_{mk}$, $d_k = \sqrt{(x - x_k)^2 + (z - z_k)^2}$, d_{mk} is the radius of influence domain of RKPM at node (x_k, z_k)

$$w(r_k) = \begin{cases} 2/3 - 4r_k^2 + 4r_k^3 & r_k \leq 1/2 \\ 4/3 - 4r_k + 4r_k^2 - 4r_k^3/3 & 1/2 < r_k \leq 1 \\ 0 & r_k > 1 \end{cases} \quad (25)$$

Eq. (17) can be rewritten into the matrix form

$$w^h(x, z) = \mathbf{B}^T \mathbf{a}_0 \quad (26)$$

where the basis function vector \mathbf{B} is

$$\mathbf{B}^T = \left[R_1 \ \dots \ R_n \ \frac{\partial R_1^{DB}}{\partial n} \ \dots \ \frac{\partial R_{n_{DB}}^{DB}}{\partial n} \ R_1^k(x, z) \ \dots \ R_{n_m}^k(x, z) \right] \quad (27)$$

The coefficient vector \mathbf{a}_0 is

$$\mathbf{a}_0^T = \{a_1 \ a_2 \ \dots \ a_n \ b_1 \ b_2 \ \dots \ b_{n_{DB}} \ c_1 \ c_2 \ \dots \ c_{n_m}\} \quad (28)$$

In Eq. (17), coefficients a_i , b_j and c_k can be confirmed by n nodes values in the influence domain and n_{DB} nodes derivative values on the boundary.

$w(x_l, z_l)$ can be obtained by the n nodes in the influence domain.

$$w(x_l, z_l) = \sum_{i=1}^n R_i(x_l, z_l) a_i + \sum_{j=1}^{n_{DB}} \frac{\partial R_j^{DB}(x_l, z_l)}{\partial n} b_j + \sum_{k=1}^{n_m} R_k^m(x_l, z_l) c_k \quad (29)$$

where $l = 1, 2, \dots, n$.

$\frac{\partial w_l^{DB}}{\partial n}$ can be got by n_{DB} nodes on the boundary.

$$\begin{aligned} \frac{\partial w(x_l^{DB}, z_l^{DB})}{\partial n} = \\ \sum_{i=1}^n \frac{\partial R_i(x_l^{DB}, z_l^{DB})}{\partial n} a_i + \sum_{j=1}^{n_{DB}} \frac{\partial^2 R_j^{DB}(x_l^{DB}, z_l^{DB})}{\partial n^2} b_j + \sum_{k=1}^{n_m} \frac{\partial R_k^m(x_l^{DB}, z_l^{DB})}{\partial n} c_k \end{aligned} \quad (30)$$

where $l = 1, 2, \dots, n_{DB}$.

The following constraint is applied to get the unique solution

$$\sum_{i=1}^n R_k^m(x_i, z_i) a_i + \sum_{j=1}^{n_{DB}} R_k^m(x_j, z_j) b_j = 0 \quad (31)$$

where $k = 1, 2, \dots, n_m$.

Simultaneous Eqs. (29)-(31), the matrix equation can be expressed as

$$\mathbf{W}_s = \begin{Bmatrix} w(x_i, z_i) \\ \frac{\partial w(x_l^{DB}, z_l^{DB})}{\partial n} \\ 0 \end{Bmatrix} = \begin{Bmatrix} \mathbf{R}_0 & \mathbf{R}_{DB1} & \mathbf{R}_{m1} \\ \mathbf{R}_{DB2} & \mathbf{R}_c & \mathbf{R}_{DB} \\ \mathbf{R}_{m1}^T & \mathbf{R}_{m2}^T & 0 \end{Bmatrix} \begin{Bmatrix} a \\ b \\ c \end{Bmatrix} = \mathbf{G} \mathbf{a}_0 \quad (32)$$

where \mathbf{G} is generalized torque matrix, and it is constituted by torque matrix.

RKPM torque matrix can be structured by n nodes.

$$\mathbf{R}_{m1}^T = \begin{bmatrix} R_1^m(x_1, z_1) & R_1^m(x_2, z_2) & \dots & R_1^m(x_n, z_n) \\ R_2^m(x_1, z_1) & R_2^m(x_2, z_2) & \dots & R_2^m(x_n, z_n) \\ \vdots & \vdots & \ddots & \vdots \\ R_{n_m}^m(x_1, z_1) & R_{n_m}^m(x_2, z_2) & \dots & R_{n_m}^m(x_n, z_n) \end{bmatrix}_{(n_m \times n)} \quad (33)$$

$$\mathbf{R}_{n_2}^T = \begin{bmatrix} R_1^m(x_1, z_1) & R_1^m(x_2, z_1) & \dots & R_1^m(x_{n_{DB}}, z_{n_{DB}}) \\ R_2^m(x_1, z_1) & R_2^m(x_2, z_2) & \dots & R_2^m(x_{n_{DB}}, z_{n_{DB}}) \\ \vdots & \vdots & \vdots & \vdots \\ R_{n_m}^m(x_1, z_1) & R_{n_m}^m(x_2, z_2) & \dots & R_{n_m}^m(x_{n_{DB}}, z_{n_{DB}}) \end{bmatrix}_{(n_m \times n_{DB})} \quad (34)$$

The first-order derivative values of RKPM torque matrix

in n_{DB} nodes are

$$\mathbf{R}_{DB} = \begin{bmatrix} \frac{\partial R_1^m(x_1^{DB}, z_1^{DB})}{\partial n} & \frac{\partial R_2^m(x_1^{DB}, z_1^{DB})}{\partial n} & \dots & \frac{\partial R_{n_m}^m(x_1^{DB}, z_1^{DB})}{\partial n} \\ \frac{\partial R_1^m(x_2^{DB}, z_2^{DB})}{\partial n} & \frac{\partial R_2^m(x_2^{DB}, z_2^{DB})}{\partial n} & \dots & \frac{\partial R_{n_m}^m(x_2^{DB}, z_2^{DB})}{\partial n} \\ \vdots & \vdots & \ddots & \vdots \\ \frac{\partial R_1^m(x_{n_{DB}}^{DB}, z_{n_{DB}}^{DB})}{\partial n} & \frac{\partial R_2^m(x_{n_{DB}}^{DB}, z_{n_{DB}}^{DB})}{\partial n} & \dots & \frac{\partial R_{n_m}^m(x_{n_{DB}}^{DB}, z_{n_{DB}}^{DB})}{\partial n} \end{bmatrix}_{(n_{DB} \times n_{DB})} \quad (35)$$

The RBFs torque matrix of n nodes are

$$\mathbf{R}_0 = \begin{bmatrix} R_1(x_1, z_1) & R_2(x_1, z_1) & \dots & R_n(x_1, z_1) \\ R_1(x_2, z_2) & R_2(x_2, z_2) & \dots & R_n(x_2, z_2) \\ \dots & \dots & \dots & \dots \\ R_1(x_n, z_n) & R_2(x_n, z_n) & \dots & R_n(x_n, z_n) \end{bmatrix}_{(n \times n)} \quad (36)$$

The first-order RBFs derivative values of torque matrix in n_{DB} nodes are

$$\mathbf{R}_{DB1} = \begin{bmatrix} \frac{\partial R_1^{DB}(x_1, z_1)}{\partial n} & \frac{\partial R_2^{DB}(x_1, z_1)}{\partial n} & \dots & \frac{\partial R_{n_{DB}}^{DB}(x_1, z_1)}{\partial n} \\ \frac{\partial R_1^{DB}(x_2, z_2)}{\partial n} & \frac{\partial R_2^{DB}(x_2, z_2)}{\partial n} & \dots & \frac{\partial R_{n_{DB}}^{DB}(x_2, z_2)}{\partial n} \\ \dots & \dots & \dots & \dots \\ \frac{\partial R_1^{DB}(x_n, z_n)}{\partial n} & \frac{\partial R_2^{DB}(x_n, z_n)}{\partial n} & \dots & \frac{\partial R_{n_{DB}}^{DB}(x_n, z_n)}{\partial n} \end{bmatrix}_{(n \times n_{DB})} \quad (37)$$

$$\mathbf{R}_{DB2} = \begin{bmatrix} \frac{\partial R_1(x_1^{DB}, z_1^{DB})}{\partial n} & \frac{\partial R_2(x_1^{DB}, z_1^{DB})}{\partial n} & \dots & \frac{\partial R_n(x_1^{DB}, z_1^{DB})}{\partial n} \\ \frac{\partial R_1(x_2^{DB}, z_2^{DB})}{\partial n} & \frac{\partial R_2(x_2^{DB}, z_2^{DB})}{\partial n} & \dots & \frac{\partial R_n(x_2^{DB}, z_2^{DB})}{\partial n} \\ \dots & \dots & \dots & \dots \\ \frac{\partial R_1(x_{n_{DB}}^{DB}, z_{n_{DB}}^{DB})}{\partial n} & \frac{\partial R_2(x_{n_{DB}}^{DB}, z_{n_{DB}}^{DB})}{\partial n} & \dots & \frac{\partial R_n(x_{n_{DB}}^{DB}, z_{n_{DB}}^{DB})}{\partial n} \end{bmatrix}_{(n_{DB} \times n_{DB})} \quad (38)$$

The second-order RBFs derivative values of torque matrix in n_{DB} nodes are

$$\mathbf{R}_c = \begin{bmatrix} \frac{\partial}{\partial n} \left(\frac{\partial R_1^{DB}(x_1^{DB}, z_1^{DB})}{\partial n} \right) \frac{\partial}{\partial n} \left(\frac{\partial R_2^{DB}(x_1^{DB}, z_1^{DB})}{\partial n} \right) \dots \frac{\partial}{\partial n} \left(\frac{\partial R_{n_{DB}}^{DB}(x_1^{DB}, z_1^{DB})}{\partial n} \right) \\ \frac{\partial}{\partial n} \left(\frac{\partial R_1^{DB}(x_2^{DB}, z_2^{DB})}{\partial n} \right) \frac{\partial}{\partial n} \left(\frac{\partial R_2^{DB}(x_2^{DB}, z_2^{DB})}{\partial n} \right) \dots \frac{\partial}{\partial n} \left(\frac{\partial R_{n_{DB}}^{DB}(x_2^{DB}, z_2^{DB})}{\partial n} \right) \\ \dots & \dots & \dots \\ \frac{\partial}{\partial n} \left(\frac{\partial R_1^{DB}(x_{n_{DB}}^{DB}, z_{n_{DB}}^{DB})}{\partial n} \right) \frac{\partial}{\partial n} \left(\frac{\partial R_2^{DB}(x_{n_{DB}}^{DB}, z_{n_{DB}}^{DB})}{\partial n} \right) \dots \frac{\partial}{\partial n} \left(\frac{\partial R_{n_{DB}}^{DB}(x_{n_{DB}}^{DB}, z_{n_{DB}}^{DB})}{\partial n} \right) \end{bmatrix}_{(n_{DB} \times n_{DB})} \quad (39)$$

\mathbf{G} is inverse matrix, so \mathbf{a}_0 can be obtained by solving the Eq. (32)

$$\mathbf{a}_0 = \mathbf{G}^{-1} \mathbf{W}_s \quad (40)$$

Substituting Eq. (40) into Eq. (26), we can got

$$w^h(x, z) = \mathbf{B}^T \mathbf{a}_0 = \mathbf{B}^T \mathbf{G}^{-1} \mathbf{W}_s = \boldsymbol{\Phi}^T \mathbf{W}_s \quad (41)$$

$$\boldsymbol{\Phi}^T = \mathbf{B}^T \mathbf{G}^{-1} = [\phi_1 \ \phi_2 \ \dots \ \phi_n \ \phi_1^H \ \dots \ \phi_{n_{DB}}^H \ \phi_1^p \ \dots \ \phi_{n_m}^p]_{(n_{DB} + n_m) \times 1} \quad (42)$$

where $\boldsymbol{\Phi}$ is shape function vector.

Substituting Eq. (42) into Eq. (41), the approximate function can be got

$$w^h(x, z) = \sum_{i=1}^n \phi_i w_i + \sum_{j=1}^{n_{DB}} \phi_j^H \frac{\partial w_j^{DB}}{\partial n}$$

$$= [\phi_1 \ \phi_2 \ \dots \ \phi_n \ \phi_1^H \ \phi_2^H \ \dots \ \phi_{n_{DB}}^H] \begin{bmatrix} w_1 \\ w_2 \\ \vdots \\ w_n \\ \frac{\partial w_1^{DB}}{\partial n} \\ \frac{\partial w_2^{DB}}{\partial n} \\ \vdots \\ \frac{\partial w_{n_{DB}}^{DB}}{\partial n} \end{bmatrix} = \hat{\mathbf{N}} \hat{\mathbf{w}} \quad (43)$$

$$w^h(x, z)_x = \hat{\mathbf{N}}_x \hat{\mathbf{w}} \quad (44)$$

$$w^h(x, z)_z = \hat{\mathbf{N}}_z \hat{\mathbf{w}} \quad (45)$$

$$w^h(x, z)_{xx} = \hat{\mathbf{N}}_{xx} \hat{\mathbf{w}} \quad (46)$$

$$w^h(x, z)_{zz} = \hat{\mathbf{N}}_{zz} \hat{\mathbf{w}} \quad (47)$$

$$w^h(x, z)_{xz} = \hat{\mathbf{N}}_{xz} \hat{\mathbf{w}} \quad (48)$$

where $\mathbf{N}_{,x}$, $\mathbf{N}_{,z}$, $\mathbf{N}_{,xx}$, $\mathbf{N}_{,zz}$, $\mathbf{N}_{,xz}$ are the matrices containing the x , z , second x , second z , and x - z derivatives of the approximate function, respectively.

IV. DISCRETIZATION: GOVERNING EQUATIONS OF PIEZOELECTRIC MATERIAL

Once the approximation function is established, the next step is to discretize the partial differential equations. In this paper, the collocation method is used to discretize the governing equations. In the two-dimensional plane, piezoelectric material has three unknown values associated with every node in the domain, which are the displacement in the x -direction, the displacement in the z -direction and the electric potential. The collocation method forces the unknown values of each node to satisfy the governing equations or the corresponding boundary conditions.

The mechanical governing equations are discretized into

$$c_{11}\mathbf{N}_{,xx}\hat{\mathbf{u}} + c_{55}\mathbf{N}_{,zz}\hat{\mathbf{u}} + (c_{13} + c_{55})\mathbf{N}_{,xz}\hat{\mathbf{w}} + (e_{31} + e_{15})\mathbf{N}_{,xz}\hat{\varphi} = 0 \quad (49)$$

$$(c_{13} + c_{55})\mathbf{N}_{,xz}\hat{\mathbf{u}} + c_{33}\mathbf{N}_{,zz}\hat{\mathbf{w}} + c_{55}\mathbf{N}_{,xx}\hat{\mathbf{w}} + e_{33}\mathbf{N}_{,zz}\hat{\varphi} + e_{15}\mathbf{N}_{,xz}\hat{\varphi} = 0 \quad (50)$$

The electrostatic governing equation is discretized into

$$(e_{31} + e_{15})\mathbf{N}_{,xz}\hat{\mathbf{u}} + e_{15}\mathbf{N}_{,xx}\hat{\mathbf{w}} + e_{33}\mathbf{N}_{,zz}\hat{\mathbf{w}} - \xi_{11}^{\varepsilon}\mathbf{N}_{,xx}\hat{\varphi} - \xi_{33}^{\varepsilon}\mathbf{N}_{,zz}\hat{\varphi} = 0 \quad (51)$$

The unknown values of the nodes on the boundary are constructed to satisfy the corresponding boundary condition equations by the approximate function.

The mechanical boundary conditions for any node are given as

$$\sigma_x = 0 \Rightarrow c_{11}\mathbf{N}_{,x}\hat{\mathbf{u}} + c_{13}\mathbf{N}_{,z}\hat{\mathbf{w}} + e_{31}\mathbf{N}_{,z}\hat{\varphi} = 0 \quad (52)$$

$$\sigma_z = 0 \Rightarrow c_{13}\mathbf{N}_{,x}\hat{\mathbf{u}} + c_{33}\mathbf{N}_{,z}\hat{\mathbf{w}} + e_{33}\mathbf{N}_{,z}\hat{\varphi} = 0 \quad (53)$$

$$\tau_{xz} = 0 \Rightarrow c_{55}\mathbf{N}_{,z}\hat{\mathbf{u}} + c_{55}\mathbf{N}_{,x}\hat{\mathbf{w}} + e_{15}\mathbf{N}_{,x}\hat{\varphi} = 0 \quad (54)$$

$$u = 0 \Rightarrow \mathbf{N}\hat{\mathbf{u}} = 0 \quad (55)$$

$$w = 0 \Rightarrow \mathbf{N}\hat{\mathbf{w}} = 0 \quad (56)$$

Similarly, the electrostatic boundary conditions for nodes are

$$\varphi_{,x} = 0 \Rightarrow \mathbf{N}_{,x}\hat{\varphi} = 0 \quad (57)$$

$$\varphi = V \Rightarrow \mathbf{N}\hat{\varphi} = V \quad (58)$$

Finally, the governing equation can be expressed as the matrix form by the Hermit-type RRKPM

$$\begin{bmatrix} \mathbf{K}_{uu} & \mathbf{K}_{uw} & \mathbf{K}_{u\varphi} \\ \mathbf{K}_{wu} & \mathbf{K}_{ww} & \mathbf{K}_{w\varphi} \\ \mathbf{K}_{\varphi u} & \mathbf{K}_{\varphi w} & \mathbf{K}_{\varphi\varphi} \end{bmatrix} \begin{bmatrix} \hat{\mathbf{u}} \\ \hat{\mathbf{w}} \\ \hat{\varphi} \end{bmatrix} = \begin{bmatrix} \mathbf{F}_u \\ \mathbf{F}_w \\ \mathbf{F}_{\varphi} \end{bmatrix} \quad (59)$$

In the x -direction, the mechanical equilibrium equations are

$$\mathbf{K}_{uu} = c_{11}\mathbf{N}_{,xx} + c_{55}\mathbf{N}_{,zz} \quad (60)$$

$$\mathbf{K}_{uw} = (c_{13} + c_{55})\mathbf{N}_{,xz} \quad (61)$$

$$\mathbf{K}_{u\varphi} = (e_{31} + e_{15})\mathbf{N}_{,xz} \quad (62)$$

$$\mathbf{F}_u = 0 \quad (63)$$

In the z -direction, the mechanical equilibrium equations are

$$\mathbf{K}_{ww} = (c_{13} + c_{55})\mathbf{N}_{,xz} \quad (64)$$

$$\mathbf{K}_{ww} = c_{33}\mathbf{N}_{,zz} + c_{55}\mathbf{N}_{,xx} \quad (65)$$

$$\mathbf{K}_{w\varphi} = e_{33}\mathbf{N}_{,zz} + e_{15}\mathbf{N}_{,xx} \quad (66)$$

$$\mathbf{F}_w = 0 \quad (67)$$

The electrostatic equilibrium equations are

$$\mathbf{K}_{\varphi u} = (e_{33} + e_{15})\mathbf{N}_{,xz} \quad (68)$$

$$\mathbf{K}_{\varphi w} = e_{15}\mathbf{N}_{,xx} + e_{33}\mathbf{N}_{,zz} \quad (69)$$

$$\mathbf{K}_{\varphi\varphi} = -\xi_{11}^{\varepsilon}\mathbf{N}_{,xx} - \xi_{33}^{\varepsilon}\mathbf{N}_{,zz} \quad (70)$$

$$\mathbf{F}_{\varphi} = 0 \quad (71)$$

V. NUMERICAL EXAMPLES

Take an 1.0×1.0 mm ($L=1.0\text{mm}$, $2h=1.0\text{mm}$) piezoelectric strip as the example to analyze the bending deformation, polarized in the z -direction. The strip is subjected to a linear stress in the x -direction and an applied voltage in the z -direction (shown in Fig.1). The properties of the piezoelectric strip and other values are summarized in Tab.1.

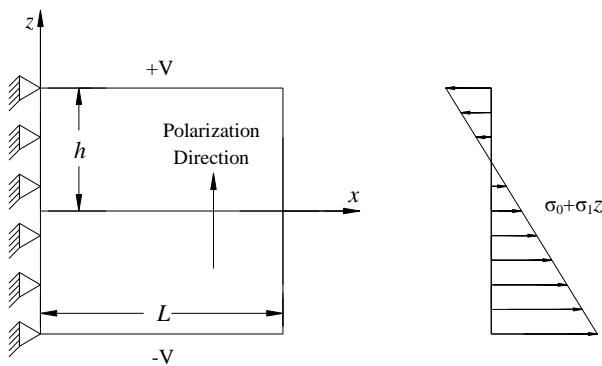


Fig.1 The piezoelectric strip subjected to a linear stress and the voltage

Tab.1 Material properties, dimensions, and other constants

s_{11}	$1.64 \times 10^{-5} \frac{(\text{mm})^2}{\text{N}}$	d_{31}	$-1.72 \times 10^{-7} \frac{\text{mm}}{\text{V}}$
s_{13}	$-7.22 \times 10^{-6} \frac{(\text{mm})^2}{\text{N}}$	d_{33}	$3.74 \times 10^{-7} \frac{\text{mm}}{\text{V}}$
σ_0	$10 \frac{\text{N}}{(\text{mm})^2}$	ξ_{33}^σ	$1.505 \times 10^{-7} \frac{\text{N}}{\text{V}^2}$
σ_1	$-50 \frac{\text{N}}{(\text{mm})^3}$	V	1500 V
L	1.0 mm	h	0.5 mm

The mechanical and electrostatic boundary conditions are

$$\phi(x, z = \pm h) = \pm V \quad \sigma_z(x, z = \pm h) = 0 \quad \tau_{xz}(x, z = \pm h) = 0$$

$$\phi_x(x = L, z) = 0 \quad \sigma_x(x = L, z) = \sigma_0 + \sigma_1 z \quad \tau_{xz}(x = L, z) = 0$$

$$\phi_x(x = 0, z) = 0 \quad u(x = 0, z) = 0 \quad w(x = 0, z = 0) = 0$$

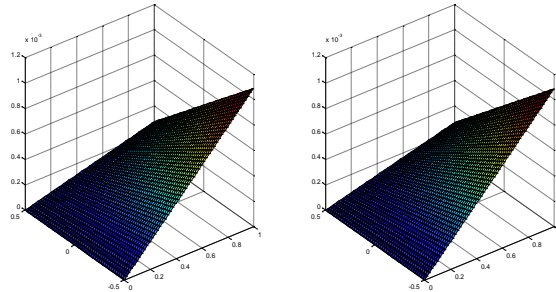


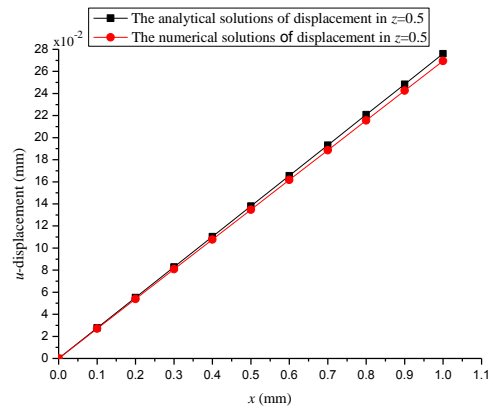
Fig.2 The comparison between the analytical solutions and numerical solutions

There are two factors to lead to the bending deformation of the piezoelectric strip: (a) The electric field is the same direction as polarization, causing the piezoelectric strip to extend along the x-direction and contract in the z-direction; (b) the piezoelectric strip bends upwards when a linear stress is

applied. The deformation of the piezoelectric strip is the result of the electric field, magnetic field and a linearly stress.

(1) In the x-direction, the analytical solutions of nodal displacements and the numerical solutions obtained by the proposed method are shown, in Fig.2.

The nodal displacements between the analytical solutions and the numerical solutions in $z=0.5$ are compared (shown in Fig.3).

Fig.3 The nodal displacements between the analytical solutions and the numerical solutions in $z=0.5$

In the x-direction, the relative errors of the nodal displacements of the piezoelectric strip in $z=0.5$ can be got (shown in Tab.2).

Tab.2 The relative errors of the nodal displacements

x-coordinate	z-coordinate	analytical solutions	numerical solutions	relative errors
0	0.5	0	0	0
0.1	0.5	2.760E-05	2.695E-05	2.355%
0.2	0.5	5.520E-05	5.390E-05	2.355%
0.3	0.5	8.280E-05	8.085E-05	2.355%
0.4	0.5	1.104E-04	1.078E-04	2.355%
0.5	0.5	1.380E-04	1.347E-04	2.355%
0.6	0.5	1.656E-04	1.617E-04	2.355%
0.7	0.5	1.932E-04	1.886E-04	2.355%
0.8	0.5	2.208E-04	2.156E-04	2.355%
0.9	0.5	2.484E-04	2.425E-04	2.355%
1	0.5	2.760E-04	2.695E-04	2.355%

In the x -direction, the numerical solutions of the piezoelectric strip displacements are very close to the analytical solutions. The maximum relative error is 2.355%, shown in Tab.2

(2) In the z -direction, the analytical solutions and numerical solutions of nodal displacement are shown in Fig.4.

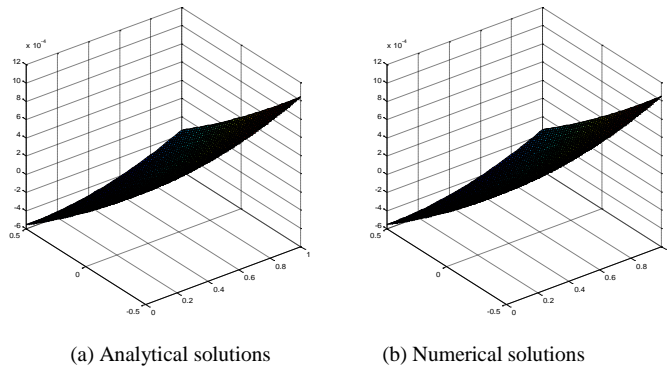


Fig.4 The comparison between analytical solutions and numerical solutions

Fig.5 shows the nodal displacements of the analytical solution and the numerical solution in $z=0.5$.

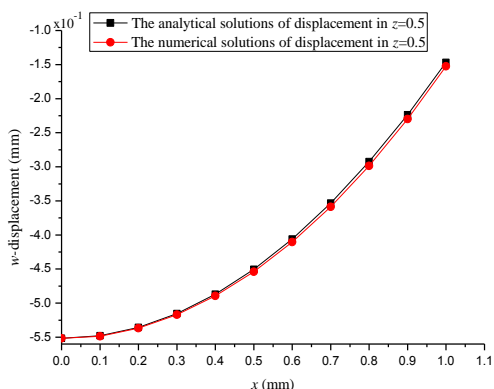


Fig.5 The nodal displacements of the analytical solution and numerical solution in $z=0.5$

Tab.3 shows the relative errors of the nodal displacement calculated by the proposed method and the analytical method in $z=0.5$.

Tab.3 The relative errors of the nodal displacement

x -coordinate	z -coordinate	analytical solutions	numerical solutions	relative errors
0	0.5	-5.518E-04	-5.518E-04	0

0.1	0.5	-5.477E-04	-5.485E-04	-0.15%
0.2	0.5	-5.356E-04	-5.368E-04	-0.23%
0.3	0.5	-5.153E-04	-5.171E-04	-0.35%
0.4	0.5	-4.870E-04	-4.895E-04	-0.52%
0.5	0.5	-4.505E-04	-4.540E-04	-0.78%
0.6	0.5	-4.060E-04	-4.104E-04	-1.10%
0.7	0.5	-3.533E-04	-3.587E-04	-1.53%
0.8	0.5	-2.926E-04	-2.985E-04	-2.03%
0.9	0.5	-2.237E-04	-2.319E-04	-3.67%
1	0.5	-1.468E-04	-1.535E-04	-4.60%

From Tab.3, it can be found that the maximum relative error is -4.43% in $z=0.5$, and the numerical solution of the displacement of the piezoelectric strip is very close to the analytical solution.

(3) The analytical solutions and numerical solutions of nodal potential are shown in Fig.6.

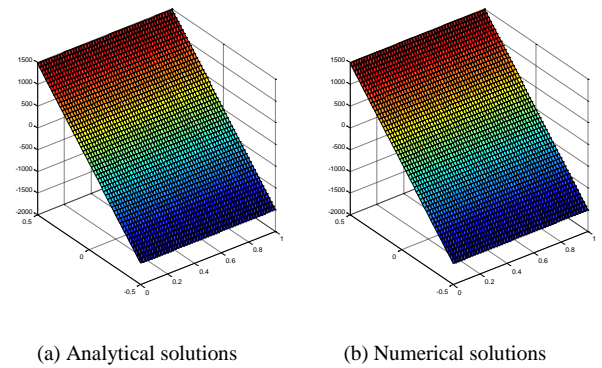


Fig.6 The comparison between analytical solutions and numerical solutions

The nodal potential between the analytical solutions and the numerical solutions in $z=0$ are compared (shown in Fig.7).

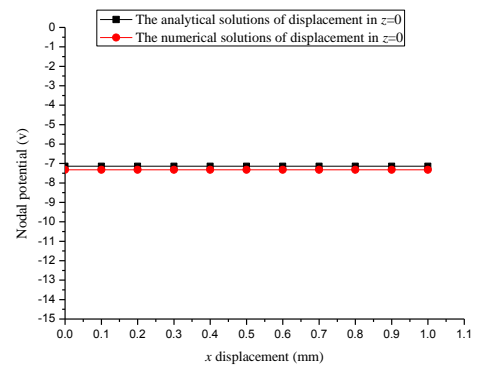


Fig.7 The nodal potential between the analytical solutions and the numerical solutions in $z=0$

Tab.4 shows the relative errors of the nodal potential calculated by the proposed method and the analytical method in $z=0$.

Tab.4 The relative errors of the nodal potential

x -coordinate	z -coordinate	analytical solutions	numerical solutions	relative errors
0	0	-7.14	-7.32	-2.52%
0.1	0	-7.14	-7.32	-2.52%
0.2	0	-7.14	-7.32	-2.52%
0.3	0	-7.14	-7.32	-2.52%
0.4	0	-7.14	-7.32	-2.52%
0.5	0	-7.14	-7.32	-2.52%
0.6	0	-7.14	-7.32	-2.52%
0.7	0	-7.14	-7.32	-2.52%
0.8	0	-7.14	-7.32	-2.52%
0.9	0	-7.14	-7.32	-2.52%
1	0	-7.14	-7.32	-2.52%

From Tab.4, it can be found that the maximum relative error is -2.52% in $z=0$, and the numerical solution of the potential for the piezoelectric strip is very close to the analytical solution.

VI. CONCLUSIONS

In this paper, the Hermit-type RRKPM is proposed to solve the electromechanical coupling partial differential equations of piezoelectric materials. The results obtained by the two methods are very close. So the Hermit-type RRKPM can accurately and effectively solve the electromechanical coupling partial differential equations of piezoelectric materials.

ACKNOWLEDGMENT

This work was supported by the National Natural Science Foundation of China [grant numbers 11271234].

REFERENCES

- [1] Y.T. He, J.H. Liu, L. Li and J.H. He, "A novel capacitive pressure sensor and interface circuitry," *Microsyst. Technol.*, vol. 19, pp. 25-30, 2013.
- [2] T. Kawada, H. Suzuki, T. Shimizu and M. Katsumata, "Agreement in regard to total sleep time during a nap obtained via a sleep polygraph and

accelerometer: A Comparison of Different Sensitivity Thresholds of the Accelerometer," *Int. J. Behav. Med.*, vol. 19, pp. 398-401, 2012.

- [3] R.R. Paccola, M.S.M. Sampaio and H.B. Coda, "Continuous stress distribution following transverse direction for FEM orthotropic laminated plates and shells," *Appl. Math. Model.*, vol. 40, pp. 7382-7409, 2016.
- [4] X. Zhang, M.W. Lu and J.L. Wegner, "A 2-D meshless model for jointed rock structures," *Int. J. Num. Meth. Engng.*, vol. 47, pp. 1649-1661, 2000.
- [5] L. Chen, Y.M. Cheng and H.P. Ma, "The complex variable reproducing kernel particle method for the analysis of Kirchhoff plates," *Comput. Mech.*, vol. 55, pp. 591-602, 2015.
- [6] Y. Strozecki, "On enumerating monomials and other combinatorial structures by polynomial interpolation," *Theory. Comput. Syst.*, vol. 53, pp. 532-568, 2013.
- [7] I. Mantegh, M.R.M. Jenkin and A.A. Goldenberg, "Path planning for autonomous mobile robots using the boundary integral equation method," *J. Intell. Robot. Syst.*, vol. 59, pp. 191-220, 2010.
- [8] Y.J. Deng, C. Liu, M.J. Peng and Y.M. Cheng, "The interpolating complex variable element-free Galerkin method for temperature field problems," *International Journal of Applied Mechanics*, vol. 7, pp. 1550017, 2015.
- [9] X.L. Li and S.G. Zhang, "Meshless analysis and applications of a symmetric improved Galerkin boundary node method using the improved moving least-square approximation," *Appl. Math. Model.*, vol. 40, pp. 2875-2896, 2016.
- [10] M.B. Liu and G.R. Liu, "Smoothed particle hydrodynamics (SPH): An overview and recent developments arch," *Comput. Meth. Eng.*, vol. 17, pp. 25-76, 2010.
- [11] A. Žilinskas, "On similarities between two models of global optimization: statistical models and radial basis functions," *J. Glob. Optim.*, vol. 48, pp. 173-182, 2010.
- [12] O. Christensen and P. Massopust, "Exponential B-splines and the partition of unity property," *Adv. Comput. Math.*, vol. 37, pp. 301-318, 2012.
- [13] D. Mirzaei and R. Schaback, "Solving heat conduction problems by the Direct Meshless Local Petrov-Galerkin (DMLPG) method," *Numer. Algor.*, vol. 65, pp. 275-291, 2014.
- [14] M. Tatari, M. Kamranian and M. Dehghan, "The finite point method for the p-Laplace equation," *Comput. Mech.*, vol. 48, pp. 689-697, 2011.
- [15] J.C. Ma, G.F. Wei, D.D. Liu and G.T. Liu, "The numerical analysis of piezoelectric ceramics based on the Hermite-type RPIM," *Applied Mathematics and Computation*, vol. 309, pp. 170-182, 2017.
- [16] H.F. Gao and G.F. Wei, "Complex Variable Meshless Manifold Method for Elastic Dynamic Problems," *Mathematical Problems in Engineering*, pp. 5803457, 2016.

A Physics Evoked Meshfree Method

MA Zhi-bo

Institute of Applied Physics and Computational
Mathematics
Beijing, China
mazhibo@iapcm.ac.cn

Abstract—In mesh free methods, discrete equations are built according to physics information of micro-bodies arbitrarily spread in vicinal space. As the requirements about topology of micro-bodies are reduced, simulations with Lagrangian approach may be easier even with large distortions. Owing to the insufficiency of topological information, there is a challenge for mesh-free method to reflect physics especially as discontinuities exist. Based on the physical laws and developing trend of numerical simulation, a new mesh free systematic method PECM (Physics Evoked Cloud Method) with excellent applicability has been developed. High fidelity to physics of the method is demonstrated through five 1-dimentional challenging problems in which strong discontinuities exist.

I. INTRODUCTION

The ability of numerical computation and its accuracy are the determinants of practicality for modeling and simulations [1-3]. One of the key technique for simulation is to solve nonlinear differential equations by numerical methods. For discontinuous problems such as shock wave, derivatives may not exist, the numerical method is usually constructed according to the ideas put forwarded by Von Neumann or Godunov. Neumann method captures physical discontinuity by adding artificial viscosity terms [4], whereas Godunov method does that by Riemann solutions [5]. In this paper, we call the artificial terms as modularizing factors in simulations as they represent the microscopic phenomena through physical quantities corresponding to macroscopic discrete volumes and time steps.

Since 1977, the meshfree method SPH (Smoothed Particle Hydrodynamics) based on Neumann idea has won a very wide attention and has undergone 40 years development [6-7], but there are two shortcomings: one is the instability or non-physical solutions in dynamic computations, and the other is the accuracy decays near free boundary owing to the information imperfectionness in support domains [8-13]. In 1995, Swegle gave out a stability condition of SPH via Fourier analysis [14]. Liu proposed RKPM (Reproducing Kernel Particle Method) method in 1995, in which the kernel function was corrected [15-16]. After that, Chen proposed CSPM (Corrective Smoothed Particle Method) method in 1999 [17], and Zhang proposed MSPH (Modified Smoothed Particle Hydrodynamics) method in 2004 [18].

According to Taylor's idea, all functions can be approximated as algebraic sums of several polynomial basic functions. The basic functions and their derivatives are known, so they can be used to construct the correct functions. All the above methods used this mechanism to improve the accuracy

ZHAO Ya-zhou

Institute of Geology and Geophysics
Chinese Academy of Science
Beijing, China
asiabuaasa@163.com

of kernel estimation. However, these improvements originated only from mathematical aspect, the potential requirements of physical laws to the numerical algorithms are not fully reflected. For engineering problems such as detonation and impact in which discontinuities exist, the improvement is not remarkable, and it is still difficult to avoid the numerical oscillation and non-physical solutions.

In this paper, the shortcomings of SPH are explored in view of the incompatibility of numerical schemes to physics. Based on the demands in application and the elicitations from physical analysis, the idea of PECM (Physics Evoked Cloud Method) is proposed, from which the SPH method is modified. Finally, the simulation abilities and effects of the new method is shown with five challenging examples.

II. FLOW GOVERNING EQUATIONS

This paper performs analysis of the algorithm from the simple fluid problem. For fluid without external force, heat source and physical viscosity, the Lagrangian form of governing equations are:

$$\text{Mass} \quad \frac{d\rho}{dt} = -\rho \nabla \cdot \mathbf{v} \quad (1)$$

$$\text{Momentum} \quad \frac{d\mathbf{v}}{dt} = -\frac{1}{\rho} \nabla p \quad (2)$$

$$\text{Energy} \quad \frac{de}{dt} = -\frac{p}{\rho} \nabla \cdot \mathbf{v} \quad (3)$$

III. SPH METHOD

3.1 Kernel estimation

SPH method performs approximation by kernel function. For a compact kernel function with a smooth length of h and its support domain Ω , the kernel estimation of any function

$f(r)$ is defined as:

$$\langle \mathbf{f}(\mathbf{r}) \rangle = \int_{\Omega} \mathbf{f}(\mathbf{r}') W^{(\text{SPH})}(\mathbf{r} - \mathbf{r}', h) d\mathbf{r}' \quad (4)$$

With integration by part and Gaussian formula, the calculations of derivatives can be shifted to the kernel function, such as:

$$\langle \nabla \mathbf{f}(\mathbf{r}) \rangle = \int_{\Omega} \mathbf{f}(\mathbf{r}') \nabla_r W^{(\text{SPH})}(\mathbf{r} - \mathbf{r}', h) d\mathbf{r}' \quad (5)$$

$$\langle \nabla \cdot \mathbf{f}(\mathbf{r}) \rangle = \int_{\Omega} \mathbf{f}(\mathbf{r}') \cdot \nabla_r W^{(\text{SPH})}(\mathbf{r} - \mathbf{r}', h) d\mathbf{r}' \quad (6)$$

Where the subscript in the operator ∇_r represents the derivation with coordinates \mathbf{r} .

3.2 Modularizing factor

From [13,19], the viscosity terms in SPH are:

$$\Pi_{ij}^{(SPH)} = \begin{cases} \left(-\alpha c_{ij} \mu_{ij} + \beta \mu_{ij}^2 \right) / \rho_{ij} & (\mathbf{v}_i - \mathbf{v}_j) \cdot (\mathbf{r}_i - \mathbf{r}_j) < 0 \\ 0 & (\mathbf{v}_i - \mathbf{v}_j) \cdot (\mathbf{r}_i - \mathbf{r}_j) \geq 0 \end{cases} \quad (7)$$

where $\mu_{ij} = h_{ij}(\mathbf{v}_i - \mathbf{v}_j) \cdot (\mathbf{r}_i - \mathbf{r}_j) / [(\mathbf{r}_i - \mathbf{r}_j) \cdot (\mathbf{r}_i - \mathbf{r}_j) + \varepsilon h_{ij}^2]$.

The averages of velocity, density and smooth length of two particles are:

$$c_{ij} = (c_i + c_j) / 2, \rho_{ij} = (\rho_i + \rho_j) / 2, h_{ij} = (h_i + h_j) / 2$$

From [20], Noh's artificial heat flux terms in the SPH energy equation is:

$$H_{ij}^{(SPH)} = \sum_j 2\zeta_{ij}(e_i - e_j) / [(\mathbf{r}_i - \mathbf{r}_j) \cdot (\mathbf{r}_i - \mathbf{r}_j) + \eta h_{ij}^2] / \rho_{ij} \quad (8)$$

Where $\zeta_{ij} = (\zeta_i + \zeta_j) / 2, \zeta = g_1 hc + g_2 h^2 (\nabla \cdot \mathbf{v} - \nabla \cdot \mathbf{v})$.

3.3 Discrete equations

In order to illustrate problems, we select following discrete equations:

Mass:

$$\frac{d\rho_i}{dt} = \sum_{j=1}^N m_j (\mathbf{v}_i - \mathbf{v}_j) \cdot \nabla_i W_{ij}^{(SPH)} \quad (9)$$

Momentum:

$$\frac{d\mathbf{v}_i}{dt} = -\sum_{j=1}^N m_j \left(\frac{p_i}{\rho_i^2} + \frac{p_j}{\rho_j^2} + \Pi_{ij}^{(SPH)} \right) \nabla_i W_{ij}^{(SPH)} \quad (10)$$

Energy:

$$\frac{de_i}{dt} = \frac{1}{2} \sum_{j=1}^N m_j \left[\left(\frac{p_i}{\rho_i^2} + \frac{p_j}{\rho_j^2} + \Pi_{ij}^{(SPH)} \right) (\mathbf{v}_i - \mathbf{v}_j) + H_{ij}^{(SPH)} (\mathbf{r}_i - \mathbf{r}_j) \right] \cdot \nabla_i W_{ij}^{(SPH)} \quad (11)$$

where

$$W_{ij}^{(SPH)} = W^{(SPH)}(\mathbf{r}_i - \mathbf{r}_j, h_i)$$

The subscript of the operator ∇_i indicates the derivative calculation to the coordinates \mathbf{r}_i of the particle i . N represents the number of particles in the support domain Ω_i . In order to satisfy the compatibility condition for the kernel estimation, this paper generally uses h_i other than h_{ij} as the smooth length.

IV. RKPM METHOD

RKPM corrects the SPH kernel function by correcting function, then substitutes the corrected kernel function and its derivative into the discrete equation. The other steps are the same as the SPH.

The RKPM kernel function is:

$$W^{(RKPM)}(\mathbf{r} - \mathbf{r}', h) = C^{(RKPM)}(\mathbf{r} - \mathbf{r}', h) W^{(SPH)}(\mathbf{r} - \mathbf{r}', h) \quad (12)$$

For n -order correct function, the RKPM kernel function should meet the consistency condition as:

$$\int_{\Omega} W^{(RKPM)}(\mathbf{r} - \mathbf{r}', h) d\mathbf{r}' = 1 \quad (13)$$

$$\int_{\Omega} W^{(RKPM)}(\mathbf{r} - \mathbf{r}', h) (\mathbf{r} - \mathbf{r}')^m d\mathbf{r}' = 0, m = 1, 2, \dots n. \quad (14)$$

The discrete form of (13) and (14) are:

$$\sum_{j=1}^N b_j C_{ij}^{(RKPM)} W_{ij}^{(SPH)} = 1 \quad (15)$$

$$\sum_{j=1}^N b_j C_{ij}^{(RKPM)} W_{ij}^{(SPH)} \mathbf{r}_{ij}^m = 0, m = 1, 2, \dots n. \quad (16)$$

where

$$b_j = m_j / \rho_j, C_{ij}^{(RKPM)} = C^{(RKPM)}(\mathbf{r}_i - \mathbf{r}_j, h_i), \mathbf{r}_{ij} = \mathbf{r}_i - \mathbf{r}_j.$$

V. PROBLEM ANALYSIS

5.1 Problem Types

By correcting the kernel function and its derivatives, RKPM, CSPM and MSPH improved the accuracy only to a limited degree, as they improve the utilization of information of neighbouring particles based on mathematics rather than on physics. For the physical problems with extreme conditions, all the methods are difficult to obtain credible results.

The defects may affect the numerical results of all discrete bodies, but they are most likely exposed in the areas where discontinuities exist. If the algorithm performs well with discontinuity, the results in smooth regions should be better undoubtedly, so we can observe the problems via discontinuous models.

SPH has three types of problems in the discontinuous region which may lead to various non-physical solutions: 1) Instability of dynamic computations; 2) Notable wall heating effects; 3) Dissipation of physical variables.

5.2 Instability

SPH exhibits its instability mainly as non-physical aggregation or repulsion. Fig. 1 shows a detonator placed between explosive and heavy metal. After detonation, the shock wave in explosive will drive the metal, the two materials should keep in touch and move right together. However, the numerical results based on equation (9)-(11) lead to interface separation, as shown in Fig. 2.

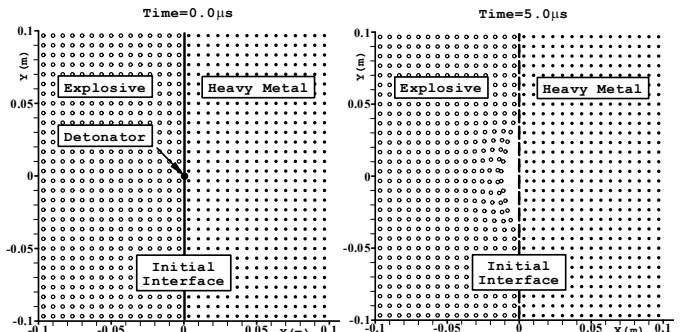


Fig. 1 Initial state of detonation model

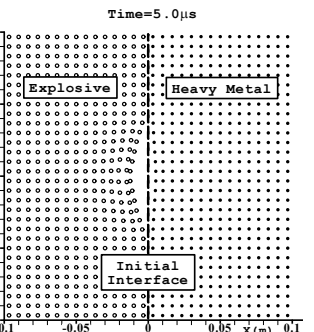


Fig. 2 Interface splitting after detonation

It is found that the instability mainly comes from the discretization of the momentum equation. In Fig. 3, we take two boundary particles "1" and "2" from explosive and metal respectively. The initial states of the left are of high pressure, low density and the right are of low pressure, high density. Given that the two particles have the same smooth length, they may approximately share the same support domain. For the right hand of equation (10), if removing the shared information

provided by neighbouring particles in the support domain, we can get their residual forms of equation (10) as:

$$\frac{d\mathbf{v}_1}{dt} = -\frac{p_1}{\rho_1^2} \sum_{j=1}^N m_j \nabla_1 W_{1j}^{(\text{SPH})} \quad (17)$$

$$\frac{d\mathbf{v}_2}{dt} = -\frac{p_2}{\rho_2^2} \sum_{j=1}^N m_j \nabla_2 W_{2j}^{(\text{SPH})} \quad (18)$$

$\nabla_1 W_{1j}^{(\text{SPH})}$ is equal to $\nabla_2 W_{2j}^{(\text{SPH})}$ and they are anti-symmetric in the respective support domain, m_j is a shared information. Since the density of the two sides are different, m_j is not symmetrical, so the sums in the right of (17) and (18) are equal but are not zero. Note that $p_1/\rho_1^2 \gg p_2/\rho_2^2$, it can be easily explained that the explosive particles move left and lead to interface separation.

We think the problem is caused by imposing an inappropriate kernel function on equation (2). In kernel estimation, SPH allocates the weights according to volumes and spatial positions of adjacent particles, this is suitable to the mass and energy equations, but not suitable to the momentum equation. In the expression of Newton's second law $\mathbf{a} = \mathbf{f}/m$, mass is as the denominator of the fraction. Therefore, the weights should be allocated according to particle mass rather than the volume. This principle can be actualized by reconstructing the kernel function of momentum equation, in which the particle's volume and density are both included.

In order to show the role of mass in the approximation, we design a 1-dimensional model in Fig. 4. If the two micro-bodies are regarded as a system Θ , then the theoretical acceleration of Θ is:

$$a_x^* = \frac{(p_1 - p_3)}{s(\rho_1 + \rho_2)} \quad (19)$$

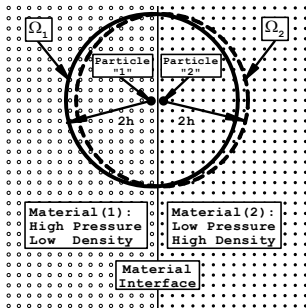


Fig. 3 Support domains of particles near interfaces

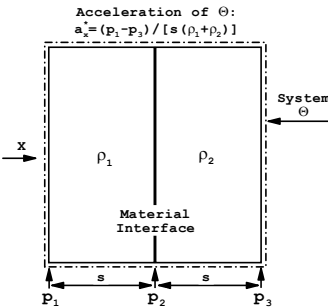


Fig. 4 Conjugent acceleration of adjacent particles

Firstly, we take mass as the weighting factor, then the estimate is equal to the theoretical value as

$$a_x^{\text{mass}} = \frac{s\rho_1}{s(\rho_1 + \rho_2)} \frac{(p_1 - p_2)}{s\rho_1} + \frac{s\rho_2}{s(\rho_1 + \rho_2)} \frac{(p_2 - p_3)}{s\rho_2} = a_x^* \quad (20)$$

If volume is taken as the weighting factor, the estimate may not equal to the theoretical value, such as

$$a_x^{\text{volume}} = \frac{s}{s+s} \frac{(p_1 - p_2)}{s\rho_1} + \frac{s}{s+s} \frac{(p_2 - p_3)}{s\rho_2} = \frac{(p_1 - p_2)}{2s\rho_1} + \frac{(p_2 - p_3)}{2s\rho_2} \neq a_x^* \quad (21)$$

It is easy to understand that when the pressure and density vary continuously and the discrete scale tends to zero, a_x^{volume} converges to a_x^* .

The computational error can also be regarded as the discontinuity information that may be propagated to the next time step. The kernel estimation which is purely based on spatial information may lead to larger errors and non-physical solution of equation (10).

5.3 Wall heating

The generation of wall heating effect is related to artificial viscosity. As the artificial viscosity is based on the macroscopic quantities, and the simulation process cannot capture the dynamic equilibrium process at infinitesimal scales of time and space, then, in the first few time steps, the overestimation of the relative velocity will result in a larger viscous pressure and lead to wall heating.

Without the use of artificial heat flux, excess energy generated by wall heating will stay in the micro-bodies in the vicinity of the discontinuity. Although the artificial heat flux can disperse part of the internal energy to other micro-bodies and reduce the oscillation, but the total energy has not fundamentally changed, the excess energy still remains in the material, it is better to suppress the generation of wall heating through numerical algorithms.

It is easy to understand that a new kinetic equilibrium would immediately establish in a very thin space where discontinuities exist, in which the pressure, acceleration and velocity are continuous at the microscopic level. Since the velocity is the integral of the acceleration, and the acceleration is determined by the spatial distribution of the pressure, we can try to construct a modularizing factor to restrain the wall heating effect by rectifying the overestimation of the relative velocity, in which the differences of pressure between micro-bodies are used to modify the relative velocities of the micro-bodies, as depicted in the following text.

5.4 Dissipation

In the discrete equations of SPH, physical laws and engineering requirements have not been sufficiently reflected. Discrete equations (9) and (11) will lead to dissipation of density and internal energy respectively.

When different materials contact with each other, the discontinuities of density and internal energy are realities both in macroscopic or microscopic scales. Dissipations will make the numerical results failed to present these realities, from which the density and energy may be blurred near the material interfaces. In order to faithfully show such discontinuities, it is necessary to identify the physical quantities that should or should not be subjected to kernel approximations for the mass and energy equations.

VI. PECM METHOD

6.1 Main ideas

Due to the complexity and diversity of the engineering systems, a numerical method is often expected to be widely applicable to the coexistence problems of multi-materials and multi-physics. The complexity of engineering problems lies in the coexistence and coupling of multiple behavior patterns and multiple physical phenomena from different materials. In order to analyse the relationship between physical properties and computational methods, we can classify the matters into real and virtual types.

Real matters usually present significant macroscopic densities and consistent behaviours with micro-bodies as they generally have high degree of aggregations in space and exist in thermodynamic equilibrium states, so they usually play leading roles in physical processes. The future behaviors of some real matters may depend on their past experiences. Most of the engineering materials can be regarded as real matter, which exist in the forms of solid, liquid, gas or particles, droplets etc.

Virtual matters usually have lower macroscopic densities and inconsistent behaviours with micro-bodies as they generally have low degree of aggregations in space and exist in thermodynamic nonequilibrium states, so they are usually dominated by real matters in physical processes. The future behaviors of virtual matters do not have relationships with their past experiences. Electromagnetic fields, gravitational fields, and x-rays, α -rays, γ -rays, neutrons, electrons can be regarded as virtual matters.

As the existence and movement of the real matters may also be a problem to be solved, and the evolutions may be affected by their historical experiences, Lagrangian methods would be more propitious to complex problems. Considering that the methods with meshes will meet with austere challenges for large deformation computations, the Lagrangian meshfree methods should generally be the best approach for real matters.

According to the above analysis, this paper proposes a meshfree method called PECM (Physics Evoked Cloud Method), where “cloud” means the discrete mass group, which may be a micro-body in a continuum, or a micro-cluster made of solid particles or liquid droplets. PECM is a kind of algorithm system composed of meshless algorithm classes which are guided by physical laws. There are no specific limits for its technical details such as approximations, modularizing factors and discrete forms of governing equations, but it should observe the following ideas: 1) Lagrangian meshfree methods are applied for real matters; 2) The commonnesses and individualities of the algorithms are loaded on the inheritances and derivations of the material classes respectively; 3) There is a platform without man made slide curves to exchange physical information; 4) Trustily represents the continuities or discontinuities in reality; 5) Can express the mass transfer owing to the sub-scale diffusion between the micro-bodies; 6) Correctly reflects the objective physical laws.

In the following sections, we show the kernel functions, modularizing factors and discrete equations of PECM with computations of fluid dynamics.

6.2 Kernel functions

In this paper, we correct the SPH kernel function of the momentum equation guided by PECM ideas, the RKPM kernel function is followed in mass and energy equations.

Let $b_j = m_j / \rho_j$ represent the volumes of the clouds in the support domain, PECM gives the kernel estimation for momentum equation as:

$$\left\langle -\frac{1}{\rho} \nabla p \right\rangle_i = \int_{\Omega} \left(-\frac{1}{\rho} \nabla_{r'} p \right) \rho W^{(\text{PECM})}(\mathbf{r}_i - \mathbf{r}', h_i) d\mathbf{r}' = - \sum_{j=1}^N b_j p_j \nabla_i W_{ij}^{(\text{PECM})} \quad (22)$$

where the kernel function of PECM is:

$$W^{(\text{PECM})}(\mathbf{r} - \mathbf{r}', h) = C^{(\text{PECM})}(\mathbf{r} - \mathbf{r}', h) W^{(\text{SPH})}(\mathbf{r} - \mathbf{r}', h) \quad (23)$$

For the n -order correction $C^{(\text{PECM})}(\mathbf{r} - \mathbf{r}', h)$, the PECM kernel function should satisfy the consistency condition as:

$$\int_{\Omega} \rho(\mathbf{r}') W^{(\text{PECM})}(\mathbf{r} - \mathbf{r}', h) d\mathbf{r}' = 1 \quad (24)$$

$$\int_{\Omega} \rho(\mathbf{r}') W^{(\text{PECM})}(\mathbf{r} - \mathbf{r}', h) (\mathbf{r} - \mathbf{r}')^m d\mathbf{r}' = 0, m = 1, 2, \dots, n. \quad (25)$$

The discrete form of the correction function should be solved by:

$$\sum_{j=1}^N b_j \rho_j C_{ij}^{(\text{PECM})} W_{ij}^{(\text{SPH})} = 1 \quad (26)$$

$$\sum_{j=1}^N b_j \rho_j C_{ij}^{(\text{PECM})} W_{ij}^{(\text{SPH})} r_{ij}^m = 0, m = 1, 2, \dots, n. \quad (27)$$

6.3 Modularizing factors

The pressure factor is:

$$\Pi_{ij}^{(\text{PECM})} = \begin{cases} (-\alpha c_{ij} \mu_{ij} + \beta \mu_{ij}^2) \rho_{ij} & (\mathbf{v}_i - \mathbf{v}_j) \cdot (\mathbf{r}_i - \mathbf{r}_j) < 0 \\ 0 & (\mathbf{v}_i - \mathbf{v}_j) \cdot (\mathbf{r}_i - \mathbf{r}_j) \geq 0 \end{cases} \quad (28)$$

The heat flux factor is:

$$\mathbf{H}_{ij}^{(\text{PECM})} = 2\zeta_{ij} \rho_{ij} (\mathbf{e}_i - \mathbf{e}_j) (\mathbf{r}_i - \mathbf{r}_j) / [(\mathbf{r}_i - \mathbf{r}_j) \cdot (\mathbf{r}_i - \mathbf{r}_j) + \eta h_{ij}^2] \quad (29)$$

The velocity factor is:

$$\Phi_{ij}^{(\text{PECM})} = \delta h_{ij} (\mathbf{r}_i - \mathbf{r}_j) (\rho_i - \rho_j) / [(\mathbf{r}_i - \mathbf{r}_j) \cdot (\mathbf{r}_i - \mathbf{r}_j) + \theta h_{ij}^2] / \bar{c}_{ij} / \bar{\rho}_{ij} \quad (30)$$

In the above three formulas, $\alpha, \beta, \mu_{ij}, \zeta_{ij}, c_{ij}, \rho_{ij}, h_{ij}$ have the same definitions that in SPH, δ, θ are used in the velocity modularizing factor introduced by PECM.

The velocity factor $\Phi_{ij}^{(\text{PECM})}$ can suppress the wall heating significantly and consequently reduces the dependence of heat flux modularizing factor in numerical computations.

6.4 Discrete equations

In order to faithfully present the physical discontinuities of density and energy, the kernel estimation should not be exerted on density in mass and energy equations, from which we have PECM discrete equations as (31) – (33).

Mass equation:

$$\frac{d\rho_i}{dt} = \rho_i \sum_{j=1}^N b_j (\mathbf{v}_i - \mathbf{v}_j + \Phi_{ij}^{(\text{PECM})}) \cdot \nabla_i W_{ij}^{(\text{RKPM})} \quad (31)$$

Momentum equation:

$$\frac{d\mathbf{v}_i}{dt} = -\sum_{j=1}^N b_j \left(p_j + \Pi_{ij}^{(\text{PECM})} \right) \nabla_i W_j^{(\text{PECM})} \quad (32)$$

Energy equation:

$$\frac{de_i}{dt} = \frac{1}{\rho_i} \sum_{j=1}^N b_j \left[\left(p_i + \frac{\Pi_{ij}^{(\text{PECM})}}{2} \right) (\mathbf{v}_i - \mathbf{v}_j + \Phi_{ij}^{(\text{PECM})}) + \mathbf{H}_{ij}^{(\text{PECM})} \right] \cdot \nabla_i W_j^{(\text{RKPM})} \quad (33)$$

VII. EXAMPLES

This paper provides five examples, the corresponding entity models and physical models are listed in Table 1 and Table 2 respectively. The computational parameters including initial

size Δx , initial smooth length h_0 of micro-bodies, time step $\Delta t = \tau h / (c + |\mathbf{v}|)$ and modularizing factors or so on are shown in Table 3. Figure 5 to Figure 9 illustrate the numerical results and their comparisons with exact solutions.

In the first three examples, the high pressure gas in the left and right regions move in directions away from each other at subsonic speeds (Example 1), sonic speeds (Example 2) and supersonic speeds (example 3) respectively. With the increase of the speeds, the density of the materials in the intermediate regions is gradually reduced until it becomes vacuum, in which the prediction ability of free boundary is demonstrated.

Table 1 Entity models of examples

Examples numbers	Region names	Distributions x/m	Density $\rho_0/\text{kg.m}^{-3}$	Energy $e_0/\text{J.kg}^{-1}$	Pressure p_0/Pa	Velocity $v_0/\text{m.s}^{-1}$
1		[-1.0, 0.0]	2.400×10^3	6.000×10^6	2.88×10^{10}	-3.00×10^3
2		[-1.0, 0.0]	2.400×10^3	6.000×10^6	2.88×10^{10}	-6.00×10^3
3	Left	[-1.0, 0.0]	2.400×10^3	6.000×10^6	2.88×10^{10}	-9.00×10^3
4		[-1.0, 0.0]	1.575×10^4	15.87	1.000×10^6	0.000
5		[-1.0, 0.0]	1.575	0.000	0.000	0.000
1		[0.0, 1.0]	2.400×10^3	6.000×10^6	2.88×10^{10}	3.00×10^3
2		[0.0, 1.0]	2.400×10^3	6.000×10^6	2.88×10^{10}	6.00×10^3
3	Right	[0.0, 1.0]	2.400×10^3	6.000×10^6	2.88×10^{10}	9.00×10^3
4		[0.0, 1.0]	2.470×10^3	7.085×10^6	3.50×10^{10}	0.000
5		[0.0, 1.0]	1.575×10^4	3.175×10^5	2.00×10^{10}	0.000

Table 2 Physics models of examples

Examples numbers	Region names	Equation of state	Equation of sound speed	Exponent	Sound speed $c_0/\text{m.s}^{-1}$
1		$p = (\gamma - 1)\rho e$	$c = \sqrt{\gamma(\gamma - 1)e}$	3.0	6000.0
2		$p = (\gamma - 1)\rho e$	$c = \sqrt{\gamma(\gamma - 1)e}$	3.0	6000.0
3	Left	$p = (\gamma - 1)\rho e$	$c = \sqrt{\gamma(\gamma - 1)e}$	3.0	6000.0
4		$p = c_0^2 (\rho - \rho_0) + (\gamma - 1)\rho e$	$c = \sqrt{c_0^2 + (\gamma - 1)(e + p / \rho)}$	5.0	1290.0
5		$p = c_0^2 (\rho - \rho_0) + (\gamma - 1)\rho e$	$c = \sqrt{c_0^2 + (\gamma - 1)(e + p / \rho)}$	1.4	760.0
1		$p = (\gamma - 1)\rho e$	$c = \sqrt{\gamma(\gamma - 1)e}$	3.0	6000.0
2		$p = (\gamma - 1)\rho e$	$c = \sqrt{\gamma(\gamma - 1)e}$	3.0	6000.0
3	Right	$p = (\gamma - 1)\rho e$	$c = \sqrt{\gamma(\gamma - 1)e}$	3.0	6000.0
4		$p = c_0^2 (\rho - \rho_0) + (\gamma - 1)\rho e$	$c = \sqrt{\gamma(\gamma - 1)e}$	3.0	6520.0
5		$p = c_0^2 (\rho - \rho_0) + (\gamma - 1)\rho e$	$c = \sqrt{\gamma(\gamma - 1)e}$	5.0	2520.0

Table 3 Parameters of numerical computation

$\Delta x/\text{mm}$	h_0/mm	τ	α	β	ϵ	g_1	g_2	η	δ	θ	n
0.5	0.75	0.5	1.0	2.0	0.01	0.1	0.2	0.01	0.5	0.01	2

In Example 4, the left side with low pressure and high density imitates heavy metals, the right side with high pressure and low density imitates explosive product, from which the initial ratios are $p_{20}/p_{10} = 3.5 \times 10^4$, $\rho_{10}/\rho_{20} \approx 6.38$, $e_{20}/e_{10} \approx 4.5 \times 10^6$, $(p_{20}/\rho_{20})/(p_{10}/\rho_{10}) \approx 2.23 \times 10^5$. This model is built mainly to reflect the process in which the detonation wave drives a high-density metal to accelerate, and it is easily leading to non-physical numerical solution. PECM can give stable and accurate solutions in this case even if the heat flux modularizing factor is not applied.

In Example 5, a material that has very low density, zero

pressure and zero internal energy is on the left side imitating thin gas, and the right side with high pressure and high density intimates the heavy metal that will rapidly expand after being compressed by shock. The initial ratios are $p_{20}/p_{10} = \infty$, $\rho_{20}/\rho_{10} = 1.0 \times 10^4$, $e_{20}/e_{10} = \infty$, $(p_{20}/\rho_{20})/(p_{10}/\rho_{10}) = \infty$. This model reflects another typical problem encountered in detonation system in which a high pressure heavy metal drives rarefied gas to accelerate. Its main characteristics are the very big ratios of initial density, energy and pressure. It is very difficult to stably obtain the correct solutions. PECM can also be stable and give accurate solutions about the density, energy, pressure and velocity. Application of the modularizing factor

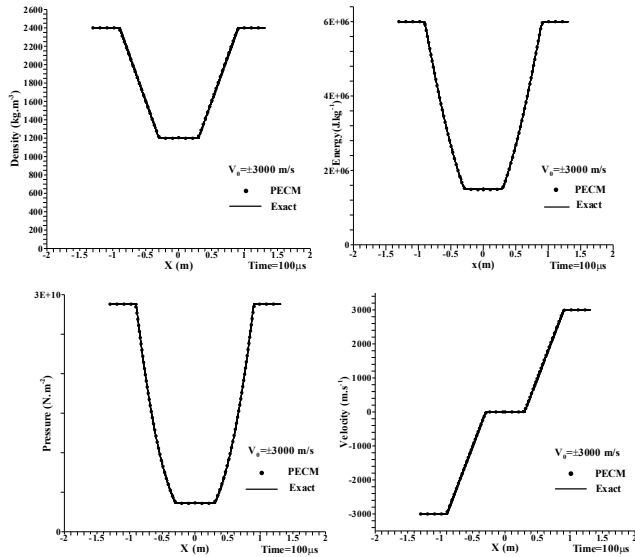


Fig. 5 Numerical results about Example 1

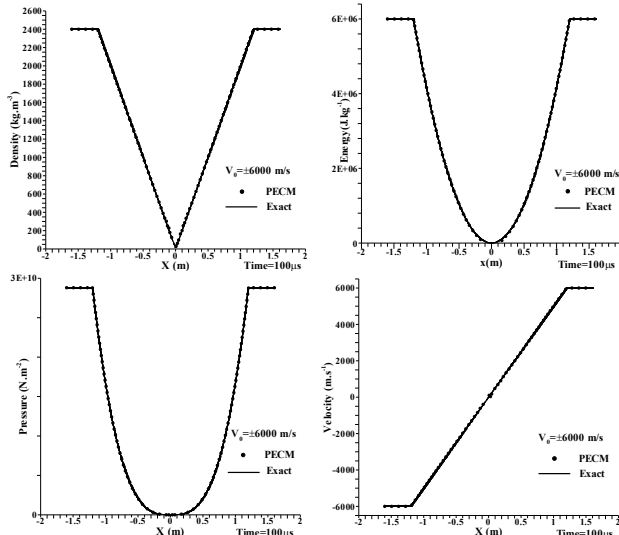


Fig. 6 Numerical results about Example 2

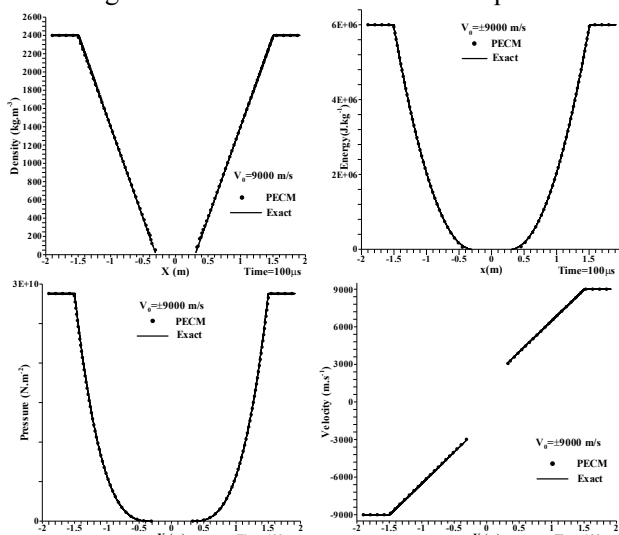


Fig. 7 Numerical results about Example 3

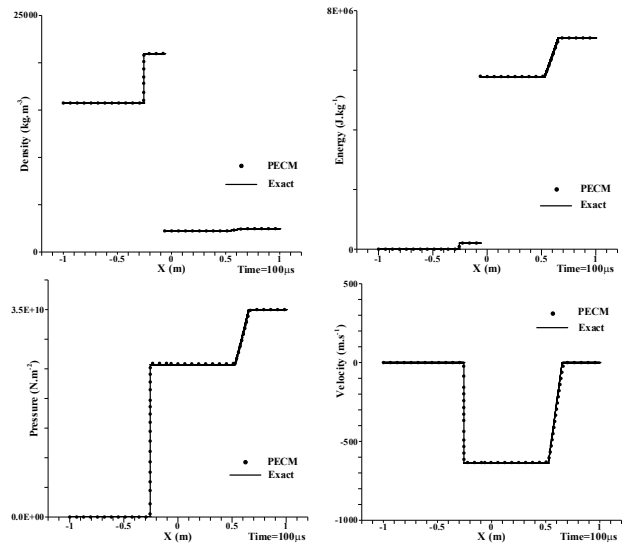
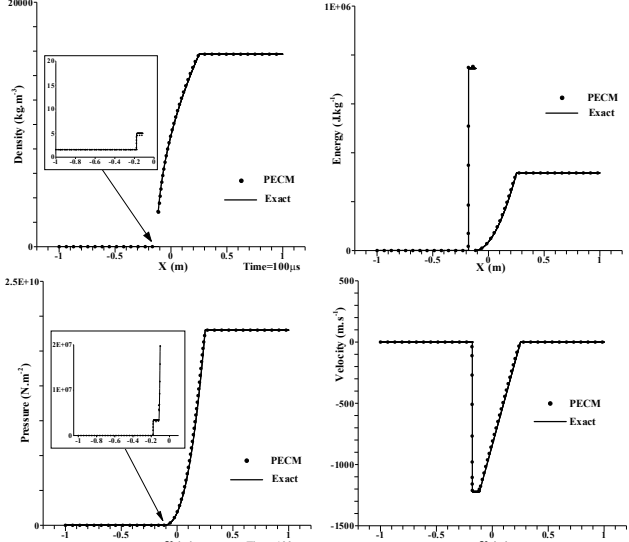


Fig. 8 Numerical results about Example 4

Fig. 9 Numerical results about Example 5
of heat flux could improve the wall heating effect.

All the computations in this paper are based on the numerical simulation software HAUC (How Are Universes Cuddling?) developed by Ma Zhibo.

VIII. CONCLUSIONS

Engineering systems are often diversified and complex, so it is needed to develop advanced algorithms for simulation codes applied in engineering. Inspired by applications and physical laws, the mesh free systematic method with fidelity to physics and universality in application is constructed according to the relationships of inheritances and derivations of the material behaviours. The numerical tests for fluid dynamics show that the new method can represent the physical process more accurately even strong discontinuities exist, which reveal the importance of cognition on physics when designing a meshfree method.

ACKNOWLEDGEMENT

This work has been supported in part by the National Natural Science Foundation of China (Grant No.11371066).

REFERENCES

- [1] MA Zhibo, ZHENG Miao, et al. Quantification of uncertainties in detonation simulations [J]. Chinese Journal of Computational Physics, 2011, 28(1): 66-74.
- [2] MA Zhibo, LI Haijie, et al. Uncertainty quantification of numerical simulation for reliability analysis [J]. Chinese Journal of Computational Physics, 2014, 31(4): 424-430.
- [3] MA Zhibo, YIN Jianwei, et al. Uncertainty quantification of numerical simulations subjected to calibration [J]. Chinese Journal of Computational Physics, 2015, 32(5): 514-522.
- [4] VON Neumann J, RICHTMYER R D. A method for the numerical calculation of hydrodynamic shocks [J]. Journal of Applied Physics, 1950, 21(3): 232-237.
- [5] GODUNOV S K. A finite difference method for the computation of discontinuous solutions of the equations of fluid dynamics [J]. Mathematics of the USSR-Sbornik, 1959, 47: 357-393.
- [6] GINGOLD R A and MONAGHAN J J. Smoothed particle hydrodynamics: Theory and application to non-spherical stars [J]. Monthly Notices of the Royal Astronomical Society, 1977, 181(3): 375-389.
- [7] LUCY L B. A numerical approach to the testing of the fission hypothesis [J]. Astronomical Journal, 1977, 82(82): 1013-1024.
- [8] GINGOLD R A and MONAGHAN J J. Kernel estimates as a basis for general particle methods in hydrodynamics [J]. Journal of Computational Physics, 1982, 46(3): 429-453.
- [9] MONAGHAN J J and GINGOLD R A. Shock simulation by the particle method SPH [J]. Journal of Computational Physics, 1983, 52(2): 374-389.
- [10] MONAGHAN J J. Particle methods for hydrodynamics [R]. Computer Physics Reports, 1985, 3(2): 71-124.
- [11] CLEARY P W and MONAGHAN J J. Conduction modelling using smoothed particle hydrodynamics [J]. Journal of Computational Physics, 1999, 148(1): 227-264.
- [12] PETSCHEK A G and LIBERSKY L D. Cylindrical smoothed particle hydrodynamics [J]. Journal of Computational Physics, 1993, 109(1): 76-83.
- [13] ZHANG Suochun. Smoothed particle hydrodynamics (SPH) method (A review) [J]. Chinese Journal of Computational Physics, 1996, 13 (4): 385-397.
- [14] SWEGLE J W, HICKS D L, ATTAWAY S W. Smoothed particle hydrodynamics stability analysis [J]. Journal of Computational Physics, 1995, 116(1): 123-134.
- [15] LIU W K, JUN S, LI S F, et al. Reproducing kernel particle methods for structural dynamics [J]. International Journal for Numerical Methods in Engineering, 1995, 38(10): 1655-1679.
- [16] YIN Jianwei, MA Zhibo. Reproducing kernel particle method in smoothed particle hydrodynamics [J]. Chinese Journal of Computational Physics, 2009, 26 (4):553-558.
- [17] CHEN J K, BERAUN J E, JIH C K. An improvement for tensile instability in smoothed particle hydrodynamics [J]. Computational Mechanics, 1999, 23(4): 279-287.
- [18] ZHANG G M, BATRA R C. Modified smoothed particle hydrodynamics method and its application to transient problems [J]. Computational Mechanics, 2004, 34(2): 137-146.
- [19] MONAGHAN J J. SPH and Riemann solvers [J]. Journal of Computational Physics, 1997, 136(2): 298-307.
- [20] SIGALOTTI L D G, López H et al. A shock-capturing SPH scheme based on adaptive kernel estimation [J]. Journal of Computational Physics, 2006, 212(1): 124-149.

Analysis of the hydrological safety of dams using numerical tools: Iber and DualSPHysics

J. González-Cao, O. García-Feal, A.J.C. Crespo, J.M. Domínguez, M. Gómez-Gesteira

Enviromental Physics Laboratory (EPHYSLAB)

Universidade de Vigo, Campus As Lagoas

Orense, Spain

email: jgcao@uvigo.es

Abstract— The analysis of the hydrological safety of dams is a critical issue to avoid failures that can affect people or material goods. In this work a numerical methodology to analyse the safety of the “Belesar” dam (Northwest of Spain) based in two different numerical codes is presented. The first one is a mesh-based code named Iber suited to deal with large domains in which 2-D assumptions can be adopted. The second one is a mesh-free code named DualSPHysics very suited to deal with complex and violent 3-D flows. Iber is used to simulate the impoundment associated to the dam while DualSPHysics is used to simulate one of the spillways of the dam starting from the results obtained with Iber. The analysed conditions correspond to the maximum expected inflow to the impoundment assuming that the initial water level of the reservoir is equal to the maximum value. These values of maximum inflow and maximum water depth are obtained from the technical specifications of the dam.

I. INTRODUCTION

The probability of failure of the exceedance structures (spillways and outlet works) of a dam defines its hydrological safety. This failure can be categorised into two types: structural and performance failures. The former one is related to dam breaks and the latter one is related to water excess in the impoundment associated to the dam. These failures can generate high impacts downstream the dam causing serious damage to population or infrastructures. For example, in February 2017 the damage of main and emergency spillways of the Oroville dam, in Northern California, prevented the opening of their gates causing the rising of the level of the impoundment over the crest of the dam (overtopping) during a high precipitation phenomenon. To avoid the collapse of the weir caused by this overtopping, the gates of the spillways were open causing the erosion of the main spillway of the dam. More than 100,000 people living downstream the Oroville dam were evacuated. Figure 1 shows the main spillway of the Oroville dam during this crisis.

In this work the hydrological safety of “Belesar” dam is analysed by means of two numerical codes: Iber [1] and DualSPHysics [2]. In order to analyse the hydrological safety of the dam, first, the water elevation and the outflow of the spillways associated with the maximum expected flow of the “Miño” river were obtained using the numerical code Iber [1]. Iber is a mesh-based numerical code that solves the

Shallow Water Equations in 2D using finite volume schemes. This numerical code is suited to analyse the behaviour of rivers or impoundments defined in large domains where only the horizontal components of the velocity and the water depth are involved, such as flooding hazards analysis. In [3] the reader can find an application of Iber to this type of flooding analysis. The numerical domain defined for this simulation considers the real geometry of the “Belesar” dam and its associated impoundment. The geometry was obtained from raster files downloaded from the IGN website and edited by means of the software QGIS [4].



Figure 1. Main spillway of the Oroville dam during the crisis on February of 2017. Source: https://en.wikipedia.org/wiki/Oroville_Dam_crisis

Once the water elevation and the outflow of the spillways were obtained with Iber, the behaviour of the left spillway was analysed using the numerical code DualSPHysics [2]. DualSPHysics is a mesh-free numerical code highly suited to analyse free-surface phenomena where complex dynamics of fluid are observed (3-D effects), such as non-linear wave-structure interaction ([5, 6]) in small and medium size domains. These features allow DualSPHysics to overcome the limitations of Iber when analysing 3-D flows. The geometry of the spillway was obtained using the software Blender [7] according to the technical specifications of the dam.

II. CASE OF STUDY

The “Belesar” dam was built in 1962 with the main purposes of hydroelectric use, basin regulation and control of floods of the “Miño” river. The dam is 127 meters high (from the heel to the crest) and its crest length is equal to 500 m. The elevation of the crest of the dam is equal to 332 m.a.s.l. The impoundment associated to this dam is supplied by the hydrological network of the “Miño” river and it is 50 km long. The main exceedance structures of the dam are two spillways located at both sides of the dam and four low level outlets. Both spillways were designed using scaled models (1:75). According to the technical specifications of the dam, the maximum level of the pool is equal to 330 m.a.s.l. and the maximum expected flow of “Miño” river is equal to 4,000 m³/s. The location of the dam, its impoundment and a detailed aerial image including both spillways are shown in Figure 2.

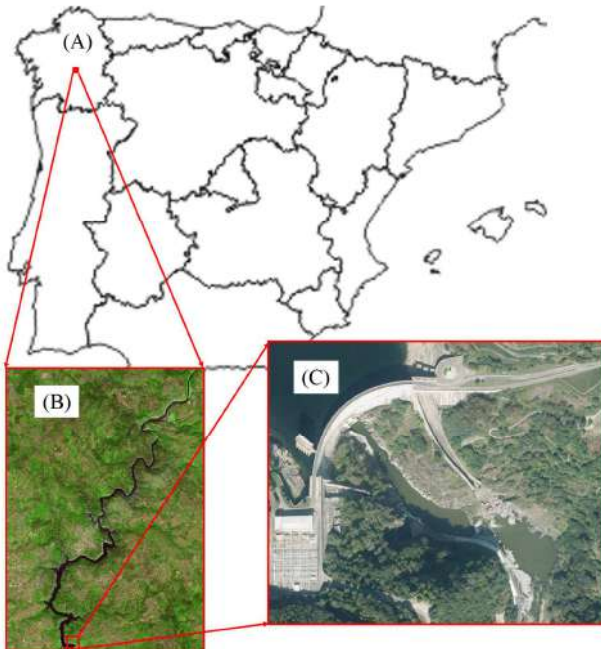


Figure 2. Location of “Belesar” dam (A), impoundment associated to the dam (B) and aerial image of the dam (C). The figures showed in panels B and C were obtained from <http://www.ign.es/iberpix2/visor/#> (PNOA courtesy of © Instituto Geográfico Nacional).

III. MATERIALS AND METHODS

In this paragraph a brief description of the numerical codes used to carry out the simulations and the parameters defined for these simulations are presented.

A. Iber

Iber is a numerical code that solves the Shallow Water Equations in 2D (Eq. 1) by means of finite volume schemes. Actually, Iber is composed by three modules: hydrodynamic, turbulence and sediment transport modules. In this work, only the hydrodynamic one is used. This code can be freely downloaded from <http://iberaula.es/web/index.php>.

$$\begin{cases} \frac{\partial h}{\partial t} + \frac{\partial hU_x}{\partial x} + \frac{\partial(hU_y)}{\partial y} = 0 \\ \frac{\partial(hU_x)}{\partial t} + \frac{\partial}{\partial x}\left(hU_x^2 + g\frac{h^2}{2}\right) + \frac{\partial}{\partial y}(hU_x U_y) = \\ -gh\frac{\partial Z_b}{\partial x} - \frac{\partial\tau_{s,x}}{\rho} - \frac{\partial\tau_{b,x}}{\rho} + \frac{\partial}{\partial x}\left(hv_t\frac{\partial U_x}{\partial x}\right) + \frac{\partial}{\partial y}\left(hv_t\frac{\partial U_x}{\partial y}\right) \\ \frac{\partial(hU_y)}{\partial t} + \frac{\partial}{\partial x}\left(hU_y^2 + g\frac{h^2}{2}\right) + \frac{\partial}{\partial y}(hU_x U_y) = \\ -gh\frac{\partial Z_b}{\partial y} - \frac{\partial\tau_{s,y}}{\rho} - \frac{\partial\tau_{b,y}}{\rho} + \frac{\partial}{\partial x}\left(hv_t\frac{\partial U_y}{\partial x}\right) + \frac{\partial}{\partial y}\left(hv_t\frac{\partial U_y}{\partial y}\right) \end{cases} \quad (1)$$

In Eq. (1) h refers to the water depth, U_x and U_y refer to the horizontal components of the velocity of the flow, g is the acceleration of gravity, Z_b is elevation of the bottom of the channel, ρ is the density of the water (constant), $\tau_{s,x}$ and $\tau_{s,y}$ are the friction derived from the wind in the x and y direction, $\tau_{b,x}$ and $\tau_{b,y}$ are the friction in bottom of the channel in the x and y direction and v_t is the turbulent viscosity.

The assumptions, usually fulfilled in rivers and in tidal estuaries, of the 2D Shallow Water Equations are:

- The velocity vector varies in the horizontal direction of the flow;
- The slopes of the bottom are small;
- No erosion is considered;
- The flow is considered as incompressible and with constant density.

The friction between the water and the bottom of the channel is an important parameter to model the hydrodynamics of flows in different applications. This parameter is modelled by means of the known Manning’s formula:

$$C_f = g \frac{n^2}{h^{1/3}} \quad (2)$$

where C_f is a non-dimensional roughness coefficient, g is the acceleration of gravity, n is the Manning coefficient and h is the water depth.

The friction stress in the bottom of the channel can be obtained using Eq. (3) where $|U|$ is the average bottom velocity of the fluid.

$$\tau_b = \rho C_f |U|^2 \quad (3)$$

The Manning’s coefficients associated to the land uses of the study area can be assigned in two ways: manually and automatically. The first one allows the user to define by hand the different Manning’s coefficient of the areas of study and is based in a tool implemented in Iber. The second one is based on an automatic tool developed by the EPHYSLAB group that allows defining in automatic way, starting from the land uses defined by the Sistema de Información sobre Ocupación del Suelo de España (SIOSE) in shape files, the

land uses and the Manning's coefficients of the study area. Depending on the extension of the study area more than 1000 land uses can be defined. This is a very useful tool to study runoff processes. Figure 3 shows an example of the automatic assignment.

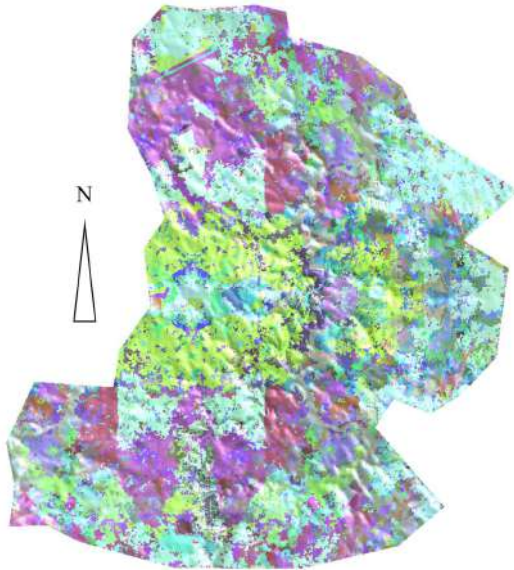


Figure 3. Land uses assigned using the automatic tool.

Two simulations were carried out using the numerical code Iber [1] to analyse the behaviour of the impoundment. In the first simulation, with the purpose of analysing the inflow conditions, the crest of the dam was raised to obtain the total elevation of the water near the dam considering that the gates of the spillways were closed. In the second simulation the gates of the spillways were open. The simulation time of both numerical simulations were 8 hours each one. The numerical domain was discretised, for both simulations carried out with Iber, defining a mesh of 180,000 triangular elements. Figure 4 shows a detail of the defined mesh near the dam.



Figure 4. Detail of the mesh defined to simulate the impoundment using the numerical code Iber. Image PNOA courtesy of © Instituto Geográfico Nacional.

The boundary conditions of the numerical simulation were an inlet flow of $4000 \text{ m}^3/\text{s}$ (Figure 5) defined 50 km upstream the dam and two outflows defined in the dam near the position of the spillways. These two outflows were only

considered in the second simulation of the impoundment where the gates of the spillways were fully open. The inlet flow corresponds to the maximum expected flow defined in the technical specifications of the dam. The initial condition was equal to the maximum elevation of water of the dam, i.e., 330 m.a.s.l.

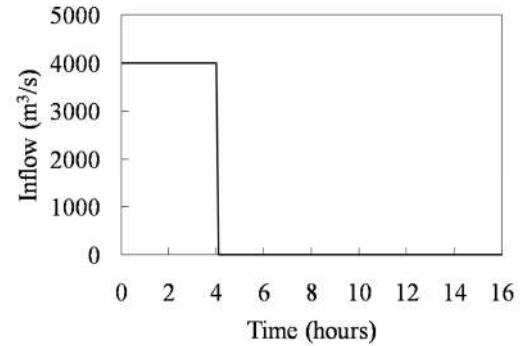


Figure 5. Inlet flow defined as boundary condition.

Two land uses were prescribed using the assignment tool implemented in the numerical code Iber. The first one corresponds to the river and the second one corresponds to sparse vegetation. The values of these Manning's coefficients are $0.025 \text{ s/m}^{1/3}$ and $0.08 \text{ s/m}^{1/3}$, respectively. Figure 6 shows the land uses defined for this simulation.

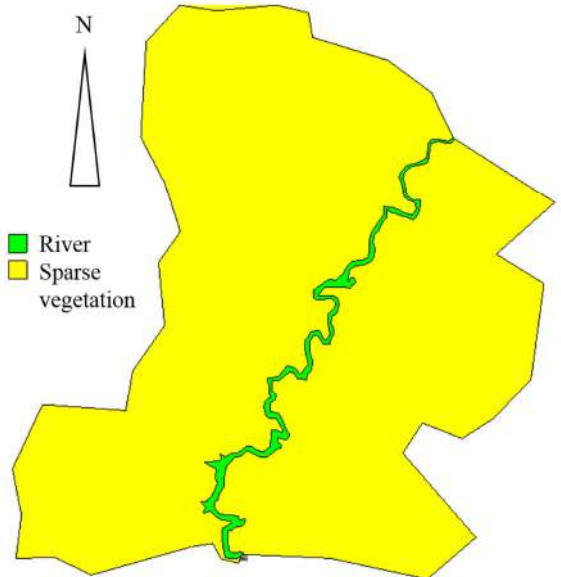


Figure 6. Land uses defined for the numerical simulation of the impoundment using Iber.

B. DualSPHysics

DualSPHysics is a numerical code based on the Smoothed Particle Hydrodynamics (SPH) method. DualSPHysics was conceived to use SPH for real engineering problems. The model is open source and can be freely downloaded from <http://www.dual.sphysics.org>. DualSPHysics includes a software that can be run on either CPUs or GPUs (graphics cards with powerful parallel

computing). GPUs offer greater computing power than CPUs, and they are an affordable option to accelerate SPH modelling. This software also includes pre-processing and post-processing tools. A complete description of DualSPHysics can be found in [2] and [8].

DualSPHysics has been widely used to analyse wave propagation and their interaction with fixed and moving bodies. The walls of the Spillway were discretized using Dynamic Boundary Conditions (DBC) which are implemented in DualSPHysics using [9]. The work of [10] presented a new functionality of DualSPHysics where inlet and outlet conditions are implemented. This new option allows us to define inlet conditions imposing velocity, density or water depth. In this work inlet conditions with prescribed velocity will be used.

There are two spillways in the dam, but only the left spillway was considered. Figure 7 shows the real and the numerical geometry of the spillway. The initial interparticle spacing defined for the numerical simulations of DualSPHysics was equal to 0.3 m and the physical time to be simulated was 30 s.

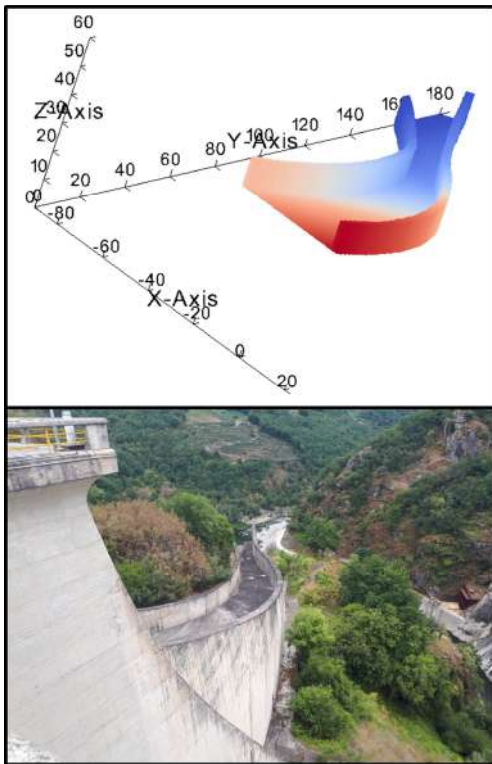


Figure 7. Geometry of the left spillway of the “Belesar” dam obtained with the software Blender [7] (upper panel) and real image of the spillway (lower panel).

Figure 8 shows the right spillway of the “Belesar” dam and its gates.

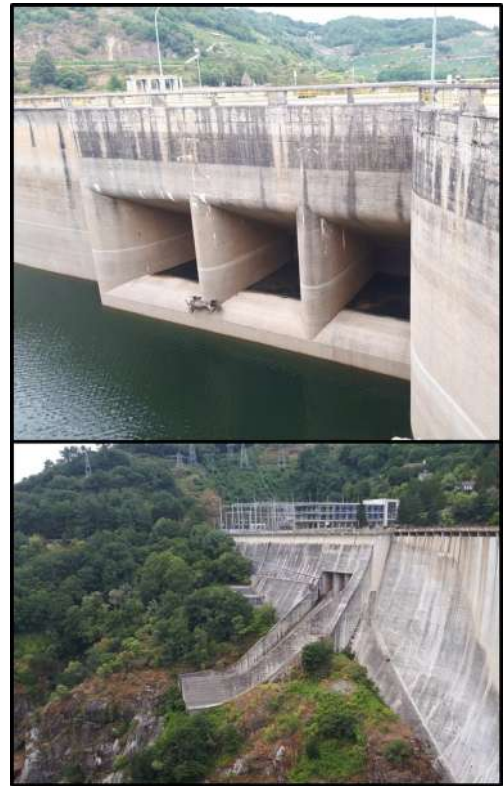


Figure 8. Geometry of the gates of the right spillway of the Belesar dam (upper panel) and the spillway (lower panel).

Previously to the simulation of left spillway of the “Belesar” dam two simulations were carried out to verify the accuracy of the results obtained using DualSPHysics when dealing with two different 2-D spillways. The first one corresponds to an ogee spillway and the second one corresponds to a broad crested weir.

IV. RESULTS AND DISCUSSIONS

In this section the numerical results obtained in the simulations of the impoundment and the left spillway of the “Belesar” dam will be shown. First the results of the simulations carried out using Iber will be displayed and then the numerical results of the left spillway obtained with DualSPHysics are showed.

A. Simulation of the reservoir using Iber

As mentioned before, two simulations were carried out using the numerical code Iber. In the first simulation the crest of the dam was raised to 350 m.a.s.l. to obtain the total elevation of the water near the dam considering that the gates of the spillways were closed and in the second simulation the gates were open to obtain the outflows of the spillway.

Figure 9 shows the water elevation near the right and left spillways obtained in the first simulation with Iber. Hence, this shows that the water elevation near the left spillway is equal to the water elevation obtained near the right spillway. In the first two hours the water elevation decreases from the initial depth (330 m.a.s.l.) to near 327 m.a.s.l. due the general dynamics of the water movement in the reservoir. Then water

elevation increases to near 333 m (time equal to 7 hours). The elevation of the crest of the dam is reached for a time equal to 6 hours. Therefore, the gates of the spillways would need to be opened 6 hours after the inflow starts into the reservoir to avoid the overflow of the dam.

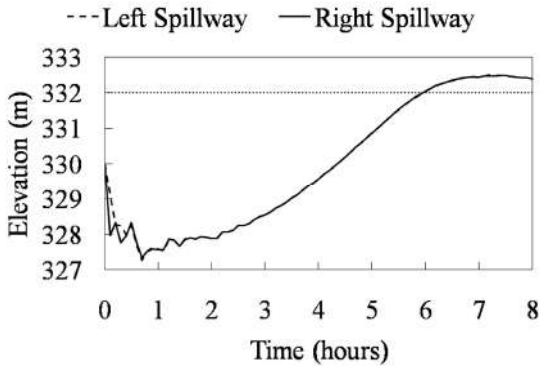


Figure 9. Water elevation near left (dashed line) and right (solid line) obtained in the first simulation using Iber. The dotted line represents the elevation of the crest of the dam (332 m.a.s.l.).

Figure 10 shows the water elevation obtained in the first simulation using Iber near the dam for a time equal to 6 hours. Figure 10 shows that the water elevation in the entire area near the dam is equal to the elevation of the crest of the dam.

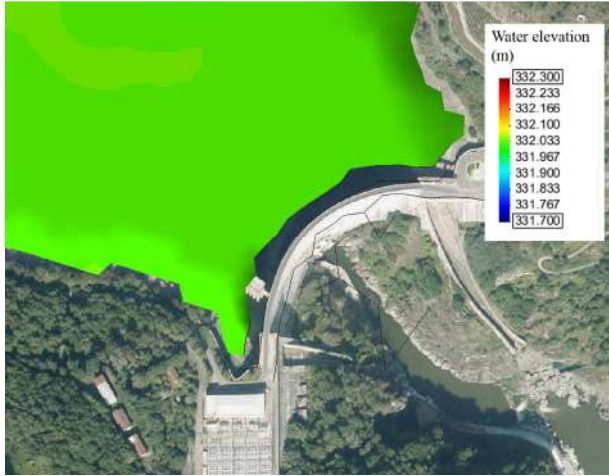


Figure 10. Water elevation near the dam for time equal to 6 hours.

Once the water elevation was obtained, a second simulation with Iber was carried out considering that the gates of the spillways were completely opened. Figure 11 shows the outflow of the left spillway obtained using Iber. Figure 11 shows that the maximum outflow through the left spillway is near $1200 \text{ m}^3/\text{s}$ at the beginning of the simulation. This flow decreases in a quasi-linear way to $700 \text{ m}^3/\text{s}$.

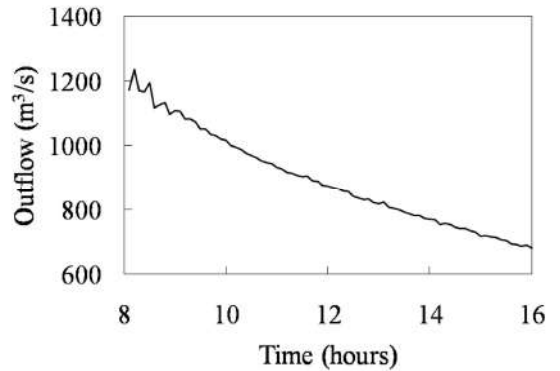


Figure 11. Outflow near the left spillway obtained with Iber.

B. Simulation of the left spillway using DualSPHysics

To verify the accuracy of the results obtained with DualSPHysics, two simulations of different 2-D spillways were carried out. The first one corresponds to a typical ogee spillway and the second one corresponds to a crested weir. The numerical results obtained with DualSPHysics were compared to experimental data. Figure 12 compares the numerical and the experimental results obtained for these simulations. In the upper panel of Figure 12 the 0-line represents the vertical wall of the ogee spillway and in the lower panel the red rectangle represents the lateral view of the broad crested weir. The figure shows that the water profiles obtained with DualSPHysics are similar to those obtained in the experimental tests. These results show that DualSPHysics is a suited tool to analyse these types of flow over such spillways. The reader can obtain a detailed analysis of these types of simulations in [11].

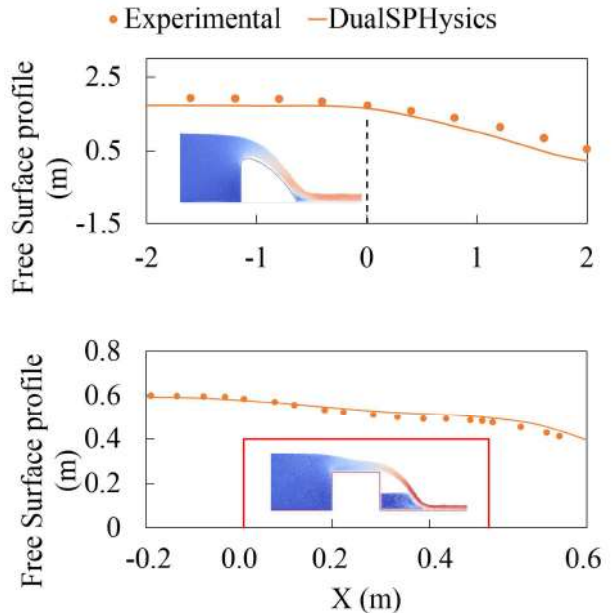


Figure 12. Free surface profile from experiment (dots) and obtained using DualSPHysics (solid line) in two different spillways: ogee spillway (upper panel) and broad crested weir (lower panel).

Once the results of DualSPHysics were verified for these type of simulations the numerical simulation of the spillway were carried out. The inlet condition in DualSPHysics is defined using the velocity of the flow that is computed starting from the outflow obtained with Iber (Figure 11) and considering a lateral area of the gates of the spillway equal to 300 m².

Figure 13 shows three different snapshots of the SPH simulation of the spillway. It can be observed how at the beginning of the simulation (time equal to 2.9 seconds) the velocity of the water flow is greater in the right side of the spillway than in the left side. This effect is due to the geometry of the spillway. Then (time equal to 6.1 seconds) the water impacts onto the right wall of the spillway while the left side of the spillway remains dry. Finally (time equal to 29.8 seconds) the flow is homogeneously distributed in the last section of the spillway. This shows that the steady state of the working operations of the spillway is reached for a time near to 30 seconds.

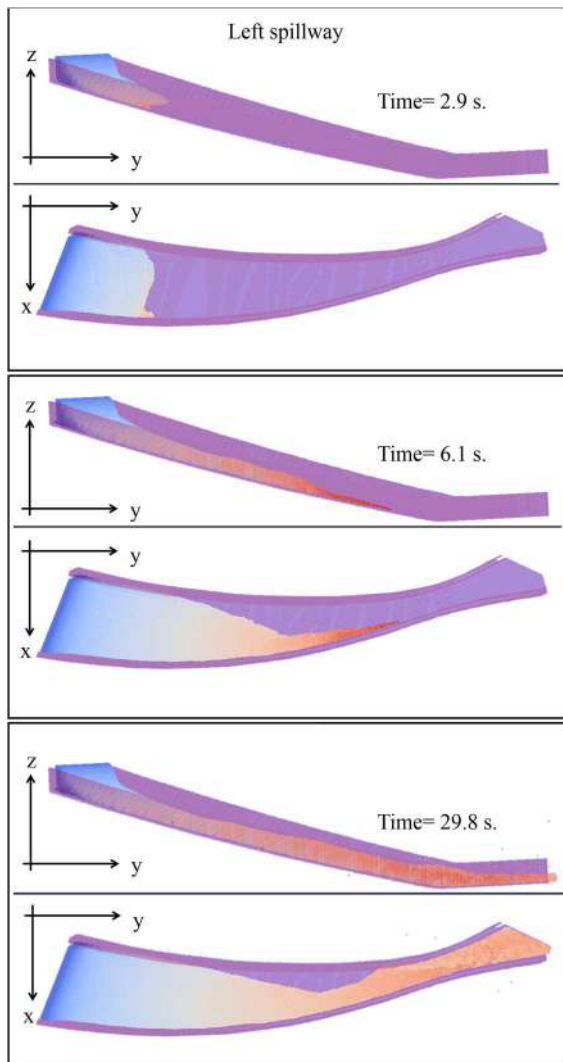


Figure 13. Different snapshots of the numerical simulation of the left spillway of the “Belesar” using DualSPHysics. Colour of particles correspond to velocity values.

The time series of the water depth computed in different positions of the spillway are depicted in Figure 14. It shows that the maximum water depth was obtained near the right wall of the spillway being close to 6 meters. The water depth near the inlet in P1 (≈ 3 m) is greater than the water depth obtained at P2 (≈ 1.5 m). At the end of spillway (points P4 and P5) the water depth remains constant and near 4 meters. Since the walls of the spillway are 10 meters high, no overflow was observed during the simulation of the spillway for the analysed conditions.

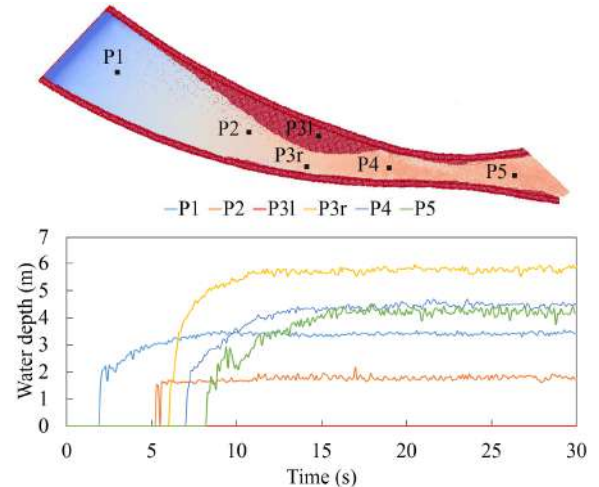


Figure 14. Locations of the depth sensors in the spillway (upper panel) and time series of water depth (lower panel) obtained in these locations of the spillway using DualSPHysics.

Figure 15 shows the time series of the components of force exerted onto the bottom of the spillway near the inlet of the flow. Near the inlet the flow direction is equal to y-direction so the force in x-direction is equal to 0 N. The maximum (in absolute value) component of the force exerted onto the floor of the spillway is F_z and is equal to -10 MN. The force in y-direction is equal to -3 MN.

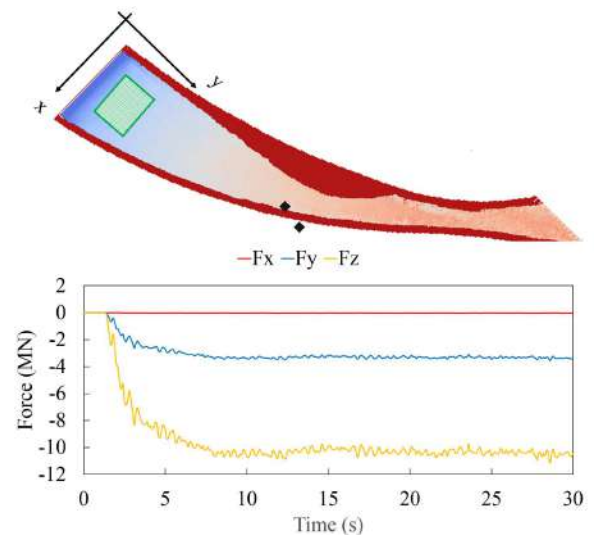


Figure 15. Time series of the force (lower panel) exerted onto the floor of the spillway near the flow inlet (shaded area in the upper panel).

Figure 16 shows the time series of force components exerted onto the vertical wall of the curve of the spillway. The vertical force is equal to 0 N whereas the x and y components of the force are greater than 0 N. Both horizontal components have a similar maximum values (≈ 1 MN) but the y-component is always less than the x-component. The profile of the time series of the horizontal components of the force is quite similar.

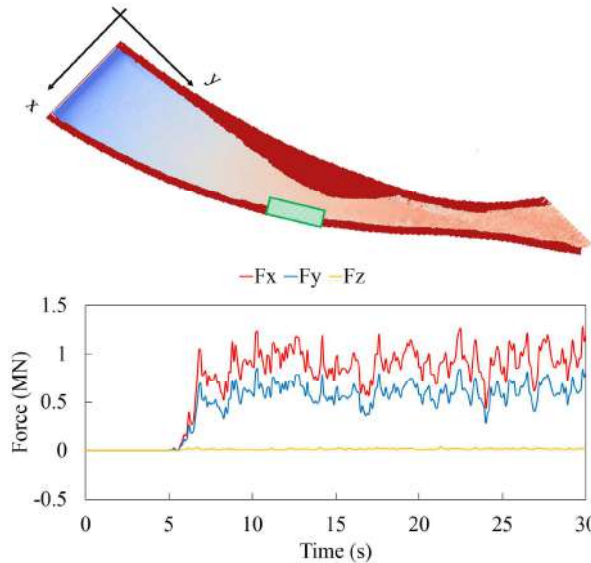


Figure 16. Time series of the force components (lower panel) exerted onto the vertical wall of the spillway in outer edge of the curve (shaded area in the upper panel).

V. CONCLUSIONS

A mesh-based code, Iber, and a mesh-less code, DualSPHysics are used together to analyse the safety of “Belesar” dam. In fact, the inlet conditions of DualSPHysics are obtained starting from the results of the Iber simulations.

The numerical results obtained with Iber and DualSPHysics show that the left spillway of “Belesar” dam is well designed to evacuate outflows associated to the limit conditions defined in the technical specification of the dam.

The numerical simulations of the impoundment carried out with Iber show that no overflow is observed if gates are open up 6 hours after the inflow starts.

The numerical simulation of the left spillway carried out with DualSPHysics shows that the spillway works properly with the conditions defined in this work. The water depth was computed in six different positions inside the spillway. The maximum water depth obtained was equal to 6 m. This value is less than the height of the lateral walls of the spillway so no overflow is observed. The forces in two locations, near the

inlet flow and in the vertical wall of the spillway, were also analysed. In the first location the maximum force a quasi-vertical force and it is near -10 MN. The force exerted in the vertical wall of the spillway is in the horizontal direction and its modulus is near to 1 MN.

ACKNOWLEDGEMENT

This work is partially supported under projects IMDROFLOOD (Water JPI - WaterWorks 2014), and Programa de Consolidación e Estructuración de Unidades de Investigación Competitivas (GRC2013-001) and Risc_ML (Interreg Program, European Regional Development Fund, ERDF). One of the authors, A.J.C.C., is funded by a “Ramón y Cajal” grant of the “Ministerio de Economía y Competitividad del Gobierno de España” (RYC-2013-12617).

REFERENCES

- [1] E. Bladé, L. Cea, G. Corestein, E. Escolano, J. Puertas, E. Vázquez-Cendón, J. Dolz, A. Coll, “Iber: Herramienta de simulación numérica del flujo en ríos”, Revista Internacional de Métodos Numéricos para Cálculo y Diseño en Ingeniería, vol. 30(1), pp. 1-10, 2014.
- [2] A.J.C. Crespo, J.M. Domínguez, B.D. Rogers, M. Gómez-Gesteira, S. Longshaw, R. Canelas, R. Vacondio, A. Barreiro and O. García-Feal, “DualSPHysics: open-source parallel CFD solver on SPH”, Computer Physics Communications, vol. 187, pp. 204-216, 2015.
- [3] R. Bonasia, O.S. Areu-Rangel, D. Tolentino, I. Mendoza-Sánchez, J. González-Cao and J. Klapp. “Flooding hazard assessment at Tulancingo (Hidalgo, Mexico)”, Journal of Flood Risk Management, 2017. Article in press.
- [4] QGIS Development Team. QGIS Geographic Information System. Open Source Geospatial Foundation Project. 2016.
- [5] C. Altomare, A.J.C. Crespo, B.D. Rogers, J.M. Domínguez, X. Gironella and M. Gómez-Gesteira “Numerical modelling of armour block sea breakwater with Smoothed Particle Hydrodynamics”, Computers and Structures, vol. 130, pp. 34-45, 2014.
- [6] C. Altomare, A.J.C. Crespo, J.M. Domínguez, M. Gómez-Gesteira, T. Suzuki and T. Verwaest, “Applicability of Smoothed Particle Hydrodynamics for estimation of sea wave impact on coastal structures”, Coastal Engineering, vol. 96, pp. 1-12, 2015.
- [7] Blender. <https://www.blender.org>
- [8] A.J.C. Crespo, M. Gómez-Gesteira, R.A. Dalrymple, “Boundary conditions generated by dynamic particles in SPH methods”. Computers, Materials and Continua, vol. 5(3), pp. 173-184 (2007).
- [9] C. Altomare, J.M. Domínguez, A.J.C. Crespo, J. González-Cao, T. Suzuki, M. Gómez-Gesteira and P. Toch, “Long-crested wave generation and absorption for SPH-based DualSPHysics model”. Coastal Engineering, vol. 127, pp. 37-54 (2017).
- [10] A.Tafuni, J.M. Dominguez, R. Vacondio and A.J.C. Crespo, “Accurate and efficient SPH open boundary conditions for real 3-D engineering problems”, 12th International SPHERIC workshop, Orense, Spain (2017).
- [11] S.M. Husain, J.R. Muhammed, H.U. Karunaratna and D.E. Reeve, “Investigation of pressure variations over stepped spillways using smooth particle hydrodynamics”. Advances in Water Resources, vol. 66, pp. 52-69 (2014).

Numerical simulation of water entry with improved SPH method

Jiaru Shao

College of Mechanical Engineering
Chongqing University of Technology
Chongqing, China
e-mail: shaojiaru@cqut.edu.cn

Moubin Liu*

Abstract—Water entry problems are very common in engineering and sciences. When objects move with relatively high speed, bubble cavities will be generated, and the behaviour of moving objects will also be affected conversely. In this paper, The water entry problems are studied using smoothed particle hydrodynamics (SPH) method, which has special advantages in modelling free surfaces, moving interfaces. Firstly, an improve fluid-solid interface treatment (I-FSIT) algorithm are presented, whose effectiveness is validated by a water entry of a buoyant cylinder. Then the water entry with different velocities and directions are researched. It is found that the velocities, angles of the moving objects will affect the movement of the object greatly, and the SPH model can give optimal predication of these corresponding conditions.

Keywords: smoothed particle hydrodynamic(SPH), water entry, bubble cavity, moving object

I. INTRODUCTION

Water entry problem can be frequently observed in daily life and engineering sciences, and can be of utmost importance both in theory and practice. Typical examples include movement of torpedo, diving of sportsman, and landing of aircrafts onto water. If the objects move at high speed, bubble cavities will appear. Numerical simulation of water entry involves rapid movement of solid objects, evolution of the bubble cavity changing, breakup of free surfaces, and violent fluid-solid interaction.

During the last decades, numerical simulations have been more and more important in investigating water entry problems. A number of researchers have provided comprehensive reviews on this problem, and the related numerical simulation methods. Conventional Lagrangian grid based methods such as FEM is difficult in treating large flow deformations, while conventional Eulerian grid-based methods such as FVM and FEM need special algorithms to track or capture the moving free surfaces and moving objects, which usually complicate the problem [1-4].

Recent developments in so-called meshfree and particle methods provide alternates for traditional numerical methods in modeling fluid-solid interaction such as underwater movement. Among the meshfree and particle methods, smoothed particle hydrodynamics (SPH) [5,6] is unique and has some obvious advantages. In SPH, the state of a system is represented by a set of particles, which possess individual material properties

College of Engineering,
Peking University
Beijing, China
e-mail: mbliu@pku.edu.cn

* Corresponding author

and interact with each other within a certain range defined as a support domain by a weight function or smoothing function [7]. The meshfree nature of SPH method remove the difficulties due to large deformations since SPH uses particles rather than mesh as a computational frame to approximate related governing equations.

There are a few literatures addressing the application of SPH method to water entry problems. For example, Oger et al. [8] studied the entry of water of a free falling wedge using a weakly compressible SPH (WCSPH) model. Shao [9] numerically simulated similar water entry problems using an incompressible SPH model . Marrone et al. [10] presented a 2D+t SPH model to study the breaking wave pattern generated by fast moving ships. Xu and Liu [11] simulated the slamming process of a two dimensional bow flare section. Gonget al. [12] Simulated the water entry of a wedge to validate a SPH boundary treatment method. Yang et al. [13] studied the water entry of a cylinder with LANS turbulence model.These works have demonstrated the feasibility of SPH method in modeling water entry problems. However, it is noted that previous works are generally based on traditional SPH method, and some deficiencies are still existed, such as the accuracy and boundary treatment. In addition, in these work, the impact time of objects and water is very short, the process of bubble cavity evolution is not described in detail.

In this paper, an improved Fluid-Solid boundary treatment algorithm are presented based on our previous work [14,15], and the effectiveness is validated by a water entry of a buoyant cylinder. Then the water entry with different velocities and directions are researched.

II. SPH METHODOLOGY

In SPH method, the state of a system is represented by a set of particles, and flow field variables can be obtained through approximating the governing equations which are discretized on the set of particles. A field function and its derivative can then be written in the following forms [16]

$$\langle f(\mathbf{x}_i) \rangle = \sum_j \frac{m_j}{\rho_j} f(\mathbf{x}_j) W(\mathbf{x}_i - \mathbf{x}_j, h), \quad (1)$$

$$\langle \nabla \cdot f(\mathbf{x}_i) \rangle = \sum_j \frac{m_j}{\rho_j} f(\mathbf{x}_j) \nabla_i W_{ij}, \quad (2)$$

where $\langle f(\mathbf{x}_i) \rangle$ is the approximated value of particle i ,

$\langle f(\mathbf{x}_j) \rangle$ is the value of $f(\mathbf{x})$ associated with particle j , \mathbf{x}_i and \mathbf{x}_j are the positions of corresponding particles, m , h denote mass and smooth length, W is smoothing function, and ω_j represents a weighted contribution of particle j to particle i .

A. Governing Equations for viscous fluid

For viscous hydrodynamic problems, the Lagrangian form governing Navier-Stokes equation can be written as

$$\frac{d\rho}{dt} = -\rho \nabla \cdot \mathbf{v}, \quad (3)$$

$$\frac{d\mathbf{v}}{dt} = -\frac{1}{\rho} \nabla P + \frac{\mu}{\rho} \nabla^2 \mathbf{v} + \mathbf{g}, \quad (4)$$

where \mathbf{v} , P , \mathbf{g} , μ denote velocity vector, pressure, gravity, and dynamic viscosity separately. According to equations (1) and (2), the SPH equations of motion for the N-S equation can be obtained as follows

$$\frac{d\rho_i}{dt} = \sum_j m_j \mathbf{v}_{ij} \nabla_i W_{ij}, \quad (5)$$

$$\begin{aligned} \frac{d\mathbf{v}_i}{dt} = & -\sum_j m_j \left(\frac{p_i}{\rho_i^2} + \frac{p_j}{\rho_j^2} \right) \nabla_i W_{ij} \\ & + \sum_j \frac{4m_j (\mu_i + \mu_j)}{(\rho_i + \rho_j)^2 (x_{ij}^2 + 0.01h^2)} \mathbf{v}_{ij} + \mathbf{g} \end{aligned}, \quad (6)$$

B. Equation of motion for moving rigid body

For a moving rigid body, the equation of motion is simply the Newton's law of motion. The centre of mass can be written as follows

$$\frac{d\mathbf{u}_o}{dt} = \frac{\mathbf{F}}{M} + \mathbf{g}, \quad (7)$$

where \mathbf{u}_o is the velocity of the centre of mass, \mathbf{F} is the summation of forces without gravity around the rigid body, M is the mass of the rigid body. For two-dimensional problems, the equation for the angular velocity is

$$\frac{d\omega}{dt} = \frac{\mathbf{J}}{I}, \quad (8)$$

where ω is the angular velocity, I is the moment of inertia, and \mathbf{J} is the total moment of force on the rigid body about the centre of mass. The velocity of a point i on the rigid body is

$$\mathbf{u}_i = \mathbf{u}_o + \omega \times \mathbf{r}_{oi}, \quad (9)$$

where \mathbf{r}_{oi} is the vector from the centre of mass o to point i . For the motion of moving rigid body, the force and momentum of the rigid body can be expressed in SPH as follows

$$\mathbf{F} = \sum_j \mathbf{f}_j, \quad (10)$$

$$\mathbf{J} = \sum_j \mathbf{r}_{oj} \times \mathbf{f}_j, \quad (11)$$

where \mathbf{f}_j denotes the force on particle j due to fluids. The summation is over all rigid body particles. Finally, the SPH

equations of motion for rigid body can be obtained as

$$\frac{d\mathbf{u}_o}{dt} = \frac{\sum m_j \mathbf{a}_j}{M} + \mathbf{g}, \quad (12)$$

$$\frac{d\omega_o}{dt} = \frac{\sum m_j (\mathbf{r}_j - \mathbf{R}_o) \times \mathbf{a}_j}{I_o}, \quad (13)$$

where \mathbf{R}_o is the position of the centre of mass.

C. Equation of state

It is noted that when underwater objects move in a low speed, water can be considered as incompressible. In contrast, when the underwater objects move in a high speed, compressibility of water must be considered, especially for water close to the moving objects. For the case with low velocity, the SPH method usually uses an artificial compressibility technique to model the incompressible flow as a slightly compressible flow. The artificial compressibility considers that every theoretically incompressible fluid is actually compressible. Therefore, it is feasible to use a quasi-incompressible equation of state to model the incompressible flow. The purpose of introducing the artificial compressibility is to produce the time derivative of pressure. A possible artificial equation [17] of state is

$$p = c^2 \rho, \quad (14)$$

where c is the sound speed which is a key factor that deserves careful consideration. For the case with high velocity, a true equation of state which can take account of the compressibility of water must be used.

D. Improved fluid-solid interface treatment algorithm

Boundary condition [18-21] is very important for the SPH simulation, which will affect the calculation accuracy greatly. In this work, an improved Fluid-solid interface treatment (I-FSIT) algorithm is used to construct the interface, which can improve the accuracy of the fluid-solid interface.

In this I-FSIT algorithm, field variable of the Ghost particles (Type A, B and C, as shown in Fig. 1) can be dynamically evolved and obtained from SPH approximation of neighbor particles within the support domain.

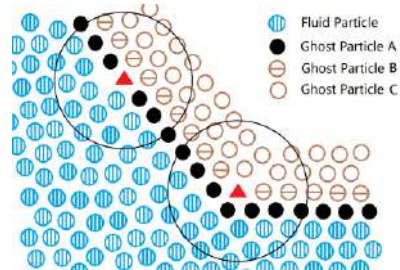


Figure 1. Illustration of the improved Fluid-solid interface treatment

The interpolation domains of different kinds of Ghost particles are different. The information of ghost particle A only comes from fluid particles, and the information of ghost particle B comes from both fluid and type A particles. Similarly, the information of ghost particle C comes from both fluid and

ghost particle A and B. It is known that the support domains of the fluid particles intersect the solid boundary with insufficient neighbor particles for conventional SPH particle approximation schemes. Therefore, to restore the consistency of SPH particle approximation, Shepard filter method [21] or moving least square (MLS) method [22] can be used in the I-FSIT algorithm for approximating both the fluid and ghost particles. Therefore, the pressure of the ghost particles can be obtained as follows,

$$P_i = \sum_j P_j W_{ij}^I \frac{m_j}{\rho_j}, \quad (15)$$

where W^I is the improved kernel function, which represents the new function obtained by the Shepard Filter or Moving Least Square method separately.

Usually, the density of the rigid body is different from the fluid. In approximating density of ghost particle , Equation(5) cannot be directly used as it is valid only for particles from the same materials. For approximations with particle from different materials, the possible large density inhomogeneity may produce large numerical oscillation in the interface region. As such, in the interface region, the density change rate (continuum equation) can be corrected by the density ratio of solid particles to fluid particles as follows

$$\frac{d\rho_j}{dt} = \sum_j m_j v_{ij} \nabla_i W_{ij} \frac{\rho_i}{\rho_j}. \quad (16)$$

It is clear that in this equation, if particle j is from the same material as particle i , as $\rho_i = \rho_j$, Equation (16) is close to (5). If particle j is a neighboring fluid particle, its contribution to $d\rho/dt$ is underestimated as the density of particle j is lower than that of particle i . Adding a corrective term of ρ_i/ρ_j can help to balance the underestimation of density change rate from particle j .

For the particles from fixed solid boundary, the density is usually set to be the same as the fluid particles. Take non-slip boundary condition for example, the variables of the boundary particles can be obtained from the following equations

$$\rho_i = \sum_{j=1}^N \rho_j W_{ij}^I \frac{m_j}{\rho_j} = \sum_{j=1}^N m_j W_{ij}^I, \quad (17)$$

$$v_i = -\sum_{j=1}^N v_j W_{ij}^I \frac{m_j}{\rho_j}. \quad (18)$$

III. NUMERICAL SIMULATIONS AND DISCUSSIONS

Water entry is a typical underwater movement, which involves breakup of the free surfaces, fluid-solid interactions and complex turbulence and vortex generation. In this part , the water entry with different velocities and directions will be researched, and the formation, growth of the bubble cavities will be analyzed. Fig. 2 shows the geometry of the water entry system. The length and height of the water is L and H separately. At the beginning, the moving body (buoyant cylinder or rectangular object) will impact the water surface with different velocity v .

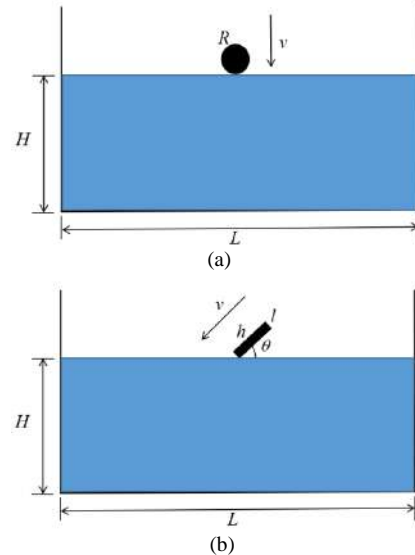


Figure 2. Sketch of the water entry
(a: buoyant cylinder, b: rectangular object)

A. Validation example

To validate the effectiveness of IFSIT algorithm, water entry of a buoyant cylinder is simulated. As shown in Figure 2(a), the length and height of the water is 2m and 1m separately, and the radius of the cylinder is 5.5 mm, which has the same density with water. At first, the cylinder moves downward with an initial velocity 2.955 m/s. These data are consistent with the experiment by Greenhow [23].

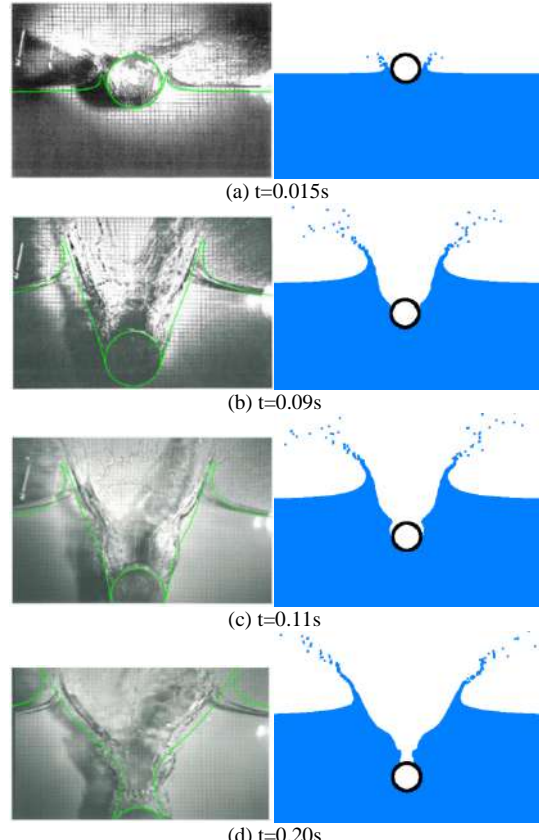


Figure 3. The process of water entry of a buoyant cylinder based on experiment [23], BEM [24] and SPH

Fig 3 shows the snapshots of the SPH results and existing experimental results [23] and boundary element method (BEM) simulation result [24] (the line on the experimental results) at $t=0.015, 0.09, 0.11$ and 0.2 s. It is clear that SPH simulation obtain similar results with the experiment and BEM. Fig. 4 shows the experimental observations by Greenhow and SPH results with coupled dynamic SBT algorithm. It is clear that the obtained SPH results are close to experimental observations, and this I-FSBT algorithm is effective for moving solid boundaries. It is noted that the SPH method can not only well predict the free surface morphology and position of the horizontal cylinder before its exit from water, but also well describe the water detachment, breakup, splash and wave generation.

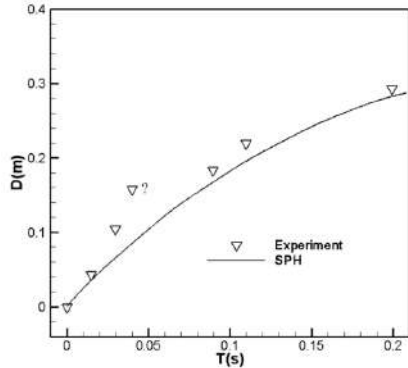


Figure 4. Comparison between the penetration depth measured experimentally [23] and predicted by the SPH method.

B. Water entry with initial velocity 5m/s.

To research the influence of different directions in water entry problem, three cases are simulated. As shown in Fig 2(b), the length and height of the water is $L=4$ m, $H=2$ m separately, and the length and height of the rectangular object is $l=0.05$ m, $h=0.3$ m. θ is the tilt angle between the object and the water surface, and in the three case, θ is $30^\circ, 60^\circ$ and 90° separately. The density of the rectangular object is 6648kg/m^3 . Initial particle spacing is 0.005 m, and about 330000 particles are used in the simulation. In the three case, the size of initial velocities are all 5m/s . Take $\theta=30^\circ$ for example, $v_x=-4.33\text{m/s}$, $v_y=-2.5\text{m/s}$, and the other can also be obtained in similar way.

Fig 5, 6 and 7 show the pressure evolution of water entry with $\theta=30^\circ, 60^\circ$ and 90° . When the rectangular object impacts the water surface, a pressure wave produces and then transmits to bottom. After the interaction with the solid wall, the pressure wave changes its direction and forms a reflection wave. In the process of interaction between objects and fluids, the velocity of the fluid is lower than the velocity of the object, and a large cavity is formed. Then, under the action of gravity and impact force, the cavity begin to close, and the shape of the cavity is constantly changing and the volume is shrinking, with a high pressure appeared in the end of the cavity. It is obvious that the evolution of the cavity is greatly influenced by the tilt angle θ . When $\theta=30^\circ$, the cavity begin to close and shrink after $t=0.35\text{s}$. However, when $\theta=60^\circ$ and 90° , the cavities have begun to shrink at $t=0.2\text{s}$. when the tilt angle is different, the change of the cavity is also very large.

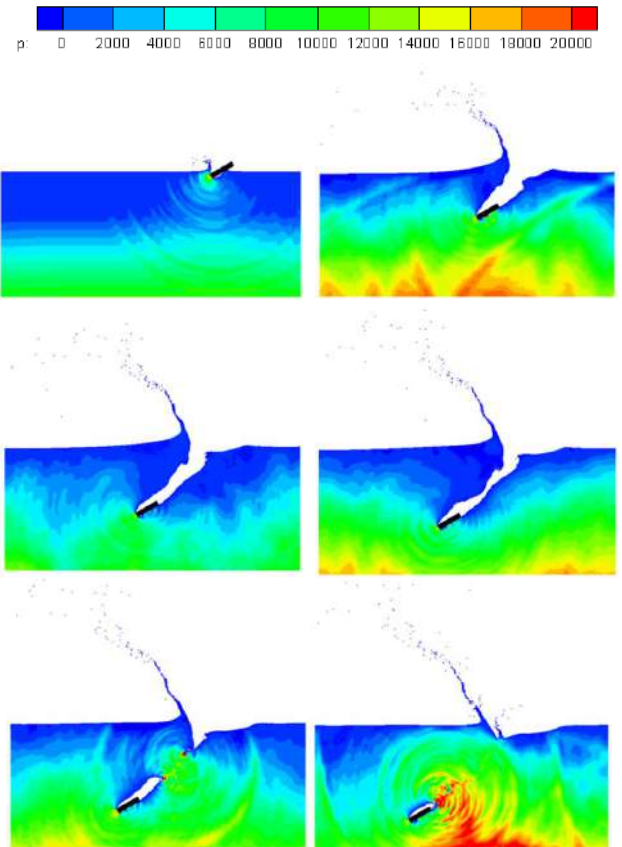


Figure 5. Pressure evolution of water entry with $\theta =30^\circ$ at $0.03, 0.2, 0.3, 0.35, 0.4$ and 0.45s .

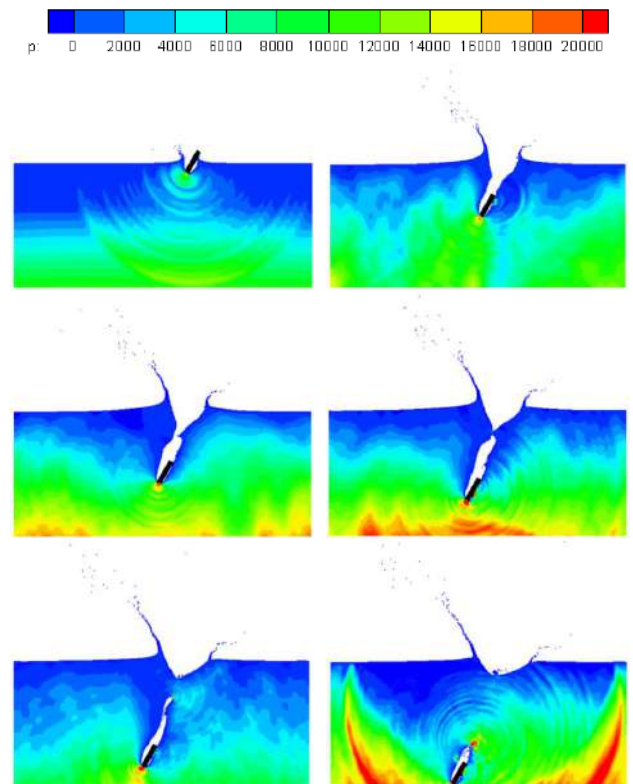


Figure 6. Pressure evolution of water entry with $\theta = 60^\circ$ at 0.03, 0.15, 0.2, 0.25, 0.3 and 0.35s.

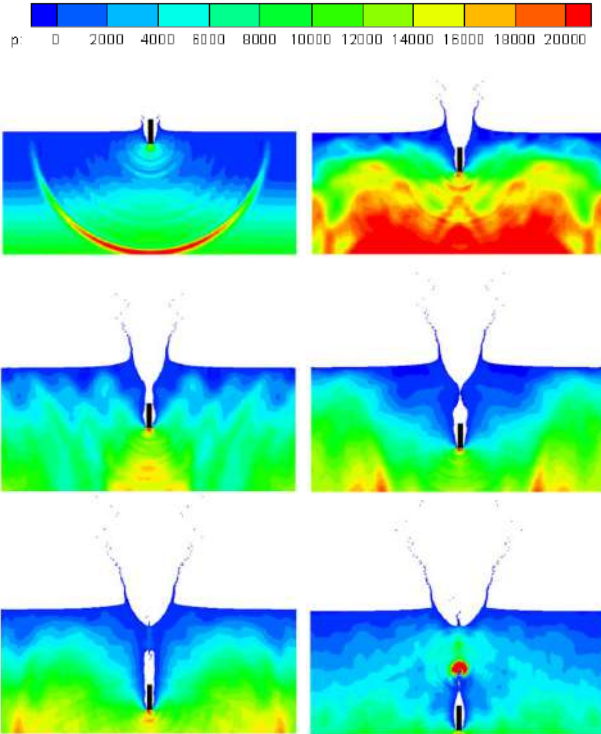


Figure 7. Pressure evolution of water entry with $\theta = 90^\circ$ at 0.03, 0.1, 0.15, 0.2, 0.25 and 0.3s.

In the three cases, the displacements of the centroid are also be researched, as shown in Fig. 8. It is obvious that before $t=0.1$ s, the displacements of the three cases are similar. With time increases, the difference of the displacement is getting bigger, and the smaller the tilt angle, the greater the resistance of the object from the water.

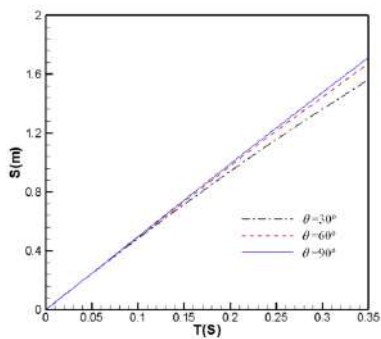


Figure 8. Displacement of the centroid with initial velocity 5m/s ($\theta = 30^\circ, 60^\circ, 90^\circ$)

C. Water entry with initial velocity 20m/s.

In water entry problem, the initial velocity will effect the fluid field greatly. Therefore, to research the influence of different velocity, three cases are simulated in these section. Except for the initial velocity 20m/s, all other data are same as the last three case.

p: 0 10000 20000 30000 40000 50000 60000 70000 80000 90000 100000

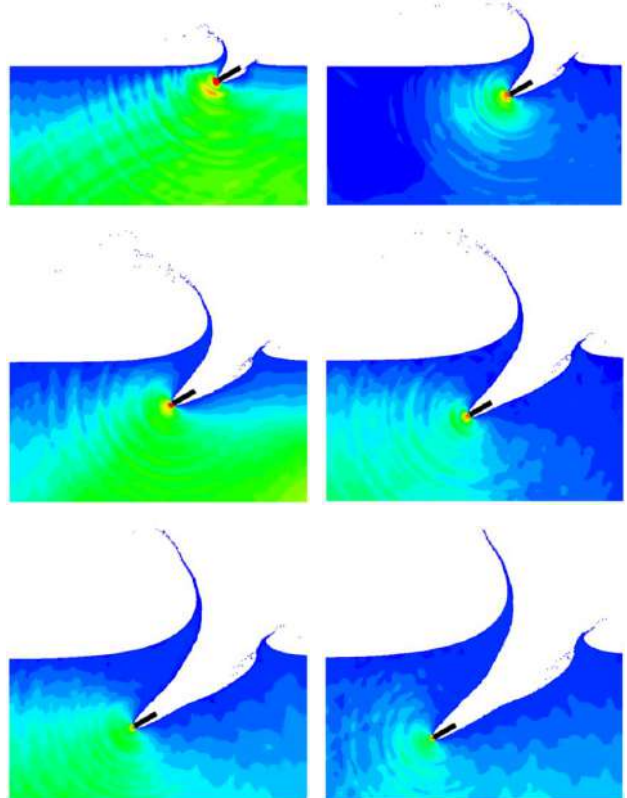


Figure 9. Pressure evolution of water entry with $\theta = 30^\circ$ at 0.02, 0.4, 0.6, 0.8, 0.10 and 0.12s.

p: 0 10000 20000 30000 40000 50000 60000 70000 80000 90000 100000

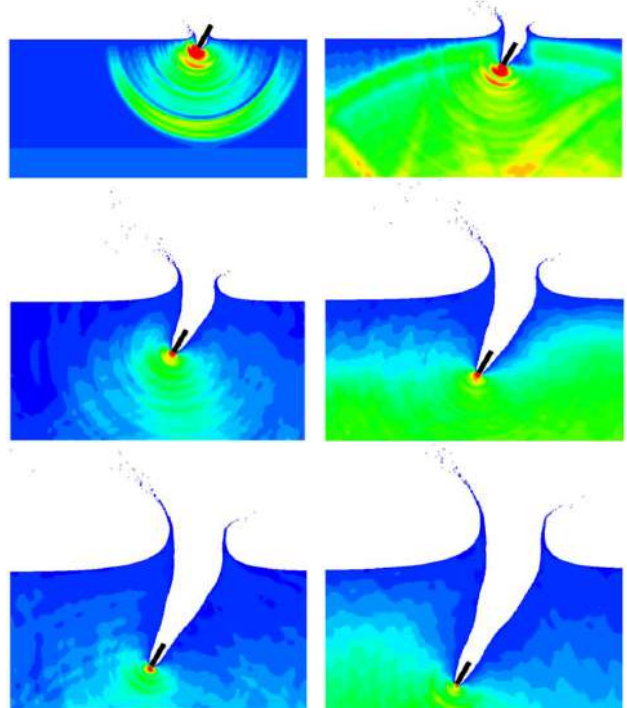


Figure 10. Pressure evolution of water entry with $\theta = 60^\circ$ at 0.006, 0.02, 0.04, 0.06, 0.08, and 0.1s.

Fig. 9, 10 and 11 show the pressure evolution of water entry with $\theta = 30^\circ$, 60° , 90° and a initial speed 20m/s. Comparing with the Fig 5, 6 and 7, there are big differences in the flow pattern. In the whole process of the water entry, the fluid near the rectangular objects is still separated from each other. The cavities are always in an increasing state. The closure and shrinkage of the cavity has never appeared. However, the tilt angle has a great influence on the flow field pressure distribution. Comparing with the cases with initial velocity 5m/s, the domain with high pressure is always at the forefront of the rectangular objects.

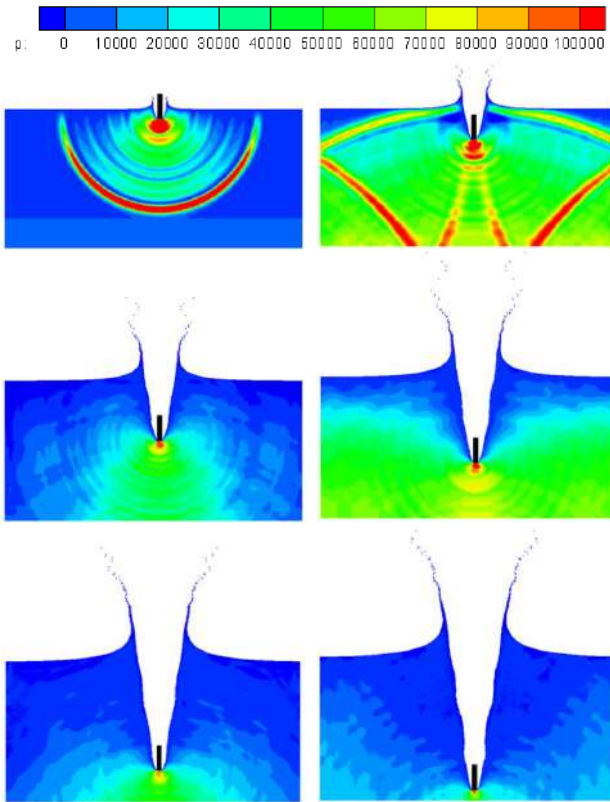


Figure 11. Pressure evolution of water entry with $\theta = 90^\circ$ at 0.006, 0.02, 0.04, 0.06, 0.08 and 0.1s.

In the three cases, the displacements of the centroid are also be researched, as shown in Fig 12. It can be observed that the displacements of the centroid are similar in the process of the movement. Even if the time continues to increase, the differences are still very small. It indicate that, for the water entry problem with a relatively high speed, the effect of the tilt angle on the displacement is very small.

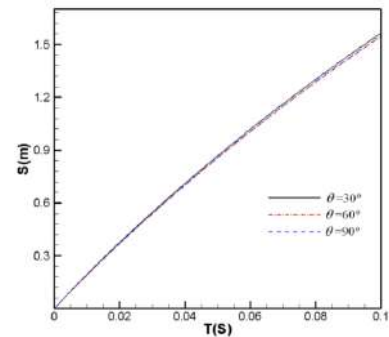


Figure 12. Displacement of the centroid with initial velocity 20m/s ($\theta = 30^\circ$, 60° , 90°)

IV. CONCLUSIONS

This paper presents a study of water entry problems with improved SPH method. An improve fluid-solid interface treatment (I-FSIT) algorithm are used to deal with the interface between fluid and moving bodies. Several water entry cases with different velocities and tilt angles are simulated, their effects to fluid field and movement of the rigid body are researched. The following conclusions can be drawn:

- 1) The I-FSIT algorithm presented in this paper can simulated the interaction between the fluid and moving bodies accurately.
- 2) For the moving body with low speed, the evolution of the cavity is greatly influenced by the tilt angle, and the smaller the tilt angle, the greater the resistance of the object from the water.
- 3) For the moving body with relatively high speed, the closure and shrinkage of the cavity didn't appeared. Even if the tilt angles are very different, their displacement curve of the centroid are similar.

ACKNOWLEDGEMENT

This work has been supported by the National Natural Science Foundation of China (11602045, 21676037), NSAF (Grant No.U1530110), Natural Science Foundation of Chongqing (cstc2016jcyjA0373), STRPCMEC (Grant No.KJ1600918).

REFERENCES

- [1] A. Anju, A. Maruoka and M. Kawahara, "2D fluid structure interaction problems by an arbitrary lagrangian-eulerian finite element method," International Journal of Computational Fluid Dynamics, 1997, vol.8, pp. 1-9.
- [2] P. Z. Lin, "A fixed-grid model for simulation of a moving body in free surface flows," Computers & Fluids, 2007, vol.36, pp. 549-561.
- [3] Q. T. Chen, B. Y. Ni, S. P. Chen and J. G. Tang, "Numerical simulation of the water entry of a structure in free fall motion," Journal of Marine Science and Application, 2014, vol. 13, pp. 173–177.
- [4] W. Peng and Q. Wei, "Solving 2-D water entry problems with a CIP method and a parallel computing algorithm," Marine Systems & Ocean Technology, 2016, vol. 11, pp. 1-9.
- [5] R. A. Gingold and J. J. Monaghan, "Smoothed particle hydrodynamics-theory and application to non-spherical stars," Monthly Notices of the Royal Astronomical Society. 1977, vol.181, pp. 375-89.
- [6] L.B. Lucy, "A numerical approach to the testing of the fission hypothesis," The Astronomical Journal. 1977, vol. 82, pp. 1013-24.
- [7] M. B. Liu and G. R. Liu, "Smoothed particle hydrodynamics (SPH): an overview and recent developments," Archives of Computational

- Methods in Engineering, 2010, vol.17, pp. 25-76.
- [8] G. Oger, M. Doring, B. Alessandrini and P. Ferrant, "Two-dimensional sph simulations of wedge water entries," Journal Of Computational Physics, 2006, vol. 213, pp. 803-822.
 - [9] S. D. Shao, "Incompressible sph simulation of water entry of a free-falling object," International Journal For Numerical Methods In Fluids, 2009, vol.59, pp. 91-115.
 - [10] S. Marrone, A. Colagrossi, M. Antuono, C. Lugni and M. P. Tulin, "A 2d+ δ sph model to study the breaking wave pattern generated by fast ships," Journal of Fluids and Structures, 2011, vol.27, pp. 1199-1215.
 - [11] F. Xu, H. Liu, "Numerical simulation of 2-D bow flare slamming using SPH method, " Chinese Journal of Hydrodynamics. 2013, vol.28, pp. 585-590.
 - [12] K. Gong, H. Liu and B. L. Wang, "An Improved Boundary Treatment Approach for SPH Method," Chinese Quarterly of Mechanics. 2008, vol.29, pp. 507-514.
 - [13] X. F. Yang, S. L. Peng and M. B. Liu, "Simulation of Water Entry with Smoothed Particle Hydrodynamics Method," Chinese Journal of Computational Physics. 2011, vol. 28, pp. 523-528.
 - [14] M. B. Liu, J. R. Shao and J. Z. Chang, "On the treatment of solid boundary in smoothed particle hydrodynamics," Science China Technological Sciences, 2012, vol.55, pp. 244-254.
 - [15] M. B. Liu, J. R. Shao and H. Q. Li, "Numerical simulation of hydro-elastic problems with smoothed particle hydro-dynamics method," Journal of Hydrodynamics, 2013, vol. 25, pp. 673-682.
 - [16] G. R. Liu and M. B. Liu, "Smoothed particle hydrodynamics: A meshfree particle method," 2003, World Scientific Pub Co Inc.
 - [17] J. P. Morris, "Analysis of smoothed particle hydrodynamics with applications," PhD Thesis, Monash University, 1996.
 - [18] J. P. Morris, P. J. Fox and Y. Zhu, "Modeling low reynolds number incompressible flows using SPH," Journal of computational physics, 1997, vol.136, pp. 214-226.
 - [19] B. Rogers and R. Dalrymple, "SPH modeling of tsunami waves," Advanced Numerical Models for Simulating Tsunami Waves and Runup, 2007, pp. 75-101
 - [20] G. M. Gomez and R. A. Dalrymple, "Using a three-dimensional smoothed particle hydrodynamics method for wave impact on a tall structure," Journal of Waterway Port Coastal and Ocean Engineering-Asce, 2004, vol.130, pp. 63-69.
 - [21] A. Colagrossi and M. Landrini, "Numerical simulation of interfacial flows by smoothed particle hydrodynamics," Journal of computational physics, 2003, vol.191, pp. 448-475.
 - [22] T. Rabczuk, T. Belytschko and S. Xiao, "Stable particle methods based on Lagrangian kernels," Computer Methods in Applied Mechanics and Engineering, 2004. vol.193, pp. 1035-1063.
 - [23] M. Greenhow and W. M. Lin, "Nonlinear free surface effects: Experiments and theory," Department of Ocean Engineering, 1983, Report No.83.
 - [24] H. Sun and O. M. Faltinsen, "Water impact of horizontal circular cylinders and cylindrical shells," Applied Ocean Research, 2006, vol.28, pp. 299-311.

Construction of Two-dimensional SPH Numerical Wave Tank

Jingyu Wang, Fei Xu, Yang Yang

School of Aeronautics

Northwestern Polytechnical University

Xi'an China

xufei@nwpu.edu.cn

Abstract—a numerical wave tank is established based on the SPH method and accompanied with relevant numerical processing techniques. In the construction of the numerical tank, apart from the swinging plate at the upstream that excites the motion of water to generate the required waves, an artificial viscosity sponge layer is introduced at the downstream to remove the unwanted wave reflections from the boundaries, which ensures the wave characteristic of the workspace. The results from the SPH model show relatively good agreement with the theory solution. At the same time, the reason of errors has been discussed for the further study.

I. INTRODUCTION

Wave research has always been a hot topic in hydrodynamics. In order to better study the mechanism and characteristics of wave propagation, fragmentation and interaction with various structures, physical tanks are established to narrow these problems to the lab. Notwithstanding that, there are some problems in the experiments in physical tank. Model tests in physical tank are not only time-consuming but also strenuous. Its results are easily affected by testing instruments. With the development of computer technology and numerical calculation techniques, the establishment of numerical wave tanks to carry out simulations has displayed a bright future. In recent decades, many researchers have devoted themselves to the study of numerical wave tanks, the core of which is the generation, propagation and elimination of waves. As the wave-maker and wave eliminator occupy the important position in a physical tank, an excellent numerical wave tank should also be able to generate the various wave fields required for systematically study.

In this context, the SPH(Smoothed Particle Hydrodynamics) method, which has advantages in dealing with strong nonlinear wave problems such as overturning, breaking of free surface etc., has been used to establish a simple numerical wave tank to simulate regular waves.

II. NUMERICAL PROCESSING TECHNIQUES

In the present work we use WSPH (the fluid is weakly-compressible) to construct the numerical tank. WSPH is generally more suited for free-surface flows since the boundary condition along the free surface is implicitly

satisfied [1]. Details about WSPH are not repeated and we will list the specific details as follows.

A. The solid boundary treatment

Repulsive function is employed in this context to simulate the interaction between the water and solid boundary. The force/mass on fluid SPH particle i due to boundary particle j is normally written in the form[2]:

$$f_{ij} = \frac{K}{r_{ij}^2} r_{ij} W(r_{ij}/h) \frac{2m_i}{m_i + m_j}. \quad (1)$$

where m_i and m_j denotes the mass of particle i and j respectively. The constant $K = 0.01 c_s^2$, where c_s is the speed of sound.

B. Artificial viscosity

The viscosity ensuring the stability of the numerical algorithm is determined by Π_{ij} for which we choose the form:

$$\Pi_{ij} = \frac{\alpha c_s v_{ij} \cdot r_{ij}}{\rho_{ij} |r_{ij}|} \quad (2)$$

In this expression α is a constant, and the corresponding numerical kinematic viscosity is theoretically given in two dimension by[3]

$$\nu = \alpha c_s h / 8 \quad (3)$$

where h is the smooth length, and the constant α will be discussed later.

C. Free surface detection

In the process of making wave, it is necessary to obtain the time history of wave height at the fixed point. Therefore, the free surface particle detection becomes the key technology in the numerical wave tank by SPH method. In this paper, the following free surface detection method is used [4]:

$$\nabla \cdot r_i = \sum_{j=1}^N \frac{m_j}{\rho_j} r_{ij} \cdot \nabla_i W \quad (4)$$

For the particles inside the fluid, the theoretical value of $\nabla \cdot r_i$ for the one-dimensional problem equals one, and for the two-dimensional problem the value equals two. The value would be much below 2 for surface particles since the number of neighbouring particles are smaller than what it should be. Through uninterruptedly attempting, a criterion of 1.4 is used to determine surface particles.

D. δ -SPH

Although the SPH method has great potential in dealing with the wave problem, the main factor that restricts its development is the instability of the pressure field and attenuation of wave. An alternative approach proposed by Antuono et al.[5], in a manner, improves this problem. A numerical diffusive term has been used inside the continuity equation as follows.

$$\frac{D\rho_i}{Dt} = -\rho_i \sum_j \frac{m_j}{\rho_j} v_{ji} \cdot \nabla_i W_{ij} + \delta h c_s D_i \quad (5)$$

where $\delta = 0.1$, and D_i is the diffusive term. For more details we address the reader to Antuono[5].

III. NUMERICAL MODEL

As shown in figure 1, the numerical wave tank in this work is 50m long, and its water depth is 3m. In the construction of the numerical tank, apart from the swinging plate at the upstream that excites the motion of water to generate the required waves, an artificial viscosity sponge layer is introduced at the downstream to remove the unwanted wave reflections from the boundaries, which ensures the wave characteristic of the workspace. The particle distance in this model is 0.05m, and the smooth length is 1.5 times that of the particle distance.

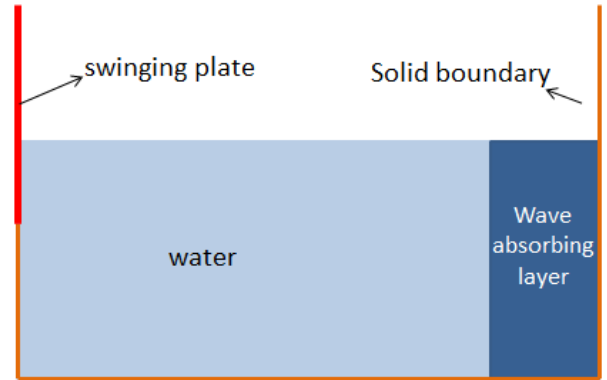


Figure 1. Model of two-dimensional wave tank

A. Upstream boundary condition

Swinging plate is set at the upstream, with simple harmonic motion, to generate regular waves. The amplitude of swinging plate e is as follow:

$$e(y) = 0, 0 \leq y \leq (h-l); \\ e(y) = \frac{E}{l} (y - h + l), (h-l) < y \leq h. \quad (6)$$

The abscissa x is:

$$x = e(y) \sin(\omega t) \quad (7)$$

In this expression ω is the circular frequency of the wave.

The equation of wave profile η in front of the swinging plate can be obtained according to the linear wave-maker theory[6]:

$$\eta(x, t) = C_0 \sinh(k_0 h) \cos(k_0 x - \omega t) + \sum_{n=1}^{\infty} C_n \sin(k_0 y) e^{-k_0 x} \sin(\omega t) \quad (8)$$

$$C_0 = \frac{2E}{k_0 l} \frac{k_0 l \sinh(k_0 h) - \cosh(k_0 h) + \cosh(k_0 h - k_0 l)}{k_0 h + \sinh(k_0 h) \cosh(k_0 h)} \\ C_n = \frac{2E}{k_n l} \frac{k_n l \sinh(k_n h) - \cosh(k_n h) + \cosh(k_n h - k_n l)}{k_n h + \sinh(k_n h) \cosh(k_n h)} \quad (9)$$

where k_0 represents the wave number, h is the depth of the tank, E indicates the amplitude of the swinging plate at the water surface, and l denotes the immersion of the swinging plate. In this work, l is set equal to 1m. The first part on the right side of the expression (8) is the traveling wave, and the second part is the standing wave, which can be ignored after

leaving a certain distance from the swinging plate. Therefore the motion parameters of the swinging plate have been determined.

B. Downstream boundary condition

According to the characteristics of SPH method, a special artificial viscosity term is added to the momentum equation at the downstream of the numerical wave tank. The area where the artificial viscosity is much larger than the viscosity in the other area is called wave-absorbing layer, which has removed the influence of the solid boundary at the end of the tank. The special artificial viscosity follows:

$$\Pi_{ij} = \frac{x - x_0}{l_s} \frac{\alpha c_s v_{ij} \cdot r_{ij}}{\rho_{ij} |r_{ij}|} \quad (10)$$

where x_0 is the abscissa at the beginning of the layer, and x is the abscissa of the particle in the layer. l_s is the length of the layer, which is 1.5 times to twice as much as wavelength(1.5 times is used in this paper). α is a constant that control the effect of eliminating wave. Generally we choose the value in the range [0.6-1.0].

IV. RESULTS AND CONCLUSION

A. Generation of the wave

The influence of speed and amplitude of the swinging plate on the wave generation is elaborated distinctly by the linear wave-maker theory.

In the following H is the height of the wave and λ indicates the length of the wave. Here $\lambda = C_0 \sin(k_0 h)$. There are corresponding amplitude and circular frequency of the swinging plate for different H and λ . For the condition that $H = 0.4\text{m}$, $\lambda = 8\text{m}$, E is calculated from the expression (9), equaling 0.35m. The circular frequency $\omega = \sqrt{2\pi/\lambda}$, which is given by the theory of small-amplitude waves, and is equal to 2.77.

B. Elimination of the wave

In order to check out the performance of the method of elimination the wave used in this paper, we calculated the velocity field in the tank at different times. Before the waves reach the wave-absorbing layer, as is seen in the figure 2, the wave form is stable. By contrast, as the waves enter the layer, the velocity of the particle in the wave will gradually attenuate.

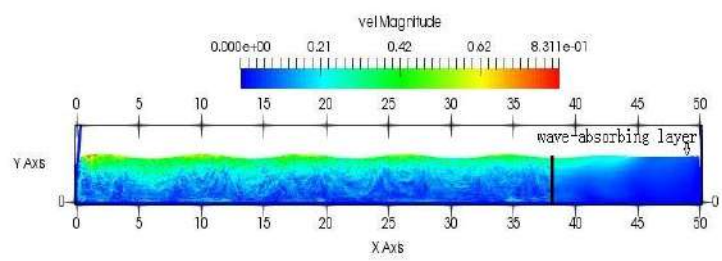


Figure 2. The velocity field of fluid at $t=30\text{s}$

Figure 3 shows the time history of free surface at $x=48$ in the wave-absorbing layer, and figure 4 shows the attenuation of the average wave height in the layer. From this, we can find out that the wave-absorbing layer is able to remove the unwanted wave reflections from the boundaries well.

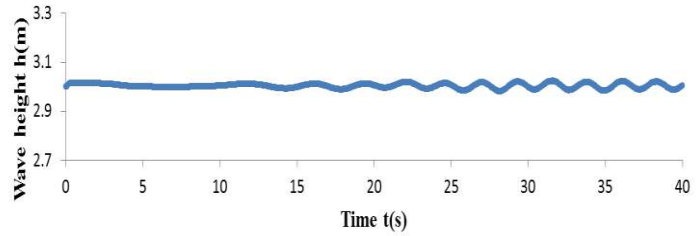


Figure 3. The time history of free surface at $x=48$ in the wave-absorbing layer

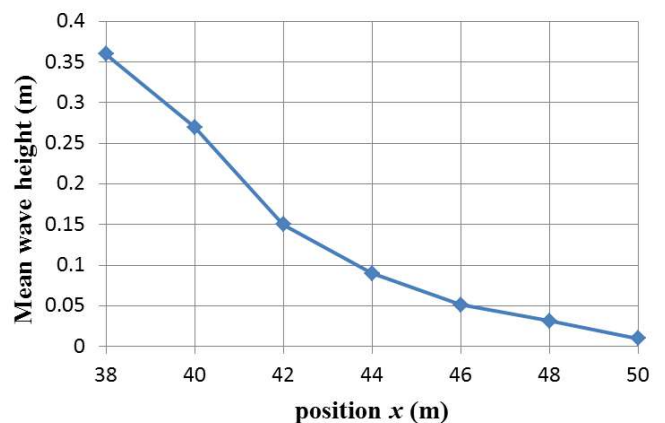


Figure 4. Results of the variation of mean wave height during the wave-absorbing layer

C. Propagation of the wave

When H is 0.4m, and λ is 8m, the time history of free surface at different measure point at workspace calculated by SPH method compared results with theoretical date has been shown in figure 4. Despite of the good agreement with theoretical results which has been shown in the time history, it is obvious that the wave height has gradual attenuation with the propagation of the wave. This is exhibited more clearly from the figure 5.

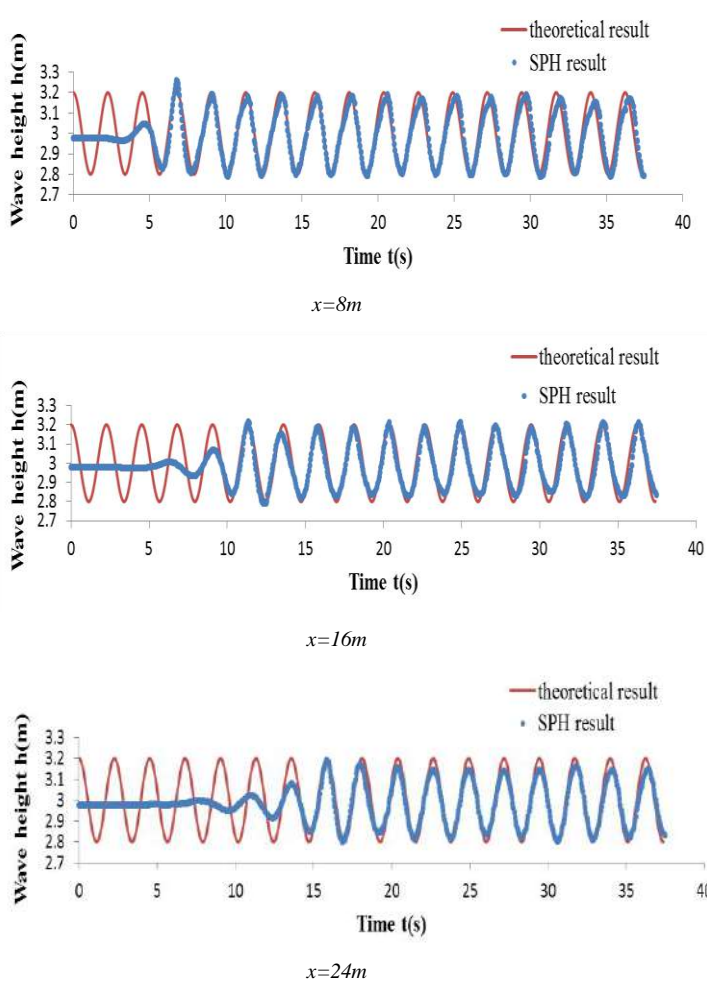


Figure 4. The time history of free surface at different measure point at workspace calculated by SPH method compared results with theoretical date

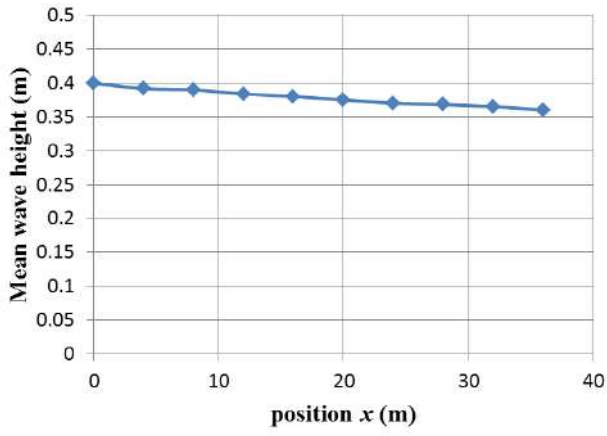


Figure 5. Results of the variation of mean wave height during the tank

We suspect that there may be the following reasons resulting the attenuation:

Firstly, the artificial viscosity causes loss of energy and numerical damping of the wave height. Vaughan[7] has given the law of attenuation, and Antuono[8] also discussed an estimation of the damping effects. As a consequence, the constant α becomes particularly important. If the value of α is too large, a large damping is observed in the long time simulations. So we take a small value, equal to 10^{-6} , to make the waveform smoother.

Secondly, the particle distance dx may have effect on the simulation and result the loss of accuracy. In theory, the smaller the particle distance is, the better the simulation becomes. However, small particle distance will inevitably bring a huge amount of calculation. It is difficult to have both effectiveness and high-accuracy. Therefore particle distance is a parameter that needs to be carefully adjusted to achieve the desired effects. A preliminary discuss about the effect of the ratio λ / dx is carried out in this work and we find not only the wave height but also the wave length has deformed because of inappropriate particle distance. When λ / dx less than about 160, the wave length will get longer as the wave propagates. This condition will be improved if the value of λ / dx becomes greater, and further work remains to be done.

Apart from this, on account of the absence of the integral of the fluid particles near the free surface in the SPH method, the continuity of the field has decreased and the waves have been attenuated during the propagation process. This is the next work we are going to conduct.

REFERENCES

- [1] A. Colagrossi, M. Antuono, D. Le Touzé. Theoretical considerations on the free surface role in the SPH model, Phys. Rev. E 79 (5) (2009) 056701
- [2] Monaghan J J, Kajtar J B. SPH particle boundary forces for arbitrary boundaries[J]. Computer Physics Communications, 2009, 180(10):1811-1820.
- [3] J.J. Monaghan. Smoothed particle hydrodynamics, Rep. Progr. Phys. 68 (2005) 1703–1759.
- [4] Lee E S, Moulinec C, Xu R, et al. Comparisons of weakly compressible and truly incompressible algorithms for the SPH mesh free particle method[J]. Journal of Computational Physics, 2008, 227(18):8417-8436.
- [5] Antuono M, Colagrossi A, Marrone S. Numerical diffusive terms in weakly-compressible SPH schemes[J]. Computer Physics Communications, 2012, 183(12):2570-2580.
- [6] ZHANG Yaqun. The control and realization of wave maker[D]. Wuhan:Wuhan University of Technology,2007:6-10.
- [7] Vaughan G L, Healy T R, Bryan K R, Sneyd, A. D., & Gorman, R. M. An SPH Numerical Wave Tank , Civil Engineering in the Ocean, 2006,6:95~107
- [8] Antuono M, Colagrossi A, Marrone S, et al. Propagation of gravity waves through an SPH scheme with numerical diffusive terms[J]. Computer Physics Communications, 2011, 182(4):866-877.

SPH for the Interaction between Tsunami Wave and Upright Cylindrical Groups

Jing-jun Li & Lei Tian & Yongsen Yang & Liu-Chao Qiu & Yu Han

China Agricultural University

Beijing, China

Lijunjed@163.com

Abstract—The Smoothed Particle Hydrodynamics (SPH) method has proven to be potential in dealing with the wave-structure interactions since it is good at modelling the large deformation and the free surface. Based on the SPH method, this paper verifies the accuracy of a piston-type wave maker for Tsunami wave generation and its application to modelling of the wave interaction with upright cylindrical groups. The weakening effect of the upright cylindrical group on the waves is proven by SPH simulation. The influences of the number of cylindrical layers and the layout of the cylindrical group on the wave weakening have been investigated. (Abstract)

I. INTRODUCTION

Circular cylindrical structures are commonly used in the support structures of offshore wind turbines, oil and gas platforms, offshore mooring dolphins in deep and intermediate waters and near shore coastal structures. But the tsunami poses a serious threat to these structures [1, 2]. Upstanding cylindrical construction engineering group always been built in the offshore areas to eliminate waves to protect buildings on the coast. It can help to dissipate incoming wave energy, regulate water levels, and increase bank stability. Understanding the interaction of waves with these structures is important for accurate design.

There are generally two classes of models for wave simulations. The Laplace equation with fully nonlinear boundary conditions was used for simple wave problems In the early years[3-5], while the Navier–Stokes (N-S) equations with more realistic physical boundary conditions were solved in recent numerical models [6,7]. As a result, various numerical schemes, such as the finite element, finite volume and finite difference methods have been used to solve the N-S equations to investigate the nonlinear water wave propagation and its interaction with the structures [8,9].

The Smoothed Particle Hydrodynamics (SPH) method has emerged as a promising mesh-free Lagrangian modelling technique in the last two decades. The SPH has the advantage of tracking the free surface in an easy and accurate way although the SPH model may use more CPU time than the grid counterpart in some cases. The governing equations are discretized and solved by the individual particles within the computational domain in this approach. SPH was originally developed for the study of astrophysics [10] and then employed to study the wave propagating and

overtopping over coastal structures [11]. A strict incompressible algorithm of the SPH model [12] was developed based on the algorithm of the Moving Particle Semi-implicit (MPS) approach [13] and SPH projection method [14]. Meanwhile it was further improved to simulate wave breaking and post-breaking [15]. The major difference between the incompressible SPH(ISPH) [12] and the standard weakly compressible SPH (WCSPH) [10] lies in that the former employs a strict incompressible formulation to solve the pressure implicitly by a pressure Poisson equation (PPE), while the latter calculates the fluid pressure explicitly by using an equation of state. Both the WCSPH and ISPH show limitations and capabilities. The pressure field has also been improved by different form of diffusive terms in the continuity equation for wave–structure interaction problems [16,17]. For WCSPH, it has been highlighted the better possibility to parallelize the numerical code for simulations in real conditions [18]. Furthermore, the acoustic components related to the use of the state equation can be eliminated by an appropriate filtering in the data post-processing to recover the incompressible solution [19].

In this paper, the WCSPH model will be used to simulate the interaction between tsunami wave and upright cylindrical groups with different condition. And the influence factors of eliminating the wave are studied by numerical simulation, which includes the influence of the number of rows and arrangement of the upright cylindrical groups.

II. METHODOLOGY

A. SPH governing equations

In the SPH method, any particle quantity, f , at the location of \bar{x} is estimated by[20] :

$$f(\bar{x}) \approx \sum_b W(\bar{x} - \bar{x}_b) f_b V_b \quad (1)$$

where W is the weighting function (smoothing kernel) and V_b is equal to m_b/ρ_b . m_b and ρ_b are the mass and density of the b -th particle, respectively. And V_b is the volume of the b -th particle at the location of \bar{x}_b with the scalar quantity f_b .

The SPH method is based on the weakly compressible formulation in this paper, which involves conservation of mass and momentum in their Lagrangian form[21]:

$$\frac{d\rho_a}{dt} = -\sum_b m_b (\bar{u}_b - \bar{u}_a) \cdot \nabla_a W_{ab} \quad (2)$$

$$\frac{d\bar{u}_a}{dt} = -\sum_b m_a \left(\frac{p_a}{\rho_a^2} + \frac{p_b}{\rho_b^2} + \Pi_{ab} \right) \nabla_a W_{ab} + \vec{g} \quad (3)$$

where t is time, g is gravity acceleration, ρ_a is density of particle a . b is the index of the particles neighbor to the particle a . m_b is the mass of the particle b , \bar{u}_a and \bar{u}_b are velocity vectors of the particles a and b , respectively. p_a and p_b are pressures of the particles a and b , respectively. ∇_a stands for the gradient with respect to the coordinates of . Π_{ab} stands for viscous effects, which damps out instability due to chaotic particle movement and also prevents particle interpenetration. In this work, the Sub-Particle Scale (SPS) method [22], is used to represent the turbulent features of the flow.

Particle movement is governed by the XSPH correction method[21]:

$$\frac{d\bar{x}_a}{dt} = \bar{u}_a + \varepsilon \sum_b m_b \left(\frac{\bar{u}_a - \bar{u}_b}{\rho_{ab}} \right) W_{ab} \quad (4)$$

where $\varepsilon=0.5$ is a parameter and $\rho_{ab}=1/2(\rho_a+\rho_b)$.

The below equation of state, relates the pressure to the flow density[10]:

$$p = B \left(\left(\frac{\rho}{\rho_0} \right)^{\gamma} - 1 \right) \quad (5)$$

where $\rho_0=1000 \text{ kg/m}^3$ is the reference density of flow, $\gamma=7$ is a parameter for water, and B is selected such that compressibility of flow is kept under 1%.

The Symplectic algorithm is used for time-stepping [20]. This technique has shown more accurate results comparing to others [23].

To overcome pressure fluctuations, the Moving Least Squares (MLS) approach is used to re-assign a density to each particle[24] in every 30 time-steps according to:

$$\rho_a^{new} = \sum_b \rho_b \tilde{W}_{ab} \frac{m_b}{\rho_b} \quad (6)$$

where \tilde{W}_{ab} is the corrected kernel, calculated as follow:

$$\tilde{W}_{ab} = \{ \psi_0(\bar{x}_a) + \psi_{1x}(\bar{x}_a)(x_a - x_b) + \psi_{1z}(\bar{x}_a)(z_a - z_b) \} W_{ab} \quad (7)$$

with x and z are the coordinates denoting horizontal and vertical positions, respectively. ψ is the correction vector which can be calculated according to:

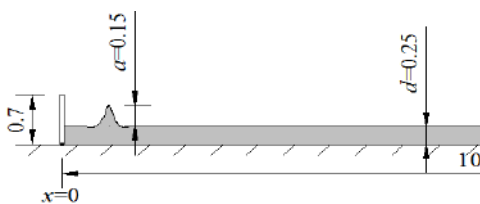


Figure 1. Prototype size(m)

$$\psi_0(\bar{x}_a) = \begin{Bmatrix} \psi_0 \\ \psi_{1x} \\ \psi_{1z} \end{Bmatrix} = \left[\sum_b w_b(\bar{x}_a) [\Phi] V_I \right]^{-1} \begin{Bmatrix} 1 \\ 0 \\ 0 \end{Bmatrix} \quad (8)$$

matrix $[\Phi]$ is given by:

$$[\Phi] = \begin{bmatrix} 1 & (x_a - x_b) & (z_a - z_b) \\ (x_a - x_b) & (x_a - x_b)^2 & (z_a - z_b)(x_a - x_b) \\ (z_a - z_b) & (z_a - z_b)(x_a - x_b) & (z_a - z_b)^2 \end{bmatrix} \quad (9)$$

B. Boundary conditions

In SPH, due to particles move according to their Lagrangian velocities, so no kinematic boundary condition is needed at the location of the free surface (in the absence of surface stresses). For solid walls, dynamic boundary condition is implemented. In this way, the boundary fluid particles are either fixed in their positions, or move according to a prescribed law, e.g. wavemaker motion[25].

In the numerical flume, the solitary wave was generated by the paddle movement. The required motion of the wave maker is given by Goring as[26]:

$$x_p(t) = \frac{a}{k_p} (\tanh \chi(t) + \tanh(\frac{k_p}{h} \lambda)) \quad (10)$$

where $x_p(t)$ is the time history of the paddle location, t represents the time, a is the solitary wave height, k_p is defined as $(3a/4h)^{0.5}$, h is the still water depth, λ is $3.8/k_p$. The parameter $\chi(t)$ is calculated by using:

$$\chi(t) = \frac{k_p}{h} (c_w t - x_p(t) - \lambda) \quad (11)$$

in which c_w is $(g(h+a))^{0.5}$. It is clear that $x_p(t)$ appears in the above two equations and can be found by iteration methods such as Newton-Raphson.

III. VERIFICATION OF THE MODEL

In order to show the effectiveness of SPH technique, an numerical simulation of a solitary wave propagation and impact on a solid wall with 120° inclination was performed. The corresponding physical experiment was carried out by Zheng et al.[27] in a 3-D wave flume with piston wave maker in Harbin Engineering University (HEU). The schematic diagram of the wave tank is shown in Figure 1. The wave tank length is $L = 10 \text{ m}$, the water width is 0.7 m and the water depth is $d = 0.25 \text{ m}$. The solitary wave height is $a = 0.15 \text{ m}$. In the SPH computations, the initial particle spacing is chosen to be 0.02 m and the time step kept constant as 0.00001 s .

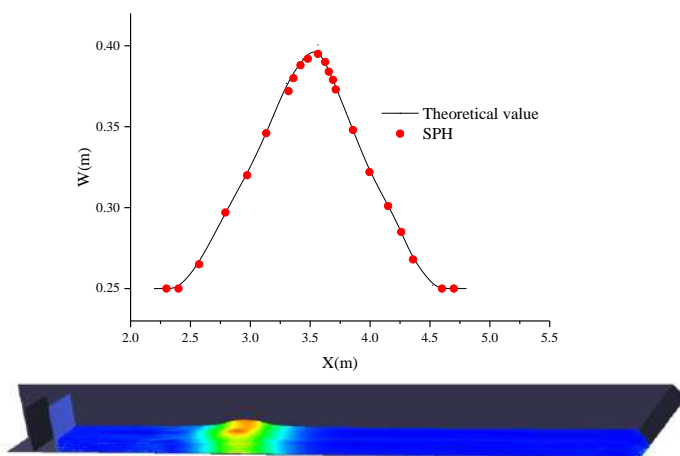


Figure 2. Validation of piston-type wave maker condition in SPH

Figure 2 shows the computed free surface profile with the analytical solution the wave. It shows that the numerical wave surfaces agree well with the analytical ones.

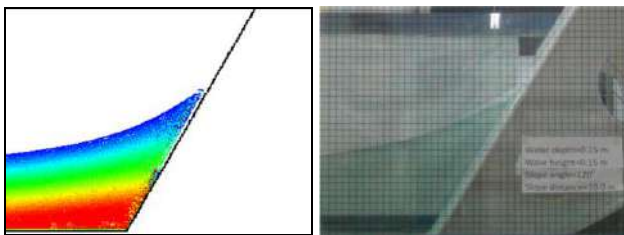


Figure 3. The interaction between waves and slopes: Comparison of SPH (left) to experimental value (right)

A snapshot of the computed wave profile with the experimental photo is be shown as Figure3, including the pressure contour distributions in the fluid domain. It shows again that the wave elevation profile obtained by SPH can achieve a good agreement with the laboratory photograph, and the pressure distribution of wave field is quite stable and noise-free.

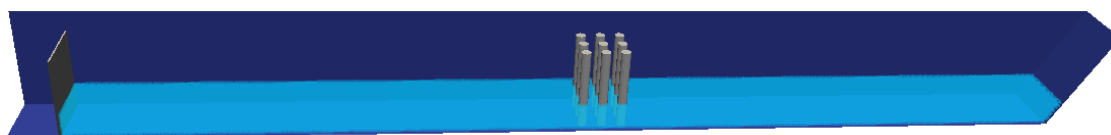
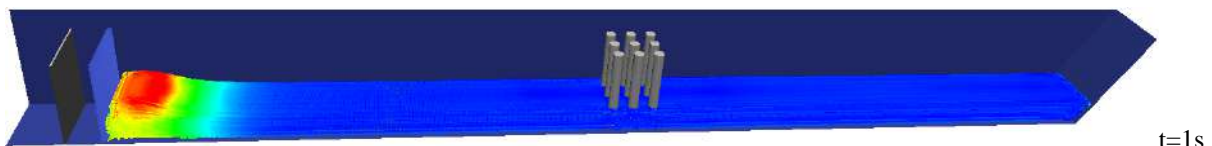


Figure 5. The establishment of the model

Figure 6 shows the propagation of waves under three rows of arrangement.



IV. THE WAVE INTERACTION WITH UPRIGHT CYLINDRICAL GROUPS

The presence of the cylinde in water can weaken the elevation of the waves. Therefore, the strength of the waves can be weakened by constructing a cylindrical group, thereby reducing the erosion effect of the waves on the bank and shore structures. In this section, we mainly study the effect of different cylindrical layers and different arrangement of different groups on the wave. The types of solitary waves used in this chapter are the same as those in Chapter 3, and are therefore not repeated here.

A. The impact of different layers

This section mainly simulates the effect of the number of rows of cylindrical groups on the weakening effect of waves under the same wave area. The simulation conditions include the following four as free wave,one-row arrangement,two-row arrangement and three-row arrangement. A schematic diagram illustrating the numerical setup is given in Figure 4.

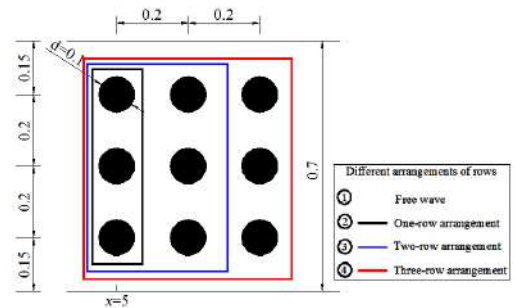


Figure 4. Cylindrical group layout(m)

By increasing the set of cylinders, the model of Figure 5 is established on the basis of the model of Figure 1.

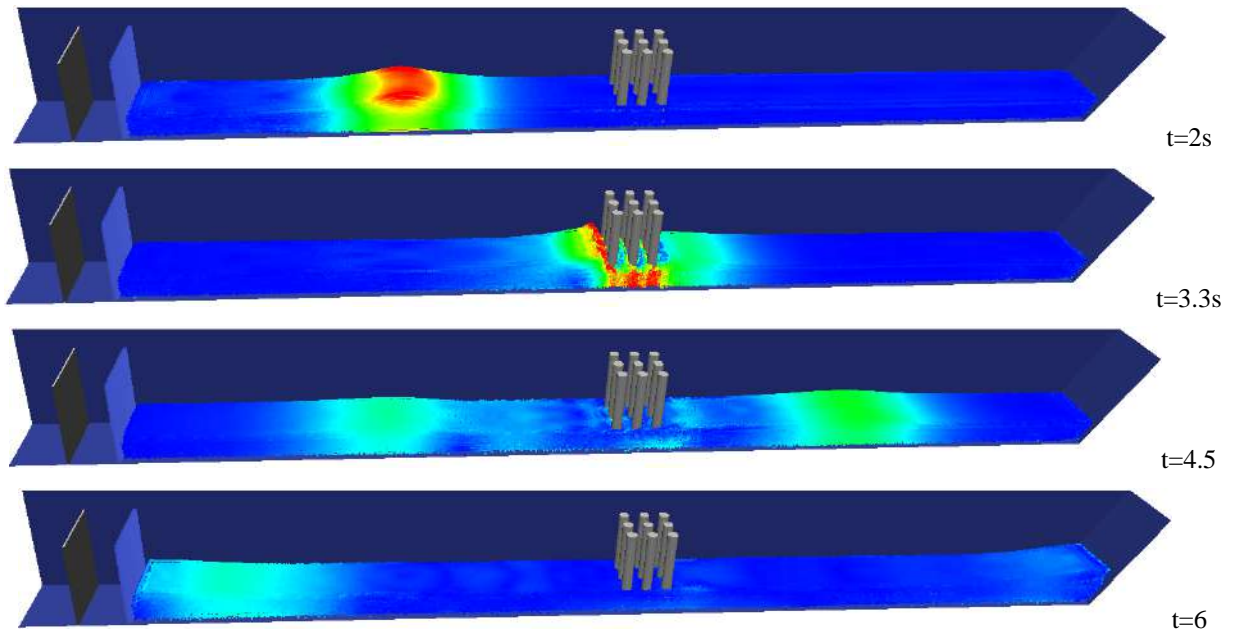


Figure 6. A snapshot of the computed wave propagation

When the waves pass through the cylindrical group, the cylinder will have a hindrance to it. Draw the water level elevation line along the middle section as shown in Figure 7.

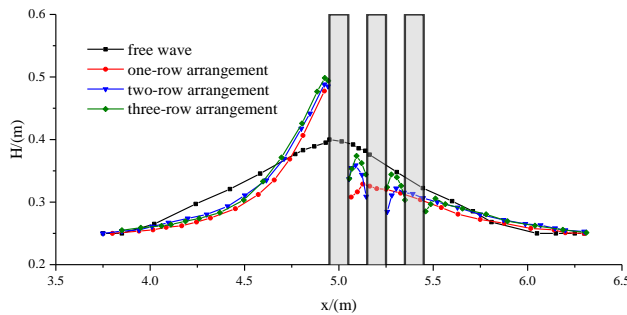


Figure 7. The free surface of the midline section of the cylindrical group under different working conditions

From Figure 7, the phenomenon could be seen that the setting of the cylinder in the group can play a role in weakening the crest. Along the middle section of the water level elevation line, the cylinder has the effect of blocking the waves. It produces the phenomenon of backwater and slows down the role of fluctuations. With the increase in the number of rows of cylindrical groups, the water level in front of the first row of cylinders gradually increased. When there is no cylinder group, the water level is the water level at the crest 0.4m. After the addition of the cylindrical group, from one row to three rows of arrangement, the water level elevation before the first row of cylinders along the center line is 0.477m, 0.488m and 0.498m respectively. Compared with the non-cylindrical group, the water level increased 19.3%, 22.0% and 24.5% respectively. The increase in water level will affect the force of the first row of cylinders. The force between the water wave and the cylinder is higher than the hydrostatic pressure. The local pressure diagram is shown in Figure 8.

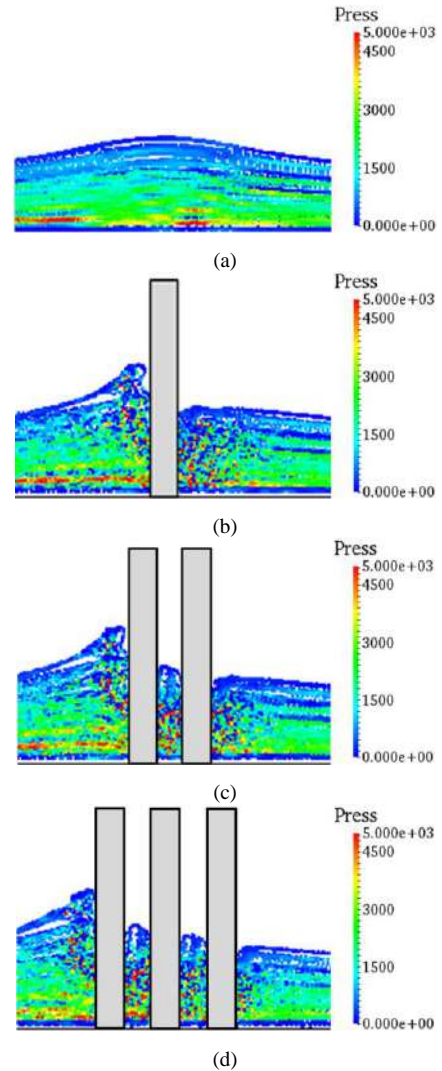


Figure 8. pressure curve of midline section of cylindrical group under different working conditions at 6s((a) free wave; (b) one-row arrangement; (c) two-row arrangement; (d) three-row arrangement).

A reference point A is set on the upstream side of the bottom of the first row of the middle cylinders to detect the pressure and to plot the pressure (Figure 9) under different working conditions.

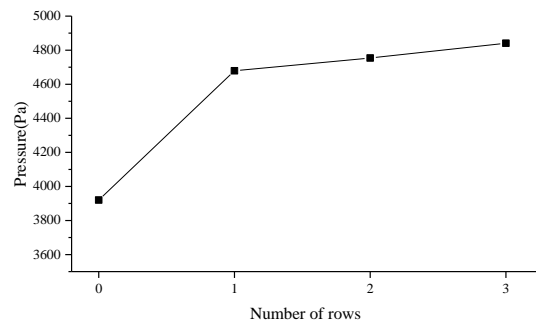


Figure 9. Pressure at point A

In Figure 9, with the increase in the number of rows of cylindrical groups, the pressure value at point A is gradually increased. Therefore, in the process of designing the bearing capacity of the cylinder, the number of rows of the cylinder should be taken into account.

By setting the slope section and observing the climbing height of the wave in the slope section, the weakening effect of the group on the wave can be observed intuitively. Figure 10 show the free surface of the slope section when the wave climbs to the highest point.

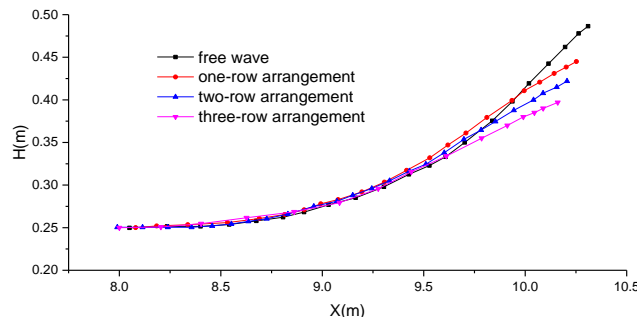


Figure 10. Free surface at the slope

With the increase in the number of rows of the cylindrical groups, the cylinder group acted as a weakening effect on the waves, and the climbing height of the wave gradually decreased. When there is no cylinder group, the climb height of the wave is 0.486m. After the addition of the cylindrical group, from one row to three rows of arrangement, the climb height of the wave is 0.445m, 0.422m and 0.397m respectively. Through the climb height of the wave, draw the relationship between the elimination coefficient and the number of rows of columns as Figure 11.

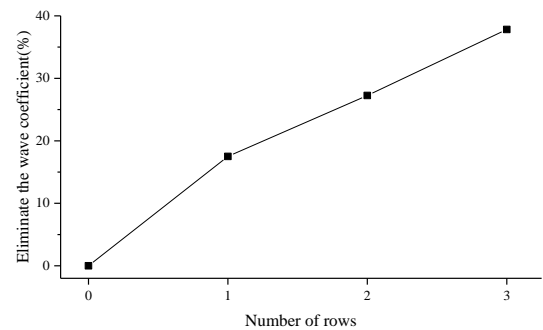


Figure 11. Eliminate the wave coefficient

The eliminate the wave coefficient is 17.51% while only one-row arrangement. The two is 27.25%. The three is 37.82%. So by increasing the number of layers of the cylinder can enhance the ability to weaken the waves in the actual project.

B. Different arrangement

This section mainly simulates the effect of different arrangement of cylindrical groups on the weakening effect of waves under the same wave area. In this paper, the analysis of the cylindrical group layout as following, rectangular arrangement, triangular arrangement (as Figure 4) and quincunx arrangement, the working conditions shown in the Figure 12.

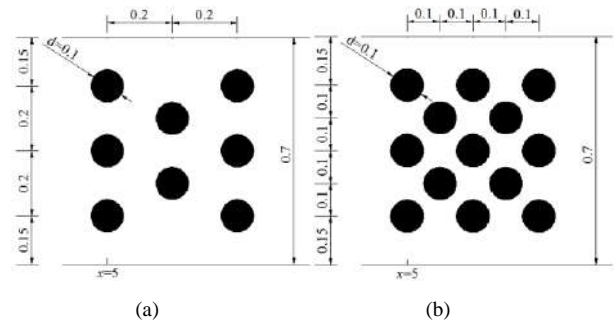


Figure 12. triangular (a) and quincunx (b) arrangement(m)

Figure 13 and Figure 14 show the water level elevation lines of the intermediate interface under the triangular arrangement and the quincunx arrangement.

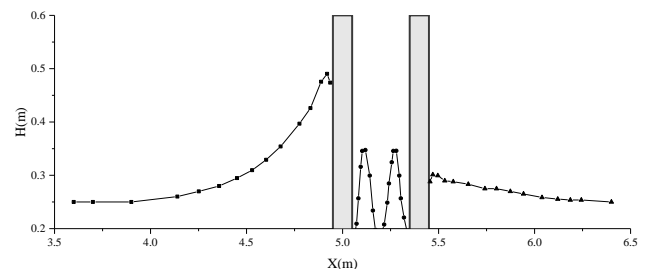


Figure 13. The free surface of triangular arrangement in the midline section of the cylindrical group

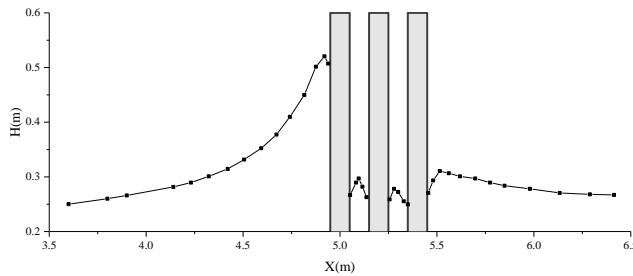


Figure 14. The free surface of quincunx arrangement in the midline section of the cylindrical group

Compared with the three-row arrangement in Figure 7, the water level of the triangular arrangement and the quincunx arrangement are 0.490m and 0.520m. The water level of the quincunx arrangement is the higher, and the pressure on the cylinder is also greater.

The free surface of the slope section is shown as Figure 15.

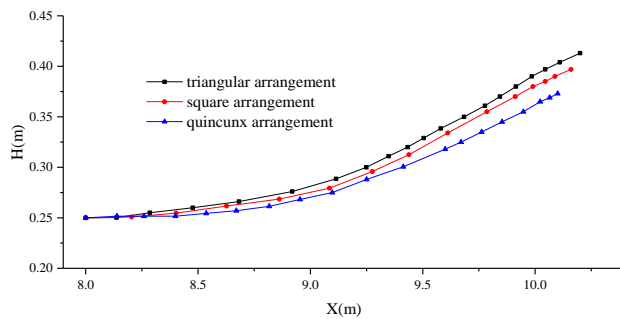


Figure 15. Free surface at the slope

Wave in the slope of the climb height is also different with different arrangements. The climb height of triangular arrangement is 0.490m; the square arrangement is 0.498; the quincunx is 0.520m. Draw a comparison of the elimination wave coefficients as Figure 16.

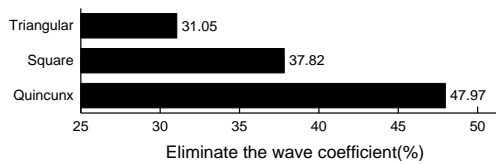


Figure 16. Eliminate the wave coefficient

The eliminate the wave coefficient of triangular arrangement is 31.05%, the square arrangement is 37.82% and the quincunx arrangement is 47.99%. In the case of the same area of the wave, the quincunx arrangement is the best, but The number of cylinders is the largest, there are as many as 13; square arrangement followed, the number is 9; triangular arrangement effect is poor, but the number of cylinders is the least by 8.

RESULTS AND DISCUSSIONS

In this paper, the wave making process is well simulated through SPH. The calculated results of the height of the wave are found to be in a reasonable range compared with the

experimental results. The numerical calculation verifies the accuracy of the SPH method for the simulated wave and the wave height after climbing on the slope. By using this method, this paper simulates the weakening effect of upright cylindrical group on the wave. The results show that the elimination of the wave group is getting better and better with the increase of the number of layers of the wave group. In the same layout area, the laying of the cylindrical group of different ways to eliminate the effect of the waves is different. Commonly arranged in a quincunx arrangement, square layout, triangular layout. From the perspective of eliminating the waves, in turn from the quincunx arrangement, square layout, triangular layout of the anti-wave effect is gradually reduced.

ACKNOWLEDGEMENT

The authors are grateful for funding from the National Natural Science Foundation of China (Grant No. 11772351 and Grant No. 11172321) and the Scientific Research and Experiment of Regulation Engineering for the Songhua River Mainstream in Heilongjiang Province, P.R. of China (Grant No. SGZL/KY-12).

REFERENCES:

- [1] M.R. Motley, H.K. Wong, X. Qin, A.O. Winter, M.O. Eberhard, Tsunami-Induced Forces on Skewed Bridges, Journal of Waterway Port Coastal & Ocean Engineering, 142(2015) 4015025.
- [2] H.K. Wong, Three-Dimensional Effects of Tsunami Impact on Bridges, (2015).
- [3] S.T. Grilli, P. Guyenne, F. Dias, A fully non - linear model for three - dimensional overturning waves over an arbitrary bottom, Int J. Numer Meth Fl, 35(2015) 829-867.
- [4] M.S. Celebi, Fully Nonlinear 3-D Numerical Wave Tank Simulation, J. Ship Res, Vol.42(1998) 33-45.
- [5] Q.W. Ma, G.X. Wu, R.E. Taylor, Finite element simulations of fully non - linear interaction between vertical cylinders and steep waves. Part 2: numerical results and validation, Int J. Numer Meth Fl, 36(2001) 287-308.
- [6] W. Yue, C.L. Lin, V.C. Patel, Numerical simulation of unsteady multidimensional free surface motions by level set method, Int J. Numer Meth Fl, 42(2003) 853-884.
- [7] D. Greaves, Simulation of interface and free surface flows in a viscous fluid using adapting quadtree grids, INT J. Numer Meth Fl, 44(2004) 1093-1117.
- [8] P. Wang, Y. Yao, M.P. Tulin, An efficient numerical tank for non - linear water waves, based on the multi - subdomain approach with BEM, Int J. Numer Meth Fl, 20(2010) 1315-1336.
- [9] G.X. Wu, Z.Z. Hu, Simulation of Nonlinear Interactions between Waves and Floating Bodies Through a Finite-Element-Based Numerical Tank, Proceedings of the Royal Society A Mathematical Physical & Engineering Sciences, 460(2004) 2797-2817.
- [10] J.J. Monaghan, Simulating Free Surface Flows with SPH, J. Comput Phys, 110(1994) 399-406.
- [11] M. Gómez-Gesteira, D. Cerqueiro, C. Crespo, R.A. Dalrymple, Green water overtopping analyzed with a SPH model, Ocean Eng, 32(2005) 223-238.
- [12] S. Shao, E.Y.M. Lo, Incompressible SPH method for simulating Newtonian and non-Newtonian flows with a free surface, Adv Water Resour, 26(2003) 787-800.
- [13] S. Koshizuka, Y. Oka, Moving-Particle Semi-Implicit Method for Fragmentation of Incompressible Fluid, Nuclear Science & Engineering, 123(1996) 421-434.
- [14] S.J. Cummins, M. Rudman, An SPH Projection Method, J. Comput Phys, 152(1999) 584-607.
- [15] Khayyer, Gotoh, Shao, S. D, Corrected Incompressible SPH method for accurate water-surface tracking in breaking waves, Coast Eng, 55(2008) 236-250.

- [16]A.S. Extended, F. Instance, T.U.F. See, E. G, Assessment of Dynamic Pressures at Vertical and Perforated Breakwaters through Diffusive SPH Schemes, Mathematical Problems in Engineering,2015,(2015-3-1), 2015(2015) 1-10.
- [17]D.D. Meringolo, F. Aristodemo, P. Veltri, SPH numerical modeling of wave - perforated breakwater interaction, Coast Eng, 101(2015) 48-68.
- [18]A.J.C. Crespo, J.M. Dom ínguez, B.D. Rogers, M. Gómez-Gesteira, S. Longshaw, R. Canelas, R. Vacondio, A. Barreiro, O. Garc ía-Feal, DualSPHysics: Open-source parallel CFD solver based on Smoothed Particle Hydrodynamics (SPH), Comput Phys Commun, 187(2015) 204-216.
- [19]D.D. Meringolo, A. Colagrossi, S. Marrone, F. Aristodemo, On the filtering of acoustic components in weakly-compressible SPH simulations, Journal of Fluids & Structures, 70(2017) 1-23.
- [20]B.G.R. Liu, M.B. Liu, Smoothed particle hydrodynamics : a meshfree particle method, World Scientific, 2004.
- [21]D. Violeau, B.D. Rogers, Smoothed particle hydrodynamics (SPH) for free-surface flows: past, present and future, J. Hydraul Res, (2016) 1-26.
- [22]R.A. Dalrymple, B.D. Rogers, Numerical modeling of water waves with the SPH method, Coast Eng, 53(2006) 141-147.
- [23]A.A. Marjani, Advancement in Smoothed Particle Hydrodynamics for Applying to Ocean Wave Energy Conversion., Dissertations & Theses - Gradworks, (2013).
- [24]A. Colagrossi, M. Landrini, Numerical simulation of interfacial flows by smoothed particle hydrodynamics, J. Comput Phys, 191(2003) 448-475.
- [25]A.J.C. Crespo, M. Gomez-Gesteira, R.A. Dalrymple, Boundary conditions generated by dynamic particles in SPH methods, Cmc -Tech Science Press-, 3(2007) 173-184.
- [26]D.G. Goring, Tsunamis—The propagation of long waves onto a shelf, California Institute of Technology, (1979).
- [27]X. Zheng, Z. Hu, Q.W. Ma, W.Y. Duan, Incompressible SPH Based on Rankine Source Solution for Water Wave Impact Simulation, Procedia Engineering, 126(2015) 650-654.

Numerical and Experimental Investigation of Two Porous Wave-breaking Structures

HU Wenqing, FAN Qing, ZHAN Jiemin, CAI Wenhao

Department of Applied Mechanics and Engineering

Sun Yat-sen University

Guangzhou, China

stsjm@mail.sysu.edu.cn

Abstract—Compared with the traditional breakwater, floating breakwater has the advantages of simple construction and low cost. The design of the porous structure has been paid more attention because it can effectively reduce the loss of the structure by wave and maintain the wave absorbing ability. In this paper, the difference of the wave absorbing ability between two kinds of porous structures with the same porosity under the periodic wave is investigated by combining experimental measurement and SPH method. Furthermore, the computational results by SPH method have been compared with that by VOF (Volume of Fluid) method. The results show that the SPH method is suitable for the real complicated engineering application.

I. INTRODUCTION

The forms of porous structure are widely found within the structures in the oceans, rivers, lakes or shore-protection dikes. The traditional breakwater [1] such as vertical type and oblique type have higher cost, which increases greatly with the increase of water depth, and the construction difficulty is also increased significantly. Wave research reveals a fact that 98% wave energy is concentrated in the range of water depth about three times of the wave height, counting below the free surface level [2]. Therefore, compared with the traditional breakwater, the floating breakwater is increasingly used in many fields due to its low price and flexible deployment, such as deepwater aquaculture, coastal protection and marine tourism, etc.

At present, the structures of floating breakwaters are mainly composed of floating boxes, pontoon and floating raft, etc [1, 3]. Wave dissipation methods of floating breakwaters vary with different structures, but mainly can be divided into reflection, wave break, friction, vortex generation, resonance and other types [4]. Porous structure is one of the most common structural forms of breakwater facilities, which makes it a hotspot in breakwater research. Mani[5] tests on floating boxes, pontoon and tethered breakwaters show that the ratio of breakwater width to incident wave length (W/L) has a great impact on wave transmission coefficient. Bayram[6] studies a tilted buoy breakwater, it is found that the amplitude of the incident wave has little influence on the wave transmission coefficient, and the shorter the period of the incident wave is, the better the wave attenuation effect is. Huang Lu [7] studied the wave attenuation performance of T type breakwater.

Recent years, the meshless Smoothed Particle Hydrodynamics (SPH) method has been developed rapidly. Since Monaghan [8] firstly simulated a simple dam break problem using SPH method, it has been successfully applied to many fluid mechanics problems. Many studies of wave interaction with coastal structures are presented [9, 10].

In this paper, two kinds of porous structures with the same porosity under the periodic wave is investigated by combining experimental measurement and SPH method.

II. TESTING MODELS

Two kinds of testing models are presented in this paper, of which the cross sections are illustrated in Fig. 2. They have the same porosity, but with different pore sizes. The full size of the models cross section is 24 cm×12 cm with the porosity 0.5 and different inner rectangular pillar widths 2 cm (referred to as model 1) and 1 cm (referred to as model 2). The lengths of the pillars are 60 cm, which is the width of experimental flume.



Figure 1. The photo of testing model 1

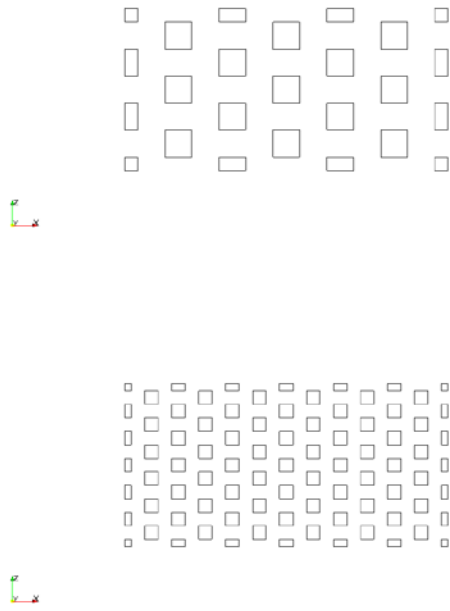


Figure 2. The cross sections of testing models

III. EXPERIMENTAL CONFIGURATION

The experiments are carried out in the wave-generating experimental flume in Department of Applied Mechanics and Engineering, Sun Yat-sen University. The length of the flume is 15 m, and the width 60 cm. The water depth in this experiment is kept to 37 cm.

The porous models are suspending-installed, as show in Fig. 3. The rectangular pillars are fixed in the two ending plates, which have supporting structures inside. And the two ending plates are fixed to the flume structure. The top side of the model is kept of the free surface level of water.

The paddle-type wavemaker is installed at one ending of the flume. The wave presented in this paper has amplitude of 2 cm, frequency of 1 Hz.



Figure 3. Model installation

Two wave height meters are installed at the locations 1m in front of and 1 m back of the models.

IV. NUMERICAL CONFIGURATION

Two computational softwares are used, DualSPHysics[11] and ANSYS Fluent[12]. They have different configuration for making wave. DualSPHysics has straightforward way to simulate the paddle wavemaker, with specifying the paddle's rotation axis, frequency, amplitude, phase and duration of a sinusoidal rotational motion. In ANSYS Fluent, wave is made by using Second Order Stokes wave theory with VOF method.

With different wave making methods, detailed numerical configuration varies in the two codes. Here the attention is focused on DualSPHysics. As illustrated in Fig. 4, the length of the calculation area is 15 m, which is the length of experimental flume. The depth of water is 37 cm. The calculation is 2D, thus the width is not important. And the paddle is configured at 1 m from one of the ending of the area. Be consistent with the experimental configuration, the distance between model and paddle is 3 m.

Other options of DualSPHysics are: laminar+SPS viscosity formulation, Wendland kernel and Simple precision in particle interaction.

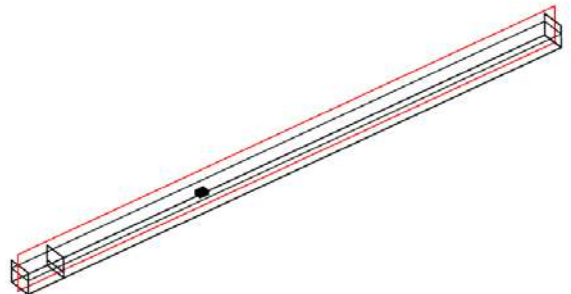


Figure 4. DualSPHysics calculation geometry configuration

By using DesignSPHysics[13], a user interface for DualSPHysics, it is convenient for setting up the calculation area and the options for computation.

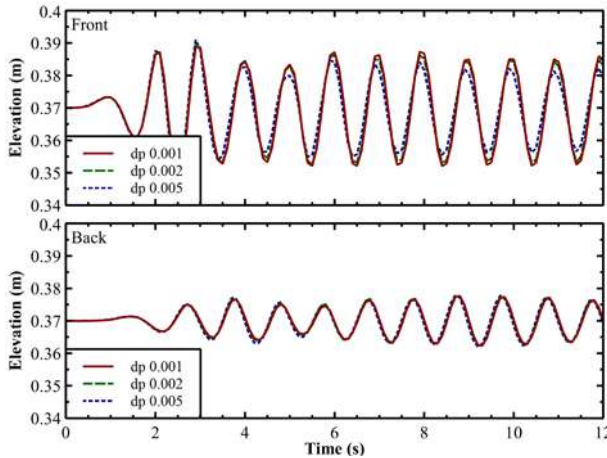


Figure 5. Water elevation before and after model with different inter-particle distance (dp)

V. RESULTS

The calculations are first performed on a smaller calculation area, to check the results dependency on inter-particle distance (dp). As shown in Fig. 5, water elevations at the locations 1m in front of and 1 m back of model 1 vary small between dp 0.002 m and dp 0.001 m. And the results of dp 0.002 m are used thereafter.

Fig. 6 and Fig. 7 show the water elevation changes 1 m in front of and 1 m back of model 1 and model 2 respectively. Results are compared with experiment data and the results calculated by using ANSYS Fluent. Due to the fact that, it is hard to make sure the beginning collecting time to be the beginning of making wave in experiment, and the fact that, the methods used to making wave are different in DualSPHysics and ANSYS Fluent, the results are shifted along x-axis separately.

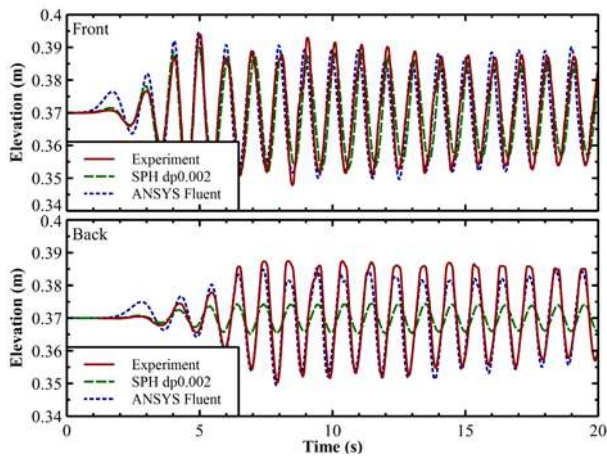


Figure 6. Water elevation before and after model 1

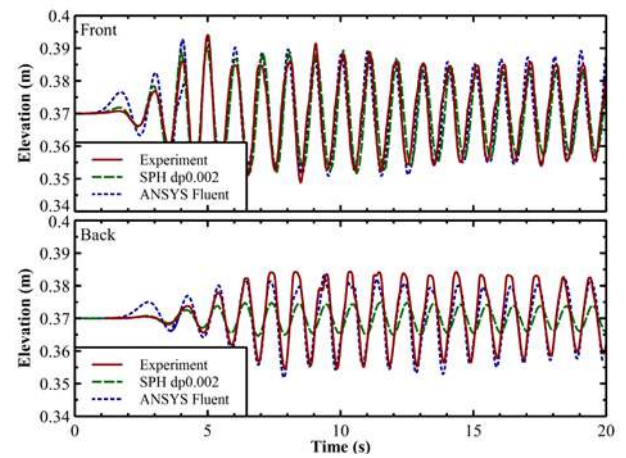


Figure 7. Water elevation before and after model 2

It can be shown in Fig. 6 and Fig. 7, DualSPHysics performs better at the onset of wave. This may benefit from that the SPH code simulates well the method of making wave in experiment. Both DualSPHysics and ANSYS Fluent give reasonable results at the locations before models. The results at the locations after the models are much better when ANSYS Fluent is used. This may due to the wave attenuation during propagation found when using DualSPHysics, which is not found when using ANSYS Fluent (Fig. 8).

Fig. 8 shows water elevations at different locations. No model is introduced into these calculations. And the distance is from the wavemaker. It is clear that, configurations used here caused wave attenuation during propagation in DualSPHysics calculation, which is not present in ANSYS Fluent calculation. We conjecture that, this kind of attenuation maybe one reason which leads to the deviation of calculated results from experiment data.

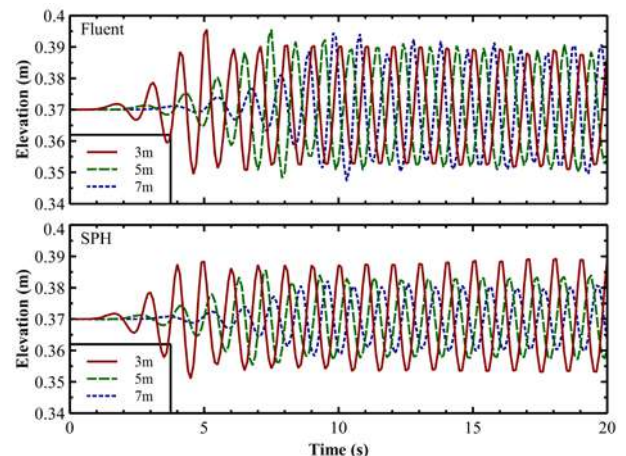


Figure 8. Water elevations at different locations

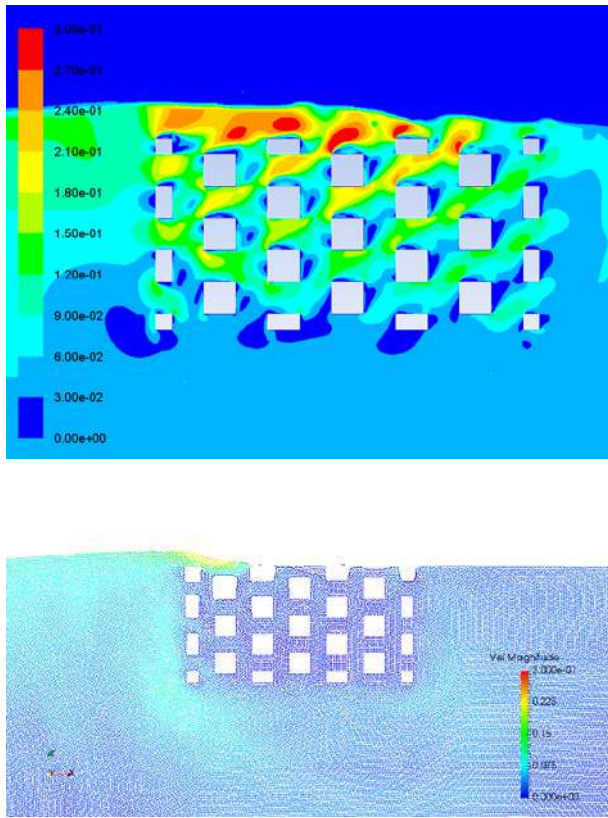


Figure 9. Velocity fields calculated by ANSYS Fluent (above) and DualSPHysics (below)

With this attenuation in wave, one can expect the attenuation in velocity field, which can be seen in Fig. 9. However, whether if it is the attenuation in wave that caused these phenomena or not is just conjecture, needed to be confirmed.

VI. CONCLUSION

The velocity fields around two kinds of porous models which have the same porosity are calculated by using DualSPHysics and ANSYS Fluent, and the wave elevations before and after models are extracted and compared with experiment data. Due to the method used for making wave, DualSPHysics performs well at the onset of wave. Wave attenuation during propagation is found in DualSPHysics calculation, this maybe one reason which leads to the deviation of calculated results from experiment data and attenuation in velocity fields. Further work is needed to confirm or deny it.

From the results, it is shown that, SPH simulates well as a real wavemaker, and is convenient for setting up the calculating model. It is suitable for real complicated engineering application.

ACKNOWLEDGEMENT

This paper is supported by the Special Fund of Marine-Fishery Science-Technology Extension in Guangdong Province, China (Grant No. A201401B08).

REFERENCES

- [1] WANG Huan-yu. Experimental study and numerical simulation of a porous floating breakwater. Dalian University of Technology, 2010
- [2] YU Yu-xiu. A new progress in technology of rubble mound breakwater and vertical wall breakwater. Port Engineering Technology, 2000 (4):1-4.
- [3] Mccartney B L. Floating breakwater design. Journal of Waterway Port Coastal & Ocean Engineering, 1985, 111(2):304-318.
- [4] TONG Chao-feng, YAN Yi-xin. Study on the decaying wave feature of floating breakwater. Port & Waterway Engineering, 2002, (8):32-35.
- [5] Mani J S. Design of Y-frame floating breakwater. Journal of Waterway Port Coastal & Ocean Engineering, 1991, 117(2):105-119.
- [6] Bayram A. Experimental study of a sloping float breakwater. Ocean Engineering, 2000, 27(27):445-453.
- [7] HUANG Lu. The analysis of wave scattering performance of T-type breakwater. Dalian University of Technology, 2013.
- [8] J.J. Monaghan, Simulating free surface flows with SPH, *J. Comput. Phys.* 110(1994) 399–406.
- [9] Wen H, Ren B, Dong P, et al. A SPH numerical wave basin for modeling wave-structure interactions. *Applied Ocean Research*, 2016, 59:366-377.
- [10] Altomare C, Crespo A J C, Domínguez J M, et al. Applicability of Smoothed Particle Hydrodynamics for estimation of sea wave impact on coastal structures. *Coastal Engineering*, 2015, 96(96):1-12.
- [11] A. J. C. Crespo et al., “DualSPHysics: Open-source parallel CFD solver based on Smoothed Particle Hydrodynamics (SPH),” *Computer Physics Communications*, vol. 187, pp. 204–216, 2015.
- [12] ANSYS INC. Ansys 15.0 fluent UDF manual. USA: Ansys Incorporated, 2013.
- [13] Andrés Vieira, DesignSPHysics. <http://design.sphysics.org/>

DualSPHysics: a numerical tool to simulate real breakwaters

Feng ZHANG, Shaoping SHANG

Xiamen University

Xiamen, China

zhangfeng@stu.xmu.edu.cn

Alejandro CRESPO, Jos éDOM NGUEZ & Moncho GÓMEZ-GESTEIRA
Universidade de Vigo, Spain
alexbexe@uvigo.es, jmdominguez@uvigo.es,
mggesteira@uvigo.es

Abstract—The open-source code DualSPHysics is used in this work to compute the wave run-up in an existing dike in the Chinese coast using realistic dimensions, bathymetry and wave conditions. The GPU computing power of DualSPHysics allows us to simulate real-engineering problems that involve complex geometries using high resolution at reasonable computational times. The code is first validation by comparing numerical surface elevation and time series of run-up with physical data in a wave flume. Those experiments include a smooth dike and an armored dike with two layer of cubic blocks. After validation, the code is applied to the real case, so that, wave run-up is obtained for different incident wave conditions. The use of active wave absorption allows avoiding spurious reflection from the wavemaker in order to mimic the real open sea.

I. INTRODUCTION

Coastal defences are built to protect the population and infrastructure in coastal zones. These defences protect infrastructures against storm surge and large waves that may cause run-up and overtopping on structures such as breakwaters or dikes. The wave run-up height is a key parameter in design of such kind of coastal structures to define the breakwater crest height.

The simulation of breakwaters using numerical models is a difficult task due to the complex geometries and the violent hydrodynamics involved in the problem. Mesh-based methodologies present some limitations in about those aspects that can be easily overcome by the mesh-less formulation implemented in SPH. An important issue about the numerical modelling of these coastal structures is to reproduce the porosity of the armoured layer to allow the fluid to flow between the blocks and dissipate its energy reducing the run-up process

DualSPHysics is an SPH-based model conceived to be an efficient and user-friendly numerical technique for a wide range of application in the field of hydraulic, naval and coastal engineering. Thanks to the power of GPUs (graphics cards with powerful parallel computing), real engineering problems can be simulated with DualSPHysics using high resolution at a reasonable time. When applied to coastal engineering, the

Corrado ALTOMARE,

Flanders Hydraulic Research & Ghent University, Belgium

corrado.altomare@mow.vlaanderen.be,

corrado.altomare@ugent.be

Andrea MARZEDDU,
Universitat Politècnica de Catalunya, Spain
andrea.marzeddu@upc.edu

model has been demonstrated to accurately reproduce wave propagation and transformation and wave-structure interaction phenomena. The code is devised to mimic an experimental facility (wave flume or wave basin) and therefore implements automatic wave generation and integrated active wave absorption (AWAS) techniques. Moving boundaries are used to mimic the displacement of the wavemaker used in a physical facility. In the present study, a piston-type wavemaker that moves with a pre-imposed displacement is considered to generate regular wave trains.

The DualSPHysics code is used here to model the wave run-up over breakwaters and dikes. In a first step, the code is validated with experiments in a flume where surface elevation and wave run-up were obtained simulating the interaction of regular waves with a smooth and an armoured breakwater. Once the model is validated with data from physical tests, DualSPHysics is applied to simulate the interaction of realistic waves with an existing dike in the Chinese coast. DualSPHysics includes an implementation to generate regular and irregular waves of the desired wave height and period. The idea is that the numerical flume resembles a physical wave facility, so that, the moving boundaries mimic the action of a piston-type wavemaker. DualSPHysics also includes systems of passive and active wave absorption. The passive absorption is employed to avoid wave reflection by using a dissipative beach or sponge layers, while the active wave absorption is employed to absorb the reflected waves that travel back to the numerical piston. The details of wave generation algorithms, passive and active absorption techniques are described in [1].

The aim of this paper is the modelling of the hydrodynamic interaction of waves with an existing dike and to compute the wave run-up for different incident wave conditions in the Chinese coast.

II. DUALSPHYSICS MODEL

The DualSPHysics code [2] is developed by researchers from Universidade de Vigo (Spain) and The University of Manchester (U.K.). DualSPHysics has been developed to use SPH for real engineering problems with software that can be

run on either CPUs or GPUs (graphics cards with powerful parallel computing). GPUs offer now a higher computing power than CPUs and they are an affordable option to accelerate SPH with a low economic cost. Thereby, the simulations can be performed using a GPU card installed on a personal computer. In addition, for the purpose of providing a general model, relevant modes of interaction are not always evident, in which case high spatial and temporal resolutions must be attainable. Furthermore, some simulations may require remarkably large domains. This stresses the need for high performance codes and implementations and it means that DualSPHysics is a perfect candidate since it is the most efficient SPH code worldwide ([3]).

DualSPHysics is open source and can be freely downloaded from www.dual.sphysics.org. The first validation of the GPU implementation of the code was presented in [4] and more details about DualSPHysics can be found in [2]. Recently, DualSPHysics code was applied to coastal engineering problems, e.g. to study the run-up on a real armour block coastal breakwater in [5] and to estimate sea wave impact on coastal structures in [6] where the numerical results have been validated with the experimental data for typical cases from the Belgian coast.

The main features of the DualSPHysics code are described in detail in [2] and we will only refer here to the main features of the method. Weight functions play a fundamental role in SPH method. They should be constructed following several conditions such as positivity, compact support, normalization, monotonically decreasing and delta function behaviour ([7]). A quantic kernel developed by [8] was used in our simulations. Using this normalized kernel, the basic equations of conservation can be represented in SPH notation following [9]. The fluid is treated as compressible in our approach, which allows the use an equation of state to determine fluid pressure, rather than solving an equation. However, the compressibility is adjusted to slow the speed of sound so that the time steps in the model (based on the sound speed) are reasonable. Changes in the fluid density were calculated by means of the differential equation given by [9] instead of using a weighted summation of mass terms, which leads to an artificial density decrease near fluid interfaces. The relationship between pressure and density was assumed to follow the equation of state given by [10]. A Symplectic algorithm ([11]) was used in the present work to integrate variables in time. A variable time step was calculated according to [12], involving the CFL (Courant-Friedrich-Lewy) condition, the force terms and the viscous diffusion term.

A. Boundary conditions

In DualSPHysics, the boundary is described by a set of particles that are considered as a separate set to the fluid particles. The Dynamic Boundary Condition (DBC) is the default method provided by DualSPHysics ([13]. This method uses boundary particles that satisfy the same equations as fluid particles, however they do not move according to the forces exerted on them. Instead, they remain either fixed in position or move according to an imposed/assigned motion function (i.e. moving objects such as gates or wave-makers). When a fluid particle approaches a boundary and the distance between the boundary particles and the fluid particles becomes smaller

than twice the smoothing length (h), the density of the affected boundary particles increases, resulting in a pressure increase. In turn, this results in a repulsive force being exerted on the fluid particle due to the pressure term in the momentum equation. Stability of this method relies on the length of time step taken being suitably short in order to handle the highest present velocity of any fluid particles currently interacting with boundary particles and it is therefore an important issue when considering how the variable time step is calculated. Validations with dam-break flows and sloshing tanks have been published with good results and also comparing these BCs with other approaches ([14]). In addition, DBC have been shown to be suitable to reproduce complex geometries ([5]).

B. Wave generation

The waves are generated in DualSPHysics by means of moving boundaries that aim to mimic the movement of a wavemaker as in physical facilities. The wave generation using moving boundary in DualSPHysics consists of piston- and also flap-type wavemakers.

First- and second-order wave generation theories are implemented in DualSPHysics. For second-order wave generation of monochromatic waves, the reader is referred to the solution proposed by [15] where the author advises to use it only for $HL^2/d^3 < 8\pi/3$, where H and L are the wave height and wavelength respectively (referred to a case of monochromatic waves) and d is the water depth at the wavemaker location in still water conditions. The first-order wave generation for monochromatic waves is extended to random waves in DualSPHysics based on the method described in [16]. Then, the solution for random waves is extended to second-order wave generation to suppress spurious long waves. The method implemented in DualSPHysics is based on the correction for the signal of the wavemaker that is described in [17]. Two standard wave spectra are implemented and used to generate random waves: JONSWAP and Pierson-Moskowitz spectra. The generation system allows having different random time series with the same significant wave height (H_{m0}) and the same peak period (T_p), just defining different phase seeds. In this way, wave height, wave period and depth are the key input parameters in DualSPHysics, therefore the time series of wavemaker displacement is computed using the aforementioned wave theory.

C. Active wave absorption

Active wave absorption is used in physical facilities to absorb the reflected waves at the wave-maker in order to avoid that they will be reflected back into the domain. In this way, the active absorption prevents the introduction into the system of extra spurious energy that will bias the results. With active absorption, the position of the wave maker is corrected every time step. The active wave absorption system (AWAS) implemented in DualSPHysics is based on the approach that appears in [18]. The water surface elevation η at the wave-maker position is used and transformed by an appropriate time-domain filter to obtain a control signal that corrects the wave paddle displacement in order to absorb the reflected waves every time step. Hence, the target wave-maker position is

corrected to avoid reflection at the wave-maker. The position in real time of the wave-maker is obtained through the velocity correction of its motion. For a piston-type wave-maker the velocity correction is calculated using linear long wave theory in shallow water ([18], [19]). For that it is necessary to estimate the free-surface elevation of the reflected waves, η_R , to be absorbed comparing the target incident water surface elevation, η_I , with the measured one in front of the wave-maker, η_{SPH} . The corrected wave-maker velocity is then the summation of velocity correction and the theoretical incident wave-maker velocity. For further details, the reader is referred to [1].

III. VALIDATION

This study is the first that compares SPH results with experimental time series of run-up for a smooth and armoured dike. Hence, numerical results of wave run-up have been validated against data from physical model tests carried out at the Universitat Politècnica de Catalunya (UPC). A small-scale wave flume named CIEMito is part of the experimental infrastructures of the CiemLab.

A. Initial setup

The experimental campaign investigated the propagation and breaking processes of regular waves running up a smooth beach and an armoured dike. CIEMito has a total length of 18m, with a useful section of 0.38m wide and 0.56m high and a maximum water depth of 0.36m. The support structure consists of square section metal sections and both laterals and bottom walls are of tempered glass. The initial configuration of the SPH simulation is based on the real dimensions of the experiment, so that the numerical tank is 7 m long, 0.37 m wide and 0.36 m tall. The initial water level is 0.25 m. On the left of the flume there is a piston type wavemaker, and at the end of the flume a slope (28.3°). A sketch of wave flume is shown in Figure 1. V1 and V2 are acoustic Doppler velocimetry to measure the velocities. The wave gauges WG1, WG2, WG3 and WG4 are used to obtain the surface elevation. Two more wave gauges (WG5 and WG6) are located on the slope in order to measure wave run-up and run-down.

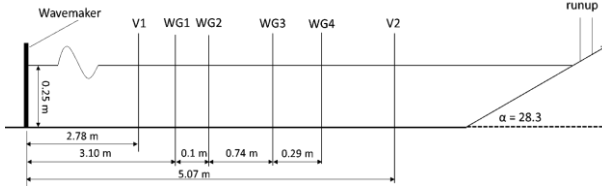


Figure 1. Sketch of the wave flume with beach used in the SPH

In the numerical simulation, the initial particle spacing (dp) is set to 0.008 m, that leads to a smoothing length of 1.36 cm in 2-D cases and 0.17 cm in 3-D cases.

Different regular waves were generated varying the wave height (H) and the wave period (T) with a constant depth ($d=0.25$ m) as shown in Table I. These different wave conditions lead to three type of wave breakers on the dike; “spilling breaker”, “plunging breaker” and “surging breaker”.

TABLE I. Wave conditions in the validation cases.

	H (m)	T (s)	Breaking type
Wave#1	0.08	0.87	Plunging
Wave#2	0.08	1.40	Collapsing
Wave#3	0.08	1.73	Surging
Wave#4	0.06	1.21	Collapsing
Wave#5	0.10	0.79	Plunging
Wave#6	0.10	1.56	Collapsing

B. Smooth dike: EXP vs SPH

Six different numerical cases are simulated to reproduce the six wave conditions shown in Table I with the smooth dike. These simulations have a 2-D behaviour, however both 2-D and 3-D cases have been performed to check this. The initial particle distance mentioned before ($dp=0.008$ m) leads to a total number of particles of 22,862 in 2D and 1,033,976 in 3D. The 2-D simulations took 15 min to simulate 15 seconds of physical time using the GeForce GTX TITAN GPU card.

Figure 2 shows the experimental and numerical surface elevation at WG1, WG2, and WG3 during 15 seconds of the test. It can be observed how the SPH results with Wave#6 ($H=0.1$ m, $T=1.56$ s, $d=0.25$ m) are in good agreement with experiments. Results of the 2-D and 3-D cases provide the same accuracy.

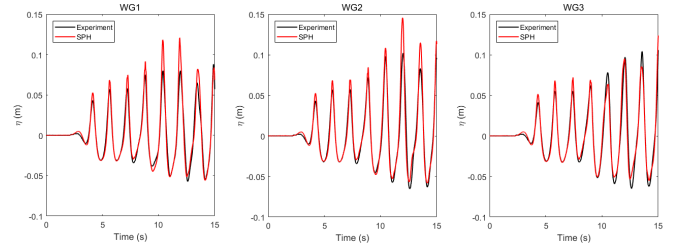


Figure 2. Comparison of the experimental and numerical surface elevation for Wave#6 with smooth dike.

Once the waves have been proven to be generated and propagated with accuracy (according to the good agreement observed in Figure 2), the experimental time series of the wave run-up can be compared with the results obtained with DualSPHysics. Figure 3 shows the comparison between experimental and numerical values of run-up during the 15 seconds of the test.

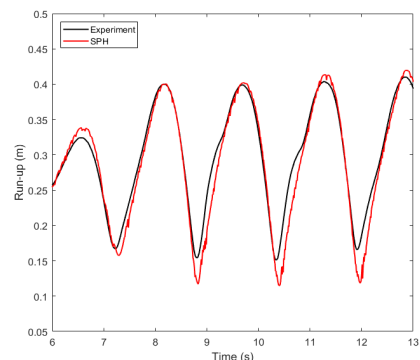


Figure 3. Comparison of the experimental and numerical run-up for Wave#6 with smooth dike.

C. Armoured dike: EXP vs SPH

In the second set of simulations, a dike with an outer layer of armour blocks is studied. Figure 4 shows the initial setup of the experiment. The same configuration shown in Figure 1 is also used now but the dike with two layers of cubic blocks is included instead of the smooth beach. Regular waves with $H=0.08$, $T=0.87$ s, $d=0.25$ m (Wave#1 in Table I) are simulated now. Only 3-D simulations were performed.

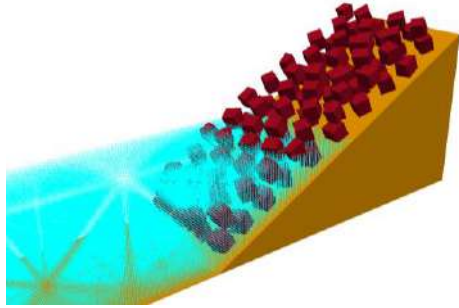


Figure 4. Initial setup of the experiment with the armoured dike.

The same initial configuration of the blocks in the experiment is considered in the simulations (Figure 5). The positions of the cubic blocks of two layers were digitized and converted into a 3D model (STL format) that the pre-processing tools of DualSPHysics can convert into a set of boundary particles.

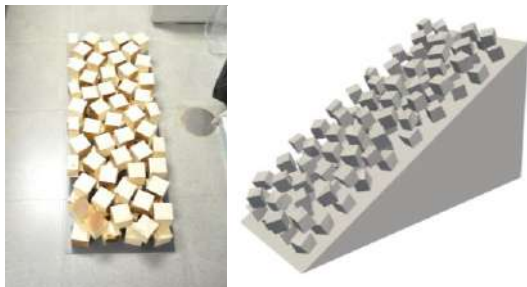


Figure 5. Left: image of the blocks in the experiment. Right: STL model in DualSPHysics.

The initial particle distance, dp , needs to guarantee a minimum number of fluid particles to move between the gaps of the blocks. This fact defined the choice of $dp=0.008$ m that we also used in the case of the smooth dike, which already provides good accuracy when computing surface elevation and wave run-up for that case. With this resolution, a total number of 1,135,818 are simulated. The simulation of 15 seconds physical time took 17.5h using the GeForce GTX TITAN GPU card.

As studied before in the case of the smooth dike, both surface elevation at different positions along the wave flume and wave run-up at the location of the dike are numerically computed and compared with the experimental data performed in CIEMito. Therefore, Figure 6 plots the time series of surface elevation at WG1, WG2, WG3 and WG4 where a very good agreement is observed between SPH and experiment.

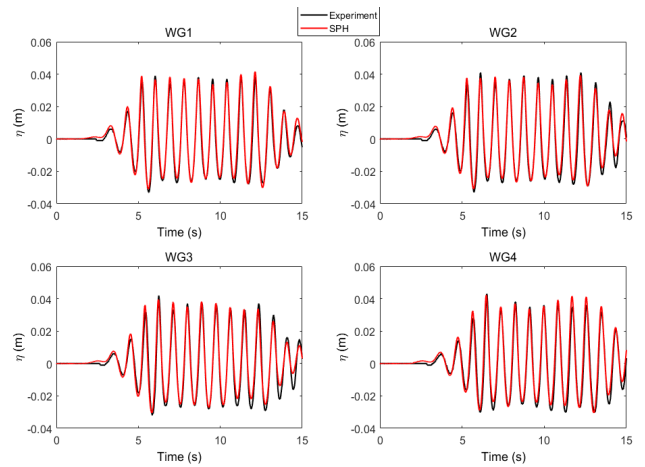


Figure 6. Comparison of the experimental and numerical surface elevation for Wave#1 with armoured dike.

Run-up is numerically computed at 52 positions along the width of the tank to catch the 3-D behaviour. However only two positions were used in the experiments. These two filaments can be observed in Figure 7. Hence, the black line in Figure 8 corresponds to the average between the two experimental probes while the different red lines correspond to the different numerical measurements.



Figure 7. Wave gauges in the armoured dike during the experiment.

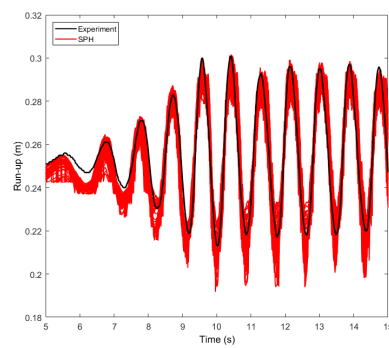


Figure 8. Comparison of the experimental and numerical run-up for Wave#1 with armoured dike.

IV. APPLICATION

Once the model was properly validated with experiments it can be now applied to study real situations in the Chinese coast. Hence, in this section, DualSPHysics is used to study a real problem using the dimensions of a dike in China, in particular, in the coast of Chongwu. The SPH modelling will allow computing the values of wave run-up in this dike under realistic wave conditions. A picture of the dike can be seen in Figure 9. The dike is located in Fujian province, made of cement with steps.



Figure 9. Picture of the dike in the coast of Chongwu.

Several considerations are taking into account in the initial design of the numerical tank: (i) 2-D behaviour is assumed due to the section of the dike, (ii) the length of the tank is large enough to guarantee the proper wave generation and propagation (2-3 times L, being L the wavelength), (iii) the dimensions of the dike are the real ones, (iv) the numerical piston-type wave-maker generates regular waves according to wave theory using the wave heights and periods measured in that area and (v) the active wave absorption system (AWAS) described in is used to absorb reflected waves at the wave-maker.

Figure 10 shows the dimensions of the numerical tank that consists of a piston to generate the typical waves of that coast, an area of wave propagation following the realistic depth of the area and the dike at the end. The channel has a length of 100 m. The still water level at the piston location correspond to a water depth of d=5 m.

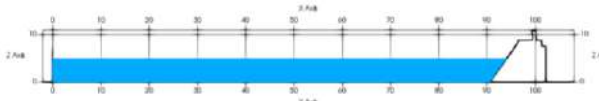


Figure 10. Initial setup of the case of application.

As mentioned before, the piston moves to generate waves with typical values of height and period in that coast. To define the sea state, three months wave data are measured at 100 m from the dike toe. Regular and irregular (JONSWAP spectrum) waves will be numerically reproduced. The different wave conditions are shown in Table II. The values of relative depth (d/L) indicate that waves belong to intermediate depths and the Stokes 2nd order wave theory is used to determine the wave kinematics for all tests.

TABLE II. Wave conditions in the case of study.

	H (m)	T (s)	d (m)	L (m)
Wave#1	1.24	7.03	5	45
Wave#2	0.76	5.29	5	33

Before analysing the interaction between the incident waves and the dike, wave propagation is validated by comparing numerical values with theoretical ones. A modified wave tank (Figure 11) is used with constant depth ($d=5$ m) and a sponge layer at the end of the tank to avoid wave reflection.

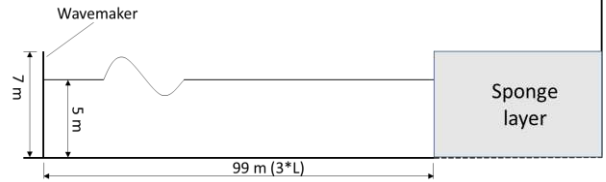


Figure 11. Numerical domain to study wave propagation.

Figure 12 and 13 show the numerical and theoretical time series of the surface elevation at 45, 68 and 90 meters far from piston for Regular Wave#1 and Wave#2, respectively. While Figures 14-15 show the numerical and theoretical results for Irregular waves. The SPH results follow the Stokes 2nd order wave theory in terms of surface elevation, so it is demonstrated that waves are being properly generated and propagated.

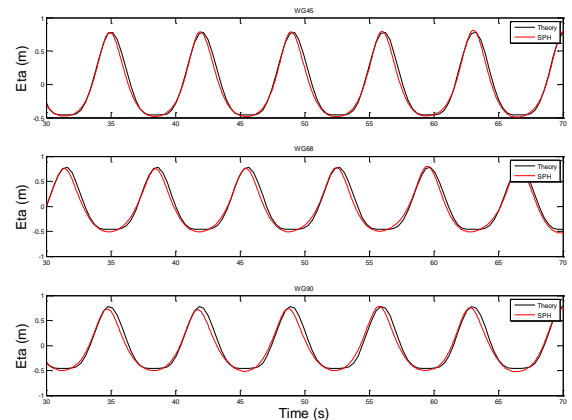


Figure 12. Comparison of the experimental and numerical surface elevation for regular Wave#1 with sponge layer.

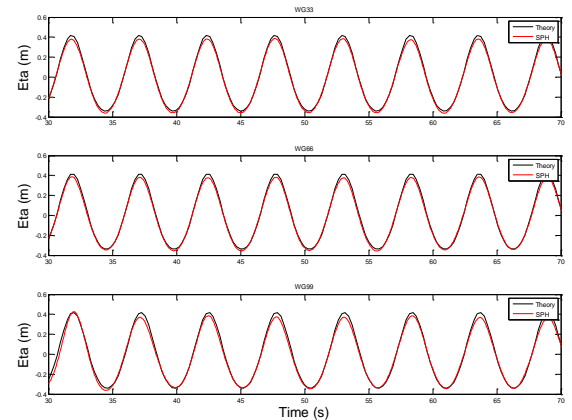


Figure 13. Comparison of the experimental and numerical surface elevation for regular Wave#2 with sponge layer.

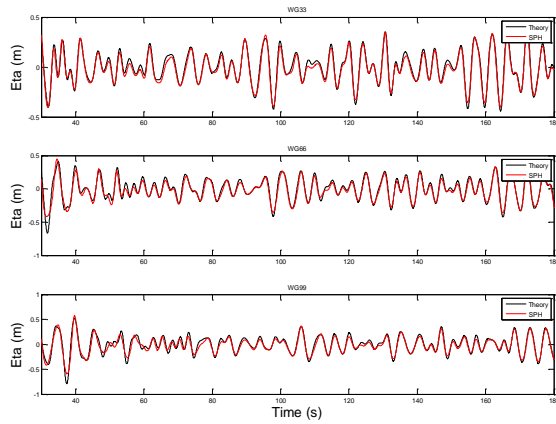


Figure 14. Comparison of the experimental and numerical surface elevation for irregular Wave#1 with sponge layer.

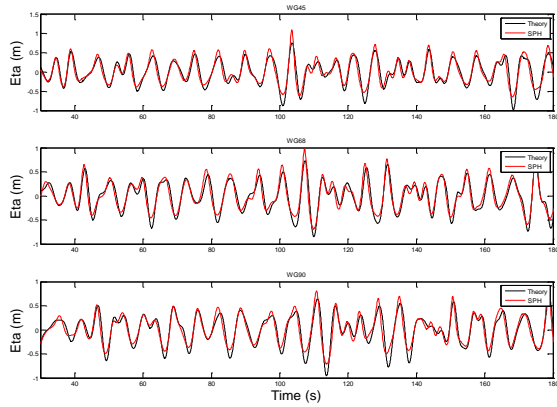


Figure 15. Comparison of the experimental and numerical surface elevation for irregular Wave#2 with sponge layer.

The sponge layer is used in the numerical tank to avoid wave reflection. Table III contains the values of the incident (H_i) and reflected (H_r) components and the reflection coefficients (CR). Wave reflection is considered very low with values of CR lower than 10%.

TABLE III. Values of incident and reflected wave height, and reflection coefficient for Regular Wave#1 and Wave#2 with sponge layer.

	H_{theory} (m)	H_i (m)	H_r (m)	CR (%)
Regular Wave#1	1.24	1.32	0.06	4.35
Regular Wave#2	0.76	0.75	0.03	3.74
Irregular Wave#1	1.24			7.00
Irregular Wave#2	0.76			6.40

Once wave generation and propagation have been proven to be accurate, the interaction between realistic waves and a dike in the coast of Chongwu are studied with DualSPHysics. The dike will reflect part of the wave energy, creating reflected waves that will travel back towards the wave-maker. This re-reflection can introduce spurious waves and extra energy into

the system that will bias the results. Thus, an active wave absorption system (AWAS) is implemented to absorb the reflected waves at the piston to mimic the behaviour of an open sea where reflected waves propagate outside the simulated domain. The setup shown in Figure 16 represents the case of study.

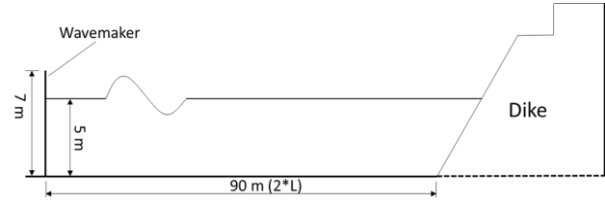


Figure 16. Numerical domain to study wave-dike interaction.

Therefore, we need first to prove that the use of AWAS system avoids re-reflection and only the desired incident waves are interacting with the real dike. Figure 17 and 18 demonstrate that the surface elevation of regular waves using AWAS show oscillations of the same amplitude and period, as it should be expected if re-reflection at the piston is observed. Note that when AWAS is not employed the surface elevation at different locations become chaotic without a regular pattern.

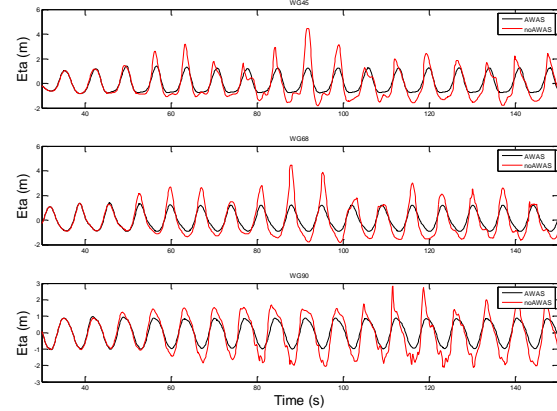


Figure 17. Comparison of the numerical surface elevation obtained with and without AWAS for regular Wave#1.

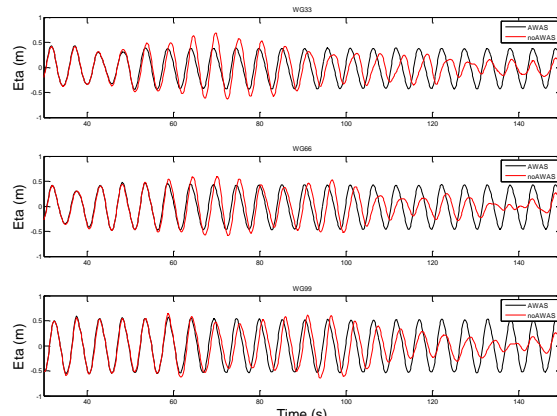


Figure 18. Comparison of the numerical surface elevation obtained with and without AWAS for regular Wave#2.

In order to check the correct behaviour of AWAS, we can also use theoretical results of surface elevation assuming a value of the reflection coefficient that corresponds to dikes similar to the one reproduced here. A value of CR=75% can be used, so that Figure 19 shows the numerical and theoretical solutions using the theory of [20].

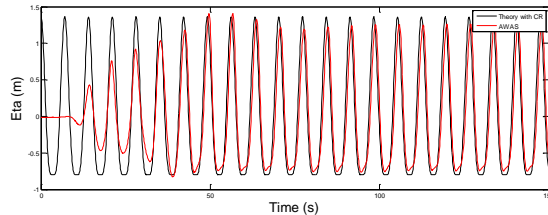


Figure 19. Comparison of the theoretical solution using CR=75% and the numerical surface elevation obtained with AWAS for regular Wave#1 at WG45.

One third option to prove the correct behaviour of AWAS is to compute forces exerted onto the dike. If re-reflection is removed, then regular cycles are observed in the time series of the force, as it can be observed in Figure 20 and 21 for regular Wave#1 and Wave#2, respectively.

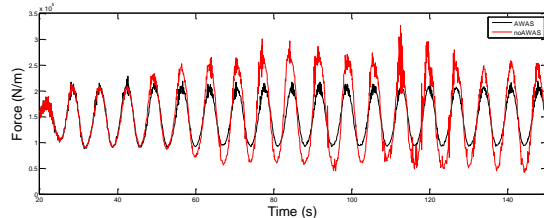


Figure 20. Comparison of the numerical force exerted against the structure obtained with and without AWAS for regular Wave#1.

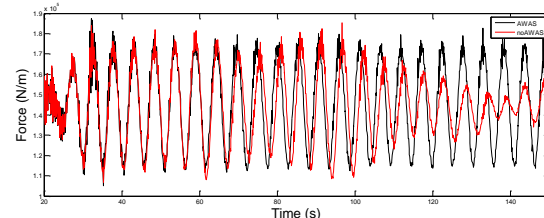


Figure 21. Comparison of the numerical force exerted against the structure obtained with and without AWAS for regular Wave#2.

In the case of irregular waves, the best option to analyse if AWAS is working as expected is to perform an spectral analyses of the incident components (Figures 22 and 23) of the wave. Without AWAS, the incident wave includes also the re-reflected wave (reflected wave hits the piston and moves again in the incident direction). In the case of using a dissipative beach that, acting as pasive absorption of reflection, we should have only indicent component. So that, if AWAS is removing the re-reflected wave, the incident component using AWAS should be the same as the incident when a dissipative beach is included in the numerical domain.

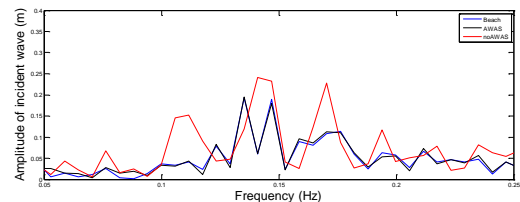


Figure 22. Spectrum analysis of incident wave for irregular Wave#1.

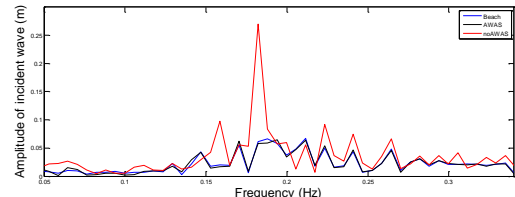


Figure 23. Spectrum analysis of incident wave for irregular Wave#2.

After of these previous checks, we can assume that the numerical tank can mimic a real sea state since the piston with AWAS reproduces the behaviour of an open sea. Therefore, we can now compute the values of wave run-up at the dike. Figure 24 and 25 collects the time series of the numerical run-up computed with DualSPHysics for regular waves and irregular waves, respectively.

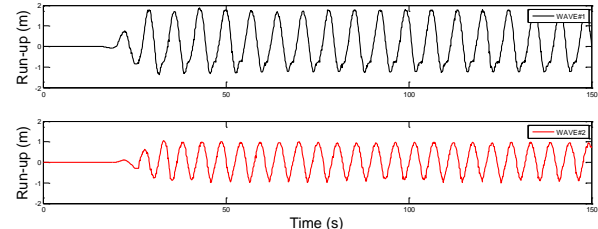


Figure 24. Time series of the wave run-up with regular Wave#1 and Wave#2.

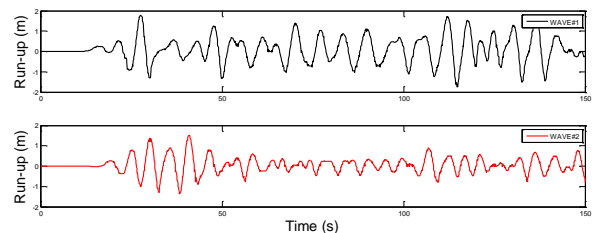


Figure 25. Time series of the wave run-up with irregular Wave#1 and Wave#2.

V. CONCLUSIONS

The DualSPHysics code has been validated in terms of wave run-up on a breakwater. The numerical results are compared with experimental data of a smooth dike and a dike with two layers of cubic blocks. Several different wave conditions are simulated and overall good accuracy is obtained for both wave surface elevation and time series of the run-up. The code is then applied to study a real case, using the real dimensions of a dike, the bathymetry and wave conditions from the coast of Chongwu (China).

As first novelty, a proper validation of run-up is here performed since we have compared the numerical and experimental time series of water surface elevation and time series of wave run-up. Previous work [5] presented a validation for run-up, but only a maximum value for different incoming waves was compared with experimental and literature data.

The second novelty is the application of the SPH model to a real problem using the dimensions of a dike in China. In this case wave conditions are imposed based on real wave condition *in situ* and AWAS is employed to compensate the wave reflection at the numerical wavemaker. This is mandatory to mimic the real open sea. Therefore, the model has been properly validated with experiments and it can be applied to study real situations in the coast of China.

ACKNOWLEDGEMENT

This work was partially financed by Xunta de Galicia (Spain) under project “Programa de Consolidación e Estructuración de Unidades de Investigación Competitivas (Grupos de Referencia Competitiva) GRC2013-001” and under project “NUMANTIA ED431F 2016/004”. The work is also funded by the Ministry of Economy and Competitiveness of the Government of Spain under project “WELCOME ENE2016-75074-C2-1-R”.

REFERENCES

- [1] C. Altomare, J.M. Domínguez, A.J.C. Crespo, J. González-Cao, T. Suzuki, M. Gómez-Gesteira, P. Troch. Long-crested wave generation and absorption for SPH-based DualSPHysics model. *Coastal Engineering*, 127 (2017) 37-54.
- [2] A.J.C. Crespo, J.M. Domínguez, B.D. Rogers, M. Gómez-Gesteira, S. Longshaw, R. Canelas, R. Vacondio, A. Barreiro and O. García-Feal, O, “DualSPHysics: open-source parallel CFD solver on SPH”, *Computer Physics Communications*, 187, (2015) 204-216.
- [3] J.M. Domínguez, A.J.C. Crespo, D. Valdez-Balderas, B.D. Rogers, M. Gómez-Gesteira. New multi-GPU implementation for Smoothed Particle Hydrodynamics on heterogeneous clusters. *Computer Physics Communications* 184, (2013) 1848-1860.
- [4] A.J.C. Crespo, J.M. Domínguez, A. Barreiro, M. Gómez-Gesteira, B.D. Rogers. GPUs, a new tool of acceleration in CFD: Efficiency and reliability on Smoothed Particle Hydrodynamics methods. *PLoS ONE* 6(6), (2011) e20685.
- [5] C. Altomare, A.J.C. Crespo, B.D. Rogers, J.M. Domínguez, X. Gironella, M. Gómez-Gesteira, Numerical modelling of armour block sea breakwater with smoothed particle hydrodynamics, *Comput. Struct.* 130 (2014) 34–45.
- [6] C. Altomare, A.J.C. Crespo, J.M. Domínguez, M. Gómez-Gesteira, T. Suzuki, T. Verwaest, Applicability of Smoothed Particle Hydrodynamics for estimation of sea wave impact on coastal structures, *Coast. Eng.* 96 (2015) 1–12.
- [7] G.R. Liu, M.B. Liu. *Smoothed Particle Hydrodynamics: a meshfree particle method*, World Scientific (2003).
- [8] H. Wendland. Piecewise polynomial, positive definite and compactly supported radial functions of minimal degree. *Advances in Computational Mathematics* 4, (1995) 389–396.
- [9] J.J. Monaghan. Smoothed particle hydrodynamics. *Annual Review of Astronomy and Astrophysics* 30, (1992) 543–574.
- [10] G.K. Batchelor. *Introduction to fluid dynamics*. Cambridge University Press, (1974).
- [11] B.J. Leimkuhler, S. Reich, R.D. Skeel. *Integration Methods for Molecular dynamic IMA Volume in Mathematics and its application*. Springer (1996).
- [12] J.J. Monaghan, Smoothed particle hydrodynamics, *Annu. Rev. Astron. Astrophys.* 30 (1992) 543–574.
- [13] A.J.C. Crespo, M. Gómez-Gesteira, R. Dalrymple, Boundary Conditions Generated by Dynamic Particles in SPH Methods, *Comput. Mater. Contin.* 5 (2007) 173–184
- [14] J.M. Domínguez, A.J.C. Crespo, J.L. Cercos-Pita, G. Fourtakas, B.D. Rogers, R. Vacondio. Evaluation of reliability and efficiency of different boundary conditions in an SPH code. In: *Proceedings of the 10th SPHERIC International Workshop*, Parma, Italy (2015).
- [15] P. A. Madsen, D. R. Fuhrman, and H. A. Schäffer, “On the solitary wave paradigm for tsunamis”, *J. Geophys. Res.*, 113, (2008) C12012.
- [16] Z. Liu, P. Frigaard, Generation and Analysis of Random Waves, *Laboratoriet for Hydraulik og Havnebygning, Instituttet for Vand, Jord og Miljøteknik, Aalborg Universitet*, (2001).
- [17] F.C. Barthel, V., Mansard, E, P., Sand, S.E., Vis, Group bounded long waves in physical models, *Ocean Eng.* 10 (1983) 261–294.
- [18] H.A. Schaffer, G. Klopman, Review of multidirectional active wave absorption methods, *J. Waterw. Port, Coast. Ocean Eng.* 126 (2000) 88–97.
- [19] E. Didier, M.G. Neves. A Semi-Infinite Numerical Wave Flume Using Smoothed Particle Hydrodynamics. *International Journal of Offshore and Polar Engineering* 22(3), (2001) 193-199.
- [20] O.S. Madsen, On the generation of long waves, *J. Geophys. Res.* 76 (1971) 8672–8683.

Numerical simulation of green water using SPH method

Liang-Jun WEN

China Ship Scientific Research Center,
Wuxi, China
18706171527@163.com

Qian-Dong FENG

China Ship Scientific Research Center,
Wuxi, China

Abstract— When the ship is navigating in the sea, it is inevitable to meet the rough sea condition. In this case, the ship can suffer great danger from green water, and severe green water can cause structure damages. The flows tend to be highly dynamic, with large amounts of free surface deformation. A numerical method to simulate the phenomenon of the green water on deck is established by taking advantage of SPH method.

The paper aims to extend this method to deal with green water. The ship motion is given by potential flow theory. The ship model is regard as rigid body. Numerical results of water flow on deck and green water loads on the deck structure are compared with the corresponding experimental data. It is shown that the SPH method can be applied to describe and analyze green water.

Keyword: Green water; Smoothed Particle Hydrodynamics (SPH); wave loads;

I. INTRODUCTION

In ocean engineering realm, such phenomena like green water loading on the deck equipment, water wave strike on the ship side are quite common. Severe water on deck may not only cause active speed loss and course changing of ships, but also damage equipment and superstructure.

At present, studies on the green water have made great progress, which can be mainly classified into three groups: the theoretical prediction, the experimental research^[1] and numerical simulations.

Green water experiments have been carried out on the international standard ship model S-175, by which the essence of green water and prediction methods have been studies. Buchner conducted a series of FPSO model test in MARIN basin, and discussed the influence of wave height, wave period, current velocity and the shape of breakwaters on the ship motion and the impact loading on superstructures. The model test shows that the green water phenomenon is similar to dam breaking. Fonseca carried out a series of model tests to study how the bow of a containership affects the green water. Model tests were carried out using S-175 containership in head regular and irregular waves of large amplitude. They measured the relative motions, the structural loads, the height of water and the impact pressure on the deck. The effect of the horizontal impact pressure and total force on the bow was discussed. B.Hamoudi considered the probability of green water occurrence and got some conclusions, as follows. The deck wetness occurs when the relative motions exceed the freeboard. The probability of deck wetness occurrence and number of wetting depends mainly on the freeboard parameter.

Theoretical research is another way to study green water phenomenon. This method always takes some simplification of physical problems. Most theoretical methods are based on potential flow theory. These methods are efficient to predict the water shape flowing on the deck in different theory models with experimental formulae, but inaccurate when predicting the green water.

With the rapid development of computational technology, the Computational Fluid Dynamics (CFD) has been widely applied in the field of ocean engineering. CFD can be classified into two groups: grid methods and meshless methods. Grid methods include Finite Element Method (FEM), Finite Different Method (FDM), Finite Volume Method (FVM), and so on. Due to the existence of free surface and its large deformation in ocean engineering, green water belongs to the complex strong nonlinear problems. Grid method may encounter a lot of difficulties deal with this problem.

During the past three decades, many researches have been conducted on development and application of meshless methods^[2-3], including SPH (smoothed particle hydrodynamics) and MPS (moving particle semi-implicit) methods, for different fields of engineering, including ocean engineering. Due to their mesh-free, lagrangian nature, particle methods have been proven to provide a substantial potential for simulation of free-surface fluid flows, especially dealing with large deformation ,splashing and fragment.

Due to this reason, SPH method is applied in many engineering problems such as dam-breaking, sloshing and green water and so on^[4].The main challenge is to devise a SPH scheme that balances spatial and temporal accuracy with an efficient computer implementation to produce accurate simulations at a reasonable computing cost. The proposed SPH methods were coded in the open source parallel code DualSPHysics. DualSPHysics has been recently applied to free-surface flow problems and it has been proven to give accurate results in agreement with physical model and data.

II. MUMERICAL MODEL

Green water phenomenon is mainly the affected by two mechanisms: wave propagation and ship motion. Green water and its impact on superstructures may cause damage on a ship. So it is essential to accurately simulate the process of green water phenomenon. Based on the open source code DualSPHysics , wave propagation is included^[5-6]. DualSPHysics has been successfully applied to various hydrodynamics applications. The main aims of this work are to apply a smoothed particle hydrodynamics (SPH) method for simulating green water in ship

model, and then verify and validate the numerical results with experimental data^[7-9].

A. Governing equations

The Weakly-Compressible SPH formulation is adopted in DualSPHysics, the continuity equation and the momentum equation, expressed in particle notation as follows:

$$\frac{d\rho_a}{dt} = \sum_b m_b \mathbf{v}_{a,b} \cdot \nabla_a W_{a,b} \quad (1)$$

$$\frac{dv_a}{dt} = -\sum_b m_b \left(\frac{p_a + p_b}{\rho_a \rho_b} + \prod_{ab} \right) \nabla_a W_{ab} + \mathbf{g} \quad (2)$$

Here a is the target particle, b is the interpolating particle within the kernel support region, and the notation \cdot_{ab} indicates $(\cdot_a - \cdot_b)$. The density, mass, and velocity of a fluid particle are indicated with ρ , m , and \mathbf{v} , respectively, whereas P denotes the pressure. The viscosity term \prod_{ab} is given by:

$$\prod_{ab} = \begin{cases} \frac{-\alpha \overline{c}_{ab} \mu_{ab}}{\rho_{ab}} & v_{ab} \cdot r_{ab} < 0 \\ 0 & v_{ab} \cdot r_{ab} > 0 \end{cases} \quad (3)$$

where $\mathbf{r}_{ab} = \mathbf{r}_a - \mathbf{r}_b$ and $\mathbf{v}_{ab} = \mathbf{v}_a - \mathbf{v}_b$ with r_k and v_k being the particle position and velocity respectively.

$\mu_{ab} = h \mathbf{v}_{ab} \cdot \mathbf{r}_{ab} / (r_{ab}^2 + \eta^2)$, $\overline{c}_{ab} = 0.5(c_a + c_b)$ is the mean speed of sound, $\eta^2 = 0.01h^2$ and α is a coefficient that needs to be tuned in order to introduce the proper dissipation. The value of $\alpha = 0.01$ has proven to give the best results in the validation of wave flumes to study wave propagation and wave loadings exerted onto coastal structures.

The latter is computed following the standard WCSPH practice of coupling pressure and density through an equation of state:

$$P = b \left[\left(\frac{\rho}{\rho_0} \right)^\gamma + 1 \right] \quad (5)$$

Where $\gamma = 7$ and $\rho_0 = 1000 \text{ kg/m}^3$ for water, and $b = c_0^2 \rho_0 / \gamma$. The value of c_0 represents a numerical speed of sound that is conveniently reduced to obtain reasonable time-steps.

B. Wave generation

Wave generation is included in Dualsphysics. In this way, the numerical model can be used to simulate a physical wave fume. The transfer function links the displacement of the piston-type wavemaker to the water surface elevation, under the hypothesis of monochromatic sinusoidal waves in one dimension in the x -direction:

$$\eta(x, t) = \frac{H}{2} \cos(\omega t - kx + \delta) \quad (6)$$

where H is the wave height, d the water depth, x is distance and δ is the initial phase. The quantity $\omega = 2\pi/T$ is the angular frequency and $k = 2\pi/L$ is the wave number with T equal to the wave period and L the wave length. The initial phase δ is given by a random number between 0 and 2π . Equation (6) expresses the surface elevation at infinity that Biesel defined as the far-field solution. The Biesel function can be derived for the far-field solution and for a piston-type wavemaker as:

$$\frac{H}{S_0} = \frac{2 \sinh^2(kd)}{\sinh(kd) \cosh(kd) + kd} \quad (7)$$

where S_0 is the piston stroke. Once the piston stroke is defined, the time series of the piston movement is given by:

$$e_1(t) = \frac{S_0}{2} \sin(\omega t + \delta) \quad (8)$$

C. Ship motion

The motions are given by potential theory. The numerical calculation is based on the Sesam soft. Based on the numerical results, the changing in the heave and pitch are apparent under regular waves. The results are shown in Fig 1.

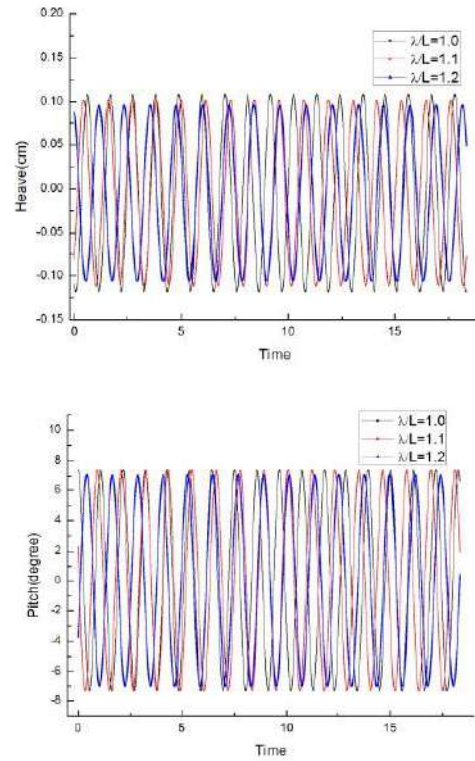


Fig 1. heave (upper)and pitch(down) motion(λ is the wave length, L is the ship length)

III. GEOMETRY AND CONDITION

A. Geometry

In the present work, the ship model is applied to study the green water problems. A baffle was added at the bow to simulate the influence of green water on the superstructures. The geometry of the ship model is shown in Fig 2. Main particulars of ship model at both full scale and model scale are shown in Table 1.

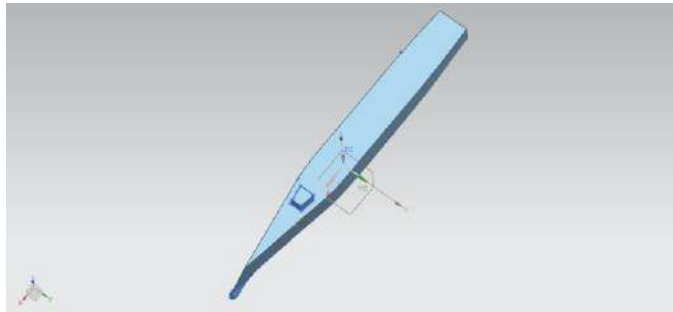


Fig 2. the geometry of ship model

Table 1. Main particulars of ship model

Main particulars	Ship model
Length(stern to bow)/(m)	4.497
Width/(m)	0.555
Height(keel to deck)/(m)	0.395
Designed draft/(m)	0.180
displacement	228.659(kg)

B. Case conditions

The Deck wetness occurs depends mainly on the relative motion. For this reason, three different wavelengths with the same height were chosen to investigate the influence of wavelength on green water phenomenon. The wave height and the wavelengths are shown in the table 2. The speed of ship model is 0.732 m/s.

Table 2. Case conditions

Wave length(m)	Wave height(m)
4.50	0.15
4.95	0.15
5.40	0.15

The ship model is placed in a tank having a depth of 2 metres when the water within is initially at rest. The vessel opposes a type piston that generates undulating travelling waves at the free surface.

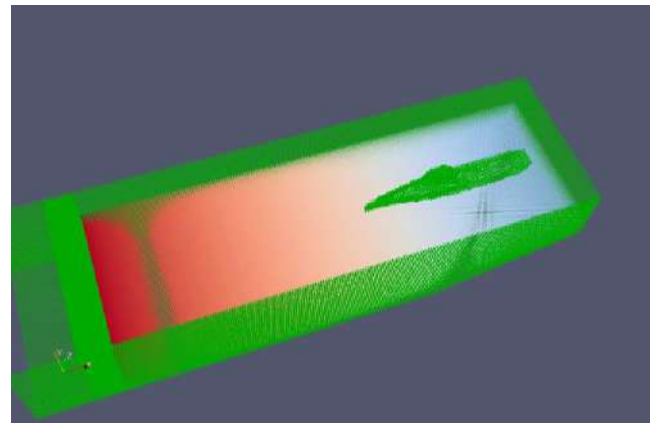


Fig 3. Particles of ship model

These waves travel along the vessel's axis of symmetry. As they interact with the ship, it is given prescribed pitch and heave movements. The potential theory can calculate the movement and in the regular wave, the numerical results are compared well with the experimental data. Consider the challenge that produces accurate simulations at a reasonable computing cost, the particle size is limited. The numerical model is shown in Fig 3.

Four pressure sensors are located on the deck of the ship to record pressure when deck flooding occurs. The positions of the sensors are placed in Figure 4 and table 3. The total real time of the simulation is 20 seconds. All the signals are collected by the data collecting system and recorded into computer system. The experiments are carried out at China Ship Research Centre.

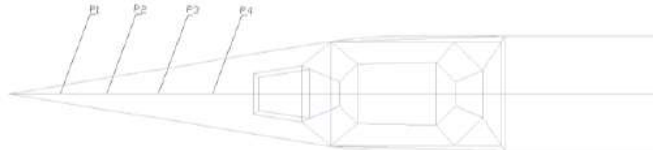


Fig 4. Layout of pressure sensors

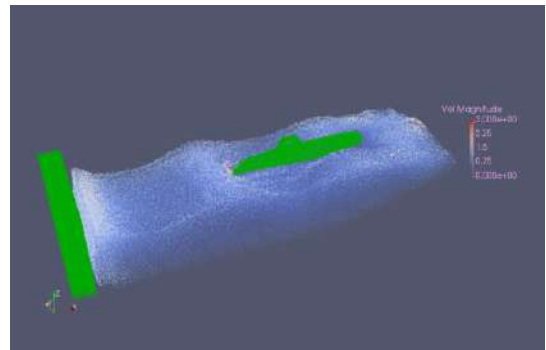
Table 3. Location of pressure sensors

	The location		
	X axial(to ordinate)	Y axial	Z axial
P1	1.750m	0.0m	On the deck
P2	1.531m	0.0m	On the deck
P3	1.313m	0.0m	On the deck
P4	0.952m	0.0m	On the deck

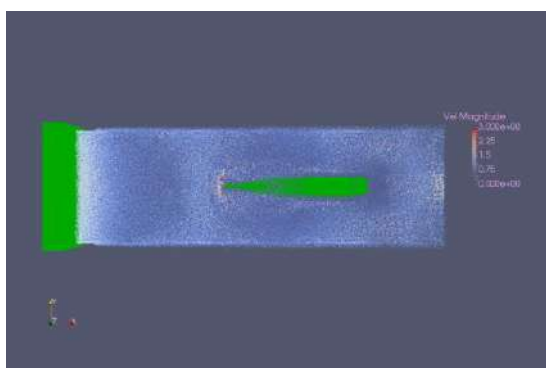
IV. RESULTS AND DISCUSSION

A prism domain with dimensions $15\text{m} \times 4\text{m} \times 2.0\text{m}$ is used, while the ship model length is approximately 4.5 m. The total number of SPH particles is approximately 7.8×10^5 .

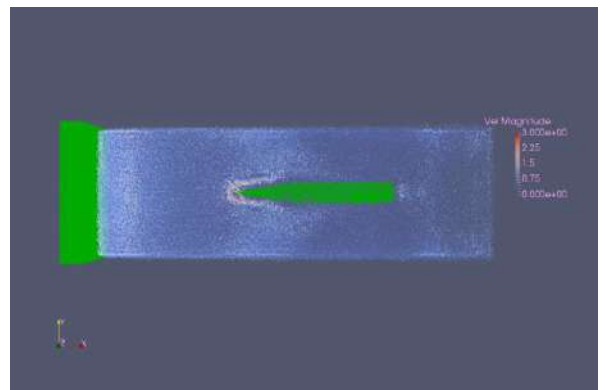
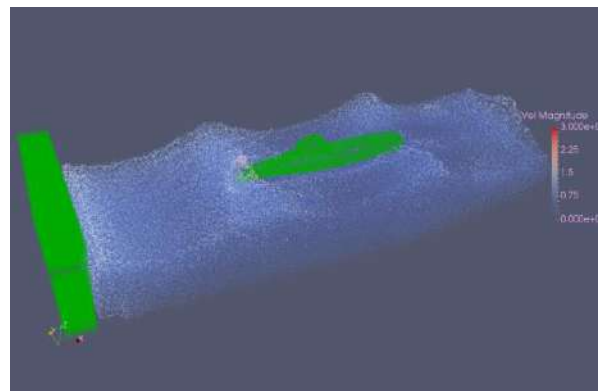
The results of numerical simulation are shown in Fig 5, the water moves towards the bow due to the effect of trim by bow. Then pitch motion makes the upcoming wave begin to run up and cross the freeboard under the ship-wave interaction. When the ship pitches deeper into the water, water around the bow will cross the freeboard from the direction normal to the deck edge. Due to the bulwark and the relative motions between the bow and the surrounding water, the inflows of green water normally had a vertical velocity component. Therefore, green water flows tended to take off the deck edge before plunging back on deck. These processes are similar with the dam break model. As the water landed back on the deck due to gravity, it causes green water to happen. Because of the horizontal relative motion between ship and wave, the water moves along the deck and falls down on the deck due to gravity. The severe green water may cause damage to the superstructure.



a. Phase one



b. Phase two



c. Phase three

Fig 5. Numerical simulation of green water

The snapshot from the experiment is depicted in Fig 6. The model tests are carried out in China Ship Research Centre.

From the pictures, we can see the numerical simulation can capture some details that agree well with the experiment. These pictures show case 1(wave length is 4.5m)condition.



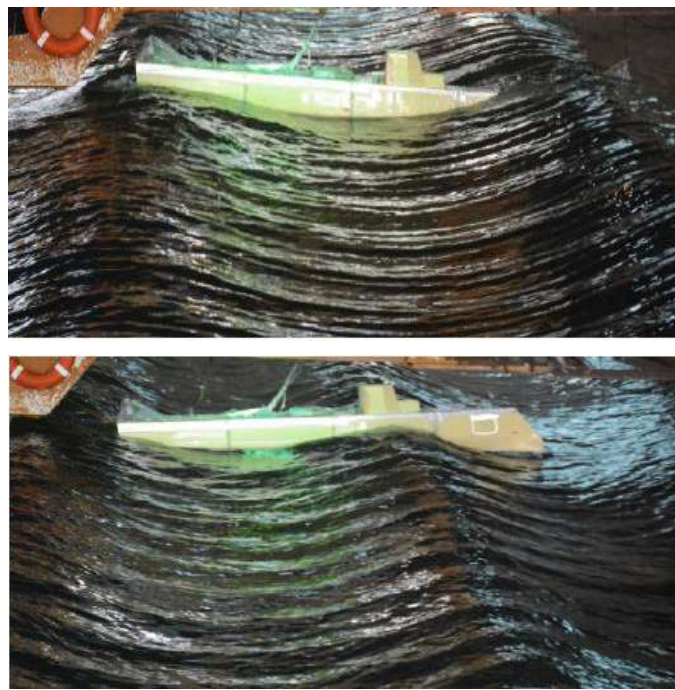


Fig 6. Physical model test

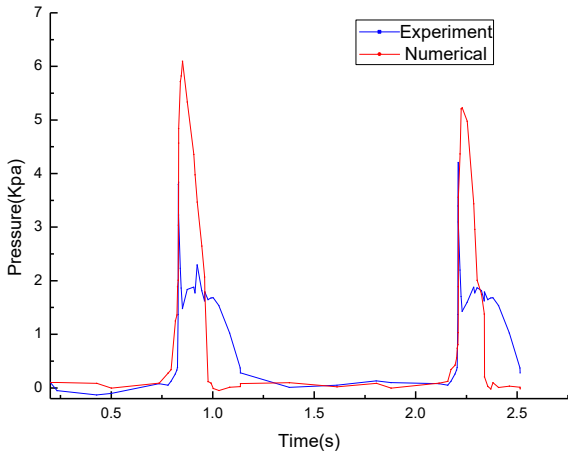


Fig 7. Comparison between experimental recordings and numerical results about pressure

A comparison between experimental water pressure measurements and those predicted by SPH method is presented in Fig 7. Due to the limited space, only the sensor 1 is presented here.

From the result, the predicted maximum water pressure magnitudes are more than those measured experimentally. This disagreement can be attributed to the size of particle or others. And the period of green water is last longer in the model test than numerical simulation.

We can see that the pressure drop abruptly to the half in the experiment, but the numerical results can't reveal this phenomenon. There may be some factors that are not considered in the numerical simulation, such as Reynolds number, viscosity.

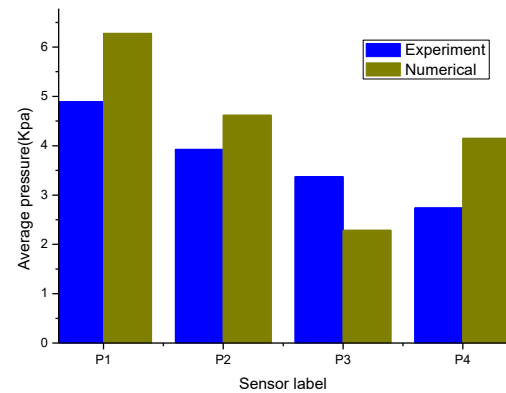
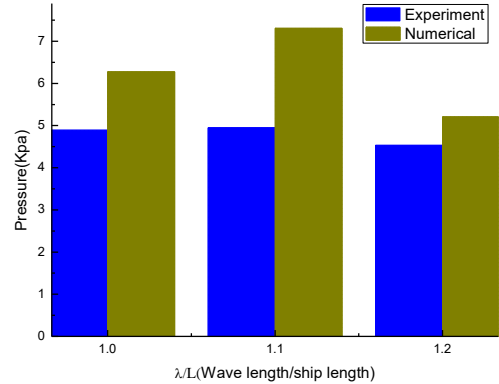


Fig .8 Comparison between experimental recordings and numerical results about average maximum pressure

Fig 9. Comparison between experimental recordings and numerical result about water pressure(P1)
in different wave lengths

At the same time, we compare the maximum pressure averages of the experimental and numerical simulations for a given period of time. This is very important value in engineering applications, and it can provide effective evaluation information about ship. For this reason, four pressured test points are compared. The results is shown in Fig 8. From the picture, the numerical results are close to the experimental ones. Due to the strong nonlinear problem, the error is accepted. For three different wave lengths, only the test point P1 is listed here in the Fig 9. From the picture, the water pressures from numerical calculation are relatively close to the ones from model test. Through a series of numerical calculations and comparisons, it can be seen that the SPH method is stable, accurate and reliable.

V. CONCLUTIONS

In this paper, SPH method has been used to predict green water flooding on a ship's deck in three dimensions. Four pressure sensors on the deck are used for recording the water pressure. These data are then compared to the experimental work. With the aim of simulating engineering problems, we can get some conclusions.

SPH method is feasible to apply on the green water phenomenon. Due to the meshless, the large deformation of free surface can be simulated more close to the physical experiment. When the water flows beat the deck, the flows has a x-axial velocity and then the flows will hit superstructure. This phenomenon is captured by SPH method.

Although there is a certain deviation, the results of numerical calculation and experimental simulation are relatively close, and the four pressure test points are relatively stable. Four test points are also verified by comparison of pressure at three different wavelengths. The deviations here are not only due to numerical calculations, but also possible deviations from the tests. Above all, the numerical results are accepted and need to be improved in the future.

At the same time, there are several problems needed to be solved in the engineering realm. In the three dimension wave generation, wave decay due to the energy dissipation in some degree. Stability, reliability, accuracy and time consume are all important sides in engineering applications. These sides are expected to improve with resolution.

REFERENCES

- [1] B.Hamoudi , K.S. Varyani, "Significant load and green water on deck of offshore units/vessels," Ocean Engng, Vol.25,No.8, pp:715-731,1998
- [2] Hitoshi, Abbas Khayyer, "Current achievements and future perspectives for projection-based particle methods with applications in ocean engineering," J.Ocean Eng.Mar.Energy(2016)2:251-278.
- [3] Kai Pan, "Simulating Fluid-Solid Interaction Using Smoothed Particle Hydrodynamics Method," PhD thesis, Massachusetts Institute of Technology.
- [4] Mashy David Green, "Sloshing simulations with the smoothed particle hydrodynamics (SPH) method," PhD thesis, Imperial College London.
- [5] Angelantonio Tafuni, Jos éM. Dom íguez, Renato Vacondio , Alejandro J. C. Crespo, "Accurate and efficient SPH open boundary conditions for real 3-D engineering problems," 12th International SPHERIC Workshop, At Ourense, Spain.
- [6] C. Altomare, T. Suzuki , J.M. Dom íguez, A. Barreiro, A.J.C. Crespo and M. Gómez-Gesteira, "Numerical wave dynamics using Lagrangian approach: wave generation and passive & active wave absorption ,," 10th International SPHERIC Workshop, Parma, Italy.
- [7] D. Le Touz é A. Marsh, G. Oger, P.-M. Guilcher, C. Khaddaj-Mallat, B. Alessandrini, P. Ferrant, "SPH simulation of green water and ship flooding scenarios," 9th International Conference on Hydrodynamics, Shanghai, China, pp231-236
- [8] Zhenghao Liu, Decheng Wan, "Numerical simulation of green water on S-175 containership," The Second Conference of Global Chinese Scholars on Hydrodynamics, Wuxi, China.
- [9] Canelas RB, Dom íguez JM, Crespo AJC, Gómez-Gesteira M, Ferreira RML. (2015). "A Smooth Particle Hydrodynamics discretization for the modelling of free surface flows and rigid body dynamics. International Journal for Numerical Methods in Fluids", 78: 581-593.

Application of Improved SPH Solid-Wall Boundary Model in Missile Waterexiting

Zheng Hua-lin

Xi'an Hi-Tech Institute
Xi'an 710025, China
zero2one@aliyun.com

Qiang Hong-Fu

Xi'an Hi-Tech Institute
Xi'an 710025, China

Chen Fu-Zhen

Xi'an Hi-Tech Institute
Xi'an 710025, China

Sun Xin-ya

Xi'an Hi-Tech Institute
Xi'an 710025, China

Abstract—For its meshfree nature, smoothed particle hydrodynamics (SPH) faces challenges on solving solid-wall interaction problems. By correcting the condition and force direction between fluid particles and boundary particles, an improved SPH solid-wall boundary model is proposed by LiuHu, which can apply boundary condition effectively. The classical water entry of a eccentric block problem are simulated, which are respectively compared with the experimental results and another simulation results. And with this treatment, the 2-D missile waterexiting problem is simulated, which explores the changes of the longitudinal load on the process of missile waterexiting. The present study expands application of SPH method in solving solid-fluid interaction problems, and with the help of it, the stable flow field, smooth velocity and pressure fields could be obtained.

I. INTRODUCTION

Submarine-launched missile waterexiting is a very complex fluid-solid coupling process. Missile launched from the submarine tube to the water surface after ignition is very fast with variable factors and complex environment, which directly affects the performance of the later missile performance.

With the continuous development of computer technology and the improvement of numerical calculation, it is an important means to use the computer to carry on the effective numerical simulation on this complex process. At present, the NS equations of the coupled multiphase flow model are solved to simulate the missile waterexiting process. The multiphase flow model can be divided into free interface tracking method such as MAC^[1], VOF^[2] methods, as well as soft drinks mixed models such as the Mixture model. These models have their own advantages and disadvantages, which can achieve a good application effect in the numerical calculation.

In recent years, a meshless smooth particle hydrodynamic method (SPH method)^[3,4] has also been developed in numerical simulation of interface deformation problems and fluid-solid coupling problems. In the whole flow field, the flow field media is separated into a series of particles, which carry all the flow field variables and are controlled by the constraints in the space for a certain degree of movement. The two-dimensional simulation of the

process of submarine-launched missile was carried out. In order to simplify the model, the gas, air, cavitation and phase change are ignored in the simulation.

II. SPH METHODOLOGY

A. Governing equation and State equation

For a viscous incompressible fluid, the governing equations can be written in Lagrangian form as:

$$\frac{d\rho}{dt} = -\rho \nabla \cdot \mathbf{v} \quad (1)$$

$$\frac{d\mathbf{v}}{dt} = -\frac{1}{\rho} \nabla p + -\frac{1}{\rho} \nabla \cdot \boldsymbol{\tau} + \mathbf{g} \quad (2)$$

$$\frac{d\mathbf{r}}{dt} = \mathbf{v} \quad (3)$$

where ρ , p , \mathbf{v} , \mathbf{r} , \mathbf{g} are density, pressure, velocity, position and body force, respectively, and $\boldsymbol{\tau}$ is the viscous stress tensor.

The traditional SPH method treats the incompressible fluid as weakly compressible, and the pressure is calculated from the following equation of state:

$$p = p_0 \left[\left(\frac{\rho}{\rho_0} \right)^\gamma - 1 \right] \quad (4)$$

where ρ_0 is the initial density of the fluid, p_0 is the reference pressure, constant $\gamma = 7$. Following the analysis of Monaghan, $P_0 = \frac{c_s^2 \rho}{\gamma}$, and the sound speed c_s is artificial, it is suggested to be at least 10 times of the maximum of the flow velocity, which can limit the variation of the density to less than 1%.

B. SPH discretization

In SPH method, the computation domain is discretized into a set of particles. Particles interact with each other within a specified range through kernel functions. Any function and its derivative can be approximated as:

$$\langle f(\mathbf{r}_i) \rangle = \sum_{j=1}^N \frac{m_j}{\rho_j} f(\mathbf{r}_j) W(\mathbf{r}_i - \mathbf{r}_j, h) \quad (5)$$

$$\langle \nabla \cdot f(\mathbf{r}_i) \rangle = \sum_{j=1}^N \frac{m_j}{\rho_j} f(\mathbf{r}_j) \cdot \nabla_i W(\mathbf{r}_i - \mathbf{r}_j, h) \quad (6)$$

where i, j are the index of the particles, N is the number of particle in the support domain, $m_j, \rho_j, \mathbf{r}_j, f(\mathbf{r}_j)$ are the mass, density, position and function value of particle j . $\langle f(\mathbf{r}_i) \rangle, \langle \nabla \cdot f(\mathbf{r}_i) \rangle$ are the approximated values of function and derivative of particle i positioned at \mathbf{r}_i . h is the smoothing length. $W(\mathbf{r}_i - \mathbf{r}_j, h)$, $\nabla_i W(\mathbf{r}_i - \mathbf{r}_j, h)$ are kernel function and its derivative with respect to particle i .

In this work, the cubic spline is used as the kernel function^[5]:

$$W(r, h) = \alpha_d \times \begin{cases} 1 - \frac{3}{2}q^2 + \frac{3}{4}q^3, & 0 \leq q \leq 1 \\ \frac{1}{4}(2-q)^3, & 1 \leq q \leq 2 \\ 0, & q > 2 \end{cases} \quad (7)$$

where $q = \frac{r}{h}$, and α is a normalization constant with values of $\frac{1}{h}$, $\frac{15}{7\pi h^2}$ and $\frac{3}{2\pi h^3}$ in one, two and three dimensions.

Using the above-mentioned SPH approximation, the governing equations(1)-(3) can be discretized as:

$$\frac{d\rho_i}{dt} = \sum_{j=1}^N m_j \mathbf{v}_{ij} \cdot \nabla_i W_{ij} \quad (9)$$

$$\frac{d\mathbf{v}_i}{dt} = -\sum_{j=1}^N m_j \left(\frac{p_i + p_j}{\rho_i \rho_j} + \Pi_{ij} \right) \nabla_i W_{ij} + \sum_{j=1}^N m_j \frac{\mu_i + \mu_j}{\rho_i \rho_j} \mathbf{v}_{ij} \frac{\mathbf{r}_{ij} \cdot \nabla_i W_{ij}}{r_{ij}^2} + \mathbf{g}_i \quad (10)$$

$$\frac{d\mathbf{r}_i}{dt} = \mathbf{v}_i \quad (11)$$

where $\mathbf{v}_{ij} = \mathbf{v}_i - \mathbf{v}_j$, $\mathbf{r}_{ij} = \mathbf{r}_i - \mathbf{r}_j$, μ_i, μ_j are dynamic viscosities of particle i and j . Π_{ij} is artificial viscosity:

$$\Pi_{ij} = \begin{cases} -\frac{\alpha_{av} \bar{h}_{ij} c_s}{\bar{\rho}_{ij}} \frac{\mathbf{v}_{ij} \cdot \mathbf{r}_{ij}}{r_{ij}^2 + \varepsilon \bar{h}_{ij}^2}, & \mathbf{v}_{ij} \cdot \mathbf{r}_{ij} < 0 \\ 0, & \mathbf{v}_{ij} \cdot \mathbf{r}_{ij} \geq 0 \end{cases} \quad (12)$$

where $\bar{h}_{ij} = \frac{h_i + h_j}{2}$, $\bar{\rho}_{ij} = \frac{\rho_i + \rho_j}{2}$, $\varepsilon = 0.01$ is introduced to prevent a singularity. In this work, artificial viscosity is used to remove numerical oscillations with $\alpha_{av} = 0.05$.

C. Improved Solid-Wall Boundary model

In order to implement the coupling calculation between solid and fluid state and solve the problem of boundary application effectively, an improved SPH solid-wall boundary application model based on dummy particle method is applied, which may avoid particle penetration near the solid-wall boundary and numerical shock problem.

The solid-wall boundary model is represented according to the following equations^[6]:

$$\left(\frac{d\rho_i}{dt} \right)_b = \begin{cases} m_b \mathbf{v}_{ib} \cdot \nabla_i W_{ib}, & \text{if } \mathbf{v}_{ib} \cdot \mathbf{n}_b \neq 0 \\ 0, & \text{else} \end{cases} \quad (13)$$

$$(8) \quad \left(\frac{d\mathbf{v}_i}{dt} \right)_b = \begin{cases} -m_b \left(\frac{p_i + p_b}{\rho_i \rho_b} \right) \mathbf{n}_b \cdot \nabla_i W_{ib} \mathbf{n}_b, & \text{if } (p_i + p_b) > 0 \\ 0, & \text{else} \end{cases} \quad (14)$$

where subscripts $\left(\frac{d\rho_i}{dt} \right)_b$ and $\left(\frac{d\mathbf{v}_i}{dt} \right)_b$ denote the density, velocity increment due to the action of boundary particle b towards the fluid particle i . \mathbf{n}_b is the unit normal vector of the boundary dummy particle b .

D. Time stepping scheme

The equations of motion are integrated in time using a Leap-frog scheme:

$$\phi_i(t + \frac{\Delta t}{2}) = \phi_i(t - \frac{\Delta t}{2}) + \phi_i(t) \Delta t \quad (15)$$

$$\mathbf{r}_i(t + \frac{\Delta t}{2}) = \mathbf{r}_i(t) + \mathbf{v}_i(t + \frac{\Delta t}{2}) \Delta t \quad (16)$$

where ϕ_i stands for the density or velocity of particle i .

The time step Δt is limited for stability reasons, in this work, the CFL, viscous and body force conditions are considered^[7]:

$$\Delta t_{CFL} = \min_i \left(\frac{h_i}{c_s} \right) \quad (17)$$

$$\Delta t_{av} = \min_i \left(\frac{h_i}{c_s + 0.6\alpha c_s} \right) \quad (18)$$

$$\Delta t_{pv} = \min_i \left(\frac{h_i^2}{\nu_i} \right) \quad (19)$$

$$\Delta t_g = \min_i \left(\frac{h_i}{|\mathbf{g}_i|} \right)^{\frac{1}{2}} \quad (20)$$

where $\nu_i = \frac{\mu_i}{\rho_i}$ is the kinematic viscosity of particle i.

Finally, the time step Δt is chosen as:

$$\Delta t = \min(0.25\Delta t_{CFL}, 0.4\Delta t_{av}, 0.125\Delta t_{pv}, 0.25\Delta t_g) \quad (21)$$

III. NUMERICAL TESTS

A. Water entry of eccentric block

Water entry of eccentric block is a typical free surface problem with fluid-rigid interactions, which simulates the rotation and sinking process of the rigid block in the viscous fluid. This kind of model needs to solve the problems of interaction between hydrodynamics and solid dynamics and free surface flow. The test model is shown in Figure 1 and compared with Barcarolo[8] using the finite volume particle method (FVPM) in 2013.

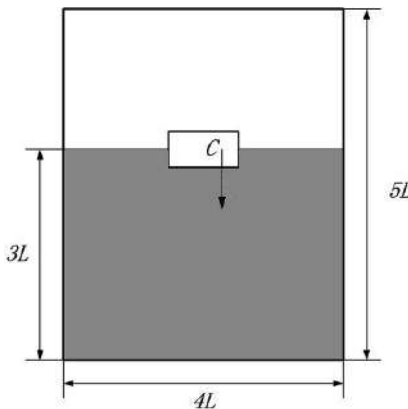


Figure 1. Schematic of water entry of eccentric block

As shown in Figure 1, the model is the same as Barcarolo, the block size is $1.0m \times 0.5m$, and the center of gravity C is initially located at $(0.25m, 3m)$, with $M = 1kg$, $I = 0.083kg \cdot m^2$, $g = 1m/s^2$, $\rho_0 = 1kg/m^3$, and $\nu = 2 \times 10^{-3} m^2/s$. The initial state of block is static. In the numerical calculation, the total number of particles is 32718, of which the fluid particles are

29349, the total number of dummy particles is 3369. All the boundary is set with 4 layers of dummy particles. Particle spacing $\Delta l_b = 0.02m$, time step $\Delta t = 5.0 \times 10^{-4}s$, sound velocity $c_s \approx 24.5m/s$. The surrounding flow field, the pressure distribution were calculated at different times as shown in Figure 2.

As is shown in Figure 2(a), the block begins to gradually tilt by gravity because the center of gravity of the block is not in the geometric center, and the block begins to sink gradually because the density of the block is greater than that of the fluid. In Figure 2 (b), $t = 1.50s$, the right side of the block gradually formed a cavity, then the block continues to rotate down, and the cavity gradually closed, and the block was impacted by the right side of the fluid. By applying the improved solid-wall boundary model, the wall pressure distribution is normal, without any pressure shock or particle penetration. After $t = 2.0s$ in Figure 2 (c), the rotational speed of the block is gradually reduced to zero due to the pressure of the left fluid and continues to drop to the bottom at a rotation angle.

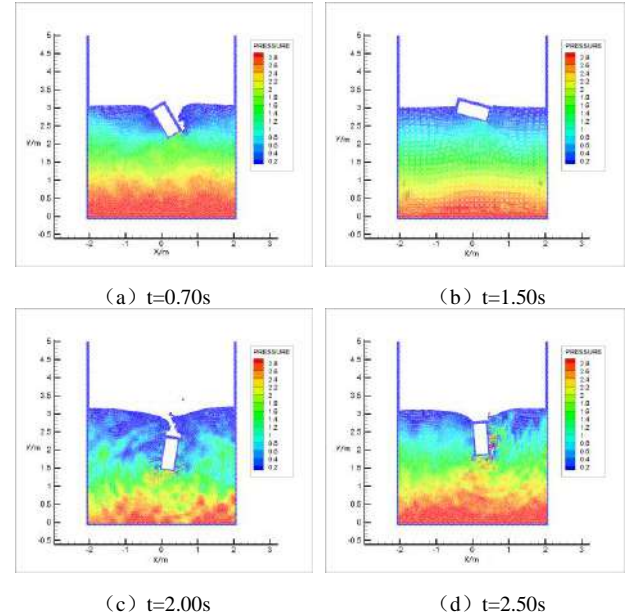
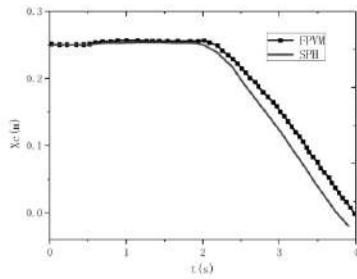
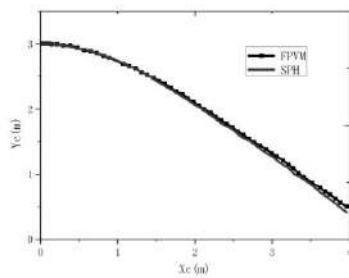


Figure 2. Surrounding flow field and the pressure distribution at different time

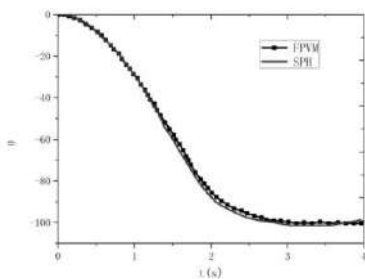
The position of the center of gravity and the deflection angle of the block are compared with the FVPM result (Barcarolo2013). It is found that the SPH method and the FVPM method are similar to those calculated as is shown in Figure 3. In Figure 3. (a), the slight deviation with FVPM in the X direction in the late movement may be due to the use of weak pressure algorithm caused by pressure wave echo. However but SPH has a lot saving in the calculation compared to FVPM method.



(a) Changes of the center of gravity X-axis Xc over time



(b) Changes of the center of gravity Y-axis Yc over time



(c) Changes of the deflection angle of the falling block over time

Figure 3. Comparison of Position Parameters for Simulating water entry of eccentric block by Different Methods

B. Missile waterexitting

The size of two-dimensional missile model is set as 2m \times 12m as shown in Figure 4, and the center of gravity C is initially located at (0m, -6m), with $M = 1.96 \times 10^4 \text{ kg}$, $I = 2.368 \times 10^6 \text{ kg} \cdot \text{m}^2$, $g = 9.8 \text{ m/s}^2$. The missile head is shaped as a single hood blunt. The tank is set as 20m \times 60m with $\nu = 2 \times 10^{-3} \text{ m}^2/\text{s}$. As shown in Figure 5, the total number of particles is 208832, of which the number of fluid particles is 200000, the number of missile dummy particles is 2400, and the tank is set with four layers of dummy particles with a total of 6432 particles. Time step $\Delta t = 5.0 \times 10^{-4} \text{ s}$, sound velocity $c_s \approx 300 \text{ m/s}$.

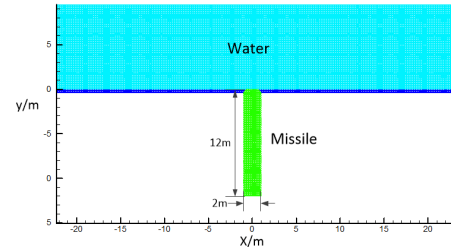


Figure 4. missile model with single hood blunt head

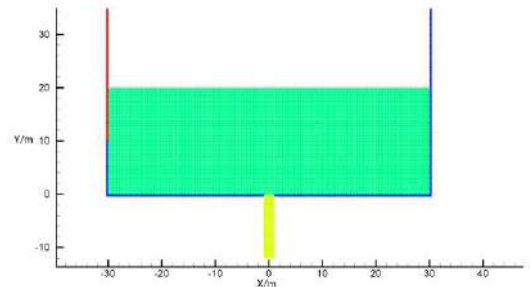
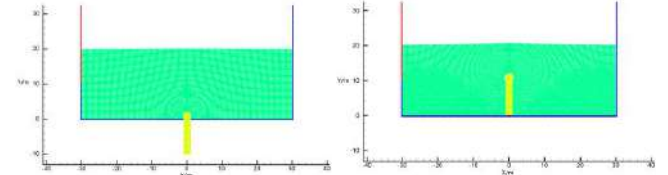


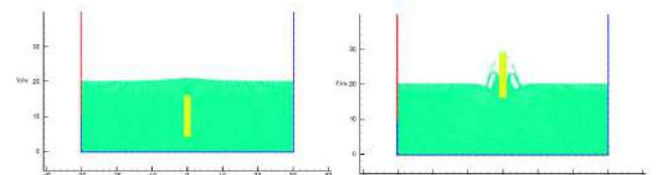
Figure 5. model of missile waterexitting

The waterexitting process of 2-D missile from ignition to water surface is simulated. The missile head is 20m away from the surface and the speed is 30m/s initially.



(a) t=0.1s

(b) t=0.8s



(a) t=0.1s

(b) t=0.8s

Figure 6. missile waterexitting process over time at $V = 30 \text{ m/s}$

As is shown in Figure 6, the location of the missile and surface deformation at different times can be seen. With the missile close to the surface, the water gradually becomes redundant, broken and splash out. The vertical acceleration in the process of missile waterexitting is as shown in Figure 7. At the initial ignition time, the missile was subjected to a great impact, reaching 3.8 g of acceleration, and the resistance in water was 2 g besides its own gravity. As the missile rises, the resistance decreases gradually. At $t = 1.07 \text{ s}$, the missile is subjected to a positive impact, which is caused

by the jet impingement generated by the return of the tail of the missile, resulting in a greater damage to the missile.

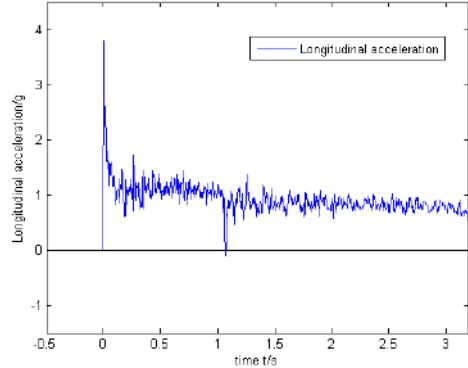


Figure 7. Longitudinal load change curve during the missile waterexiting

IV. CONCLUSIONS

In this paper, based on the SPH method and the improved solid-wall boundary model, the water entry of a eccentric block is simulated. The results are compared with the experimental results and the effectiveness of the SPH method and the improved wall boundary model are verified. In order to simplify the model, the gas, air, cavitation and phase transition are ignored in the simulation. Furthermore, The water exiting process of 2-D missile from ignition to water surface is simulated. Through the analysis of the simulation results, the longitudinal load changes in the process of missile water exiting are obtained. Based on these,

the presence of air and gas will be further considered in the future. To provide the accuracy and efficiency of the calculation, the least squares method, the non-reflective boundary conditions and the particle splitting algorithm will be studied further. On the basis of above all, a more systematic simulation of the process of missile water exiting should be carried out to further acknowledge the influence of the water depth, submarine speed and seawater movement on missile trajectory and outlet attitude, and lay the foundation for engineering application.

REFERENCES

- [1] C. W. Hirt and B. D. Nichols. Volume of fluid (VOF) method for the dynamics of free boundaries[J]. Journal of Computational Physics, 1981, Vol.39: 201-225
- [2] Stanley Osher and James A Sethian. Fronts propagating with curvature-dependent speed: Algorithms based on Hamilton-Jacobi formulations[J]. Journal of Computational Physics, 1988, Vol.79: 12-49
- [3] J.J. Monaghan, Simulating Free Surface Flows With SPH[J]. Journal of Computational Physics, 1994, 110: 399-406.
- [4] Monaghan J. J. An Introduction to SPH [J]. Computer Physics Communications. 1988, 48:89-96.
- [5] Qiang Hongfu, Han Yawei, Wang Kunpeng, Gao Weiran. Numerical simulation of water filling process based on new method of penalty function SPH [J]. Engineering Mechanics. 2011, 28(1): 245-250.
- [6] Liu Hu, Qiang Hongfu, Chen Fuzhen, Han Yawei, Fan Shujia. A new boundary treatment method in smoothed particle hydrodynamics. Acta Physica Sinica, 2015(09):384-397.
- [7] Monaghan J J. Smoothed particle hydrodynamics[J]. Annual Review of Astronomy and Astrophysics, 1992, 30:543-574.
- [8] Barcarolo, D.A., et al., Adaptive particle refinement and derefinement applied to the smoothed particle hydrodynamics method[J]. Journal of Computational Physics, 2014. 273: p. 640-657.

Aircraft tire water spray simulation using SPH

Yongkang HU, Yingfei RONG,
Dexin LENG
National Engineering Laboratory
Triangle Tire R&D
Weihai, China
huyongkang@triangle.com.cn

Fei XU, Xiangyang GAO
The College of Aeronautics
Northwest Polytechnical University
Xi'an, China

Rengang CAO, Wei DING,
Jun LV
Landing Gear System & Wheels
COMAC
Shanghai, China

Abstract—The sprays produced by aircraft tire running in water are complex and depends on the aircraft speed, tire shape and load, also the water depth. The serious consequence of water spray ingestion is the loss of engine power which will impact on the take-off and landing operations.

The present paper aims to investigate the chine design parameters of aircraft tire in function of water spray performance. Detailed aircraft tire construction models are being built with different chine design parameters using Abaqus/Explicit. The interaction between the aircraft and water is modeled using general contact of SPH elements on tire structure elements.

The numerical simulations at different loading and aircraft speeds are performed with different chine design models. It can be concluded that the chine design parameters have clear impacts on water spray pattern, position and speed.

I. DESCRIPTION OF AIRCRAFT TIRE WATER SPRAY

The sprays produced by aircraft tire running in water are complex and depends on the aircraft speed, tire shape and load, also the water depth. The serious consequence of water spray ingestion is the loss of engine power which will impact on the take-off and landing operations.

There are three directions to describe the aircraft movement, namely forward (X, 1), lateral (Y, 2) and vertical (Z, 3).

Figure 1 and Figure 2 show respectively the side spray at 90 and 110 knots.

It can be observed that the water spray at 110 knots is mainly lateral side whereas at 90 knots the water sprays both lateral side and also tire front side. There is a clear trace line formed by water spray and this trace line has certain angles with respect to the forward, lateral and vertical directions.



Figure 1. water spray at 90 knots.



Figure 2. water spray at 110 knots.

Figure 3 illustrates the water spray of short spool at different time.

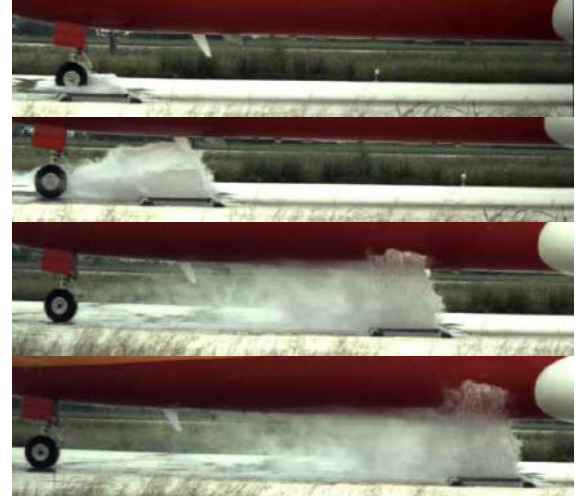


Figure 3. short water spool.

Figure 3 shows that the water moves up mainly in the lateral and vertical directions after the tire impacts the water spool with certain speed when observing the water spray at a fixed point on the ground.

II. AIRCRAFT TIRE WATER SPRAY ANALYSIS

Based on the observation from the trace line in Fig. 1 and Fig. 2, also the water movements in Fig. 3, the water spray characteristics can be defined by an angle and two velocities. The two velocities are the lateral (V2) and vertical (V3) speeds. The angle formed by vertical speed V3 to the lateral speed V2 is named as Frontview angle (FVA), illustrated in Figure 4.

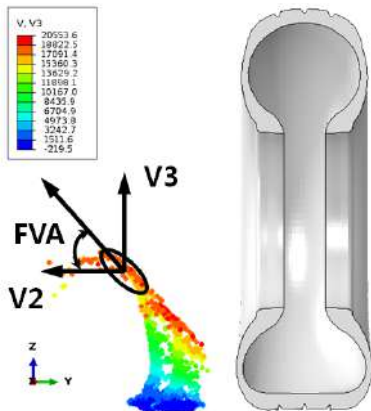


Figure 4. The definition of the water spray characteristics.

III. AIRCRAFT TIRE WATER SPRAY MODELING

The model to simulate the aircraft tire water spray has two parts, one is the aircraft tire model and the other is water spool model.

The aircraft tire size is 24x7.7 with and without chine design. The chine is an extra rubber ring to deflect the water spray trajectory.

The water spool model has the sizes of 1200x300x16 mm in X, Y and Z directions. The SPH method is used to model the water spool and the USUP type of EOS is defined as water properties. The Abaqus V6.14-5 was used to predict the aircraft tire water spray. Fig. 5 to 9 show the water spray tire and water models. Fig. 9 shows the position of the water particles to post process the simulation results. A typical model has near 3 million of DOFs and it takes about 7 hours using 16 cores.

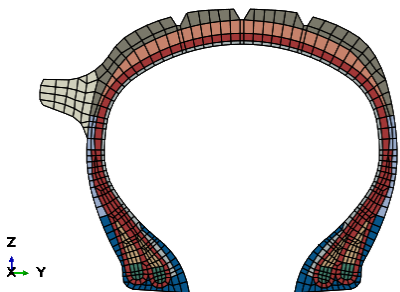


Figure 5. Aircraft tire cross section model with chine design.

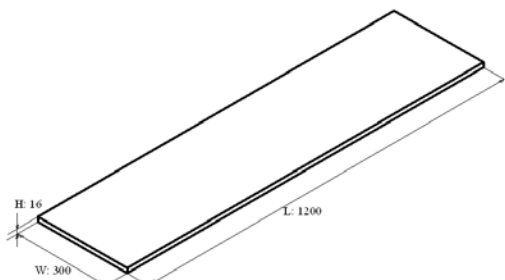


Figure 6. Water spool geometry model.

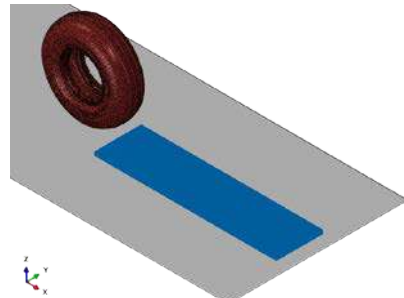


Figure 7. Tire and water spool assembly model.

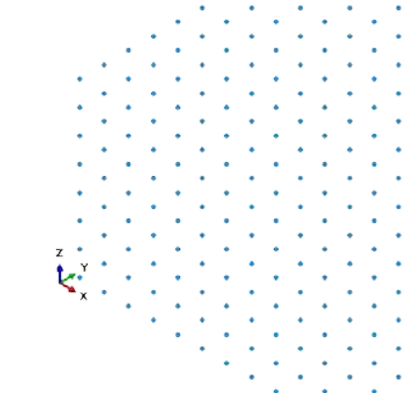


Figure 8. Water SPH particles model.

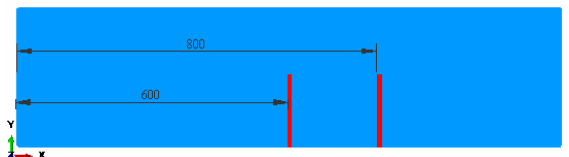


Figure 9. Position of water particles used for postprocessing

IV. INFLUENCE ON WATER SPRAY OF TIRE DESIGN PARAMETERS

Many tire design parameters and loading conditions can be modified to investigate the influence on water spray characteristics. In this paper, the water spray characteristics are focused on the chine design parameters and the tire load also the aircraft velocity.

A. Chine design parameters

The chine design parameters like chine width and height change the chine geometrical shape. The aim for chine design is to reduce both the water spray velocities (V2 &V3) and the Frontview angle (FVA).

Figure 10 illustrates 4 chine designs: G0 is the original tire without chine, G1 is the tire with original chine design, D and H are the modified chine designs.

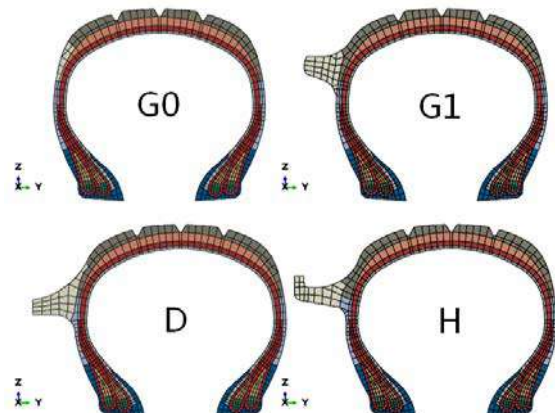


Figure 10. Chine designs

B. Tire loads and aircraft velocities

Aircraft tire has to be operated at specific load range and inflation pressure. The standard load for this aircraft tire is of 22266.4 N and the inflation pressure is of 0.869 MPa.

In this paper, the inflation pressure keeps constant while the tire load has three levels: 50%, 100% and 150% of the standard load. The aircraft velocity has also three levels: 90, 100 and 110 knots.

Figure 11 illustrates the influence of the chine design on the water spray. It can be observed the chine design impact significantly the water spray pattern. H design shows the best capability to prevent the water spray.

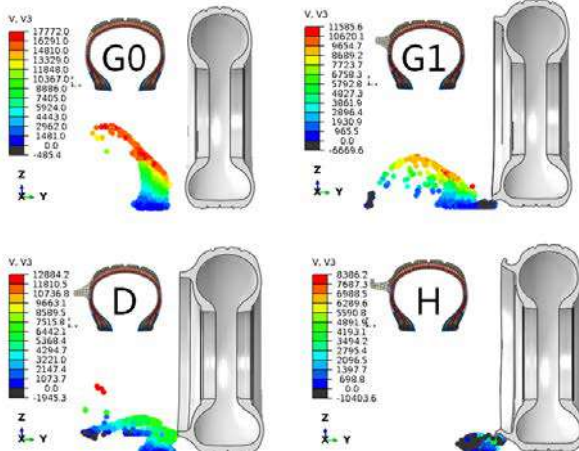


Figure 11. Water spray pattern at 90 knots (Loads=22266.4 N, Pressure=0.869 MPa)

Figure 12 provides the impact of the tire loads on the water spray at high speed. It shows tire load has different influence on the water spray. D design shows a decrease of the FVA with the increase of tire load whereas H design shows an increase of the FVA with the increase of tire load.

Figure 13 gives the influence of aircraft velocity on water spray at heavy tire load. Both D and H design show an increase of FVA with the increase of aircraft velocity, especially H design.

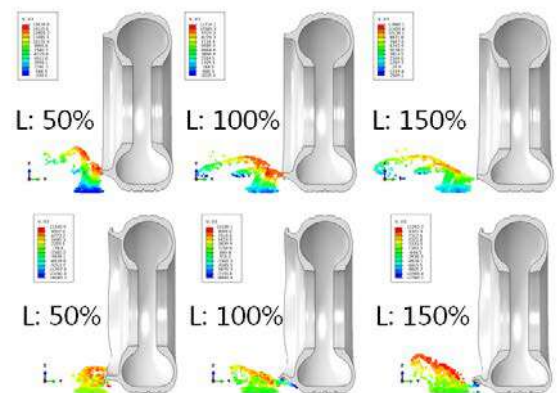


Figure 12. Tire load influence on water spray at 110 knots.

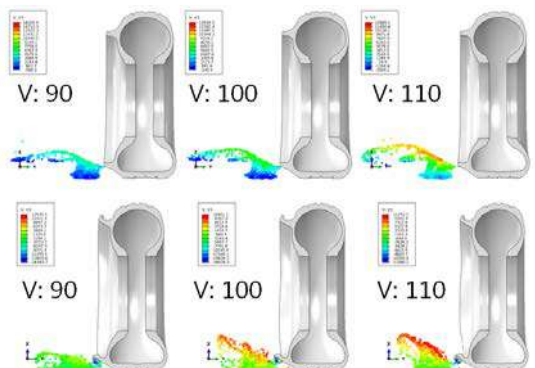


Figure 13. Aircraft velocity on water spray at 150% load.

V. COMPARISON WITH EXPERIMENTS

Several real scale aircraft tests were performed to test the different chine design at specific aircraft speed range.

Figure 14 to Figure 17 provide the experiment results for D and H chine design at 90 and 110 knots. It can be observed both D and H chine designs cannot prevent totally the water from spraying into aircraft engine, especially at high speed.



Figure 14. D design at 90 knots (2015.11)



Figure 15. D design at 110 knots (2015.11)



Figure 16. H design at 90 knots (2016.11)



Figure 17. H design at 110 knots (2016.11)

VI. CONCLUSIONS

SPH method can be used to predict the water spray of aircraft tire running into water spool. The tire chine design has significant impact on water spray pattern. Good trend of the prediction was obtained compared with experiments.

Further analyses and model prediction improvements are still being needed to correlate better the experiment results, especially at high speed, in order to prevent totally the water sprayed into aircraft engine, which remains a challenging issue to be solved.

ACKNOWLEDGEMENT

The authors would like to thank COMAC to provide the partial funding for this project. Special thanks go to other colleagues in Triangle tire for different tasks like mesh generation, SPH benchmark testing, different chine design and manufacture, etc.

REFERENCES

- [1] ESDU report 83042, Estimation of spray patterns generated from sides of aircraft tyres running in water or slush, D.J. Mitchell, 1998.
- [2] NASA TM X-72695, The effect of chine tires on nose gear water-splay characteristics of a twin-engine propjet airplane, Thomas J. Yager, 1975.
- [3] SAE aerospace information report 1904B, Tire spraysuppression-airplane design and consideration for, 2006.

Numerical Simulation Research on Multi - Floor Building

Breaking by Conical Projectile with SPH Methods

Qiang Hongfu, Sun Xinya, Chen Fuzhen,
Zheng Hualing, Shi Chao, Zhang Guoxing,
Department of Power Engineering,
Xi'an Hi – Tech Institute,
Xi'an, China
1430167246@qq.com

Qiang Hongfu, Sun Xinya, Chen Fuzhen,
Zheng Hualing, Shi Chao, Zhang Guo Xing,
Department of Power Engineering,
Xi'an Hi – Tech Institute,
Xi'an, China
1430167246@qq.com

Abstract: In the modern war, it is an important means to win the war by effectively breaking the enemy important military facilities, such as the command center of the ground floor. Based on sph method with fully variable smoothing lengths, the HJC constitutive model and SDPH method are used to deal with the deformation and damage of concrete slab under impact load and the free scattering of dead concrete particles, and the numerical simulation of the process of striking the multi - floor building . The damage degree of multi - floor buildings is analyzed, and the damage calculation and evaluation model of high - speed penetration of multi - storey buildings is established. Through the theoretical analysis, it is reasonable to show that the numerical simulation results are reasonable, which has some guiding value for predicting the impact performance of the missile and the effective fire strike.

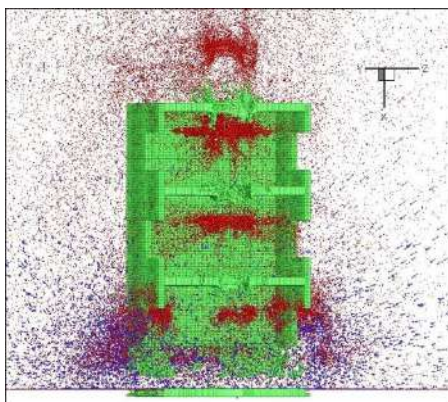


Figure 2-Schematic diagram of calculation of

I. INTRODUCTION

Penetration warhead is a conventional warhead of the combined action of penetration and explosion, which is wide

-ly used in modern warfare as an effective means of attacking concrete building floor (such as enemy ground command post, communication station, presidential palace). Penetration warheads compared with ordinary bombs, one has a certain depth of penetration, filling effect was significantly strengthened; Second, to ensure the warhead have a certain degree of penetration, the strength of the missile structure and stiffness requirements higher, The shell is usually thicker, so it is greatly influenced by the shell of the combat department to explosive damage. In order to effectively assess the penetration of the warhead damage, it is necessary to study the impact of its numerical simulation, and for strengthening the national defense System under the conditions of high-tech warfare viability and effective against the enemy's military objectives is of great significance.

The study of concrete penetration at home and abroad has been studied for many years, and some empirical formulas and experimental models of simulated penetration process have been obtained from experimental data. Frew et al. [4] demonstrated the empirical formula of Forrestal invasion by experiment, and further discussed the problem of parameter determination in empirical formula. Ou Yangchun and Zhao Zhiguo [5] based on the three-way stress cavity expansion theory, combined with experimental data Influence of Different Concrete Materials Model on Penetration Results. But the study of multi-storey buildings has not been reported in detail. Smoothed particle hydrodynamics (SPH) method, as a kind of meshless particle method, can avoid grid

re-division and algorithm coupling in large deformation calculation of concrete impact and explosion, so it is very suitable to solve such problem. The earliest use of SPH method to simulate the explosion can be traced back to J.W.Swiegle, et al, and L.D.Libersky et al [9] first put the SPH method used for the field of high-speed impact, Qiang Hongfu et al. [13] used the modified SPH method proposed by F.Ott et al. [8] to simulate the jet process, and analyzed the effect of different detonation methods on the jet. In this paper, based on the full-smooth-length SPH method proposed by Qiang Hongfu et al. [13], the modified SPH method [8] and the SDPH method are used to penetrate the multi-storey buildings and locate the damaged buildings. The physical image of the penetration process is obtained and compared with the actual phenomenon.

II. BASIC THEORY

A. SPH and SDPH method

In the SPH method, any physical quantities $f(x)$ and $\nabla f(x)$ can be represented by the sum of all the particles in their domain:

$$\langle f(x_i) \rangle = \sum_{j=1}^N \frac{m_j}{\rho_j} f(x_j) W_{ij} \quad (1)$$

$$\langle \nabla f(x_i) \rangle = \sum_{j=1}^N \frac{m_j}{\rho_j} f(x_j) \nabla_i W_{ij} \quad (2)$$

Where m is the mass and ρ is the density of the particle; N is all the particles in the Calculation area; $W_{ij} = W(x_i - x_j, h)$ is the kernel function; h is the smooth function, usually use cubic spline function.

In order to better track and simulate the characteristics of random motion of particles and solve the problem of large computational complexity in particle tracing, SDPH method is adopted in this paper. The method considers particles as a quasi-fluid from the point of view of particle dynamics. Assuming that there are n particles in the flow field area, the average volume of the particles is V_p , the average mass is m_p , the total volume of space is V_0 , for the particles to be fluid, the effective density $\hat{\rho}_p$ of the particles can be expressed as:

$$\hat{\rho}_p = \alpha_p \rho_p = \frac{nV_p}{V_0} \rho_p = \frac{m_p}{\frac{V_0}{n}} = m_p \sum W = \rho_{SPH} \quad (3)$$

Where $\sum W = \frac{n}{V_0} = \frac{1}{V_{\text{eff}}}$, p is the Particle subscripts, α_p is the Particle volume fraction and ρ_p is the Particle density. Thus establishes the relationship between the density of the SDPH particles and the effective density of the particles and the volume of the SDPH particles and the volume of the particles.

In order to simulate the problem of violent changes in medium density and smooth length during the penetration process, this paper adopts the completely smooth slippery length. The method starts from a symmetric kernel approximation and regards the smooth length as a function of space and time. The SPH equations based on the complete smoothed length algorithm are:

$$\begin{aligned} \frac{d\rho_i}{dt} &= m_i \sum_{j=1}^N [v_{ij} \cdot \nabla_i W_{ij} + \frac{1}{2} (\frac{dh_i}{dt} + \frac{dh_j}{dt}) \frac{\partial W_{ij}}{\partial h}] \\ \frac{dv_i}{dt} &= - \sum_{j=1}^N m_j \left(\frac{f_i \sigma_i + f_j \sigma_j}{\rho_i \rho_j} + \Pi_{ij} \right) \nabla_i W_{ij} \\ \frac{de_i}{dt} &= (\frac{\sigma_i}{\rho_i \rho_j} + \Pi_{ij}) \frac{d\rho_i}{dt} \\ \frac{dh_i}{dt} &= - \frac{1}{d} \frac{h_i}{\rho_i} \frac{d\rho_i}{dt} \\ f_i &= (1 + \frac{h_i}{d \rho_i}) \sum_{j=1}^n m_j \frac{\partial W_{ij}}{\partial h_i} - 1 \end{aligned} \quad (4)$$

Where σ is the total stress tensor, Π_{ij} is the artificial viscosity, it is difficult to solve the problem for the smooth length change rate $\frac{dh_i}{dt}$ and the density change rate $\frac{d\rho_i}{dt}$, we use the iterative method to solve the density equation and the smooth length.

B. The state equation and parameters of the material

In this paper, TNT is used in the simulation. The detonation velocity is 6930m / s. The detonation gas' state uses the JWL equation(Eq.(5)).

$$p(e, v) = A \left(1 - \frac{w}{R_1 v} \right) \exp(-R_1 v) + B \left(1 - \frac{w}{R_2 v} \right) \exp(-R_2 v) + \frac{w \rho_0 e}{v} \quad (5)$$

Where $\rho_0 = 1630 \text{ kg/m}^3$ is the initial density of the

TNT explosive, $\nu = \rho_0 / \rho$ is the ratio of the initial density of the explosive and the detonation gas, e is the specific energy of the detonation gas, and A, B, R_1, R_2, w are coefficients obtained from the test fitting, the values as following: $A = 371.2 \text{ GPa}$, $B = 3.231 \text{ GPa}$, $R_1 = 4.15$, $R_2 = 0.95$, $w = 0.3$.

The state equation of the penetration warhead is chosen by the Mie-Grüneisen equation of state^[15] (Eq.(6)and Eq.(7)).

$$p(\rho, e) = (1 - \frac{1}{2} \Gamma \eta) p_H(\rho) + \Gamma \rho e, \quad \eta = \frac{\rho}{\rho_0} - 1 \quad (6)$$

$$p_H = \begin{cases} a_0 \mu + b_0 \eta^2 + c_0 \eta^3 & \eta > 0 \\ a_0 \mu & \eta < 0 \end{cases} \quad (7)$$

Where $\rho_0 = 7850 \text{ kg/m}^3$ is the initial density. $\Gamma = 1.99$, $c_s = 3940 \text{ m/s}$, $S_s = 1.489$.

The HJC constitutive model is adopted for concrete, the model is divided into three parts: the intensity model (Fig.1), the cumulative damage model (Fig.2) and the state equation (Fig.3).

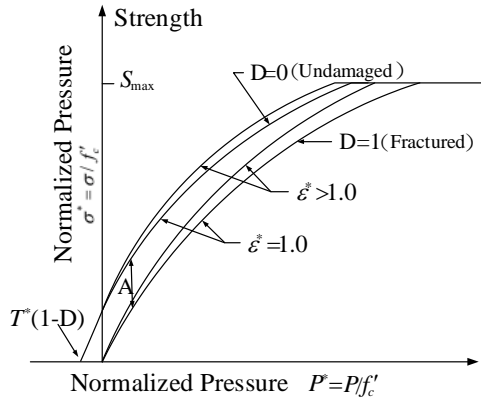


Figure 1. intensity model

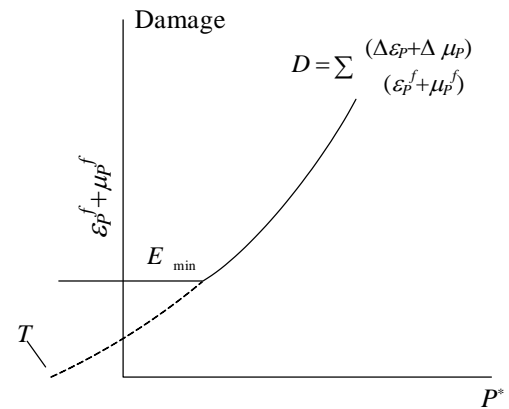


Figure 2.cumulative damage model

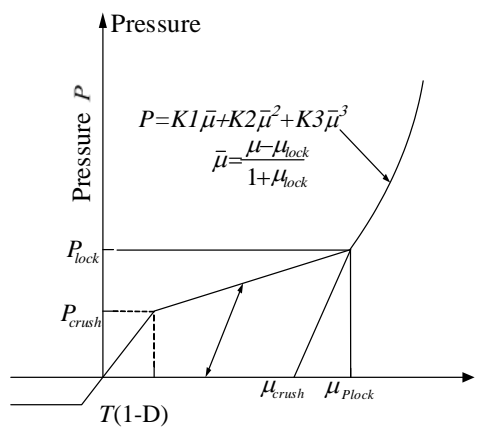


Figure 3. the state equation

The concrete modulus of the concrete target^[14]:

$G = 14.8 \text{ GPa}$ is the shear modulus; $\rho_0 = 2450 \text{ kg/m}^3$ is the initial density; $A = 790 \text{ MPa}$ is the ratio of complete breaking strength to no damage strength for given hydrostatic pressure; $B = 1600$ is the pressure strengthening factor; $N = 0.61$ is the Hardening factor; $\dot{\epsilon}_0 = 1.0$ is the reference strain rate; $C = 0.007$ is the strain rate sensitivity factor; $f'_c = 48 \text{ MPa}$ is the quasi-static uniaxial compressive strength; $S_{\max} = 7.0$ is the maximum normalized strength that concrete can achieve; $D_1 = 0.04$ and $D_2 = 1.0$ are concrete damage constant; $\epsilon_{p,\min}^f = 0.01$

is the concrete crushing of the smallest plastic strain; $P_c = 16.0 \text{ MPa}$ is the crushing pressure; $\mu_c = 0.001$ is the crushing volume strain; $P_i = 800 \text{ MPa}$ is the compaction pressure; $\mu_i = 0.1$ is the volume strain; $T = 2.5 \text{ MPa}$ is the maximum tensile hydrostatic pressure ; $K_1 = 85 \text{ GPa}$, $K_2 = -171 \text{ GPa}$ and

$K_l = 208Gpa$ are the concrete material constant.

The motion state of the rigid body is determined by the conservation of momentum and momentum moment. Equation (8) is the motion equation of the rigid body.

$$\frac{d}{dt}(mv_c) = \mathbf{F} \quad (8)$$

Where m is the mass of the rigid body; v_c is the heart rate of the rigid body; F is combined with external force, including surface force, gravity and so on. As the missile is penetrating the concrete, don't consider the rotation of the missile body.

III. NUMERICAL SIMULATION

A. Building model

Numerical simulation of the warhead used in the multi-storey building model as shown in Fig.4 (a), the warhead model composed by three parts of the end and warhead charge, warhead shell. Missile material is selected D6A Steel, diameter of 450mm, length of 2000mm, missile head cone section length of 500mm, using rigid body model. Multi-floor building's materials is the concrete, the structure of the four corners is the rectangular form, floor and wall's thickness are taken 300mm, each building size 8000mm, 5000mm, 4000mm (length, width, height). The specific particle configuration as Fig.4 (b), the particle spacing is 30mm, the kinetic energy is broken into 45310 particles, and the concrete target is scattered to 716153 particles.

In the calculation, the XSPH parameters $\varepsilon=0.3$ were used. The failure of the concrete particles was characterized by SDPH particles, the kernel function was chosen as the cubic spline function [14], the smooth length was 1.5 times the particle spacing, and the time integral was in the leapfrog, the time step was $0.1\mu s$. The impact speed of Penetration warhead to the surfaces of multi-storey building is 1500m /s, and use the delay point fixed detonation way, the timing of the warhead pressure is the first time to reach the maximum, the delay is 14ms, the starting point is (0,70mm). Penetrating the warhead impact stress is much smaller than its own material strength limit, so treat the warhead to the rigid body.

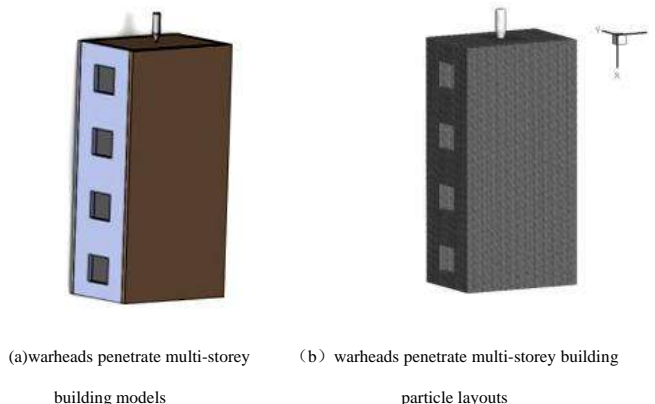


Figure 4. Example model structure

B. Results analysis

Fig.5 shows the stress change trend of the building's top floor at $26.3\mu s$ (the warhead reaches the surface of the building). The compressive stress (258.6Mpa) at the collision point A (-11.04, -0.77, 5.96) is much higher than that of concrete of the ultimate compressive strength of 48Mpa [14], the point of concrete is failure and to spread around the compressed wave.

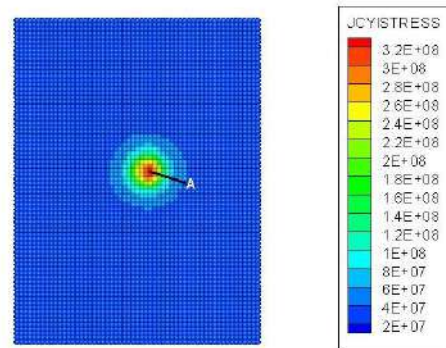


Figure 5. Change of stress on the top floor of the building

Fig.6 presents the numerical simulation map of the warhead penetrating multi-storey building. At first, the warhead penetrates the concrete floor under the kinetic energy and the impact of the end of the head (a, b). After reaching the intended detonation location (the second floor), the interior of the warhead is ignited and the building is damaged under the action of an explosive shock wave(c, d). After 24.3ms, the superstructure collapsed down under the action of gravity (e, f). Fig.7 shows the actual effect of

warhead penetrating the floor of the building, the comparison between the simulation results and the actual results are similar, indicating that the simulation results are correct.

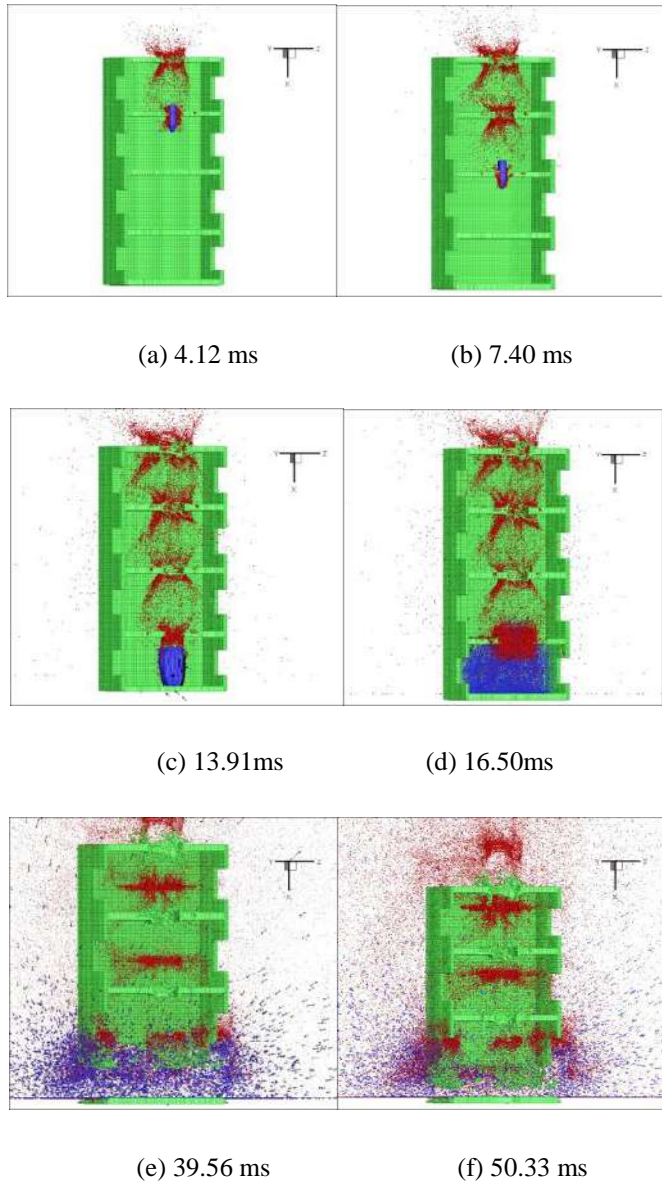


Figure 6. Numerical simulation of the penetration of the building

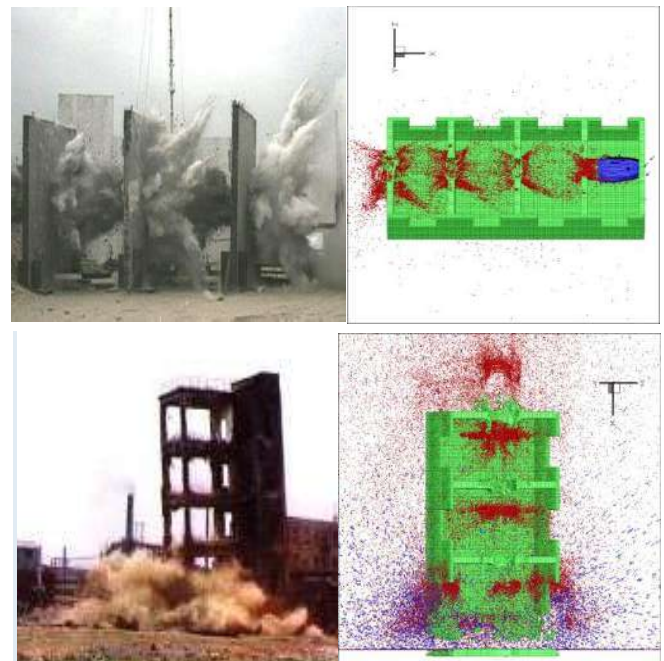


Figure 7. attack tough fighting Department of the building through the floor effect map

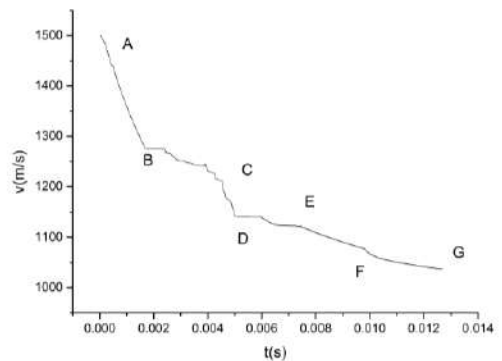


Figure 8. The graphs of missile velocity-time

Fig.8. shows the speed changes during the warhead penetrating the multi-storey building. The warhead speed changes under the penetration resistance. AB segment that penetrate the first floor, due to the relatively large, by the concrete floor of the reaction force is relatively large, the rate of change is relatively large; CD, EF, FG, respectively, penetrate the second, three, four Floor section, with the speed of decline, the rate of change is relatively small; BC section, DE section, respectively, said the movement in the floor, due to almost no external force, so the speed remains basically

unchanged.

IV. CONCLUSION

Using the method of mesh less SPH to calculate the process of Penetration and Explosion of Multi - floor Buildings, we know:

(1) SPH method can effectively solve the traditional method in high-speed impact and large deformation problems in the Euler grid interface tracking complex or Lagrange grid distortion and winding. Using F.Ott to modify the SPH method, it effectively solves the dramatically varies of the smooth length in the explosion and the impact, and the computational instability caused by the large density discontinuity at the multi-media interface.

(2) Using SDPH single particle to characterize the real particle group method with a series of specific particle size distributions, the particle group in the failure state after the ultra-high speed collision is processed by discrete particle phase, it makes the real particle system use less SDPH particles to characterize, it can solve the problem that the random motion process of the simulated particles is complicated and the computational complexity of the particle tracking process is large.

(3) The HJC constitutive model and the equation of state are used to describe the deformation and damage characteristics of concrete under high speed impact, it effectively simulate the damage of multi-storey concrete building in the case of penetration and explosion, it is in accordance with the actual physical phenomena.

REFERENCES

- [1] Qiang Hongfu, Fan Shujia, Chen Fozing, et al. Numerical simulation of concrete target penetrating concrete target based on SPH [J]. *Explosion and shock*, 2016, 36 (4): 516-524.
- [2] Wang Jintao, Yu Wenli , Wang Tao, et al. Application of SPH algorithm in penetration of long rods into multi - layer spacing targets [J]. *Explosion and shock*, 2011, 31 (5): 533-539.
- [3] Duan Jian, Yang Qianlong, Zhou Gang, et al. Experimental study on the penetration of concrete targets by tandem with the warhead [J]. *Explosion and Shock*, 2007,27 (4): 364-369.
- [4] Swegle J W, Attaway S W. On the feasibility of using smoothed particle hydrodynamics for underwater explosion [J]. *Computational Mechanics*, 1995, 17 (3): 151-168.
- [5] Libersky L D, Petscheck A G. Smoothed particle hydrodynamics with strength of materials [C] // TreaseH, Fritts J, Crowley W. Proceedings of the Next Free Lagrange Conference. NY: Springer Verlag, 1991, 395: 248-257.
- [6] Zhang Suochun. Smoothed particle hydrodynamics (SPH) method: a review [J]. *Computational physics*, 1996, 13 (4): 385-397.
- [7] Xu Zhihong, Tang Wenhui, Luo Yong,.SPH algorithm for high speed penetration [J]. *Journal of National University of Defense Technology*, 2005, 27 (4): 45-48. J
- [8] Ott F, Schnetter E. A modified SPH approach for fluids with large density differences [J]. *Arxiv Physics E-prints*, 2003:3112.
- [9] Liber sky L D, Pets check A G, Carney T C, et al. High strain Lagrangian hydrodynamics: A three-dimensional SPH code for dynamic material response[J]. *Journal of Computational Physics*, 1993, 109(1) : 67-75.
- [10] Liu M B, Liu G R , Zong Z, et al. Computer simulation of high explosive explosion using smoothed particle hydro dynamics methodology [J]. *Computers & Fluids*, 2003, 32 (3) : 305-322.
- [11] Liu M B, Liu G R , Lam K Y, et al. Mesh free particle simulation of the detonation process for high explosives in shaped charge unlined cavity configurations [J]. *Shock Waves*, 2003, 12(6) : 509-520.
- [12] Livermore Software Technology Corporation. LS-DYNA keyword user's manual [M]. Livermore: Livermore Software Technology Corporation, 2012: 17-45.
- [14] Monaghan J J. Smoothed particle hydrodynamics [J]. *Reports on Progress in Physics*, 2005, 68 (8) : 1703-1759.
- [15] Zhang Fangju, Chen Xiaowei, Xie Jose. Study on small scale reduction test of ground penetrating artillery ZW-D-2004102[R]. Miyanang: Institute of Engineering Physics, General Research Institute, 2004

Numerical study of the mechanism of explosive/impact welding using an improved SPH method

Z. L. Zhang

BIC-ESAT, College of Engineering
Peking University
zlhzzhang@pku.edu.cn

M. B. Liu

BIC-ESAT, College of Engineering
Peking University
mbliu@pku.edu.cn

Abstract—Explosive welding (EXW) involves processes like the detonation and explosion of explosive, impact of metal structures and strong fluid-structure interaction with complex features such as interfacial waves and jet generation. The whole EXW process has not been well modelled before due to the large deformation and moving interfaces while the associated mechanism inherent in EXW is also not well understood. In this paper, a novel smoothed particle hydrodynamics (SPH) model is developed to simulate explosive welding. In the SPH model, a kernel gradient correction algorithm is used to achieve better computational accuracy. A density adapting technique which can effectively treat large density ratio is also used to treat variable large density ratio in EXW. Typical phenomena in EXW such as the wavy interface, jetting formation, temperature and pressure distribution at the interfaces are investigated by the present SPH simulations, which are usually difficult for grid based methods. The mechanisms of wave formation are investigated. Two well-known mechanisms namely, the jet indentation mechanism and the vortex shedding mechanism are studied with the present simulations.

I. INTRODUCTION

It was occasionally found during the Second World War that shrapnel might be bonded tightly together after the detonation of explosives. Based on such observations, ideas of welding two or more kinds of metals together by using the explosion of explosives were developed to design new composite plates with controllable thermal conductivity and electric conductivity, good welding property and even better erosion resistance than a plate with single material. In 1960s, DuPont developed the explosive welding (EXW) technique for commercial applications [1]. Compared to the traditional ways of welding, explosive welding technique provides broader selections of metals (same material or different materials), such as aluminium-aluminium welding [2], steel-steel welding [3], and steel-titanium welding [4].

Bahrani and Crossland studied the morphology of the welding surface and the mechanism of the explosive welding process with an experimental investigation. Fig. 1 shows the schematic of the experiment conducted by Bahrani et al. [5]. In the experiment, two metal plates, namely the flyer plate and the base plate were placed with an angle φ_0 initially. The explosive was set on the flyer plate. After the ignition of explosives, the flyer moves towards the base plate at a very high impact velocity. These two plates were eventually welded together with properly chosen explosive charge as well as the initial welding angle φ_0 . In theoretical analysis and numerical simulations of

EXW process, the effect of buffer layer is usually neglected due to its thinner thickness and weaker strength compared to the flyer and base plates (as shown in Fig. 2).

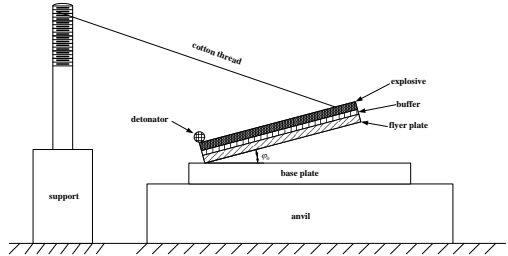


Fig. 1. Experimental facility of explosive welding by Bahrani et al. [5].

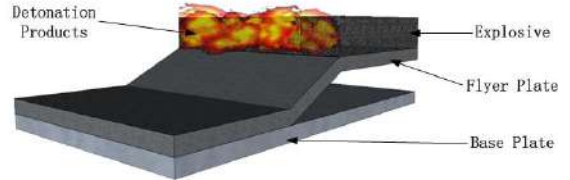


Fig. 2. Schematic diagram of explosive welding.

In reality, the explosive welding process completes in a very short duration, when rather complex chemical reactions (e.g., detonation of explosives) and physical processes (e.g., driving effects of the explosion on flyer and base plates, metallurgical bonding of two plates) take place. It is very difficult to capture such coupled complex processes experimentally or by using highly simplified analytical methods such as the Gurney formula [6]. Hence recently more and more researchers tend to numerically study EXW as numerical modeling provides an alternate to explore the inherent physics with greatly reduced costs. However, in most existing numerical models, explosive welding process is modeled with a simplified process as the impact of the flyer plate onto the base plate at a high speed. This is usually referred to as *high velocity impact welding* (HVIW) since the detonation and explosion of the explosive as well as the driving effect on the flyer plate and on the base plate are ignored. In real EXW, the explosion effect and the interaction between the explosive gas and the flyer plate need to be considered. The numerical results from such models are naturally more realistic than those from simplified models (such as HVIW) as more physical effects and multi-dimensional effects are considered. However, modeling real EXW is numerically challenging due to the reasons mentioned before. Development of advanced numerical methods to model real explosive

welding process rather than using simplified models is thus necessary.

Recently, different numerical methods have been proved to be efficient for modeling HVIW and EXW. Lagrangian grid-based methods suffer from mesh distortion which may abort the computation when the large deformation of the materials becomes serious. Despite the defects, this kind of method can predict the waveless interfaces and detect the onset of jetting phenomenon, but it is not suitable for predicting the wavy interface pattern (as mentioned in literature [7]). To overcome the mesh distortion problems, the Arbitrary Lagrangian-Eulerian (ALE) method can be adopted in modeling EXW problems while treating large deformations [7-9]. However, it can be observed in ALE simulation results from these literatures, the mesh deformation at the interface is not explicitly evidenced and the jetting cannot be well reproduced [10]. Meshfree particle methods use a set of arbitrarily distributed nodes or particles without fixed connectivity to represent the physical domain and approximate governing equations on the nodes/particles. Therefore, meshfree particle methods provide alternate approaches different from the grid-based methods and have special advantages in modeling problems with large deformations and rapidly moving interfaces or free surfaces [11-15], e.g. EXW problem.

Smoothed particle hydrodynamics (SPH) is a truly meshfree, particle class method which was originally invented for modeling astrophysical problems in three-dimensional open space [7, 8], and then it was widely used in continuum mechanics field [9]. In SPH method, the matter was discretized by a series of particles, and the particles carry out all the properties (e.g., mass, density and pressure) of the matter. By solving the governing equations, the physical information of particles at each time step could be obtained. Since the invention of SPH method, it has good applications in modeling problems with large deformation or large energy release, such as explosion, high velocity impact, penetration and shaped charge problem [10-18]. Also due to its advantages in modeling explosion and impact, some researchers tried to use SPH to simulate explosive welding [16, 17]. Again, HVIW model is used and it may not show the real physics in the explosive welding process as the detonation and explosion of the high explosive as well as the driving effect on the flyer plate and on the base plate are ignored.

In this paper, the density adaptive SPH method is used to model the entire process of real explosive welding and investigate the mechanisms inherent in EXW. To improve the numerical accuracy of the conventional SPH method, a kernel gradient correction (KGC) algorithm [18, 19] is used to enhance the computational accuracy. A density adaption algorithm is also used in SPH modeling to resolve the instability problem originated from large density inhomogeneity in EXW. The improved SPH methodology and the simulation models are briefed in Section II and III respectively. In section IV, the classical characteristics in EXW such as the wavy interface, jetting formation, temperature and pressure distribution at the interfaces are investigated. Two important wave formation mechanisms

are studied in section V. This paper concludes in the Section VI with some remarks.

II. SPH METHODOLOGY

A. SPH approximation techniques

In SPH method, the governing partial differential equations are approximated in two steps, the kernel approximation and the particle approximation. In kernel approximation, the kernel function W is introduced to reflect the interaction between SPH particles, and a field function $f(\mathbf{x})$ and its derivative $\nabla \cdot f(\mathbf{x})$ at position \mathbf{x} can then be written as

$$\langle f(\mathbf{x}) \rangle = \int_{\Omega} f(\mathbf{x}') W(\mathbf{x} - \mathbf{x}', h) d\mathbf{x}', \quad (1)$$

$$\langle \nabla \cdot f(\mathbf{x}) \rangle = - \int_{\Omega} f(\mathbf{x}') \nabla W(\mathbf{x} - \mathbf{x}', h) d\mathbf{x}', \quad (2)$$

where h is the smoothing length, $\langle \cdot \rangle$ is the SPH approximation sign. The Gaussian kernel [20] is used in this paper,

$$W(S, h) = \alpha_d e^{-S^2}, \quad (3)$$

where $S = |\mathbf{x} - \mathbf{x}'| / h$, h is the smoothing length defining the support domain of the kernel function, α_d is a dimension-dependent constant and it is $1/\pi h^2$ or $1/\pi^{3/2} h^3$ in two or three-dimensional spaces.

In SPH particle approximation, by summing over all the neighboring particles around particle i within its support domain, the field function and its derivative can be given by

$$\langle f(\mathbf{x}_i) \rangle = \sum_{j=1}^N \frac{m_j}{\rho_j} f(\mathbf{x}_j) W(\mathbf{x}_j - \mathbf{x}_i), \quad (4)$$

$$\langle \nabla \cdot f(\mathbf{x}_i) \rangle = \sum_{j=1}^N \frac{m_j}{\rho_j} f(\mathbf{x}_j) \nabla_i W_{ij}, \quad (5)$$

where m_j and ρ_j are the mass and density of a particle j . N is the total number of neighboring particles for a certain particle i . In following sections, the SPH approximation sign $\langle \cdot \rangle$ is ignored for the sake of conciseness.

B. Governing equations

In HVI process, the projectile and the crater region of the target plate can behave like fluids and can even be gasified if the impacting velocity is extremely high. In contrast, in regions far away from the crater, the plate is a solid. For hydrodynamics of fluids and solids with material strength, the following governing equations of continuum mechanics apply

$$\begin{cases} \frac{d\rho}{dt} = -\rho \frac{\partial \mathbf{v}^\beta}{\partial \mathbf{x}^\beta} \\ \frac{d\mathbf{v}^\alpha}{dt} = \frac{1}{\rho} \frac{\partial \sigma^{\alpha\beta}}{\partial \mathbf{x}^\beta}, \\ \frac{de}{dt} = \frac{\sigma^{\alpha\beta}}{\rho} \frac{\partial \mathbf{v}^\alpha}{\partial \mathbf{x}^\beta} \end{cases} \quad (6)$$

where ρ , t and e are the scalar density, time and internal energy separately. \mathbf{v}^α , \mathbf{x}^α and $\boldsymbol{\sigma}^{\alpha\beta}$ are velocity component, spatial coordinates and total stress tensor respectively, in which α and β are the indices of a tensor from 1 to the number of dimensions. As for stress tensor $\boldsymbol{\sigma}$, it can be written as

$$\boldsymbol{\sigma} = -P\mathbf{I} + \mathbf{S}, \quad (7)$$

where \mathbf{I} is the unit tensor, P is the pressure and \mathbf{S} is the residual deviator part of the stress tensor. By using the conventional SPH approximation method to discretize formula (6), the following SPH equations of motion are given as

$$\begin{cases} \frac{d\rho_i}{dt} = \rho_i \sum_{j=1}^N \frac{m_j}{\rho_i} (\mathbf{v}_i^\beta - \mathbf{v}_j^\beta) \frac{\partial W_{ij}}{\partial \mathbf{x}_i^\beta} \\ \frac{d\mathbf{v}_i^\alpha}{dt} = -\sum_{j=1}^N m_j \left(\frac{\boldsymbol{\sigma}_i^{\alpha\beta}}{\rho_i^2} + \frac{\boldsymbol{\sigma}_j^{\alpha\beta}}{\rho_j^2} + \mathbf{\Pi}_{ij} \right) \frac{\partial W_{ij}}{\partial \mathbf{x}_i^\beta} \\ \frac{de_i}{dt} = \frac{1}{2} \sum_{j=1}^N m_j \left(\frac{P_i}{\rho_i^2} + \frac{P_j}{\rho_j^2} + \mathbf{\Pi}_{ij} \right) (\mathbf{v}_i^\beta - \mathbf{v}_j^\beta) \frac{\partial W_{ij}}{\partial \mathbf{x}_i^\beta} + \frac{1}{\rho_i} \mathbf{S}_i^{\alpha\beta} \boldsymbol{\epsilon}_i^{\alpha\beta} \\ \frac{d\mathbf{x}_i^\alpha}{dt} = \mathbf{v}_i^\alpha \end{cases}, \quad (8)$$

where $\boldsymbol{\epsilon}_i^{\alpha\beta}$ is the strain tensor and $\mathbf{\Pi}_{ij}$ stands for the artificial viscosity tensor [21], which will be described in the next section. \mathbf{v}_i^α is the component of the velocity vector of the particle i .

C. Kernel gradient correction

The conventional SPH method has been successfully applied to hydrodynamics with material strength [22-26] and shows its good capability in dealing with large material deformation and moving interfaces. However, the conventional SPH method was often referred to as a low order computational method since it cannot exactly reproduce quadratic and linear functions, and even cannot exactly reproduce a constant, especially when particles are irregularly distributed [27].

During the last decade, different approaches have been proposed to improve the particle inconsistency and hence improve the SPH approximation accuracy. Some involve reconstruction of a new smoothing function so as to satisfy the discretized consistency conditions. One typical example is the reproduced kernel particle method (RKPM) proposed by Liu and his co-workers [14]. Recently, one popular way is to construct improved SPH approximation schemes based on Taylor series expansion on the SPH approximation of a function and/or its derivatives. Typical examples include the corrective smoothed particle method (CSPM) by Chen et al. [28] and the finite particle method (FPM) by Liu et al. [27, 29]. Both CSPM and FPM do not need to reconstruct smoothing function. It is noted that in the conventional SPH method, a field function and its derivatives are approximated separately. Instead, in CSPM, the derivatives are approximated through solving a coupled matrix equation while the field function is approximated separately. In FPM, both the field function and its

derivatives are coupled together and can be approximated simultaneously through solving a general matrix equation.

In this paper, the kernel gradient correction (KGC) technique [18, 19] is adopted to improve the accuracy of the gradient of the kernel functions. In the KGC technique, a modified or corrected kernel gradient is obtained by multiplying the original kernel gradient with a local reversible matrix $L(\mathbf{r}_i)$, which is obtained from Taylor series expansion method. In two-dimensional spaces, the new kernel gradient of the smoothing function $\nabla_i^C W_{ij}$ can be obtained as follows

$$\nabla_i^C W_{ij} = L(\mathbf{r}_i) \nabla_i W_{ij}, \quad (9)$$

$$L(\mathbf{r}_i) = \left(\sum_j \begin{pmatrix} x_{ji} \frac{\partial W_{ij}}{\partial x_i} & y_{ji} \frac{\partial W_{ij}}{\partial y_i} \\ x_{ji} \frac{\partial W_{ij}}{\partial y_i} & y_{ji} \frac{\partial W_{ij}}{\partial x_i} \end{pmatrix} V_j \right)^{-1}, \quad (10)$$

where $x_{ji} = x_j - x_i$, $y_{ji} = y_j - y_i$. x , y are the two components of the position vector.

It is noted from equation (9) that for gradient correction, since only the gradients of the smoothing function (or kernel gradients) are corrected, there is no need to significantly change the structure of SPH computer programs and procedure of SPH simulations.

D. Density adaption technique

SPH method has special advantages in simulating explosive welding problem, and it can naturally track the moving interfaces between different materials. It is also attractive in describing complex physics in explosive welding including phase change of materials, high strain rate and large deformation. These features are usually difficult for conventional grid-based methods. However, as EW involves the interaction of explosive gas and metal at large density ratio, and this leads to sharp discontinuity at the material interface. Just as in other grid-based or meshfree methods [30, 31], large density ratio can lead to numerical instability and further cause the SPH simulation failure.

There are two approaches in the solution of the density in SPH. One is the density summation approach and the other is the continuity approach which solves the continuity equation to update density [32]. The density summation approach is mainly used in modeling fluid flows to ensure mass conservation. When modeling impact and explosion problems, the following continuity approach is usually more preferred,

$$\dot{\rho}_i = -\rho_i \nabla \cdot \mathbf{v}, \quad (11)$$

where the “.” above the variable represents the first derivative of the variable versus time. By using SPH particle approximation, the continuity equation can be written as

$$\dot{\rho}_i = -\rho_i \sum_{j=1}^N \frac{m_j}{\rho_j} \mathbf{v}_j^\beta \cdot \frac{\partial W_{ij}}{\partial \mathbf{x}_i^\beta}. \quad (12)$$

Combing equation (12) with following formula

$$\rho_i \mathbf{v}_i^\beta \nabla \mathbf{1} = \rho_i \mathbf{v}_i^\beta \sum_{j=1}^N \frac{m_j}{\rho_j} \cdot \frac{\partial W_{ij}}{\partial \mathbf{x}_i^\beta} = 0, \quad (13)$$

a frequently used SPH continuity equation can be obtained as

$$\dot{\rho}_i = \rho_i \sum_{j=1}^N \frac{m_j}{\rho_j} \mathbf{v}_{ij}^\beta \cdot \frac{\partial W_{ij}}{\partial \mathbf{x}_i^\beta}. \quad (14)$$

By using a simple operation to include density in the gradient operator as

$$\dot{\rho} = -\rho \nabla \cdot \mathbf{v} = -(\nabla(\rho \mathbf{v}) - \mathbf{v} \cdot \nabla \rho), \quad (15)$$

another commonly used SPH continuity equation can be obtained as

$$\dot{\rho}_i = \sum_{j=1}^N m_j \mathbf{v}_{ij}^\beta \cdot \frac{\partial W_{ij}}{\partial \mathbf{x}_i^\beta}. \quad (16)$$

Equations (14) and (16) are two widely used SPH continuity equations to evolve density and they do not appear to differ much at the first sight. However, considering that conventional SPH does not have 0th and 1st order consistency [27], equation (38) is not satisfied exactly

(i.e., $\sum_{j=1}^N \frac{m_j}{\rho_j} \cdot \frac{\partial W_{ij}}{\partial \mathbf{x}_i^\beta} \neq 0$) especially for irregular distributed

particles, boundary and interface areas and therefore equation (14) is also not exactly satisfied. Different from equation (14), equation (16) is obtained from exact mathematical transformation and should be more rigorous and have better accuracy. However, as no density appears on the right-hand-side (RHS) of equation (16), when modeling problems with large density ratio, contributions from different materials (with density discontinuity) for interface particles may not be properly estimated. This can cause numerical oscillation (instability) around the interface and can further terminate the simulation. For example, Colagrossi [33] noticed that equation (14) is usually better than equation (16) when modeling multiphase flows with large density ratios. Monaghan also pointed out that equations (14) and (16) are all suitable for solving continuity equation when the density ratio of two fluids is less than or equal to 2 [34]. When the density ratio is bigger than 2, equation (14) is more preferred for more stable simulations.

When modeling explosive welding with SPH, the explosive detonation produces explosive gas, which rapidly expands with quickly reducing density. However, during EW process, the density of flyer and base plates does not change violently. As such, the density ratio of metal to explosive gas can be larger than 10. This big density inhomogeneity causes additional difficulty to numerical simulation and this may be the reason why people usually use the HVIW model for simulating explosive welding as a simplified approach.

As equation (16) is more accurate with a symmetric approximation and equation (14) is more stable for high density ratio, it is natural to use a hybrid approach, which can possess the advantages of equations (14) and (16). Therefore, in this paper, an adaptive density formulation is presented to deal with multi-material problems with high

density ratio. The time rate of change of density can be approximated using following expression

$$\dot{\rho}_i = \sum_{j=1}^N \frac{\rho_i + \psi_i \rho_j}{\rho_j(1 + \psi_i)} m_j \mathbf{v}_{ij}^\beta \cdot \frac{\partial W_{ij}}{\partial \mathbf{x}_i^\beta}. \quad (17)$$

It is seen that through adjusting the control parameter ψ , it is possible to control the contributions to density approximation from equations (14) and (16). For a system with different materials, a density adaption can be conducted when density ratio is huge.

Let's define a dimensionless variable k_i as

$$k_i = \frac{\rho_{i,\max}}{\rho_{i,\min}}, \quad (18)$$

where $\rho_{i,\min}$ and $\rho_{i,\max}$ represent for the maximal and minimal density values of the particles for a concerned particle i in its support domain. If $k_i \rightarrow 1$ and $\psi_i \rightarrow \infty$, there is no density difference in particle approximation within the support domain, and the change rate of density is approximated only using equation (16). Instead, if $k_i \rightarrow \infty$, the density difference in the support domain approaches infinite and the change rate of density is only calculated using equation (14). Hence, we aim to obtain a function relationship $\psi_i = \psi(k_i)$ which is adaptive with the change of density, as shown in Fig. 1. In SPH simulation of explosive welding, the explosive particles with relatively low density are more likely to be unstable. Since pressure of the explosive gas is calculated from density using the

JWL equation of state, and it is on the scale of $e^{-\frac{1}{\eta}}$, the instability due to density ratio will lead to pressure instability in a scale of $e^{-\frac{1}{\eta}}$. Based such considerations,

$\psi_i = \frac{1}{\ln k_i}$ is adopted in this paper.

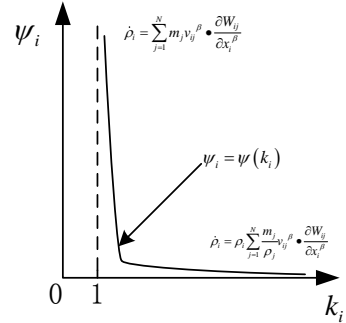


Fig. 1. Schematic diagram of function $\psi_i = \psi(k_i)$

III. NUMERICAL SIMULATION MODELS

A. Constitutive modeling

Johnson-Cook model [35] adopted in this paper is a widely used constitutive model for numerical simulations of impact and penetration, and the yield stress is given by

$$\sigma_y = (A + B \varepsilon^{p^n})(1 + C \ln \dot{\varepsilon}^*) (1 - T^{*m}), \quad (19)$$

$$T^* = \frac{T - T_{room}}{T_{melt} - T_{room}}, \quad (20)$$

where T is the temperature, and T^* is a dimensionless quantity related to temperature. T_{room} and T_{melt} are the room temperature and the metal melting temperature respectively. ε^p and $\dot{\varepsilon}^*$ are the effective plastic strain and the dimensionless strain rate separate. A , B , C , n and m are all material constants obtained by different experiments. The parameters of aluminum and steel used in IMW and EXW modeling are listed in Table 1.

Table 1
Parameters used in the Johnson-Cook model for steel and aluminum.

	$A(Mpa)$	$B(Mpa)$	C	n	m	$T_{room}(K)$	$T_{melt}(K)$
Steel	792	510	0.014	0.26	1.03	294	1793
Al	175	380	0.0015	0.34	1.00	273	775

B. Equation of state (EOS)

For explosive gas, the standard Jones-Wilkins-Lee (JWL) equation of state [36] can be employed as

$$P = A_1 \left(1 - \frac{\omega\eta}{R_1}\right) e^{-\frac{R_1}{\eta}} + B_1 \left(1 - \frac{\omega\eta}{R_2}\right) e^{-\frac{R_2}{\eta}} + \omega\eta\rho_0 e_0, \quad (21)$$

where η is the ratio of the density of the explosive gas to the initial density of the original explosive. e_0 is the initial internal energy of the high explosive per unit mass. A_1 , B_1 , R_1 , R_2 and ω are the coefficients obtained from the fitting of the experimental data. The values of the specific parameters are listed in Table 2.

Table 2
Parameters used in the JWL equation for TNT.

$\rho_0/kg\cdot m^{-3}$	A_1/GPa	B_1/GPa	R_1	R_2	ω	$e_0/kJ\cdot kg^{-1}$
1630	317.2	3.21	4.15	0.95	0.30	4290

The Mie-Gruneisen equation of state [37] is used for steel to describe the relation between pressure P , density ρ and internal energy E as

$$P = \begin{cases} \frac{\rho_0 C_0^2 \mu \left[1 + \left(1 - \frac{\gamma}{2}\right) \mu - \frac{\alpha \mu^2}{2} \right]}{\left[1 - (S_1 - 1)\mu - \frac{S_2 \mu^2}{\mu + 1} - \frac{S_3 \mu^3}{(\mu + 1)^2} \right]^2} + (\gamma + \alpha\mu) E_0; & \mu > 0 \\ \rho_0 C_0^2 \mu + (\gamma + \alpha\mu) E_0; & \mu \leq 0 \end{cases}, \quad (22)$$

where $\mu = \rho/\rho_0 - 1$ and ρ_0 is the initial density. γ is the Gruneisen Parameter and E_0 is the initial internal energy of the metal per unit mass. The specific parameters are listed in Table 3.

Table 3
Parameters used in the Mie-Gruneisen equation for steel.

$\rho_0/kg\cdot m^{-3}$	C_0/ms^{-1}	S_1	S_2	S_3	γ	α	$E_0/kJ\cdot g^{-1}$
7830	4569	1.49	0.00	0.00	2.17	0.46	0.00

C. Model set-ups

There are two models used in this paper, i.e., HVIW (Fig. 2(a)), EXW with explosive charge and flyer plate obliquely deployed (Fig. 2 (b)). In the HVIW model (or Model A), the flyer plate and base plate (4340 steel) are simulated using 250,000 particles while the particle spacing is 0.002 cm. In the EXW model with obliquely placed explosive (Model B), the base plate is modeled with 84,000 SPH particles with the particle spacing 0.005cm. The flyer plate is 60 mm long, and has the same particle spacing with the base plate. The length of the high explosive is the same as the flyer plate with changed thickness for different explosive charges.

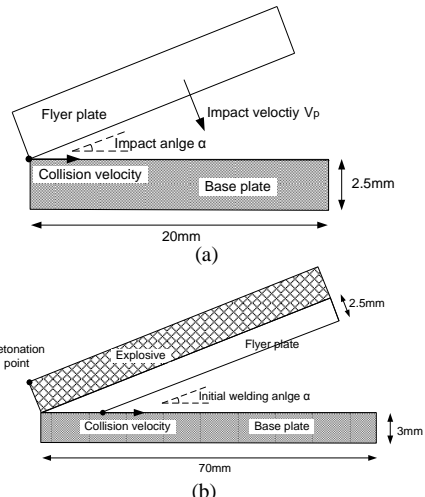


Fig. 2. Initial model set-up for (a) IMW and (b) EXW.

IV. SIMULATION RESULTS

A. Straight and wavy interface

The formation of wavy interface and the generation of jets are often regarded as two most important features of a successful explosive welding [38-41]. It is experimentally observed that the shape of the interface can be roughly divided into three categories as straight, smooth wavy and wavy with vortex shedding [42]. The wave formation is related to many influencing factors including plastic strain, temperature, contact pressure and etc. For a specific experimental setup with determined materials of flyer and base plate, the welding quality is only determined by the initial welding angle and the amount of explosive. Changing these two factors, the above-mentioned three types of interfacial morphologies in EXW can be obtained.

Fig. 3 shows the experimental snapshots of straight to wavy interfaces in steel-steel EXW conducted by Bahrami et al. [5]. As the welding angle increases from 0 ° to 21 °, the amplitude and length of the wave increase to a maximum value. Thereafter the amplitude decreases although the length of wave still increases. Fig. 4 shows the present SPH simulations of EXW with the same material at different welding angles (Model B). It is seen that present SPH model can well reproduce the same physics observed in experiments. As shown in Fig. 4 (a) to (d), the wavelength increases with the increase of welding angle. In

contrast, the amplitude of the wave increases first to a maximal value as the welding angle increases, and then decreases afterwards. It is noted that HVIW, as a simplified model of EXW, ignores the driving effect of the flyer plate on the base plate, and hence it is not able to reproduce the evolution of interfacial wave with varying wave length and amplitude. Therefore the present SPH modeling of EXW (Model B) is more reasonable with more comprehensive physics.

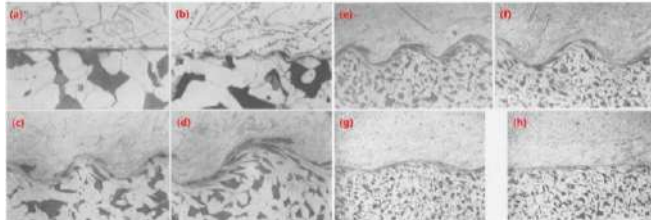


Fig. 3. Illustration of straight to wavy interfaces in the experimental steel-steel EXW conducted by Bahrani et al. [5]. The direction of the welding is from right to left, and the welding angle increases from (a) 0 ° to (h) 21 °.

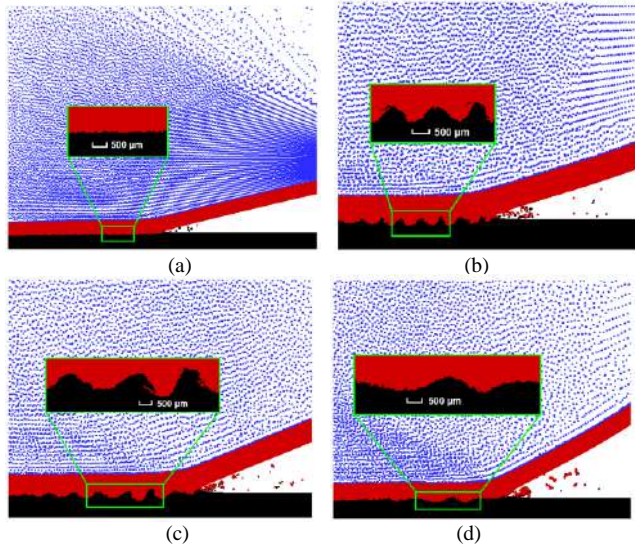


Fig. 4. Illustration of the straight to wavy interfaces in the steel-steel EXW obtained by present SPH simulations (Model B). From (a) to (d), the initial welding angles are 5 °, 10 °, 15 ° and 20 ° separately.

B. Jet formation

As mentioned early, jet formation is believed to be a sign of a successful welding [40, 42]. In most cases, jet formation means that the flyer plate and the base plate have been well bonded together. The jets could also strip away the surface contaminant, oxides and impurities occurring in EXW. The present SPH simulation could well capture the typical jetting phenomenon in EXW while the jets are in a bundle of fluids which are firstly ejected from the welding front point. It is found that the welding angle must exceed a minimal value so that the pressure is large enough to ensure that the metal plates exceed the dynamic elastic limit and to generate a jet [40]. As shown in Fig. 5 (a), at the initial welding angle of 5 °, only few particles are ejected from the bonding region of two plates and the jet does not form. At

the initial angle of 10 ° however, it is clearly seen that more particles in a bundle of fluids are ejected out. As the initial welding angle increases to 15 °, more particles are ejected out with more evident jet formation.

From present SPH simulations, it is also found that welding angle and the amount of explosive (or impact velocity of the flyer plate) have little influence on the composition of the jets. As shown in Fig. 5 (a)-(d), the jets originate from both flyer and base plates under different initial welding angles. In other cases of simulative steel-steel welding with different amount of explosive, the jets are also from both flyer and base plates.

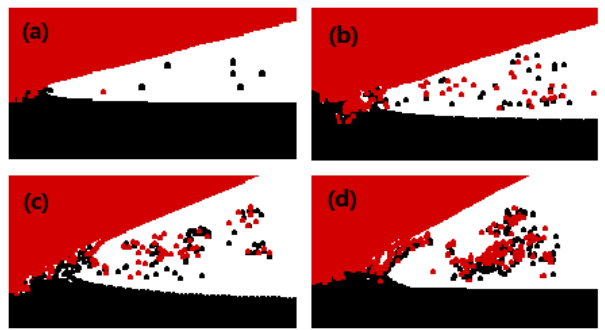


Fig. 5. Zoom-in view of jets in Fig. 4 at the same time (from (a) to (d)), the initial welding angles are 5 °, 10 °, 15 ° and 20 ° respectively

C. Pressure distribution

Fig. 6 (a) shows the pressure distribution in the impacting plates in HVIW (Model A) obtained using the developed SPH method. At the interface, the pressure surrounding the collision point is the highest with a maximal value over 15 GPa. The decrease of the pressure from the welding point is in a circular shape. From present simulation results of HVIW, it is found increasing impact angle can lead to smaller maximal pressure close to the collision point when the impact velocity is fixed. This is similar to the observations in literature [40]. Fig. 6 (b) shows the pressure distribution during the EXW process at two typical instants (Model B). It is seen that as the detonation initiates, the detonation wave propagates rightward across the explosive and the resultant explosive gas quickly expands leftwards with the rarefaction wave traveling inward. When the explosion wave reaches the left-bottom corner of the flyer plate, the high pressure explosive gas then strongly interacts with the flyer plate, and causes the flyer plate to deform, accompanied with a shock wave traveling through the flyer plate. The pressure attenuation around the collision point in EXW is similar to that in HVIW. In summary, the pressure distribution in the impacting plates as well the explosion waves can be well captured by the present SPH simulations.

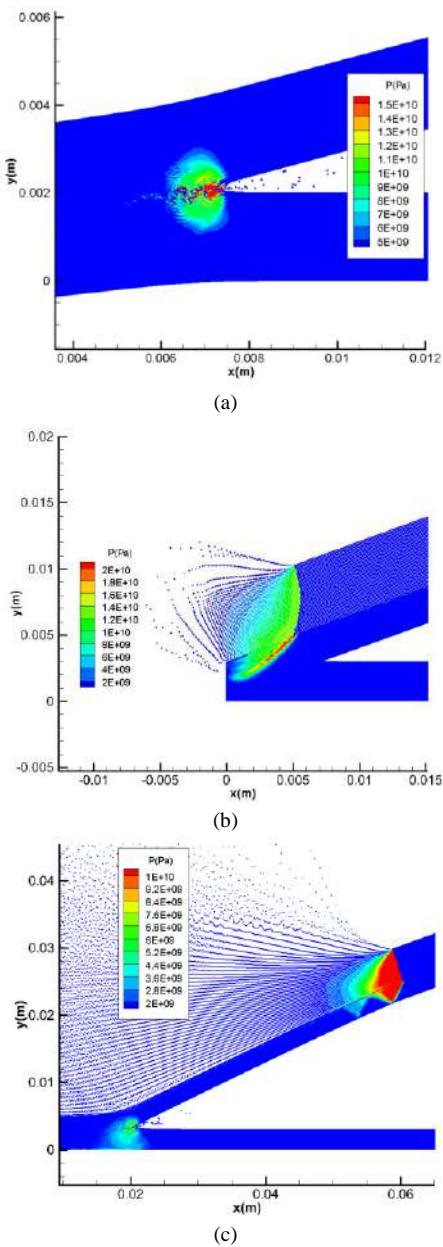


Fig. 6. The pressure distribution of impacting plates and explosives in IMW and EXW at corresponding time respectively. (a) IMW with impact velocity $V_p=850$ m/s and impact angle $\alpha=15^\circ$ (b) EXW with $M_{\text{explosive}}/M_{\text{plate}}=0.1596$ and initial welding angle $\alpha=15^\circ$

D. Temperature around the interface

Capturing the temperature field around the welding interface is also very important as whether the interfacial materials melt are closely related to the quality of explosive welding [7, 8], and this will be further discussed in the next section. The Johnson-Cook equation includes the effect of temperature on flow stress and on the plastic strain. The present SPH simulation models using Johnson-Cook constitutive equations can obtain the welding temperature field of the materials. As shown in Fig. 7 (a), when the impact velocity $V_p=850$ m/s, the temperature of the material at the welding interface locally exceeded the

melting point of the material, although the wavy morphology is well reproduced. Such case is assumed to be the upper limit of impact velocity for a given welding, because melting or diffusion are assumed to be detrimental to welding quality [8]. As the impact velocity reduces, the ideal temperature of the material and the wavy morphology can be obtained (illustrated in Fig. 7 (b)), and the bonding in this case is regarded to be a solid-state welding.

As shown in Fig. 8, the initial model set-ups in two cases are the same with different explosive charges. When the amount of explosive is relatively large, the temperature of the material close to the interface will exceed the melting point of the material (illustrated in Fig. 8 (a)), which is similar to that in the above case (Model A for HVIW). As the explosion and driving effect of explosive on the flyer plate is so rapid, the temperature is locally high around the interface region. Fig. 8 (b) shows the temperature distribution after the EXW with proper amount of explosive. The interfacial temperature is lower than the melting point of the material, but is high enough for the occurrence of phase changes. This is similar to what happens in tempering or martensitic formation in steels [40]. With fixed amount of explosive, an ideal metal-metal bond without melting or diffusion can be obtained from present SPH simulations, and this is very important for determine the desired weldability windows for EXW.

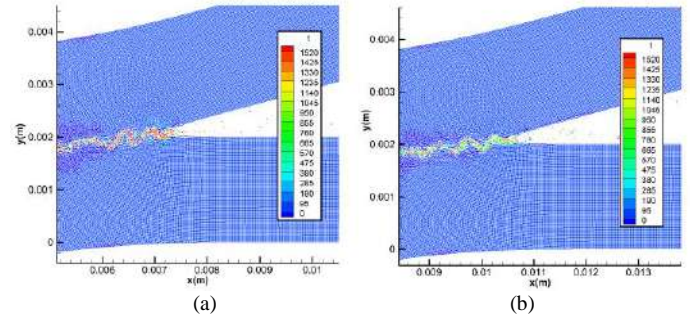


Fig. 7. Temperature distribution in IMW (Model A) at 3.2 μ s (a) and 750 m/s (b), the initial impact angle is 15° . The unit of the temperature in this figure and the following figures are all centigrade degrees.

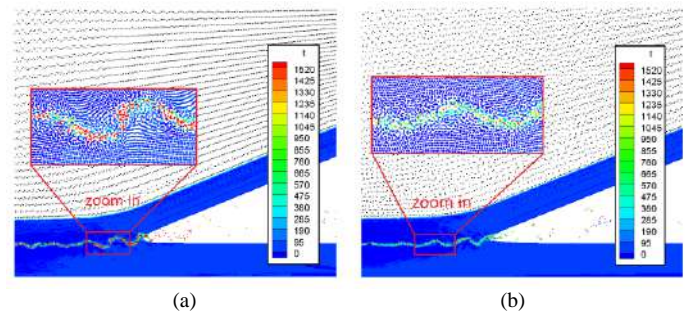


Fig. 8. Temperature distribution in EXW (Model B) at 15 μ s with $M_{\text{explosive}}/M_{\text{plate}}=0.1596$ (a) and 0.1915 (b), the initial welding angle is 15° .

V. MECHANISMS OF WAVE FORMATION

Wave formation is important for a successful welding, and the mechanism of wave formation in EXW has been

studied for years. As mentioned in literature [42], it is difficult to reach a reliable conclusion about the mechanism regarding to the formation of the waves. As the present SPH simulation can well reproduce the formation of wave and the interface evolution in EXW, it is possible to revisit the the Bahrani Mechanism (or named the Jet Indentation Mechanism) and the vortex shedding mechanism.

A. The Bahrani Mechanism

The Bahrani mechanism is a type of phenomenological mechanism proposed by Bahrani et al. [5], and it can well explain the formation of wave in EXW. As shown in Fig. 9 (right), according to the Bahrani Mechanism, the pressure around the collision point is much larger than the yield strength of the materials, and the materials at the collision regions behave like liquids of low viscosity. When two impact plates collide at a high velocity, the flyer plate is divided into a re-entrant jet and a salient jet by the stagnation point S (illustrated in Fig. 9 (a)). The base plate deforms under the collision of the salient jet, hence a hump is formed in the base plate ahead of the collision point. As the size of hump increases to a maximal value, the stagnation point transfers to the top of the hump (shown in Fig. 9 (b) as S'). Then the re-entrant jet skips over the stagnation point and collides the base plate ahead of the hump, during which process a trough of wave is formed and some of the materials are ejected as a jet (illustrated in Fig. 9 (b) and (c)). As the movement of flyer plate, the stagnation point transfers from the crest to the trough of the wave again and a new hump begins to form.

Fig. 9 (left) shows the formation of a wave during EXW process obtained using the present SPH method. It can be seen that the wave formations obtained from SPH simulation and from the Bahrani Mechanis are in good agreement. In another word, the SPH simulation results reveal the effectiveness of the Bahrani Mechanis in explaining the wave formation in EXW.

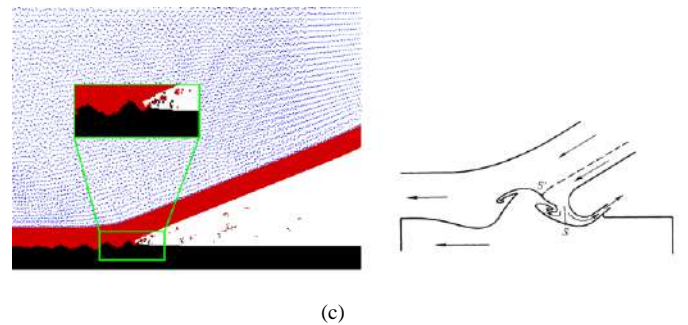
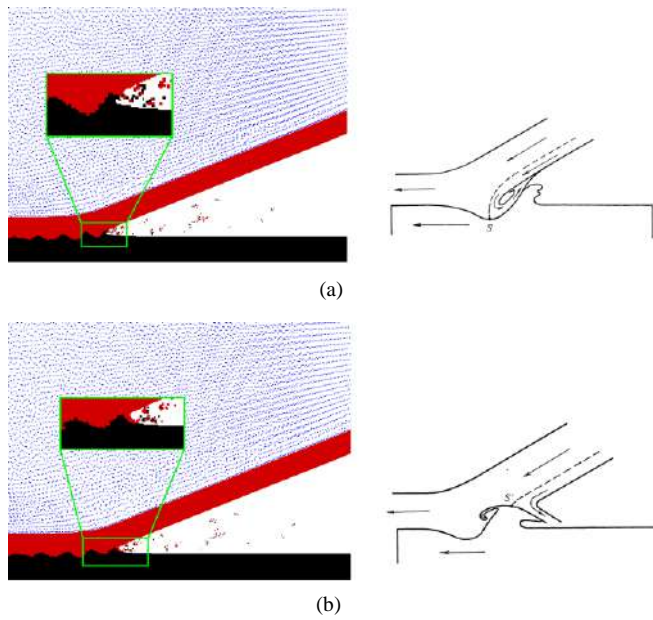
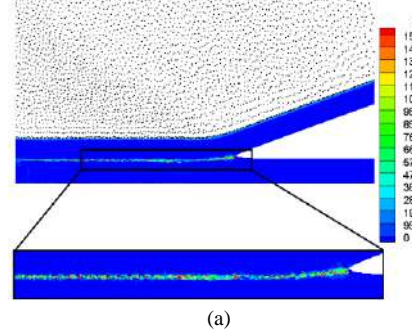


Fig. 9. Illustration of the formation of one wave (from (a) to (c)) given by the present simulation (left) and the Bahrani mechanism (right) [5].

B. The Vortex Shedding Mechanism

As shown in literatures [43, 44], the wavy interfaces formed due to the Vortex Shedding Mechanism is similar to the formation of the von Kármán Vortex Street, which can be obtained from the flow of a viscous fluid after an obstacle. Besides, the transition of the interfacial morphology from smooth to wavy versus the increase of collision or impact velocity can be predicted quantitatively from a universal critical value of a Reynolds number defined in terms of average density and hardness of the two metals. In the experiments conducted by Cowan et al. [44], the interfacial morphology changes from straight to wavy and then to wavy with vortex shedding as the collision velocity increases (illustrated in Fig. 12 (a)-(c)). As shown in Fig. 10 and Fig. 11, the present simulations can reproduce this phenomenon precisely, and these vortices are very similar to that obtained from the flow of a viscous fluid after an obstacle in literature [44]. Different from the experimental set-up, the welding in present simulations is from left to right. For comparison with the experimental results, single wave is adopted from Fig. 10 and is zoomed in Fig. 11 separately. Fig. 12 (b) and (e) show typical wavy interfaces without vortex shedding, from which it can be seen the left slope of the wave is slow while the shape of right slope is on the contrary. Fig. 12 (c) and (f) show the wavy interfaces with vortex shedding in EXW. The shape and position of the vortex, the shapes of the wave crest and trough are very close for both the experimental and simulative results. The melting zone from present simulations corresponds well with the grayscale of the experimental wavy interface. Unfortunately, the welding materials in the experiments by Cowan et al. [44] and present simulations are similar but not exactly the same, and therefore the comparisons in Fig. 12 are only qualitative.



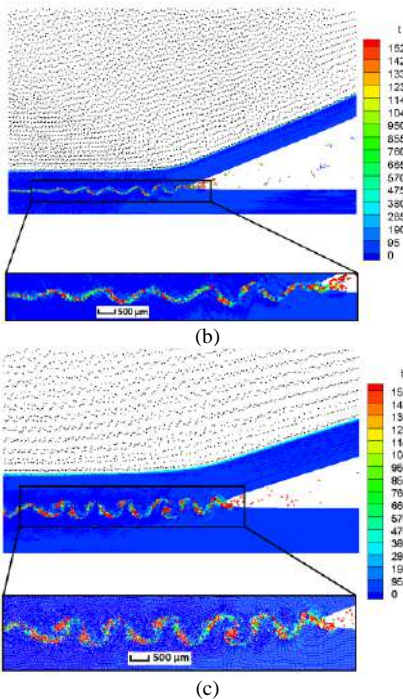


Fig. 10. The temperature distribution in the base and flyer plates in EXW with different initial set-ups. (a) $M_{\text{exploding}}/M_{\text{plate}}=0.09576$, (b) $M_{\text{exploding}}/M_{\text{plate}}=0.1596$ and (c) $M_{\text{exploding}}/M_{\text{plate}}=0.1915$.

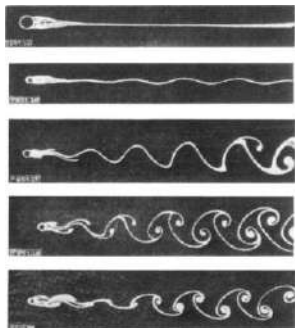


Fig. 11. Photographs of fluid flow behind cylinders at increasing values of the Reynolds number, obtained by Homann et al. [44].

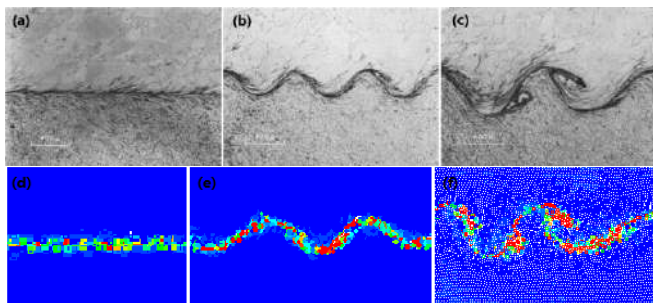


Fig. 12. Bond zones in experiments [44] and present SPH simulations of EXW. (a), (b) and (c) are experimental observations of nikel-steel welding conducted at different collision velocities, i. e., 1600 m/s, 1900 m/s and 2500 m/s. (d), (e) and (f) are simulation results of steel-steel welding conducted at corresponding collision velocities.

According to the Vortex Shedding Mechanism, Cowan et al. [44] linked wave formation in EXW to fluid flow

around an obstacle. Hence the critical Reynolds number ($R_{\text{transition}}$) for laminar to turbulent flow is used to determine the transition of the interface morphology from straight to wavy in EXW, and is given by

$$R_{\text{transition}} = \frac{(\rho_{\text{flyer}} + \rho_{\text{base}})V_c^2}{2(H_{\text{flyer}} + H_{\text{base}})}, \quad (23)$$

where R represents for the Reynolds number, ρ and H stand for density (kg/m^3) and Vicker's hardness (N/m^2) respectively. V_c (m/s) stands for flow velocity of the flyer material into the collision point, and it approximately equals the welding velocity under low collision angles [45]. Corresponding to the present SPH simulations (steel-steel welding), when the transition of the interfacial morphology happens, the V_c obtained from the analytical formula (22) gives by

$$V_c = \sqrt{\frac{2R_{\text{transition}}(H_{\text{flyer}} + H_{\text{base}})}{\rho_{\text{flyer}} + \rho_{\text{base}}}} \approx 1960 \text{ m/s}, \quad (24)$$

where $R_{\text{transition}}$ is obtained from literature [45] by experimental approaches at welding angle of 12 degree. The present simulation of V_c is about 2100 m/s at transition situation of the interfacial morphology, which agrees well with the analytical result according to the Vortex Sheding Mechanism.

VI. CONCLUSION

In this paper, an improved smoothed particle hydrodynamics method is used for modelling the explosive welding process. The difficulties of EXW modelling are associated with large material deformation, moving interface and huge density ratio. The improved SPH method uses a kernel gradient correction algorithm to enhance the computational accuracy of the SPH particle approximation. An adaptive density model is incorporated into the SPH method to deal with the huge metal-explosive gas density ratio.

The whole process of EXW (i.e., the explosion of the explosives, driving effect of the explosion on the flyer plate and metallurgical bonding of two plates) as well as the classical characteristics such as the wavy interface, jetting formation, temperature and pressure at the interface can be well modeled by the improved SPH methods. Based on the simulation results, important wave formation mechanisms are studied, and two classical mechanisms of wave formation (i.e., the Jet Indentation Mechanisms and the Vortex Sheding Mechanism) are revealed. It is demonstrated that the present SPH modeling is able to explain the formation of one wave and the transition of wavy interfaces respectively.

ACKNOWLEDGEMENT

This work has been supported by the National Natural Science Foundation of China (Grant Nos. U1530110 and 51779003).

REFERENCES

- [1] D. Cutler, "What you can do with explosion welding, *Welding Journal*, 5 (2006) 177-199.

- [2] F. Grignon, D. Benson, K.S. Vecchio, M.A. Meyers, "Explosive welding of aluminum to aluminum: analysis, computations and experiments," *International Journal of Impact Engineering*, 30 (2004) 1333-1351.
- [3] R. Kacar, M. Acarer, "An investigation on the explosive cladding of 316L stainless steel-din-P355GH steel," *Journal of Materials Processing Technology*, 152 (2004) 91-96.
- [4] N. Kahraman, B. Gülenç, F. Findik, "Joining of titanium/stainless steel by explosive welding and effect on interface," *Journal of Materials Processing Technology*, 169 (2005) 127-133.
- [5] A.S. Bahrani, B. Crossland, "The mechanics of wave formation in explosive welding," *Proceedings of the Royal Society A*, 296 (1967) 123-136.
- [6] S.A.L. Salem, L.G. Lazari, S.T.S. Al-Hassani, "Explosive welding of flat plates in free flight," *International Journal of Impact Engineering*, 2 (1984) 85-101.
- [7] T. Sapanathan, R.R. Nirina, E. Padayodi, N. Buiron, M. Rachik, "Depiction of interfacial characteristic changes during impact welding using computational methods: Comparison between Arbitrary Lagrangian - Eulerian and Eulerian simulations," *Materials & Design*, 102 (2016) 303-312.
- [8] A. Nassiri, G. Chini, A. Vivek, G. Daehn, B. Kinsey, "Arbitrary Lagrangian-Eulerian finite element simulation and experimental investigation of wavy interfacial morphology during high velocity impact welding," *Materials & Design*, 88 (2015) 345-358.
- [9] A. Nassiri, B. Kinsey, "Numerical studies on high-velocity impact welding: smoothed particle hydrodynamics (SPH) and arbitrary Lagrangian-Eulerian (ALE)," *Journal of Manufacturing Processes*, 24 (2016) 376-381.
- [10] A. Nassiri, S.Y. Zhang, T. Lee, T. Abke, A. Vivek, B. Kinsey, G. Daehn, "Numerical investigation of CP-Ti & Cu110 impact welding using smoothed particle hydrodynamics and arbitrary Lagrangian-Eulerian methods," *Journal of Manufacturing Processes*, 28 (2017) 558-564.
- [11] S. Koshizuka, Y. Oka, "Moving-particle semi-implicit method for fragmentation of incompressible fluid," *Nuclear Science Engineering*, 123 (1996) 421-434.
- [12] S.F. Li, W.K. Liu, "Meshfree and particle methods and their applications," *Applied Mechanics Reviews*, 55 (2002) 1-34.
- [13] G.R. Liu, "Mesh free methods moving beyond finite element method," Crc Press, 2003.
- [14] W.K. Liu, Y. Chen, S. Jun, J.S. Chen, T. Belytschko, C. Pan, R.A. Uras, C.T. Chang, "Overview and applications of the reproducing Kernel Particle methods," *Archives of Computational Methods in Engineering*, 3 (1996) 3-80.
- [15] X. Zhang, Z. Chen, Y. Liu, "The material point method - a continuum-based particle method for extreme loading cases," Elsevier, 2016.
- [16] X.J. Li, F. Mo, X.H. Wang, B. Wang, K.X. Liu, "Numerical study on mechanism of explosive welding," *Science & Technology of Welding & Joining*, 17 (2012) 36-41.
- [17] A. Nassiri, B. Kinsey, "Numerical studies on high-velocity impact welding: smoothed particle hydrodynamics (SPH) and arbitrary Lagrangian-Eulerian (ALE)," *Journal of Manufacturing Processes*, 24 (2016).
- [18] J.R. Shao, H.Q. Li, G.R. Liu, M.B. Liu, "An improved SPH method for modeling liquid sloshing dynamics," *Computers & Structures*, 100-101 (2012) 18-26.
- [19] M.B. Liu, S.M. Li, "On the modeling of viscous incompressible flows with smoothed particle hydrodynamics," *Journal of Hydrodynamics*, 28 (2016) 731-745.
- [20] R.A. Gingold, J.J. Monaghan, "Smoothed particle hydrodynamics: theory and application to non-spherical stars," *Monthly Notices of the Royal Astronomical Society*, 181 (1977) 375-389.
- [21] J.J. Monaghan, "On the problem of penetration in particle methods," *Journal of Computational Physics*, 82 (1989) 1-15.
- [22] J.W. Swegle, S.W. Attaway, "On the feasibility of using smoothed particle hydrodynamics for underwater explosion calculations," *Computational Mechanics*, 17 (1995) 151-168.
- [23] P.W. Randles, L.D. Libersky, "Smoothed particle hydrodynamics: some recent improvements and applications," *Computer Methods in Applied Mechanics & Engineering*, 139 (1996) 375-408.
- [24] M.B. Liu, G.R. Liu, K.Y. Lam, Z. Zong, "Smoothed particle hydrodynamics for numerical simulation of underwater explosion," *Computational Mechanics*, 30 (2003) 106-118.
- [25] M.B. Liu, G.R. Liu, Z. Zong, K.Y. Lam, "Computer simulation of high explosive explosion using smoothed particle hydrodynamics methodology," *Computers & Fluids*, 32 (2003) 305-322.
- [26] M.B. Liu, G.R. Liu, K.Y. Lam, "Adaptive smoothed particle hydrodynamics for high strain hydrodynamics with material strength," *Shock Waves*, 15 (2006) 21-29.
- [27] M.B. Liu, G.R. Liu, "Restoring particle consistency in smoothed particle hydrodynamics," *Applied Numerical Mathematics*, 56 (2006) 19-36.
- [28] J.K. Chen, J.E. Beraun, "A generalized smoothed particle hydrodynamics method for nonlinear dynamic problems," *Computer Methods in Applied Mechanics & Engineering*, 190 (2000) 225-239.
- [29] M.B. Liu, W.P. Xie, G.R. Liu, "Modeling incompressible flows using a finite particle method," *Applied Mathematical Modelling*, 29 (2005) 1252-1270.
- [30] X.Y. Hu, N.A. Adams, "An incompressible multi-phase SPH method," *Journal of Computational Physics*, 227 (2007) 264-278.
- [31] M.Y. Zhang, X.L. Deng, "A sharp interface method for SPH," *Journal of Computational Physics*, 302 (2015) 469-484.
- [32] G.R. Liu, M.B. Liu, "Smoothed particle hydrodynamics: a meshfree particle method," World Scientific, 2003.
- [33] A. Colagrossi, "A meshless Lagrangian method for free-surface and interface flows with fragmentation," La Sapienza: Universita di Roma, 2003.
- [34] J.J. Monaghan, "Smoothed particle hydrodynamics," World Scientific, 2005.
- [35] G.R. Johnson, W.H. Cook, "A constitutive model and data for metals subjected to large strains, high strain rates and high temperatures," In: Proceedings of seventh international symposium on ballistics, The Hague, Netherlands, 1983.
- [36] E.L. Lee, H.C. Hornig, J.W. Kury, "Adiabatic expansion of high explosive detonation products," Livermore Lawrence Radiation Lab, California Univ, 1967.
- [37] J.A. Zukas, "High Velocity Impact Dynamics," John Wiley and Sons, 1990.
- [38] P.V. Vaidyanathan, A. Ramanathan, "Design for quality explosive welding," *Journal of Materials Processing Technology*, 32 (1992) 439-448.
- [39] M. Acarer, B. Gülenç, F. Findik, "The influence of some factors on steel/steel bonding quality on there characteristics of explosive welding joints," *Journal of Materials Science*, 39 (2004) 6457-6466.
- [40] A.A.A. Mousavi, S.T.S. Al-Hassani, "Numerical and experimental studies of the mechanism of the wavy interface formations in explosive/impact welding," *Journal of the Mechanics & Physics of Solids*, 53 (2005) 2501-2528.
- [41] B. Wronka, "Testing of explosive welding and welded joints. Wavy character of the process and joint quality," *International Journal of Impact Engineering*, 38 (2011) 309-313.
- [42] X. Wang, Y. Zheng, H. Liu, Z. Shen, Y. Hu, W. Li, Y. Gao, C. Guo, "Numerical study of the mechanism of explosive/impact welding using Smoothed Particle Hydrodynamics method," *Materials & Design*, 35 (2012) 210-219.
- [43] S.R. Reid, "A discussion of the mechanism of interface wave generation in explosive welding," *International Journal of Mechanical Sciences*, 16 (1974) 399-413.
- [44] G.R. Cowan, O.R. Bergmann, A.H. Holtzman, "Mechanism of bond zone wave formation in explosion-clad metals," *Metalurgical & Materials Transactions B*, 2 (1971) 3145-3155.
- [45] A. Vivek, B.C. Liu, S.R. Hansen, G.S. Daehn, "Accessing collision welding process window for titanium/copper welds with vaporizing foil actuators and grooved targets," *Journal of Materials Processing Technique*, 214 (2014) 1583-1589.

A SPH model of root growth

Matthias MIMAULT^{*}, Mariya PTASHNYK[†], Lionel X. DUPUY^{*}

Abstract

In this work we use the Smoothed Particle Hydrodynamics method to describe the growth of a plant root. This method solves partial differential equations using a particle discretization. To model the root growth we use the framework of poroelasticity coupled with a microscopic description of the plant cell growth.

Keywords: Poroelasticity, Root growth model, Smoothed particle hydrodynamics.

1 Introduction

Plants are the most primary producers on earth. Through the photosynthesis process taking place in the leafs, they fix the carbon and supply food to most of the actors of the ecosystem. What is happening in the soil, although less visible, is of considerable importance to plant photosynthesis functions. Plants must acquire water and a multitude of mineral elements. This is a challenge because soil resources are heterogeneously distributed in the ground, sometimes available at great depth (deep sandy soils) or only at certain times (seasonal rotation). Additionally resources may not be available to the plant and have to be processed in association with soil micro-organisms. To achieve such functions,

plants grow root systems of considerable complexity. How a plant performs growth in such diverse conditions is still poorly understood. There has been much work done with imaging and providing new observations, yet the challenge remains to understand how growth and developmental processes, determined biologically at the cellular level, evolves at macroscopic scale in interaction with the granular media.

Biological studies are benefiting immensely from emerging optical imaging technologies, but the study of soil biota does not benefit much from them because most soil organisms cannot be cultured in current artificial substrates, whilst others have their functions strongly affected by the medium they are grown in [8]. It requires new transparent substrates [2], new visualisation techniques [3] and new models to integrate them all.

The roots acquire nutrients and water through complex interactions with bacterial colonies and chemical distribution in the ground [12]. Roots provide also support to aerial stems and increase the cohesion of the surrounding land [9]. The differentiation of the roots is genetically induced but also dependent on the heterogeneity of the soil [6].

In this paper we propose a framework to model the growth of roots using the Smoothed Particle Hydrodynamics (SPH) method, first developed in astrophysics by Lucy [7] and by Gingold and Monaghan [5], then extended to fluid dynamics

^{*}The James Hutton Institute

[†]University of Dundee

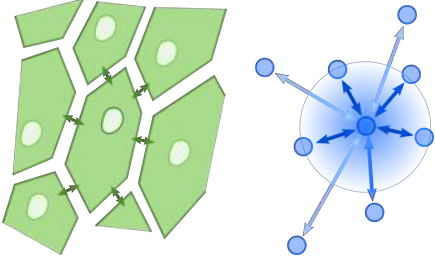


Figure 1: Schematic representation of the cell nucleus and the particle approximation kernel.

problems [10], structure problems [4] and interactions between fluids and structures [1].

The model consists of a poroelastic material description coupled with a microscopic growth model. The SPH is used to solve the elasticity equations, while for the microscopic description of the growth the numerical particles are identified with plant cells, see Fig. 1. In part 2 we describe the equations and the implementation of the SPH. We evaluate in part 3 the convergence, the stability and the sensitivity of the model in illustrative test cases. Finally we discuss the results and the perspectives in the part 4.

2 Model equations

We define the model of plant root tissues in the framework of poroelasticity. The extremal part of the root, called the *meristem*, is represented as a one dimensional elastic bar and depends on the turgor pressure.

2.1 Governing equations

The continuity equation for the density is based on mass conservation which is

$$\frac{\partial \rho}{\partial t} = -\rho \frac{\partial u}{\partial x}, \quad (1)$$

where ρ is the dry matter density, t is the time, u is the velocity and x is the space. In the case of mass growth, (1) becomes a balance law

$$\frac{\partial \rho}{\partial t} = -\rho \frac{\partial u}{\partial x} + S \quad (2)$$

with a source term which S will be explained later.

The equation of motion without gravitation is

$$\frac{\partial u}{\partial t} = -\frac{1}{\rho} \frac{\partial \sigma}{\partial x}, \quad (3)$$

where $\sigma = P + p$, with P being the internal pressure of the material and p the *turgor pressure*, identified as the pore pressure.

2.2 SPH formulation

The SPH method is based on a particle interpolation of a continuum, using a kernel approximation. The kernel represents the evaluation of the continuous function as an integral, discretized over a set of particles and is denoted by $W(x - x', h)$. It is essentially an approximation of the Delta function

$$\delta(x - x') = \begin{cases} 1 & \text{if } x = x' \\ 0 & \text{otherwise} \end{cases},$$

such that $\lim_{h \rightarrow 0} W(x - x', h) = \delta(x - x')$. h is called the *smoothing length* and $x - x'$ represents the distance between two particles.

The particle approximation of the continuous integral representation of a function $f(x)$ at a particle a is

$$\langle f(x) \rangle_a = \sum_{b=1}^N m_b \frac{f(x_b)}{\rho_b} W(x - x_b, h),$$

$$\left\langle \frac{\partial f}{\partial x} \right\rangle_a = \sum_{b=1}^N m_b \frac{f(x_b)}{\rho_b} \frac{\partial W(x - x_b, h)}{\partial x},$$

where N is the number of particles, W is the approximation kernel and x_b , m_b , ρ_b are respectively the position, the mass and the density at a particle b .

Using the SPH approximation, we reformulate (1) and (3)

$$\left\langle \frac{\partial \rho}{\partial t} \right\rangle_a = \sum_b m_b (u_a - u_b) \frac{\partial W_{ab}}{\partial x_a}, \quad (4)$$

$$\begin{aligned} \left\langle \frac{\partial u}{\partial t} \right\rangle_a &= \\ &- \sum_b m_b \left[\left(\frac{\sigma_a}{\rho_a^2} + \frac{\sigma_b}{\rho_b^2} \right) + \Pi_{ab} \right] \frac{\partial W_{ab}}{\partial x_a}, \end{aligned} \quad (5)$$

where $W_{ab} = W(x_a - x_b, h)$ and the artificial viscosity Π_{ab} is defined by

$$\Pi_{ab} = \begin{cases} \frac{-\alpha_a c_0 \mu_{ab} + \alpha_b \mu_{ab}^2}{\bar{\rho}_{ab}} & \text{if } (u_a - u_b) \cdot (x_a - x_b) \geq 0, \\ 0 & \text{elsewhere,} \end{cases}$$

with α_a , α_b constants, $\bar{\rho}_{ab} = \frac{\rho_a + \rho_b}{2}$ and

$$\mu_{ab} = h \frac{(u_a - u_b) \cdot (x_a - x_b)}{|x_a - x_b|^2 + (0.1h)^2}.$$

See [11] for more details.

2.3 Constitutive equations

A plant root tissue us mainly composed of incompressible materials. We describe it as a weakly compressible material, with a linearized pressure equation depending on density

$$P(\rho) = c_0^2 (\rho - \rho_0), \quad (6)$$

where $c_0 = \sqrt{\frac{K}{\rho_0}}$, with K being the compressibility modulus and ρ_0 the equilibrium density.

We assume that the mass of cells increases due to nutrient uptake. We model this mechanism

with a source term in the continuity equation, depending on the difference between cell density and a constant equilibrium density, representing the fact that water flows inside a plant cell when the turgor pressure is lower than the pressure in the extracellular space

$$S(\rho) = \lambda (\rho_0 - \rho), \quad (7)$$

where λ is the rate of growth.

For the pore pressure we assume a linear distribution depending on space

$$p(x) = p_0 \frac{|x|}{L}. \quad (8)$$

It might also depends microscopically on the length of cell v

$$p(x, v) = p_0 \frac{|x|}{L} g(v), \quad (9)$$

where g is an arbitrary function depending v .

3 Numerical application

In this section we analyse the convergence, stability and sensitivity to the model parameters of SPH simulations.

3.1 Model settings

A part of a plant root tissue is represented by a one dimensional bar of length L , fixed on the left side and free on the right side. We apply mirror conditions on the fixed boundary with N_{bd} ghost particles negatively indexed

$$\begin{cases} v_{-b} = -v_b & \text{for } b < N_{bd}, \\ \rho_{-b} = \rho_b & \text{for } b < N_{bd}. \end{cases}$$

The bar is divided in N particles of initial spacing $\Delta x = \frac{L}{N}$ and mass $m = \frac{L\rho_0}{N}$. The time step is chosen as

$$\Delta t = 0.4 \frac{h}{c_0}.$$

The kernel used in the simulations presented here is the *cubic spline* kernel, proposed by [11]

$$W(r, h) = \frac{2}{3h} \begin{cases} 1 - \frac{3}{2} \left(\frac{r}{h}\right)^2 + \frac{3}{4} \left(\frac{r}{h}\right)^3 & \text{if } 0 \leq r < h, \\ \frac{1}{4} \left(2 - \frac{r}{h}\right)^3 & \text{if } h \leq r < 2h, \\ 0 & \text{elsewhere.} \end{cases}$$

The update of the forces acting on the particles is performed using an Euler time integration scheme with the SPH approximations (4) and (5)

$$\begin{aligned} \rho^{n+1} &= \rho^n + \Delta t \left\langle \frac{\partial \rho}{\partial t} \right\rangle^n, \\ v^{n+1} &= v^n + \Delta t \left[\left\langle \frac{\partial v}{\partial t} \right\rangle^n - \nu v^n \right], \\ x^{n+1} &= x^n + \Delta t v^{n+1}, \end{aligned}$$

with a motion damping applied in addition to the artificial viscosity to increase the convergence of the equilibrium.

3.2 Tests

To analyse the behaviour of the root model, we simulate two situations

1. Only-elongation model: $\lambda = 0$, $g(v) = 1$,
2. Growth-elongation model: $\lambda = 0.5$,
 $g(v) = 1, \bar{v} - v$,

The length of the initial domain is $L = 5 \text{ mm}$, starting at equilibrium density 1 mg.mm^{-3} . The motion damping $\nu = 0.2$ and $\alpha_a = \alpha_b = 1.0$.

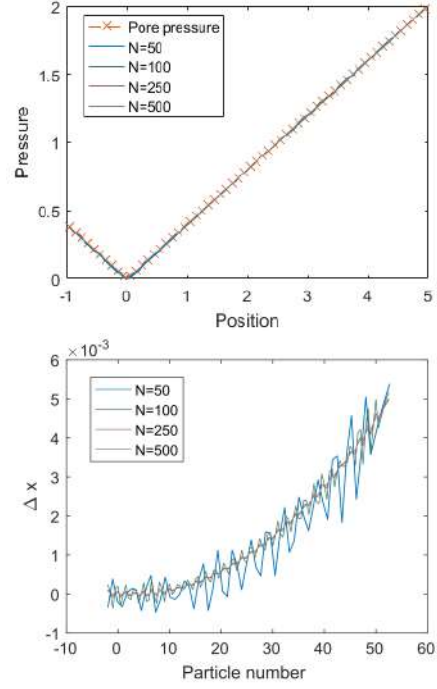


Figure 2: Pressure distribution and relative displacement for $N = 50, 100, 250$ and 500 .

We will consider as outputs the pressure distribution in with respect to the space variable x and the relative displacement of the particles with respect to their initial position.

3.2.1 Only-elongation

In this test, we assert the convergence and stability of the model under the linear distribution of pore pressure (8) for different particle numbers. We have $N = 50, 100, 250, 500$, $p_0 = 2 \text{ kPa}$ and $T_{\max} = 50 \text{ ms}$. As we can see in Fig 2, the inner pressure matches the pore pressure distribution and the maximal elongation is $5.2 \times 10^{-3} \text{ mm}$. Moreover, the oscillations in the relative displacement are vanishing as the number of par-

ticles increases.

3.2.2 Growth-elongation

Here we consider a coupling between the poroelastic model and a plant root growth model, and its impact on the relative displacement and the mass of particles. The mass evolution will depends on the difference of the density with the equilibrium (7) and the pore pressure will depends on the cell length $v^n = \frac{m^n}{\rho^n}$ with (9). The microscopic formulation of (7) is

$$\begin{aligned} m^{n+1} &= m^n + \Delta t \lambda v^n (\rho_0 - \rho) \\ &= m^n + \Delta t \lambda m^n \left(\frac{\rho_0}{\rho} - 1 \right). \end{aligned}$$

The parameters of the test are $N = 100$, $p_0 = 2$ kPa and $T_{\max} = 50$. $\lambda = 0.5$ for the growth rate and $g(v) = 1$ in the without control case and $g(v) = \bar{v} - v$ for the cell size-dependant pore pressure, where the maximal cell size is $\bar{v} = 0.06$ mm. In Fig 3, we observe that the elongation dynamic is stronger than the mass growth (NoPoreCtrl). It leads to an unbounded but stable elongation, especially compared to the elongation-only case (NoGrowth). In the case of cell size-dependant control of the pore pressure (PoreCtrl), we have an appreciable elongation, with the inner pressure converging to zero as the pore pressure vanishes when the maximal cell size is reached. Fig 4 supports the smooth evolution of the growth as the relative displacement and the mass evolution do not show of instabilities.

4 Perspectives

We described a bio-mechanical model of root growth based on the SPH method. It produced good results regarding convergence and stability

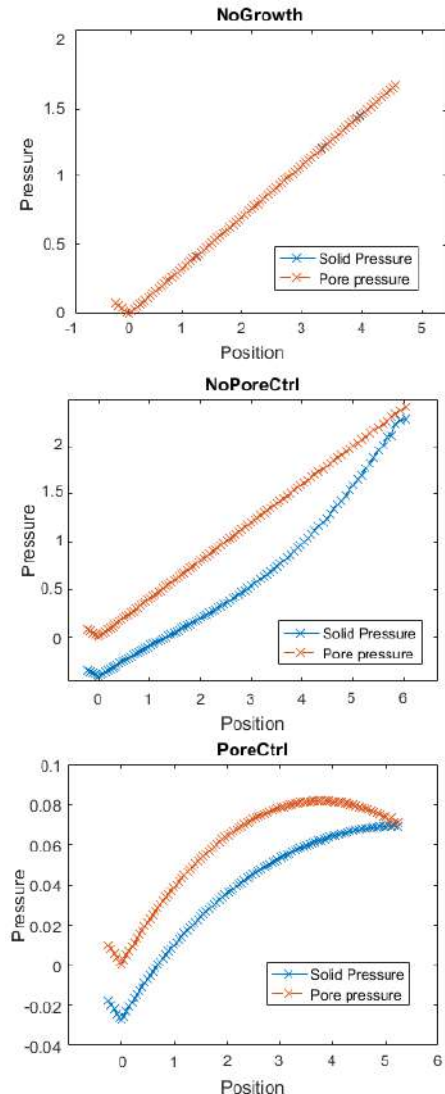


Figure 3: Pressure distribution and relative displacement for the Growth-elongation test

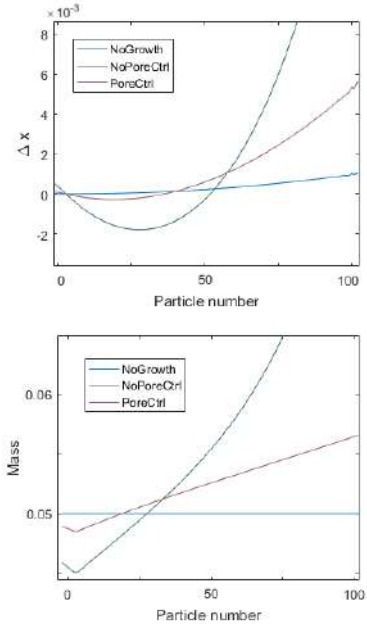


Figure 4: Relative displacement and the mass evolution for $N = 100$.

and allowed us to consider the different dynamics involved in the coupling of poroelasticity with cell growth. Future work will include the extension of the model to three dimensions, with the exploration of more physical biological models of turgor pressure, nutrient assimilation and soil interaction. Moreover the model will be also used in a visualisation framework to integrate experimental data from lab imaging.

5 Acknowledgement

This research was supported by a consolidator fellowship from the European Research Council (ERC SENSOILS-647857). The James Hutton Institute receives support from the Scottish Government Rural and Environment Science and Analytical Services Division (RESAS, Workpackage 3.3 and 3.4). Financial support for this project came also from the Institute of Mathematics and its Applications (Small Grant SGS17-46).

References

- [1] C. Antoci, M. Gallati, and S. Sibilla. Numerical simulation of fluid–structure interaction by sph. *Computers & Structures*, 85(11):879 – 890, 2007. Fourth MIT Conference on Computational Fluid and Solid Mechanics.
- [2] H. Downie, W. Otten, A. Spiers, T. Valentine, and D. LX. Transparent soil for imaging the rhizosphere. *PLoS ONE*, 7(9), 2012.
- [3] F. Federici, L. Dupuy, L. Laplaze, M. Heisler, and H. Jim. Integrated genetic and computation methods for in planta cytometry. *Nature Methods*, 9:483—485, 2012.

- [4] M. D. Fuller. *The Application Of Smooth Particle Hydrodynamics To The Modelling Of Solid Materials*. PhD thesis, University of Leicester Engineering Department, July 2010.
- [5] R. A. Gingold and J. J. Monaghan. Smoothed particle hydrodynamics - Theory and application to non-spherical stars. *Monthly Notices of the Royal Astronomical Society*, 181:375–389, Nov. 1977.
- [6] A. Hodge, D. Robinson, B. S. Griffiths, and A. H. Fitter. Why plants bother: root proliferation results in increased nitrogen capture from an organic patch when two grasses compete. *Plant, Cell & Environment*, 22(7):811–820, 1999.
- [7] L. B. Lucy. A numerical approach to the testing of the fission hypothesis. *Astronomical Journal*, 82:1013–1024, Dec. 1977.
- [8] J. E. Malamy. Intrinsic and environmental response pathways that regulate root system architecture. *Plant, Cell & Environment*, 28(1):67–77, 2005.
- [9] A. Mäkelä, J. Landsberg, A. Ek, T. Burk, M. Ter-Mikaelian, G. Ågren, C. Oliver, and P. Puttonen. Process-based models for forest ecosystem management: Current state of the art and challenges for practical implementation. *Tree Physiology*, 20(5-6):289–298, 3 2000.
- [10] J. Monaghan. Simulating free surface flows with sph. *Journal of Computational Physics*, 110(2):399 – 406, 1994.
- [11] J. J. Monaghan. Smoothed particle hydrodynamics. *Annual review of astronomy and astrophysics*, 30:543–574, 1992.
- [12] A. Smucker. Carbon utilization and losses by plant root systems. *Roots, Nutrient and Water Influx, and Plant Growth*, page 27–46, 1984.

Modeling the Melting Process of Quartz Glass using SPH Method

Zhongyi Liu, Qianli Ma, Haisheng Fang

School of Energy and Power Engineering
Huazhong University of Science & Technology (HUST)
Wuhan, P.R. China
hafang@hust.edu.cn

Abstract—Owning to excellent performance in optics and thermo-physics, quartz glass is widely used in aerospace, semiconductor, fiber-optic communication, laser weapon and so on. There are many complex phenomena coupled with heat transfer in melting process of quartz glass, such as large surface deformation, free surface flow and fluid-solid interaction. Smoothed Particles Hydrodynamics (SPH), a mesh-free Lagrange method, has been proved an effective tool to deal with such problems. The challenges to simulate quartz glass melting are the following two aspects: incompressible flow with a high viscosity and radiative heat transfer in semi-transparent material. During study, both the physical viscosity model and the Monaghan artificial viscosity model are applied to compute viscous force. The heat radiation from the heater is simplified through adding a heat source at the ingot surface, and the radiation in participating media is approximated by an effective thermal conductivity from Rosseland model. Then Fourier law in SPH format is employed to calculate the evolution of temperature field. A simple algorithm based on SPH is developed to solve the velocity and temperature field of quartz glass melting process.

Keywords: quartz melting, radiative heat transfer, smoothed particles hydrodynamics, viscosity

I. INTRODUCTION

Quartz glass is an indispensable material in modern technology and industry because of its good thermo-physical properties, excellently optical performance and outstanding electrical properties, which make it as “King of Glass” by material specialist [1]. The popular techniques to produce quartz glass include fused process, flame fused process, chemical vapor deposition (CVD), and plasma chemical vapor deposition (PCVD). The high-purity quartz glass is mainly synthesized by fusing purified silica sand powders (natural quartz glass), or by chemical reaction of silicon tetrachloride (SiCl_4) with oxyhydrogen flame (synthetic quartz glass). The natural quartz glass has less bubble, better transparency and higher productivity than synthetic quartz glass, while the latter is more excellent in optical homogeneity, purity and irradiance resistance performance. Both of the glasses suffer from the composition defect, high concentrations of hydroxyl. Hydroxyl (OH), contained in the quartz sand or generated from the flame fused process, weakens the strength of Si-O band, thus remarkably degrading the chemical stability and the mechanical strength [1]. Besides, optical performance is extremely sensitive to the concentration of OH, and

refractivity changes 1×10^{-6} per 10 ppm of Hydroxyl content fluctuation [2]. Thus, hydroxyl content has become one of the most important factors to affect optical homogeneity. Reduction of hydroxyl in quartz glass has become a common goal throughout quartz industry, which encourages researchers investigating new synthesis technologies. A new two-step process has been developed by modifying the technique in existence. A porous silica ingot is firstly obtained by flame fused technique. Then the ingot is put into an electrical melting vacuum furnace where hydroxyl is removed. High-purity and low-hydroxyl quartz glass could be produced after melting and solidification. The new process contains various complex phenomena coupling to heat transfer, including large surface deformation, free surface flow and fluid-solid interaction. It will be very significant to understand clearly the melting process for achieving qualified products.

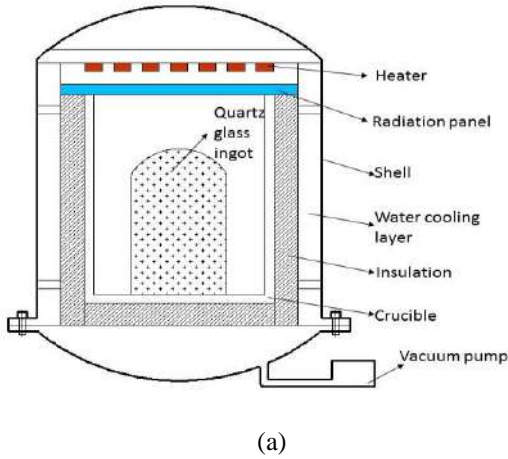
Smoothed Particles Hydrodynamics (SPH) has been proved a more effective tool to deal with the melting process than the traditional grid-based algorithm. SPH, a mesh-free Lagrangian method, is first put forward by Lucy [3] and Monaghan and Gingold [4] in 1977, aiming to solve the astrophysics problem in three-dimensional open space. And now it is universally applied in the hydrodynamics investigation with large deformation. The early SPH method is confined to the non-viscous flow due to the difficulty of solving the second derivative of the physical viscosity term in the generalized Navier-Stokes equation. A series of viscosity models has been proposed. The Monaghan type of artificial viscosity proposed by Monaghan [5] is the most widely used. Morris et al. [6] developed a model to simulate low Reynolds number incompressible flow. Cleary et al. [7] simulated heat conduction of multi-materials with a similar way as Morris. Suprijadi et al. [8] studied the melting process of ice with experimental verification.

This paper focuses on extending the SPH method into quartz glass synthesis with highly viscous flow and heat transfer. During study, both the physical viscosity model and the Monaghan artificial viscosity model are applied to compute viscous force. The challenge is how to deal with thermal radiation transfer in SPH framework. In the current modelling, a strategy to simplify the radiative heat transfer is developed based on the CFD results. A heat source is added to the surface to replace the surface-to-surface radiation. The radiation in participating media is approximated by an effective thermal conductivity from Rosseland model.

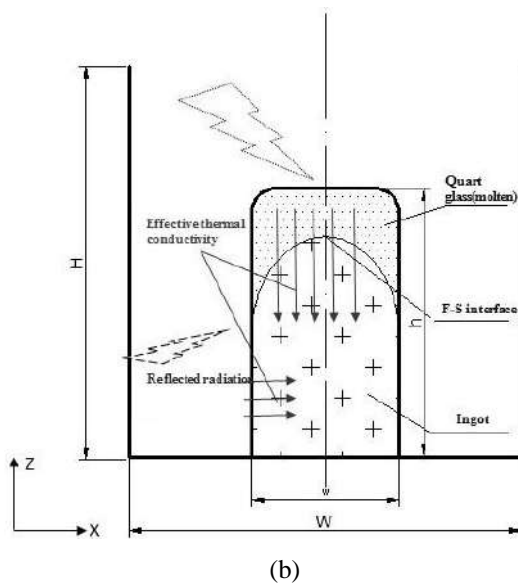
II. SIMULATION

A. Model Description

The quartz ingot electric melting vacuum furnace is illustrated in Fig. 1a, which mainly contains electric heater, radiation panel, supporters, heat insulation, crucible and vacuum pump. The resistive heater is mounted at the top of furnace. And a radiation panel is below to help heating quartz ingot homogeneously. Further down, the crucible is enclosed by heat insulation. The external shell of the furnace is cooled by room temperature water. Vacuum pump is located at the bottom, which could benefit from the porous structure of un-melted ingot. A diagram of heat transfer during melting is shown in Fig. 1b, which describes an ideal melting process. And the ideal melting process is layer-by-layer from the top to the bottom along the ingot. The radiation energy from the heater reaches the high-reflective crucible walls firstly, and then to the ingot surface rapidly. As revealed in CFD modelling, temperature at the whole surface of the quartz ingot except the bottom rises up almost in the same time. To simplify, all particles on the surface except bottom is set to a uniform temperature, T_h .



(a)



(b)

Figure 1. (a) Schematic diagram of the quartz ingot in an electric melting furnace, and (b) description of heat transfer during the ingot melting.

B. Governing Equations

Motion of the melted quartz is described by Navier-Stokes (N-S) equations. In Lagrangian frame, the governing equations take the forms:

$$\frac{D\rho}{Dt} = -\rho \nabla \cdot v, \quad (1)$$

$$\frac{Dv^\alpha}{Dt} = -\frac{1}{\rho} \nabla p + \mu \nabla^2 v^\alpha + F, \quad (2)$$

$$\frac{De}{Dt} = \frac{p}{\rho} \nabla \cdot v + \nabla \cdot (\kappa_{eff} \nabla T), \quad (3)$$

where the superscript α represents the coordinate direction. And ρ , p , v , e , F and μ are density, pressure, velocity, energy, body force and dynamic viscosity, respectively. The uppercase T and lowercase t denotes temperature and time separately. The κ_{eff} is effective thermal conductivity, and will be explained in detail later.

The artificial compressibility is introduced into the model. Pressure can be directly calculated by a function of density by it. The Monaghan model is employed [9] in current study,

$$p = B((\frac{\rho}{\rho_o})^\gamma - 1). \quad (4)$$

And the γ is a constant, equalling to 7 usually; ρ_o is reference density and B is a varying parameter with the specific issues.

C. Numerical Scheme

The cores of constructing governing equations in SPH form are kernel approximation and particle approximation. Kernel approximation, also called integral representation, is used to discretize the governing equations using integral of interpolation:

$$\langle f(r) \rangle = \int_Q f(r') W(r - r', h) dr'. \quad (5)$$

And the kernel approximation operator is marked by angle bracket $\langle \rangle$, and the value of function f at position r can be attained by integrating the product of function f and W throughout entire space here. The function W is smoothing kernel, and parameter h defines the influence area. In the SPH frame, the system is described by a series of particles with mass and position. The integral representation of functions needs to be converted into discretized forms of summation over all the particles inside the support domain, which is the second step: particle approximation.

$$\langle f(r_i) \rangle = \sum_{j=1}^N \frac{m_j}{\rho_j} f(r_j) \cdot W(r_i - r_j, h), \quad (6)$$

where the letters i and j are the identifier of particles.

The approximation of spatial derivative is another important element. After a skilful derivation, the divergence at particle i takes forms,

$$\nabla \cdot f(r_i) = \frac{1}{\rho_i} \left[\sum_{j=1}^N m_j [f(r_j) - f(r_i)] \cdot \nabla_i W(r_i - r_j, h) \right], \quad (7)$$

or

$$\nabla \cdot f(r_i) = \rho_i \left[\sum_{j=1}^N m_j \left(\frac{f(x_j)}{\rho_j^2} + \frac{f(x_i)}{\rho_i^2} \right) \cdot \nabla_i W(r_i - r_j, h) \right]. \quad (8)$$

Using the (7) or (8), then, the Navier-Stocks equation can be derived as:

$$\frac{D\rho_i}{Dt} = \rho_i \sum_{j=1}^N \frac{m_j}{\rho_j} v_{ij} \cdot \nabla_{ij} W, \quad (9)$$

$$\frac{Dv_i^\alpha}{Dt} = \sum_{j=1}^N m_j \left(\frac{p_j}{\rho_i^2} + \frac{p_i}{\rho_j^2} \right) \frac{\partial W_{ij}}{\partial x_i^\alpha} + F + \theta, \quad (10)$$

$$\frac{De_i}{Dt} = \frac{1}{2} \sum_{j=1}^N m_j \left(\frac{p_i}{\rho_i^2} + \frac{p_j}{\rho_j^2} \right) v_{ij} \nabla_{ij} W + \nabla \cdot (\kappa_{eff} \nabla T)_i. \quad (11)$$

And the θ in the momentum equation denotes viscous force which will be calculated by the physical viscosity model and the Monaghan artificial viscosity model. Both thermal conductivity of energy equation and viscosity of momentum equation contain derivative of second order which is an intricate term for SPH, and an similar SPH estimation is employed according to Cleary and Monaghan[7, 10].

$$\nabla \cdot (\kappa_{eff} \nabla T)_i = \sum_{j=1}^N \frac{4m_j}{\rho_j \rho_i} \frac{\kappa_i \kappa_j}{(\kappa_i + \kappa_j)} (T_i - T_j) \frac{r_{ij} \cdot \nabla_{ij} W}{r_{ij}^2 + \zeta^2}, \quad (12)$$

$$(\mu \nabla^2 v)_i^\alpha = \sum_{j=1}^N m_j \frac{\mu_i + \mu_j}{\rho_i + \rho_j} v_{ij}^\alpha \frac{r_{ij} \cdot \nabla_{ij} W}{r_{ij}^2 + \zeta^2}, \quad (13)$$

$$r_{ij} = r_i - r_j, \quad v_{ij} = v_i - v_j. \quad (14)$$

As to viscous force, the model, Monaghan type artificial viscosity, is also incorporated into pressure term of momentum equation directly. The formulation is as below:

$$\pi_{ij} = \begin{cases} \frac{-\alpha_I \bar{c}_{ij} \phi_{ij} + \beta_I \phi_{ij}^2}{\rho_{ij}}, & v_{ij} \cdot r_{ij} < 0, \\ 0, & v_{ij} \cdot r_{ij} \geq 0; \end{cases} \quad (15)$$

where

$$\phi_{ij} = \frac{h_{ij} v_{ij} \cdot x_{ij}}{|x_{ij}|^2 + \varphi^2}. \quad (16)$$

The c and ρ with over-line represent average speed of sound and average density; the r_{ij} and v_{ij} is same as above (14). And the φ is set to $0.1h_{ij}$ in order to avoid numerical divergence when particles approach each other.

D. Radiation Dalculation

Radiation in participating media is a non-ignorable phenomenon during quartz glass melting process. The radiation heat flux is much larger than the pure conduction heat flux because of the high temperature. Rosseland approximation is available to determine the effective thermal conductivity[11], relying on the hypotheses that the participating media is optically thick, i.e. the optical thickness far outweighs 1. The optical thickness is defined by the integral of absorption coefficient along a typical optical path. Supposing that the quartz glass is a grey media, the radiation heat flux can be evaluated by[12]

$$q_r = - \frac{4\sigma}{3\beta_r} \nabla(n^2 T^4). \quad (17)$$

And if the refractive index is a constant, the (17) can be simplified as $q_r = -\kappa_r \Delta T$ where κ_r is effective thermal conductive due to radiation heat flux.

According to Rosseland approximation, the radiation effective thermal conductivity is calculated by

$$\kappa_r = \frac{16n^2 \sigma T^3}{3\beta_r}, \quad (18)$$

where n , σ , T , and β_r are refractive index, Stefan-Boltzmann constant, temperature and mean extinction coefficient, respectively. Then the system effective thermal conductivity equates to

$$\kappa_{eff} = \kappa + \kappa_r = \kappa + \frac{16n^2 \sigma T^3}{3\beta_r}, \quad (19)$$

in which κ is inherent thermal conductivity.

E. Surface Detection

The investigation uses the strategy of adding heat source into surface particles to replace surface-to-surface thermal radiation, so detecting particles located at surface in real time becomes crucial for the simulation. Particle number density could be used as the criteria. As shown in Fig. 2, the particles located at free surface have a lower particle number density than that at inner. The particle number density equation in SPH style is:

$$N_i = \sum_j \left(\frac{m_j}{\rho_i} \right) W(r_i - r_j, h). \quad (20)$$

Birds et al. [13] employed $N_i < 0.84N_{max}$ as the condition of determining the free surface particle. According to current study, the coefficient “0.84” will result in obvious bias for our model. The influence of

coefficient will be explained at next section, and a more eligible one will be adopted.

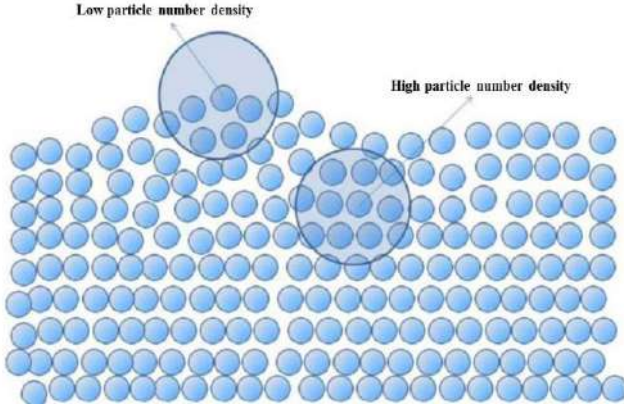


Figure 2. Surface detection using particle number density[8]

III. RESULTS

A. Overview of Temperature and Velocity Field

The process of quartz glass ingot melting and collapse with the radiation heating is illustrated in Fig. 3a-f where the left is temperature field and the right is velocity field. There is a two-dimensional areal model in which height and length are both 0.5 meters. And the glass ingot is 0.3 meters * 0.4 meters, and represented by 3240 particles. Besides, additional 303 particles are employed as boundary particles, which exert the boundary force to the nearby fluid particles. The initial temperature, specific heat capacity and equivalent thermal conductivity equal to 1650 K, 1500 J/(K*kg) and 500 W/(m*K), respectively. And the coefficient α of artificial viscosity is unit. Based on the results of simulation, the distribution of temperature and velocity agrees with the reality and traditional CFD calculation liberally.

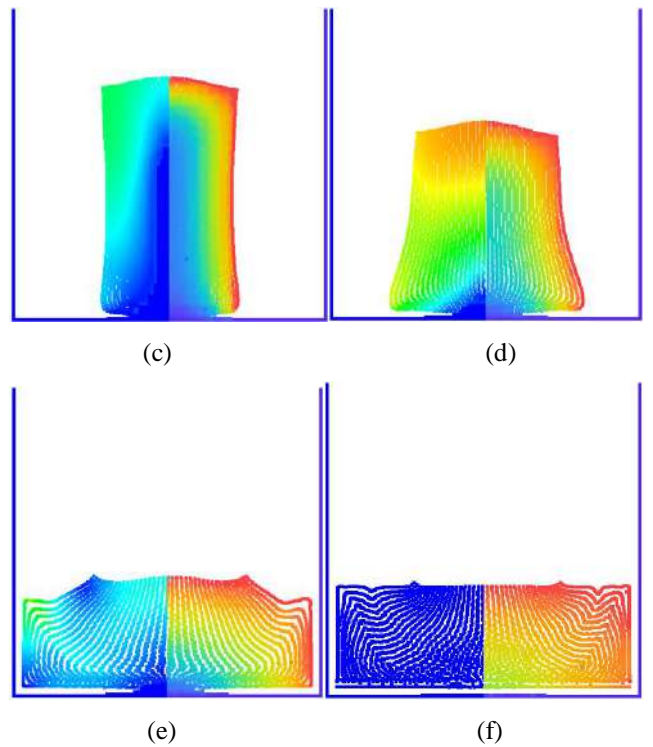
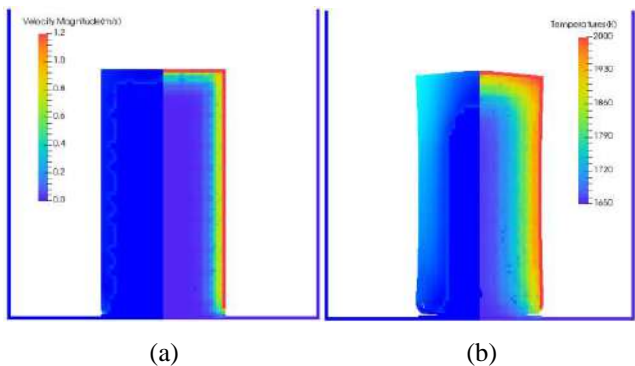


Figure 3. Velocity field and temperature field distribution of quartz glass melting process (artificial viscosity model). (a) ~ (f) are describing at the step time 0,5,10,20,35 and 140 respectively. And the left is the velocity field, the right is the temperature field at each time step.

B. Detection Coefficient Effect

The paper defines the ratio of individual particle number density to the maximum particle number density as detection coefficient. As mentioned above, the detection coefficient in free-surface tracing algorithm is applied as a condition to distinguish the particles located at the surface. During the simulation, a heat source is added to the surface for considering radiation heating. Accurate determination of the surface directly affects calculation of radiative heat transfer in the model, thus, affects calculation accuracy of the system temperature and velocity fields.

Birds et al. [13] used the value of 0.84 as the detection coefficient. However, it is not suitable for the current study. With increase of the particle disorder, the selection criterion of $N_i < 0.84N_{max}$ makes a large number of inner particles be improperly considered as surface particles. As shown in Fig. 4 d, when the melting process proceeds to a certain extent, most of the inner particles would be identified as the surface particles, thus causing the wrong heating, and a sudden melting of the quartz. The glass ingot collapses unreasonably.

The following study takes 0.54, 0.64, 0.74 and 0.84 as the detection coefficient in the surface tracing algorithm to explore its influence on the modelling. The results are shown in Fig. 4. It can be seen that the surface determination affects the melting process significantly. The coefficient of 0.54 is too small to trace the free surface

accurately. For the values of 0.74 and 0.84, although the surface at the early time can be tracked effectively, at the late stage more and more internal particles are mistakenly considered as the surface particles due to the increase of disorder degree. When it is set to 0.64, the maximum misidentified coefficient (the ratio of the particles predicted at the surface to the particles at the actual surface) is less than 20%. The deviation mainly occurs in the area A (as illustrated in Fig. 4b), where the heating of particle has little effect on the overall temperature and velocity fields. In a summary, the detection coefficient should be very careful chosen to reduce or avoid the error of surface tracking. Therefore, in the current model, the coefficient of 0.64 is adopted.

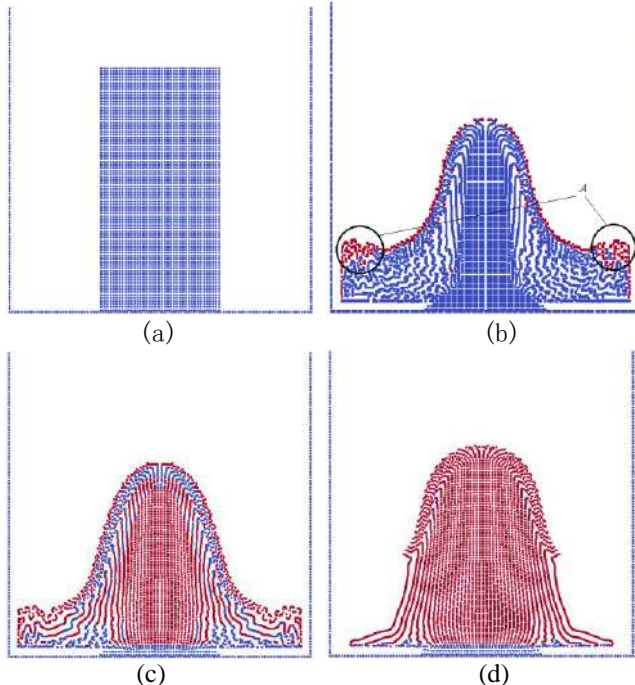


Figure 4. The results of the free surface determination under different detection coefficients. The red represents the free surface, and the blue represents the internal particles. The coefficients in (a)~(d) are 0.54, 0.64, 0.74 and 0.84, respectively.

C. Dynamic Viscosity Effect

As shown in the above governing equations, viscosity plays an important role in the accurate calculation of the velocity field. Using the artificial viscosity model proposed in Section A, the obtained results are found close to industrial experience. In this section, the physical viscosity model proposed by Morris is further adopted. In the model, the dynamic viscosity μ is employed as the calculation variable. The calculation formula of the physical viscosity is closer to the real melt properties, which is significant for future application of the algorithm in industrial optimization.

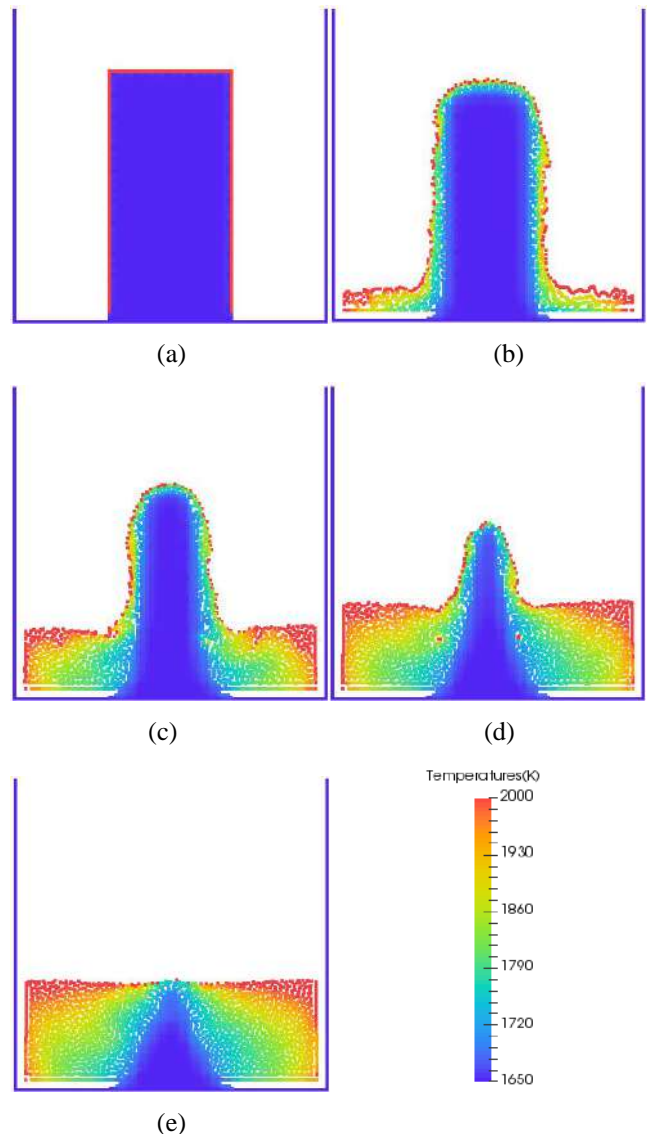


Figure 5. Temperature and morphology evolutions of the quartz melting calculated with the physical viscosity model

Fig. 5 shows the quartz glass melting process using the physical viscosity model. The physical viscosity model uses a similar setting as the artificial viscosity model, and its dynamic viscosity μ equals to 10. The physical viscosity model results in a similar morphology and temperature distribution as the artificial viscosity model. It should be noted that the specific morphology depends on the relative relationship between viscosity and temperature. Influences of viscosity on the effective thermal conductivity are further discussed. The viscosity is calculated at 10, 300, 500 and 1000 Pa·s. It can be found that the physical viscosity model proposed by Morris has good stability under the condition of high viscosity. The quartz glass melting morphologies with different viscosities at the same melting time are illustrated at Fig. 6. When the viscosity is small, the molten glass of the heated surface flows along the surface of the quartz ingot (as illustrated in Fig. 5) as the layer-by-layer

melting. As the viscosity increases, the molten glass becomes more and more difficult to flow along the ingot surface, and the heat transfer rate gets faster than the flow velocity of the molten glass. As a result, the inner temperature reaches the soften point simultaneously, causing the ingot collapse in a whole (as illustrated in Figs. 6b-d).

D. Incomplete Melting Phenomenon

Figure 7 shows the morphology of the late stage during the melting process. It can be observed clearly that a piece of un-melted quartz glass is enclosed by quartz melt. The un-melted quartz may cause critical defects degrading optical uniformity of the final product of the quartz glass. The inconsistency melting is mainly due to the fact that the loose quartz located at the bottom of the crucible is surrounded by the circumjacent molten glass, and the energy of the heater is difficult to reach the loose body. Therefore, increasing the heat transfer of the melt, for example improving melt convection, may reduce the incomplete melting of the ingot, and improve optical performance and uniformity of the glass products.

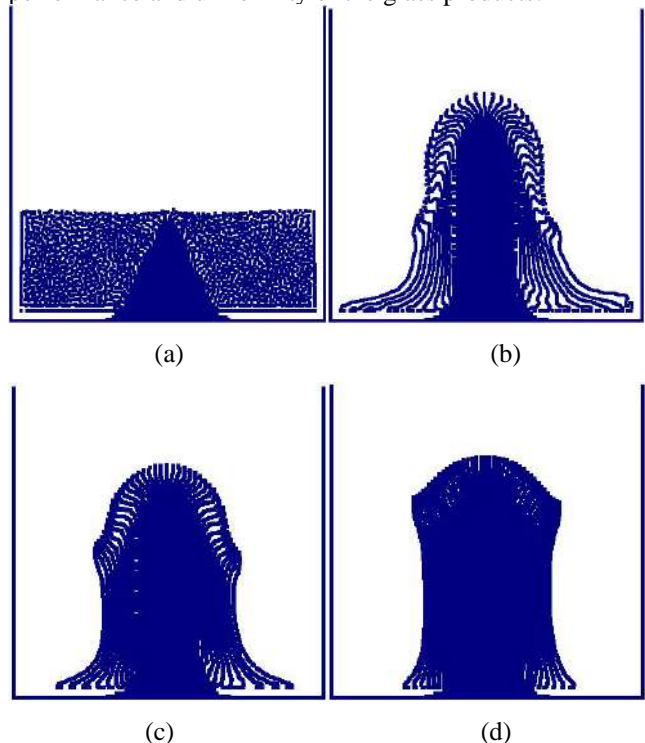


Figure 6. Melting morphology comparation of different viscosities at the same time. The viscosities of a, b, c and d are 10, 300, 500 and 1000 Pa·s, respectively.

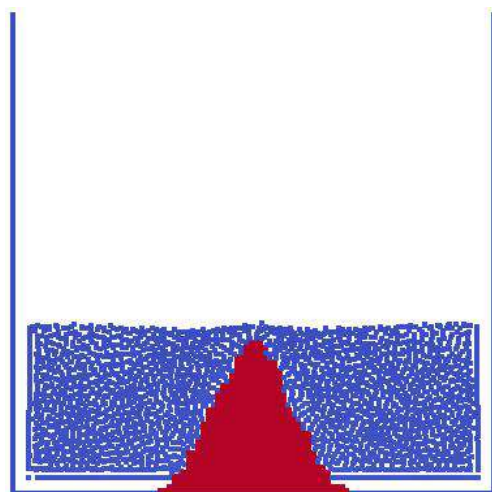


Figure 7. Morphology with dynamic viscosity equaling to 10 at the end of the melting process. The red represents the solid, and the blue represents the melt.

IV. CONCLUSION

In the paper, a SPH algorithm coupled heat transfer and high-viscosity flow are developed. Based on analysis of the two-dimensional melting process of the quartz glass ingot, the following conclusions can be drawn:

(1) Artificial viscosity model and physical viscosity model proposed by Morris take good account of the dissipation phenomenon in highly viscous fluid flow, and are able to carry out a reliable process modelling. However, physical viscosity model is more practical in physical significance.

(2) The algorithm based on the particle density is applied to track the free surface, and a suitable detection coefficient is found to be 0.64 in the current study.

(3) By analysing the cases, the morphology of the melting process is found dependent on the combined effect of the liquid viscosity and the heat transfer rate: when the heat transfer is slow, and the viscosity is small, the quartz ingot tends to melt in layers. Vice versa, it tends to collapse.

(4) According to the modelling results, there would be solid quartz in the centre of the crucible that cannot be melted due to weak heat transfer to the center. Strengthening convection of the fused quartz could promote better heat transfer to the central area, thus avoiding the incomplete melting phenomenon.

ACKNOWLEDGEMENT

This work is supported by the grants from National Key Research and Development Program (2016YFB0303801).

REFERENCES

1. Fanderlik, I., *Silica glass and its application*. 2013: Elsevier.
2. Hetherington, G. and K. Jack, "Water in Vitreous Silica—Part I: Influence of Water" Content on the Properties of Vitreous Silica," *Phys. Chem. Glasses*, 1962. 3(4): p. 129-33.

3. Lucy, L.B., *A numerical approach to the testing of the fission hypothesis*. The Astronomical Journal, 1977. **82**: p. 1013-1024.
4. Gingold, R.A. and J. Monaghan, *Smoothed particle hydrodynamics: Theory and application to non-spherical stars*. Monthly Notices of the Royal Astronomical Society, 1977. **181**(3): p. 375-389.
5. J. J.Monaghan, *On the problem of penetration in particle methods*. Journal of Computational Physics, 1989. **82**(1): p. 1-15.
6. Morris, J.P., P.J. Fox, and Y. Zhu, *Modeling low Reynolds number incompressible flows using SPH*. Journal of computational physics, 1997. **136**(1): p. 214-226.
7. Cleary, P.W. and J.J. Monaghan, *Conduction Modelling Using Smoothed Particle Hydrodynamics*. Journal of Computational Physics, 1999. **148**(1): p. 227-264.
8. Suprijadi, F. Faizal, and R.R. Septiawan, *Computational Study on Melting Process Using Smoothed Particle Hydrodynamics*. Journal of Modern Physics, 2014. **05**(03): p. 112-116.
9. Monaghan, J.J., *Simulating Free Surface Flows with SPH*. Journal of Computational Physics, 1994. **110**(2): p. 399-406.
10. Monaghan, J., *Heat conduction with discontinuous conductivity*. Applied Mathematics Reports and Preprints, 1995. **95**(18): p. 7.1.
11. Jin, Z.L., et al., *Influence of temperature-dependent thermophysical properties of sapphire on the modeling of Kyropoulos cooling process*. Journal of Crystal Growth, 2014. **405**: p. 52-58.
12. Modest, M.F., *Radiative heat transfer*. 2013: Academic press.
13. Bird, R., W. Stewart, and E. Lightfoot, *Interphase Transport in Non Isothermal Systems*. Transport phenomena, 2002: p. 422-450.

An elasto-plastic- μ (I) SPH model for landslide induced debris flow

Zhang Wentao, An Yi

Laboratory for Mechanics in Fluid Solid Coupling Systems
Institute of Mechanics, Chinese Academy of Sciences
Beijing, China
anyi@imech.ac.cn

Liu Qingquan

Department of Mechanics
Beijing Institute of Technology
Beijing, China

Abstract—In the landslide induced debris flow problem, the soil slope experiences four stages: slope instability, large deformation, debris flow and deposition. Although the SPH method has been applied in geotechnical problems such as slope instability since Bui et al. [1], the numerical simulation of this whole process, esp. which includes phase change between solid and fluid, is very few. In this study, the elasto-plastic viscous implementation with the Drucker-Prager yield criterion for solid stage and μ (I) rheology for the fluid stage is developed based on DualSPHysics. The model is validated with laboratory dry-granular dam break experiments. Good agreement is observed between the simulated results and the laboratory data on both the shape evolution and the velocity field. Moreover, the simulation could also provide the shear band distribution which is essential for an understanding of the mechanism in this problem. Almost all parameters involved in the simulation have their physical meaning and could be available from experiment. Some artificial parameters focusing on numerical stability are selected according to previous studies without tuning. This model could serve as a powerful tool for the landslide induced debris flow study.

I. INTRODUCTION

Granular material can behave like a solid, a liquid or a gas during its movement. These different flow regimes can also coexist in a single configuration and occur from state to state transitions [2]. For each individual state, a large number of theoretical and empirical constitutive models have been proposed to describe granular material's mechanical properties. Granular interact mainly by friction in the granular solid state, researchers often adopt elasto-plasticity constitutive relation to describe it. In granular gaseous regime, granular interact mainly by binary collisions, the analogy between agitated grains in gaseous regime and molecules in a gas caused the development of kinetic theories of granular media that provide constitutive equations for rapid and diluted granular flows. For a granular liquid, granular interact with each other through friction as well as collision. The μ (I) rheology was widely adopted in granular liquid regime since Jop et al. [3] as it can describe many granular flow phenomena successfully.

For the landslide induced debris flow problem, engineering practices need information regarding (a) when and where the failure will take place; (b) how many materials will slip, i.e. what the slip surface will look like; and (c) how far the

collapsed soil mass will flow. To answer (a) and (b), numerical models should be able to describe landslide stage when granular in the solid regime where stress distribution and plastic yield are important; While when we deal with the debris flow stage, numerical models should able to simulate the granular in the liquid regime to answer (c). As the solid stage is inseparably connected with the flow stage, a well-developed numerical model should able to describe the motion of granular in the solid-like regime and liquid-like regime at the same time.

Actually, many of previous numerical models, especially those models based on meshfree methods such SPH, have been developed for the first two stages. Some of them, such as our previous model [4] - a three-dimensional extension of the Bui et al.'s work [1], could simulate some characteristics of the fluid-like stage, although not intently. That is because the physical and numerical viscosity in the model could act as a viscous damper when the soil reaches plastic yield criteria. In other words, an elasto-plastic-constant-viscous model is actually build in these previous works, although the viscosity is artificially determined. Considering the fact that the μ (I) rheology is believed to be able to characterize the fluid-like soil such as avalanche or debris flow, this study focus on the set up of an elasto-plastic- μ (I) model with the Drucker-Prager (D-P) yield criterion in the framework of the SPH method.

II. MODEL DESCRIPTION

We extend our earlier work [4] to consider the motion of granular in liquid-like regime. We assume granular flow after plastic yielding could be described with the μ (I) rheology borrowed from dense granular flow theory. Then the 3D D-P elasto-plastic- μ (I) SPH model for simulating granular solid and granular liquid is described as follows.

A. Governing equations

The governing equations of geo-materials consist of mass and momentum conservation

$$\begin{cases} \frac{D\rho}{Dt} = -\rho \frac{\partial v^\alpha}{\partial x^\alpha} \\ \frac{Dv^\alpha}{Dt} = \frac{1}{\rho} \frac{\partial \sigma^{\alpha\beta}}{\partial x^\beta} + f^\alpha \end{cases} \quad (1)$$

where α, β denote the Cartesian components x, y, z with the Einstein convention applied to repeated indices; ρ is soil

density; v is soil velocity; f^α is the component of acceleration caused by external force, which is the gravitational acceleration in this work; σ represents the total stress tensor of soil and its expression can be obtained from the constitutive model.

B. Constitutive model for granular solid regime

In geotechnical mechanics, the total strain rate tensor is defined as

$$\dot{\varepsilon}^{\alpha\beta} = \frac{1}{2} \left(\frac{\partial v^\alpha}{\partial x^\beta} + \frac{\partial v^\beta}{\partial x^\alpha} \right) \quad (2)$$

Moreover, the total strain rate tensor can be decomposed into an elastic and a plastic part

$$\dot{\varepsilon}^{\alpha\beta} = \dot{\varepsilon}_e^{\alpha\beta} + \dot{\varepsilon}_p^{\alpha\beta} \quad (3)$$

The elastic strain rate tensor $\dot{\varepsilon}_e^{\alpha\beta}$ is normally computed by the generalized Hooke's law

$$\dot{\varepsilon}_e^{\alpha\beta} = \frac{\dot{S}^{\alpha\beta}}{2G} + \frac{1-2\nu}{3E} \dot{\sigma}^{\gamma\gamma} \delta^{\alpha\beta} \quad (4)$$

Where $\dot{\sigma}^{\gamma\gamma}$ is the sum of three principal stress rates

$$\dot{\sigma}^{\gamma\gamma} = \dot{\sigma}^{xx} + \dot{\sigma}^{yy} + \dot{\sigma}^{zz} \quad (5)$$

Similarly, $\dot{\varepsilon}^{\alpha\beta}$ is the sum of three principal strain rates

$$\dot{\varepsilon}^{\alpha\beta} = \dot{\varepsilon}^{xx} + \dot{\varepsilon}^{yy} + \dot{\varepsilon}^{zz} \quad (6)$$

By applying the plastic flow rule, the plastic strain rate $\dot{\varepsilon}_p^{\alpha\beta}$ is defined as

$$\dot{\varepsilon}_p^{\alpha\beta} = \dot{\lambda} \frac{\partial g}{\partial \sigma^{\alpha\beta}} \quad (7)$$

The soil hydrostatic pressure P can be obtained directly from the constitutive equation by the standard definition of mean stress

$$P = -\frac{\sigma^{\gamma\gamma}}{3} = -\frac{1}{3}(\sigma^{xx} + \sigma^{yy} + \sigma^{zz}) \quad (8)$$

The Drucker–Prager model with non-associated plastic flow rules is adopted here. The yield condition $f(I_1, J_2)$ and plastic potential function $g(I_1, J_2)$ have the following forms, respectively

$$f(I_1, J_2) = \sqrt{J_2} + \alpha_\phi I_1 - k_c = 0 \quad (9)$$

$$g(I_1, J_2) = \sqrt{J_2} + \alpha_\psi I_1 - \text{constant} \quad (10)$$

where I_1 and J_2 are, respectively, the first and second invariants of the stress tensor; C is an arbitrary constant; α_ϕ and k_c are Drucker–Prager's constants, which are related to the Coulomb's material constants c (cohesion) and ϕ (internal friction); α_ψ has the same expression as α_ϕ and is related to the dilatancy angle ψ of geo-materials:

$$\alpha_\phi = \frac{\tan \phi}{\sqrt{9+12\tan^2 \phi}} \quad k_c = \frac{3c}{\sqrt{9+12\tan^2 \phi}} \quad \alpha_\psi = \frac{\tan \psi}{\sqrt{9+12\tan^2 \psi}} \quad (11)$$

for the 2D plane strain condition. While

$$\alpha_\phi = \frac{2\sin \phi}{\sqrt{3}(3-\sin \phi)} \quad k_c = \frac{6c\cos \phi}{\sqrt{3}(3-\sin \phi)} \quad \alpha_\psi = \frac{2\sin \psi}{\sqrt{3}(3-\sin \psi)} \quad (12)$$

for the 3D condition in which the Drucker–Prager failure surface coincides with the outer cone of the Mohr–Coulomb hexagonal surface, corresponding to triaxial compression.

Comparing with plastic deformation, smaller elastic deformation of volume can be ignored in the present model. The plastic deformation of volume can be represented by the dilatancy angle, ψ . The stress–strain relationship is therefore expressed as

$$\frac{D\sigma_i^{\alpha\beta}}{Dt} = 2G\dot{\varepsilon}_i^{\alpha\beta} + K\varepsilon_i^{\gamma\gamma}\delta_i^{\alpha\beta} - \dot{\lambda}_i \left[3\alpha_\psi K\delta^{\alpha\beta} + \frac{G}{\sqrt{J_2}} s_i^{\alpha\beta} \right] \quad (13)$$

where $\dot{\lambda}_i$ is the rate of change of the plastic multiplier and is determined by the elasto-plastic function, equation (9); $\dot{\varepsilon}_i^{\alpha\beta}$ is the deviatoric shear stress rate tensor; $\dot{\varepsilon}_i^{\alpha\beta}$ is the deviatoric shear strain rate tensor; δ is Kronecker's delta; K and G are, respectively, the elastic bulk modulus and the shear modulus, which are related to the Young's modulus, E , and Poisson ratio, ν , through the following equations

$$K = \frac{E}{3(1-2\nu)} \quad G = \frac{E}{2(1+\nu)} \quad (14)$$

A general technique to treat finite strain problems is to compute a field variable for the next time step by way of its rate of change during the current time step. Considering the effect of rigid body rotation on the current stress rate, the Jaumann rate of Cauchy stress is used here

$$\dot{\sigma}_J^{\alpha\beta} = \dot{\sigma}^{\alpha\beta} - \dot{\omega}^{\alpha\gamma} \cdot \sigma^{\gamma\beta} - \dot{\omega}^{\beta\gamma} \cdot \sigma^{\alpha\gamma} \quad (15)$$

where ‘·’ denotes the derivative with respect to time; subscript J designates the Jaumann rate; and $\dot{\omega}$ is the spin rate tensor

The stress rate tensor in a finite strain framework is converted to

$$\dot{\sigma}^{\alpha\beta} = \dot{\sigma}_J^{\alpha\beta} + \dot{\omega}^{\alpha\gamma} \cdot \sigma^{\gamma\beta} + \dot{\omega}^{\beta\gamma} \cdot \sigma^{\alpha\gamma} \quad (16)$$

The integration of rate equations is dependent on the assumption of infinitesimal strain between two adjacent configurations. This formulation is adopted in the current study and this treatment is acceptable as long as the time increments are small.

Finally, the normal form of the stress–strain relationship for elasto-plastic materials can be expressed as

$$\frac{D\sigma_i^{\alpha\beta}}{Dt} = \sigma_i^{\alpha\gamma} \dot{\omega}^{\beta\gamma} + \sigma_i^{\gamma\beta} \dot{\omega}^{\alpha\gamma} + 2G\dot{\varepsilon}_i^{\alpha\beta} + K\varepsilon_i^{\gamma\gamma}\delta_i^{\alpha\beta} - \dot{\lambda}_i \left[3\alpha_\psi K\delta^{\alpha\beta} + \frac{G}{\sqrt{J_2}} s_i^{\alpha\beta} \right] \quad (17)$$

where the two first terms are the results from the Jaumann stress rate tensor, the third and fourth terms refer to the elastic behaviour, and the last term relates to the plastic deformation.

C. Constitutive model for granular fluid regime

Dense granular flow theories have been developed rapidly in recent years. A phenomenological constitutive law, the so-called $\mu(I)$ constitutive law, that is based on dimensional

analysis have been widely used. $\mu(I)$ constitutive law was proposed by GdR MiDi [5] and Jop et al. [3] propose 3D generalization of $\mu(I)$ constitutive law for granular material. In the $\mu(I)$ constitutive law

$$\sigma_{vi}^{\alpha\beta} = \mu(I)P \frac{\dot{\varepsilon}^{\alpha\beta}}{\|\dot{\varepsilon}^{\alpha\beta}\|} \quad (18)$$

the term $\mu(I)P/\|\dot{\varepsilon}^{\alpha\beta}\|$ can be seen as an effective viscosity of the material depending on shear rate and pressure. The friction coefficient μ was related to inertial number I by

$$\mu(I) = \mu_s + \frac{\mu_2 - \mu_s}{1 + I_0/I} \quad (19)$$

where I_0 is a dimensionless constant, μ_s and μ_2 represent static frictional coefficient and frictional coefficient for extreme high inertial number, respectively.

The inertial number, which is the square root of the Savage number or of the Coulomb number, is defined by

$$I = \frac{\|\dot{\varepsilon}^{\alpha\beta}\|d}{\sqrt{P/\rho_s}} \quad (20)$$

where d denotes grain diameter and ρ_s represents the grain density. The inertial number can be interpreted in terms of the ratio between two time scales: $t_{micro} = d/\sqrt{P/\rho_s}$ which is a microscopic time scale related to the typical time scale of granular rearrangements and $t_{macro} = 1/\|\dot{\varepsilon}^{\alpha\beta}\|$ which is a macroscopic time scale related to the mean shear rate.

III. NUMERICAL IMPLEMENTATION

Our elasto-plastic-viscous implementation with Drucker-Prager yield criterion for solid stage and $\mu(I)$ rheology for fluid stage is developed based on the DualSPHysics [6]. To suppress the tension instability in the calculation, the kernel function proposed by Yang & Liu [7] is used in this study instead of classical kernel functions included in DualSPHysics.

The artificial viscosity term was usually used to stabilize the SPH numerical system in the past. But the artificial viscosity term would cause too much energy dissipation if used with a value that is too large, or lead to numerical instability if too small. This problem exist no more in this study as the artificial viscosity term is replaced by $\mu(I)$ viscosity which was proven to be more realistic. Numerical instability is not observed in this study although a simple treatment is necessary as the viscosity become infinity when the strain rate goes to zero.

The Verlet scheme is adopted in the proposed model to discretise equations. Time-step control is dependent on the Courant–Friedrichs–Lowy (CFL) condition, the forcing terms and the viscous diffusion term. A variable time step is calculated according to Monaghan & Kos [8] here. Automatic time-step adjustment technique is also developed to reduce the occurrence of overestimation of stress when the stress status approaches the plastic yield stage [4].

IV. MODEL VALIDATION

A. Granular column collapse

The granular column collapse is a classical problem to investigate different regimes of granular flows and transition between them. It contains granular solid regime and granular liquid regime at the same time. So it is an appropriate problem to examine our numerical model. The granular column collapse experiment is carried out in transparent glass box which has a length of 1m, a height of 0.3m and a width of 0.05m. The initial granular pile is formed behind a glass plate in the right part of the box as shown in Fig. 1. The granular pile has dimensions (L, H, W) , where L is the length of the pile, H is the depth, W is the width. We keep the W unchanged and vary the L, H in experiments. When the experiment begins, the glass plate is removed away suddenly from the granular pile, and the granular pile begins to collapse. The time for the glass plate to leave t_l is short compared to the time for granular column collapse t_c ($t_l/t_c \approx 1/20$), so we ignore the glass plate in numerical simulation. A high speed camera is used to record the whole process with a speed of 8000 frames per second. The experiment was repeated for three times to exam the experimental repeatability.

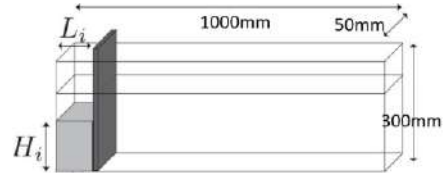


Figure 1. Experimental configuration

The granular media we used is quartz sand. The diameter d of the granular media ranged from 20 mesh to 40 mesh. The Young's module E and Poisson's ratio ν of the quartz sand is 77.8GPa and 0.17, respectively, and its friction angle ϕ is about 36°. The granular density ρ_s is 2200 kg/m³ and volume fraction ϕ is kept about 0.57 in all experiments. It has been proven (Fei et al. [9]) that the boundary effect of a channel can be ignored if $d/W < 1/20$ where d is the mean particle diameter. In our experiments, $d/W \approx 1/20$ which enabled the lateral walls effect to be safely ignored. A mount of 5% dyed quartz sand was added in each experiment to implement the Digital Image Correlation (DIC) technique. The Ncorr Software [10] was used to get the velocity profiles.

B. Numerical results

The collapse is a quasi-2D process, thus simulation is carried out in two-dimensional space. The original spacing between material points is 0.0005 m. Very large c and φ are used in the simulation to reach the initial steady state first, then the strength is suddenly reduced to the actual value, the granular column begin to collapse. We set dilatancy angle ψ to be 0° although the volume change might be up close to 10% in wide steep channel [12]. And rheological parameters are chosen to be identical with those usually used in past research $I_0 = 0.279$, $\mu_2 - \mu_s = 0.24$ (Jop et al. [3], Largé et al. [11], Martin et al. [12]).

The experimental and numerical results are compared in Fig. 2, from which we can see the numerical results match well with experimental data on both the shape evolution and the velocity field. Moreover, the simulation could also provide the shear band distribution which is essential for understanding of the mechanism in this problem (shown in Fig. 3). However, it could be found that the front of final deposit in numerical modeling is a slightly behind that in experiment as shown in Fig. 4. This might be due to there is very thin layer of granular in the front, the continuum assumption is not applicable there.

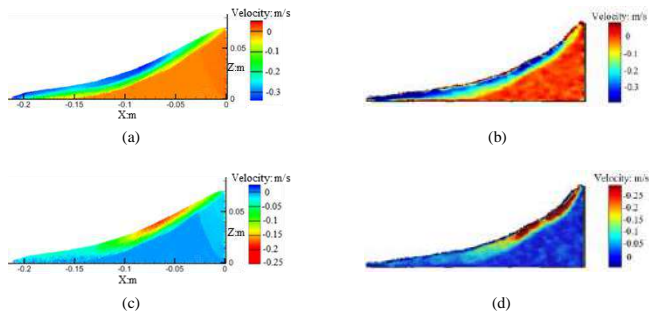


Figure 2. Comparison of velocity of experimental and numerical results at $t=0.3s$. (a) and (c) show velocity of X direction and Z direction in experiment. (b) and (d) show velocity of X direction and Z direction in numerical modeling.

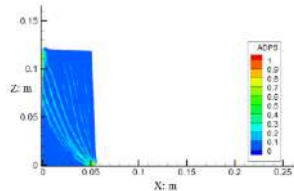


Figure 3. The accumulated plastic strain(ADPS) in the initial stage.

The granular column collapse can be divided into three stages. In the first stage, the collapse process is controlled by the free-fall behavior of the column, the top left part of the column is mainly in vertical motion. In the second stage of collapse, the granular in the front is dominated by lateral motion. Behind the front, those granular close to free surface flow along the slope. In the last phase of granular column's motion, the lateral motion almost cease, there only remain a thin layer of granular avalanche across the free surface to stabilize the steep part of the pile. The free surface of final deposition can be depicted by two straight line as shown in Fig. 4.

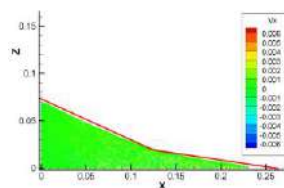


Figure 4. Comparison of final deposit of experimental and numerical results. The red straight line represent shape of final deposit in experiment.

V. CONCLUSIVE REMARKS

We have developed an elasto-plastic- $\mu(I)$ SPH model for landslide induced debris flow problem. The model is able to describe the motion of granular in solid-like regime and liquid-like regime at the same time. The model is validated using a set of granular column collapse experiments. Good agreement on both shape and the velocity field in the collapse process is observed. Almost all parameters involved in the simulation have their physical meaning and could be available from experiment. This model could serve as a powerful tool for the landslide induced debris flow study.

ACKNOWLEDGEMENT

This work was financially supported by the National Natural Science Foundation of China (No. 11672310, No. 11432015) and the National Basic Research Program of China (No. 2014 CB04680202).

REFERENCES

- [1] Bui, H. H., Fukagawa, R., Sako, K. & Ohno, S. (2008). Lagrangian meshfree particles method (SPH) for large deformation and failure flows of geomaterial using elastic–plastic soil constitutive model. *Int. J. Numer. Anal. Meth. Geomech.* 32: 1537–1570. doi:10.1002/nag.688
- [2] Andreotti B, Forterre Y, Pouliquen O. (2013). Granular Media Between Fluid and Solid. Cambridge University Press.
- [3] Jop, P., Forterre, Y. and Pouliquen, O. (2006). A constitutive law for dense granular flows. *Nature*. 441: 727–730.
- [4] An, Y., Wu, Q., Shi, C. Q. & Liu, Q. Q. (2016). Three-dimensional smoothed-particle hydrodynamics simulation of deformation characteristics in slope failure. *Géotechnique*. 66, 8: 670–680.
- [5] GdR MiDi. (2004). On dense granular flows. *Eur. Phys. J. E*. 14: 341–365.
- [6] Crespo A.J.C., Domínguez J.M., Rogers B.D., Gómez-Gesteira M., Longshaw S., Canelas R., Vacondio R., Barreiro A., García-Feal O. (2015). DualSPHysics: open-source parallel CFD solver on Smoothed Particle Hydrodynamics (SPH). *Computer Physics Communications*, 187: 204–216.
- [7] Yang, X. F. & Liu, M. B. (2012). Improvement on stress instability in smoothed particle hydrodynamics. *Acta Physica Sinica*. 61, No. 22: 224701 (in Chinese).
- [8] Monaghan, J. J. & Kos, A. (1999). Solitary waves on a Cretan beach. *J. Waterway, Port, Coastal Ocean Engng.* 125, 3: 145–154.
- [9] Fei, M. L., Sun, Q. C., Xu, X. R., Jin, F. & Zhou, G. D. (2016). Simulations of multi-states properties of granular materials based on non-linear granular elasticity and the MiDi rheological relation. *Powder Technol.* 301: 1092–1102.
- [10] Blaber J., Adair B., Antoniou A., (2015). Ncorr: open-source 2D digital image correlation Matlab software. *Experimental Mechanics*. 55, 6: 1105–1122
- [11] Largé P Y., Staron L., Popinet S. (2011). The granular column collapse as a continuum: validity of a two-dimensional Navier–Stokes model with a $\mu(I)$ -rheology. *J. Fluid Mech.* 686: 378–408.
- [12] Martin N., Ionescu I R., Mangeney A., Bouchut F. & Farin M. (2017). Continuum viscoplastic simulation of a granular column collapse on large slopes: $\mu(I)$ rheology and lateral wall effects. *Phys. Fluids*. 29: 013301.

Overview of SPH-ALE applications for hydraulic turbines in ANDRITZ Hydro

M. Rentschler, J.C. Marongiu, M. Neuhauser, E. Parkinson

R&D Department, ANDRITZ Hydro
Vevey, Switzerland

martin.rentschler@andrirtz.com

Abstract— Over the past 13 years, ANDRITZ Hydro has developed an in-house tool based on the SPH-ALE method for applications in flow simulations in hydraulic turbines. The initial motivation is related to the challenging simulation of free surface flows in Pelton turbines, where highly dynamic water jets interact with rotating buckets, creating thin water jets traveling inside the housing and possibly causing disturbances on the runner. The present paper proposes an overview of industrial applications allowed by the developed tool, including design evaluation of Pelton runners and casings, transient operation of Pelton units and free surface flows in hydraulic structures.

I. INTRODUCTION

The Pelton turbine is a hydraulic impulse machine that is best adapted for high head (from 200 to around 2000 meters) and low discharge installations (up to 50 m³/s). The largest units worldwide of BIEUDRON in Switzerland can deliver up to 420MW each, thanks to a water head of more than 1800 meters. The main components of a Pelton turbine are the distributor, the injectors (up to 6), the runner and the housing (Figure 1). While the flow is confined in the distributor and injectors, a free jet of water exits from the injectors' nozzles and a free surface flow develops in the rotating runner and the housing. The runner is composed of buckets whose design is of primary importance for the proper conversion of kinetic energy of water jets into mechanical energy of the turbine shaft. However each component influences the overall performance of the machine. Consequently each component is analysed with numerical simulation.

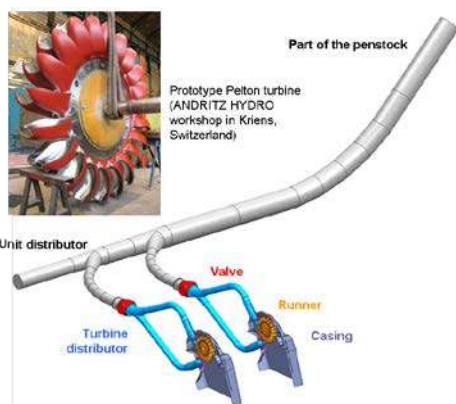


Figure 1 Exemplary layout of 2 units of 2-jet horizontal Pelton turbines.

Components of a Pelton turbine involving an internal flow can be simulated with state of the art mesh-based solvers, giving a good prediction of their behaviour ([1], [2]). These numerical approaches can also represent the free surface boundary condition, either implicitly through a two-phase model treating the free surface as an interface between phases ([3], [4]), or explicitly through single phase models as for example when using deformable meshes ([5], [6]). It is technically feasible to simulate free surface flows inside a Pelton turbine with classical mesh-based CFD tools. However a proper tracking of the water inside the housing is very demanding, as mesh-based techniques naturally diffuse the free surface. Moreover, the meshing of a Pelton casing requires time and expertise, while mesh quality can strongly influence the numerical flow. These intrinsic characteristics push classical CFD tools to the limit of their cost-effectiveness.

The SPH approach presents intrinsically attractive features for the proper handling of free surface flows in Pelton turbines. Its complete mesh-free numerical stencil offers great flexibility and robustness for highly distorted media. The ability of solving free surface flows with calculation points only in the liquid phase can trigger great computational costs savings when the liquid occupies only a small volume in the simulation domain. For these reasons, ANDRITZ Hydro has been developing along the last 13 years an in-house simulation tool based on the SPH-ALE numerical method. The main features of this method will be recalled in Section 2. The tool is nowadays embedded in the design and verification processes of Pelton turbine components. Section 3 will present some applications illustrating the usage of the mesh-less approach for hydraulic turbines.

II. SPH-ALE METHOD

A. Arbitrary Lagrange-Euler description

In the classical SPH approach, calculation points (in the following called particles) are displaced by following exactly the flow trajectory, making SPH a purely Lagrangian method. Adopting an Arbitrary Lagrange-Euler description, a separate transport velocity noted v_0 is introduced and governs the displacement of particles. It offers an additional flexibility, as it is then possible to set up

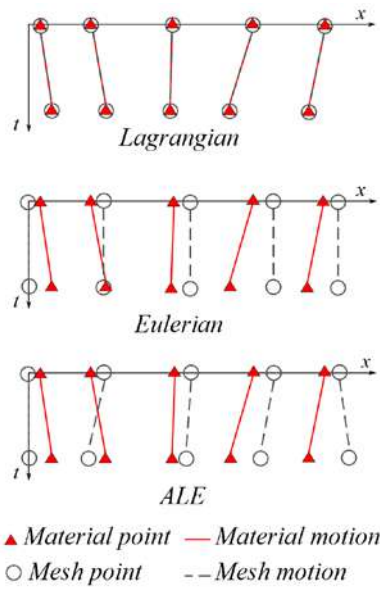


Figure 2. Different particle motions (adapted from [7])

specific particle motions depending on the application. In particular, $\mathbf{v}_0 = \mathbf{0}$ defines an Eulerian description where particles are steady and $\mathbf{v}_0 = \mathbf{v}$ (the flow velocity) defines a Lagrangian description. Other choices are possible (see Figure 2). The counterpart of this modified and arbitrary transport velocity is the necessary explicit management of convective fluxes in the conservation equations, as they are no longer included in the (Lagrangian) displacement of particles. In order to keep the treatment of free surface boundary conditions as simple as it can be in the classical SPH method, particles located at and near the free surface are displaced with a Lagrangian motion.

B. System of discrete equations

The SPH-ALE (Smoothed Particle Hydrodynamics – Arbitrary Lagrange-Euler) method was originally introduced by Vila ([8]) as a variant of the weakly compressible SPH approach. It introduces the above presented transport velocity \mathbf{v}_0 and an explicit computation of convective fluxes, leading to the following system of discrete equations to be solved for a particle of interest indexed by subscript i :

$$\frac{d}{dt}(\mathbf{x}_i) = \mathbf{v}_0(\mathbf{x}_i, t) \quad (1)$$

$$\frac{d}{dt}(\omega_i) = \omega_i \sum_{j \in D_i} \omega_j (\mathbf{v}_0(\mathbf{x}_j, t) - \mathbf{v}_0(\mathbf{x}_i, t)) \nabla_i W_{ij} \quad (2)$$

$$\frac{d}{dt}(\omega_i \rho_i) + \omega_i \sum_{j \in D_i} \omega_j 2\rho_{ij}^E (\mathbf{v}_{ij}^E - \mathbf{v}_0(\mathbf{x}_{ij}, t)) \cdot \nabla_i W_{ij} = 0 \quad (3)$$

$$\frac{d}{dt}(\omega_i \rho_i \mathbf{v}_i) + \omega_i \sum_{j \in D_i} \omega_j [\rho_{ij}^E \mathbf{v}_{ij}^E \otimes (\mathbf{v}_{ij}^E - \mathbf{v}_0(\mathbf{x}_{ij}, t)) + p_{ij}^E I] \cdot \nabla_i W_{ij} = \omega_i \rho_i \mathbf{g} \quad (4)$$

In these equations, subscript j refers to a particle included in the neighbourhood D_i of particle i , \mathbf{x} is the position, \mathbf{v} is the fluid velocity, ρ and p stand for fluid density and pressure, respectively. ω is the particle weight (or volume). W and ∇W are the kernel function and

gradient. Superscript E denotes interaction values in-between a pair of neighbouring particles as described in following Section C. Finally the term $\mathbf{v}_0(\mathbf{x}_{ij}, t)$ represents the velocity of the fictitious interface between particles i and j .

Equations (3) and (4) translate the mass and momentum conservation, respectively. It should be noted that these two equations involve convective mass and momentum flux terms which do not necessarily vanish even when adopting a Lagrangian transport velocity. As a consequence the SPH-ALE method allows variations of particles' mass, contrarily to the classical SPH approach where particles have a constant mass. Nevertheless both approaches conserve mass globally.

Equation (1) simply reflects the motion of particles with the arbitrary transport field \mathbf{v}_0 . Finally (2) is an additional equation that computes variations of the particles' volume because of the relative displacement of particles.

The system requires an equation of state to relate pressure and density, the popular so-called Tait equation is used:

$$p = \frac{\rho_0 c_0^2}{\gamma} \left[\left(\frac{\rho}{\rho_0} \right)^\gamma - 1 \right], \gamma = 7 \quad (5)$$

where $\rho_0 = 1000 \text{ kg/m}^3$ is the reference density for water and c_0 is the reference speed of sound. In order to maintain weakly compressible assumptions valid while keeping the computational cost as low as possible, the physical speed of sound is replaced by a numerical value amounting to ten times the maximum flow velocity expected in the simulation domain.

C. Computing particle interactions

One important peculiarity of SPH-ALE is that the interaction terms, denoted with the superscript E , are obtained by solving local moving Riemann problems at the interface between two interacting particles. The benefit of introducing Riemann solvers resides in their stabilization effect without introducing any additional and artificial viscosity.

There are numerous Riemann solvers that can be used efficiently and equivalently. Experience has shown that for weakly compressible cases, the exact solver is not necessary and linearized solvers are sufficient. Pre-conditioning techniques can be introduced to improve the quality of results in regions with very low dynamics ([9]).

A simple linear Riemann solver can be written as:

$$\begin{cases} v_{ij}^E = (v_i + v_j)/2 + (p_j - p_i)/2\bar{\rho}_{ij}\bar{c}_{ij} \\ p_{ij}^E = (p_i + p_j)/2 + \bar{\rho}_{ij}\bar{c}_{ij}(v_j - v_i)/2 \end{cases} \quad (6)$$

where $\bar{\rho}_{ij}$ and \bar{c}_{ij} are some averaged density and speed of sound for the pair of particles i and j .

D. Time integration

The system of equations (1) to (4) is updated with an explicit time integration scheme. For stability and accuracy reasons, 3rd and 4th order Runge-Kutta schemes are favoured.

E. High order schemes

a) High order numerical fluxes

The Riemann solver presented in (6) is a 1st order scheme that generates an important numerical viscosity. Following well established approaches from the Finite Volumes method, a classical remedy is to use the MUSCL scheme ([10]), in which piecewise constant field values inside each particle are replaced by piecewise linear functions. In the mesh-less frame of SPH-ALE, a first approach is to base the linear estimates on the gradient of field variables computed at the centre of particles with the standard SPH approximation for gradients ([9]). The Riemann solver in (6) is accordingly modified by replacing \mathbf{v}_i and \mathbf{v}_j with extrapolated values $\tilde{\mathbf{v}}_i$ and $\tilde{\mathbf{v}}_j$, and p_i and p_j with \tilde{p}_i and \tilde{p}_j which are obtained following:

$$\tilde{f}_i = f_i + \nabla f_i \cdot (\mathbf{x}_{ij} - \mathbf{x}_i) \quad (7)$$

$$\nabla f_i = \sum_{j \in D_i} \omega_j (f_j - f_i) \nabla W_{ij} \quad (8)$$

However this approach suffers the limited accuracy of the SPH approximation of field gradients (8) and further improvements to the solution can be obtained by replacing SPH with Moving Least Squares (MLS) approximates for the field gradient. Indeed MLS not only enforce accurate computation of the gradient of a function (Figure 3) but also allows higher order (polynomial) representation of functions. Difficulties arise from the possibly disordered or truncated set of particles over which the MLS methodology is applied. In the frame of SPH-ALE it is necessary to implement order and space adaptation procedures so that stability and robustness are enforced (the detailed development and validation of these procedures can be found in [13]).

2) High order flux summation

Limitations highlighted above about the low accuracy of the SPH approximation of gradients (8) are valid also for the SPH divergence operators appearing in equations (2)-(4) and which are key ingredients for the summation of numerical fluxes. In particular, and despite the use of high order numerical fluxes, the overall convergence order of the method is not enforced ([13]). It is possible to derive divergence operators from the MLS methodology fulfilling completeness requirements and restoring the global convergence order of the complete method.

Numerical experiments have demonstrated the capability of the high order approach to improve the quality of results. In particular it was observed a reduction in both the numerical viscosity and the noise of the pressure field (Figure 3).

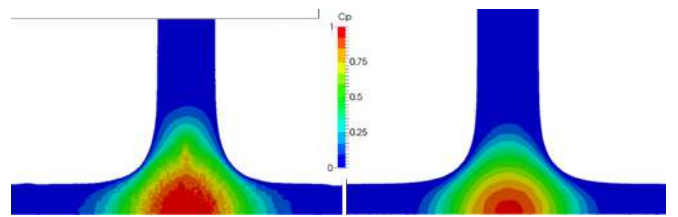


Figure 3 Simulation of a water jet impacting a flat plate in 2D. Left: standard scheme with SPH divergence. Right: high-order scheme with MLS divergence.

F. Boundary conditions

The general approach of boundary conditions in SPH-ALE is to account for their contribution in the flux summation through a surface integral term. This is rooted in the derivation of gradient and divergence operators with SPH:

$$\langle \nabla f(x) \rangle = \int_{\partial D_x} f(\mathbf{x}') W(\mathbf{x} - \mathbf{x}') \mathbf{n} dS - \int_{D_x} f(\mathbf{x}') \nabla_{\mathbf{x}'} W(\mathbf{x} - \mathbf{x}') dV \quad (9)$$

where ∂D_x stands for the intersection of the kernel support with the boundary and \mathbf{n} is the unit vector orthogonal to the boundary. The surface integral term is usually neglected as for particles located far from any boundary, it vanishes because of the compact support of the kernel function. However for particles close enough from a boundary, this term can be computed explicitly by using a discretization of the boundary surface and a quadrature formula (see for example [9], [14]).

Boundary fluxes are computed with partial Riemann solvers in the case of wall boundary conditions ([9]). Open boundaries (inlet and outlet) are managed according a Non Reflecting Characteristic Boundary Condition derived from [15].

III. FREE SURFACE APPLICATIONS FOR HYDRAULIC TURBINES

The here presented applications are obtained with SPH-ALE particles moved in a Lagrangian manner because of the presence of a free surface.

A. Hydraulic and mechanical assessment of Pelton runners

A proper design procedure of a Pelton runner aims at maximizing the hydraulic efficiency while ensuring safety and reliability of operation. On the one side thinner buckets are known to deliver a higher efficiency but on the other side thinner structures are submitted to higher stresses. Therefore the hydraulic engineer needs to make a trade-off between the optimal hydraulic design and the fatigue that limits the lifetime of a runner.

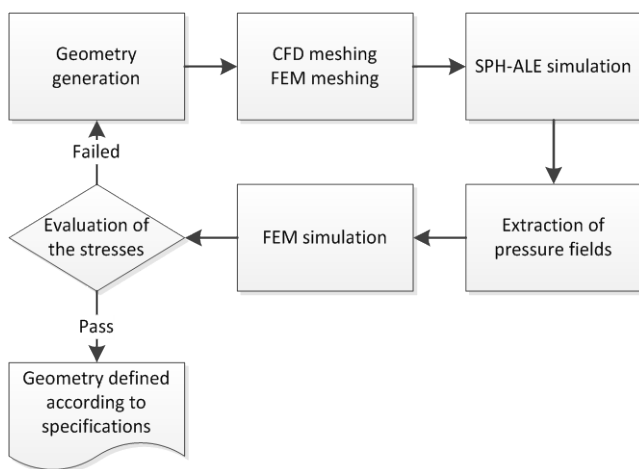


Figure 4: Design loop based on CFD.FEM evaluation

A complete numerical evaluation has been developed that combines the prediction of hydraulic performance with SPH-ALE and the prediction of mechanical stresses in the bucket with Finite Element Analysis. This evaluation is fully automatic including meshing and post-processing. At the end of the process an internal report is generated to document the result. (see Figure 4)

The typical configuration is composed of a runner sector (four to six buckets) fed with one water jet (Figure 5). A symmetry condition is imposed at the mid-plane of the runner. Only possibly wetted surfaces are included in the simulation. The simulation is done in pure Lagrangian mode and only the liquid phase is discretized.

To predict the stresses in the runner, it is necessary to sufficiently resolve the flow to predict local pressures. This pressure distribution is then used as a boundary condition for a structural calculation to predict the stresses in the runner.

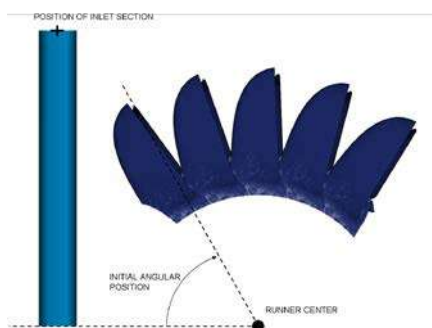


Figure 5 Initial configuration of the jet and buckets

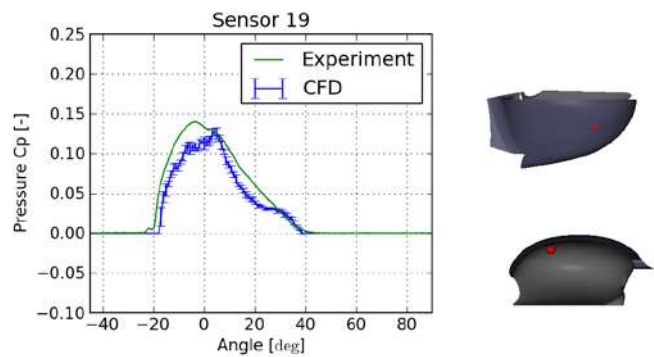


Figure 6: Validation of the pressure signal from CFD compared to model measurements.

The pressure maps as an outcome of the SPH-ALE simulation were validated against measurements. For those measurements a model scale runner was instrumented with pressure sensors.

Figure 6 shows the comparison of the experiment signal and the SPH-ALE result. The red dot is the position of the pressure sensor on the internal face of the bucket.

The pressure map is then used as a boundary condition for a FEM simulation that calculates the stresses for several positions of the runner/jet in a quasi-static approach. A safety factor is added to account for inertial effects due to the cyclic loading of the buckets.

The use of the SPH-ALE method reduces the calculation time from several days, with standard finite volumes methods to several hours using the SPH-ALE method. Due to the Lagrangian description no rotor-stator interface is necessary. A rotor-stator interface may be unstable for two-phase simulations. Robustness of the simulation process is essential for its usability in an industrial environment. Hydraulic designers require reliable and efficient tools delivering hydraulic and mechanical assessment results. Such a required robustness to simulate the flow in a Pelton bucket is difficult to achieve by a finite volume code.

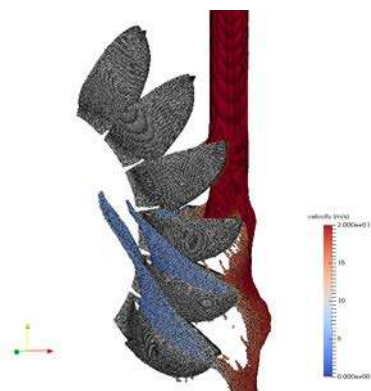


Figure 7: Detailed flow in a Pelton runner as used in the design process

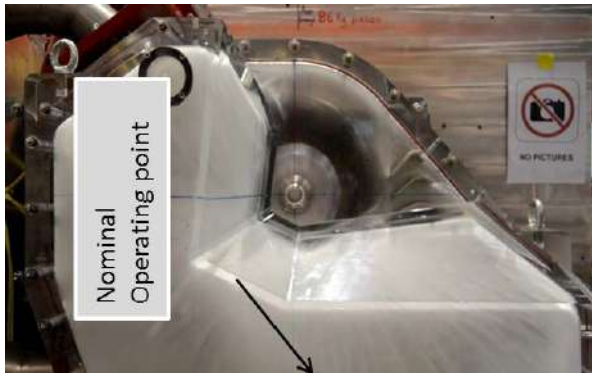


Figure 8: Observing casing flow in a model test

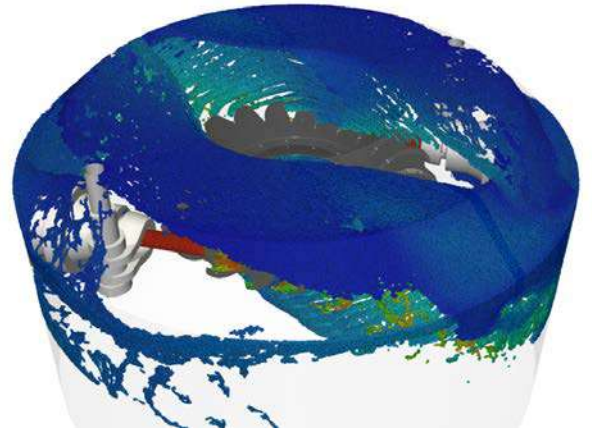


Figure 10: SPH-ALE simulation of a casing flows in a vertical 2-jets Pelton unit

B. Hydraulic assessment of Pelton casings

The flow in the casing of a Pelton turbine is an essential element in the overall efficiency of the turbine. The visualization of the flow in the laboratory is a challenge due to the presence of bubbles in the water that makes the water opaque. Figure 8 illustrates the possible observations of a model test in the ANDRITZ Pelton laboratory. The impact zone of the water is indicated by the arrow.

Simulating the casing flow using finite volume methods is computationally very expensive as the free surface needs to be captured explicitly. A fine mesh is required to represent the details of free surface using finite volume methods. The computational effort to capture major features of the casing flow is in the order of magnitude of 105 cpu h. This makes it impossible to be used in a project time frame.

The use of SPH-ALE decreases the simulation time to several days of simulation, which is affordable in the time-scale of a project. As a result the flow in the casing can be easily analysed in three dimensions (Figure 9 and Figure 10) and the casing can be adapted and optimized by inserting steel plates that guides the water out of the casing.

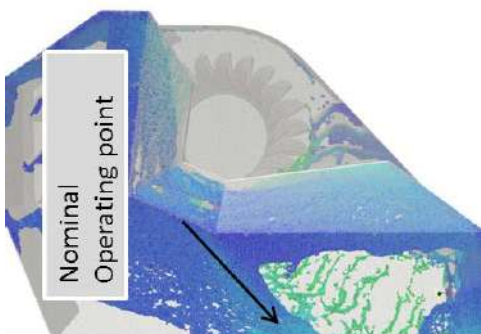


Figure 9: SPH-ALE simulation of casing flows in a horizontal 2-jets Pelton unit

In addition pressure fields are obtained to estimate stresses in all components of the runner and casing that are used for stress assessment in those inserts.

The velocity range for those simulations span two orders of magnitude, from above 100 m/s in the jets to below 1 m/s on the casing walls. For the low Mach numbers, numerical dissipation easily dominates the flow and imposes the use of higher order schemes to prevent numerical artefacts [11].

For Pelton turbines with vertical rotation axis, inserts play a minor role due to axial or cyclic symmetry of the casing. The overall flow can however create water flowing back on the runner, which reduces the hydraulic efficiency of the machine. Detailed simulations are necessary to verify that the flow in the casing will not impact in a negative way the efficiency of the machine (see Figure 10). Especially for rehabilitation projects, the prediction of the casing flow is of value, as often no experience is available with some types of vertical Pelton machine casings.

C. Deflector simulation

In case of an emergency a deflector deviates the jet away from the Pelton runner in order to prevent further acceleration of the runner. Although this device is very simple and does not require a complex hydraulic engineering in itself, it creates a high energy flow in the casing which might create leakage or damages on the installation.

Especially when effects far from the deflector are of interest, then the Lagrangian character of the SPH-ALE method permits to simulate those flows at reasonable costs. This leads to some standard checks during design phase of the Pelton turbine, to prevent issues during commissioning.

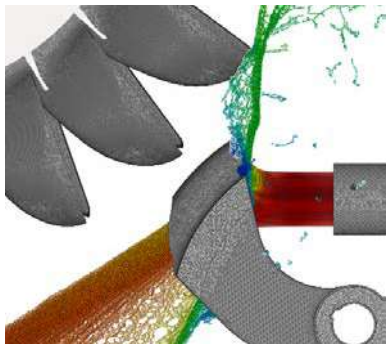


Figure 11: Flow analysis of a deflecting security device and its interaction with a Pelton runner.

One example for such a standard check is the simulation of the deflected water jet hitting the following deflector. During the commissioning of a refurbished installation, strong vibrations were observed. To understand the phenomena, SPH-ALE simulation was used to simulate a system of deflectors (see Figure 11 for a close-up view of the deflected jet and Figure 12 for the complete view of the six deflected jets and interactions with following injector).

It could be observed that the deflected water sheet from one deflector interacted slightly with the runner before hitting the next deflector. The impact of the water sheet slightly moved the next water sheet which then hit a third deflector and so on. The conclusion was to modify the roof of the injector in order to protect the deflectors from direct impacts from the previous deflector.

D. Brake jet

To slow down the Pelton units quickly, they may be equipped with so-called braking jets that impact the runner in the opposite direction of the runner rotation. This normally is only meant to be a security device which should only be used in case of emergency.

However this configuration may endanger the structural integrity because the relative velocity of the buckets and the braking jet is three times higher than the normal “driving” jet, and buckets are not designed to sustain loading on their rear side. In general the setup of the simulation is identical to what is presented in section III.A. The only difference is that the direction of the jet is inverted.

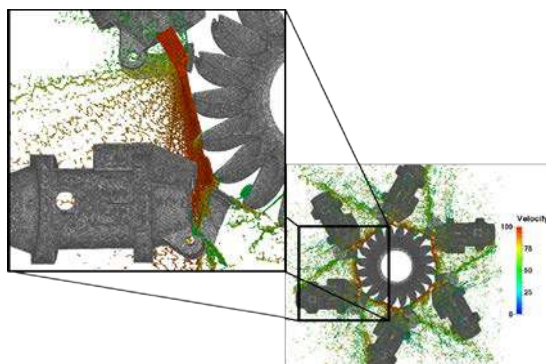


Figure 12: SPH-ALE simulation of runner and a system of deflectors for root cause analysis



Figure 13 SPH-ALE simulation of a braking jet impacting a rotating Pelton runner.

The high velocity impact and high frequency pressure variations make it difficult to setup such a simulation with a commercial finite volume code. Very small time steps would be required to simulate this configuration, and consequently the corresponding computational load with finite volumes methods would be much higher than with SPH-ALE.

Also for that application the pressure fields obtained from the SPH-ALE simulation are transferred as boundary conditions to the FE solver to calculate the stresses in the runner, even if this application is on the limit of the applicability of the quasi static FEM approach.

E. Start-up of a Pelton unit

Since the implementation of SPH-ALE on GPU the start-up of a Pelton machine including the casing can be simulated. At low rotational speed, the water leaving the runner has a high velocity and a direction which is not the one obtained at nominal speed; and therefore creates high stresses in parts of the machine. At higher runner speed, the stresses due to water impacts on static components reduce, but the periodicity of the flow increase at the frequency of the “bucket passage frequency”, which creates a high number of cycles. For the structural integrity it is therefore not always evident which runner rotational speed generates the most critical solicitations. The simulation of the full start up sequence of the machine allows the quantitative structural analysis and allows the optimisation of the sequence to guarantee a given lifetime of the machine.

To obtain a fast acceleration of the runner it is of value to increase the power on the runner as fast as possible. The simulation (Figure 14) of the start-up and the stresses in the runner are helpful to define a start-up scenario to accelerate the runner as fast as possible while keeping the stresses in an acceptable range.

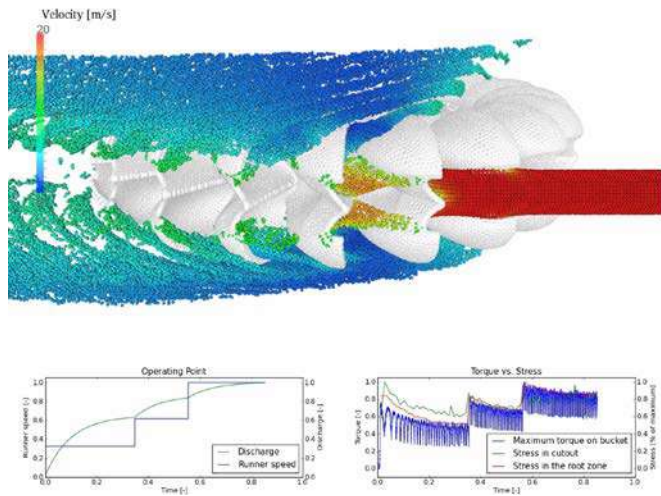


Figure 14: Start-up of a Pelton machine.

F. Free surface applications for hydraulic structures

SPH-ALE can also be used to study water intakes and other hydraulic structures of hydropower plants. Secondary flow structures like recirculation or vortices that may be present at the inlet of the penstock are carried down to the turbine units and may influence dramatically the overall performance and behaviour of the installation. For low head machines the flow in the intake directly impacts the efficiency of the turbine.

The setup of the simulation of an intake of a Hydro power plant includes a detailed bathymetry of the river bed and a detailed CAE model of the installation. The discharge is imposed at the inlet and various outlet conditions may be imposed depending on the cases, including an artificial weir which may be used downstream to control the water height close to the outlet.

As the domain occupied by the volume of liquid is compact and the free surface is almost static in normal flow

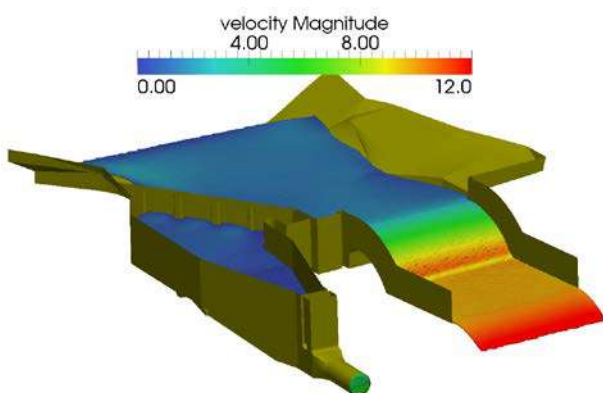


Figure 15: SPH simulation of an intake to a hydro power plant

conditions, such a flow simulation could efficiently be done using a finite volume code. However in that case the mesh generation process might be a time consuming interactive work for a calculation engineer. SPH-ALE can propose an alternative approach requiring less involvement from simulation engineers.

IV. CONCLUSION

The development of the SPH-ALE over the last 13 years has been presented with an emphasis on its applications to hydraulic machinery and especially for Pelton turbines. For the Pelton turbines this new method has become an integral part of the design process. The method has proven its accuracy and robustness during the last years by being applied to numerous projects in this industrial environment. Especially the interaction of this tool with structural analysis has shown its benefit for the projects. The implementation of the method on GPU accelerated the overall execution time and helped to further extend the field of applications and the usability in industrial projects.

REFERENCES

- [1] E. Parkinson, C. Bissel, E. Popescu and C. Tirsi, "Upgrading Pelton turbines of LOTRU-CIUNGET HPP, Romania", HYDRO Conference, Prague, Czech Republic, 2011.
- [2] E. Parkinson, M. Rentschler, S. Lais, A. Karakolcu and Th. Weiss, "Life cycle of a Pelton runner", HYDRO ASIA Conference, Colombo, Sri Lanka, 2014.
- [3] M. Sussman, P. Smereka, S. Osher, "A Level Set Approach for Computing Solutions to Incompressible Two-Phase Flow", J. Comp. Phys., 114 (1994), 146-159.
- [4] C.W. Hirt, B.D. Nichols, "Volume Of Fluid (VOF) method for the dynamics of free boundaries", J. Comp. Phys., 39 (1981), 201-225.
- [5] C.W. Hirt, A. Amsden, J.L. Cook, "An Arbitrary Lagrangian-Eulerian computing method for all flow speeds", J. Comp. Phys., 14 (1974), 227-253.
- [6] C. Münch, P. Ausoni, O. Braun, M. Farhat, F. Avellan, "Fluid-Structure coupling for an oscillating hydrofoil", Journal of Fluid and Structures, 26 (2010), 1018-1033.
- [7] J. Donea, A. Huerta, J.Ph. Ponthot and A. Rodriguez-Ferra, "Arbitrary Lagrangian-Eulerian methods", In E. Stein, R. deBorst and T. Hughes, editors, Encyclopedia of Computational Mechanics, John Wiley, 2004.
- [8] J.P. Vila, "On particle weighted methods and Smoothed Particle Hydrodynamics", Mathematical Models and Methods in Applied Sciences, 9 (1999), 161:209.
- [9] J.C. Marongiu, F. Leboeuf, J. Caro, E. Parkinson, "Free surface flows simulations in Pelton turbines using an hybrid SPH-ALE method", J. Hydr. Research, 48 (2009).
- [10] B. Van Leer, "Towards the ultimate conservative difference scheme V: a second-order sequel to Godunov's method", J. Comp. Phys., 32(1979), 101-136.
- [11] M. Rentschler, M. Neuhauser, J.C. Marongiu, E. Parkinson, "Understanding casing flow in Pelton turbines by numerical simulation", IOP Conf. Series: Earth and Environmental Science, 49 (2016)
- [12] T. Belytschko, Y. Krongauz, J. Dolbow and C. Gerlach, "On the completeness of meshfree particle methods", Int. J. Numer. Mech. Engng., 43(1998), 785-819.
- [13] G.A. Renaut, J.C. Marongiu, S. Aubert, "High-order and adaptive procedures for SPH-ALE simulations based on Moving Least Squares method", Proceedings of the 10th Int. SPHERIC workshop, Parma, Italy, 2015.

- [14] M. Ferrand, D. Laurence, B.D. Rogers, D. Violeau and C. Kassiotis, "Unified semi-analytical wall boundary conditions for inviscid, laminar or turbulent flows in the meshless SPH method", Int. J. for Num. Meth. In Fluids, 71(2013), 446-472.
- [15] L. Selle, F. Nicoud, T. Poinsot, "Actual Impedance of Nonreflecting Boundary Conditions: Implications for Computation of Resonators", AIAA Journal, 42(2004)

AUTHOR INDEX

A		J	
Altomare, C.	228	Jin, A. F.	50, 86
An, Y.	281	Jones, B.	169
Antuono, M.	15		
C		K	
Cai, W. H.	92, 224	Khayyer, A.	23
Cai, Z. W.			
Cao, R. G.	247	L	
Chen, F. Z.	242, 251	Le Touze, D.	1
Chen, J. Q.	121	Leng, D. X.	247
Chen, X.	149	Li, J. J.	217
Chen, Z.	92	Li, N.	157
Cheng, H.	78	Lind, S.	142
Cheng, X.	163	Liu, M. B.	206, 257
Chiron, L.	1	Liu, Q. Q.	281
Colagrossi, A.	1, 15, 100	Liu, W. Y.	157
Crespo, A. J. C.	199, 228	Liu, Y.	100
D		Liu, Z. Y.	274
De Leffe, M.	1	Lu, W. H.	108, 163
De Padova, D.	9	Lv, J.	247
Deng, J.	136	M	
Ding, W.	247	Ma, J. C.	184
Domínguez, J. M.	199, 228	Ma, Q. L.	274
Douillet-Grellier, T.	169	Ma, X. J.	50, 86
Dupuy, L. X.	267	Ma, Z. B.	192
F		Maimtimin, G.	50, 86
Fair, R.	142	Marongiu, J. C.	285
Falahaty, H.	23	Marrone, S.	1, 15
Fan, Q.	224	Marzeddu, A.	228
Fang, H. S.	274	Meringolo, D. D.	100
Feng, Q. D.	236	Mimault, M.	267
G		Ming, F. R.	78
Gao, X. Y.	142, 247	Moghimi, M. H.	177
García-Feal, O.	199	Mossa, M.	9
Gómez-Gesteira, M.	199, 228	N	
González-Cao, J.	199	Neuhäuser, M.	285
Gotoh, H.	23	Ni, N.	63
Guo, X. H.		P	
H		Pan, K.	169
Han, L. H.	30	Parkinson, E.	285
Han, Y.	217	Pramanik, R.	169
Hou, D. Q.	108, 136, 163	Ptashnyk, M.	267
Hu, W. Q.	224	Q	
Hu, X. Y.	30	Qiang, H. F.	242, 251
Hu, Y. K.	247	Qiu, L. C.	217
Huang, C. Y.	136, 163	Quinlan, N. J.	115, 177

R			
Rao, C. P.	37	Wang, L.	129
Raymond, S.	169	Wei, G. F.	184
Rentschler, M.	285	Wen, L. J.	236
Rogers, B. D.	142	Wen, X.	57
Rong, Y. F.	247	Williams, J.	169
		Wu, J. S.	157
S		X	
Shang, S. P.	228	Xi, G.	63
Shao, J. R.	206	Xing, Y. X.	108, 136, 163
Shen, J. Y.	108	Xu, F.	213, 247
Shen, Y. M.	121	Y	
Shi, C.	251	Yang, Y.	213
Shi, H. B.	71	Yang, Y. S.	217
Shi, W. K.	121	Yu, X. P.	71
Shimizu, Y.	23	Z	
Sibilla, S.	9	Zhan, J. M.	224
Stansby, P. K.	142	Zhang, A. M.	15, 78
Sun, P. N.	15	Zhang, F.	228
Sun, X. Y.	242, 251	Zhang, G. X.	251
Sun, Y. J.	63	Zhang, H.	157
Sun, Z. G.	63	Zhang, W. T.	281
T		Zhang, Y. L.	43
Tian, L.	217	Zhang, Z. L.	257
Tiao, C.	92	Zhao, J.	86
Tijsseling, A. S.	108, 136	Zhao, Y. Z.	192
W		Zheng, H. L.	242, 251
Wan, D. C.	37, 43, 57, 149	Zhou, L.	92
Wang, J. Y.	213	Zong, Z.	92